CO2M: Copernicus Anthropogenic Carbon Dioxide Monitoring	Study on Spectral Sizing for CO_2 Observations: **Tech-Notes**	Version 1.1 Doc ID: SRON-CSS-TN-2020-003 Date: 30-Nov-2020

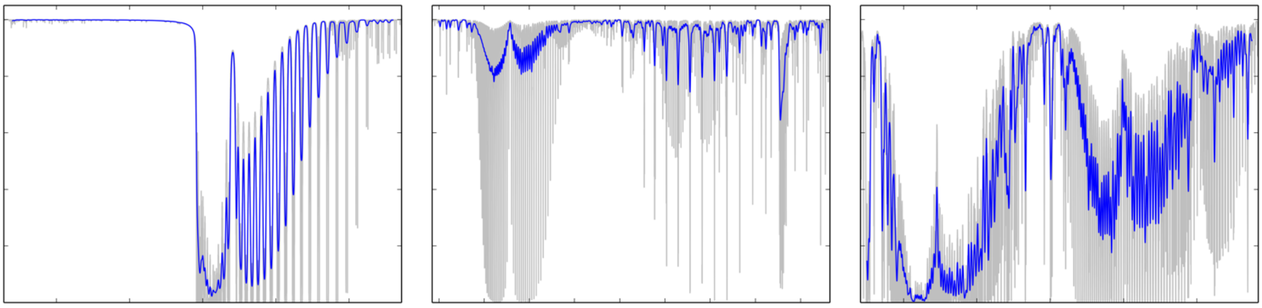

Study on Spectral Sizing for CO_2 Observations: Tech-Notes

Jochen Landgraf, Joost aan de Brugh, Lianghai Wu, Otto Hasekamp, Stephanie Rusli, Hein van Heck
SRON Netherlands Institute for Space Research, Utrecht, The Netherlands

André Butz, Kaspar Graph
Institute of Atmospheric Physics (IPA), Deutsches Zentrum für Luft- und Raumfahrt e.V. (DLR), Oberpfaffenhofen, Germany

Hartmut Boesch
Earth Observation Science Group, University of Leicester, United Kingdom

Leif Vogel
Kaioa Analytics, Bizkaia, Spain

Michael Buchwitz
Institute of Environmental Physics (IUP) / Institute of Remote Sensing (IFE), University of Bremen (UB), Bremen, Germany

Cheng Chen, David Fuertes, Yana Karol and Oleg Dubovik
GRASP SAS, Bachy, France

Table of Contents

Note

This document is a bundle of all Tech-Note deliverables of the “Study on Spectral Sizing for CO_2 observations”. Here, each Tech-Note has its independent figure and table numbering and, in most cases, an additional reference ID.

Specification of Instrument Spectral Sizing Concepts, Spectral Errors and Geo-Physical Scenarios

Jochen Landgraf and Joost aan de Brugh
SRON Netherlands Institute for Space Research

Andre Butz and Kaspar Graf
DLR German Aerospace Center

Abstract:

This document summarizes the instrument spectral sizing concepts and the modelling of instrument error sources to be used in WP2000. Additionally, we discuss and define the ensembles of measurement test data for the evaluation the sizing concepts.

Table of Contents

1 Instrument Concepts and Error Sources

1.1 Spectral sizing point

The spectral sizing points to be investigated in WP 2000 are summarized in Tab 1.

Instrument sizing point		A	B	B'	B''	C	D	ER
Spectral bands [nm]	NIR	756-773	747-773	747-773	747-773	758-772	758.35-768.65	747 – 773
	SW-1	1559-1675	1590-1675	1590-1675	1590-1675	1591-1621	1596.85-1618.55	1559 – 1675
	SW-2	2043-2095	1925-2095	1993-2095	2044-2095	2042-2081	2023.25-2050.75	1993 – 2095
Resolution [nm]/ sampling ratio	NIR	0.045/2.5	0.1/3.14	0.1/3.14	0.1/3.14	0.042/2.5	0.032/2.905	0.12 / 3
	SW-1	0.30/2.5	0.3/3.14	0.3/3.14	0.3/3.14	0.076/2.5	0.067/2.914	0.26 / 3
	SW-2	0.13/2.5	0.55/3.29	0.3/3.00	0.15/3.00	0.097/2.5	0.085/2.924	0.32 / 3
SNR coefficients a and b (Eq. 1)	NIR	2.81E-15/160540	4.47E-15/160540.	4.47E-15/160540.	4.47E-15/160540.	8.36E-016 / 2944.	8.423E-16 / 657350	4.75E-15/235000
	SW-1	2.88E-14/ 333979	2.29E-14/ 333297	2.29E-14/ 333297	2.29E-14/ 333297	4.15E-015 / 20277.	3.571E-15 / 654978	1.14E-14/ 235000
	SW-2	1.22E-14/ 324402	3.91E-14/ 323636	2.34E-14/ 307985	1.17E-14/307985	6.39E-015 / 56295.	5.670E-15 / 648609	1.47E-14/ 235000
Remark/reference		Adapted from AD-1	Adapted from AD-2	(B. Sierk, email 10.07.2017)	(B. Sierk, email 10.07.2017)	Adapted from RD-2, RD-3, RD-4, RD-5	Adapted MicroCab performance, pers. (B. Sierk, email 20.02.2017)	Based on equal resolving power concept (B. Sierk, email 19.04.218)

Table 1: Spectral sizing points. Concept A and B is simulated for the same detector readout noise of 150 electrons. The concepts B' and B'' represents two deviations of concept B with respect to spectral coverage and resolution of the SW-2 band.

The table includes coefficients of the signal to noise (SNR) ratio model

$$\mathrm{SNR} = \frac{aL}{\sqrt{aL + b}} \quad (1)$$

where L is the spectral radiance and a and b parametrizes the signal dependent and independent SNR performance of a spectral sizing concept [Sierk and Caron, 2012, RD-1]. Here, L is given in photons / (m^2 s sr μm), a has the inverse units (m^2 s sr μm) / photons, and b is unitless.

Instrument sizing point A

This instrument sizing point is based on the CarbonSat MRD 1.0 (AD-1) instrument concept but the SNR parametrization is derived from ESA's SNR model (email Bernd Sierk, 18 November, 2016).

Instrument sizing point B
This sizing point reflects the CarbonSat MRD 1.2 concept (AD-2) using the same SNR model as for instrument concept A but adapting the spectral resolution, band width and sampling in Tab. 1. Thus, both instrument sizing points A and B rely on the same instrument etendue (i.e. same pupil size and angular field of view, email Bernd Sierk, 18 November, 2016). Concept B' and B'' are to deviation altering the spectral sizing of the SW-2 band considering an enhanced spectral resolution on cost of a reduced spectral band width.

Instrument sizing point C
This instrument sizing point is adapted from the OCO-2 instrument specification as provided by RD-2 and RD-3. The SNR of the OCO-2 radiance measurements are given per spatial and spectral pixels of the individual bands by

$$\mathrm{SNR} = \frac{10\,L}{\sqrt{L_{\max}(c_1^2 \frac{L_{\max}}{100} + c_0^2 L)}} \tag{2}$$

where the coefficients c_0 and c_1 are determined during instrument calibration and $L_{\max}$ is the maximum measurable radiance signal per band. They are provided as part of the OCO-2 level-1 data product (see RD-4 and RD-5). To describe the mean instrument performance for the purpose of this study, we considered only detector pixels flagged as 'good' and averaged those coefficients c_0 and c_1 over the spatial and spectral dimension of the NIR, SWIR-1 and SWIR-2 spectral band of OCO-2. Subsequently we determined coefficient a and b in Eq. (1) by

$$a = \frac{100}{L_{\max}\, c_0^2} \text{ and } b = \frac{c_1^2}{c_0^4} \tag{3}$$

For each band, Tab. 1 reports the corresponding values.

Instrument sizing point D
This instrument point reflects the MicroCarb instrument performance. The values of coefficient a and b were fitted using the recently updated data sheet from CNES (email Bernd Sierk, 18 November, 2016). Since the fit uses only 3 data points, the reliability of the fit results is not high.

Instrument sizing point ER
This spectral sizing point adapts the noise performance of concept B but assumes an the same resolving power for all the band. Thus, the width of the SWIR-2 is reduced omitting the SWIR-2a sub-band but with an enhanced spectral resolution in the SWIR-2b and SWIR-2c spectral ranges.

1.2 Distortion of the Instrument Spectral Response Function

To describe the spectral response function (ISRF) of a future CO_2 spectrometer, we propose to use a ISRF of the form

$$S(x) = H \circ g(x) \tag{4}$$

with a scaling of the function domain by the instrument spectral resolution h,

$$g(x) = \frac{x}{h} \tag{5}$$

and the shape function

$$H(z) = A\ \exp\left[-2^{k_0} \ln 2\, |(1 + a_1 + \mathrm{sgn}(z)\ a_2)z|^{k_0 + k_1 + \mathrm{sgn}(z) k_2}\right] \tag{6}$$

(RD-6: Nadarajah, 2005; RD-7: Beirle et al., 2016). Here,

$$\mathrm{sgn}(z) = \begin{cases} 1 & \text{for } z \geq 0 \\ -1 & \text{for } z < 0 \end{cases} \tag{7}$$

is the sign function. The parameters are chosen such that the set $(k_0, k_1 = 0, k_2 = 0, a_1 = 0, a_2 = 0)$ represents the unperturbed reference ISRF and parameters k_1, k_2, a_1 and a_2 describe the shape distortion. In detail, parameter $a_1 > 0$ describes a symmetric spectral stretch of the ISRF, $k_1 > 0$ an extra flatness and a_2, k_2 indicate an asymmetric distortion. Moreover, A is the normalization constant. For the unperturbed reference case, Eq. (6) reduces to the generalized normal distribution function (RD-6: Nadarajah, 2005) and the corresponding ISRF has the full-width-half-maximum h.
To investigate the effect of ISRF distortion for the retrieval of CO_2, we simulate the measurement spectra by convolving line-by-line model spectra with a reference ISRF. To be consistent with previous studies, we choose a Gaussian ISRF, so $k_0 = 2$. The corresponding shape function H is shown in Fig. 1. For the retrieval, we assume a set of distorted ISRF, where for the first four cases we perturb only one of the parameters k_1 k_2, a_1 and a_2 such that the ISRF distortion is compliant with the corresponding requirement of the CarbonSat Mission Requirement Document (MRD) [AD-2]. Additionally, we consider two case where we perturb the parameter sets (a_1, k_1) and (a_2, k_2).

MR- OBS-140	The shape of the ISRF shall be known before launch for the spectral range where the ISRF is at least 1% of the peak value for all wavelengths and viewing angles. In this spectral range of the ISRF, the required accuracy is 1% (1-sigma) of its peak value and with a minimum absolute accuracy of 20% (i.e., in the wings of the ISRF with values between 1% and 5% of the ISRF peak value, the shape shall be known with 20% accuracy).

Table 2 summarizes the six parameter sets of distorted ISRFs and Fig. 2 depicts the corresponding distortion relative to the reference shape function. Here, the difference is expressed relative to the maximum of the reference ISRF after normalization.

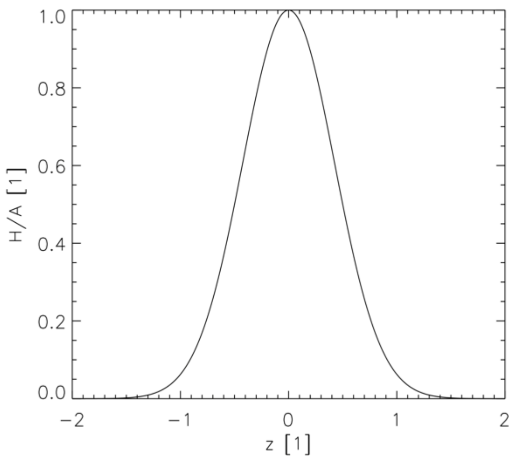

Figure 1: Gaussian shape function ($k_0 = 2$, $k_1 = k_2 = a_1 = a_2 = 0$)

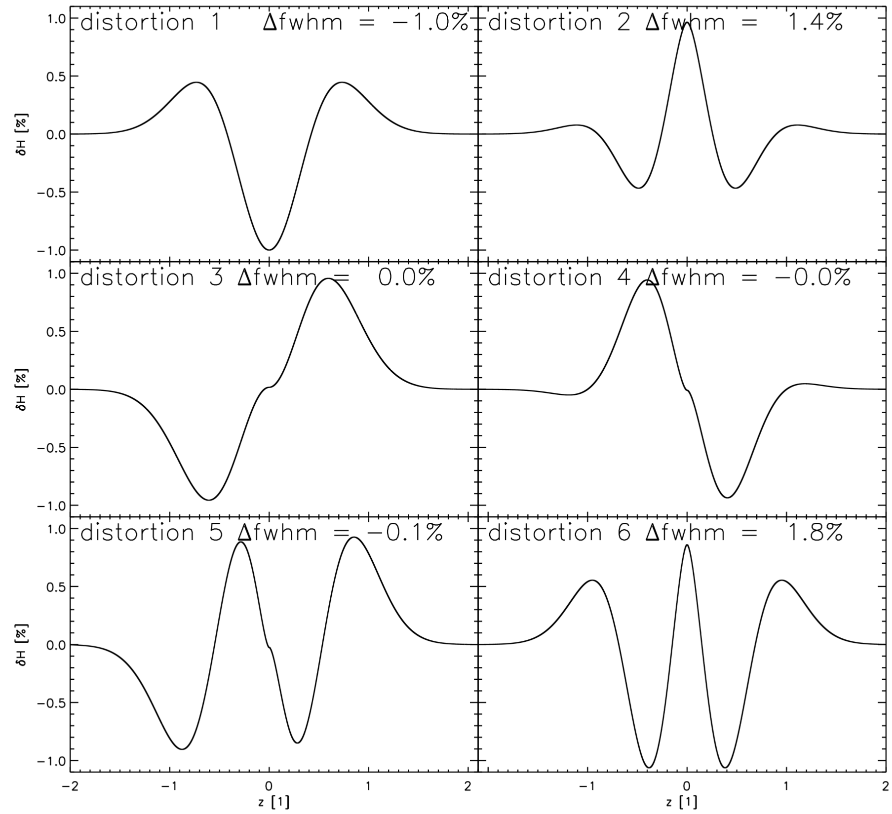

Figure 2: ISRF distortion as defined in Tab. 2. The distortion is defined relative to the maximum of the reference ISRF after normalization.

	a_1	k_1	a_2	k_2
Distortion 1	0.01	0.0	0.0	0.0
Distortion 2	0.0	0.04	0.0	0.0
Distortion 3	0.0	0.0	0.013	0.0
Distortion 4	0.0	0.0	0.0	0.036
Distortion 5	0.0	0.0	0.023	0.075
Distortion 6	0.014	0.095	0.0	0.0

Table 2: ISRF parameters for the distorted ISRFs

1.3 Stray light simulations

Usually, we mean by 'spectrometer stray light' light in the instrument, which was not intended by its design. This definition intends to contrast the real propagation of light in an instrument from its ideal performance and for the purpose of measurement simulation it has to be translated to a strict mathematical definition. Therefore, we start from a general description of the measurement process by

$$I_{ij}^{\text{meas}} = \iint dx d\lambda \; K_{ij}(x,\lambda) I_{lbl}(x,\lambda) \tag{8}$$

where I_{ij}^{meas} represents the simulated measurement by a two-dimensional detector at pixel (i,j) and $I_{lbl}(x,\lambda)$ is the geophysical spectral radiance field at a swath position x and at wavelength λ. The instrument kernel $K_{ij}(x,\lambda)$ describes the optical transmission of light through the instrument. Simulating a well-calibrated instrument, the instrument kernel must be normalized,

$$\iint dx d\lambda \; K_{ij}(x,\lambda) = 1 \tag{9}$$

Analogous, we describe the performance of an ideal instrument without any stray light by

$$I_{ij}^{\text{ideal}} = \iint dx d\lambda \; K_{ij}^{\text{ideal}}(x,\lambda) I_{lbl}(x,\lambda) \tag{10}$$

with the normalized instrument kernel K_{ij}^{ideal}. It is common to factorize K_{ij}^{ideal} by

$$K_{ij}^{\text{ideal}}(x,\lambda) = \varphi_j(x) s_i(\lambda) \tag{11}$$

with the point spread function φ_j and the ISRF s_i. Both φ and s are normalized to one. To simulate spectral measurements, we assume a Gaussian ISRF as described in Sec. 2 and a geometrical projection of the instrument entrance slit on the ground for φ, namely

$$\varphi_j(x) = \begin{cases} \frac{1}{\Delta x} & \text{for } x_j - \Delta x < x < x_j + \Delta x \\ 0 & \text{else} \end{cases} \tag{12}$$

where we assign detector index i to the spectral dimension and index j to the spatial dimension across flight direction. Here x_j is the centre of the ground pixel and Δx is the spatial sampling distance. Note that in case of spatial co-adding, we refer here to the original sampling distance before co-adding. For all spectral sizing concepts, we assume a spatial sampling distance $\Delta x = \frac{1}{3}\text{km}$ with a co-adding factor of 6, resulting in an across track sampling of 2 km.

Finally, we consider stray light I_{ij}^{stray} as an additive contribution to the actually measured signal

$$I_{ij}^{\mathrm{meas}} = I_{ij}^{\mathrm{ideal}} + I_{ij}^{\mathrm{stray}} \tag{13}$$

with

$$I_{ij}^{\mathrm{stray}} = \iint dx d\lambda\ K_{ij}^{\mathrm{stray}}(x,\lambda) I_{lbl}(x,\lambda) \tag{14}$$

and stray light kernel K_{ij}^{stray}, respectively. Obviously, the stray light contribution in Eq. (13) violates the assumption of a well calibrated instrument and so Eq. (13) needs to be renormalized. For this purpose, we consider the norm of the stray light kernel

$$\kappa = \iint dx d\lambda\ K_{ij}^{stray}(x,\lambda), \tag{15}$$

which is also known as the total internal scattering (TIS) of the spectrometer. So, the renormalization yields

$$I_{ij} = \frac{1}{1+\kappa}\left\{I_{ij}^{\mathrm{ideal}} + I_{ij}^{\mathrm{stray}}\right\} \tag{16}$$

To achieve a meaningful comparison of the different sizing concepts, we assume κ to be independent on the specific spectral sizing, namely

$$\begin{aligned} \kappa_{NIR} &= 0.009 \\ \kappa_{SW1} &= 0.007 \\ \kappa_{SW2} &= 0.005 \end{aligned} \tag{17}$$

For the purpose of this study, we adapt the stray light model of [RD-8] of the CarbonSat instrument concept AD-2, which comprises in-field and in-band stray light. It is composed of

- Diffuse stray light, due to roughness and contamination of the optical surfaces
- Ghost, due to reflections on optical surfaces
- Diffraction and aberrations

and the Bidirectional Straylight Distribution Function (BSDF) is given as a function of detector indices i and j

$$BSDF(i,i_0,j,j_0) = \frac{A}{B + [(i-i_0)^2 + (j-j_0)^2]^{\frac{g}{2}}} \tag{18}$$

We modify this discrete function to the continuous stray light kernel in Eq. (14) by

$$K_{ij}^{\mathrm{stray}}(x,\lambda) = a\frac{A}{B + \left[(\frac{\lambda-\lambda_i}{\Delta\lambda})^2 + (\frac{x-x_j}{\Delta x})^2\right]^{\frac{g}{2}}} \tag{19}$$

where λ_i is the wavelength assigned to pixel (i,j), $\Delta\lambda$ is the spectral sampling interval (see appendix for further explanations). For each sampling concept, constant a is adjusted to satisfy Eq. (15).

Furthermore, we determine the stray light kernel over a domain of 150 spectral and spatial samplings and discard the inner part of the kernel defined by a rectangle of ±4 full-wdith half-maxima (±12 $\Delta\lambda$ in the spectral dimension) and ±2 km (±6Δx in the across track dimension). This domain is covered by the ISRF and the requirement of homogenous clear sky scenes of adjacent pixels. The parameters A, B and g are taken from RD-8 and are summarized in Tab. 3. Figure 3 shows an example of the stray light kernel.

	Stray light kernel parameters		
	NIR	**SWIR-1**	**SWIR-2**
log$_{10}$(A)	-3.1	-3.5	-3.6
log$_{10}$(B)	2.7	2.6	3.0
g	2.2	2.0	2.0

Table 3: Stray light kernel parameters adapted from RD-8

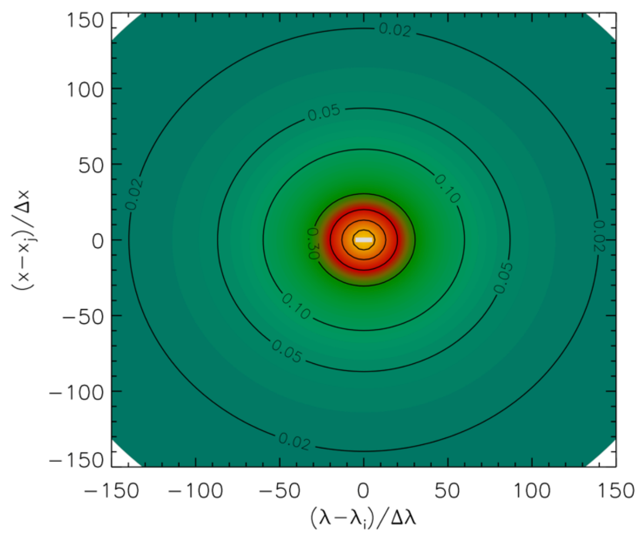

Figure 3: Stray light kernel K_{ij} for the SWIR-1 band. The domain of the ISRF is discarded at the centre of the stray light kernel.

Using our approach to model stray light, radiance line-by-line spectra are required, which include spectra outside the spectral band definition and beyond the swath of the spectrometer. Hence, the top-of-atmosphere radiance spectra of the orbit ensemble in Sec. 2.4 exceeds the spectral band definition by at least ± 100 spectral samplings and its spatial coverage includes simulation 200 km to the east and west of the spectrometer swath.

1.4 Instrument Polarization Sensitivity

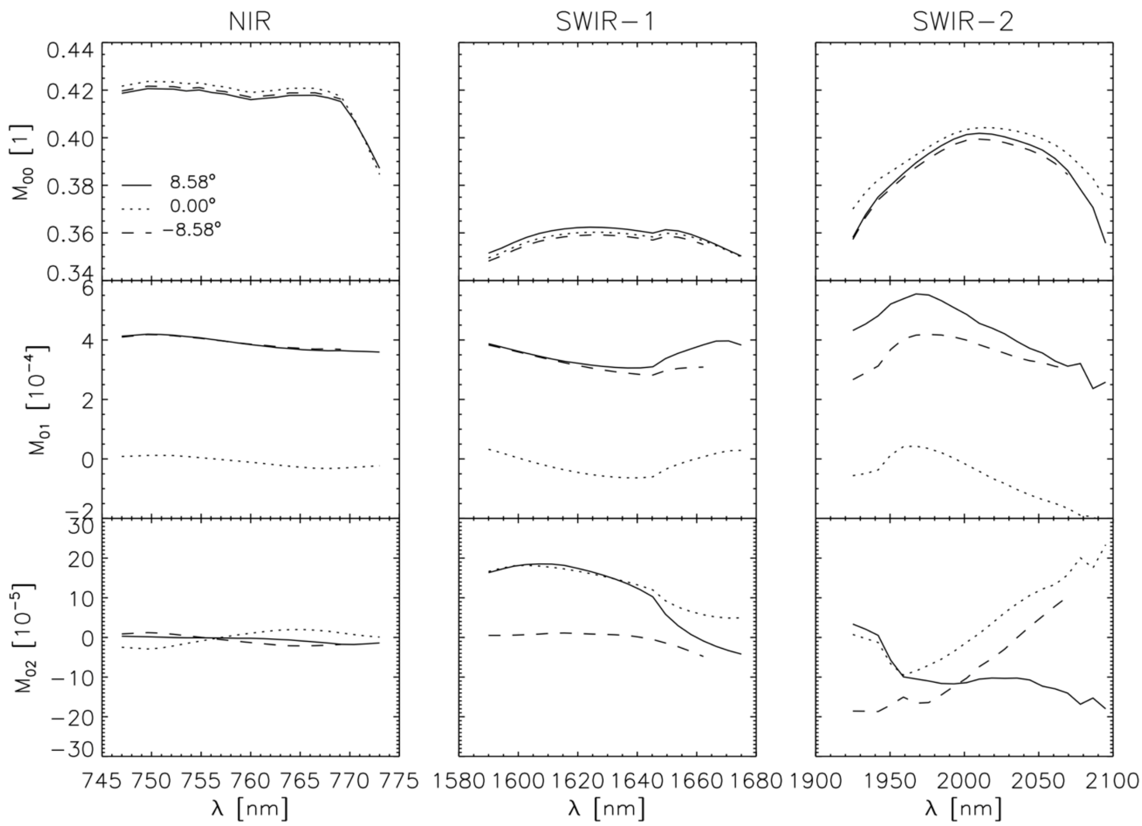

Figure 4: Instrument Müller matrix elements M_{00}, M_{01} and M_{02} for the NIR, SWIR-1 and SWIR-2 spectral bands for the left- and right-edge and sub-satellite point of the swath.

To infer CO_2 column densities from the simulated measurements, we assume as baseline a polarization insensitive instrument. A remaining polarization sensitivity of the instrument can be described as a radiometric perturbation

$$\delta I = \frac{M_{01}}{M_{00}} Q + \frac{M_{02}}{M_{00}} U \tag{10}$$

where Stokes parameter *Q* and *U* are simulated by a vector radiative transfer model for measurement ensemble G2 (see Sec 2.2). The Müller matrix elements M_{00}, M_{01} and M_{02} are adapted from instrument simulations of the CarbonSat instrument concept (email Bernd Sierk, 21-11-2016). Figure 4 shows the relevant elements with a significant dependence of the polarization sensitivity on the viewing geometry. For a proper application of Eq. 10, it is important to realize that the Stokes parameters U and Q and the Müller matrix are defined with respect to the same reference frame. The radiative transfer model LINTRAN defines U and Q with respect to the local meridian plane, which is defined by the local zenith and the propagation direction of the observed light. The Müller matrix in Figure 4 is defined with respect to the instrument plane given by the instrument entrance slit. For a nadir viewing instrument with the sub-satellite point in the slit projection, these reference frames are identical.

1.5 Radiometric offset

An uncorrected additive offset of the level-1 Earth radiance measurements has a serve impact on the CO_2 data product. To study its effect for the different instrument spectral sizing, we will study the induced CO_2 error due to a offset according to the CarbonSat requirement MRD 1.2. The radiometric offset will be superposed on the measurement simulation in absolute units [photons/(cm2 nm s sr)].

MR-OBS-200	The offset (zero-level baseline) correction accuracy under dark conditions (in photons/s/nm/cm²/sr) of the radiance shall be known to • 4.2×10^9 in NIR, • 4.3×10^9 in SWIR-1, • 5.3×10^8 in SWIR-2. NB radiance values correspond to percentages of the maximum radiance level in each band taken from the DR-min-75 scenario (see Tables 4.5); i.e., 0.15%, 0.5%, 0.14%, respectively.

1.6 Detector non-linearity

An important radiometric error on the SWIR-1 and SWIR-2 spectral measurements may be due to detector non-linearity, which addresses the radiometric response of the detector device with respect to an input signal. Generally, the linear response will be captured by the radiometric calibration of the instrument, however any deviation of a linear response may cause significant radiometric errors. For this study, we will consider the non-linear detector response as depicted in Figure 5 and 6 for instrument concept A and B of Tab. 1. The figures do not consider any correction for non-linearity as part of the L0-1 processing, however, in practice it is very likely that this processing step will include such a radiometric correction based on on-ground calibrations. The efficiency of such a correction is hard to predict for the project team and probably depends on the detector filling also shown in Figure 5 and 6. In case such a correction should be considered, input is needed from ESA on the efficiency of such a correction scheme as function of the input signal.

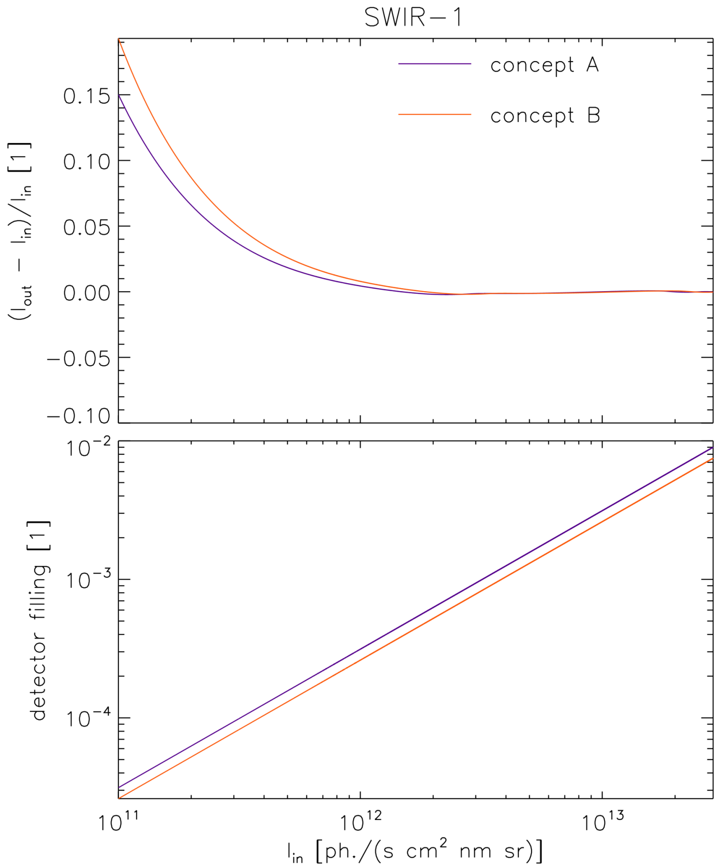

Figure 5: Relative radiometric error on the SWIR-1 output signal I_{out} as a function of the input signal I_{in} for instrument concept A (blue) and B (red) in Tab. 1 (upper panel) and the detector filling as a function of I_{in} (lower panel). Data are available at the project ftp (./WP1000/NL_Data_ESA).

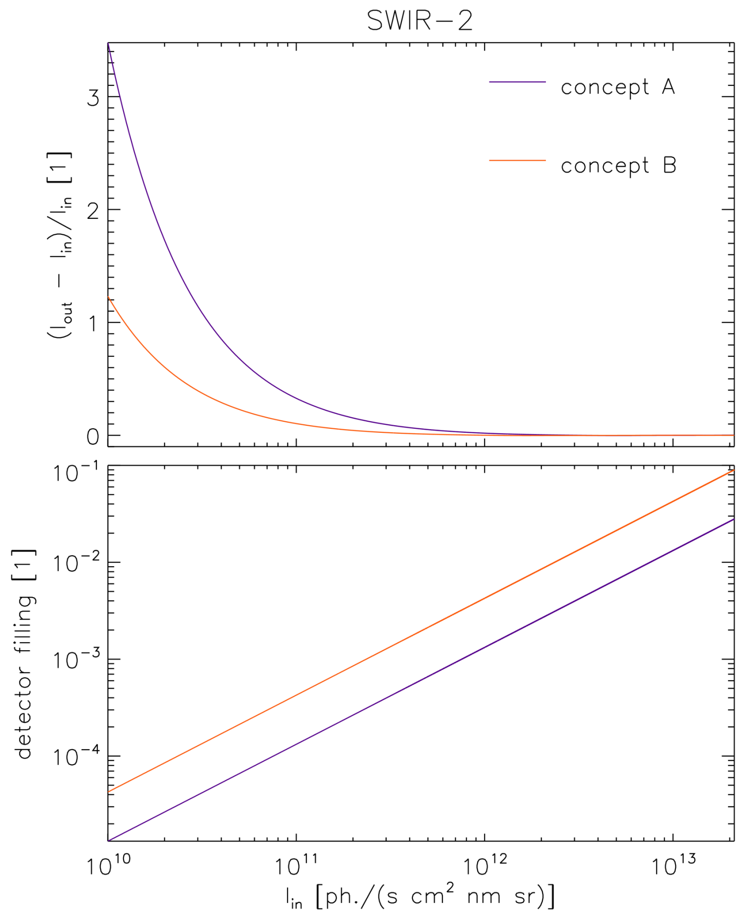

Figure 6: Same as Figure 5 but for the SWIR-2 spectral band.

2 Ensembles of model atmospheres

The Section summarizes ensembles of model atmospheres, which will be used to derive line-by-line top-of-atmosphere spectra to simulate test data sets of measurements. The spectra are simulated for the spectral ranges indicated in Tab 4.

interval	λ_i [nm]	λ_f [nm]
NIR	696.34	823.78
SWIR-1	1536.86	1729.14
SWIR-2	1869.72	2149.79

Table 4: Spectral intervals $[\lambda_i, \lambda_f]$ of the line-by-line spectra with a spectral sampling of 0.01 cm^{-1}.

2.1 Global Ensemble G1

To perform detailed sensitivity studies for the different instrument spectral sizing point, we simulate line-by-line top-of-atmosphere radiance spectra for a global ensemble of simulated spectra consisting of land-only, clear sky scenes (RD-9: Butz et al. 2012 and RD-10: Hu et al., 2016). The instrument specific aspects of the measurement, like spectral resolution and sampling and instrument noise contributions can be simulated as a posterior simulation step using these spectra. The ensemble G1 aims to simulated realistic aerosol and cirrus loaded scenes for four days, one per season, where the model approach consciously differs from the forward model of the retrieval. The test ensemble is the jumping-off point of WP2200 to investigate forward model errors for the instrument sizing point specified in Sec. 1.1.

For the simulations, trace gas profiles are adapted from different model run. Here, the profiles of CH_4 is taken from the global chemical transport model TM5 (RD-11: Houweling et al., 2014), CO_2 profiles are derived from CarbonTracker [RD-12: Peters et al., 2007], temperature, humidity and pressure profiles from ECMWF forecast data and given on a 96-model layer grid. The global distribution of the CO_2 and CH_4 total column is shown in Fig. 7 and 8. The aerosol physical properties and vertical distributions are taken from the global aerosol model ECHAM5-HAM (RD-13: Stier et al., 2005) on a ~3°×~3° latitude times longitude grid in 19 vertical layers up to the mid-stratosphere for five different chemical compositions and on a superposition of seven log-normal size distributions. The aerosol optical thickness is derived from MODIS observations (RD-14: Remer et al., 2005). Furthermore, cirrus optical properties are calculated by the raytracing model (RD-15: Hess and Wiegner,1994 and RD-16:Hess, 1998), assuming randomly oriented hexagonal ice crystals of plate and columnar shape. The cirrus size distribution follows a power-law distribution for particle sizes between 0.003 and 1.3 mm (RD-17: Heymsfield & Platt, 1984). The cirrus optical thickness and vertical extent are based on measurements by the CALIOP instrument onboard the CALIPSO satellite in the year 2007 (RD-18: Winker et al., 2007). Finally, the MODIS land albedo product at 858 nm, 1640 nm, and 2130 nm is used to approximate the NIR, SWIR-1 and SWIR-2 surface albedo, respectively. The global albedo maps for the different bands are shown in Figs. 9-11 and the sum of total aerosol and cirrus optical depth is depicted in Fig. 12. As baseline the line-by-line spectra are simulated for the nadir viewing direction and a solar zenith angle with an overpass time of 13:30 local time. In total the ensemble comprises 8633 line-by-line model.

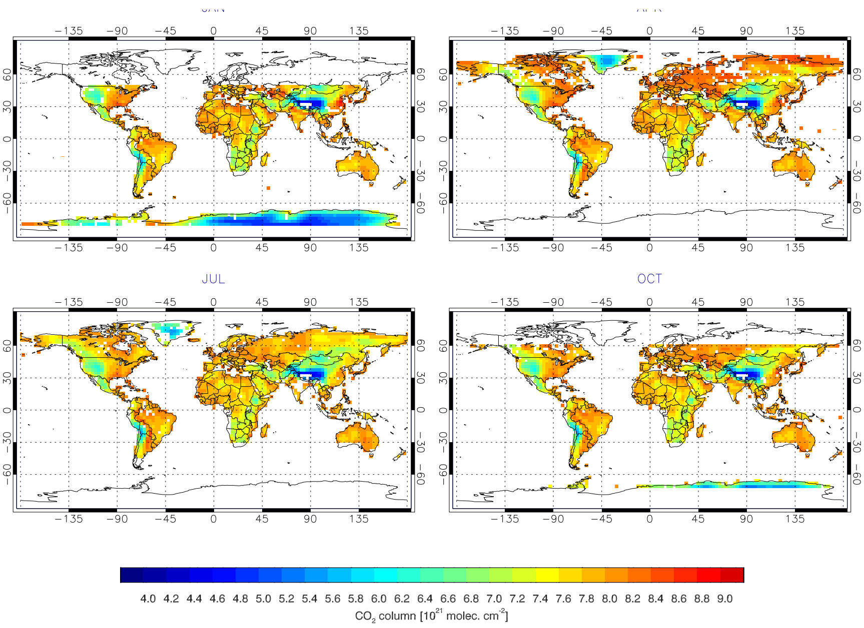

Figure 7: Global distribution of the total CO_2 column of ensemble G1 and G2

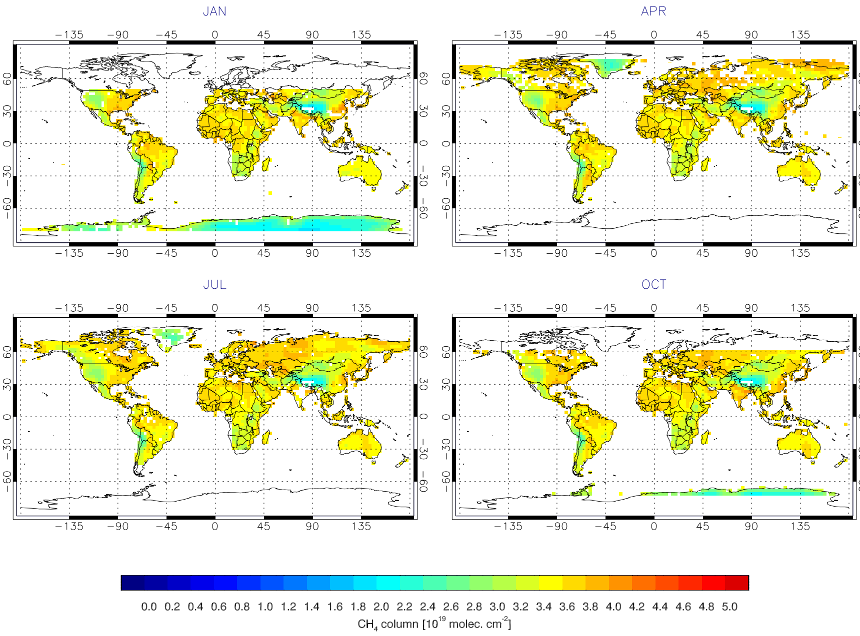

Figure 8: Same as Fig. 7 but for CH_4.

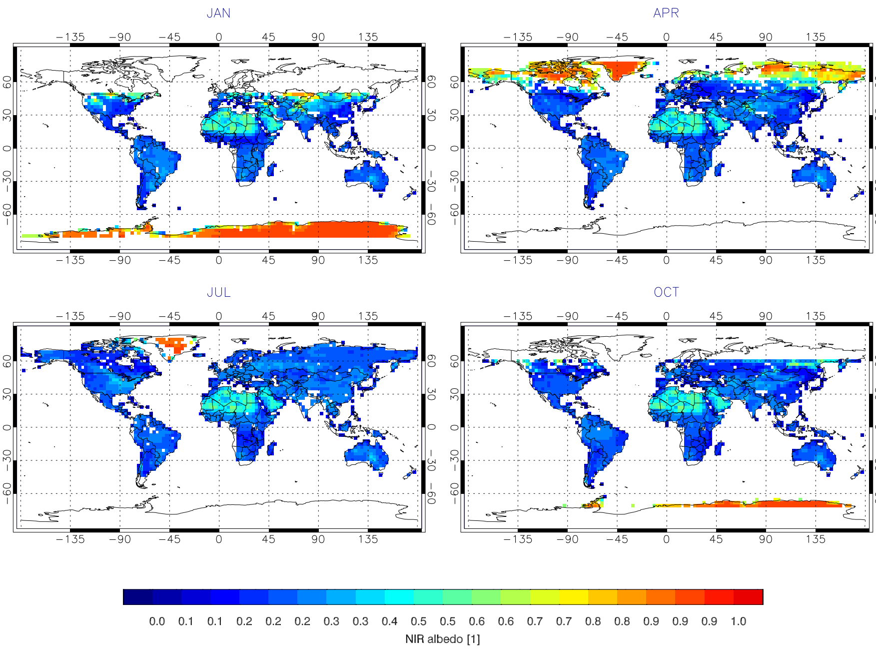

Figure 9: Global distribution of the NIR Lambertian surface albedo of ensemble G1 and G2

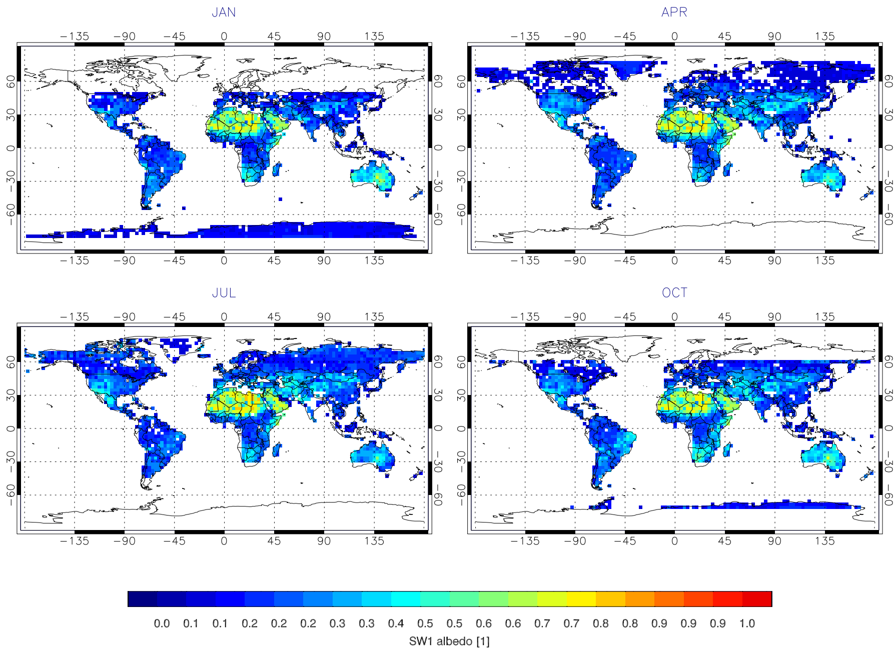

Figure 10: Same as Fig. 9 but for the SWIR-1 band

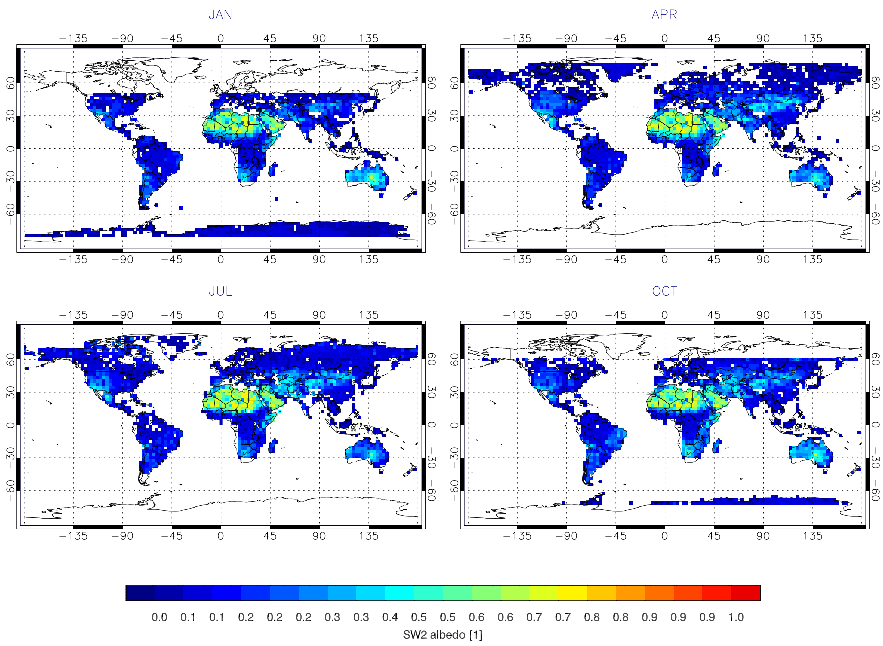

Figure 11: Same as Fig 9 but for the SWIR-2 band

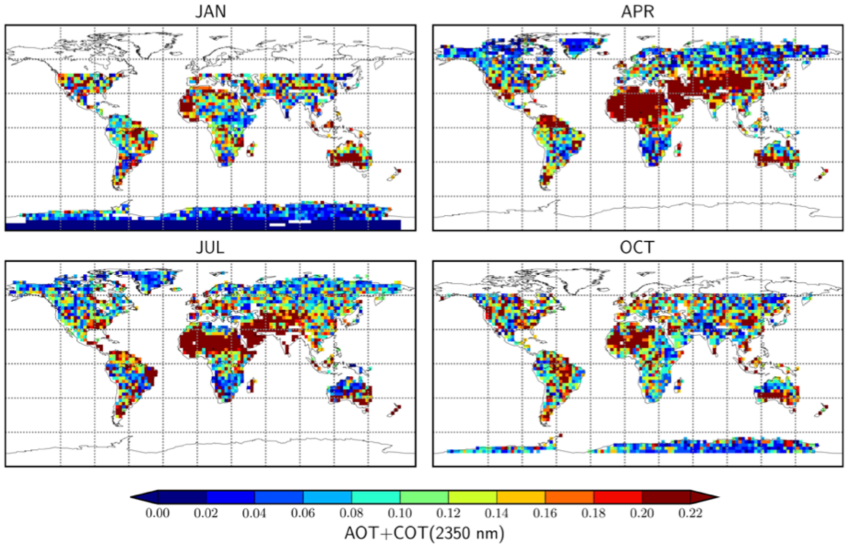

Figure 12: Global distribution of the total aerosol and cirrus optical depth of ensemble G1

2.2 Global Ensemble G2

This ensemble is developed as test environment for WP2100 to study the effect of instrument malfunction and instrument calibration errors on the CO_2 product for different spectral sizing points. Therefore, we aim to exclude forward model errors from this analysis, which are studied separately in WP2200. Thus, as a starting point WP2100 requires measurement and retrieval simulations, which are fully consistent. First, this means that the radiative transfer solver used for the line-by-line simulations and the forward model used in the retrieval must be numerically consistent; second also the model atmosphere must be described consistently in both cases. To achieve these objectives on the one hand and on the other hand to utilize the variability of global ensemble G1, we reduced the complexity of the global ensemble G1 as follows:

1. For the line-by-line simulations and for the retrieval measurement simulations, we use the same vertical grid of the model atmosphere and all profiles of ensemble G1 are reduced to a 72-layer model grid.
2. We simplify the aerosol height distribution by a Gaussian profile with fixed width of 2 km. The central height z_{aer} and the vertically integrated column number density N_{aer} are determined by a least square fitting of the Gaussian profile to the vertical aerosol distribution of ensemble G1. The global distribution of z_{aer} and the total aerosol optical depth is depicted in Fig. 13 and 14.
3. The aerosol size distribution is approximated by the power law

$$n(r) = \begin{cases} A & \text{for } r \le r_1 \\ A\left(\frac{r}{r_1}\right)^{-\alpha} & \text{for } r_1 \le r \le r_2 \\ 0 & \text{for } r > r_1 \end{cases} \tag{11}$$

   where size parameter α results from a least squares fit of Eq. 11 to the cumulated size distribution of ensemble G1. Its global map is given in Fig. 15.
4. We assume a wavelength independent complex refractive index of $1.4 - 0.01i$ in all three bands.
5. For all simulations, we ignore cirrus and the fluorescence by vegetation.

The line-by-line radiative transfer simulations are simulated using the scalar radiative transfer model in combination with the linear-k method by RD-20: Hasekamp and Butz, 2008 with fixed fulcrums.

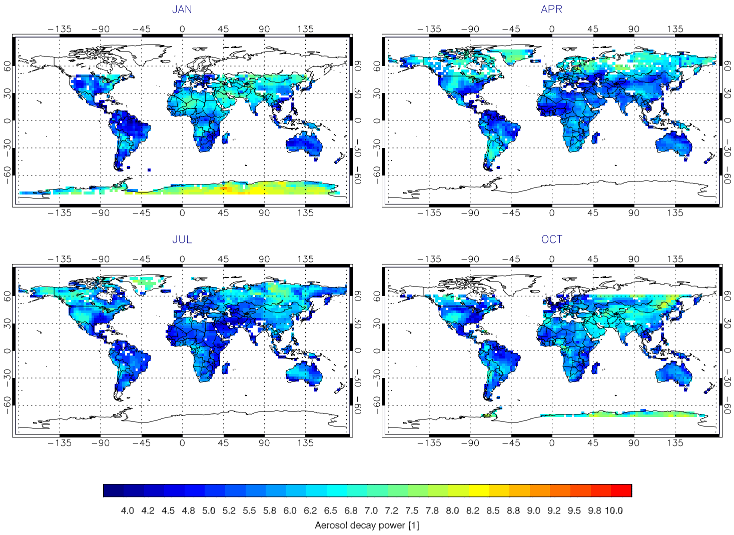

Figure 13: Aerosol size parameter α of ensemble G2

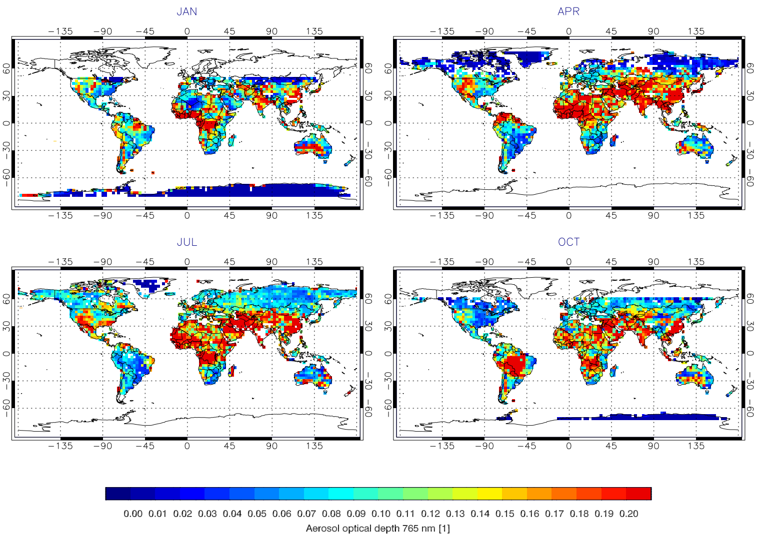

Figure 14: Aerosol optical thickness at 765 nm of ensemble G2

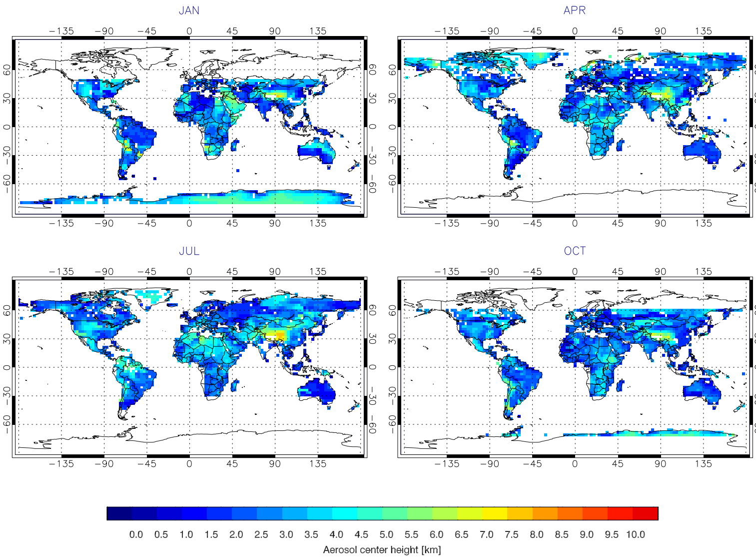

Figure 15: Aerosol central layer height z_{aer} of ensemble G2.

2.3 Global ensemble G3

To estimate the effect of the instrument polarization sensitivity on the retrieved CO_2 column for the different instrument spectral sizing concepts, a global ensemble of line-by-line spectra is required, which accounts for both the polarization of light by atmospheric scattering and by its reflection at the Earth surface. Therefore, we modify the global ensemble G2 using a global parametrization of the surface BDRF instead of the Lambertian surface model of ensemble G2. Here the BDRF is parametrized by five kernel terms, namely

$$\begin{aligned}\boldsymbol{\rho}(\Omega_{in},\Omega_{out}) = \; & c_0\,(\lambda)\boldsymbol{K}_0(\Omega_{in},\Omega_{out}) + c_0\,(\lambda)c_1\boldsymbol{K}_1(\Omega_{in},\Omega_{out}) + c_0\,(\lambda)c_2\boldsymbol{K}_2(\Omega_{in},\Omega_{out}) \\ & + c_3\boldsymbol{K}_3(\Omega_{in},\Omega_{out}) + c_4\boldsymbol{K}_4(\Omega_{in},\Omega_{out}) \end{aligned} \quad (12)$$

where ρ is the 4×4 surface BDRF that maps the four Stokes parameters I, Q, U and V of the incident light to the corresponding Stokes parameters of the reflected light as a function of the solid angles $\Omega_{in}, \Omega_{out}$. The BDRF kernels empirically describes the bidirectional reflection of the Earth surface, where kernel $\boldsymbol{K_i}$ with $i = 0{,}2$ simulates the radiance reflection with a wavelength dependent coefficient $c_0\,(\lambda)$ and two spectrally independent coefficients c_1 and c_2. Here, the kernel $\boldsymbol{K}_0$ models Lambertian isotropic reflection and so coefficient c_0 corresponds to the spectral Lambertian albedo of ensemble G2. Kernel $\boldsymbol{K_1}$ and $\boldsymbol{K_2}$ are adapted from the Ross-Li BDRF model describing anisotropic scalar reflection of land surfaces (RD-21: A. H. Strahler et al., 1999), where $\boldsymbol{K_1}$ simulates reflection of dense leaf canopy and $\boldsymbol{K_2}$ the radiance reflection of a sparse ensemble of surface objects casting shadows on the background, which is assumed Lambertian. The coefficients c_1 and c_2 are adapted from the MODIS global data set. Finally, the polarizing effect of surface reflection is expressed by the kernels $\boldsymbol{K_3}$ and $\boldsymbol{K_4}$ representing reflection properties of vegetation and soil surfaces. Here, the polarizing effect is nearly independent of wavelength as validated with RSP aircraft measurements (RD-22: Litvinov P. et al., 2012). As an estimate for the coefficients c_3 and c_4 we use the ratio of MODIS surface albedo $\alpha = \mathrm{A}_{858\mathrm{nm}}/\mathrm{A}_{2130\mathrm{nm}}$ assuming

$$c_3 = \begin{cases} 1 & \text{for } \alpha \geq 5 \\ (\alpha - 1.5)/3.5 & \text{for } 1.5 < \alpha < 5 \\ 0 & \text{for } \alpha \leq 1.5 \end{cases} \tag{13}$$

and $c_4 = 1 - c_3$. Eq. (13) is motivated by the spectral dependence of the Lambertian surface albedo of vegetation and soil, shown in Fig. 16.

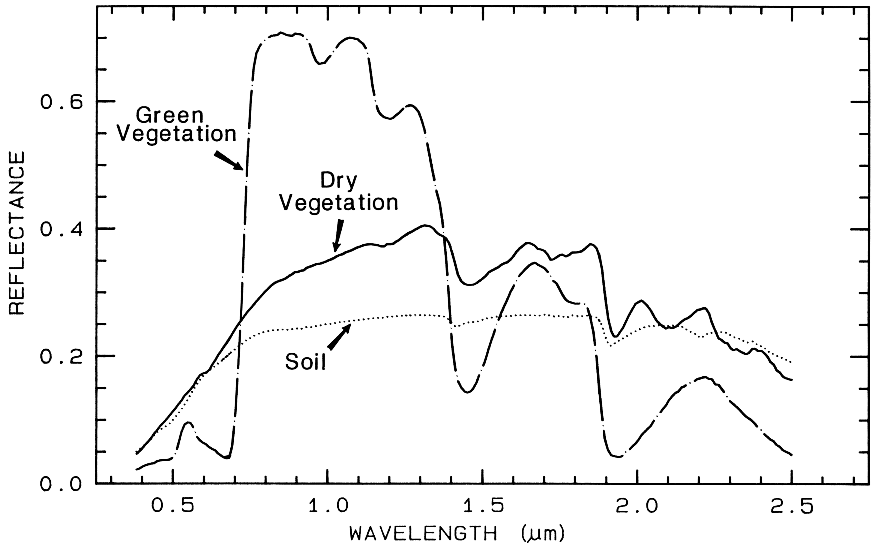

Figure 16: Spectral dependence of the Lambertian albedo for soil and vegetation surfaces (RD-23: Clark et al., 2003).

2.4 Orbit ensemble O1

The orbit ensemble O1 is generated to characterize the effect of stray light for realistic measurement condition and the different spectral sizing points, where the contrast in the Earthshine radiance in across track dimension is mainly due to the difference between clear sky and cloud sky scenes. The orbit ensemble comprises a granule of model atmospheres for a polar sun-synchronous orbit with orbit parameters summarized in Table 5 [RD-22: Brugh an de, J. 2016].

Orbit inclination [degree]	98.74
Ascending (northwards) solar equator crossing time [h]	11 pm
Date	June 19, 2012
Orbit hight [km]	836
Longitude at daytime equator pass [degree]	-1.9

Table 5: orbit parameters

The granule samples the ground scene by 1×1 km^2 over a 500 km across track extension and it includes ~526,000 spatial sampling point. For each ground pixel, the model atmosphere and solar and view geometry is given. The CO_2, CH_4, temperature and humidity profiles are taken from the model simulations of TM5, CarbonTracker and ECMWF forecast for 19 June 2012 and surface albedo for the individual spectral bands is adapted from the summer day of ensemble

G1/2. The high spatial sampling is needed to reflect the spatial variability of clouds, taken from MODIS Aqua observations. Here appropriate MODIS observations are spatially and temporally shifted such that the cities Berlin and Munich are cloud free but surrounded by clouds. The cloud fraction, cloud optical thickness and the cloud height are shown in Fig. 17. For the line-by-line model simulations, we assume a cloud with a γ-droplet size distribution, an effective radius $r_{eff} = 10\ \mu\mathrm{m}$ and an effective variance of $v_{eff} = 0.10$ and a refraction index of $n = 1.28 - 4.7\ 10^{-4} i$. Moreover, we use the MODIS cloud height to fix the top of a 1 km thick vertically homogenous cloud in the ensemble.

2.5 Orbit ensemble O2

Finally, to investigate the detection limit of CO_2 plumes for the different sizing concepts including instrument errors we define a clear-sky orbit ensemble following ensemble O1 but neglecting any cloud information for the measurement simulation. To simulate enhanced CO_2 plume concentrations due the emission of the power station, we apply the plume model of RD-22: Krings et al. 2011. We assumed the CarbonTracker CO_2 fields as background CO_2 concentration and superimpose the CO_2 plume for the coal plants listed in Tab. 6 covering a range of realistic capacities for Europe. For the simulation, we assumed a wind speed of 2 m/s and an atmospheric stability factor of 156. Figure 18 shows the CO_2 field sampled on a 1x1 km^2.

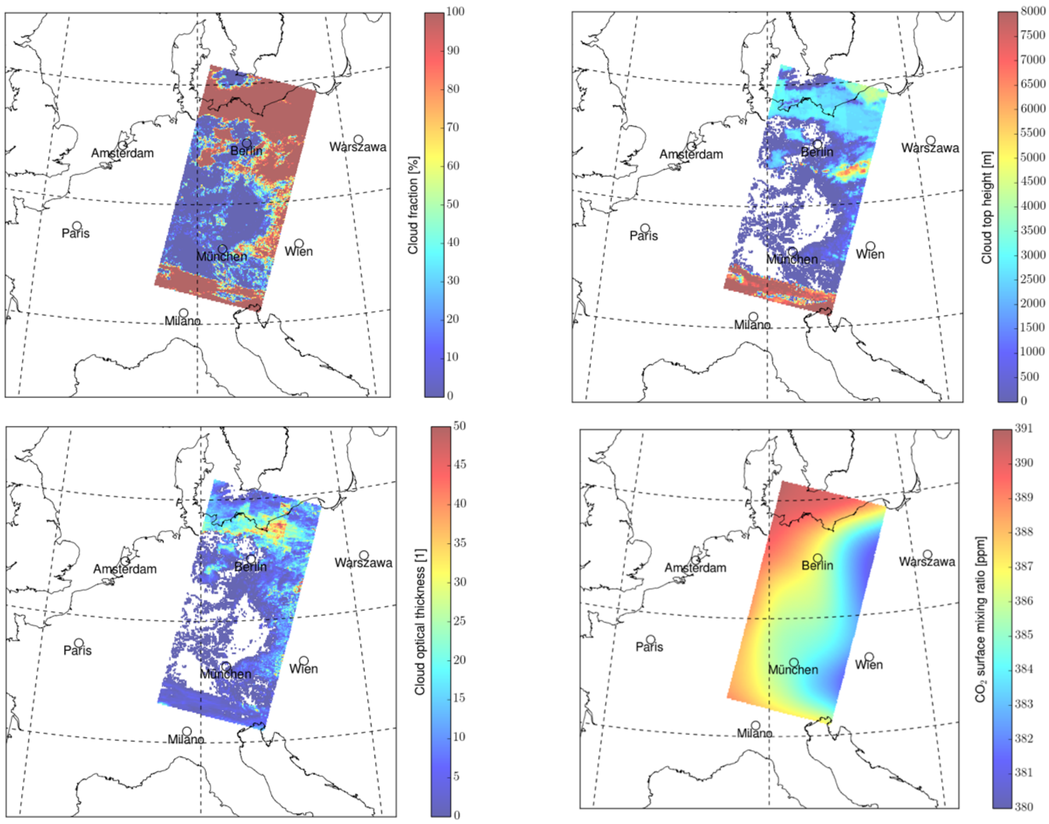

Figure 17: Cloud fraction (upper left), cloud optical thickness (upper right), cloud top height (lower left) and CO_2 mixing ratio at surface level (lower right) of orbit ensemble O1. White areas of the orbit granule indicate clear sky scenes.

#	name	Latitude [degree]	Longitude [degree]	CO_2 emission 2020 [Mt CO_2/yr]
1	München Nord	48.1805	11.6393	2.9
2	Zolling	48.4554	11.8017	3.2
3	Lippendorf	51.1822	12.3733	12.8
4	Schkpau-II	51.39845	11.9532	6.6
5	Boxberg	51.4161	14.564722	20.1
6	Schwarze Pumpe	51.529722	14.55952	10.9
7	Janschwalde	51.8347	14.4603	25.0
8	Reuter West	52.535	13.2427	4.4
9	Dolna	53.207	14.465	6.3
10	Turow	50.948	14.911	11.2

Table 6: Coal plants for plume simulation of orbit ensemble O2 (source: http://enipedia.tudelft.nl/).

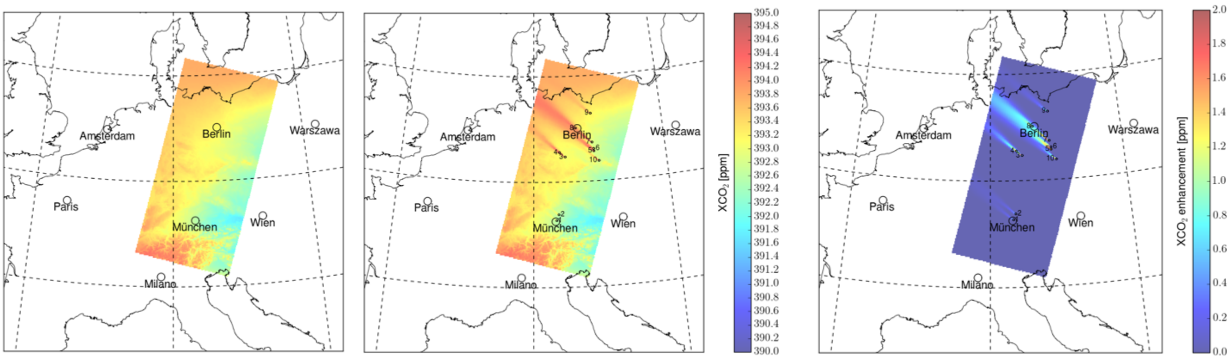

Figure 18: CO_2 total column mixing ratio of orbit ensemble O2: (left panel) without coal plant emissions, same as for ensemble O1 (middle panel) with CO_2 plumes from coal plants listed in Tab. 6, and (right panel) difference between left and middle panel.

2.6 Ensemble of generic scenarios

For preliminary performance tests, we define three different generic scenarios, which are summarized in Tab. 7. They comprise a clear sky scene over a dark surface, a corresponding spectrum for a bright surface and finally a spectrum for a cloudy atmosphere. All simulations are performed for the same amount of CH_4, H_2O and CO_2, the same aerosol load and the same solar and viewing geometries. The chosen cloud characteristics cause a similar SWIR-1 background radiance level for the cloudy scene and the bright clear sky scene. However, the SWIR-1 radiance spectra differ clearly in the depths of the telluric absorption lines.

Parameters	$L_{clr,dark}$ **clear sky dark**	$L_{clr,bright}$ **clear sky bright**	$L_{cld,dark}$ **cloudy sky dark**
Solar zenith angle	50 degree	50 degree	50 degree
Viewing zenith angle	0 degree	0 degree	0 degree

Relative azimuthal angle	0 degree	0 degree	0 degree
Lambertian albedo	A_{NIR}=0.1 A_{SWIR1}=0.05 A_{SWIR2}=0.05	A_{NIR}=0.5 A_{SWIR1}=0.4 A_{SWIR2}=0.4	A_{NIR}=0.1 A_{SWIR1}=0.05 A_{SWIR2}=0.05
Aerosol	$z_{aer} = 0\ km$ τ_{aer}=0.1	$z_{aer} = 0\ km$ τ_{aer}=0.1	$z_{aer} = 0\ km$ τ_{aer}=0.1
Mie cloud	-	-	Type: Gauss Height 5 km τ = 10 normal with r_{eff} = 10 µm and v_{eff} = 0.1 µm

Table 7: Setup of generic test scenarios, aerosol and cloud model are described in more detail in Sec. 2.2 and 2.4.

Appendix A: The Bidirectional Straylight Distribution Function (BSDF)

To simulate in-field and in-band stray light, the model of [RD-8] assumes an ideal radiance measurement, given by

$$I_{ij}^{\mathrm{ideal}} = \iint dx d\lambda\ K_{ij}^{\mathrm{ideal}}(x,\lambda) I_{lbl}(x,\lambda), \tag{A1}$$

where the kernel K_{ij}^{ideal} includes the intended ISRF and point spread function of the spectrometer. The index doublet (i,j) indicates a pixel of the two-dimensional detector pixel, where i and j represents the spectral and spatial detector dimension, respectively.

The deviation of the instrument performance from the intended performance due to stray light is described by

$$I_{ij}^{stray} = \sum_{m,n} K_{ij,mn}\ I_{mn}^{\mathrm{ideal}} \tag{A2}$$

with the stray light kernel $K_{ij,nm}$.

The total internal scattering is defined by

$$\kappa = \sum_{m,n} K_{ij,mn} \tag{A3}$$

After radiometric calibration, the measured signal becomes

$$I_{ij}^{meas} = \frac{I_{ij}^{ideal} + I_{ij}^{stray}}{1+\kappa} \tag{A4}$$

Eq. (A2) accounts for the stray light as a multiplicative correction to the ideal instrument performance and so differs from our stray light model in Eq. (14), where stray light is described by an additive contribution to the ideally performing instrument. Still, both definitions yield very similar kernels, where the stray light kernel in Eq. (A2) is defined by

$$K_{ij,mn} = \frac{dI_{ij}^{stray}}{dI_{mn}^{\mathrm{ideal}}(x_m,\lambda_n)} \tag{A5}$$

with λ_m and x_n the wavelength and spatial sampling assigned to pixel (m,n), and in Eq. (14) by

$$K_{ij}(x,\lambda) = \frac{dI_{ij}^{stray}}{dI_{lbl}(x,\lambda)} \tag{A6}$$

These definitions differ only on fine spectral scales and so Eq. (13) can be considered as a reasonable adaptation of the stray light kernel for the purpose of our study. This was confirmed by very similar simulations of stray light spectra employing both approaches.

References:

RD-1 Sierk, B., Caron J.: Optimized SNR requirement for the CarbonSat mission, ref IPD-MO-ESA-291, 2012
RD-2: Haring R., Randy Pollock R., Sutin B.M., Crisp D.: The Orbiting Carbon Observatory instrument optical design, Proc. SPIE 5523, Current Developments in Lens Design and Optical Engineering V, (14 October 2004); doi: 10.1117/12.562693
RD-3: Frankenberg, C., Pollock, R., Lee, R. A. M., Rosenberg, R., Blavier, J.-F., Crisp, D., O'Dell, C. W., Osterman, G. B., Roehl, C., Wennberg, P. O., and Wunch, D.: The Orbiting Carbon Observatory (OCO-2): spectrometer performance evaluation using pre-launch direct sun measurements, Atmos. Meas. Tech., 8, 301-313, doi:10.5194/amt-8-301-2015, 2015.
RD-4: Osterman, et al.: Orbiting Carbon Observatory–2 (OCO-2) Data Product User's Guide, Operational L1 and L2 Data Versions 6 and 6R, Version D, Data Releases 6 and 6R, March 30, 2015
RD-5: Osterman, et al.: Orbiting Carbon Observatory–2 (OCO-2) Data Product User's Guide, Operational L1 and L2 Data Versions 7 and 7R, Version D, Data Releases 7 and 7R, June 30, 2016
RD-6: Nadarajah, S.: A generalized normal distribution, Journal of Applied Statistics, 32:7, 685-694, DOI: 10.1080/02664760500079464, 2005
RD-7: Beirle, S., Lampel, J., Lerot, C., Sihler, H., Wagner T.: Parameterizing the instrumental spectral response function and its changes by a Super-Gaussian and its derivatives, Atmos. Meas. Tech. Discuss., doi:10.5194/amt-2016-307, 2016
RD-8: Stray light model, Airbus Defence & Space, pp 46, CS.ASF.TN.00003, 2015
RD-9: Butz, A., Galli, A., Hasekamp, O., Landgraf, J., Tol, P., and I., A.: TROPOMI aboard Sentinel-5 Precursor: Prospective performance of CH4 retrievals for aerosol and cirrus loaded atmospheres, Remote Sens. Envirom., 120, 267, 2012.
RD-10: Hu, H., Hasekamp, O., Butz, A., Galli, A., Landgraf, J., Aan de Brugh, J., Borsdorff, T., Scheepmaker, R., and Aben, I.: The operational methane retrieval algorithm for TROPOMI, Atmos. Meas. Tech., 9, 5423-5440, doi:10.5194/amt-9-5423-2016, 2016.
RD-11: Houweling, S., Krol, M., Bergamaschi, P., Frankenberg, C., Dlugo- kencky, E. J., Morino, I., Notholt, J., Sherlock, V., Wunch, D., Beck, V., Gerbig, C., Chen, H., Kort, E. A., Röckmann, T., and Aben, I.: A multi-year methane inversion using SCIAMACHY, accounting for systematic errors using TCCON measurements, Atmos. Chem. Phys., 14, 3991–4012, doi:10.5194/acp-14-3991- 2014, 2014.
RD-12: Peters et al, 2007, "An atmospheric perspective on North American carbon dioxide exchange: CarbonTracker", PNAS, November 27, 2007 , vol. 104, no. 48, 18925-18930
RD-13: Stier, P., Feichter, J., Kinne, S., Kloster, S., Vignati, E., Wilson, J., Ganzeveld, L., Tegen, I., Werner, M., Balkanski, Y., Schulz, M., Boucher, O., Minikin, A., and Petzold, A.: The aerosol-climate model ECHAM5-HAM, Atmos. Chem. Phys., 5, 1125–1156, doi:10.5194/acp-5-1125-2005, 2005.
RD-14: Remer, L. A., Kaufman, Y. J., Tanré, D., Mattoo, S., Chu, D. A., Martins, J. V., Li, R.-R.,

Ichoku, C., Levy, R. C., Kleidman, R. G., Eck, T. F., Vermote, E., and Holben, B. N.: The MODIS Aerosol Algorithm, Products, and Validation, J. Atmos. Sci., 62, 947–973, doi:10.1175/JAS3385.1, 2005.

RD-15: Hess, M. (1998). Scattering matrices of imperfect hexagonal ice crystals. Journal of Quantitative Spectroscopy and Radiative Transfer, 60, 301–308.

RD-16: Hess, M., & Wiegner, M. (1994). COP: A data library of optical properties of hexagonal ice crystals. Applied Optics, 33, 7740–7746.

RD-17: Heymsfield, A. J., & Platt, C. M. R. (1984). A parameterization of the particle size spectrum of ice clouds in terms of the ambient temperature and the ice water content. Journal of Atmospheric Science, 41, 846–855.

RD-18: Winker, D. M., Hunt, W. H., & McGill, M. J. (2007). Initial performance assessment of CALIOP. Geophysical Research Letters, 34, 19803.

RD-19: Guanter, L., Alonso, L., Gómez-Chova, L., Meroni, M., Preusker, R., Fischer, J., and Moreno, J.: Developments for vegetation fluorescence retrieval from spaceborne high-resolution spectrometry in the O_2 A and O_2 B bands, J. Geophys. Res.- Atmos., 115, D19303, doi:10.1029/2009JD013716, 2010.

RD-20: Hasekamp, O. P., & Butz, A.: Efficient calculation of intensity and polarization spectra in vertically inhomogeneous scattering and absorbing atmospheres. Journal of Geophysical Research, 113, 20309, 2008

RD-21: A. H. Strahler, J.-P. Muller MODIS BRDF/Albedo Product: Algorithm Theoretical Basis Document Version 5.0, MODIS Product ID: MOD43 Version 5.0 - April 1999

RD-22: Litvinov P., Hasekamp, O.P., Dubovik O., Cairns, B.:, Model for land surface reflectance treatment: physical derivation, application for bare soil and evaluation on airborne and satellite measurements, J. Quant. Spectrosc. Radiat. Transfer, 113, 2023-2039, doi:10.1016/j.jqsrt.2012.06.027, 2012

RD-22: Brugh aan de, J.: Orbit geometry simulator, SRON-CSS-TN-2016-01, version 1.0, 2016

RD-23: Clark, R. N., G. A. Swayze, K. E. Livo, R. F. Kokaly, S. J. Sutley, J. B. Dalton, R. R. McDougal, and C. A. Gent, Imaging spectroscopy: Earth and planetary remote sensing with the USGS Tetracorder and expert systems, J. Geophys. Res., 108(E12), 5131, doi:10.1029/2002JE001847, pages 5-1 to 5-44, December, 2003. http://speclab.cr.usgs.gov/PAPERS/tetracorder

AD-1: CarbonSat Mission Requirements Document, EOP-SMA/2232/PI-pi, version 1.0

AD-2: CarbonSat Mission Requirements Document, EOP-SMA/2232/PI-pi, version 1.2

Study on Spectral Sizing for CO_2 Observations (CSS)

D2 - Instrument related error for the different spectral sizing of a CO_2 instrument

Jochen Landgraf and Joost aan de Brugh

SRON Netherlands Institute for Space Research, Utrecht, The Netherlands

Andre Butz and Kaspar Graf

DLR German Aerospace Center, Oberpfaffenhofen, Germany

Abstract:

This document summarizes the analysis of instrument related errors on XCO_2 for different spectral sizing of a CO_2 spectrometer and is the delivery of WP-2100 of the 'Study on Spectral Sizing for CO_2 observations'. The instrument related errors and the measurement ensembles used for the analysis are specified in RD-1. We found that the XCO_2 retrieval performance is mostly sensitive to detector non-linearity. Here the core of the bias distributions indicates better performance of concept B with a mode error of 1.28 ppm compared to concept A with a mode error of 3.32 ppm. However, concept B includes more outliers and so has a mean bias of 7.12 ppm compared to 1.55 ppm for concept A. For the interpretation of these results it is important to note that RemoTeC does not adjust a radiometric offset to the measurements simulation. In case the radiometric offset is fitted, the corresponding XCO_2 error sensitivity diminishes. Second most important is the knowledge of the shape of the ISRF. From the investigated six different ISRF distortions, we find largest error sensitivity for ISRF deformations including a symmetrical compression. The induced XCO_2 biases are smallest for the low resolution spectral sizing of concept B with mean biases < 0.35 ppm. Generally, ISRF distortion introduces biases with significant regional dependence. For our analysis of the spectrometer stray light, we employed the CarbonSat kernel model and assumed that stray light can be corrected by a factor of 4 within the level 0 to 1 data processing. We found that for all instrument concepts this correction is sufficient and the different spectral resolutions of a measurement have only a minor impact on the stray light induced XCO_2 biases. Finally, we conclude that with respect to the investigated instrument induced XCO_2 errors, the sizing concept B is well suited for the future CO2 monitoring instrument and shows similar XCO_2 retrieval accuracy as the sizing concepts with higher spectral resolution.

Table of Contents

Instrument sizing point		A	B	B'	B''	C	D	ER
Spectral bands [nm]	NIR	756-773	747-773	747-773	747-773	758-772	758.35-768.65	747 – 773
	SW-1	1559-1675	1590-1675	1590-1675	1590-1675	1591-1621	1596.85-1618.55	1559 – 1675
	SW-2	2043-2095	1925-2095	1993-2095	2044-2095	2042-2081	2023.25-2050.75	1993 – 2095
Resolution [nm]/ sampling ratio	NIR	0.045/2.5	0.1/3.14	0.1/3.14	0.1/3.14	0.042/2.5	0.032/2.905	0.12 / 3
	SW-1	0.30/2.5	0.3/3.14	0.3/3.14	0.3/3.14	0.076/2.5	0.067/2.914	0.26 / 3
	SW-2	0.13/2.5	0.55/3.29	0.3/3.00	0.15/3.00	0.097/2.5	0.085/2.924	0.32 / 3
SNR coefficients a and b (Eq. 1)	NIR	2.81E-15/160540	4.47E-15/160540.	4.47E-15/160540.	4.47E-15/160540.	8.36E-016 / 2944.	8.423E-16 / 657350	4.75E-15/235000
	SW-1	2.88E-14/ 333979	2.29E-14/ 333297	2.29E-14/ 333297	2.29E-14/ 333297	4.15E-015 / 20277.	3.571E-15 / 654978	1.14E-14/ 235000
	SW-2	1.22E-14/ 324402	3.91E-14/ 323636	2.34E-14/ 307985	1.17E-14/307985	6.39E-015 / 56295.	5.670E-15 / 648609	1.47E-14/ 235000
Remark/reference		Adapted from AD-1	Adapted from AD-2	(B. Sierk, email 10.07.2017)	(B. Sierk, email 10.07.2017)	Adapted from RD-2, RD-3, RD-4, RD-5	Adapted MicroCab performance, pers. (B. Sierk, email 20.02.2017)	Based on equal resolving power concept (B. Sierk, email 19.04.218)

Table 1: Spectral sizing concepts

1 Introduction

In this study, we investigated the impact of instrumental errors on the XCO_2 retrieval performance depending on the spectral sizing of the spectrometers for the six sizing point summarized in Table 1. The instrument spectral sizing points reflect the spectral sizing of the CarbonSat concept before band optimization (concept A, AD-1), after band optimization (concept B, AD-2), and the OCO-2 (concept C) and MicroCarb sizing concept (concept D). Moreover, we consider two deviations of concept B with an enhanced spectral resolution and a reduced band width in the SW-2 band (concept B' and B''). Using the RemoTeC software package, we derive XCO_2 biases from simulated measurements superimposed by selected instrumental errors. Here, the error modelling is described in detail in RD-1. It is important to note that the XCO_2 error analysis is not meant to provide performance analyses for the specific instruments but aims to present a trade-off for the different spectral sizing points for a set of harmonized instrumental errors.

The Technote is structured as follows: Section 2 summarizes the main features of the global ensemble of simulated measurements. Details on the specific instrument error and data ensembles used for the analysis, can be found in RD-1. Section 3-7 presents the error analysis for (a) control runs for a signal-to-noise limited instrument, (b) ISRF distortion, (c) radiometric offset, (d) detector non-linearity, and (e) polarization sensitivity of the spectrometer. The analysis is completed with a dedicated stray light analysis in section 8, performed for an orbit granule around Berlin, which is partially covered by clouds.

2 The Global ensemble

To investigate the error sensitivity of the retrieved XCO_2 dry air column mixing ratio with respect to instrument related errors, we have simulated line-by-line top-of-atmosphere (TOA) radiance spectra for a global ensemble of clear sky scenes as described by Butz et al. 2012 [RD-7] and Hu et al., 2016 [RD-8] and specified in more detail in RD-1 for the specific error analysis. The ensemble includes a realistic variation of the Lambertian surface albedo and of the atmospheric aerosol, cirrus and trace gas composition. It comprises also information on the solar geometry for the envisaged orbit of the next-generation CO_2 mission. If not mentioned differently, all measurements are simulated for a nadir viewing geometry using a multi-order of scattering scalar radiative transfer model. Figure 1-6 show examples of the global distribution of selected parameters for four days, each representative for one season. In total the ensemble comprises 9320 model atmospheres on a ~3°×~3° latitude times longitude grid.

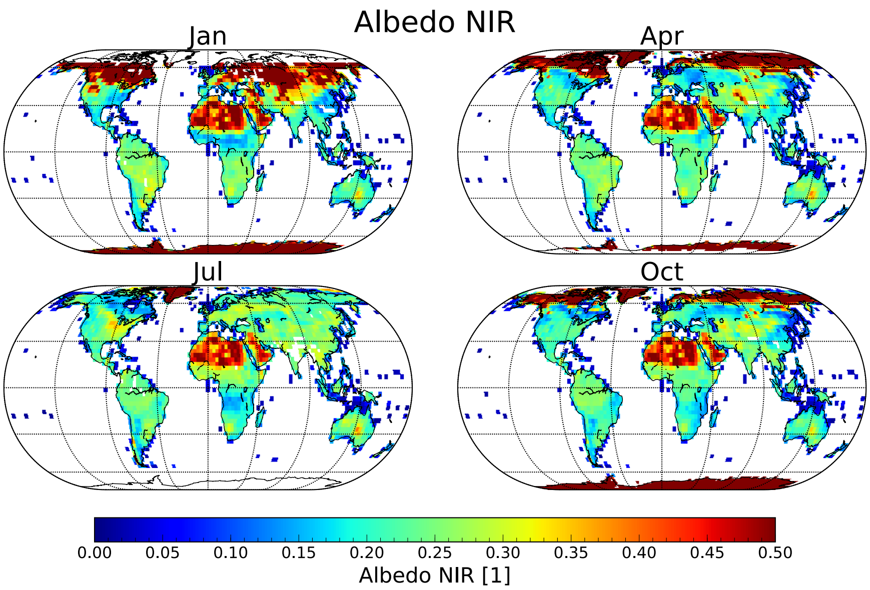

Figure 1: Global distribution of the NIR surface albedo

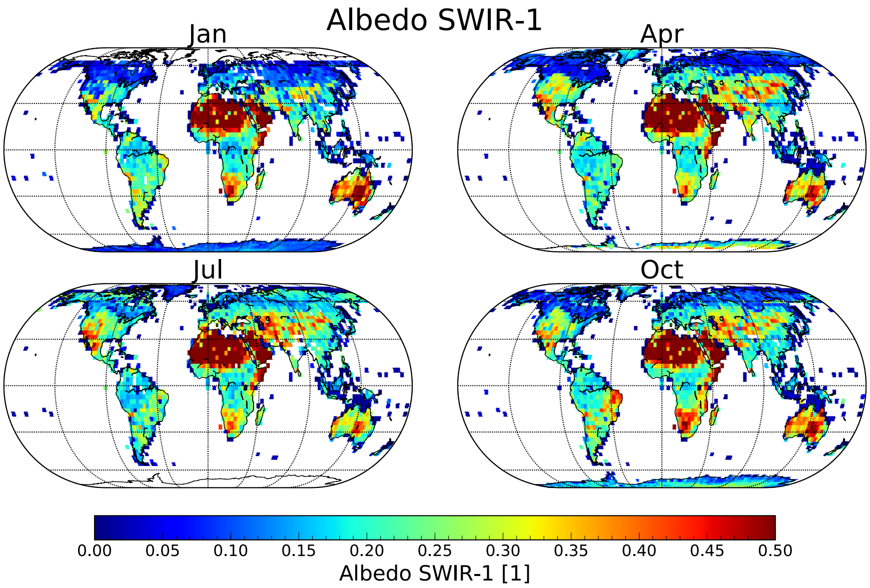

Figure 2: Global distribution of the SW-1 surface albedo

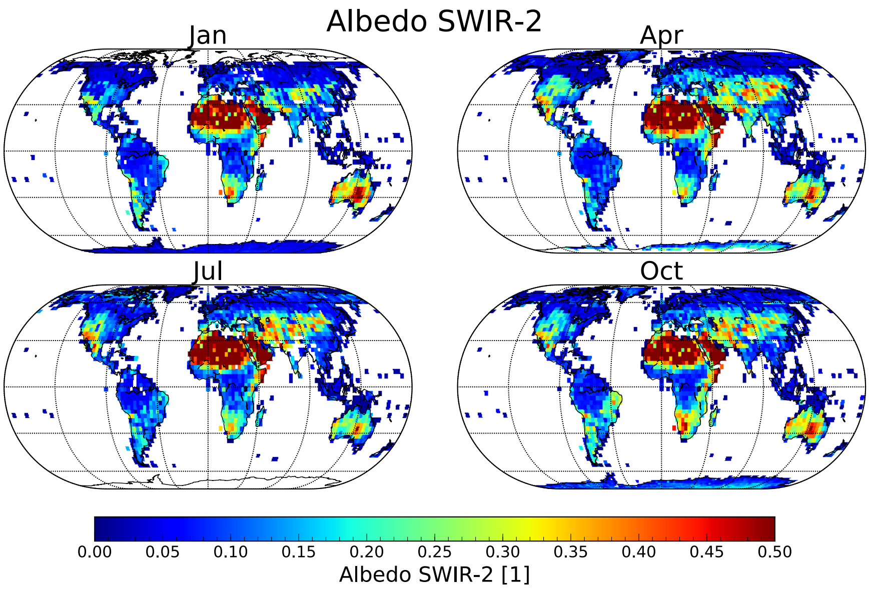

Figure 3: Global distribution of the SW-2 surface albedo

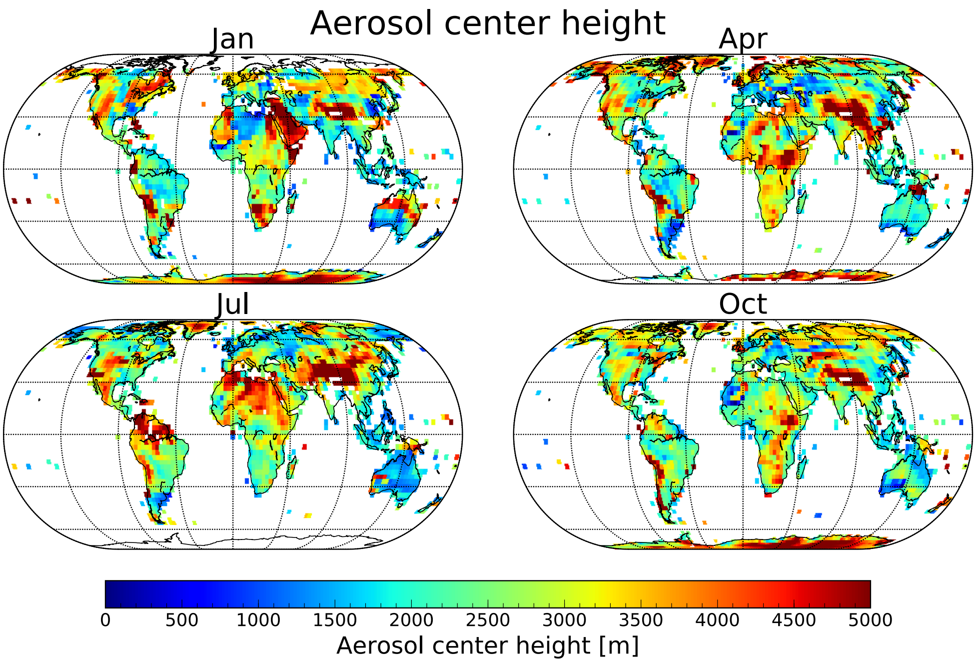

Figure 4: Global distribution of the aerosol layer center height

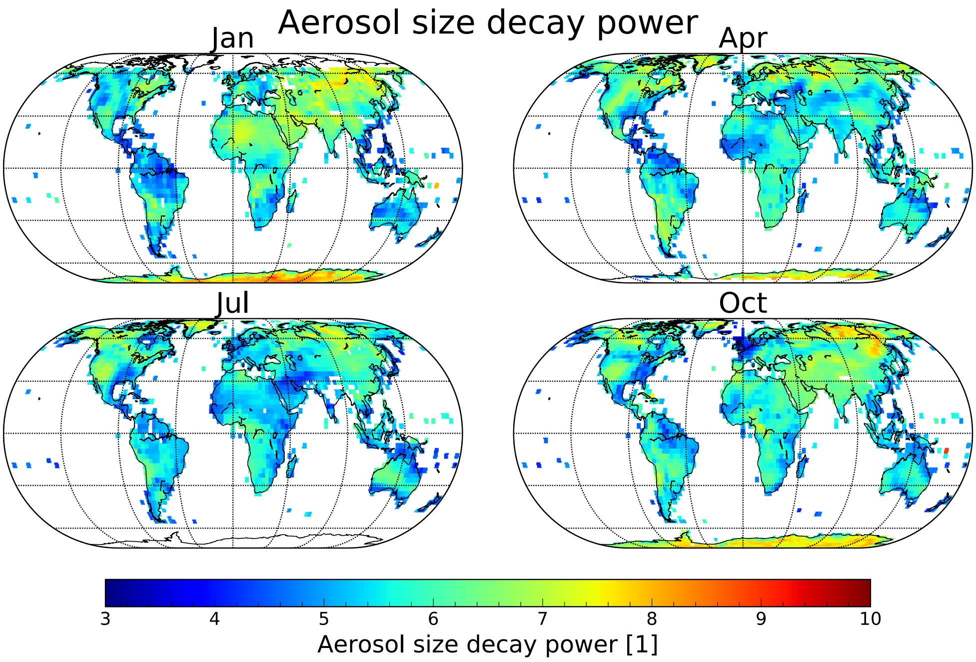

Figure 5: Global distribution of the aerosol size parameter (see Eq. 11 of RD-1)

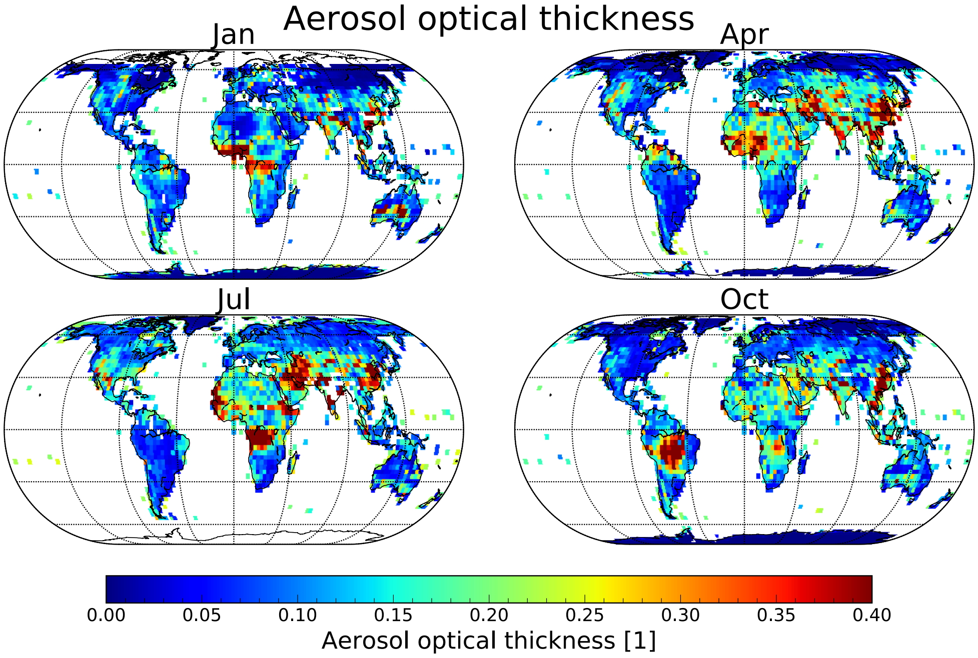

Figure 6: Global distribution of the aerosol optical depth at 765 nm

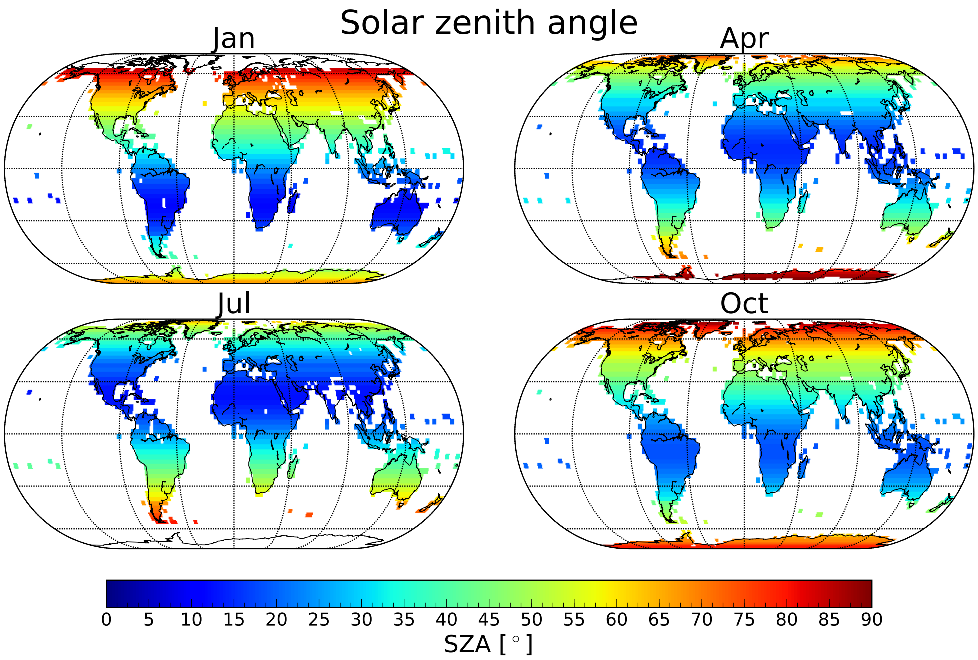

Figure 7: Global distribution of the solar zenith angle (SZA)

For the error sensitivity study, three different implementations of the global ensemble are used. The ensemble G1 aims to simulated realistic aerosol and cirrus loaded scenes for four days, one per season, where the description of the model atmosphere used for the measurement simulation and the forward simulation of the retrieval differ on purpose. The ensemble is used for the error analysis for aerosol induced error in RD-2. It represents the starting point for the measurement ensemble of this analysis, which is based on the following modification of ensemble G1.

1. **Global measurement ensemble G2**: To separate instrument related errors from aerosol induced errors, we simplified the description of aerosols of the ensemble G1 to obtain consistent measurement simulations and forward simulations as part of the retrieval. Therefore, ensemble G2 describes the atmospheric aerosol by a Gaussian height distribution with a fixed width of 2 km, a variable centre height and a height independent power law size distributions (see Eq. 11 of RD-1). The aerosol parameters are determined by least squares fitting to the original ensemble G1. All radiative transfer simulations are performed with the scalar radiative transfer model S-LINTRAN, calculating the radiance spectrum at the top of the model atmosphere (TOA).

2. **Global measurement ensemble G3:** To study the effect of the instrument polarization sensitivity, the ensemble G2 is extended to provide an estimate of the three Stokes parameters I, Q and U of the reflected light at the TOA. For this purpose, the Lambertian surface reflection model of ensemble G2 is replaced by a surface model to simulated the bidirectional reflection of the Earth surface including its polarization. Details are given in RD-1. For this ensemble, all radiative transfer simulations are performed with the vector radiative transfer solver V-LINTRAN. The degree of polarization of light depends on the scattering geometry at the Earth surface. For the CO_2 spectrometer, we assume as baseline a swath of 260 km width and so largest scattering angles occur generally at the swath edges. To account for this, we simulated a latitude dependent viewing geometry at the left (east) and right (west) edges of the swath for a satellite orbit characterized in Tab. 5 of RD-1. This leads to two global test ensembles G3-L and G3-R for the two swath geometries.

For all three ensembles G1-G3, TOA spectra are provided to ESA as part of the data package delivery of WP2000.

3 Control runs

To ensure a proper setup of the retrieval algorithm, we performed control runs the for ensemble G2 and for the instrument spectral sizing concepts A, B, C and D. Here we considered unperturbed instrument concepts, i.e. without any instrument error other than measurement noise. Figure 8 shows an example of the global XCO2 bias distribution of the measurement ensemble G2 and sizing point A. The corresponding bias probability density function (PDF) is shown in Figure 9. Ideally, the control run should indicate no retrieval bias at all. However, we observe minor biases, particular for spectral sizing points A, C and D with the fine spectral resolution with a mean bias (standard deviation) of $\mathbf{0.06}\ (\mathbf{0.07})$ ppm, $\mathbf{0.19}\ (\mathbf{0.09})$ ppm and $\mathbf{0.23}\ (\mathbf{0.11})$ ppm and a nearly ideal performance of concept B with $\mathbf{0.00}\ (\mathbf{0.01})$ ppm. These errors must be attributed to slightly different numerical implementation of the measurement and retrieval software. Although within the time constrains of the project it was not possible to fully trace the error source, it is likely that the biases are due to a slightly inconsistent ISRF convolution approach. Therefore, for the time being the XCO2 biases depicted in Figure 9 must be considered as a lower limit for a reliable error analysis of this study. Each error estimate, shown in the remaining of this document, is assured by a corresponding control run. For all cases, we found nearly bias performances, which are nearly identical to those in Figure 8 and 9.

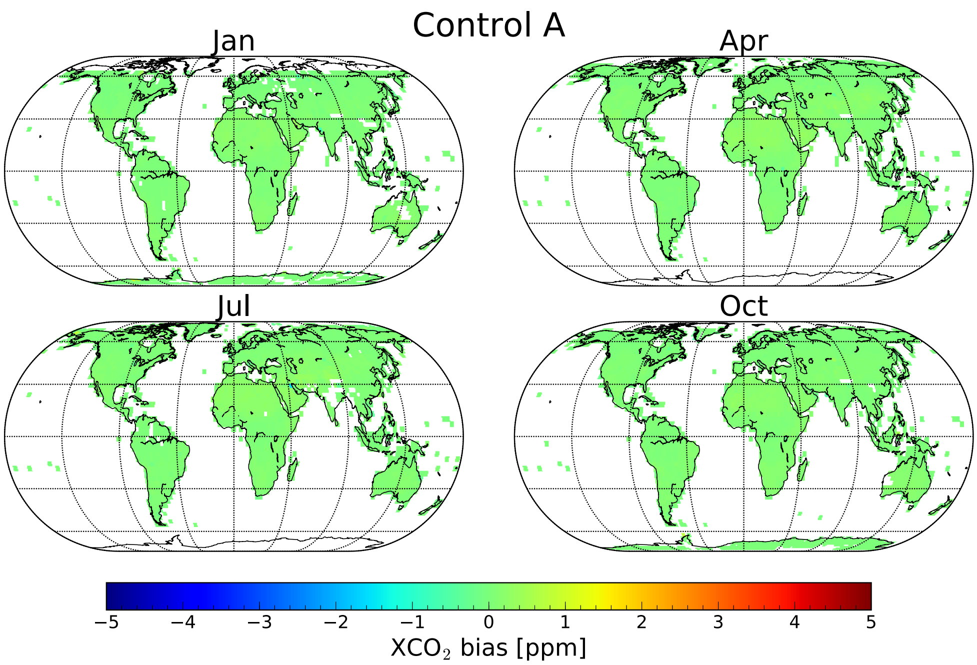

Figure 8: The global distribution of XCO$_2$ biases for the control run for ensemble G2 and instrument spectral sizing A

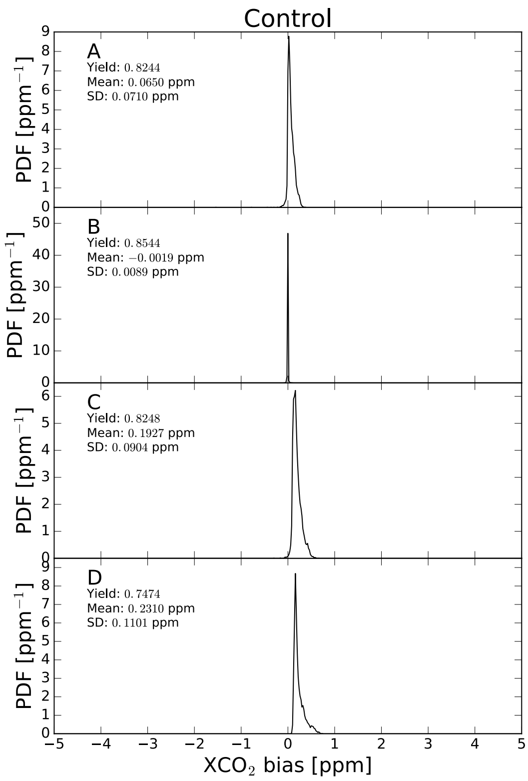

Figure 9: XCO_2 bias PDF for the ensemble G2 and instrument concepts A, B, C and D.

4 Distortion of the Instrument Spectral Response Function

At first, we considered the instrumental error contribution due to a distorted instrument spectral response function (ISRF). Therefore, we convolved the line-by-line spectra of ensemble G2 with the ISRF of the spectral sizing concepts A, B, C, and D as characterized in Table 1. We assume that the ISRF is a composite of a general Gaussian shape function, defined on a spectral scale in units of the instrument spectral resolution, which is scaled to the spectral domain of the instrument. The Gaussian shape function is distorted and so after its spectral mapping a harmonized ISRF distortion can be applied to the different spectral concepts. The distortion is described in terms of four parameters a_1, a_2, k_1 and k_2 (see Eq. 6 of RD-1). Here, parameter a_1 and k_1 yields a compression and stretching of the ISRF (distortion 1 and 2 in Figure 10) and parameter a_2 and k_2 a spectral shift (distortion 3 and 4). Additionally, the distortion 5 and 6 in Figure 10 describe more complex ISRF perturbations, where the parameters (a_1, a_2) and (k_1, k_2) are perturbed simultaneously. A detailed description of the ISRF distortion is given in RD-1.

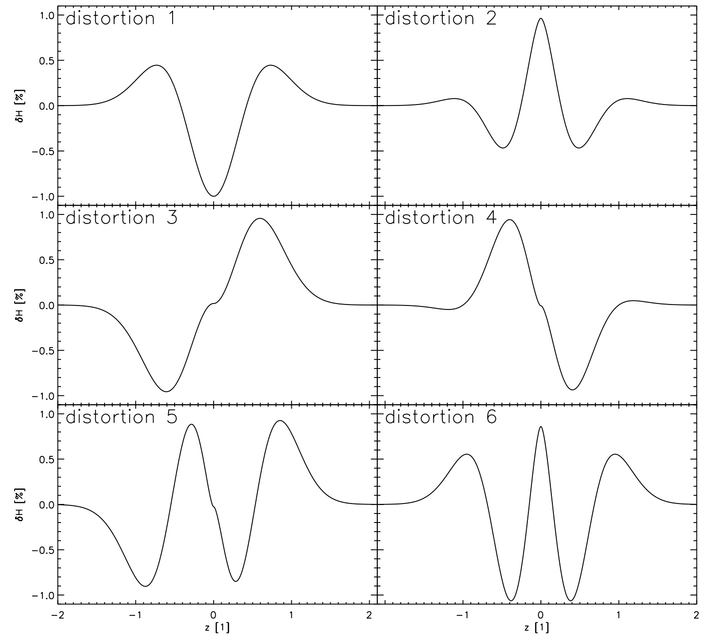

Figure 10: ISRF distortions 1-6. For more detail, see RD-1.

Figure 11 depicts the XCO_2 bias PDF for ISRF distortions 1-4 with a striking sensitivity of all spectral sizing concepts to the ISRF distortion 1, a moderate sensitivity to distortion 2 and a minor sensitivity to distortions 3 and 4. Here, distortions 3 and 4 reflect an erroneous spectral alignment of the instrument, which is mitigated by the retrieval fitting a spectral shift of the forward model. The ISRF compression of distortion 1 affects the XCO_2 bias differently for the different spectral sizing, where concept B has the smallest error sensitivity. To quantify an overall bias for the different instrumental errors, we use the mean bias b and the mode m of the PDFs. Differences between both indicates asymmetric and extended lobes of the PDFs. For the ISRF distortion 1, this are $(b,m)_A = (1.78{,}1.62)$ ppm, $(b,m)_B = (0.38{,}0.68)$ ppm $(b,m)_C = (2.73, 2.80)$ ppm, and $(b,m)_D = (2.62{,}2.30)$ ppm for concept A, B, C, and D, respectively.
For concept C, the global distribution of the XCO_2 biases are depicted in Figure 12 indicating clear regional structure of the induced errors, which results in a longitudinal averaged bias shown in Figure 13. This figure also highlights the superior low error sensitivity of the spectral sizing point B with a minor latitudinal dependence of the XCO_2 bias. For the interpretation of the CO_2 data product, the regional, latitudinal and temporal dependent biases represent a major problem.

To better understand the dependence of the XCO_2 bias on the spectral sizing, we consider an atmospheric transmission spectrum in the SW-1 spectral range for a high and low spectral resolution (see Figure 14). For the high spectral resolution (0.05 nm), the individual absorption lines can be identified in the spectrum. For lower spectral resolution (0.55 nm), these features are smeared out and only the spectral envelope of the absorption band is visible. The same spectral degradation can be observed for the CO_2 sensitivity of the spectrum. When considering the radiometric bias for the ISRF distortion 1, we can clearly identify the effect of the individual CO_2 absorption lines as spectral peaks around a zero-level baseline. Obviously, the envelope of the absorption band is not sensitive to the ISRF distortion and so the corresponding XCO_2 biases are very small for a low spectral resolution. This explains the more robust XCO2 bias performance of instrument concept B with respect to the other concepts with a higher spectral resolution.

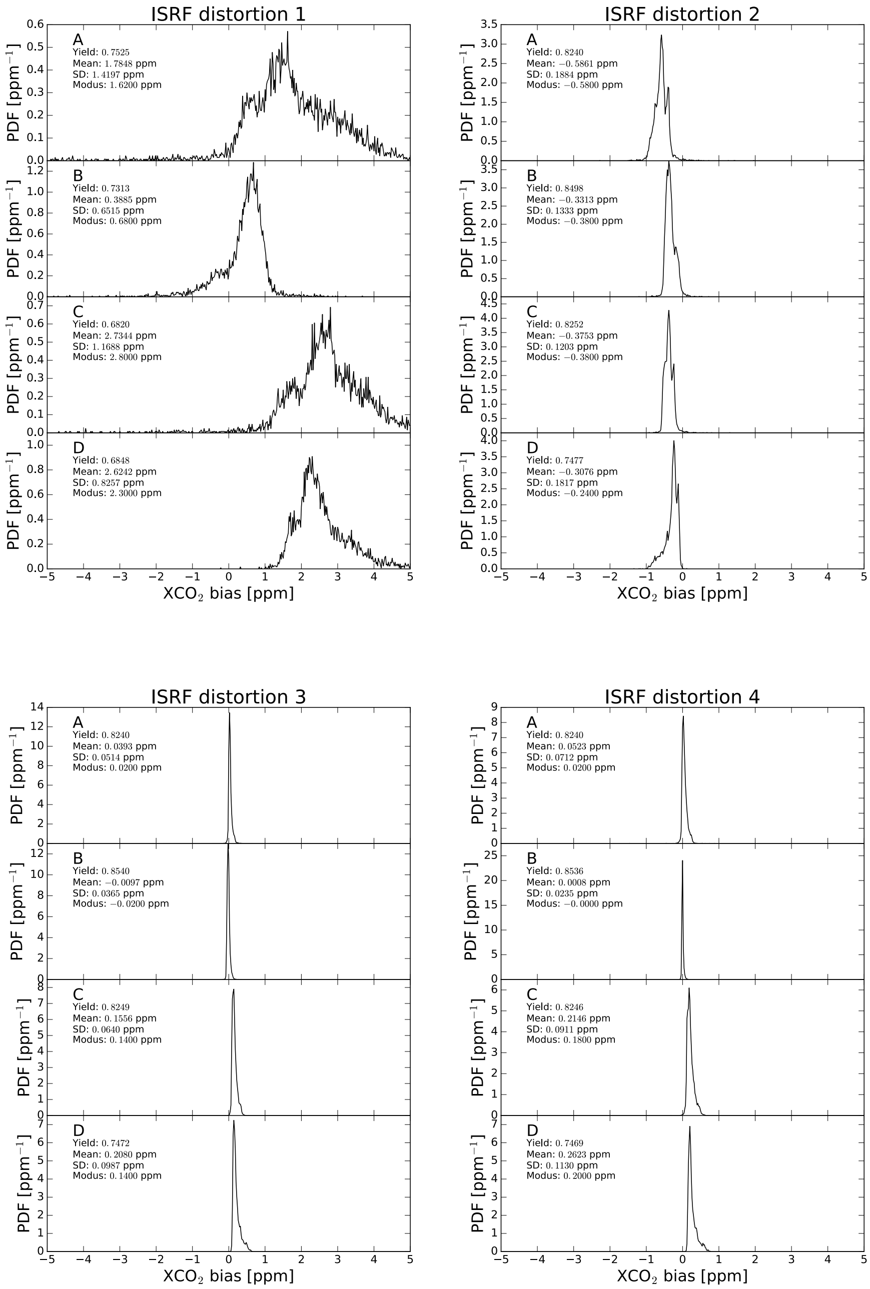

Figure 11: XCO_2 bias PDF for ISRF distortions 1-4 and instrument concepts A-D.

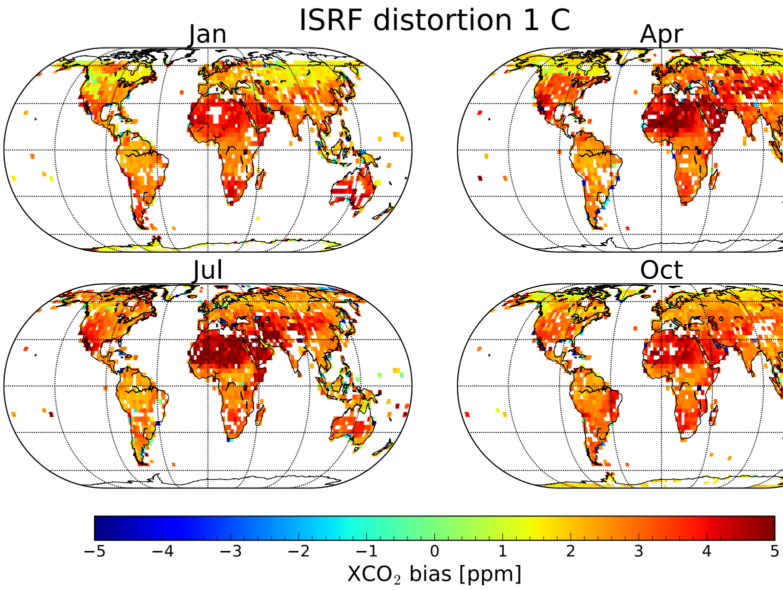

Figure 12: XCO_2 bias for instrument concept C and ISRF distortion 1.

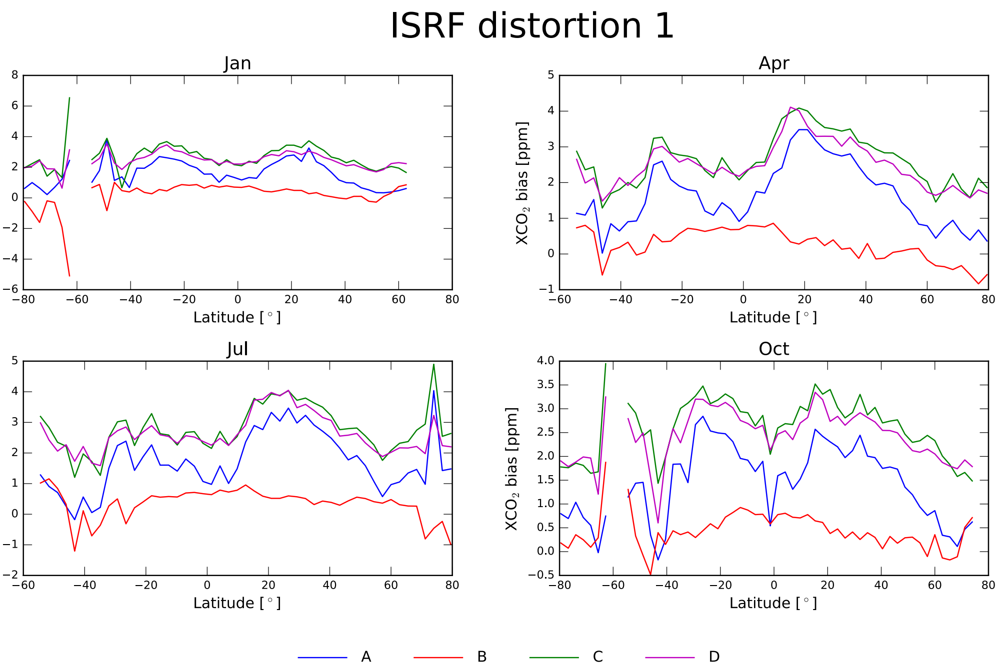

Figure 13: Longitudinal averaged XCO_2 bias for instrument concepts A, B, C, and D.

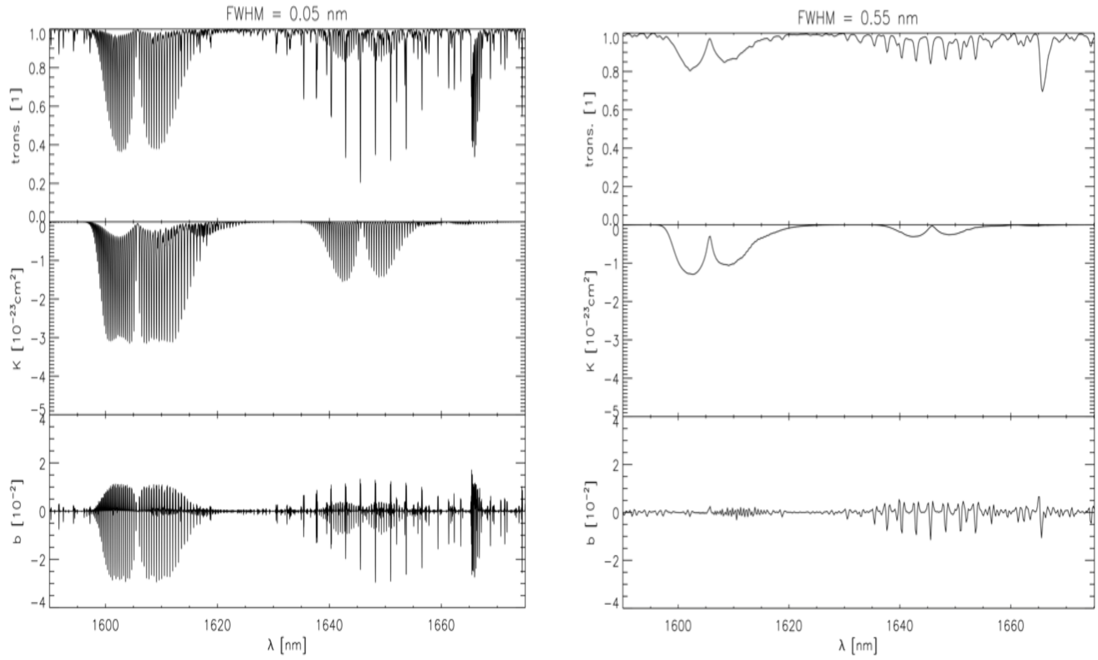

Figure 14: Atmospheric transmission spectrum between 1580 and 1630 nm (upper panels), CO_2 column sensitivity (middle panels), and radiometric bias due to ISRF distortion 1 (lower panels) for high spectral resolution (0.05 nm left) and low spectral resolution (0.55 nm, right panels).

Another obvious feature of Figure 11 is the different performance for the ISRF distortions 1 and 2. At first glance at Figure 10, one may think that distortions 1 and 2 only differ in sign. Assuming linear error propagation, one may expect similar error sensitivities for both cases, which is not confirmed by Figure 11. To check the validity of the linear error propagation, Figure 15 depicts the PDFs of the XCO_2 biases for a gradual scaling of distortion 1 with factors between -1 and +1. The results confirm nicely the linear bias dependence on the degree of the ISRF distortion and so hightlights the different error sensitivity of both ISRF distortions. A proper inspection of the distorted ISRFs shows that distortion 2 is narrower than distortion 1, yielding differences up to about 0.5 %, which is the reason for the different XCO_2 biases in Figure 11.

As a final sanity check of our ISRF analysis, we investigated the XCO_2 bias for a reduced spectral range 2022-2095 nm in the SW-2, to avoid that the concluded advantage of concept B is based on CO_2 sensitivity in the SW spectral range with extremely low signal and so large radiometric uncertainties. For this case, Figure 16 shows somewhat larger biases with $b_{B2} = 0.67$ ppm (compared to $b_B = 0.39$ ppm). However, in comparison with instrument concept C and D with $b_c = 2.73$ ppm and with $b_D = 2.62$ ppm the modified spectral sizing concept B2 is still superior with respect to the ISRF distortion 1. This conclusion is also supported by the bias analysis of the more complex ISRF distortions 5 and 6, shown in Figure 17.

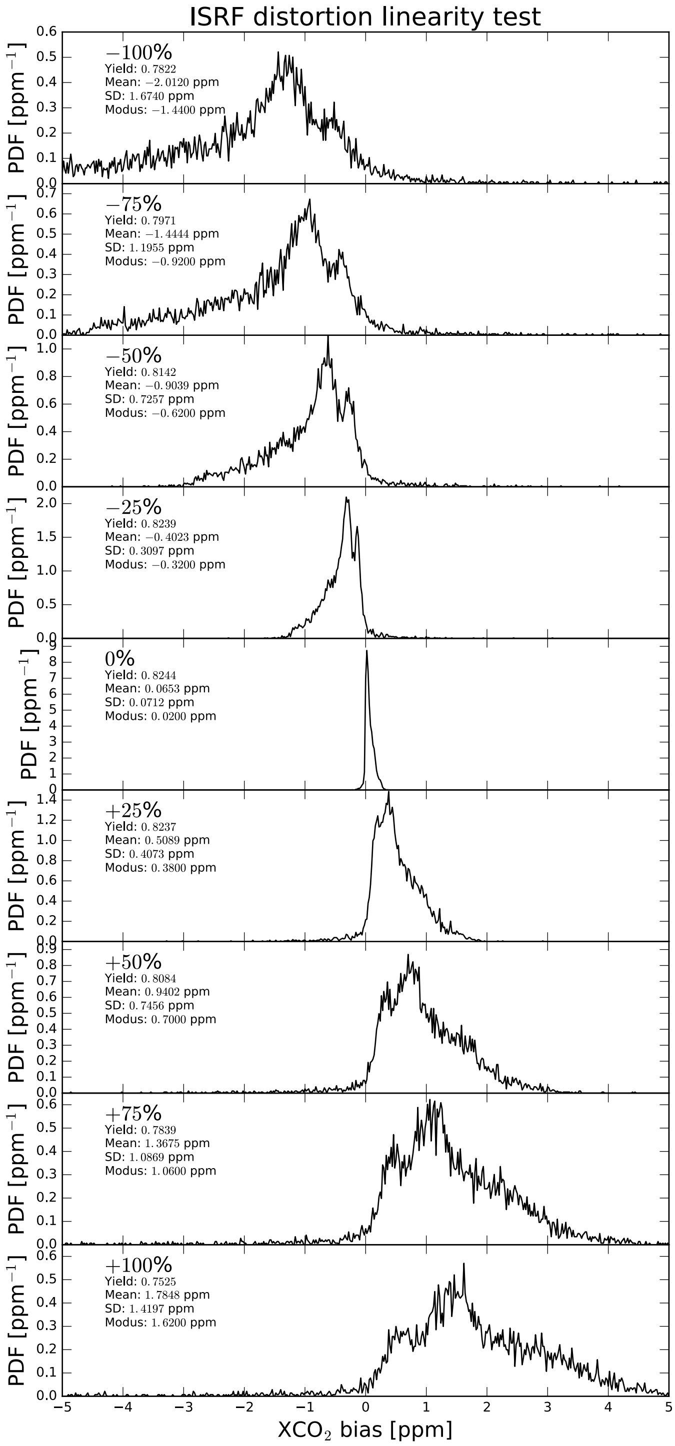

Figure 15: XCO_2 bias PDF for a linear scaling of ISRF distortion 1 for instrument concept A.

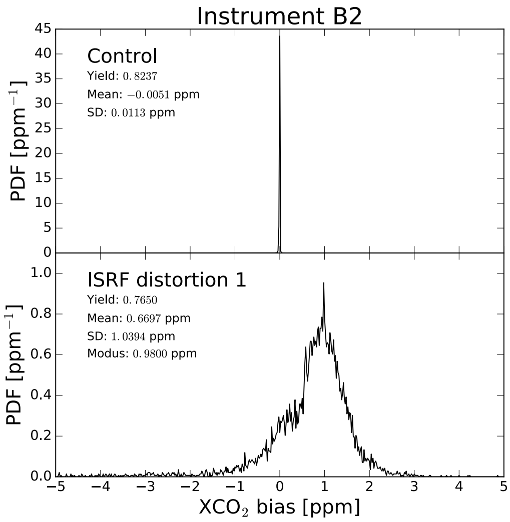

Figure 16: XCO_2 bias PDF for instrument concept B with reduced spectral coverage 2022-2095 nm in the SW-2.

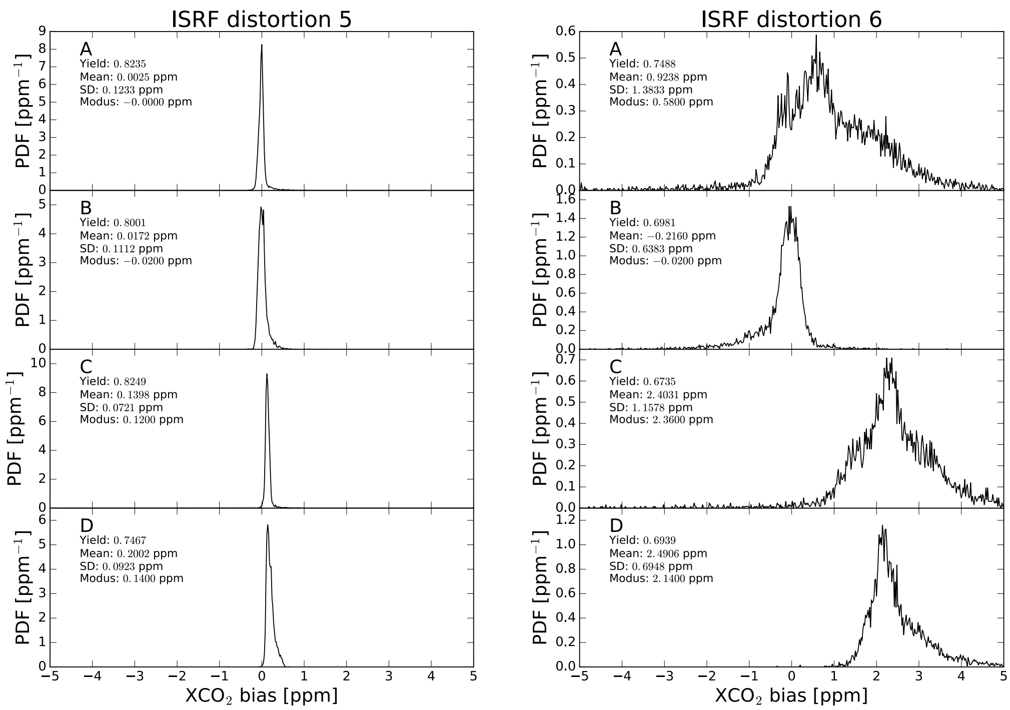

Figure 17: Same as Figure 11 but for the ISRF distortions 5 and 6.

5 Radiometric offset

Measurements in the NIR, SW-1 and SW-2 are usually subject to a radiometric offset for example due to uncorrected dark current of the detectors. To study the impact of this radiometric error, we superimpose the measurement simulations with a fixed wavelength independent radiometric offset as specified in Table 2. For the error analysis, we use the measurement simulation of the global ensemble G2 and do not fit a radiometric offset in the retrieval. For concept B, the bias distribution in Figure 18 shows clear latitudinal dependence where at high latitudes with low sun and so with low signal the biases can be -5 ppm and less. Obviously, the results require a dedicated data filtering to improve the results. Figure 19 shows the bias distribution function for no filtering, for data filtering on solar zenith angle and XCO_2 precision. Particular, filtering on XCO_2 precision improves the mean bias from $(b_A, b_B, b_C, b_D) = (-1.16, -1.06, -1.14, -0.94)$ ppm to $(b_A, b_B, b_C, b_D) = (-0.29, -0.44, -0.17, -0.06)$ ppm. Similar results can be achieved with filtering on SZA, namely $(b_A, b_B, b_C, b_D) = (-0.40, -0.58, -0.29, -0.09)$ ppm for SZA < 70° and $(b_A, b_B, b_C, b_D) = (-0.31, -0.52, -0.20, -0.01)$ ppm for SZA < 60°. Based on these findings, we consider the radiometric errors indicated Tab. 2 as less critical for all four instrument concepts and use the biases for the data filtering SZA < 70° for further referencing.

Table 2: Radiometric offset for the three spectral bands NIR, SW-1 and SW-2. Values are adopted from RD-1.

band	NIR	SW-1	SW-2
Radiometric offset [photons/(s nm cm^2 sr)]	4.2×10^9	4.3×10^9	5.3×10^8

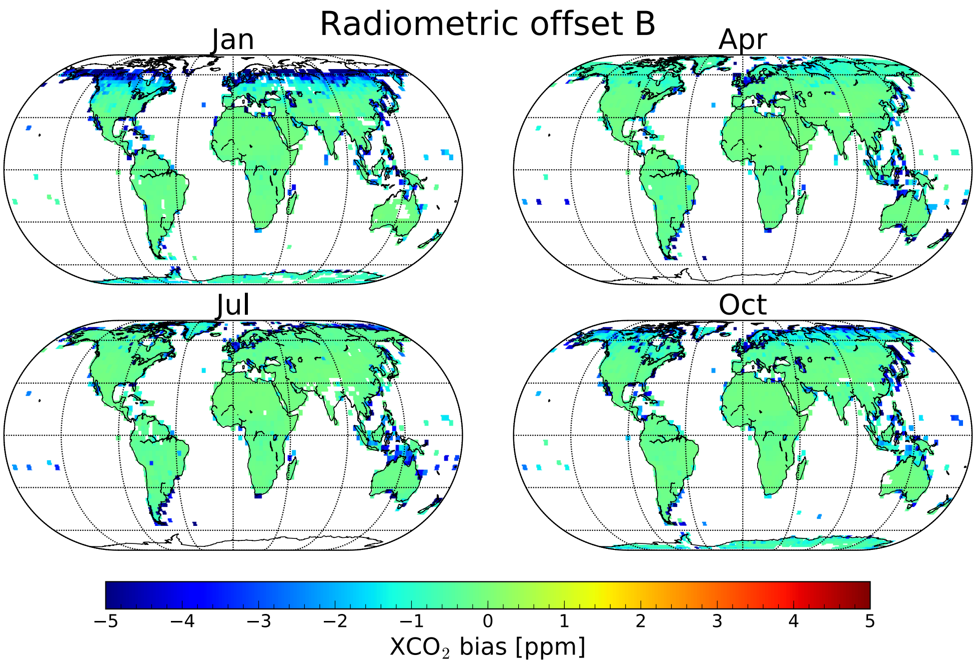

Figure 18: Global distribution of XCO2 biases due to a radiometric offset for instrument concept B.

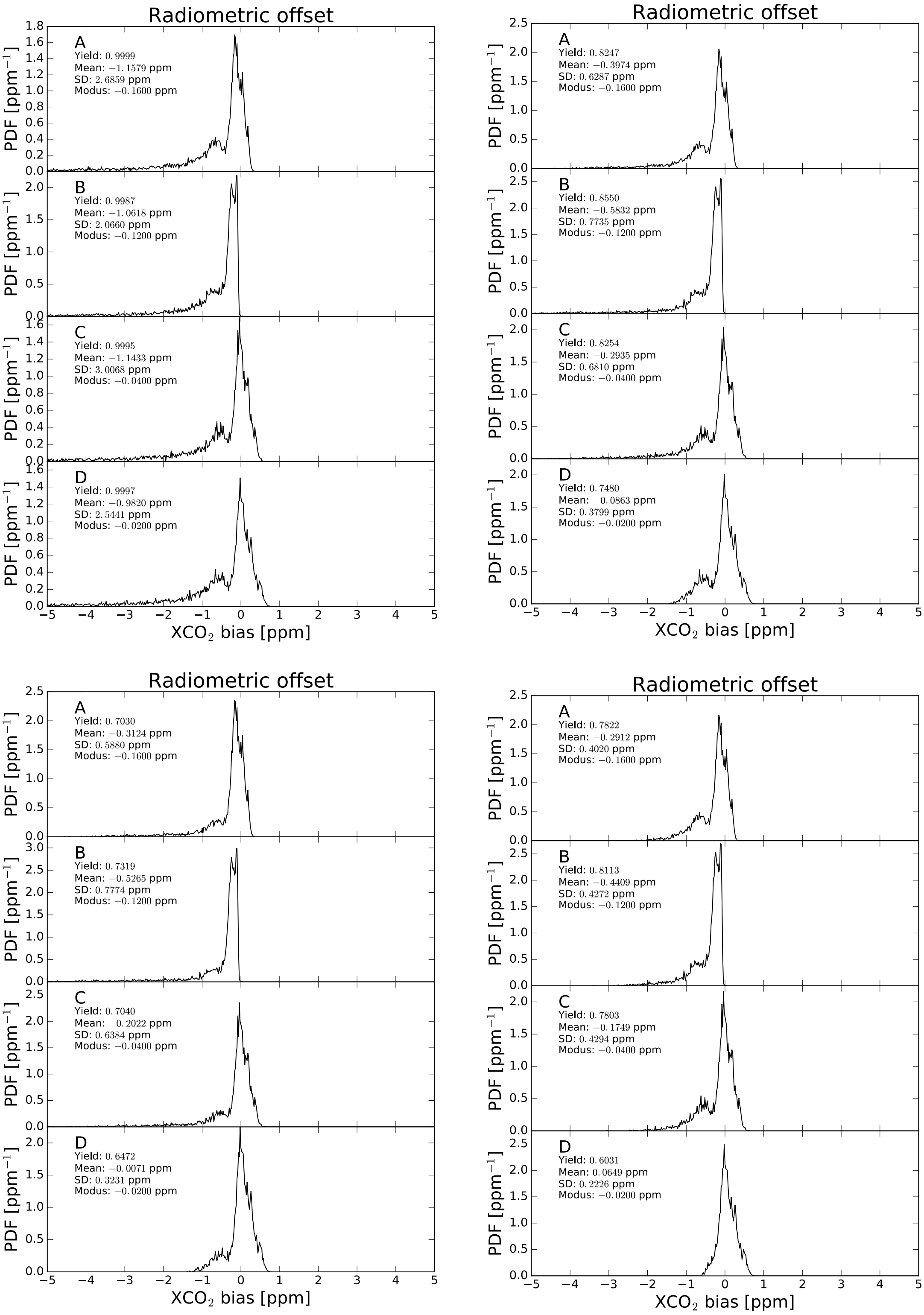

Figure 19: XCO_2 bias PDF for the global ensemble G2 and the radiometric offset defined in Tab. 2: (upper left panel) unfiltered, (upper right panel) filtered for SZA < 70°, (lower left panel) for SZA < 60°, and (lower right panel) filtered for XCO2 precision ≤ 1 ppm.

6 Detector non-linearity

The non-linear response of a detector device to the incoming signal causes a radiometric error depending on the recorded signal of each detector pixel. RD-1 give an estimate of the corresponding error for instrument concepts A and B and for the SW-1 and SW-2 band, which is also depicted in Figure 20. Here values are only provided for signal strengths between the indicated points of the non-linearity curve. For smaller signals, we extrapolate the error linearly (hence a curved line for a logarithmic x-axis). For larger signals, we use the non-linear response provided for the largest reported radiance value.

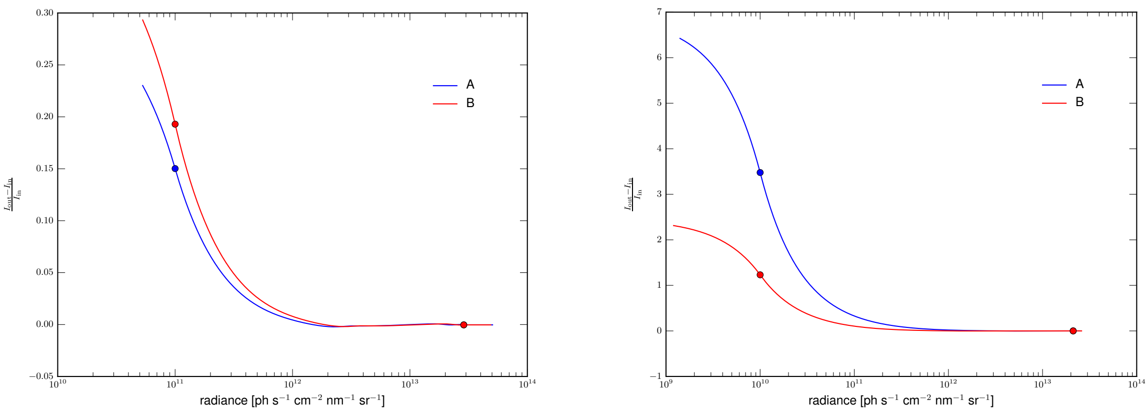

Figure 20: Detector nonlinearity for the SW-1 (left panel) and SW-2 band (right panel) both for instrument concepts A (blue) and B (red). Values between the two indicated points rely on detector characteristics of both instrument concepts. Beyond these domains, values are extrapolated.

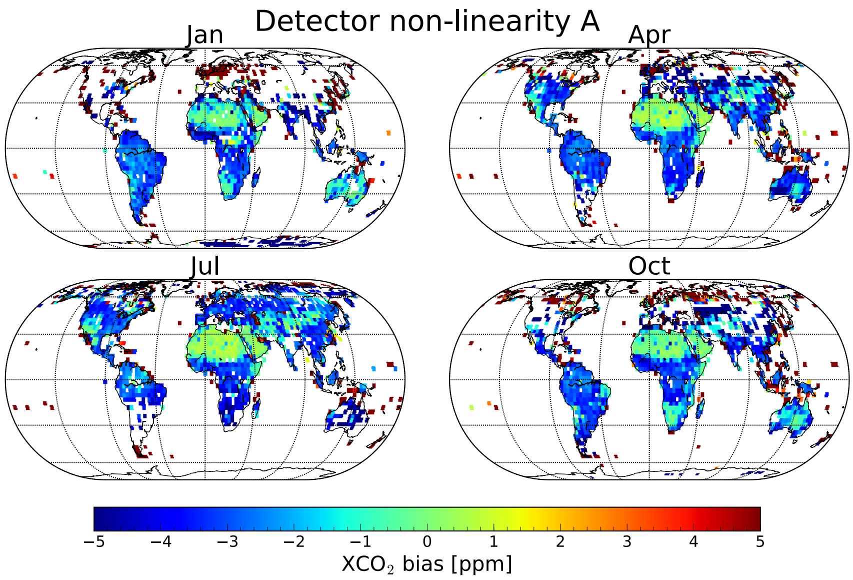

Figure 21: Global distribution of the XCO_2 bias due detector non-linearity for instrument concept A.

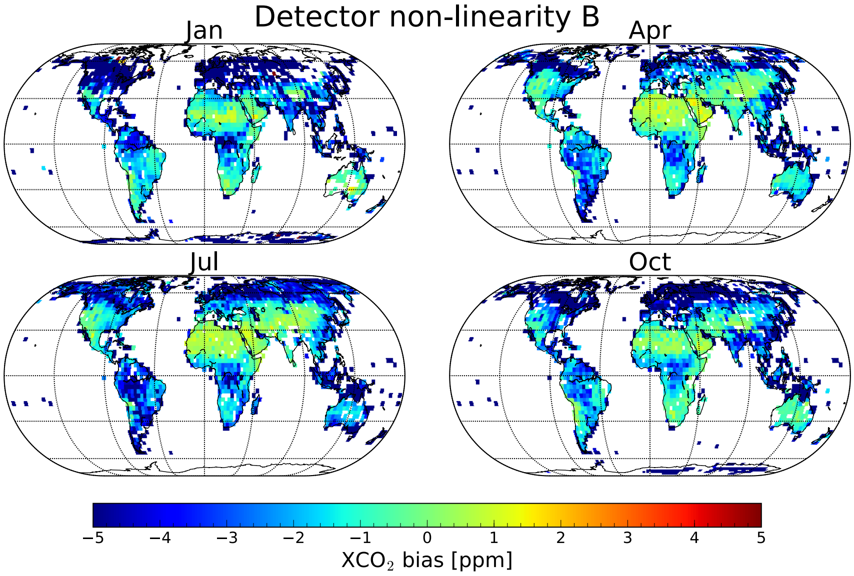

Figure 22: Same as Figure 21 but for instrument concept B.

The global distribution of the XCO_2 bias due to non-linearity is shown in Figure 21 and 22 for concepts A and B, respectively, showing distinct spatial structure on regional scale due the variation of the surface albedo superimposed by the varying solar zenith angle with latitude. Both key parameters govern the signal strength of the reflected light and so the XCO_2 bias. The corresponding PDFs of the XCO_2 bias in Figure 23 have a maximum around 3.5 and 1.5 ppm with pronounced side lobes to both sides of the maximum. A quantitative comparison of both PDFs is difficult because larger outlies are normally removed by a posteriori data filtering, which is optimized for the particular application. Focusing on the central part of the PDF, one may tend to favour concept B with a mode of -1.3 ppm over concept A with the mode of -3.3 ppm. Taking more data of the PDF into consideration, the overall performance of concept A becomes beneficial with respect to that of concept B. This performance feature is also nicely illustrated in the cumulative bias distribution in Figure 24, where concept B shows more successful retrievals with low biases but at the same time has more outliers.

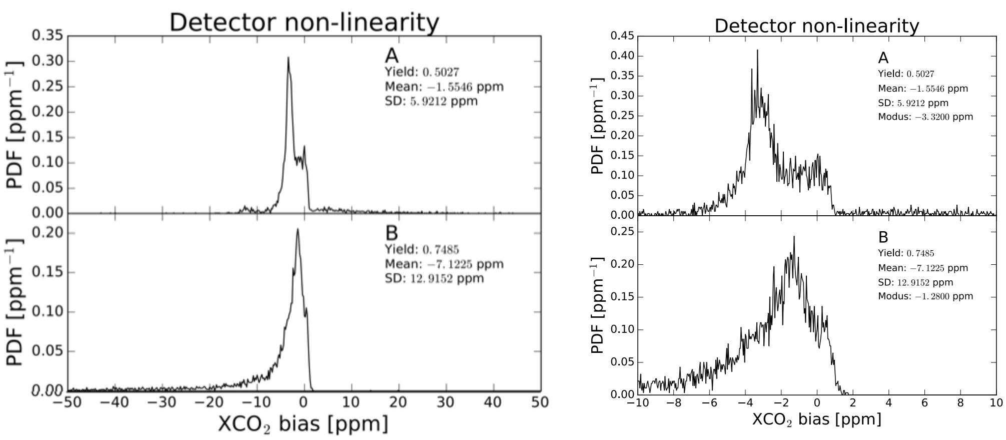

Figure 23: XCO_2 bias PDF due to non-linearity for instrument concepts A and B (left panels) and a zoom-in on the center part of the PDF (right panels).

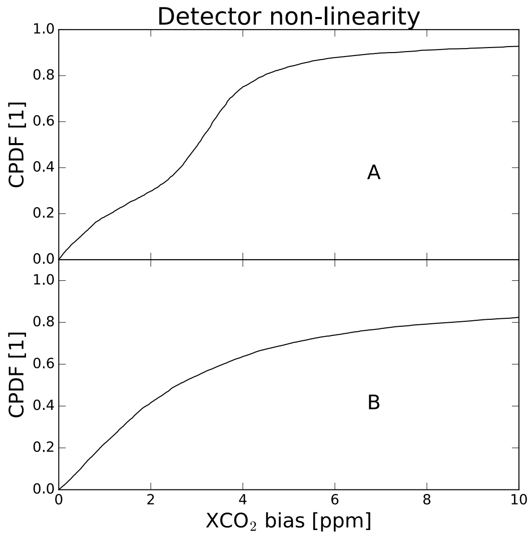

Figure 24: The cumulative distribution of the bias distribution in Figure 23 the for instrument spectral sizing concept A and B.

7 Instrument Polarization Sensitivity

To evaluate the effect of a polarization sensitive instrument for different sizing points, we use the measurement simulations of ensemble G3 and calculate the radiometric error

$$\delta I = \frac{M_{01}}{M_{00}} Q + \frac{M_{02}}{M_{00}} U \qquad (10)$$

with Stokes parameter Q and U of the ensemble. The instrument Müller matrix elements M_{00} , M_{01}, and M_{02} are taken from RD-1 and are interpolated to the viewing geometry of the left and right edge of the swath. The unperturbed measurements are modeled with the same viewing geometry as ensemble G3, but with the scalar radiative transport model S-LINTRAN, allowing us to have a consistent control run for a polarization insensitive instrument. Using this control run as baseline (and not the radiance simulation of a vector radiative transfer simulation) ensures that all biases are related to the polarization sensitivity of the instrument. The distributions of the XCO_2 bias for the ensemble G3-L and G3-R for the left and right edges of the swath are depicted in Figure 25. They are very similar to corresponding distributions of the control run in Figure 9, which indicate that the polarization sensitivity as described in RD-1 introduces only a minor error source independent from the spectral sizing point. This is true for both ensembles G3-L and G3-R.

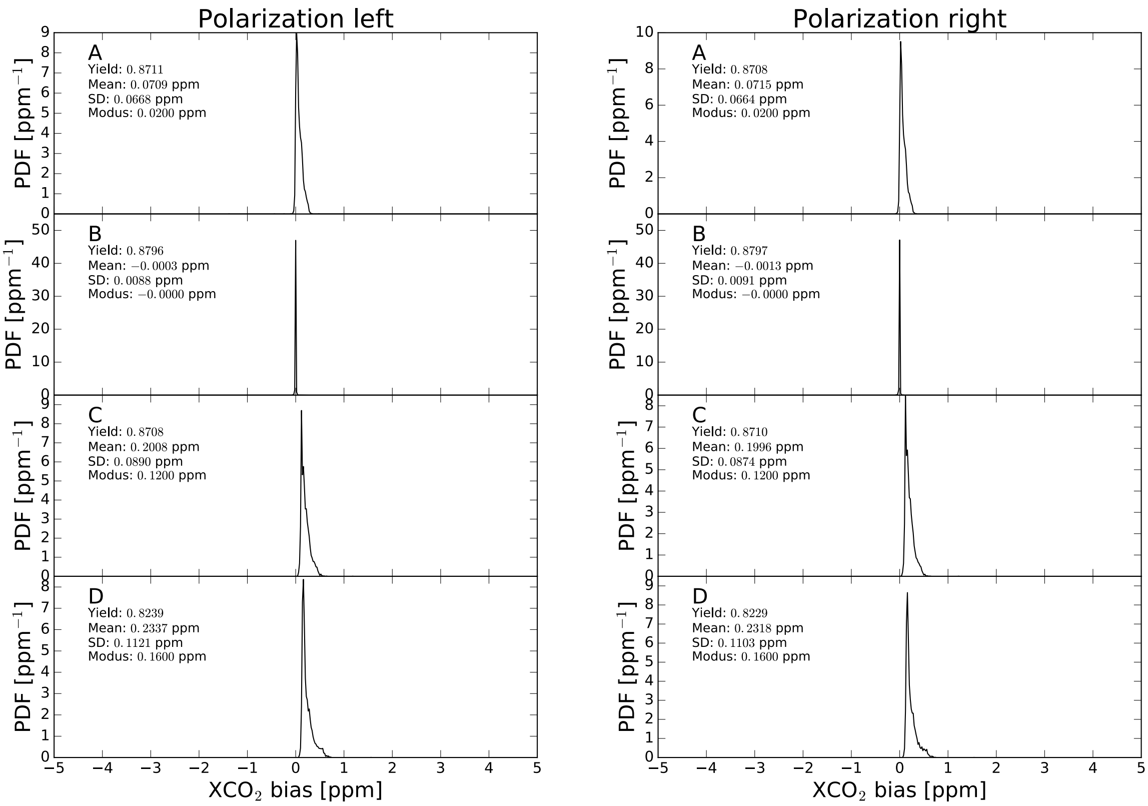

Figure 25: The XCO$_2$ bias distribution for a polarization sensitive instrument and measurement simulations of the ensemble G3-L (left panel) and G3-R (right panel) as described in Sec. 2 and in RD-1. The different instrument sizing points are indicated in the panels.

8 Stray light

8.1 Orbit ensemble

For the stray light analysis, the global ensemble of measurement simulations cannot be used because of its coarse spatial sampling. Therefore, we simulated measurements for a subset of the orbit ensemble, described in detail in RD-1. The data set is centred around Berlin and comprises TOA radiance spectra for clear sky and cloudy conditions using the MODIS cloud data shown in Figure 26. This ensemble includes spectra on a 1×1 km^2 spatial sampling with an east-west extension of 500 km. The spatial domain is needed to perform the spatio-spectral convolution of the stray light simulations (see Eq. 8 of RD-1) for an orbit with a 260-km swath including TOA radiance fields 120 km to the east and west of the swath. For the CO$_2$ atmospheric abundance, we assume a background scenario (left panel of Figure 27) and a scenario with plume emissions from coal plants in the area (right panel of Figure 28). Overall, we simulated TOA radiances for three setups of the ensemble summarized in Table 3.

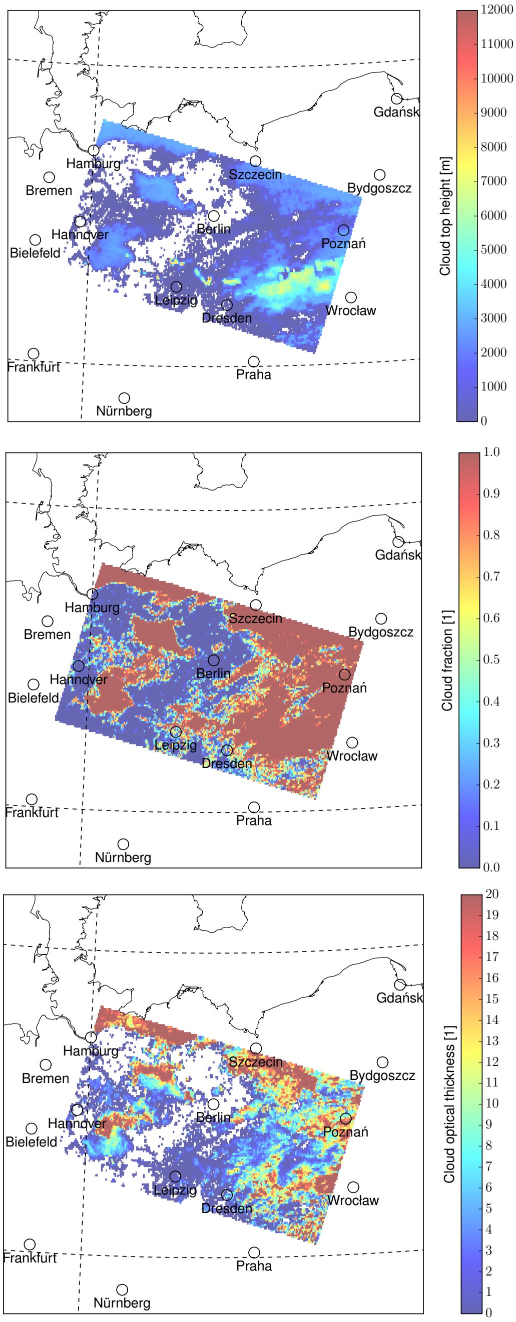

Figure 26: Cloud parameters of the orbit ensemble given on a 1×1 km² spatial sampling: cloud top height (top panel), cloud fraction (middle panel), and cloud optical thickness (bottom panel). The data set includes the spatial extension of orbit granule and 120 km beyond the east and west edges of the swath for a proper stray light simulation.

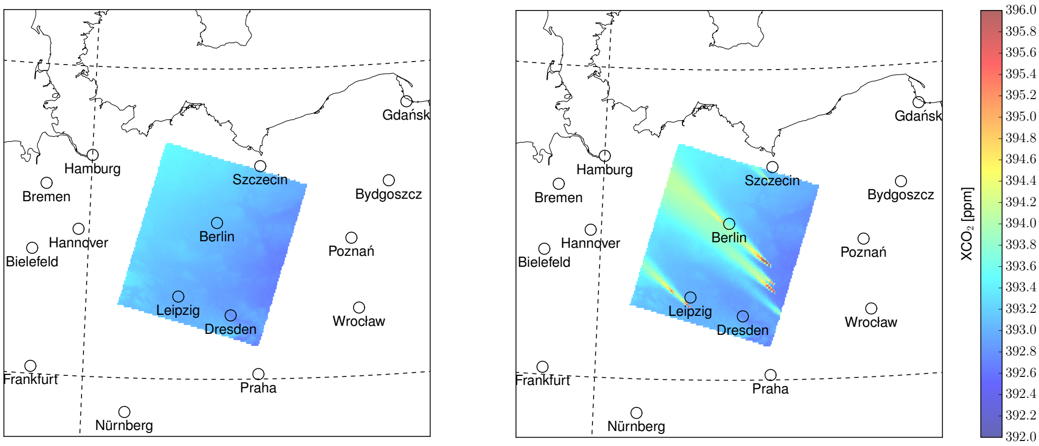

Figure 27: CO_2 fields for the simulated orbit ensemble: background scenario (left), plume scenario (right). Note that the east-west extension covers only the swath of the orbit.

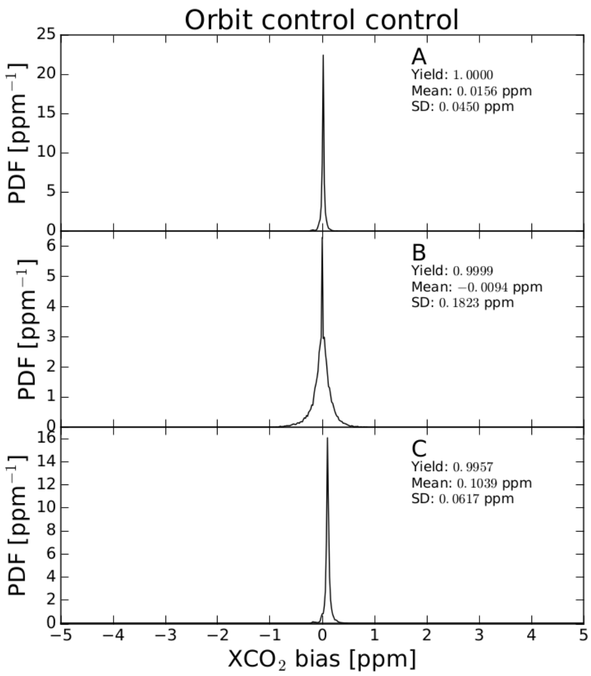

Figure 28: Control run for the spectral sizing points A, B, and C for the orbit ensemble O3, where the TOA radiance spectra are sampled on a 2×2 km² ground pixel size.

Table 3: Different setups of the orbit ensemble

Ensemble	description
O1	cloudy sky scenarios for the CO_2 background distribution
O2	clear sky scenarios considering CO_2 plumes of coal plants in addition to ensemble O3
O3	clear sky scenarios for the CO_2 background distribution

8.2 Orbit ensemble control run

The orbit ensemble requires a dedicated control run for the different sizing concepts. Therefore, we sampled spatially the ensemble O3 on 2×2 km^2 ground pixels and ignore any stray light contribution. Figure 28 shows that the corresponding XCO_2 biases are small with a mean bias < 0.1 ppm. The standard deviation of the PDFs indicates some scatter in the data due to the heterogeneity of the 2×2 km^2 ground scene, which is not accounted in the retrieval. Overall, we consider the quality of the control retrieval sufficient to study the effect of stray light on the CO_2 data product with a detection limit of about 0.1 ppm.

8.3 Stray light induced XCO2 bias

We start our stray light analysis using cloudy and clear sky measurement simulations for ensemble O1, where we perform CO_2 retrievals only for clear sky scenes, accounting for stray light from both cloudy and clear sky scenes within the corresponding swath. Figure 29 presents the XCO_2 bias for concept B both for uncorrected stray light and for a case where we reduced the stray light contribution by a factor of 4. This represents a realistic correction efficiency for stray light as part of the level 0-1 processing. In Figure 30, the corresponding bias PDFs have a mean XCO_2 bias of -3.5 ppm in case of no stray light correction and -1.2 ppm applying the stray light correction. Obviously, this error can be further reduced assuming a more efficient correction. In the remaining of this study, we apply the correction factor 4 to all stray light contribution. A close inspection of Figure 29 shows stripes of enhanced XCO_2 bias along the swath direction, where the larger bias the more cloudy scenes are present within the swath.

To understand this, we consider the depth of CO_2 absorption lines relative to the spectral continuum and simplify stray light considering its spatial component only. For different clear sky scenes within a swath, the signal may vary due to variations of the surface albedo, however, the relative depth of the absorption lines stays the same ignoring the effect of atmospheric scattering. So, superimposing spatial stray light on the spectrum does not introduce errors on the retrieved XCO_2. Moreover, the variation of atmospheric CO_2 is also small even in case of the plume ensemble O2, where the CO_2 total column enhancement with respect to the atmospheric background is typically $\leq$ 4 ppm. Hence, also in this case we expect small XCO_2 biases due to spatial stray light. The situation differs for spatial stray light from cloudy scenes, where the absorption features are generally less deep due to the light path shortening by clouds. Hence, XCO_2 gets underestimated for swaths with large stray light contributions from cloudy scenes. Moreover, cloudy scenes are usually brighter than clear sky scenes, which enhances the discussed stray light effect by cloudy scenes.

The above rationale ignores spectral and spatio-spectral contributions of the stray light kernel and so may oversimplify the problem. However, the conclusions are supported by corresponding stray light simulations both for ensemble O2, where we ignore any clouds but consider CO_2 plumes, and for ensemble O3, which assumes a background CO_2 distribution for the entire ensemble. In both cases, the induced mean XCO_2 bias in Figure 31 and 32 is about -0.67 ppm and so is significantly smaller than for the cloudy ensemble O1 with a mean bias of -1.2 ppm. Moreover, the nearly identical stray light induced bias for ensembles O2 and O3 confirms that CO_2 enhancements due to coal plants does not affect the XCO_2 retrieval errors caused by instrumental stray light.

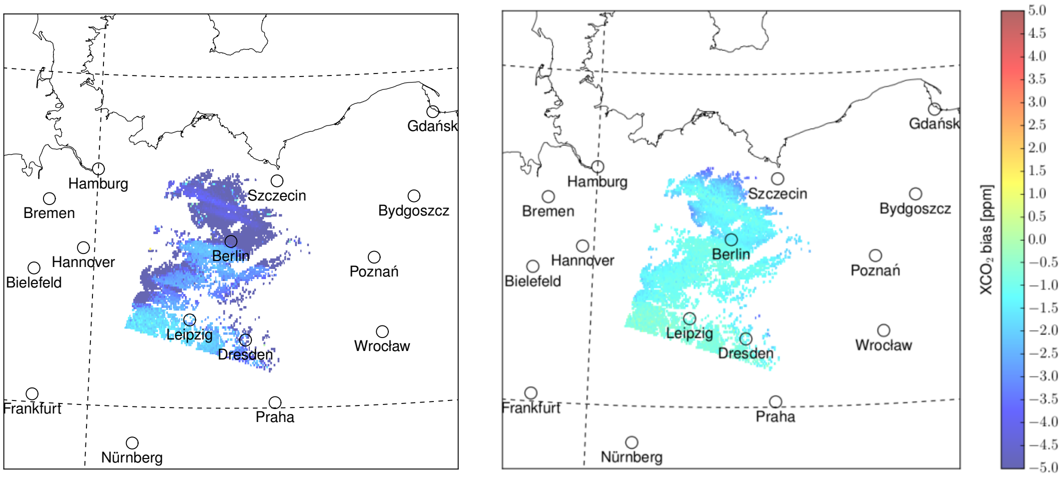

Figure 29: XCO_2 bias due to uncorrected stray light (left panel) and assuming that stray light can be suppressed by a factor of 4 (right panel) due to a corresponding correction approach as part of the data processing. Data gaps (white pixels) are due to cloud contaminated scene, which are filtered out.

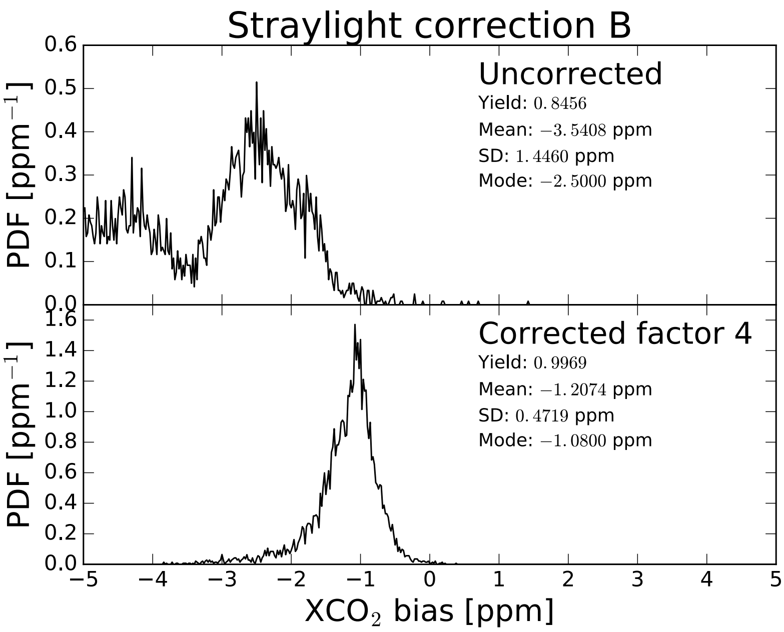

Figure 30: PDF of the XCO_2 bias as shown in Figure 29.

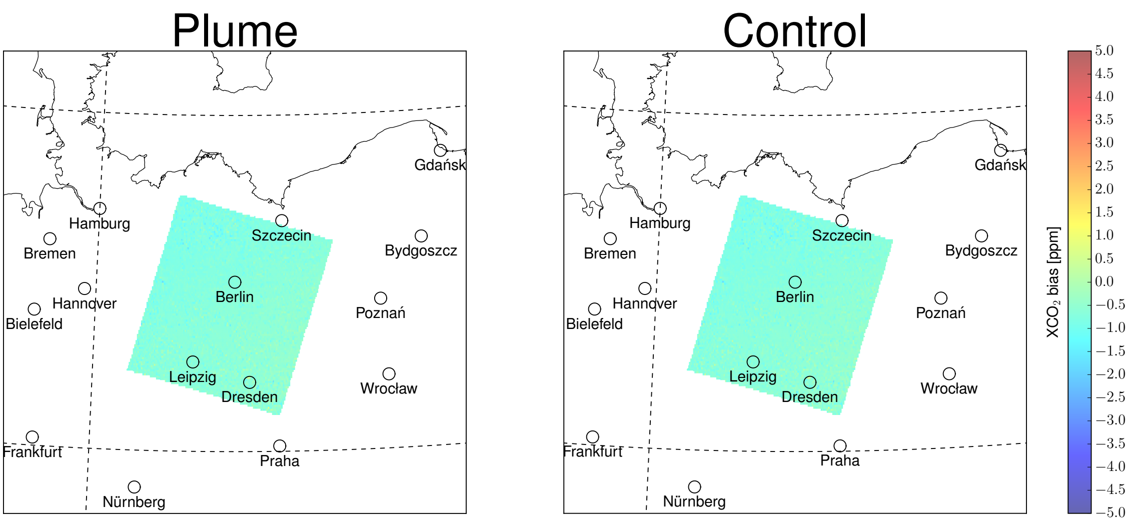

Figure 31: *Stray light induced error for ensemble O2 with CO_2 plumes from coal plants (left panel, with a mean XCO_2 bias of -0.67 ppm) and for the ensemble O3 comprising only CO_2 background concentrations (right panel, also with a mean XCO_2 bias of -0.67 ppm). For the simulations, we 'corrected' the simulated stray light spectra by a factor of 4.*

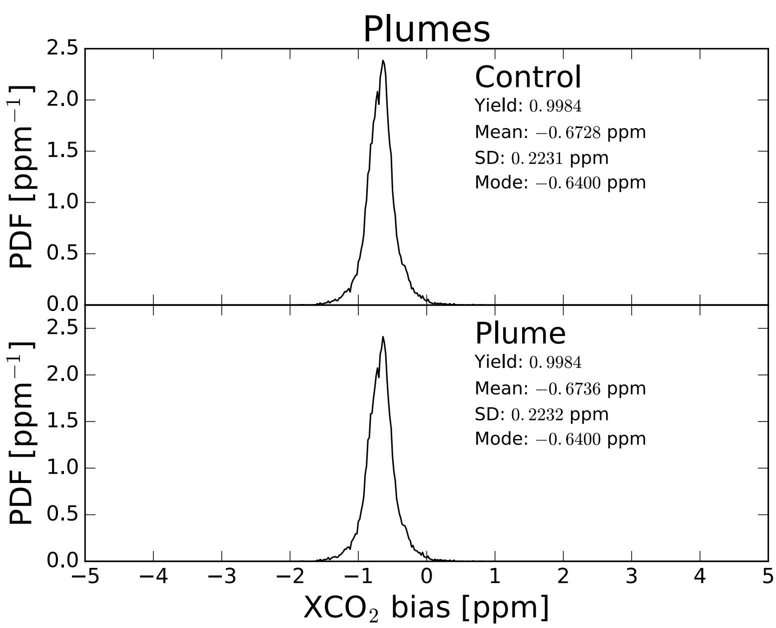

Figure 32: PDFs of the stray light induced XCO_2 error for ensemble O2 with CO_2 plumes from coal plants (lower panel, with a mean XCO_2 bias of -0.67 ppm) and for the ensemble O3 comprising only CO_2 background concentrations (right panel, also with a mean XCO_2 bias of -0.67 ppm (top panel)

Next, we investigated the XCO_2 stray light spectra for the spectral sizing points A and B. Our stray light model [RD-1] assumes that the relative amount of stray light is the same for the different sizing point and a spectrally constant stimulus. This is confirmed by stray light spectra of Figure 33 and 34. For example, at the longwave continuum of the NIR band for both concept A and B the same amount of stray light is simulated whereas in the centre of the O_2 A band the stray light is smaller for concept A than for concept B because of the finer spectral resolution. Overall, the stray light spectrum follows the low frequency features of the measurement, whereas high frequency features are smeared out because of the spectral width of the stray light kernel. The spectral dependence of stray light is more present in the NIR and SW-2 band with strong O_2 A, H_2O and CO_2 absorption bands than in the SW-1 band.

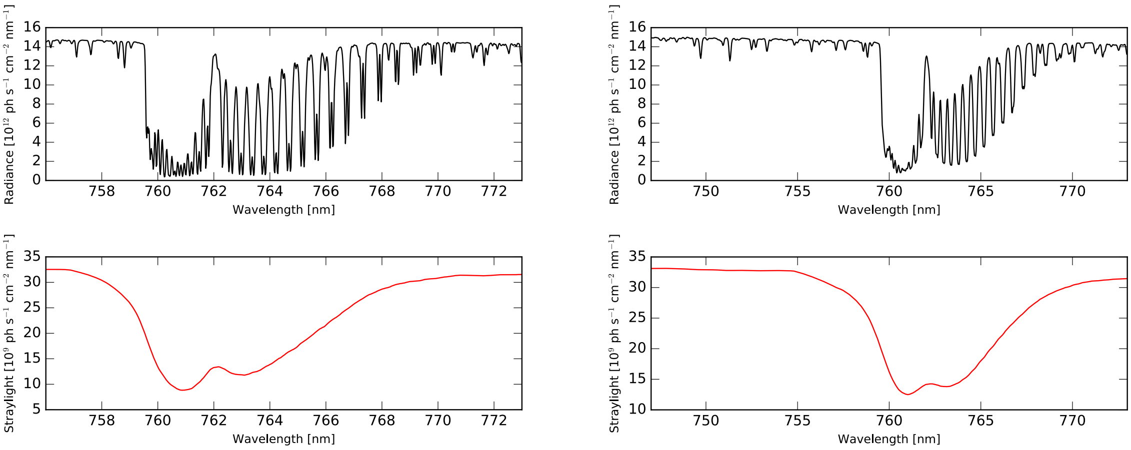

Figure 33: NIR radiance spectra (upper panels) and stray light contributions (lower panels) for the spectral sizing point A (left panels) and B (right panels) for a selected case of the orbit ensemble.

Figure 35 shows the XCO_2 bias due to the simulated stray light for the entire orbit granule and for instrument concept A, B and C. The corresponding bias PDFs are depicted in Figure 39. Overall, the stray light induced XCO_2 bias is very similar for concepts A and C and about a factor of 4-5 smaller than that for concept B with the mean biases $b_A = -0.36\,\mathrm{ppm}$, $b_B = -1.21\,\mathrm{ppm}$, $b_C = -0.24\,\mathrm{ppm}$. At first glance, these results may favour a high spectral resolution concept above a low spectral resolution concept. However, this conclusion is premature and requires further analysis. Concepts A and C differ from concept B not only in spectral resolution but also in the spectral coverage particularly in the SW-2 band. Therefore, we analysed the stray light induced error also for the deviation concepts B′ and B′′, where we gradually enhanced the spectral resolution at the cost of the spectral coverage of the SW-2 band (see Tab. 1 for further specifications). Figures 36 and 39 indicate that omitting the saturated water absorption bands below 1993 nm (the SW-2a band) reduces the biases significantly to $b_{B'} = -0.09\,\mathrm{ppm}$. Omitting also the SW-2b band (1993-2044nm) does not further improve the results with a mean bias of $b_{B''} = -0.12\,\mathrm{ppm}$. This means that the retrievals for the spectral sizing concepts B′ and B′′ are nearly insensitive to instrument stray light. These results raise the question if the improved error performance is only achieved by the reduced spectral coverage or requires at the same time the enhanced spectral resolution of the sizing concepts B′ and B′′ in the SW-2 band. To address this question, we performed XCO_2 retrievals from concept B measurement simulations for a reduced spectral fit window 1993-2095 nm (band SW-2b and SW-2c) and 2044-2095 nm (band SW-2c) adopting to the spectral coverage of concepts B′ and B′′. An example of a radiance spectrum is shown on Fig. 37. The corresponding XCO_2 biases, depicted in Figure 38 and 39 with $b_{B_{bc}} = -0.21\,\mathrm{ppm}$ and $b_{B_c} = 0.12\,\mathrm{ppm}$, are very similar to those of

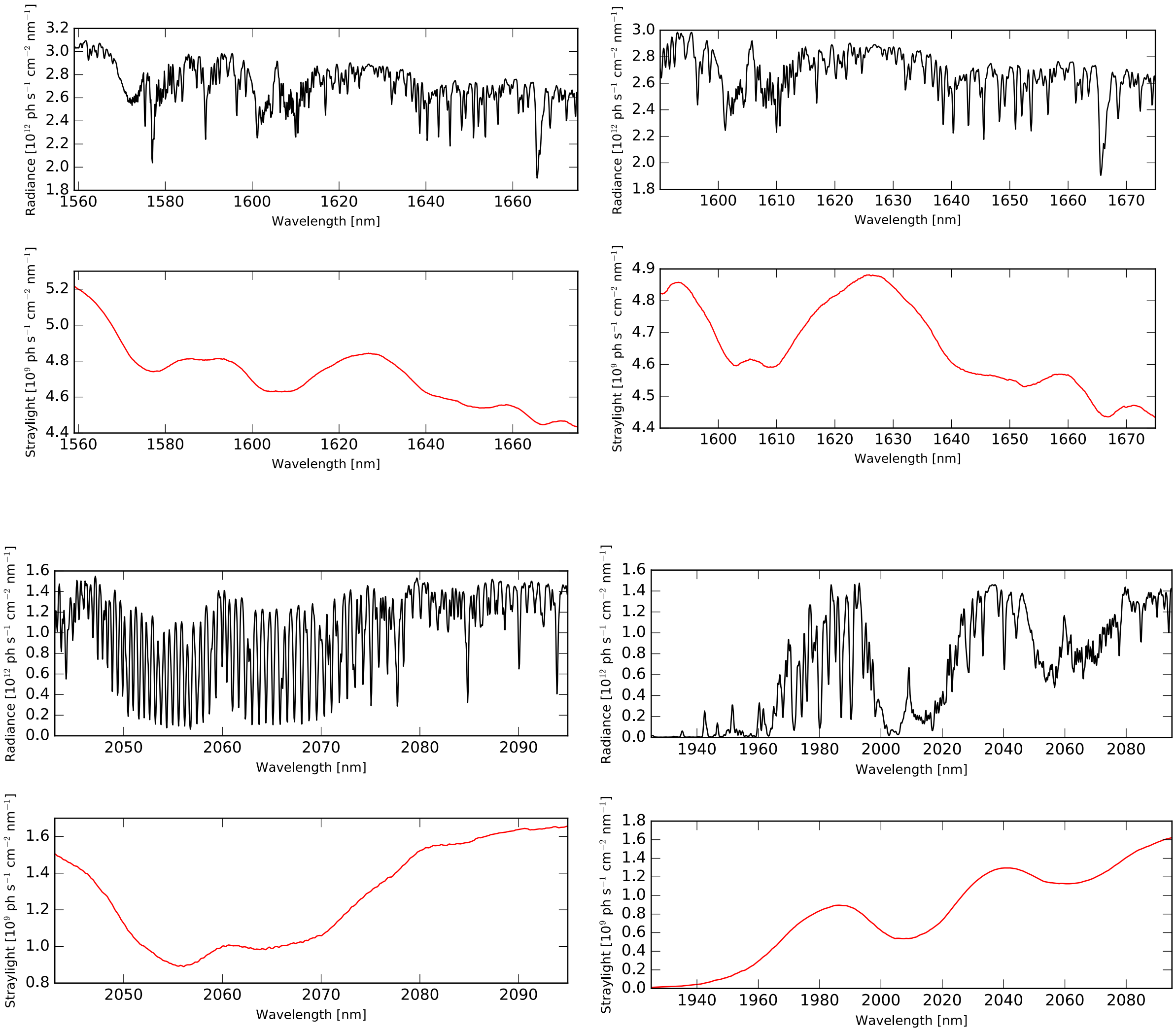

Figure 34: Same as Fig 33 but for the SW-1 (concept A upper left, concept B upper right) and SW-2 the stray light contribution (concept A lower left, concept B lower right).

concept B' and B'', which clearly suggested that the finer spectral resolution of concept B' and B'' is not required to reduce the stray light induced error.

To better understand and evaluate these results, we have to discuss the effect of stray light on the CO_2 product in more detail. Overall, in all spectral bands, stray light fills up the absorption features of the measurement spectrum and so reduces the relative absorption depth. Its impact on the retrieved XCO_2 depends on the band. Filling up of the O_2 absorption lines in the NIR means that the retrieval overestimates the aerosol amount to reduce the atmospheric light path. Consequently, this causes an overestimation of the CO_2 column inferred from the SW bands. Contrary, filling up the CO_2 absorption bands in the SW-1 yields an underestimation of the CO_2 column. For the SW-2 band, it is more difficult to estimate the stray light effect on CO_2. Here, the strong CO_2 absorption features are used to infer aerosol properties from the measurement but also constrain the CO_2 information coming from the SW-1 band. Its overall effect depends on band selection but we assume that certain choices of the retrieval method are also of relevance here.

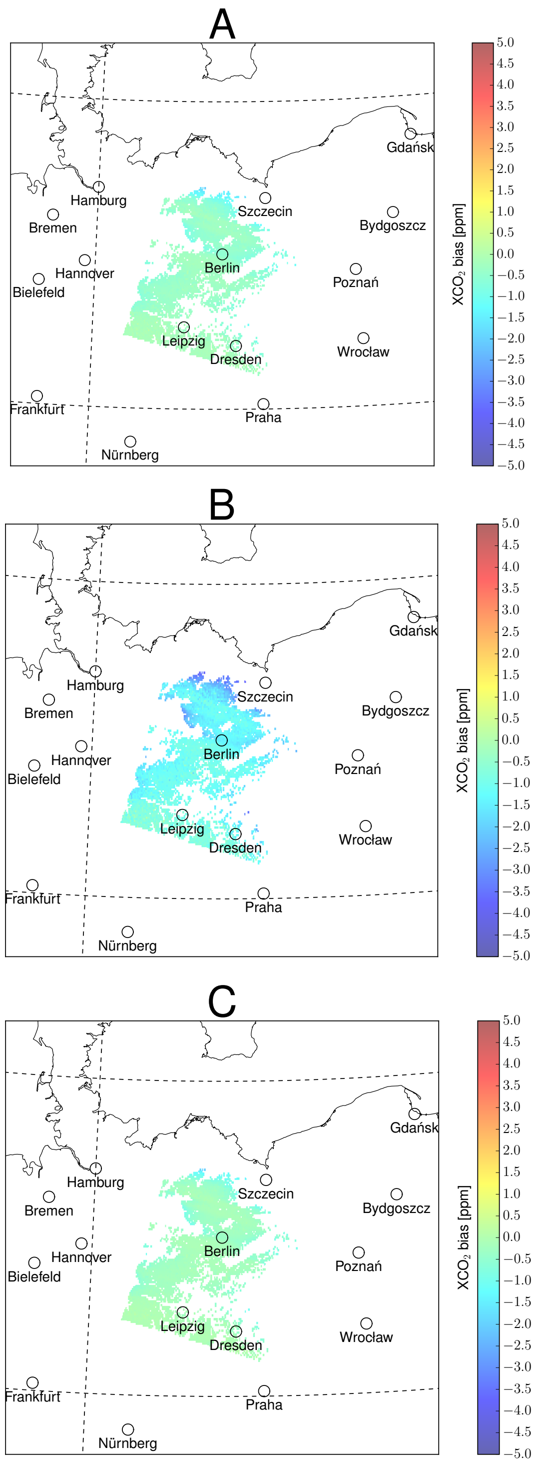

Figure 35: Stray light induced XCO_2 bias for instrument concept A (upper panel), B (middle panel) and C (bottom panel).

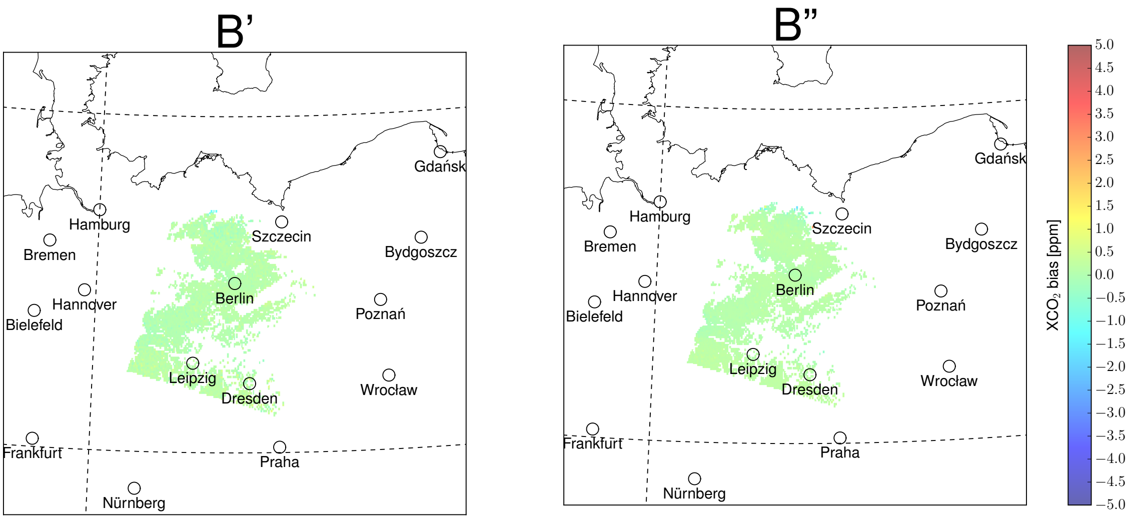

Figure 36: Stray light induced XCO_2 bias for instrument concept B' (left panel) and B'' (right panel).

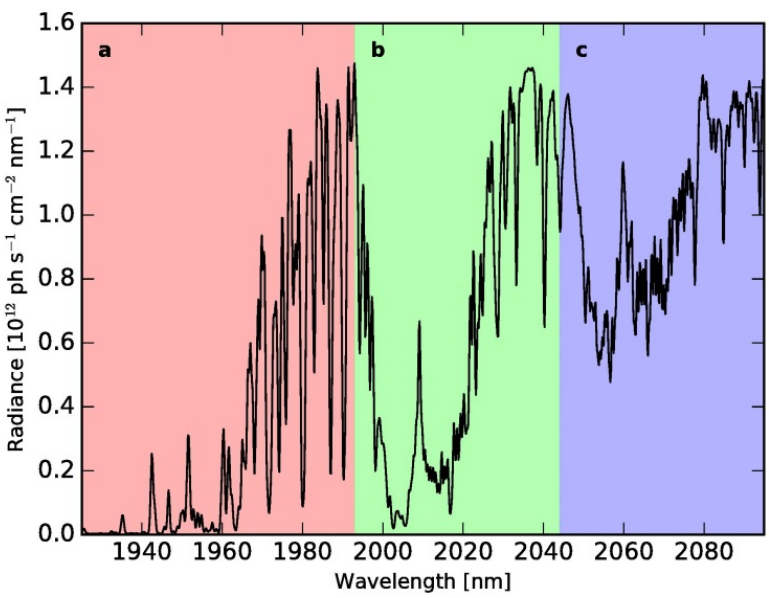

Figure 37: Radiance spectrum in the SW-2a, SW-2b and SW-2c band for spectral sizing concept B.

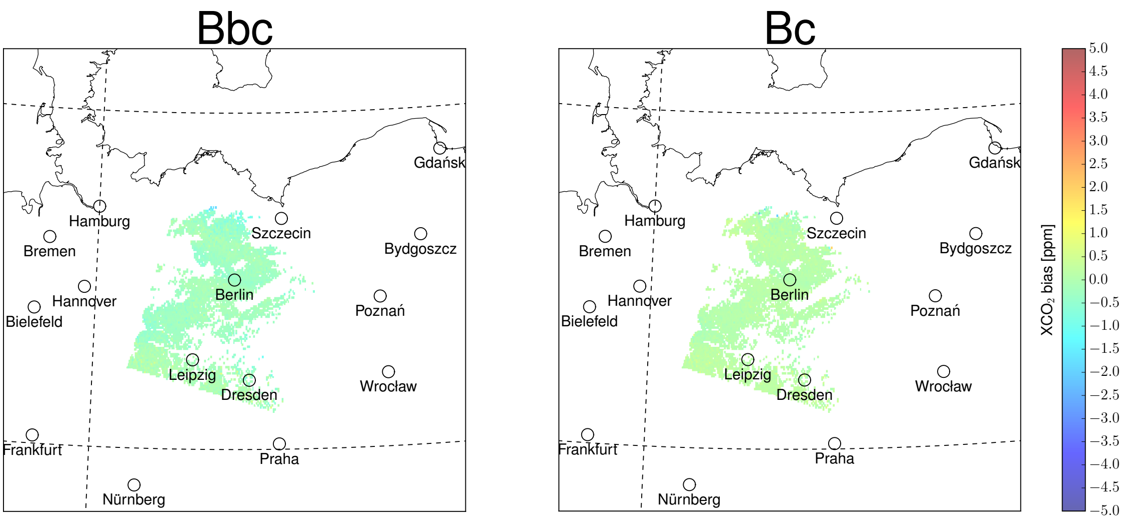

Figure 38: Stray light induced XCO_2 bias for instrument concept B using different spectral fit windows in the SW-2 (SW-2b and SW-2c, 1993-2095 nm, left panel) and (SW-2c, 2044-2095 nm, right panel). All other settings are the same as for concept B retrievals.

Figure 40-43 show the PDFs of the stray light induced biases for orbit ensemble O1 if stray light is added to measurements of all three bands and added separately to the single bands. For all instrument settings and band selections, stray light in the NIR causes an overestimation of XCO_2, whereas SW-1 stray light induced an underestimation of XCO_2, as expected. Also, SW-2 stray light causes an underestimation of XCO_2 but its relative effect with respect to the SW-1 stray light, differs very much between the concepts. Moreover, adding up the mean biases of the single band error analysis estimates very well the mean bias of three band stray light analysis. This supports the assumption of linear error propagation, which allows us to consider individual error sources for the evaluation. Moreover, it shows that the striking low stray light sensitivity of concepts A and C is not due to an overall low sensitivity but due to a beneficial cancellation of errors introduced by the different bands. The larger overall stray light induced XCO_2 bias of concept B is caused by a less beneficial distribution of biases between the bands, which could easily be changed by a different selection of fit windows (for example the retrieval simulation of case B_{bc}). Therefore, we use the performance analysis for case B_{bc} as reference for concept B. Based on this, we conclude that concepts A, B and C show a similar sensitivity to instrument stray light and correcting stray light by a factor of 4, the retrieval biases are acceptable for a future CO_2 mission.

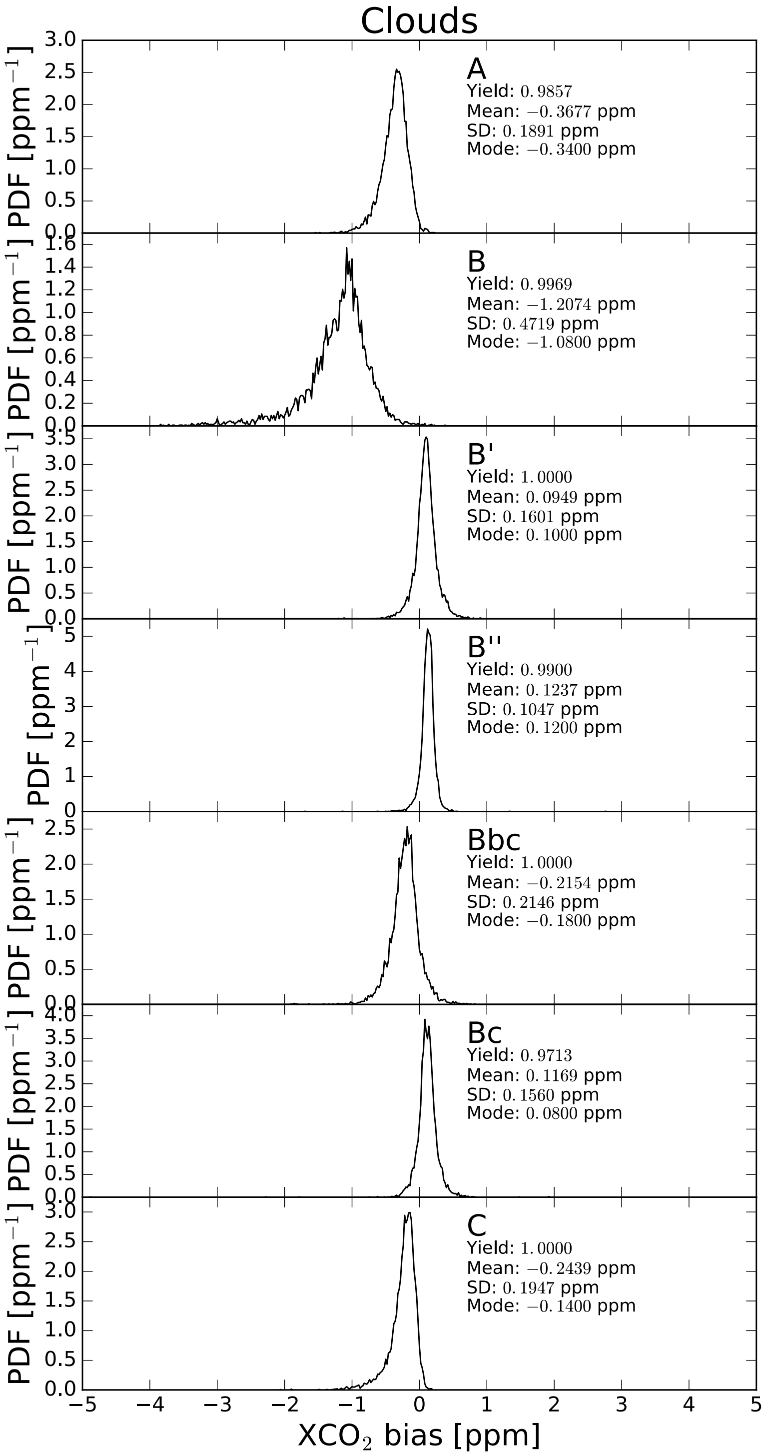

Figure 39: PDFs of the stray light induced XCO_2 bias for the measurement ensemble O1 and instrument concepts A, B, B′, B′′, and C, shown in Fig. 35 and 36. Additionally the PDFs are shown for concept B with a reduced SW-2 fit window with the XCO_2 biases depicted in Fig. 38.

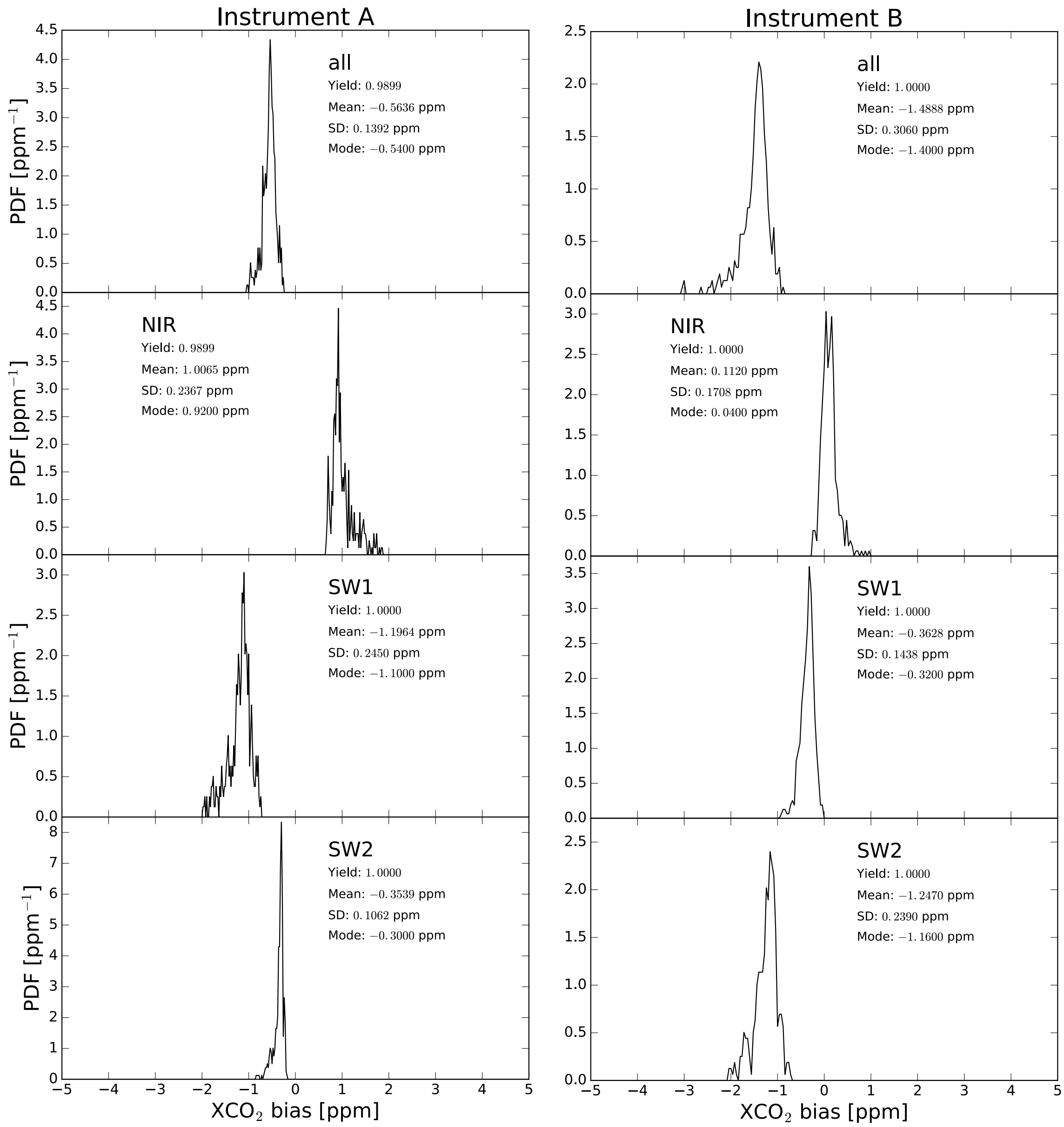

Figure 40: Bias PDF for stray light induced errors due to stray light in all three spectral band (upper panel), only in the NIR (second panel from top), only in the SW-1 (third panel from top) and only in the SW-2 (lower panel). Results are shown for concept A and B.

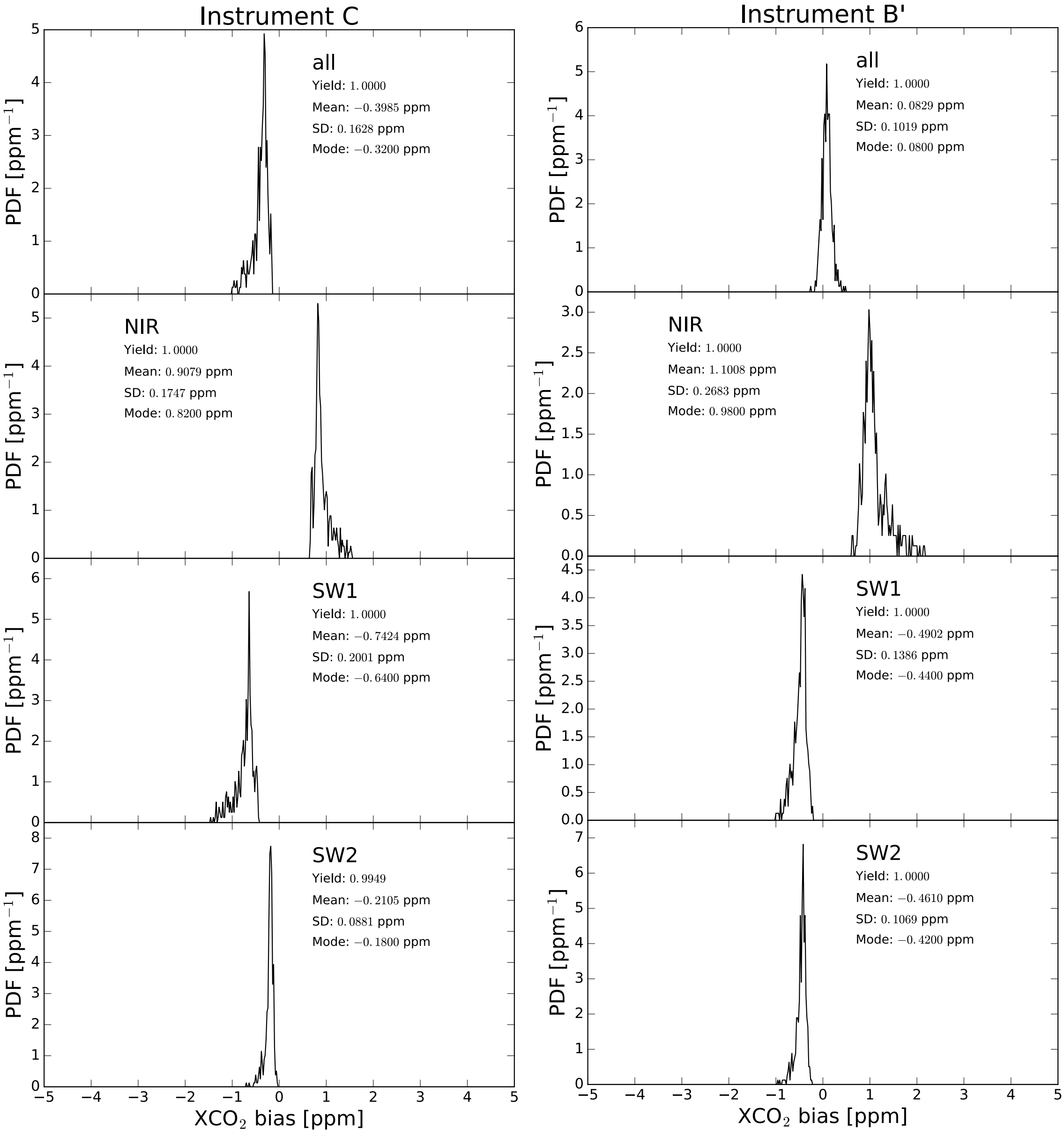

Figure 41: Same as Fig. 40 but for concept C and B'.

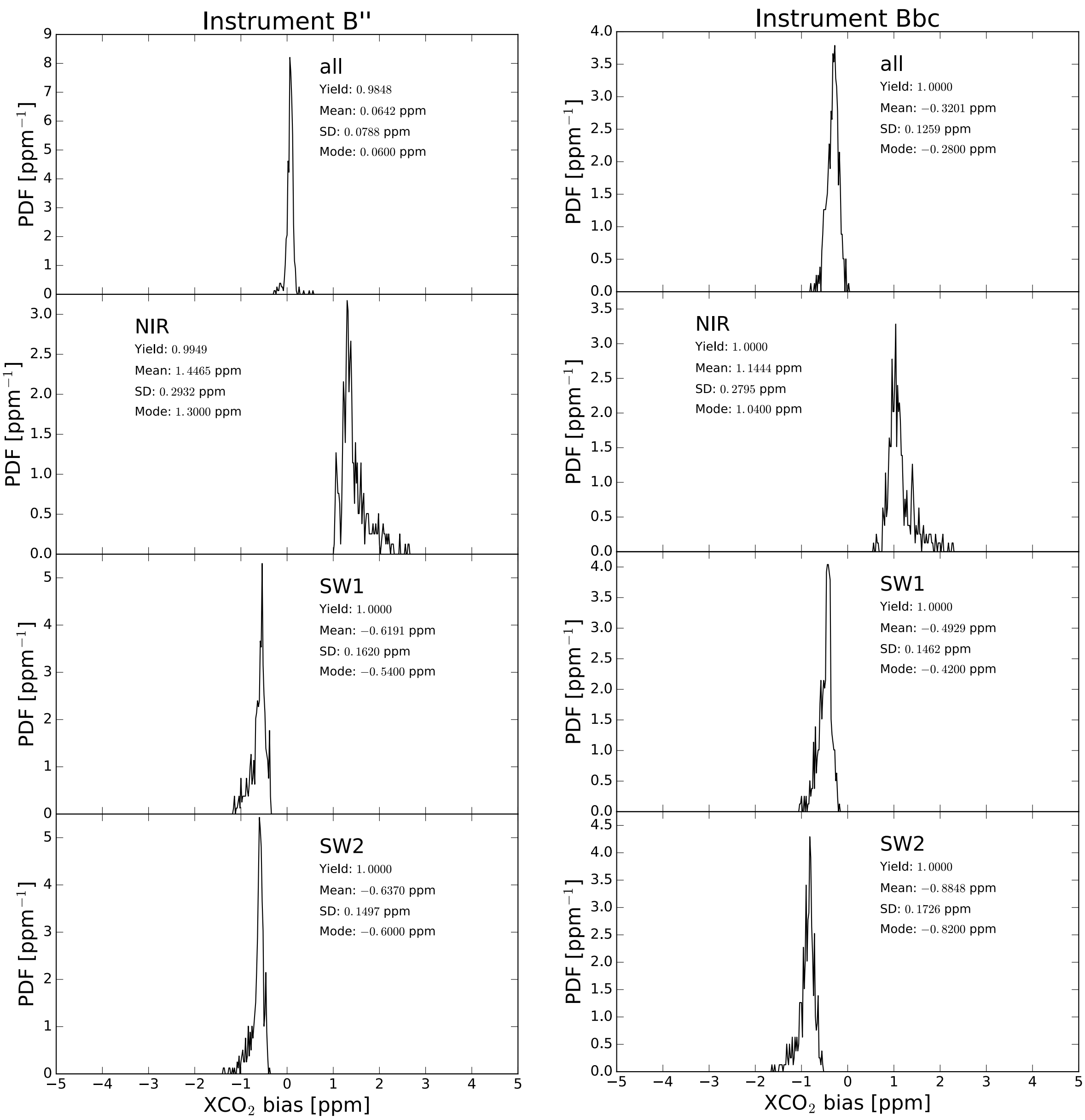

Figure 42: Same as Fig. 40 but for concept B'' and B_{bc}

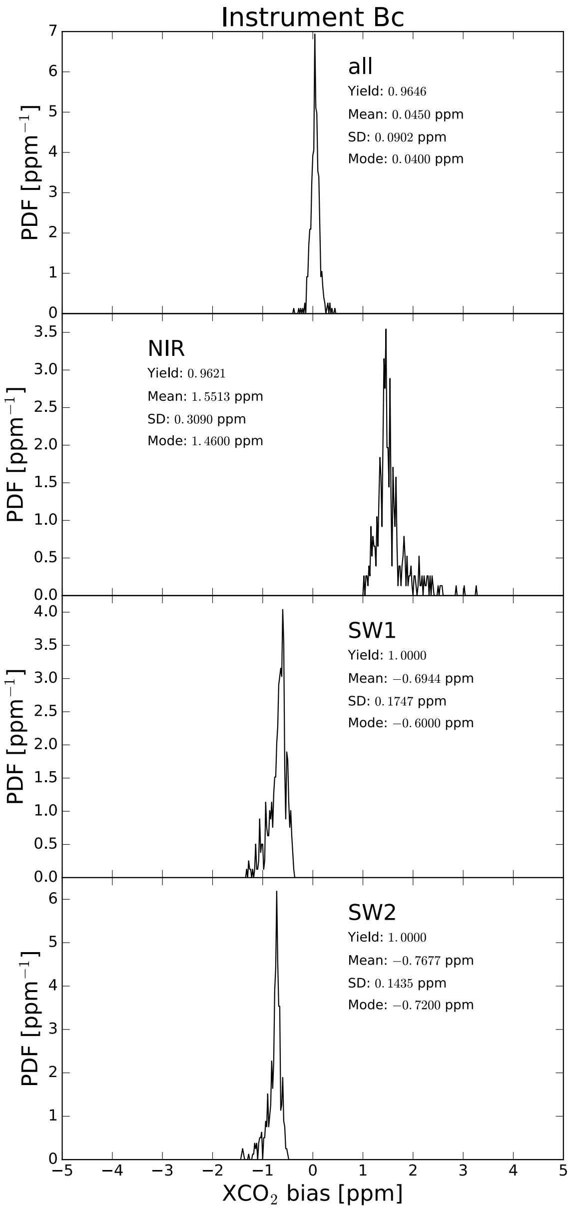

Figure 43: Same as Fig. 40 but for concept Bc

9 Conclusions

This report summarizes our results of WP 2100 on XCO_2 biases due to instrument related systematic errors for six different spectral sizing concepts covering the NIR, SW-1 and SW2 band, which adapted from designed and launched spectrometers. Here, sizing point B (CarbonSat V1.2, AD-2) has the lowest spectral resolution, whereas sizing point C (OCO-2) and D (MicroCarb) have the highest spectral resolution in all three bands. Sizing point A (CarbonSat V1.0, AD-1) can be considered as an intermediate case with high spectral resolutions in the NIR and SW-2 band and with a low spectral resolution in the SW-1 band. Moreover, we considered the deviated concept B′ and B′′, which are identical to concept B except for a higher spectral resolution of the SW-2 band on the cost of a reduced spectral band width. The SNR performance of the measurement simulation is taken from the existing instrument concepts. We analysed radiometric errors due to six different ISRF distortions, a radiometric offset, detector non-linearity, instrument polarization sensitivity and stray light within the spectrometer. Here, the spectral errors are not considered to be specific for the different spectrometers but are representative for a CO_2 grating spectrometer and are carefully adapted to the different spectral sizing point for an appropriate comparison. To draw robust conclusions, XCO_2 retrievals are performed on global and regional ensembles of simulated measurements, which allows us to evaluate the presence of large-scale and regional bias variation. All retrieval simulations are performed with the RemoTeC software with sound real-world heritage from GOSAT and OCO-2 data processing. For the ISRF distortion, we achieved largest XCO_2 biases for a compression of the ISRF shape (distortion 1) with significant regional patterns. Here the spectral sizing point B has the smallest absolute mean bias of 0.38 ppm, sizing point A, C and D have larger mean biases of 1.78, 2.73 and 2.62 ppm, respectively. The radiometric offset was adopted from CarbonSat requirements AD-2 and has only a small effect on the retrieved XCO_2. Differences are not significant enough to favour one sizing point over the others. Errors due to detector non-linearity were investigated only for sizing point A and B with a mean bias of -1.55 and -7.12 ppm. For both concepts and for the global measurement ensemble, the bias probability distributions have large side lobes with asymmetrically distributed outliers. Therefore, we are reluctant to interpret the mean bias as a valuable diagnostic tool and considered also the absolute mode m of the distribution as a relevant diagnostic with $m_A = 3.32$ ppm and $m_B = 1.28$ ppm. We concluded that for both cases an uncorrected detector non-linearity introduces significant XCO_2 biases and none of the two sizing points show a beneficial performance. Furthermore, the instrument polarisation sensitivity as provided by the agency for an elaborated instrument concept does not cause any significant XCO_2 bias for the sizing points A, B, C and D. Finally, for spectral sizing concept A, B, and C, we investigated the impact of stray light on XCO_2 for simulated measurements of an orbit granule around Berlin. Using the CarbonSat stray light model, we assumed that the instrument stray light can be corrected with a factor 4 by an appropriated correction approach as part of the Level-0 to -1 processing. The ensemble comprises realistic cloud coverage. We found very similar stray light induced errors with an absolute mean bias of 0.37, 0.09 and 0.24 ppm for the sizing point A, B, and C. Here, we used the reduced spectral fit window 1993-2095 nm (SW-2b and SW-2c) for the data processing of concept B measurement simulations. These low biases are achieved by a cancellation of errors due to stray light in the different spectral bands. Here, the degree of cancellation depends on the specific band width and can be tuned by adjusting retrieval fit windows. Therefore, we consider the differences in the stray light induced errors for the different sizing concepts as non-significant for the design of a future instrument. The error diagnostics of all instrument-induced errors are summarized in Figure 44. Overall, we conclude that the XCO_2 biases due to instrument related errors for the spectral sizing concept B are similar or even smaller than those for the other concepts.

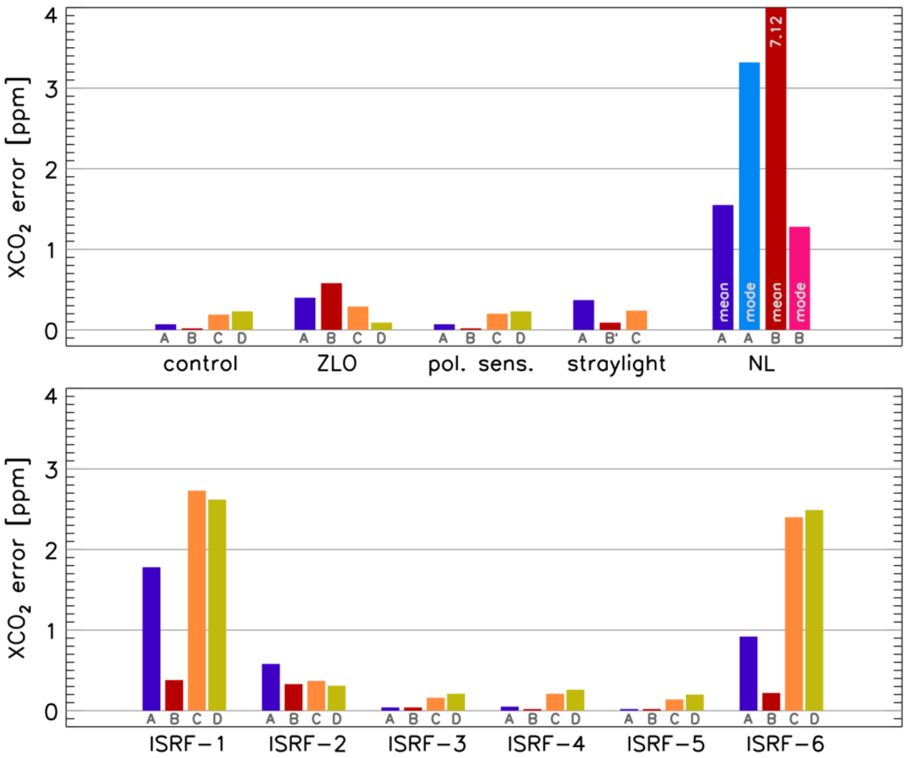

Figure 44: XCO_2 retrieval biases due to instrumental errors for spectral sizing concept A, B, C and D, derived with the RemoTeC retrieval algorithm for global and in case of stray light regional test ensembles. The figure includes the absolute mean bias for the control runs, radiometric offset (ZLO), the polarization sensitivity, spectrometer stray light, detector non-linearity (NL), and six different ISRF distortions. For detector non-linearity, also the absolute mode of the XCO_2 bias distribution is depicted.

Appendix A: The equal resolving power sizing point ER - WP A200

This section summarizes our results for the additional spectral sizing point ER as performed in WP A200 of this study, which assumes the same spectral resolving power in all three bands. The sizing point is specified in Tab 1 and compared to concept B mainly the band width of the SWIR-2 band is changed, i.e. that the SWIR-2a band is not include but covers the range 1993-2295 nm with a resolution of 0.32 nm instead of 0.3 for spectral sizing point B. To evaluate the effect of this modification, we compared the instrument specific error induced by

- ISRF distortion
- Radiometric offset
- Polarization error
- Detector non-linearity
- Straylight

as described in the Sections 4-8 of this report but for sizing point B and ER. The errors are analysed for the global ensemble G2 as described in Sec. 2.

ISRF distortion

Considering the six ISRF distortion given in Fig 10, we conclude also for the sizing point ER that the distortion 3 and 4 only induces minor errors because it is mitigated by the retrieval due to the adjusted spectral shift. The XCO2 error distribution functions for distortion 1,2,5 and 6 are depicted in Fig. 45 and shows as expected that the sensitivity to ISRF knowledge errors increases for the higher spectral resolution of sizing point ER. This is an agreement with our findings of Sec. 4.

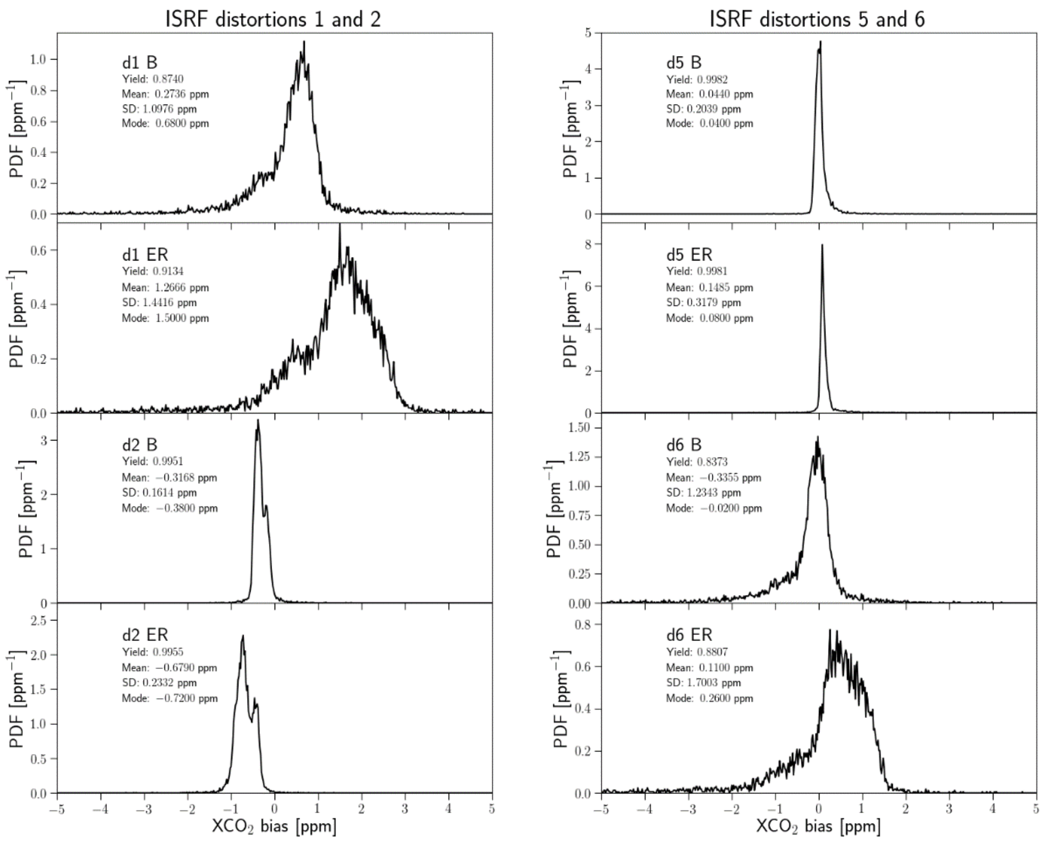

Figure 45: XCO_2 biases for the global ensemble G2 induced by the ISRF knowledge error (distortion d1,d2,d5, and d6 in Fig 10) for the spectral sizing point B and ER.

Radiometric offset

Superimposing the measurement simulation with a radiometric error given in Tab. 2, induced the XCO_2 error as depicted in Fig. 46. Both for sizing point B and ER, the biases are very similar with a mean bias pf 1.06 and 1.08 ppm for concept B and ER, respectively, a standard deviation of 2.07 ppm and 2.3ppm and a mode of 0.12 and 0.18 ppm for both distribution. Therefore, we conclude that the sensitivity of both concepts to radiometric offset is very similar and of little relevance for the evaluation of the spectral sizing point.

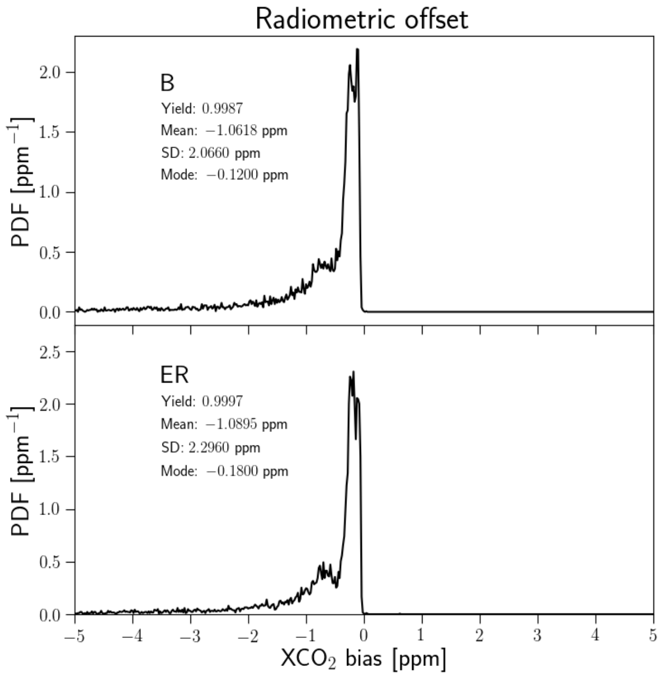

Figure 46: XCO_2 biases for the global ensemble G2 induced by a radiometric offset as specified in Tab. 2 for the spectral sizing point B (top) and ER (bottom).

In Section 7 of the document, we already concluded that the polarisation errors as described in RD-1 are of little relevance of the XCO2 uncertainty estimate. This is also confirmed for sizing point ER (not shown).

Stray light

Section already indicated spectrometer stray light as an important contribution to the XCO2 error budget. To extend the analysis by the spectral sizing point ER, Fig. 47 shows the stray light induced error for the orbit ensemble O1-O3, which include (a) cloudy sky scenarios for the CO_2 background distribution, (b) clear sky scenarios considering CO_2 plumes of coal plants, and (c) clear sky scenarios for the CO_2 background distribution. For all three ensembles, the stray light induced error is smaller than for concept B, which is mainly due to a different partitioning of errors from the different spectral bands, as depicted in Fig. 48. Here, the straylight induced error from the SWIR-2 band is significantly smaller for concept ER compared to B due to the band width, and the straylight errors from the NIR and SWIR-1 band cancel out very well for concept ER. We would like to emphasise not to overinterpret the results as an optimized stay light mitigation approach. The analysis does not include any realistic approach to correct stray light as part of the level 1A to 1B processing and so only indicates an overall sensitivity to stray light rather than a reliable error estimate for a certain instrument.

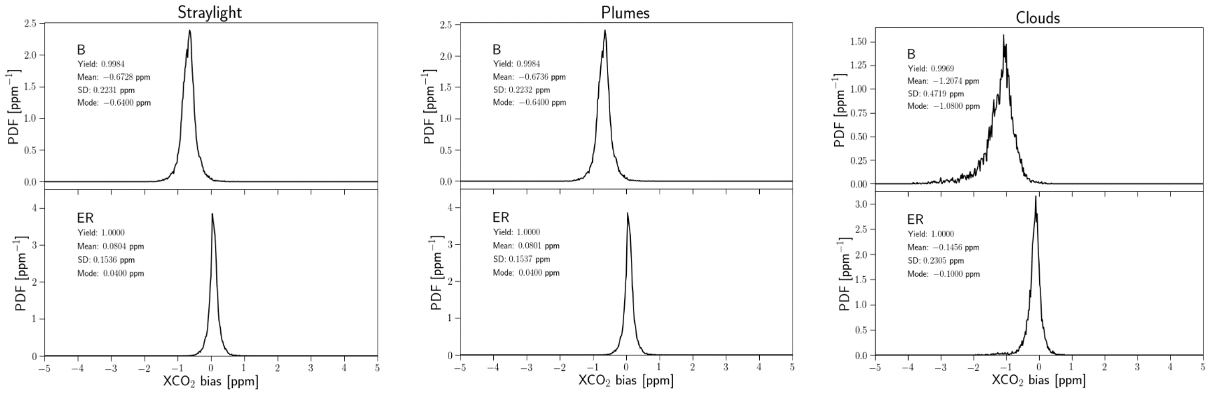

Figure 47: Stray light analysis analogous to Fig. but for spectral sizing point B and ER and the orbit ensemble O1 (right), O2 (middle), and O3 (left).

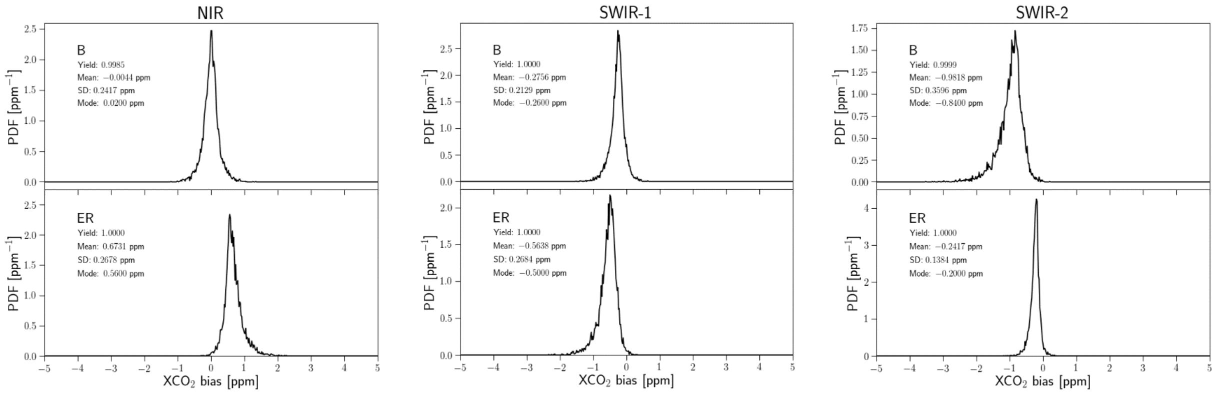

Figure 48: Band resolved stray light error for concept B (top) and ER (bottom).

Conclusion: Instrument induced errors for spectral sizing point ER

For spectral sizing point ER, all instrument induced errors preform as expected from the error analysis for the remaining sizing points. Inline with the study conclusions in Sec. 9 and due to the difference and band width and spectral resolution, we conclude that

- For spectral sizing point ER, retrievals from simulated measurements are more sensitive to ISRF knowledge error than those for sizing point B.
- Stray light induced XCO_2 errors of sizing point ER are smaller than those for sizing point B, mainly due to the reduced spectral width of the SWIR-2 band.
- For all other error sources, we found not significant difference of the sensitivity to instrument induced XCO_2 errors.

References:

RD-1: Landgraf, J., aan de Brugh, J., Butz A., Graf K., Specification of Instrument Spectral Sizing Concepts, Spectral Errors and Geo-Physical Scenarios, SRON-CSS-TN-2016-002

RD-2: Butz A. Graf, K, Landgraf, J., aan de Brugh, L., Study on Spectral Sizing for CO2 Observations (CSS) D3 – CO_2 errors due to measurement noise and atmospheric scattering for the, DLR, 2017

RD-3: Haring R., Randy Pollock R., Sutin B.M., Crisp D.: The Orbiting Carbon Observatory instrument optical design, Proc. SPIE 5523, Current Developments in Lens Design and Optical Engineering V, (14 October 2004); doi: 10.1117/12.562693

RD-4: Frankenberg, C., Pollock, R., Lee, R. A. M., Rosenberg, R., Blavier, J.-F., Crisp, D., O'Dell, C. W., Osterman, G. B., Roehl, C., Wennberg, P. O., and Wunch, D.: The Orbiting Carbon Observatory (OCO-2): spectrometer performance evaluation using pre-launch direct sun measurements, Atmos. Meas. Tech., 8, 301-313, doi:10.5194/amt-8-301-2015, 2015.

RD-5: Osterman, et al.: Orbiting Carbon Observatory–2 (OCO-2) Data Product User’s Guide, Operational L1 and L2 Data Versions 6 and 6R, Version D, Data Releases 6 and 6R, March 30, 2015

RD-6: Osterman, et al.: Orbiting Carbon Observatory–2 (OCO-2) Data Product User’s Guide, Operational L1 and L2 Data Versions 7 and 7R, Version D, Data Releases 7 and 7R, June 30, 2016

RD-7: Butz, A., Galli, A., Hasekamp, O., Landgraf, J., Tol, P., and I., A.: TROPOMI aboard Sentinel-5 Precursor: Prospective performance of CH4 retrievals for aerosol and cirrus loaded atmospheres, Remote Sens. Envirom., 120, 267, 2012.

RD-8: Hu, H., Hasekamp, O., Butz, A., Galli, A., Landgraf, J., Aan de Brugh, J., Borsdorff, T., Scheepmaker, R., and Aben, I.: The operational methane retrieval algorithm for TROPOMI, Atmos. Meas. Tech., 9, 5423-5440, doi:10.5194/amt-9-5423-2016, 2016.

AD-1: CarbonSat Mission Requirements Document, EOP-SMA/2232/PI-pi, version 1.0

AD-2: CarbonSat Mission Requirements Document, EOP-SMA/2232/PI-pi, version 1.2

Painted papers category

Study on Spectral Sizing for CO_2 Observations (CSS)

CO_2 errors due to measurement noise and atmospheric scattering for the different spectral sizing concepts of a CO_2 instrument

DLR

Document properties

Title	D3 – CO_2 errors due to measurement noise and atmospheric scattering for the different spectral sizing concepts of a CO_2 instrument
Subject	Study on Spectral Sizing for CO_2 Observations (CSS)
Institute	Institute of Atmospheric Physics (IPA), Deutsches Zentrum für Luft- und Raumfahrt e.V. (DLR), Oberpfaffenhofen, Germany Netherlands Insitute for Space Research (SRON), Utrecht, The Netherlands
Compiled by	André Butz (DLR), Kaspar Graf (DLR), Jochen Langraf (SRON), Joost aan den Brugh (SRON)
Date	May 23, 2017
Version	1.1

Index of contents

1. Summary

The retrieval of the column-average mole fraction of carbon dioxide (XCO_2) from solar backscatter soundings in the near and shortwave infrared spectral range suffers from various error sources. Here, we investigated how fully random noise errors and systematic aerosol- and cirrus induced errors propagate into XCO_2 errors for four candidate instrument concepts (A,B,C,D) of a future CO_2 monitoring satellite. These instrument concepts in particular differ in their spectral sizing (spectral coverage, spectral resolution, signal-to-noise-ratio). Concept A and B are derived from the early and the later CarbonSat concept, respectively. Concept B in particular adopts relatively low spectral resolution and thereby gains spectral coverage and signal-to-noise. Concepts C and D are derived from the OCO-2 (Orbiting Carbon Observatory) and the MicroCarb concepts, both featuring relatively high spectral resolution and narrower spectral coverage.

The error evaluation is based on retrieval simulations for a global ensemble (G1) of realistic atmospheric and surface scenarios to be encountered by a space borne observer. The ensemble covers roughly 8600 scenes. Fully random noise errors for XCO_2 are calculated via linear error analysis i.e. by Gaussian error propagation of the instrument specific measurement noise. Aerosol and cirrus induced errors are assessed by using a highly sophisticated radiative transfer model for simulating the satellite measurements and then, using an approximate radiative transfer scheme for the retrieval. The difference in radiative transfer complexity induces a forward model error for XCO_2 which we refer to as the aerosol and cirrus induced error. Essentially, an instrument concept is considered better than another one if the noise error is lower and if it succeeds in better mitigating aerosol and cirrus induced XCO_2 errors.

The XCO_2 noise errors for concepts A, B, and C are typically less than 1 ppm (0.5 ppm) for more than 90% (75%) of the geophysical test cases. Concept D shows significantly larger noise errors with about 75% (50%) of the cases below 1 ppm (0.5 ppm) implying particularly large errors for low sun and dark surfaces i.e. under high-latitude and winter conditions. Figure S1 summarizes our findings on noise errors. Beside the differences in instrument-related measurement noise, it is spectral coverage of CO_2 absorption lines which affects the propagation of noise errors into XCO_2. Since the SW-2 channel (around 2000 nm) of concept D is spectrally located in-between two CO_2 absorption bands, the number of CO_2 absorption lines contributing to the CO_2 retrieval is lower than in concepts A, B, and C.

For the systematic aerosol and cirrus induced XCO2 errors, all concepts show errors < 2 ppm for 50 % (< 4 ppm for 70 %) of the ensemble members, where the performance differences among the concepts are small. Here, concept D (63% < 2 ppm, 82% < 4ppm) is slightly better than A (58% < 2 ppm, 80% < 4ppm), A is slightly better than C (54% < 2 ppm, 76% < 4 ppm), C is almost equal to B (B1: 51% < 2 ppm, 71% < 4 ppm; B2: 55% < 2 ppm, 76% < 4 ppm; B3: 57% < 2 ppm, 78% < 4 ppm). Figure S2 summarizes our findings on aerosol and cirrus induced XCO_2 errors. Performance can be improved for all concepts by employing filters that screen complex scattering scenarios or low sun conditions.

Concept B is the only concept with such wide spectral coverage in the SW-2 band to cover the highly absorbing water vapor bands below 1950 nm wavelength. The water bands have been suggested to be used for the retrieval of cirrus cloud properties and thus, for improved XCO_2 retrievals under cirrus conditions. The retrieval software RemoTeC used here is not (yet) suited for evaluating this possible improvement. In the past, however, the 1950 nm range has already been used for successful cirrus screening.

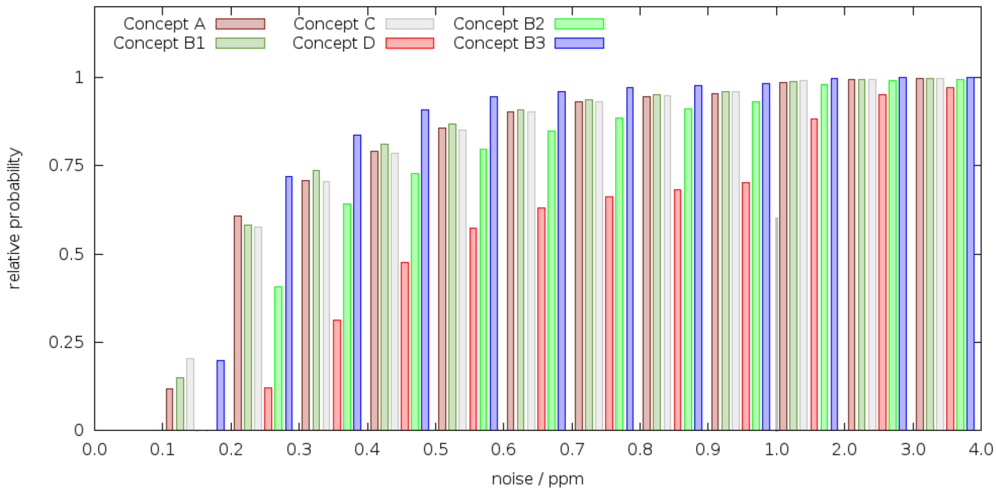

Figure S1. Cumulative histogram of the XCO_2 noise errors for the retrieval concepts A, B1, B2, B3, C, and D. B1, B2, and B3 are retrieval configurations that choose different retrievals sub-windows out of the SW-2 band of concept B. Please note the change in the x axis scale at values of 1 ppm.

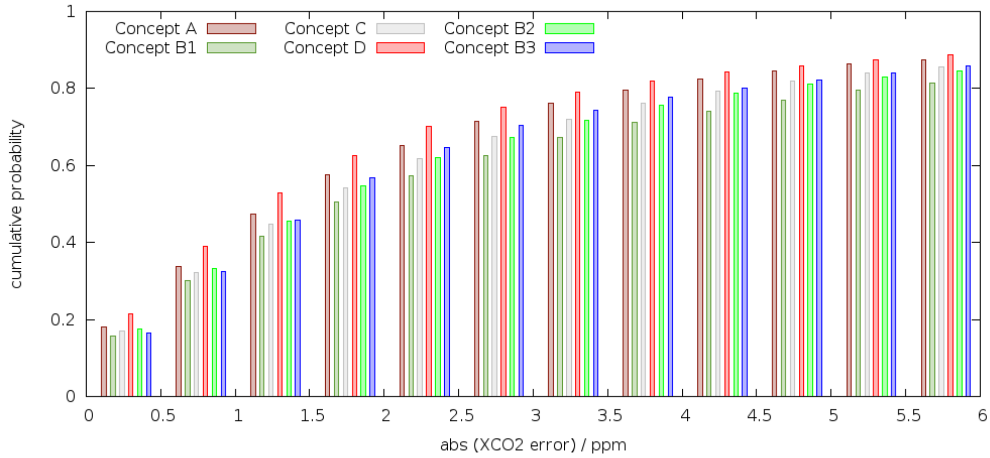

Figure S2. Cumulative histogram of the aerosol and cirrus induced XCO_2 error for the retrieval concepts A, B1, B2, B3, C, and D. B1, B2, and B3 are retrieval configurations that choose different retrievals sub-windows out of the SW-2 band of concept B. For Details see manuscript.

2. Introduction

CO_2 retrieval errors due to unaccounted lightpath modification by aerosols, cirrus and thin clouds are among the largest contributors to the systematic error budget of space-based CO_2 remote sensing missions. Thus, instrument concepts to be implemented for future carbon monitoring satellites must enable the retrieval of atmospheric scattering properties together with the targeted column-average concentrations. The ability to support such retrievals and to mitigate particle-induced CO_2 errors is an important criterion for prioritizing certain instrument designs. Typically, spectral coverage and spectral resolution are found important design factors that impact the retrieval of scattering parameters and on the other hand, somewhat depending on the type of instrument, these parameters impact the achievable signal-to-noise ratio (SNR). Thus, the spectral sizing of a CO_2 mission largely controls the budget of systematic and random retrieval errors.

Spectral coverage relates to several aspects: covering a wide spectral range, covering optically thin and optically thick absorption lines, covering absorption by molecules with a priori known atmospheric concentrations. Wide spectral coverage provides information on the spectral dependence of the particle scattering properties. They typically vary only mildly with wavelength and thus, wide coverage is required. Such spectral information relates to the microphysics of the particles i.e. the sizes (e.g. effective radii) and the optical composition (e.g. refractive indices). Wide spectral coverage also implies coverage of a range of surface reflection properties. Bright surfaces favor multiple scattering events, dark surface favor single scattering. Covering optically thin and optically thick absorption lines also allows for probing different regimes of single- and multiple-scattering effects. Regions with optical thick absorption lines are typically sensitive to single-scattering effects since heavy absorption does not allow for long atmospheric lightpaths. Optically thin regions, in contrast, can be subject to lightpath enhancing multiple scattering effects e.g. via multiple scattering events between a particle layer and the ground. Covering absorption by molecules with a priori know abundances such as O_2 has the clear advantage that residual differences between the measured and the simulated spectra cannot be due to erroneous knowledge of the absorber concentrations but must be attributed to erroneous modelling of the lightpath and thus, scattering information can be inferred. Heavy absorption by lower tropospheric gases such as H_2O can be used to attribute scattered light to scattering events above the highly absorbing gas layer in the lower atmosphere e.g. facilitating the detection of thin cirrus in the upper atmosphere.

The impact of spectral resolution on the retrieval of scattering properties refers to the ability of the spectrometer to resolve the actual depth of absorption lines, the shape of absorption lines, and the continuum in-between the absorption lines. The benefit of resolving the actual depth of the absorption lines comes along with actually resolving a wide range of absorption optical thickness and thus, different regimes of single- and multiple scattering. The shape of absorption lines carries information from different altitude in the atmosphere. If a substantial fraction of the detected photons was backscattered to the satellite at high altitude, the upper atmospheric layers (at lower pressure and temperature) would have larger relative contribution to the absorption line than the lower atmosphere. Thus, the line shape would be thinner than for a non-scattering lightpath. Resolving continuum radiances in-between lines is important to get a handle on spectral variations of surface reflection which need to be disentangled from the spectrally mildly varying scattering properties of the atmosphere.

Here, we evaluate the retrieval performance of four instrument designs proposed for a future CO_2 observing mission. The instrument concepts in particular differ by their spectral sizing, i.e. spectral coverage, spectral resolution and SNR. Our performance evaluation focuses on quantifying the systematic errors induced by unaccounted aerosol and cirrus scattering effects. For completeness, we also report the random CO_2 noise errors to be expected. To this end, we run simulated retrievals for each of the concepts for a global ensemble of realistic atmospheric scenarios. For the random noise errors, we evaluate error propagation in linear approximation. For the systematic aerosol and cirrus induced errors, we compare the retrieved column-average mole fractions of CO_2 (XCO_2) to the simulation truth.

3. Simulation and retrieval methods

3.1. The full-physics algorithm RemoTeC

Estimating the CO_2 total column concentration from solar backscatter measurements faces the challenge that the light-path from the sun to the satellite observer via backscattering at the Earth's surface is not known with sufficient accuracy. In practice, light scattering by atmospheric particles causes unknown lightpath modification. As a consequence state-of-the-art retrieval algorithms must retrieve particle properties simultaneously with the CO_2 concentration. Therefore, RemoTeC aims at retrieving the CO_2 vertical profile (with slightly more than 1 degree of freedom) and 3 scattering parameters characterizing the particle amount, size and height. Particle amount is represented through the total column number density of particles. For the particle number density size distribution, RemoTeC assumes a power-law with the power of the particle radius as retrievable parameter. The particle height distribution is a Gaussian function of center height, where center height is retrieved and the width is fixed to 2 km. Particle refractive index is assumed fixed-value at m_r=1.400 and m_i=-0.003. The retrieval method infers the CO_2 partial column concentration profile, the three aforementioned particle parameters, interfering absorber concentrations of CH_4 and H_2O as well as some auxiliary parameters such as surface albedo by iteratively minimizing the Phillips-Tikhonov cost function discussed in detail below.

Generally, remote sensing methods aim at inferring a state vector $\mathbf{x}$ (with x_j the j-th retrieval parameter) from measurements $\mathbf{y}$ (with y_i the i-th measurement). Here, the measurements are simulated spectra of sunlight backscattered by the Earth's surface and atmosphere to the space-based spectrometer at various shortwave-infrared wavelengths λ_i. The retrieval parameters are the parameters discussed above, most importantly the partial columns of CO_2 in 12 atmospheric layers. The forward model $\mathbf{F(x)}$ relates the atmospheric state $\mathbf{x}$ to the measurements $\mathbf{y}$ through

$$\mathbf{y} = \mathbf{F}(\mathbf{x}) + \mathbf{e}_{\boldsymbol{y}} + \mathbf{e}_{\mathbf{F}} \qquad (1)$$

where $\mathbf{e_y}$ is the measurement noise error, and $\mathbf{e_F}$ the forward model error.

In order to infer $\mathbf{x}$, equation (1) has to be inverted which is non-trivial since the inverse problem is generally ill-posed, ie. the measurements contain insufficient or inconsistent information on the state variables to be estimated. The method employed here is based on Philipps-Tikhonov regularization which finds the solution state $\hat{\mathbf{x}}$ by minimizing the Phillips-Tikhonov cost function

$$\hat{\mathbf{x}} = \mathrm{argmin}(\, ||\mathbf{S}_{\boldsymbol{y}}^{-\mathbf{1/2}}[\mathbf{F}(\mathbf{x}) - \mathrm{y}]||^2 + \gamma||\mathbf{L}(\mathbf{x} - \mathbf{x_a})||^2) \qquad (2)$$

where $\mathbf{S_y}$ is the measurement noise error covariance matrix, $\mathbf{L}$ a weighting matrix, γ the regularization parameter, and $\mathbf{x_a}$ an a priori estimate of the state. In our case $\mathbf{L}$ is the first order difference operator for the CO_2 elements of the state vector, the identity matrix for the aerosol parameters and 0 for all other parameters. In the limiting case γ=0, equation (2) reduces to the least-squares solution. If $\gamma > 0$, information from the measurements is supplemented by information from the physical side-constraint.

Since the forward model is non-linear the minimization problem is solved iteratively in linear approximation with the n-th iteration forward model being approximated through

$$\mathbf{F}(\mathbf{x}_{n+1}) = \mathbf{F}(\mathbf{x}_n) + \mathbf{K}(\mathbf{x}_{n+1} - \mathbf{x}_n) \tag{3}$$

with $\mathbf{K}$ the Jacobian matrix

$$\mathbf{K} = \frac{\partial \mathrm{F}}{\partial x'}, \tag{4}$$

$$\mathrm{K}_{ij} = \frac{\partial \mathrm{F}_i(\mathbf{x}_n)}{\partial x_j}. \tag{5}$$

In general, the retrieved state vector $\hat{\mathbf{x}}$ is subject to different error sources: the retrieval noise, forward model errors and instrument related errors. Overall the different contributions to the error budget represent systematic, quasi-statistical and fully random errors, which have to be treated separately. Here, we address fully random retrieval noise and systematic aerosol and cirrus induced errors. Instrument related errors are addressed by WP2100.

3.2. Error propogation and estimation

In linear approximation, the solution state vector $\hat{\mathbf{x}}$ and its error contributions can be expressed in terms of the averaging kernel $\mathbf{A}$ and the gain matrix $\mathbf{G}$

$$\hat{\mathbf{x}} = \mathbf{A}\mathbf{x}_{true} + (\mathbf{1} - \mathbf{A})\mathbf{x}_a + \mathbf{G}\mathbf{e}_y + \mathbf{G}\mathbf{e}_\mathrm{F} \ , \tag{6}$$

where $\mathbf{G}=(\mathbf{K}^T \mathbf{S}_\mathbf{y}^{-1} \mathbf{K} + \gamma\, \mathbf{L}^\mathrm{T}\mathbf{L})^{-1} \mathbf{K}^T \mathbf{S}_\mathbf{y}^{-1}$, $\mathbf{A}=\mathbf{G}\mathbf{K}$, and $\mathbf{x}_{true}$ the true state vector. The a priori vector $\mathbf{x}_a$ contains any a priori knowledge about the state vector.

Here, we design our evaluation such that we focus on systematic forward model errors $\mathbf{e}_\mathrm{F}$. Thus, we are mostly interested in

$$\Delta\hat{\mathbf{x}} = \mathbf{G}\mathbf{e}_\mathrm{F} \ . \tag{7}$$

Using the true profile as a priori, we can derive $\Delta\hat{\mathbf{x}}$ from equations (6) and (7)

$$\Delta\hat{\mathbf{x}} = \hat{\mathbf{x}} - \mathbf{x}_{true} - \mathbf{G}\mathbf{e}_y, \qquad (8)$$

where all quantities on the r.h.s. are either known from the retrieval ($\hat{\mathbf{x}}$ and $\mathbf{G}$) or from the simulation input ($\mathbf{x}_{true}$ and $\mathbf{e}_y$). For the total column CO_2 forward model error, we sum $\Delta\hat{\mathbf{x}}$ over the 12 CO_2 profile layers and divide by the air column to get XCO_2

The quantity defined by equation (8) is what we call the **residual retrieval forward model error**. In our setup, these forward model errors come from the treatment of aerosol and cirrus scattering effects being different in the simulation and in the retrieval. While the simulation uses a very sophisticated radiative transfer model to simulate atmospheric scattering properties in great detail, the retrievals use approximations on the amount, type, size and height distribution of scattering particles. We emphasize that such forward model errors are introduced by intention since it can be safely assumed that the real atmospheric physics encountered by a satellite is sufficiently more complex than the models used for retrieval which, for example, must not consume excessive computational resources.

For evaluating random retrieval noise errors, we rely on Gaussian error propagation. Mapping the measurement noise covariance $\mathbf{S_y}$ into the retrieval covariance yields

$$\hat{\mathbf{S}} = \mathbf{G}\mathbf{S_Y}\mathbf{G}^T\,. \qquad (9)$$

The diagonal elements of $\hat{\mathbf{S}}$ are the variances of the retrieval parameters. Thus, the total column CO_2 noise error is the square root of the sum of the 12x12 submatrix representing the 12 CO_2 profile layers.

3.3. Simulation settings

As outlined by the introduction the goal of the present study is to compare retrieval performance for different spectral sizing concepts. The four considered configurations A, B, C, D are shown in table 1, which is taken from Technote D1 [SRON-CSS-TN-2016-002_V3, table 1].Please note that we defined three sub-configurations B1, B2, B3 for concept B which will be used for retrieval exercises.

Figure 1 shows illustrative solar absorption spectra in the NIR, SW-1 and SW2 bands corresponding to the four instrument concepts. While all concepts cover three similar spectral bands, the concepts clearly differ in spectral resolution and spectral coverage. Concepts C and D generally adopt high spectral resolution and in consequence quite narrow spectral coverage, concept A relaxes spectral resolution in SW-1 and thereby gains spectral bandwith (allowing for coverage of methane (CH4) absorption lines), concept B further relaxes spectral resolution in NIR and SW-2 which, in particular, gains spectral coverage toward the strongly absorbing water vapor (H2O) bands below 2000 nm wavelength.

Given the signal-to-noise-ratio (SNR) coefficients of table 1, we add Gaussian noise calculated according to equation (1) in TN1 [SRON-CSS-TN-2016-002_V3] to the modelled atmospheric absorption spectra. The resulting SNR is shown in Figure 2 for the various illustrative spectra.

The instrument configurations are used to simulate absorption spectra for the geophysical scenarios of the global ensemble G1 described in TN1 [SRON-CSS-TN-2016-002_V3, section 2.1] which is in particular designed to try retrieval performance for aerosol and cirrus loaded scenes. This yields roughly 8600 geophysical cases for which we evaluate XCO_2 noise errors (section 4) and the aerosol and cirrus induced forward model errors (section 5).

Instrument concept		A	B	C	D	B1	B2	B3
Spectral bands [nm]	NIR	756-773	747-773	758-772	758.35-768.65	747-773	747-773	747-773
	SW-1	1559-1675	1590-1675	1591-1621	1596.85-1618.55	1590-1675	1590-1675	1590-1675
	SW-2	2043-2095	1925-2095	2042-2081	2023.25-2050.75	1990-2095	2022-2095	1925-2095
Resolution [nm]/ sampling ratio	NIR	0.045/2.5	0.1/3.14	0.042/2.5	0.032/2.905	0.1/3.14	0.1/3.14	0.1/3.14
	SW-1	0.30/2.5	0.3/3.14	0.076/2.5	0.067/2.914	0.3/3.14	0.3/3.14	0.3/3.14
	SW-2	0.13/2.5	0.55/3.29	0.097/2.5	0.085/2.924	0.55/3.29	0.55/3.29	0.55/3.29
SNR coefficients a and b (Eq. 1)	NIR	2.81E-15/160540	4.47E-15/160540.	8.36E-016 / 2944.	8.423E-16 / 657350	4.47E-15/160540.	4.47E-15/160540.	4.47E-15/160540.
	SW-1	2.88E-14/ 333979	2.29E-14/ 333297	4.15E-015 / 20277.	3.571E-15 / 654978	2.29E-14/ 333297	2.29E-14/ 333297	2.29E-14/ 333297
	SW-2	1.22E-14/ 324402	3.91E-14/ 323636	6.39E-015 / 56295.	5.670E-15 / 648609	3.91E-14/ 323636	3.91E-14/ 323636	3.91E-14/ 323636
Remark/reference		Adapted from AD-1	Adapted from AD-2	Adapted from RD-2, RD-3, RD-4, RD-5	Adapted MicroCab performance, pers. (B. Sierk, 18/11/2016)	Adapted from AD-2	Adapted from AD-2	Adapted from AD-2

Table 1. Spectral sizing points representing the four instrument concepts A, B, C, and D, as specified in Technote D1 [SRON-CSS-TN-2016-002_V3, table 1]. For the instrument concept B, different retrieval concepts (purple background) with different lower limits of the SW-2 band are tested.

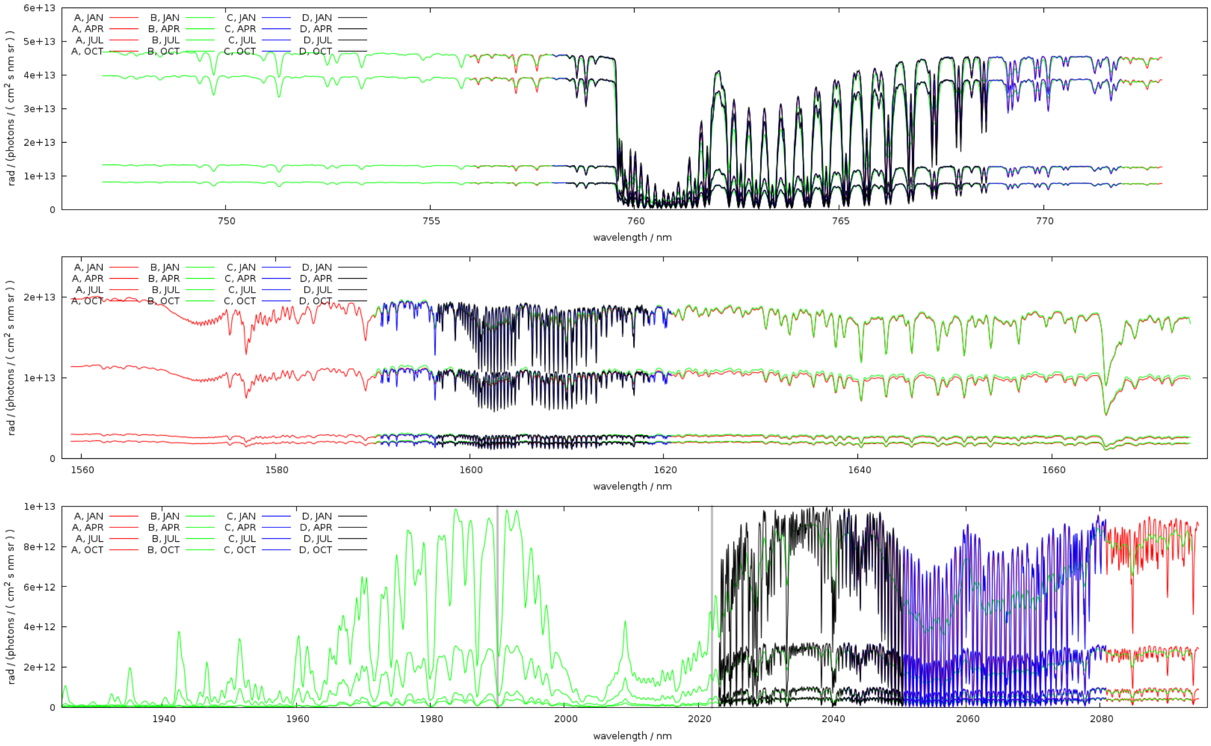

Figure 1. Solar absorption spectra in the NIR (top), SW-1 (middle) and SW2 (bottom) bands corresponding to the four instrument concepts A (red), B (green), C (blue) and D (black) for four different scenarios from the ensemble

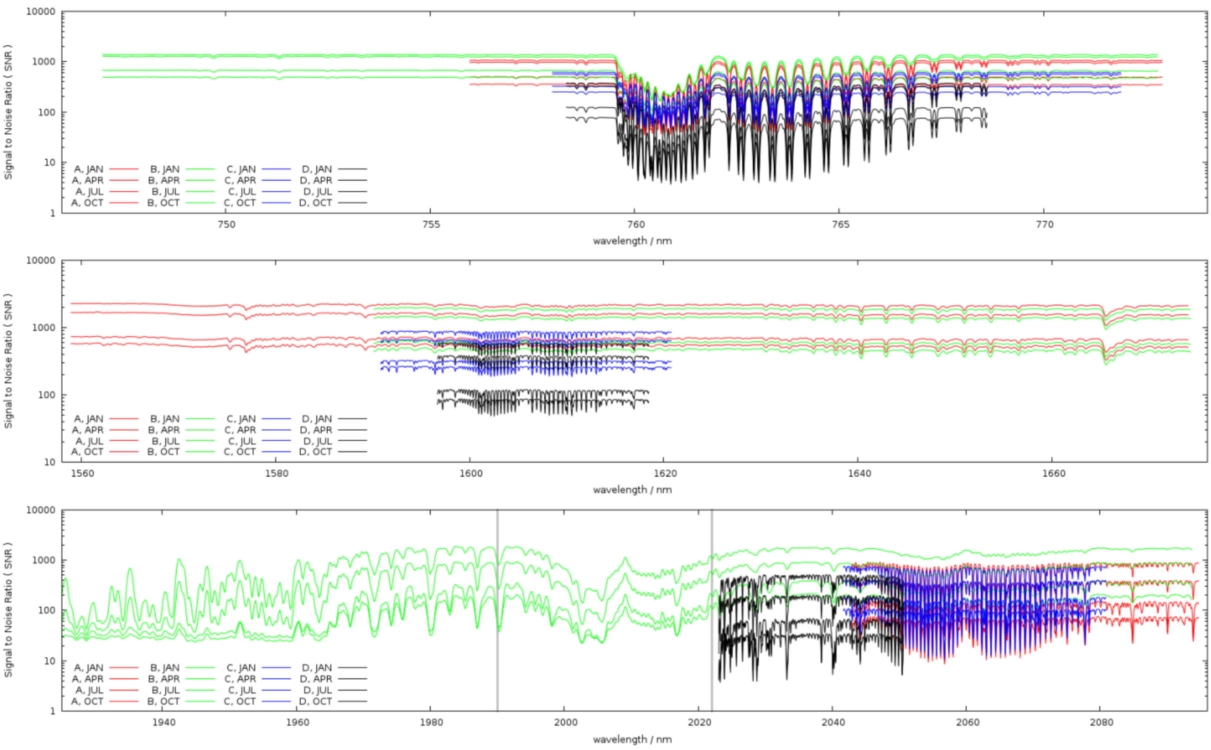

Figure 2. Same as Figure 1 but for the Signal to Noise Ratio (SNR)

4. CO_2 noise errors

The CO_2 noise errors evaluated here resuls from Gaussian error propagation of the measurement noise parameterized through the SNR coefficients given in table 1. In terms of using the CO_2 retrievals for quantifying emission (and uptake) patterns at the Earth's surface, noise errors are benign for applications which allow for (temporal and/or spatial) averaging of individual retrievals. Then, the noise errors will reduce according to the laws of error propagation. The simplest case of averaging N identical scenes results in error reduction by a factor √N. For applications, which rely on single-shot retrievals, noise errors are more problematic since reduction through averaging is not an option.

Figures 3 through 6 show the XCO_2 noise errors for retrievals from the January, April, July, and October G1 ensemble members for the configurations A, B1, C, and D after basic screening of non-convergent retrievals, solar zenith angle (SZA)>70°, and ocean surfaces. The spatial and temporal distribution of noise errors is driven by the position of the sun and by surface albedo. As expected, high latitudes reveal higher noise errors than mid- and low-latitudes, with concept D showing significantly higher errors compared to the other concepts.

Figure 7 summarizes the noise errors in a cumulative histogram comparing performance of concepts A, B1, B2, B3, C, and D. Except for concept D, all other concepts yield comparable noise errors less than 1 ppm (0.5 ppm) for more than 90% (75%) of the geophysical test cases. Concept D shows significantly greater noise errors with about 75% (50%) of the cases below 1 ppm (0.5 ppm).

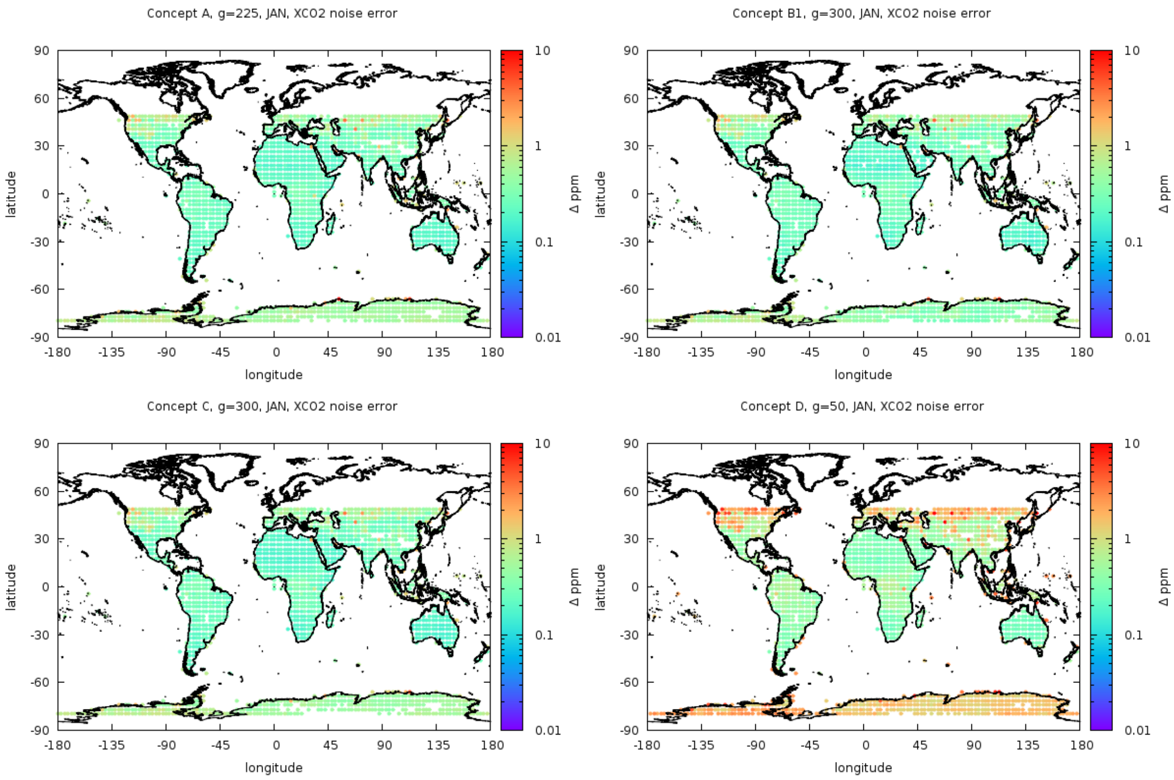

Figure 3. XCO_2 noise errors for retrievals of G1 ensemble members in January

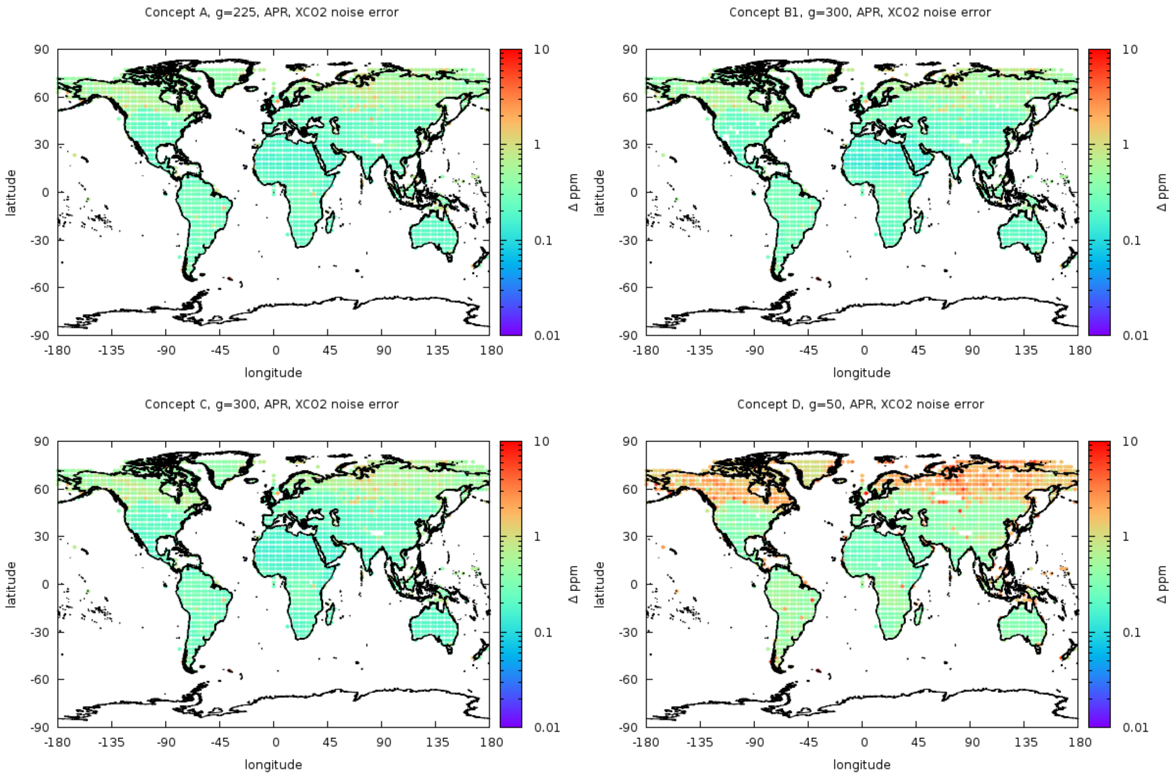

Figure 4. XCO_2 noise errors for retrievals of G1 ensemble members in April

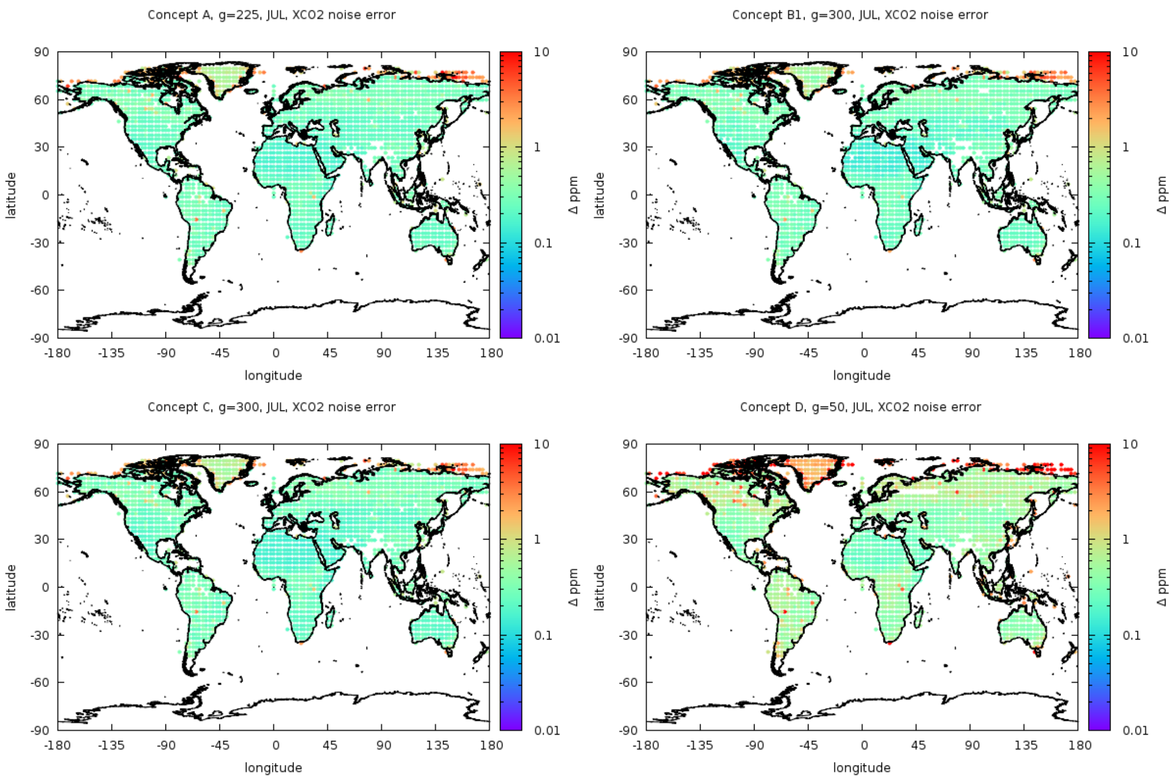

Figure 5. XCO_2 noise errors for retrievals of G1 ensemble members in July

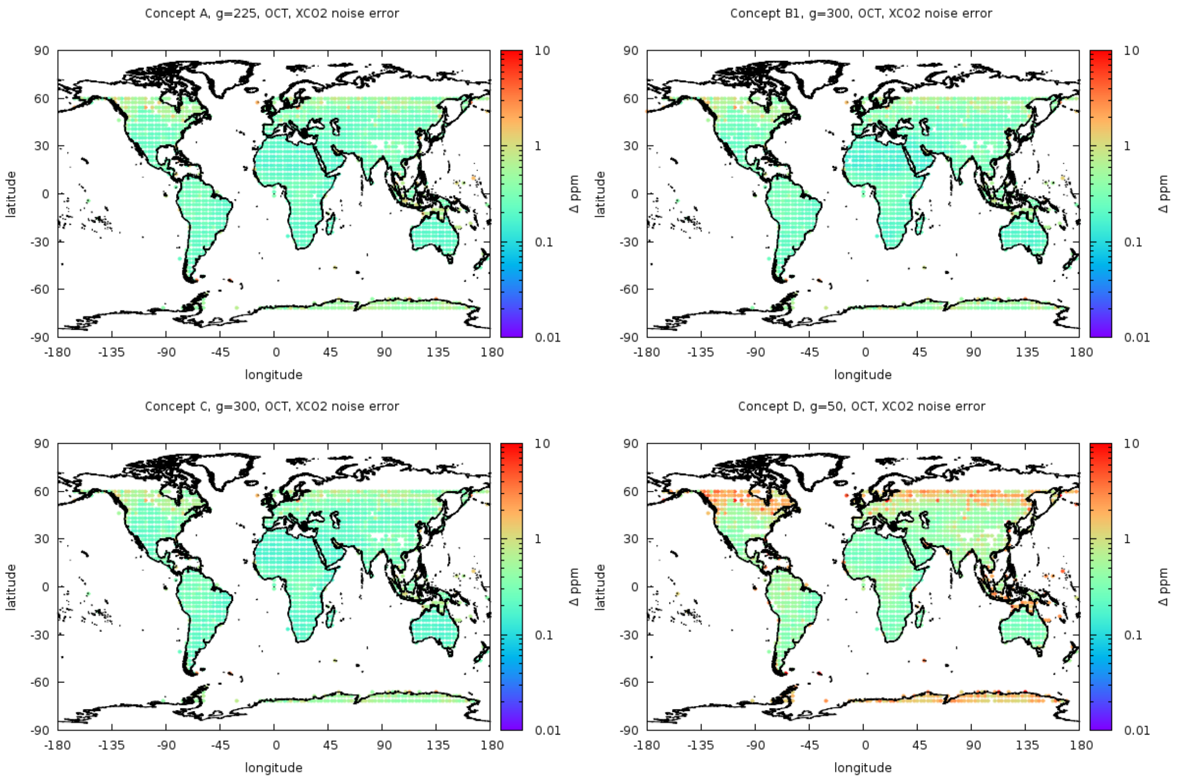

Figure 6. XCO_2 noise errors for retrievals of G1 ensemble members in October

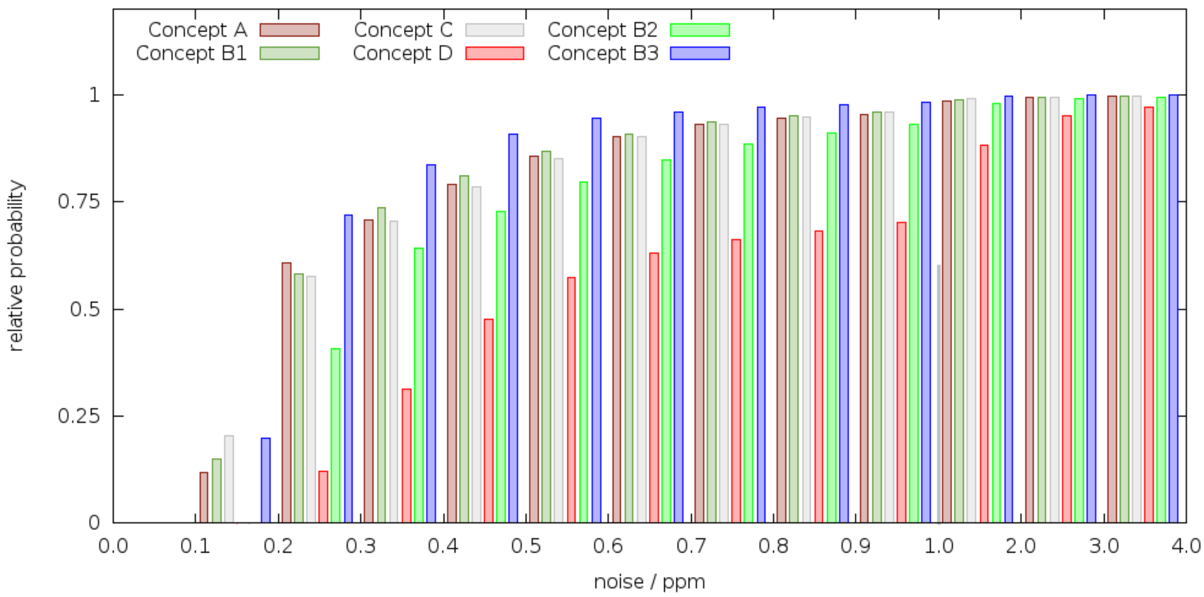

Figure 7. Cumulative histogram of the noise error for the retrieval concepts A, B1, B2, B3, C, and D. Please note the change in the x axis scale at values of 1 ppm.

5. Aerosol and cirrus induced errors

The evaluation of the aerosol and cirrus induced forward model error is needed to assess the performance of the different instrument concepts in terms of mitigating approximations to radiative transfer. For the forward simulation, challenging aerosol and cirrus loaded atmospheres are used, as specified in Technote D1 [SRON-CSS-TN-2016-002_V3, section 2.1. and figure 12].

Figures 8 through 11 show the aerosol and cirrus induced errors for retrievals from the January (Fig. 8), April (Fig. 9), July (Fig. 10), and October (Fig. 11) G1 ensemble members for the configurations A, B1, C, and D after basic screening of non-convergent retrievals, solar zenith angle (SZA)>70°, and ocean surfaces. The spatial and temporal distribution of aerosol and cirrus induced errors is driven by the solar zenith angle, the albedo, and from the amount of cirrus and aerosol content in the input. As expected, high latitudes and regions with high aerosol and cirrus load reveal higher error values than mid- and low-latitudes clear-sky regions. Figure 12 summarizes the aerosol and cirrus induced errors in a cumulative histogram comparing the performance of the retrieval concepts A, B1, B2, B3, C, and D.

All concepts show errors < 2 ppm for 50 % (< 4 ppm for 70 %) of the ensemble members, despite of the challenging global ensemble scenario referred to above. The differences among the concepts are small. Concept D (63% < 2 ppm, 82% < 4ppm) is slightly better than A (58% < 2 ppm, 80% < 4ppm), A is slightly better than C (54% < 2 ppm, 76% < 4 ppm), C is almost equal to B (B1: 51% < 2 ppm, 71% < 4 ppm; B2: 55% < 2 ppm, 76% < 4 ppm; B3: 57% < 2 ppm, 78% < 4 ppm).

Despite slightly worse aerosol and cirrus induced error performance, it should be noted that concept B allows for both, additional cirrus screening and cirrus retrieval, and further optimization of the retrieval ranges. Regarding the different retrieval concepts B1, B2, and B3, concept B2 (lower limit in SW-2 = 2022 nm) and the reference concept B3 (lower limit in SW-2 at 1925 nm) are slightly better than the B1 concept (lower limit in SW-2 at 1990 nm).

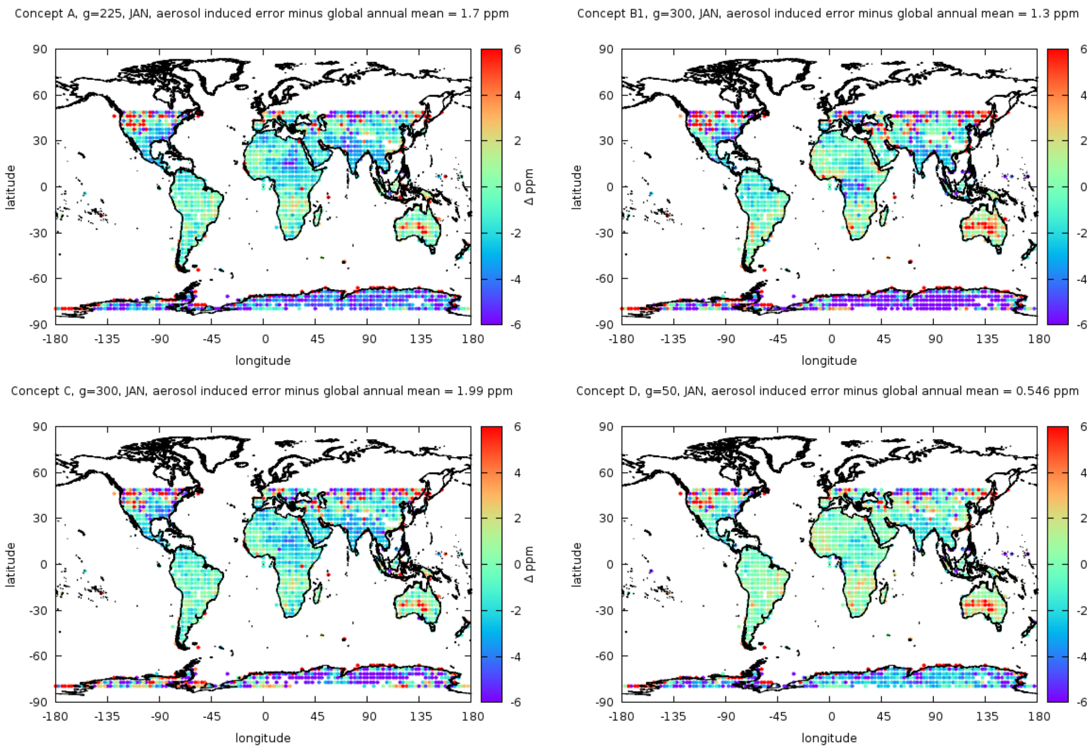

Figure 8. Aerosol and cirrus induced errors for concepts A, B1, C, D for retrievals of ensemble members in January.

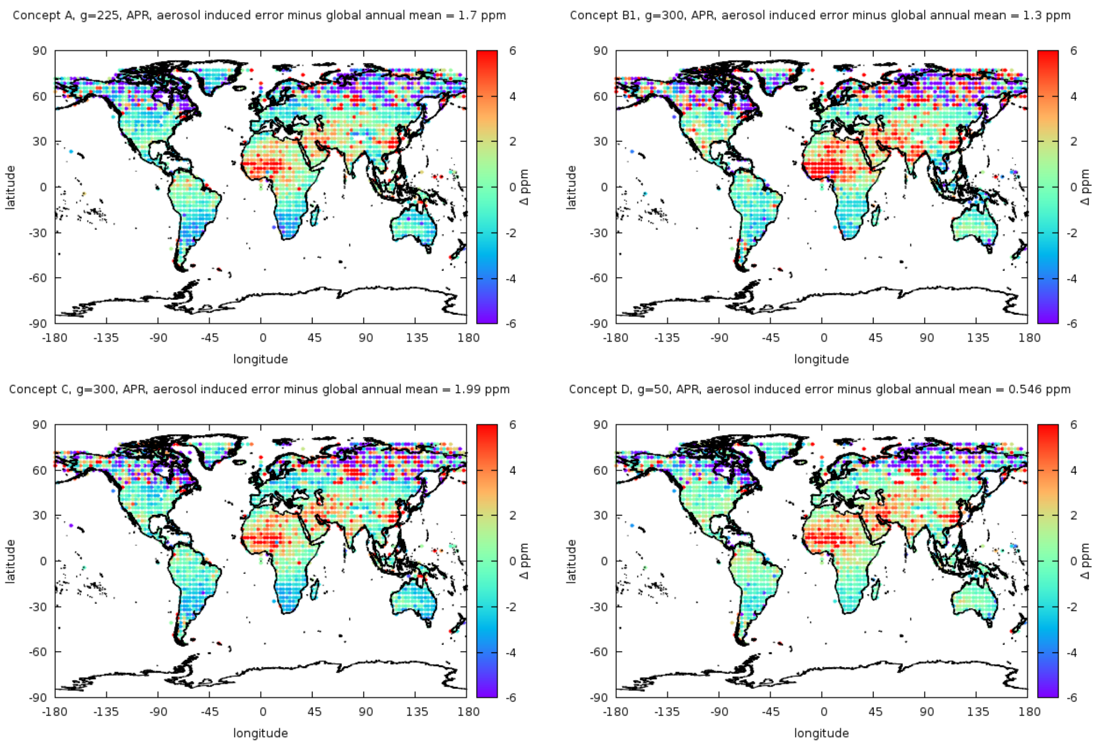

Figure 9. Aerosol and cirrus induced errors for the four concepts A, B1, C, and D in April.

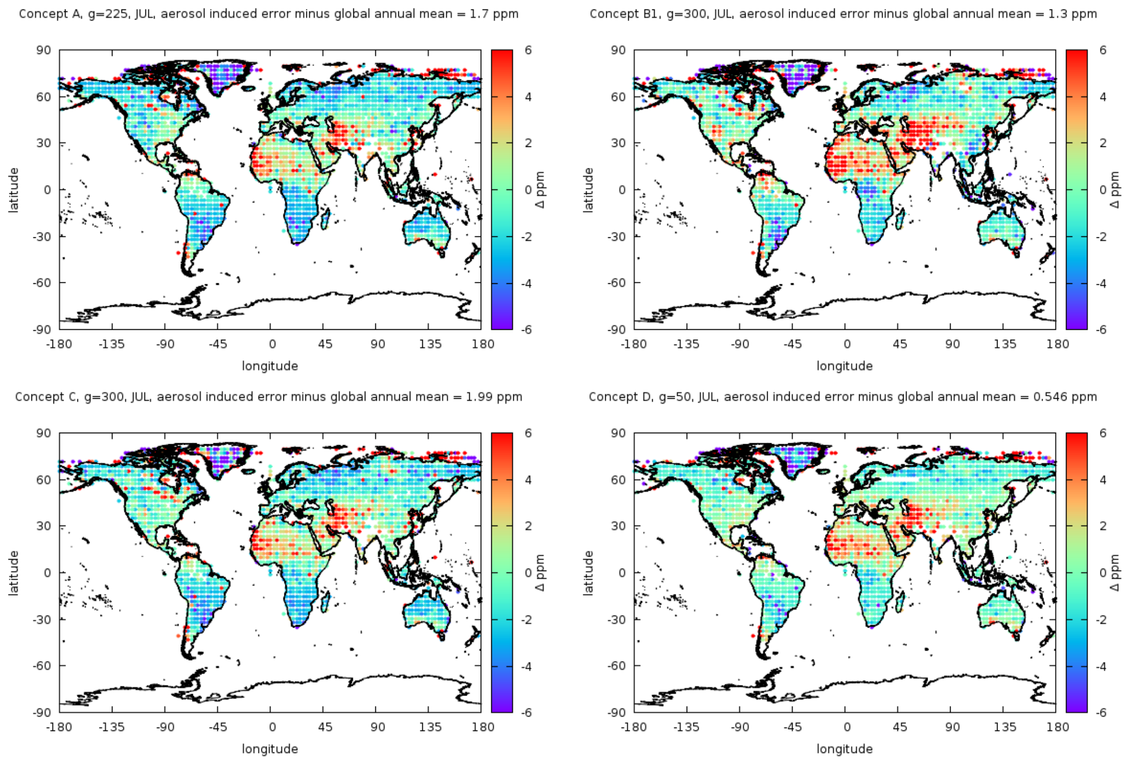

Figure 10. Aerosol and cirrus induced errors for the four concepts A, B1, C, and D in July.

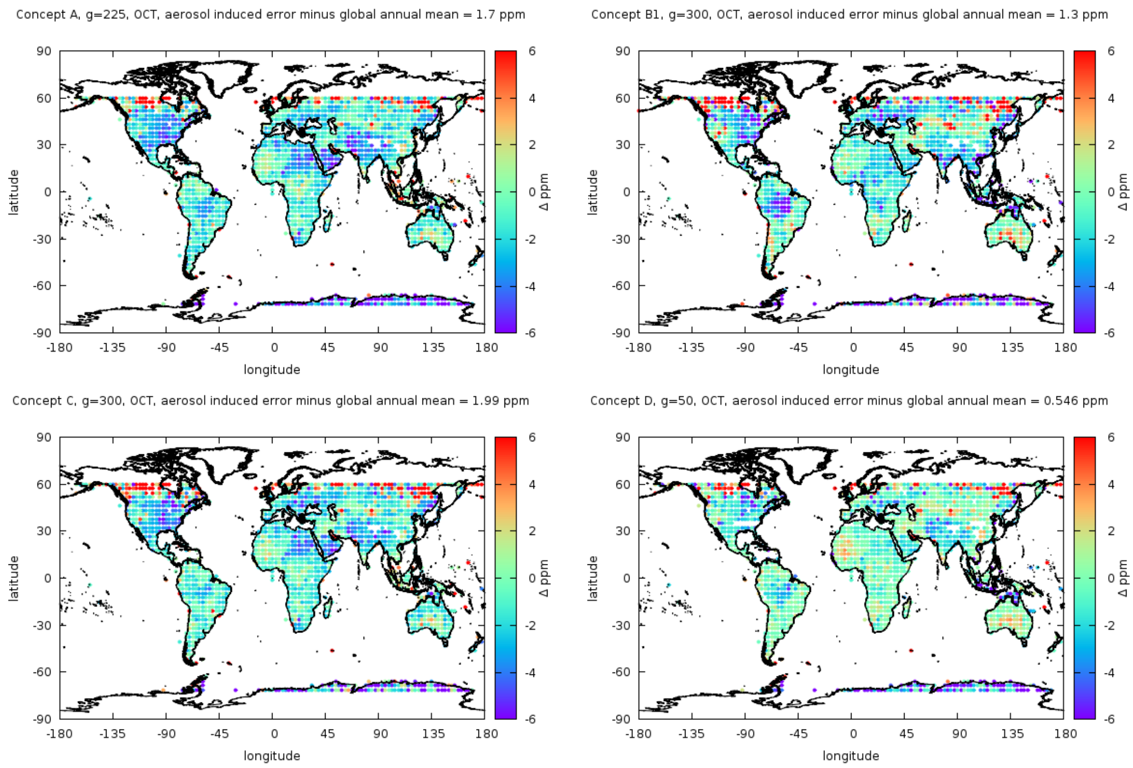

Figure 11. Aerosol and cirrus induced errors for the four concepts A, B1, C, and D in October.

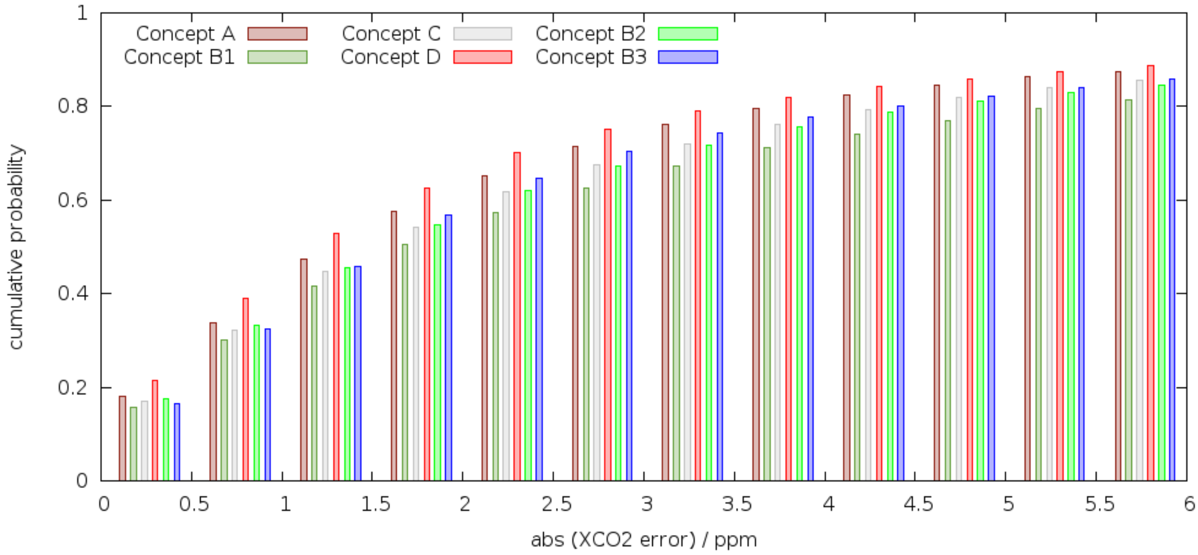

Figure 12. Cumulative histogram of the aerosol and cirrus induced error for the retrieval concepts A, B1, B2, B3, C, and D.

Further sensitivity analyses

As discussed at the PM2 meeting the regional dependencies of the aerosol induced errors are of interest. Therefore, Fig. 13 shows the cumulative histogram of the aerosol and cirrus induced error for individual continental regions. The relative performance among the four instrument concepts appears consistent among all regions except for the B3 retrieval configuration, which uses the entire SW-2 band including the strongly absorbing water vapor bands below 1950 nm wavelength. B3 performs clearly worst for the tropics and tentatively best for Australia. The other retrieval configurations, B1 and B2, derived from instrument concept B (omitting the strong water bands) do not show such a variable performance. Thus, configuration B3 needs further improvements of the retrieval concept. So far, our retrieval software RemoTeC does not retrieve cirrus particle properties and multi-layer cloud structures. The variable performance of B3 suggests that the strong water vapor bands in SW-2 actually contain information on such more complicated scattering scenarios. A retrieval that cannot exploit this information (such as RemoTeC in its current version) is subject to larger errors since the retrieval accounts for the spectral structures carrying the information. On the other hand, the performance analysis suggests that scattering information could be gained by further developing the retrieval software towards exploiting the highly saturated water vapor lines.

Further, we assessed the impact of data filtering on the overall performance statistics. Fig. 14 shows the cumulative histograms for the aerosol and cirrus induced errors for different choices of the scattering complexity filter. The complexity of the scattering scenario is determined via calculation of the complexity parameter

$$aaa = (SOT * z_c) / \alpha \qquad (10)$$

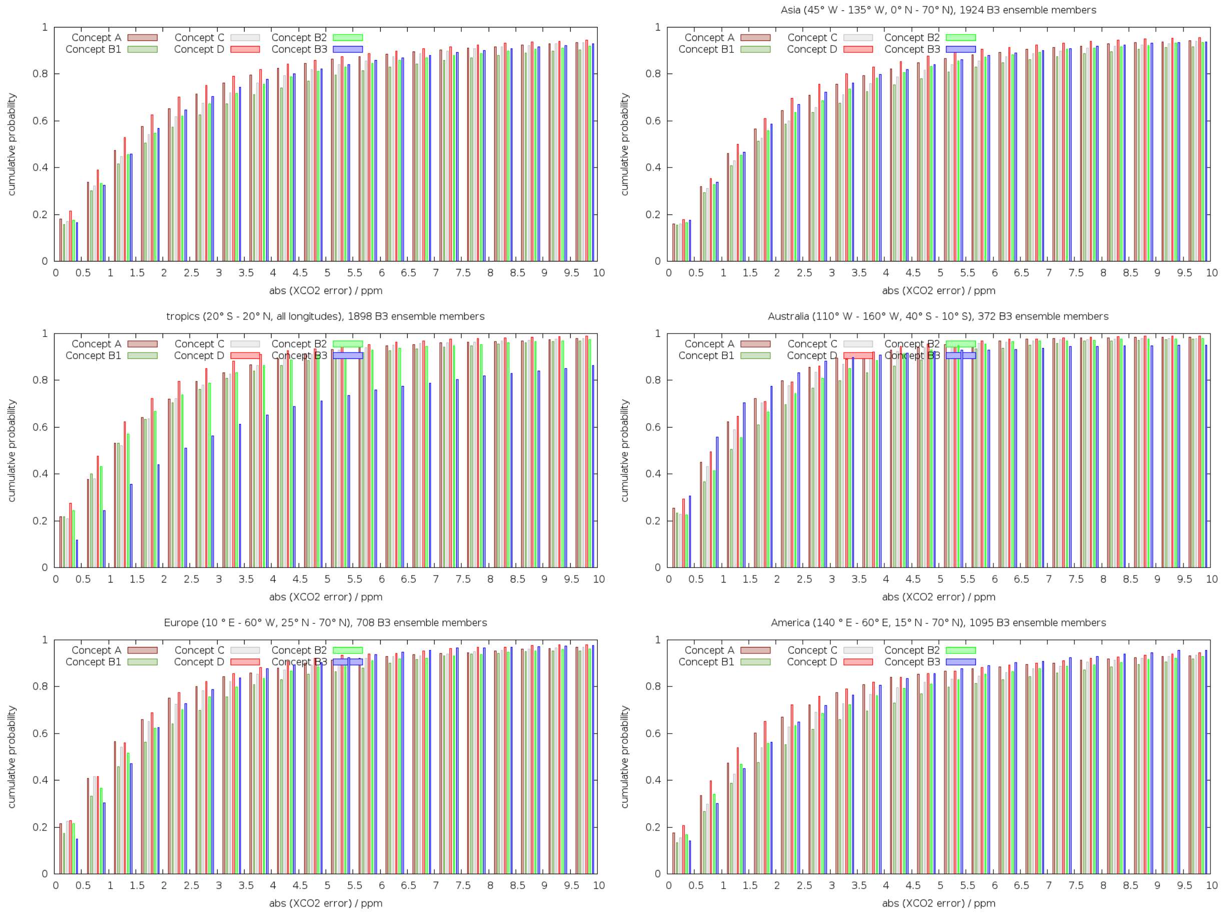

Figure 13. Aerosol and cirrus induced errors for the whole ensemble (all regions, top left), the tropics (middle left), Europe (bottom left), Asia (top right), Australia (middle right) and Northern America (bottom right).

where SOT is the retrieved scattering optical thickness, z_c is the center height of the retrieved particle height distribution, and α is the retrieved power of the power law size distribution. The aaa-filter preferentially screens scenes where scattering particles are found in large amounts at high altitudes with large particle sizes Fig. 14 compares the whole ensemble (unfiltered for aaa) with the ensemble subset with aaa < 200 m and aaa < 500 m. As expected, the less complex the aerosol scenario, the lower the aerosol induced errors. In particular, the range of very low XCO_2 errors gains weight in the histograms for stricter filtering. The number of screened scenes, however, is substantial. The number of valid retrievals decreases from roughly 9000 to about 3000 between the aaa-unfiltered and the aaa < 200 m case.

Another important filtering parameter is SZA. Fig. 15 compares the cumulative histogram of the aerosol and cirrus induced error of all ensemble members (SZA<70° is already included there) and subsets of the ensemble with SZA<60° and SZA<50°. The performance impact of the SZA filter is less pronounced as for the scattering complexity filter but there is a significant effect on the overall performance.

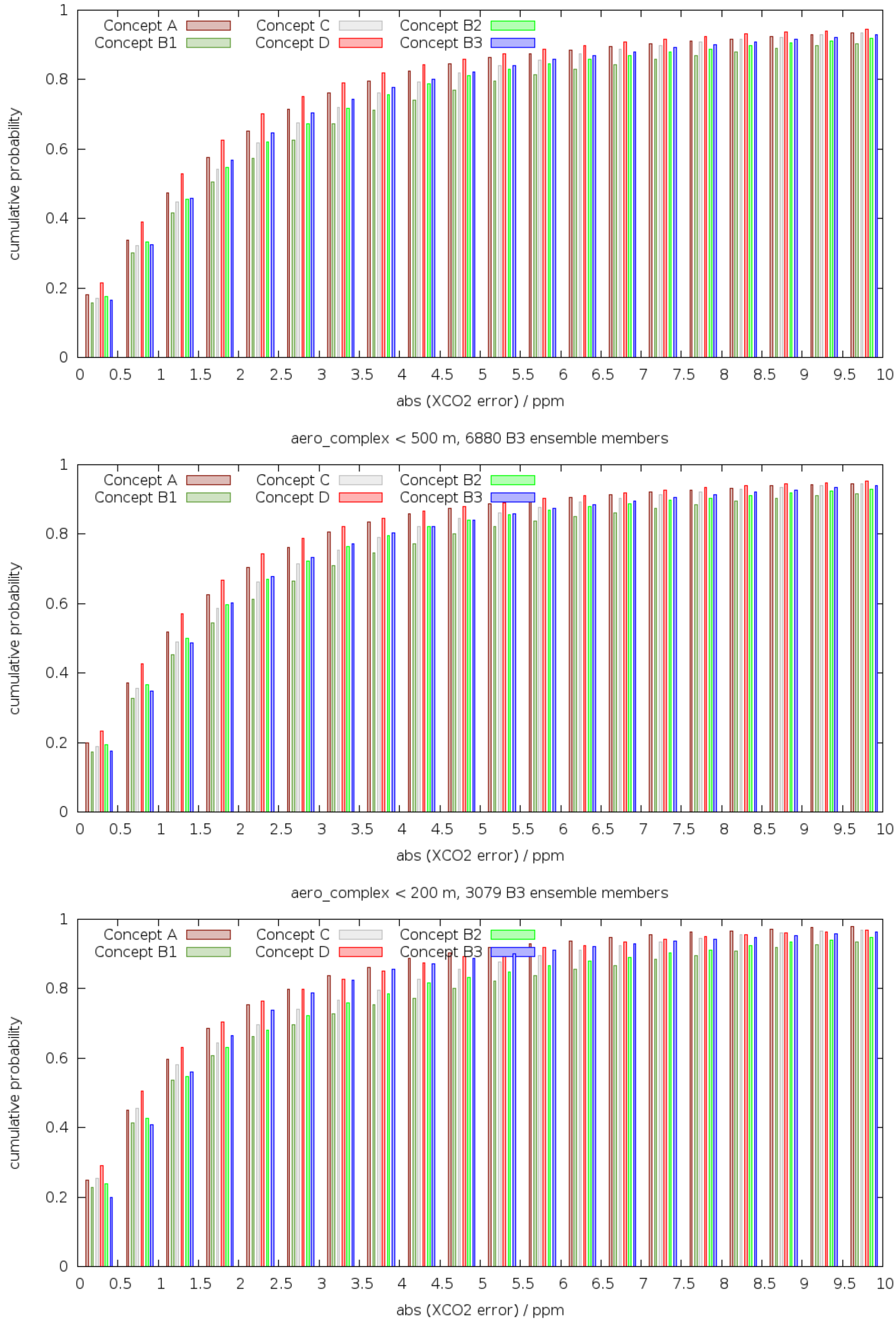

Figure 14. Cumulative histogram of the aerosol and cirrus induced error for the whole ensemble (top), the ensemble members with aerosol complexity < 500 m (middle) and < 200 m (bottom).

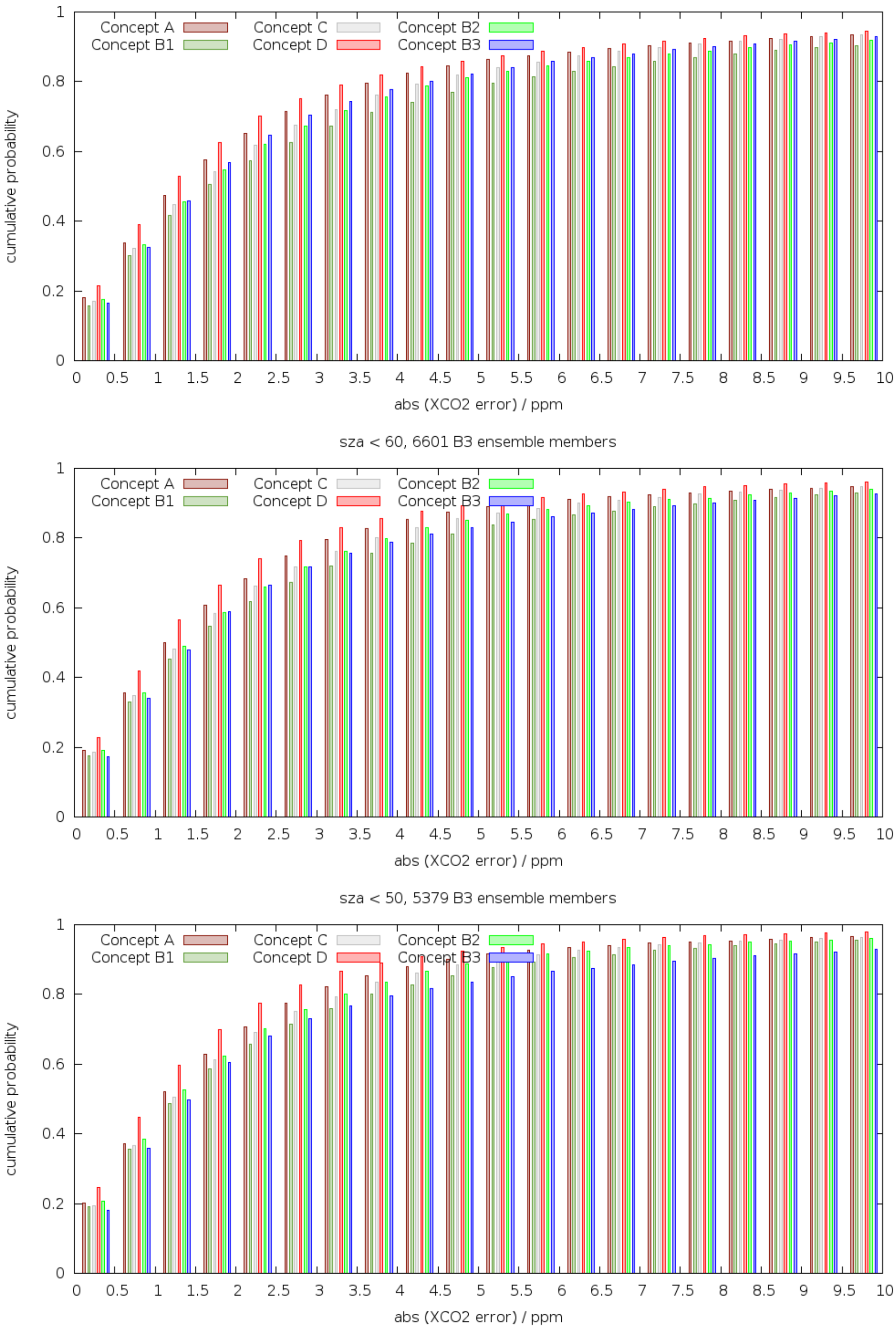

Figure 15. Cumulative histogram of the aerosol and cirrus induced error for the whole ensemble (top), the ensemble members with SZA < 60° (middle), and SZA < 50° (bottom).

List of literature

SRON-CSS-TN-2016-002_V3, Landgraf, J., aan de Brugh, Joost, Butz, A. Graf, K., Specifications of instrument spectral sizing concepts, spectral errors, and geo-physical scenarios, 2016

Optimizing Spectral Sizing Concepts

Technical Note

ESA Study CO_2 Spectral Sizing Study

Lead author:

Hartmut Boesch

Earth Observation Science Group

University of Leicester

United Kingdom

Change log

Version	Date	Status	Reason for change
Draft 1.0	15 Mar. 2018	Submitted	New document

Contents

1 Purpose of this Document

In this document an extension/update of the spectral sizing analysis, carried out by UoL within the CS L1L2-I study, is presented. Specifically, instrumental and aerosol-related retrieval errors for 4 specific sizing concepts are evaluated and a systematic analysis of a range of sizing scenarios has been conducted.

2 UoL Retrieval Algorithm and Analysis Methods

2.1 Description of the UoL Retrieval

The UoL retrieval algorithm uses an iterative retrieval scheme based on Bayesian optimal estimation to estimate a set of atmospheric/surface/instrument parameters, referred to as the state vector **x**, from measured, calibrated spectral radiances **y** by calls to the forward model and the inverse method.

The forward model describes the physics of the measurement process and relates measured radiances to the state vector. It consists of a radiative transfer (RT) model coupled to a model of the solar spectrum to calculate the monochromatic spectrum of light that originates from the sun, passes through the atmosphere, reflects from the Earth's surface or scatters back from the atmosphere, exits at the top of the atmosphere and enters the instrument. The top of atmosphere (TOA) radiances are then passed through the instrument model to simulate the measured radiances at the appropriate spectral resolution.

The forward model employs the LIDORT radiative transfer model combined with a fast 2-orders-of-scattering vector radiative transfer code (Natraj et al., 2008). In addition, the code uses the low-streams interpolation functionality (O'Dell, C.W., 2010) to accelerate the radiative transfer component of the retrieval algorithm.

The TOA spectrum calculated by the RT code is multiplied with a synthetic solar spectrum, which is calculated with an algorithm based on an empirical list of solar line parameters [G. Toon, private communication] (G. Toon). The solar line list covers the range from 550 to 15,000 cm^{-1} and is derived from FTS solar spectra: Atmospheric Trace Molecule Spectroscopy (ATMOS), MkIV balloon spectra for the range 550–5650 cm^{-1}, and Kitt Peak ground-based spectra for 5000–15,000 cm^{-1}. The solar model includes both disk centre and disk integrated line lists.

The instrument model convolves the monochromatic radiance spectrum with the IRSF. As described in (Boesch et al., 2006), the instrument model can also simulate continuum intensity scaling, zero-level offsets and channeling effects.

The inverse method employs the Levenberg-Marquardt modification of the Gauss-Newton method to find the estimate of the state vector $\hat{\mathbf{x}}$ with the maximum a posteriori probability, given the measurement **y** (Connor et al., 2008), (Rodgers, C. D., 2000). The state vector will typically include a CO_2 or CH_4 profile together with additional state vector elements. After the iterative retrieval process has converged to a solution, the error covariance matrix $\hat{\mathbf{S}}$

$$\hat{S} = \left(\mathbf{K}^{\mathbf{T}}\, \mathbf{S}_{\varepsilon}^{-1}\, \mathbf{K} + \mathbf{S}_{\mathbf{a}}^{-1}\right)^{-1} \qquad \text{Eq. 2-1}$$

and the averaging kernel matrix **A**

$$\mathbf{A} = {\partial \hat{\mathbf{x}}}/{\partial \mathbf{x}} = \hat{S}\,\mathbf{K}^{\mathbf{T}}\, \mathbf{S}_{\varepsilon}^{-1}\, \mathbf{K} \qquad \text{Eq. 2-2}$$

are calculated using the a priori covariance matrix $\mathbf{S_a}$ and the measurement covariance matrix $\mathbf{S}_\varepsilon$. XCO_2 is inferred by averaging the retrieved CO_2 profile, weighted by the pressure weighting function, **h,** such that

$$X_{CO2} = \mathbf{h}^{\mathbf{T}}\, \hat{\mathbf{x}} \qquad \text{Eq. 2-3}$$

The associated column averaging kernel for a level *j* is then given by

$$(\boldsymbol{a_{CO2}}) = \frac{\partial X_{CO2}}{\partial \mathbf{x}_j}\frac{\mathbf{1}}{\mathbf{h}_j} = (\mathbf{h}^T\mathbf{A})_j\frac{\mathbf{1}}{\mathbf{h}_j} \qquad \text{Eq. 2-4}$$

and the variance of XCO_2 by

$$\boldsymbol{\sigma_{XCO2}} = \mathbf{h}^{\mathbf{T}}\,\hat{\mathbf{S}}\,\mathbf{h} \qquad \text{Eq. 2-5}$$

The main parameters for the characterization of the XCO_2 retrieval that are calculated by the retrieval algorithm are the a posteriori XCO_2 retrieval error given by the square root of the variance σ_{XCO2} and the column averaging kernel $\mathbf{a}_{CO2}$. For the retrieval of XCH_4, the same procedure as for CO_2 is followed with CO_2 being replaced with CH_4.

2.2 Analysis Method

We first carry out simulations of spectra for different instrument concepts and geophysical scenarios with the forward model of the UoL retrieval algorithm described above. The measurement uncertainty described by the measurement covariance matrix is simulated according to the signal to noise model given in section 4. No noise is added to the simulated radiance spectra themselves.

For the assessment of aerosol-related errors, the spectra are the used as inputs for the full end-to-end retrieval and we describe the error in the retrieval by the difference between the retrieved and the true (simulated) XCO2.

To study instrument related errors, we have adopted the concept of linear error analysis. Here, the spectral error $\boldsymbol{\Delta f}$ that results from instrument uncertainties is used in conjunction with the gain matrix **G** to calculate an error in XCO2 according to (Connor et al., 2008):

$$\Delta \boldsymbol{XCO2} = \mathbf{h}^{\mathbf{T}}\,\mathbf{G}\,\Delta\mathbf{f} \qquad \text{Eq. 2-6}$$

3 Geophysical Scenarios

The geophysical scenarios for the simulation are based on a 27-level profile atmosphere for the VEG50 scenario (Solar zenith angle 50° and vegetation surface reflectance). The simulations use a single aerosol mixture reflecting dusty maritime+coarse dust (Type 2a from Kahn et al., 2001). 11 different aerosol profiles are included that are created by scaling the boundary layer (BL) part and of the boundary + free troposphere (BL + FT) of the profile according to Table 1. The reference profile consists of a boundary layer profile (BL) with constant extinction (<2 km) for an AOD of 0.06 and a free tropospheric (FT) profile with constant extinction (2-5 km) with an AOD of 0.04. We also include cirrus clouds with an assumed Gaussian-shaped extinction profiles (see Table 2 for more details). The optical properties for ice particles are from Baum et al. (2005) for r_{eff} = 60 micron.

Table 1: Aerosol scenarios used in the simulations

Aerosol extinction vertical profiles for Simulations (760 nm)		
No.	**Type**	**Comment**
1	Reference	AOD: 0.1
2	Enhanced in BL: x5.0 in 0-2 km	AOD: 0.34
3	Enhanced in BL: x3.0 in 0-2 km	AOD: 0.22
4	Enhanced in BL: x2.0 in 0-2 km	AOD: 0.16
5	Reduced in BL: x0.5 in 0-2 km	AOD: 0.07

6	Reduced in BL: x0.2 in 0-2 km	AOD: 0.052
AP 2	Enhanced in BL + FT: x5.0 in 0-5 km	AOD: 0.5
AP 3	Enhanced in BL + FT: x3.0 in 0-5 km	AOD: 0.3
AP 4	Enhanced in BL + FT: x2.0 in 0-5 km	AOD: 0.2
AP 5	Reduced in BL + FT: x0.5 in 0-5 km	AOD: 0.05
AP 6	Reduced in BL + FT: x0.2 in 0-5 km	AOD: 0.02

Table 2: Cirrus scenarios used in the simulations

Cirrus Clouds for Simulations	
Cloud Optical Depth (760 nm)	**Cloud Centre Heights [km]**
0.01, 0.02, 0.05, 0.1, 0.2	8, 10, 12

4 Instrument Setup

Four different instrument concepts labelled A to D are investigated. Each concept has specific values for spectral coverage, spectral resolution and signal-to-noise (coefficients a and b) according to Table 3. The instrument lineshape is assumed to be Gaussian shaped. The signal-to-noise is calculated from the coefficient a and b from eq. 4-1.

$$SNR = \frac{aL}{\sqrt{aL+b}} \qquad \text{Eq. 4-1}$$

An example of simulated spectra for the four instrument concepts and their signal-to-noise ratio is shown in Figure 1. Noteworthy is that the SNR for concept D is significantly lower than for the other three concepts, specifically compared to concept C which has comparable spectral resolution. It can be expected that the information content in the spectra for this concept will be lower.

Table 3: Parameters used for the 4 Instrument concepts (for concept B we give the spectral band used for the retrieval in brackets).

Instrument concept		A	B	C	D
Spectral bands [nm] (used in retrieval)	NIR	756-773	747-773	758-772	758.35-768.65
	SW-1	1559-1675 (1.59 - 1.625)	1590-1675 (1.59 - 1.625)	1591-1621	1596.85-1618.55
	SW-2	2043-2095	1925-2095 (1.99 - 2.095)	2042-2081	2023.25-2050.75
Resolution [nm]/ sampling ratio	NIR	0.045/2.5	0.1/3.14	0.042/2.5	0.032/2.905
	SW-1	0.30/2.5	0.3/3.14	0.076/2.5	0.067/2.914
	SW-2	0.13/2.5	0.55/3.29	0.097/2.5	0.085/2.924
SNR coefficients a/b (Eq. 4-1)	NIR	2.81E-15/ 160540	4.47E-15/160540.	8.36E-016/ 2944.	8.423E-16/ 657350
	SW-1	2.88E-14/ 333979	2.29E-14/ 333297	4.15E-015/ 20277.	3.571E-15/ 654978
	SW-2	1.22E-14/ 324402	3.91E-14/ 323636	6.39E-015/ 56295.	5.670E-15/ 648609

Remark/reference	Adapted from AD-1	Adapted from AD-2	Adapted from RD-2, RD-3, RD-4, RD-5	Adapted MicroCarb performance, pers. (B. Sierk, 18/11/2016)

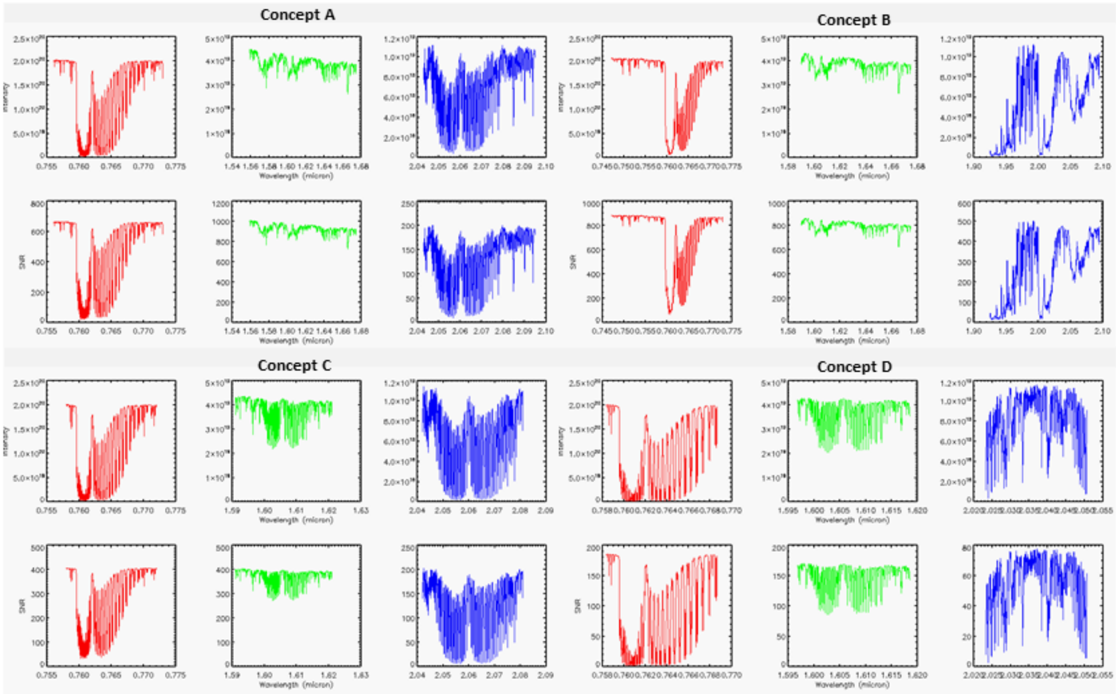

Figure 1: Example of the simulated spectra and signal-to-noise (SNR) for the four instrument concepts

5 Aerosol-Related Errors

5.1 Retrieval Setup

We have carried our 2 retrieval experiments. In the first experiment, we assume that we know the aerosol optical properties, i.e. the same aerosol optical properties are used in the retrieval and in the simulations. In the second experiment, we assume that aerosol optical properties are unknown. In this case, we use 2 retrieval types (different to the aerosol type used in the simulations) representing small and large aerosols: type 2b (Dusty maritime coarse dust) and type 5a (Carbonaceous black carbon continental) from Kahn et al. (2011).

In all cases, the a priori aerosol profile differ from the aerosol profile used in the simulations. For Aerosols, we adopt a Gaussian-shaped a priori profile with a height of 2 km, a width (FWHM) of 2 km and AOD of 0.1 and for cirrus we use a Gaussian-shaped profile at a height of 10 km and an optical depth of 0.05.

The state vector for the retrieval includes a full CO_2 profile, H_2O and Temperature scaling factors, surface pressure, albedo + tilt, log extinction profile for cirrus and aerosol, zerolevel offset in the NIR band. The a priori values for all state vector elements other than aerosol and cirrus are identical to that used in the simulations.

5.2 Results for known aerosol type

The inferred XCO2 biases for aerosol scenarios 1-6 (and cirrus) are summarised in Figure 2 and Table 4. After applying a quality filter (for number of diverging steps less or equal to 1) the observed histograms of the XCO2 biases are compact with the vast majority of values with a magnitude of less than 1 ppm. We find that the mean bias is similar and small (<0.1 ppm) for concepts A to C while the mean bias is slightly larger for concept D (0.2 ppm). The spread of the observed biases is smallest for concepts B and C, however, both concepts also show the lowest number of soundings.

Considering the aerosol scenarios where the aerosol load is varied in the free troposphere as well (AP2-6), we find that the mean bias for concept D becomes significantly larger compared to the other three concepts (1ppm vs 0.1 ppm, see Table 4). Concept D has also a much larger spread of values. However, concept D shoes a larger number of soundings and it is possible that applying a more tailored filter could bring concept D more in line with the other three concepts.

Figure 3 compares the retrieved to the true (simulated) values of AOD, COD and AOD+COD for the four instrument concepts for the aerosol scenarios 1-6. As expected, we find a tendency for large AODs to be underestimated and low ADOs to be overestimated by the retrieval due to the impact of the a priori constraint on AOD and the limited aerosol information given by the spectra. For concepts A-C, the comparison between retrieved and true AOD are similar, while results for concept D are significantly poorer. For COD, we find that all concepts reproduce the true (simulated) COD well. The result of poorer aerosol performance for concept D shown in Figure 3 is consistent with the observation of larger XCO2 biases.

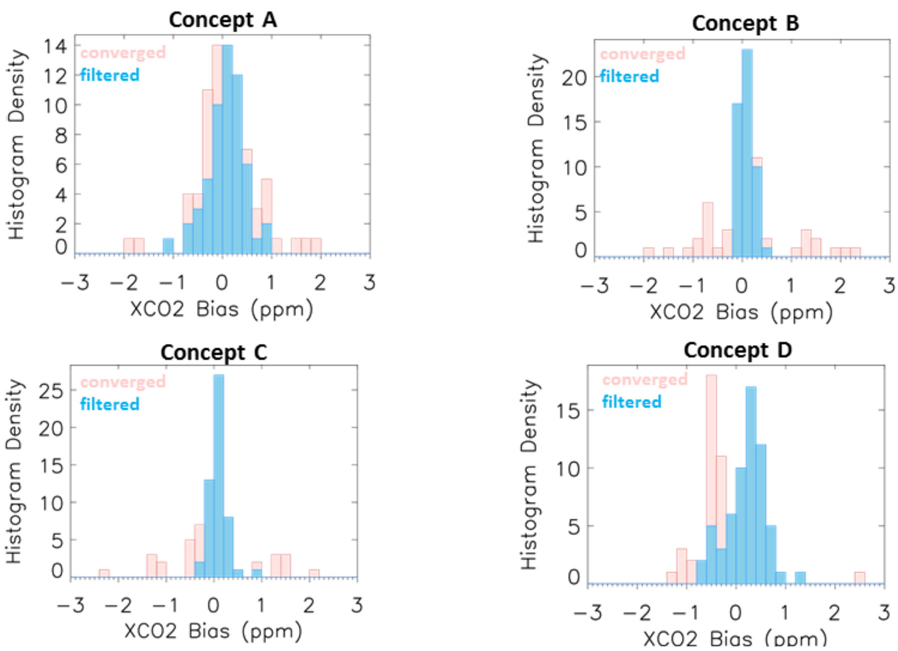

Figure 2: Histograms of XCO2 biases related to aerosols assuming a known aerosol type for instrument concepts A to D for aerosol scenarios 1-6. The results are given for all 'converged' retrievals and for retrievals filtered for number of diverging steps less or equal to 1.

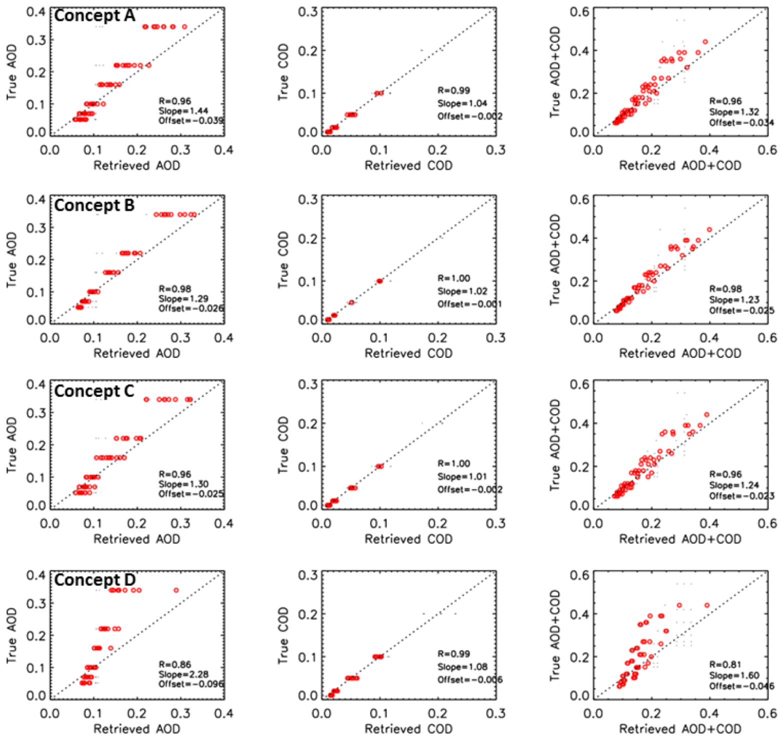

Figure 3: Comparison of retrieved and true AOD, COD and AOD+COD for the four instrument concepts.

Table 4: Summary of the XCO2 biases and their spread (given by the standard deviation) for the simulations for aerosol scenarios 1-6 and AP2-6. The values in brackets are without filtering (for number of diverging steps less or equal to 1). The number of soundings is also given.

		Concept A	Concept B	Concept C	Concept D
Mean CO_2 Bias (ppm)	1-6	0.08 (0.09)	0.07 (0.08)	0.09 (0.06)	0.21 (0.01)
	AP2-6	0.11 (0.66)	0.12 (0.43)	0.09 (0.63)	0.97 (0.67)
Standard Deviation (ppm)	1-6	0.37 (0.60)	0.15 (0.70)	0.20 (0.67)	0.40 (0.57)
	AP2-6	0.42 (1.24)	0.24 (1.01)	0.27 (1.22)	1.28 (1.49)
Number of Soundings	1-6	56 (81)	51 (77)	52 (76)	62 (90)
	AP2-6	39 (65)	33 (61)	41 (65)	55 (75)

5.3 Results for unknown aerosol type

The results of the retrieval experiment for unknown aerosol type for aerosol scenarios 1-6 for the four instrument concepts are summarized in Table 5. We find that results are comparable to the retrieval simulations for known aerosol type for concept A and B. For concept C, we find an increased spread of the biases while for concept D, the mean bias and the spread increase.

Again, concept C and D have a larger number of soundings compared to concepts A and B. To test if results can be brought into agreement between all concepts by a stricter filter, we have applied a new filter to concepts C and D that does not allow any diverging retrieval steps. The results are given in square brackets in Table 5. In the case of concept C, we find bias and spread become similar to those of concept A and B. For concept D, we find a decrease of the mean bias and the spread of the biases, but the spread is still much larger than for the other 3 concepts.

Table 5: Summary of the XCO2 biases and their scatter (given by the standard deviation) for the simulations for aerosol scenarios 1-6 assuming unknown aerosol types. The values in round brackets are

for all converged retrievals and the values in square brackets for concepts C and D are for a stricter filter that does not allow any diverging retrieval steps.

	Concept A	Concept B	Concept C	Concept D
Mean CO_2 Bias (ppm)	0.08 (-0.17)	0.13 (-0.09)	0.04 (-0.21) [0.14]	-0.32 (-0.40) [-0.14]
Standard Deviation (ppm)	0.28 (1.01)	0.15 (0.91)	0.45 (0.90) [0.18]	0.78 (0.740 [0.52]
Number of Soundings	57 (84)	55 (79)	62 (83) [49]	67 (90) [60]

6 Instrument-Related Errors

6.1 XCO2 Errors from IRSF Uncertainties

We have carried out simulations of spectra for aerosol scenarios 1-6 using the IRSF described in TN SRON-CSS-TN-2016-002 (eq. 6 in section 1.2) for a non-distorted case and the symmetric distortion 1 (Figure 4). The spectral difference between spectra calculated from the distorted and non-distorted IRSF are then used according to Eq. 6-6 to estimate the resulting error in XCO2. Three different gain matrices have been used to ensure that the calculated errors are representative for a range of scenarios.

If the IRSF distortion is applied to all bands simultaneously, we observed XCO2 errors between 1 and 3 ppm with largest errors observed for concept B and C. We can observe that errors inferred for each band separately can have positive or negative signs so that there will be a compensation of errors for the combined, simultaneous error. Since we do not know necessarily the direction of the distortion, we have also calculated the rms error from the error for each band. In this case, we observe that errors for concept A and B are lowest (except for gain matrix with high COD) while errors for concept C are largest. However, should the IRSF distortion between the bands be correlated then the simultaneous error ('All') is more representative of the expected errors.

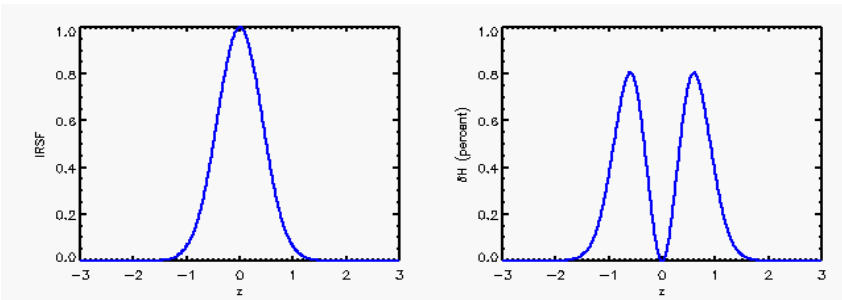

Figure 4: IRSF function and IRSF error used to evaluate the impact of IRSF errors on XCO2

Table 6: XCO2 errors in ppm resulting from an IRSF uncertainty (distortion 1) for the 4 instrument concepts. The errors are given when the distortion is applied to all 3 bands at the same time ('All'), for each band individually, and the rms error inferred from the individual errors.

	All	NIR	SWIR1	SWIR2	RMS
Concept A					
Ref	-1.67	-0.63	-0.91	-0.13	1.11
Low COD	-1.97	-0.68	-0.93	-0.36	1.21
High COD	-1.10	-0.53	-1.02	0.45	1.23

Concept B					
Ref	-1.93	-0.99	-0.76	-0.17	1.26
Low COD	-1.90	-0.86	-0.82	-0.22	1.21
High COD	-3.07	-2.23	-0.78	-0.07	2.36
Concept C					
Ref	-2.49	-0.43	-2.19	0.13	2.23
Low COD	-2.53	-0.32	-2.18	-0.03	2.20
High COD	-2.70	-0.60	-2.61	0.51	2.73
Concept D					
Norm	-1.43	0.01	-1.59	0.16	1.59
Low COD	-1.60	-0.02	-1.60	0.02	1.60
High COD	-0.92	0.19	-1.64	0.53	1.73

6.2 XCO2 Errors Zero Level Offset Uncertainties

We have assessed the XCO2 errors for a non-corrected zero level offset with the same approach used in section 6.1. The requirements on zero level offset are given in Table 7 and the resulting errors in XCO2 are given in Table 8. We find that errors are less than 1 ppm for all four instrument concept with a tendency for slightly larger errors for concept C and D when the rms error is considered.

Table 7: Zero level offset requirement for the 3 bands

Band	Zero Level Offset (10^{12} ph s^{-1} cm^{-2} μm^{-1} sr^{-1})
NIR	4.2
SWIR1	4.3
SWIR2	0.53

Table 8: XCO2 errors in ppm resulting from a zero level offset (according to Table 7) for the 4 instrument concepts. The errors are given when the zero level offset is applied to all 3 bands at the same time (‘All’), for each band individually, and the rms error inferred from the individual errors

	All	NIR	SWIR1	SWIR2	RMS
Concept A					
Norm	-0.40	0.08	-0.54	0.06	0.55
Low COD	-0.42	0.07	-0.54	0.05	0.55
High COD	-0.47	0.07	-0.67	0.12	0.68
Concept B					
Norm	-0.32	0.13	-0.45	-0.001	0.47
Low COD	-0.36	0.12	-0.48	0.003	0.50
High COD	-0.36	0.08	-0.49	0.05	0.50
Concept C					
Norm	-0.50	0.05	-0.66	0.11	0.67
Low COD	-0.50	0.06	-0.66	0.10	0.67
High COD	-0.59	0.05	-0.79	0.15	0.80
Concept D					
Norm	-0.43	0.15	-0.61	0.03	0.63
Low COD	-0.42	0.15	-0.59	0.02	0.61

High COD	-0.53	0.17	-0.75	0.04	0.77

6.3 XCO2 Errors from Straylight Uncertainties

The effects of straylight have been studies using the approach given in TN SRON-CSS-TN-2016-002 with the updates provided by B. Sierk (private communication). Essentially, a straylight kernel function in spatial and spectral direction is applied. This means that each spectral element (central element of the kernel) will receive a small fraction of light from other spectral or spatial elements. We have set the central element of the kernel to zero and normalised the kernel to a value for the Total Internal Scatter (TIS) of 0.9% (NIR), 0.7% (SWIR-1) and 0.5% (SWIR-2). The central element has been given a value of 1–TIS. This means that the central element has a value of >99%.

We have applied the straylight kernel to 2 scenarios. In the clear scenario the observed scene is given by the VEG50 scenario for all spatial rows on the detector. In this case, the straylight is only from the spectral direction. In the clear-cloudy scenario, we have assumed that half of the scene (including the scene considered for the analysis) is given by the VEG50 scenario while the other half sees a cloudy scene with cloud optical depth of 10. The resulting straylight radiance spectra are given in Figure 5.

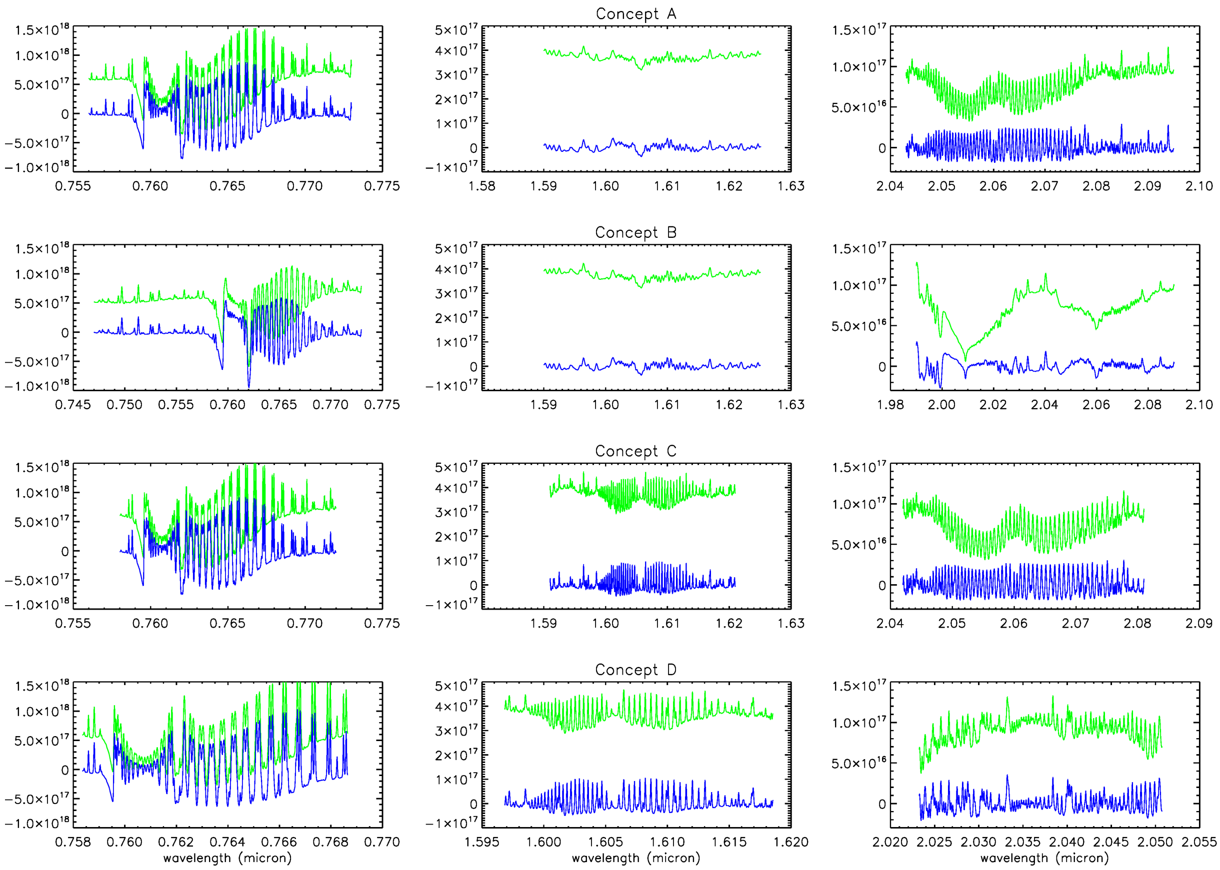

Figure 5: Spectral radiance errors (in ph/s/micron/cm^2/sr) from straylight for the 4 instrument concepts for a clear scene (blue) and a scene where half of the field of view is clear and the other half is cloudy (green).

The errors in XCO2 as a consequence of the straylight errors are inferred using linear error analysis (Eq. 6-6). Table 9 summarizes the XCO2 errors for each band and for all bands for the clear and the clear-cloudy scenario. For the clear scenario, we find total XCO2 errors between 3 and 4 ppm for concepts A-C and slightly lower errors for concept D. For concept A and B, the largest fraction of the error is from the NIR band while SWIR-1 is the largest contributor for concepts C and D reflecting the higher spectral resolution of this band for these concepts. As expected, we find much larger errors for the clear-cloudy scenes with values between 5 and 7 ppm. The largest error is now observed for concept C and the smallest error for concept B. Again, we find that straylight errors are dominated by SWIR-1 for concepts C and D. For concept A and B, NIR and SWIR-1 are contributing in a similar manner.

Table 9: XCO2 Errors (in ppm) from straylight estimated for the clear and the clear/cloudy scene

	All	NIR	SWIR1	SWIR2
Concept A				
Clear	-3.6	-2.4	-1.3	0.1
Clear-cloudy	-5.8	-2.6	-3.7	0.5
Concept B				
Clear	-3.8	-2.9	-0.9	0.1
Clear-cloudy	-5.2	-2.9	-2.8	0.5
Concept C				
Clear	-3.6	-1.1	-3.0	0.5
Clear-cloudy	-6.7	-1.1	-7.4	1.8
Concept D				
Clear	-2.7	0.1	-2.9	0.2
Clear-cloudy	-5.7	0.82	-7.3	0.7

7 Additional Sizing Concepts

We have investigated the XCO2 retrieval errors from aerosol-scattering and instrument calibration (IRSF and zero level offset) for sizing concepts that are obtained by systematically degrading the spectral resolution in all 3 bands. As a starting point, we have used instrument concept C and we have decreased the resolution by applying a multiplicative (resolution) factor to the spectral resolution in each band between 1 and 5. The same factor is applied to the intensity-dependent factor *a* in the SNR equation (Eq. 4-1). Figure 6 shows the impact of the application of this factor on the SNR.

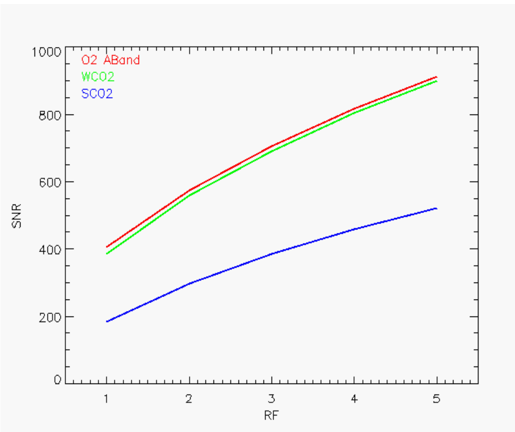

Figure 6: Signal-to-noise SNR for the 3 bands as a function of the resolution factor (RF).

We have considered two implementation option:

a) the number of spectral points remains constant

b) the oversampling ratio is kept constant and thus the number of spectral points is reduced.

We have repeated the retrieval simulations for aerosol-related errors described in section3 but limited it to aerosol scenarios 1-6. The summary for options a and b are given in Figure 7 and Figure 8, respectively. For option a, the retrieval precision remains essentially unchanged (with a value of ~0.5 ppm) as the lower SNR is compensated by the increased resolution. We find that aerosol related errors for 'known type' are very similar between the different resolutions, while for 'unknown type' we find a clear increase in the spread of errors with higher resolution (from 0.18 ppm to 0.45 ppm). The IRSF errors are larger for higher resolution while the zero level offset errors change little with resolution.

For option b, we see a clear increase in the estimated retrieval precision with resolution factor (i.e. lower resolution). Again, we find that the mean bias related to aerosol changes little with resolution. In contrast to implementation option a, we now find that the spread of the errors increase significantly with decreasing resolution. The IRSF and zero-level offset related errors are similar as before.

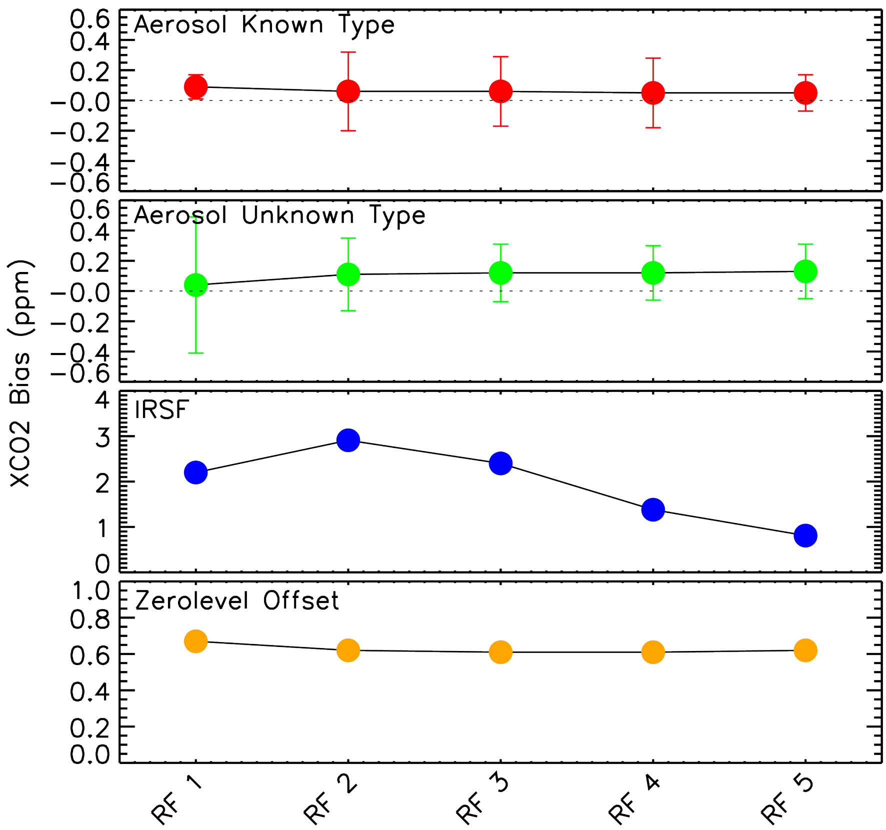

Figure 7: Summary of the XCO2 error analysis for the 5 resolution factors for implementation option a

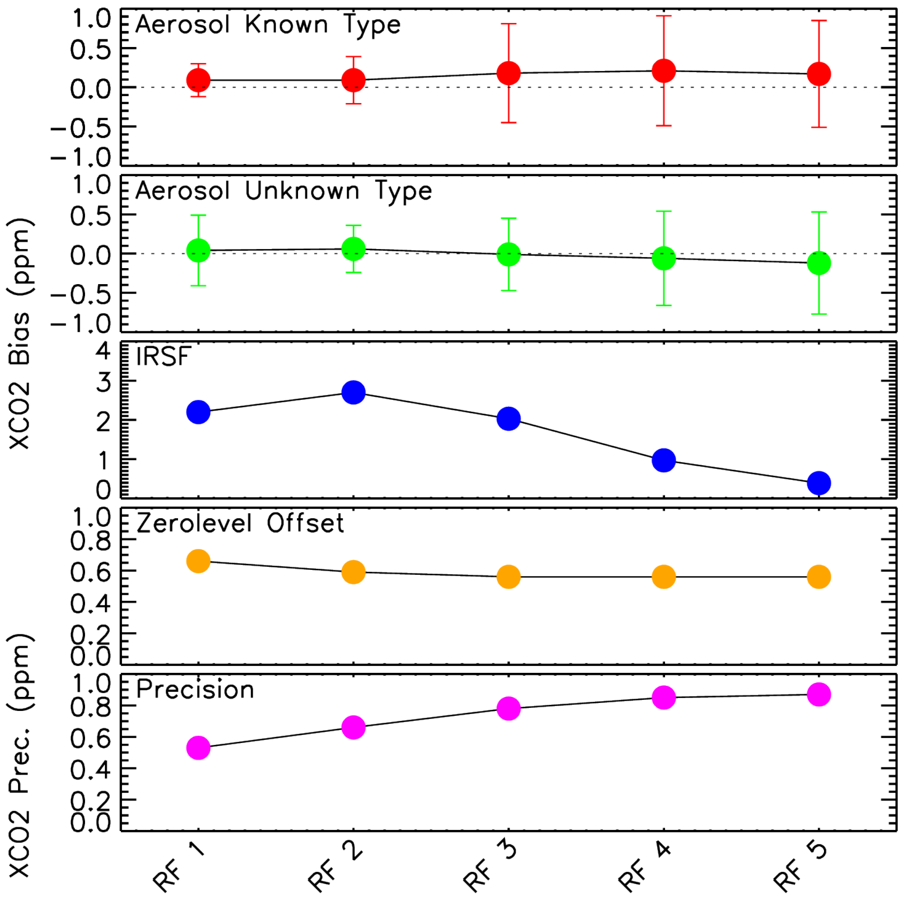

Figure 8: Summary of the XCO2 error analysis for the 5 resolution factors for implementation option b

8 Summary and Conclusion

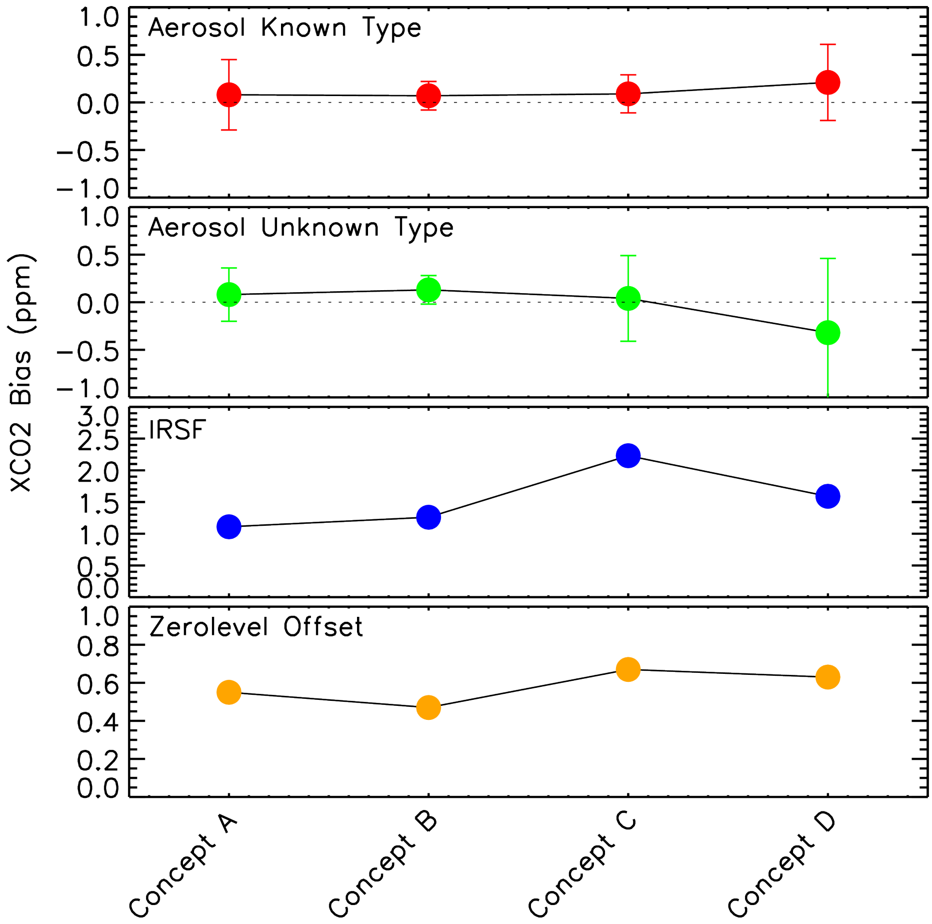

Figure 9: Summary of the XCO2 errors inferred for the 4 instrument concepts studies in section 5 and 6. Not included is the error from straylight.

We have analysed aerosol-related XCO2 errors and errors from instrument calibration uncertainties (IRSF, zero level offset and straylight) for four specific instrument concepts. Aerosol-related errors have been studied with full end-to-end retrieval simulations while linear error analysis has been used for instrument errors. Overall, we find that aerosol-related errors are similar between concepts A to C (somewhat depending on the chosen quality filter) while concept D tends to yield larger errors. It can be presumed that this is a result of the comparably low SNR assumed for concept D. We find that IRSF-related errors are significant for all concepts but are largest for concepts with higher spectral resolution (concepts C and D). Zero level offset errors tend to be similar and small for all concepts. We find that straylight errors are large but again similar for all concepts.

We have conducted an additional systematic study on the impact of changing spectral resolution and SNR of instrument concepts (section 8). This study supports the finding that aerosol-related errors are similar between different resolutions but depending on the implementation option, the higher or the lower resolution concepts are preferred. Again, we see that IRSF errors are largest for concepts with high spectral resolution.

In summary, we conclude that concept B appears as the best compromise between a high capability to mitigate aerosol-related errors and low IRSF-related errors. Note that concept B is the only instrument concept that makes use of the ‘super-strong’ CO_2 band at 2.1 micron which has no heritage from previous satellite missions.

9 References

Baum, B.A., A. J. Heymsfield, P. Yang, S. T. Bedka, Bulk Scattering Properties for the Remote Sensing of Ice Clouds. Part I: Microphysical Data and Models, J. Appl. Met., 44, 2005

Boesch, H., Toon, G. C., Sen, B., Washenfelder, R. A.,Wennberg, P. O., Buchwitz, M., de Beek, R., Burrows, J. P., Crisp, D., Christi, M., Connor, B. J., Natraj, V., and Yung, Y. L.: Space-based near-infrared CO2 measurements: Testing the Orbiting Carbon Observatory retrieval algorithm and validation concept using SCIAMACHY observations over Park Falls, Wisconsin, J. Geophys. Res., 111, D23302, doi:10.1029/2006JD007080, 2006.

Connor, B. J., H. Boesch, G. Toon, B. Sen, C. Miller, and D. Crisp, Orbiting Carbon Observatory: Inverse method and prospective error analysis, J. Geophys. Res., 113, D05305, doi:10.1029/2006JD008336, 2008.

Kahn, R.; Banerjee, P.; McDonald, D. Sensitivity of multiangle imaging to natural mixtures of aerosols over ocean. J. Geophys. Res., 106, D16.,2001.

Natraj, V., Boesch, H., Spurr, R. J. D., and Yung, Y. L.: Retrieval of *XCO*2 from simulated Orbiting Carbon Observatory measurements using the fast linearized R-2OS radiative transfer model, J. Geophys. Res., 113, D11 212, doi:10.1029/2007JD009017, 2008.

O’Dell, C.W.: Acceleration of multiple-scattering, hyperspectral radiative transfer calculations via low-streams interpolation, J. Geophys. Res., 115, D10 206, doi:10.1029/2009JD012803, 2010

Rodgers, C. D.: “Inverse Methods for Atmospheric Sounding: Theory and Practice”, World Scientific, Singapore, 2000.

Study on Spectral Sizing for CO_2 Observations:

Error analysis for CarbonSat scenarios and different spectral sizing

Technical Note

ESA Study
"Study on Spectral Sizing for CO_2 Observations"
ESA Contract Nº 4000118601/16/NL/FF/gp

Author:
Michael.Buchwitz@iup.physik.uni-bremen.de,
Institute of Environmental Physics (IUP) / Institute of Remote Sensing (IFE),
University of Bremen (UB), Bremen, Germany

Change log

Version	**Date**	**Status**	**Author**	**Reason for change**
1.0	11-Apr-2017	Submitted	M. Buchwitz, IUP-UB	New document
2.0	23-May-2017	Submitted (for MTR)	M. Buchwitz	Update of straylight assessment using updated version of SRON-CSS-TN-2016-002 (incl. improved error estimation procedure) Some editorial improvements (e.g., Fig. numbering issue)
3.0	29-June-2017	Submitted	M. Buchwitz	Update of straylight assessment considering new information from ESA Summary figure for linear error analysis added
3.1	6-July-2017	Submitted	M. Buchwitz	Improved summary figures 36 (improved colors) and 47 (improved colors and annotation)
4.0	30-April-2018	Submitted	M. Buchwitz	Additional results added: New Sects. 9 and 10

Table of Contents

1. Abstract

In the context of optimizing CarbonSat (also in terms of costs) it had been investigated in the past if high spectral resolution is mandatory for precise and accurate XCO_2 retrieval or if a somewhat less demanding spectral resolution is also acceptable taking into account that other parameters (such as spectral coverage and signal-to-noise performance) can be optimized simultaneously for compensation. According to the initial specification of CarbonSat - as given in the CarbonSat Mission Requirements Document, MRDv1.0 – a rather high spectral resolution was required. Using this specification as a starting point it had been investigated in the past to what extent the spectral resolution can be reduced. That investigation was primarily based on simulated retrievals which have been carried out by University of Bremen using the BESD/C retrieval algorithm and independently by University of Leicester using University of Leicester's XCO_2 retrieval algorithm. In addition, real GOSAT data had been analysed by SRON. Based on these past investigations it was concluded that the spectral resolution can be reduced if the signal-to-noise performance is enhanced and the spectral coverage is extended. These findings had been adopted for the final version of the CarbonSat Mission Requirements Document - MRDv1.2 - which had been used for sub-sequent assessments conducted to quantify in detail the performance of CarbonSat in the context of the Earth Explorer 8 (EE8) Report for Mission Selection (RfMS) of CarbonSat.

The purpose of this follow-on study is to repeat and extend (parts of) those past investigations, which had been carried out to define CarbonSat's instrument spectral sizing point (SSP), where SSP is defined as spectral resolution, spectral coverage and signal-to-noise performance. Specifically, it was requested to repeat the analysis as had been carried out for CarbonSat by the University of Bremen but (i) using the latest version of the BESD/C retrieval algorithm (as available at the end of the CarbonSat EE8 related activities), (ii) using the latest information on systematic instrument related errors and (iii) using four different pre-defined instrument concepts: instrument A (similar as CarbonSat MRDv1.0), instrument B (similar a CarbonSat MRDv1.2), instrument C (similar as NASA's OCO-2) and instrument D (similar as CNES's MicroCarb). Here instrument B has the lowest spectral resolution compared to the other three instruments but instrument B has highest signal-to-noise ratio and covers the largest spectral region. The purpose of this investigation is to find out if the past recommendation - which led to a CarbonSat similar as instrument B - is still valid, namely that instrument B is equivalent or even better in terms of XCO_2 random and systematic errors compared to other higher spectral resolution instrument concepts (note that instrument B is preferred for cost reasons if equivalent in terms of XCO_2 quality).

As shown in this document the following error sources have been considered: (i) instrument noise, (ii) geophysical errors (e.g., aerosols, cirrus, sun-induced fluorescence), (iii) zero-level-offset, (iv) distortions of the Instrument Spectral Response Function, (v) straylight, (vi) detector non-linearity and (vii) polarization. It is shown that instrument B has the smallest XCO_2 random error ("best precision"). For systematic errors the situation is less clear. Using full iterative retrievals it is shown that instrument B often has the smallest systematic error for the investigated scenarios but according to linear error analysis (performed to isolate instrument specific errors) the differences to the other instruments are much less pronounced (here the results show that instruments A, B and C are nearly identical). It is therefore concluded that the past recommendations - which resulted in MRDv1.2 - are still valid.

2. Executive summary

In this document an updated (and extended) analysis of a past analysis is presented. That past analysis had been conducted for the ESA Earth Explorer 8 (EE8) candidate mission CarbonSat. The results of that past analysis are reported in the Final Report (FR) of the ESA study "Level-2 and Level-1B Requirements Consolidation Study" **/Bovenmann et al., 2014/** in particular in Sect. 5.1 - 5.3. In the following that past study is referred to as CS-L1L2-I study.

A key result of that past analysis was that the spectral resolution of CarbonSat can be reduced (w.r.t. to the initial instrument configuration) - without degradation in terms of biases and precision of the main data products XCO_2 and XCH_4 - if the spectral coverage of (the initial specification of) CarbonSat bands is extended and the signal-to-noise ratio (SNR) is enhanced.

As a result, it had been recommended (and later also decided) to aim at a new "spectral sizing point" (SSP) for CarbonSat, where SSP is defined as a certain combination of spectral resolution, spectral coverage and SNR performance. The decision about the new SSP has been made quite early in CarbonSat Phase A and the resulting instrument specification had been used to update the CarbonSat Mission Requirements Document (MRD) from versions 1.0/1.1 to version 1.2.

Document MRDv1.2 had been used as input for many sub-sequent assessments and, ultimately, for the results presented in the CarbonSat EE8 Report for Mission Selection (RfMS) **/CS RfMS, 2015/**. All these assessments confirmed that a CarbonSat instrument with the new MRDv1.2 SSP will be able to meet the demanding XCO_2 and XCH_4 requirements concerning random and systematic errors (see **/Buchwitz et al., 2013a, 2013b, 2015/ /Bovensmann et al., 2015/ /CS RfMS, 2015/**).

At present, however, more details are available on various instrument related errors such as detector non-linearity and straylight. It is therefore of interest to know if the past CarbonSat findings and recommendations concerning its SSP are still valid or not. This is relevant in the context of ongoing activities related to a possible future European satellite mission to monitor fossil CO_2 emissions (see "Towards a European Operational Observing System to Monitor Fossil CO_2 emissions" **/Ciais et al., 2015/**).

In this document results from a new analysis are reported which are an update and extension of the above mentioned past analysis. Specifically, simulated retrievals have been performed for four different SSPs referred to as instrument concepts A, B, C and D in this document.

Instruments A and B correspond to CarbonSat MRD v1.0 and v1.2, respectively, except for the SNR performance (which had been updated based on the most recent information). Instrument C is similar to NASA's OCO-2 and Instrument D is similar to MicroCarb/CNES.

Simulated retrievals have been performed primarily for the 15 geophysical scenarios also used for the previous CarbonSat SSP assessments (see **/Bovenmann et al., 2014/**, in particular Sects. 5.1 to 5.3). They are defined by different CO_2, CH_4, and aerosol vertical profiles, different aerosol types, cirrus amounts and cirrus altitudes and different amounts of Sun-Induced Fluorescence (SIF). These parameters are input parameters for radiative transfer simulations. The high spectral resolution radiances - as computed with the radiative transfer model SCIATRAN - have been converted to simulated satellite instrument radiance observations using an instrument model.

The simulated radiance observations have then been inverted using the BESD/C retrieval method, which has also been used for previous CarbonSat assessments. The main output of the retrieval step is the retrieved XCO_2 and its uncertainty (essentially the XCO_2 random error due to instrument noise). Systematic XCO_2 retrieval errors are obtained by computing the difference of the retrieved and the "true" XCO_2 (the "true" XCO_2 has been computed from the known model atmosphere).

The main question to be answered via the activities described in this document is:

- Is instrument B equivalent (or even better) in terms of XCO_2 data quality compared to (some or all of) the other (higher spectral resolution) instruments or not?

This question is relevant as high spectral resolution implies high costs. This means that instrument concept B is the preferred concept if equivalent in terms of XCO_2 quality.

This question has been answered by performing simulated XCO_2 retrievals for different SSPs (i.e., different instrument concepts) using different scenarios and different instrument / calibration related errors such as straylight, detector non-linearity and zero-level-offset.

The findings can be summarized as follows: It is shown that instrument B has the smallest XCO_2 random error ("best precision") (**Figure 1**). For systematic errors the situation is less clear. Concerning systematic errors (biases) it is shown using full iterative retrievals that instrument B often has the smallest bias for the investigated scenarios (**Figure 1**). In addition, a linear error analysis has been performed in particular to (better) isolate instrument related biases. Also here instrument B shows good performance but the differences between the four instruments is much less pronounced (esp. for A, B and C) (**Figure 2**). It is therefore concluded that the past recommendations - which resulted in CarbonSat MRDv1.2 - are still valid.

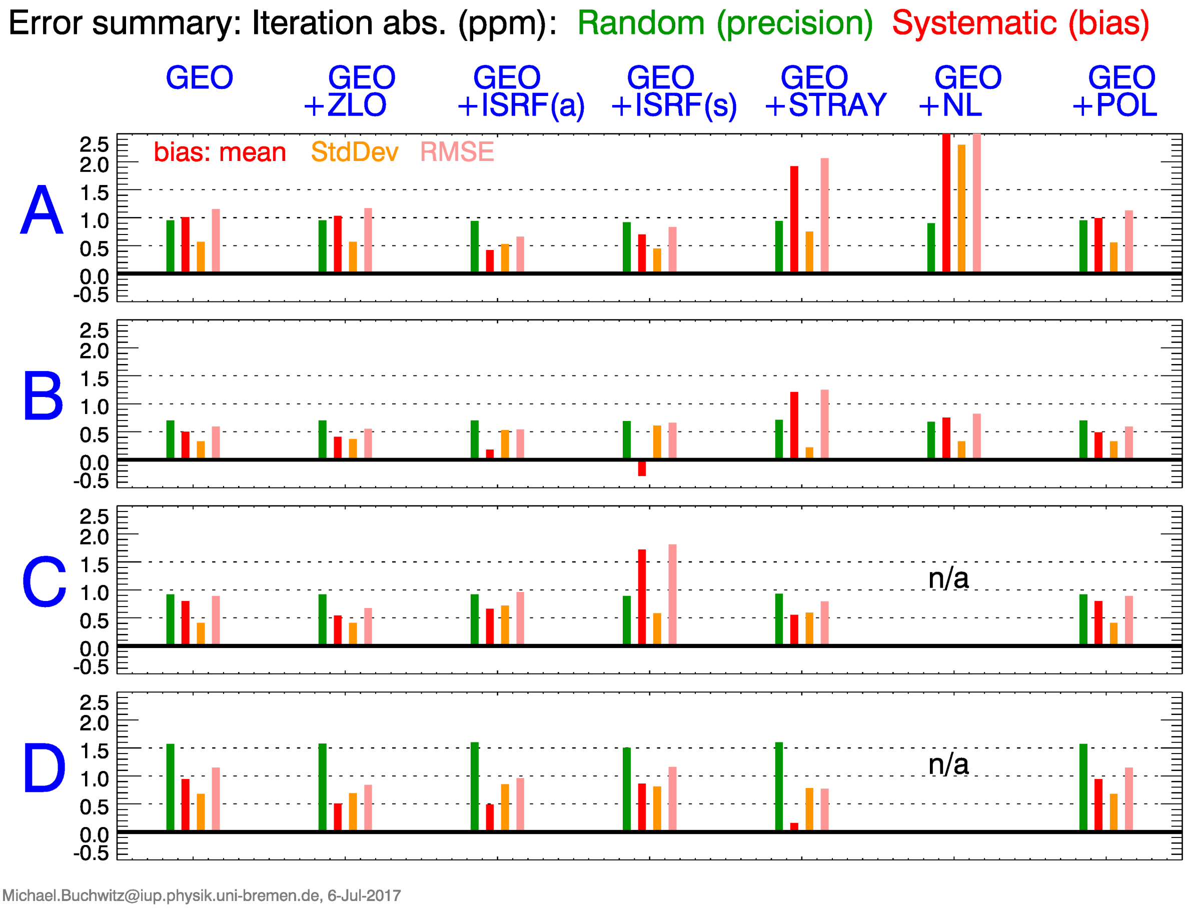

Figure 1: Summary of the error analysis results obtained using full iterative retrievals. A row corresponds to one of the four instruments A, B, C and D. A column corresponds to a certain systematic error or combination of errors: GEO: geophysical error (i.e., XCO_2 error due to aerosols, clouds, etc.), GEO+ZLO: zero-level-offset (radiance) error in addition to GEO error, ISRF: Instrument Spectral Response Function (two type of ISRF errors have been investigated (a = anti-symmetrial shape error, s = symmetrical error)), STRAY: straylight, NL: detector non-linearity (only input data for the instruments A and B were available), and POL: polarization related radiance error. The green bars show the XCO_2 random error ("precision"). The red bars show the three numbers computed to characterize XCO_2 biases (from left to right): mean bias, standard deviation of bias and root-mean-square error. As can be seen, instrument B has "best precision" (smallest random error) and typically also smallest bias (smallest systematic error). For additional details see **Sect. 6**.

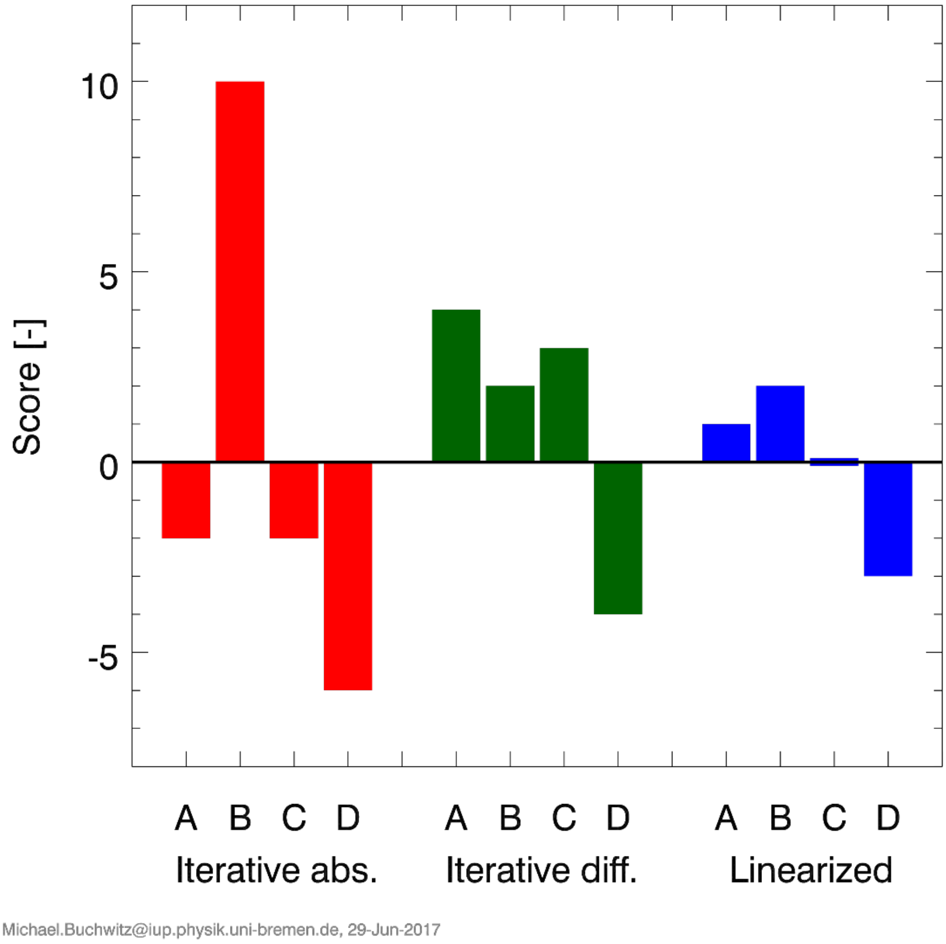

Figure 2: Overall summary of the error analysis results using scores (see **Sect. 8.1**). The higher the score, the better the instrument in terms of smaller XCO_2 biases. The red bars ("Iterative abs.") show the scores for the results obtained using full iterative retrievals. The blue bars ("Linearized") show the scores using linearized retrievals. As can be seen, instrument B is "the winner" for both methods. For additional details incl. explanation of "Iterative diff." (green bars), where the results are somewhat difficult to interpret, see **Sect. 8.1.2**.

3. Used set-up and simulation tools

3.1. Overview

The goal of this study is to investigate four different satellite instrument concepts in order to determine their characteristics with respect to the retrieval of column-averaged dry-air mole fractions of carbon dioxide (CO_2), i.e., XCO_2. Essentially it is of interest to find out which instrument is "the best" for this application and how large the XCO_2 data quality differences are (if the differences are "negligible", then other criteria for instrument selection are more relevant, e.g., costs).

However, none of the instruments is directly measuring XCO_2. Each instrument measures a radiance spectrum. This radiance spectrum needs to be "interpreted" w.r.t. XCO_2 using an inversion (or retrieval) algorithm, which is typically a quite complex algorithm using atmospheric radiative transfer modelling and a large number of input parameters. The instrument observes the atmosphere, which is defined by many parameters including CO_2. The atmospheric radiance, which enters the instrument, is modified by the instrument and is measured using a detector. The detector signals can be converted to the observed radiance using a "Level 0 to Level 1" algorithm (essentially the inverse of the instrument model) and calibration parameters. This observed radiance can then be converted to the desired quantity XCO_2. This retrieved XCO_2 can be compared with the "true XCO_2" (which is known for simulations) in order to determine the bias characteristics of the retrieved XCO_2. These characteristics depend NOT ONLY on the instrument but ALSO on the inversion (or retrieval) algorithm, i.e., on the entire Observing System (**Figure 3**). This means that - strictly speaking - the results shown in this document are valid only for the observing system, which uses BESD/C as inversion algorithm. The influence of the inversion algorithm is however considered in this study by using also other algorithms (see the corresponding technical reports and the Final Report of this study). Furthermore, linear error analysis is used in addition to full iterative retrievals.

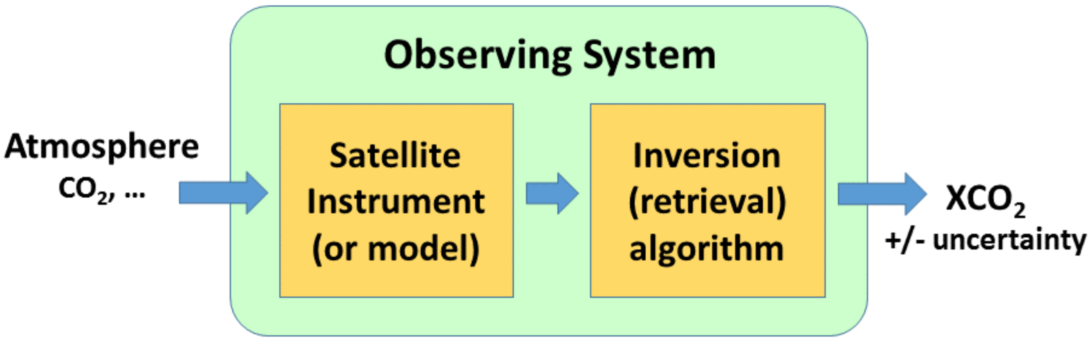

Figure 3: The XCO_2 observing system.

For the purpose of this study, it is essential to determine how certain characteristics of the Level 1 radiance spectra determine the quality of the XCO_2 Level 2 data products of the proposed CarbonSat-like instrument. To perform these assessments, the IUP-UB CarbonSat (CS) analysis system has been used, which is described in detail in **/Buchwitz et al., 2013a, 2013b, 2015/ /Bovenmann et al., 2014/**.

A more detailed overview about this analysis system is shown in **Figure 4**. The key components are:

- a Radiative Transfer Model (RTM) which computes high spectral resolution radiances based on given atmospheric, surface parameters and other parameters such as the solar zenith angle. A given set of parameters is referred to as "geophysical scenario" in the following.
- an instrument model which converts the high resolution RTM radiances into simulated satellite instrument observations taking into account the instrument characteristics as given by instrument requirements (or performance estimates) for parameters such as spectral range, spectral resolution and signal-to-noise ratio (SNR).
- the Level 1-2 retrieval program ("BESD/C") which inverts the radiance spectra in order to obtain the desired parameter XCO_2 (and XCH_4) and its statistical uncertainty (random error). The XCO_2 systematic error (bias) is computed as "retrieved minus true", where the true value of XCO_2 is obtained from the used model atmosphere.

More details on these components are given in the following sub-sections.

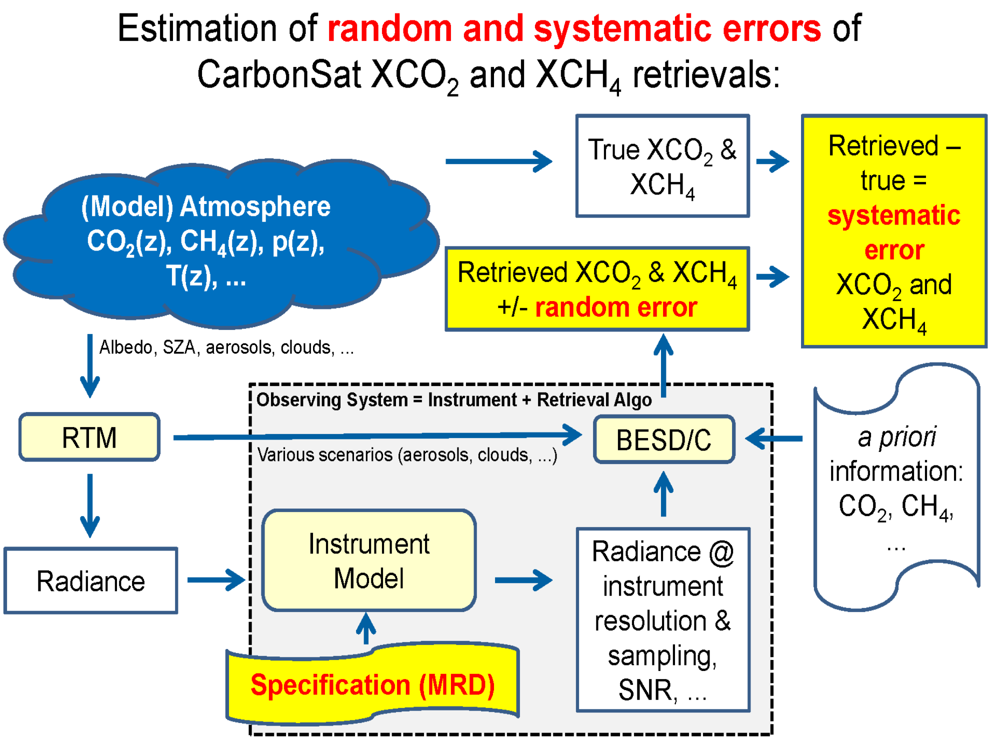

Figure 4: Overview of the IUP-UB satellite instrument Level 1 to Level 2 analysis system as used for past for CarbonSat assessments and also used in this study. Figure from **/Buchwitz et al., 2013b/**.

3.2. Retrieval Algorithm BESD/C

The retrieval algorithm used for the assessment results presented in this document is BESD/C **/Bovensmann et al., 2010/ /Buchwitz et al. 2013a/**. BESD stands for "Bremen optimal Estimation DOAS". BESD/C is an algorithm primarily designed to retrieve atmospheric dry-air column-averaged mole fractions of CO_2 and CH_4, i.e., XCO_2 and XCH_4 from satellite observed radiance spectra in the Near-Infrared / Shortwave-Infrared (NIR/SWIR) spectral region. In addition, a number of other parameters, such as Sun-Induced Fluorescence (SIF) (also referred to as Vegetation Chlorophyll Fluorescence (VCF) in this document) and cirrus optical depth (COD), can also be retrieved with this algorithm.

BESD/C is based on Optimal Estimation (OE) **/Rodgers, 2000/** and uses SCIATRAN as the forward (RT) model. SCIATRAN is a powerful state of the art RT simulation software which has been developed at the IUP of University of Bremen **/Rozanov et al. 2014/**.

BESD/C has been designed to simultaneously evaluate multiple spectral regions (e.g., O_2 A band and SWIR bands) and to retrieve scattering parameters (aerosols, clouds) in addition to XCO_2, as well as other parameters (e.g., SIF).

The radiance as used for the purpose of this study are high spectral resolution radiances (computed with SCIATRAN), which are converted to simulated satellite radiance observations using an instrument model, which is described in the following.

The same (full iterative) BESD/C retrieval algorithm has been applied to simulated radiance of all 4 instruments investigated in this study. However, some of the retrieval algorithm settings had to be adjusted due to the fact that the instruments cover different spectral regions. The only differences are the following:

- All instruments: Spectral fitting windows according to instrument specification.
- SIF and COD pre-processing:
    - A: SIF: yes (via 758 nm region); COD: no
    - B: SIF: yes (via 758 nm region); COD: yes (via 1939 nm region)
    - C: SIF: no; COD: no
    - D: SIF: no; COD: no

3.3. Instrument Simulator

The satellite instrument simulator as used for the presented assessments converts the high spectral resolution radiance and irradiance spectra as computed with RTMs such as SCIATRAN **/Rozanov et al. 2014/** into simulated spectra as measured by a satellite instrument by

- convolving the spectra using the assumed Instrument Spectral Response Function (ISRF) (spectral resolution),
- computing the wavelength grid of the satellite radiance observations using the definition of the instrument's spectral bands, spectral resolution and Spectral Sampling Ratios (SSR),
- spectral interpolation of the convolved spectra onto the instrument spectral grid and
- computation of the measurement error using the instrument signal-to-noise ratio (SNR).

Figure 5 shows example spectra for instrument B. The instrument parameters are from **/Landgraf et al., 2017b/** and described in **Sect. 5**.

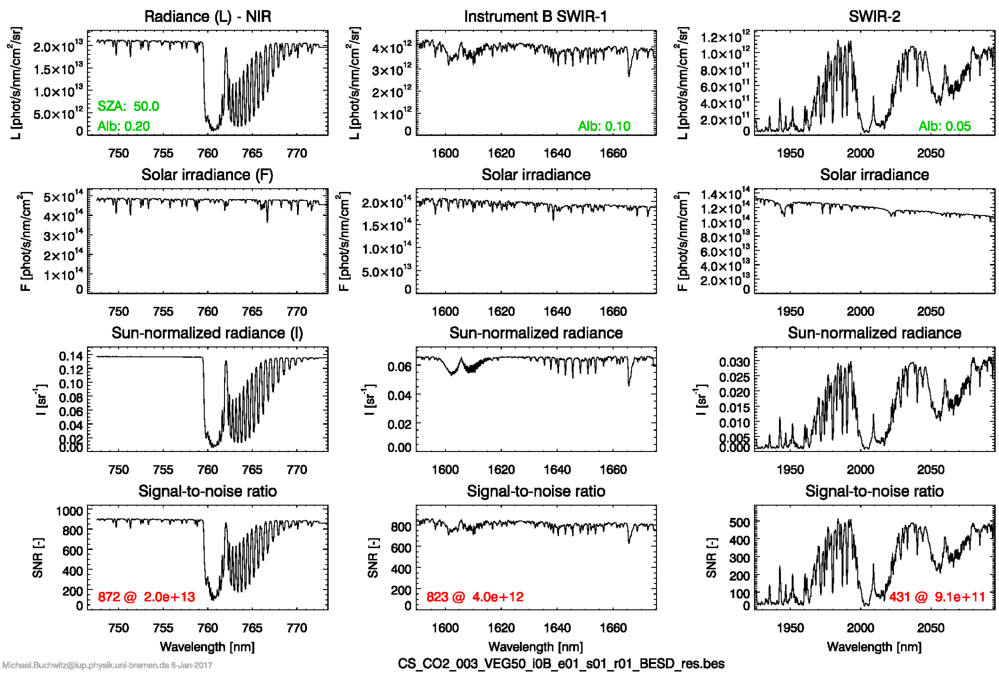

Figure 5: Simulated nadir radiance (top), solar irradiance (2nd row), sun-normalized radiance (3rd row) and signal-to-noise ratio (bottom) spectra for vegetation albedo and a Solar Zenith Angle (SZA) of 50°. Here the SSP corresponds to instrument B. The scenario is s01 (details are given below).

4. Geophysical Scenarios

4.1. Overview

For the purpose of this study we use the 15 geophysical scenarios as defined and used also in the past to optimize the SSP of CarbonSat **/Bovensmann et al., 2014/**. They are described in **/Bovensmann et al., 2014/** but also in the following sub-sections.

Key parameters which are varied and which define the used geophysical scenarios are:

- CO_2 (and CH_4) vertical profiles
- SIF
- Aerosol profile
- Aerosol type
- Cirrus optical depth (COD)
- Cirrus altitude

The focus is on simulations for vegetation surface albedo (VEG) and a solar zenith angle (SZA) of 50°. If other conditions have been used, then this is explicitly mentioned in the following.

4.2. GHG vertical profiles

Two sets of CO_2 and CH_4 vertical profiles have been used. They are shown in **Figure 6** (see also **Table 1**). One set (shown in black) corresponds to the *a priori* (= first guess) profiles as used for the retrieval. The other set (green) has been used for most of the simulated satellite observations presented in this report. It corresponds to a typical northern mid-latitude summer (MLS) scenario, where lower atmospheric CO_2 (especially in the boundary layer) is lower than average due to CO_2 uptake by growing vegetation (plant uptake) and CH_4 is higher primarily due to wetland emissions (note that the same profiles have been used for the assessments presented in **/Bovensmann et al., 2010/**). As can be seen from **Figure 6**, XCO_2 is 390 ppm for the *a priori* profile and 386.27 ppm for the MLS profile, i.e., XCO_2 is 3.7 ppm ppm lower for the MLS scenario.

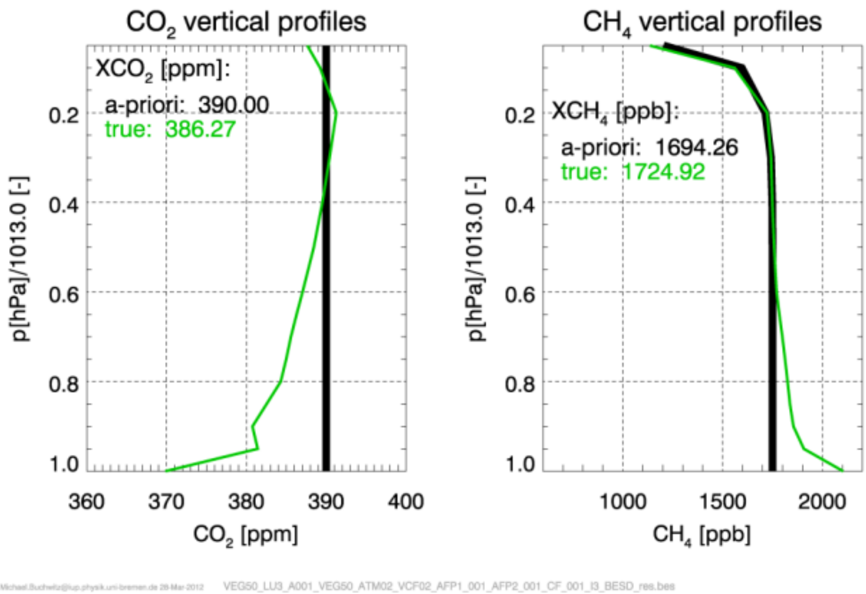

Figure 6: The two sets of CO_2 and CH_4 vertical profiles used for the assessments described in this document (black: *a priori* profiles; green: northern mid-latitude summer (MLS) profiles as used for most of the simulated satellite observations presented in this document).

Greenhouse Gas (CO_2 and CH_4) vertical profiles		
No.	**Type**	**Comment**
1	*A priori*	-
2	Perturbed	Northern hemispheric mid-latitude summer (MLS) conditions, see also **/Bovensmann et al., 2010/**

Table 1: The two sets of CO_2 and CH_4 vertical profiles used in this study. See also **Figure 6**.

4.3. Sun-Induced Fluorescence (SIF)

Four different Sun-Induced Fluorescence (SIF) / Vegetation Chlorophyll Fluorescence (VCF) emission spectra have been used for this study. They are shown in **Figure 7** (see also **Table 2**).

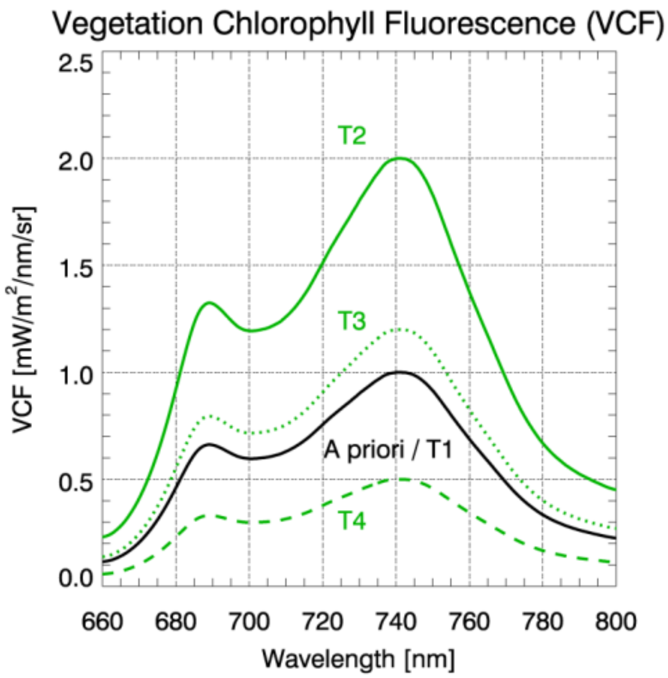

Figure 7: The four SIF/VCF emission spectra used in this study (from **/Rascher et al., 2009/**). See also **Table 2**.

Sun-Induced Fluorescence (SIF) / Vegetation Chlorophyll Fluorescence (VCF) emission spectra		
No.	**Type**	**Comment**
1	*A priori*	Peak emission: 1 $mW/m^2/nm/sr$ @ 740 nm = 0.8 $mW/m^2/nm/sr$ @ 755 nm
2	Perturbed (x2)	As 1 but scaled with x 2.0
3	Perturbed (x1.2)	As 1 but scaled with x 1.2
4	Perturbed (x0.5)	As 1 but scaled with x 0.5

Table 2: The four SIF/VCF emission spectra used in this study. See also **Figure 7**.

4.4. Aerosols

Five different aerosol types based on OPAC **/Hess et al., 1998/** have been used. They are summarised in **Table 3**. Note that they differ somewhat from the scenarios listed in Tab. 6 of **/Bovensmann et al., 2014/**. The main reason is that the latest version of the BESD/C retrieval algorithm use "OPAC continental average, 70% humidity" (here: No. 0) as *a priori* aerosol type.

Aerosol types		
No.	**Type**	**Comment**
0	*A priori*: OPAC continental average, 70% humidity (CA70)	Mixture: • 46% water soluble • 54% soot Humidity troposphere: 90%
1	OPAC continental clean (CC)	Mixture: • 100% water soluble Humidity troposphere: 70%
2	OPAC continental average, 90% humidity (CA90=CA)	Mixture: • 46% water soluble • 54% soot Humidity troposphere: 90%
3	OPAC continental polluted (CP)	Mixture: • 31% water soluble • 69% soot Humidity troposphere: 90%
4	OPAC desert (DE)	Mixture: • 87% water soluble • 12% mineral (nucleation mode) • 1% mineral (accumulation mode) Humidity troposphere: 70%

Table 3: The five aerosol types used in this study based on OPAC **/Hess et al., 1998/**.

Five different aerosol extinction profiles have been used and are summarised in **Table 4**. Note that the extinction profiles are only valid for 550 nm as the wavelength dependence of the extinction profiles depends on aerosol type. Note that the AODs differ somewhat from the values listed in Tab. 6 of **/Bovensmann et al., 2014/**. The main reason is that the *a priori* profile as used in the latest version of the BESD/C retrieval algorithm has changed.

Aerosol extinction vertical profiles (550 nm)		
No.	**Type**	**Comment**
1	*A priori*	AOD: 0.200
2	Enhanced in BL: x2.0 in 0-2 km	AOD: 0.305
3	Enhanced in BL: x1.5 in 0-2 km	AOD: 0.252
4	Reduced in BL: x0.5 in 0-2 km	AOD: 0.174
5	Reduced in BL: x0.2 in 0-2 km	AOD: 0.111

Table 4: The five aerosol extinction profiles and corresponding AODs (at 550 nm) as used in this study. BL = Boundary Layer.

4.5. Cirrus clouds

Six different cirrus clouds have been defined for this study and they are summarised in **Table 5** shown below.

Cirrus clouds		
No.	**Cloud Optical Depth (COD) [-]**	**Cloud Top Height (CTH) [km]**
1	*A priori*: 0.05	*A priori*: 10.0
2	0.10	10.0
3	0.20	10.0
4	0.20	8.0
5	0.02	12.0
6	0.05	9.0

Table 5: The six cirrus clouds defined for this study.

4.6. Summary geophysical scenarios

Fifteen different geophysical scenarios have been defined using different combinations of the parameters described in the previous sub-sections. They are presented in **Table 6**.

Note that XCO_2 is 390.00 ppm for GHG vertical profile No. 1 (XCH_4: 1694.26 ppb) and 386.27 ppm for No. 2 (XCH_4: 1724.92) (see **Figure 6**).

Overview Geophysical Scenarios					
No.	**GHG vertical profiles**	**VCF**	**Aerosol type**	**Aerosol extinction**	**Cirrus**
1	1 (~constant)	1	1 (clean, CC)	1	1 (COD 0.05 / 10 km)
2	2 (mid-lat.summer)	1	1	1	1
3	2	2 (x2.0)	1	1	1
4	1	2	1	1	1
5	2	3 (x1.2)	1	1	1
6	2	3	1	2 (x2.0)	1
7	2	3	1	2	2 (0.1)
8	2	3	1	2	3 (0.2)
9	2	3	1	2	4 (0.2 / 8 km)
10	2	3	2 (average, CA90)	2	4
11	2	3	3 (polluted, CP)	2	4
12	2	3	4 (desert, DE))	3 (x1.5)	5 (0.02 / 12 km)
13	2	4 (x0.5)	4	4 (x0.5)	5
14	2	1	1	5 (x0.2)	1
15	2	1	1	4	6 (9 km)

Table 6: The 15 geophysical scenarios defined for this study.

5. Instrument configurations

An overview of the 4 instrument configurations A, B, C and D, which have been investigated in this study, is given in **Table 7.**

Spectra for instrument B for scenario s01 are shown in **Figure 5**. The corresponding spectra for instruments A, C, and D are shown in **Figure 8**, **Figure 9**, and **Figure 10**, respectively.

Radiance ratios for all scenarios w.r.t. one reference scenario (s01) are shown in **Figure 11** (instrument A) to **Figure 14** (instrument D).

Instrument concept	Band	Spectral range [nm]	Spectral resolution FWHM [nm]	Continuum SNR [-]	SSR (per FWHM)	Comment
A	NIR SW1 SW2	756-773 1559-1675 2043-2095	0.045 0.3 0.13	622 949 167	2.5 2.5 2.5	Similar as CS MRDv1.0 except SNR
B	NIR SW1 SW2	747-773 1590-1675 1925-2095	0.1 0.3 0.55	872 823 431	3.1 3.1 3.3	Similar as CS MRDv1.2 except SNR
C	NIR SW1 SW2	758-772 1591-1621 2042-2081	0.042 0.076 0.097	405 385 170	2.5 2.5 2.5	Similar as OCO-2
D	NIR SW1 SW2	758-769 1597-1619 2023-2051	0.032 0.067 0.085	190 160 61	2.9 2.9 2.9	Similar as MicroCarb

Table 7: The four instrument configurations investigated w.r.t. XCO_2 data quality. SSR is the Spectral Sampling Ratio = FWHM/SSI, where FWHM is the "Full Width Half Maximum" of the satellite Instrument Spectral Response Function (ISRF). The Signal-to-Noise Ratios (SNRs) are valid for the following radiances (given in photons/s/cm^2/nm/sr): NIR: $2x10^{13}$, SW1: $4x10^{12}$, SW2: $9.1x10^{11}$. The instrument parameters are from **/Landgraf et al., 2017b/**.

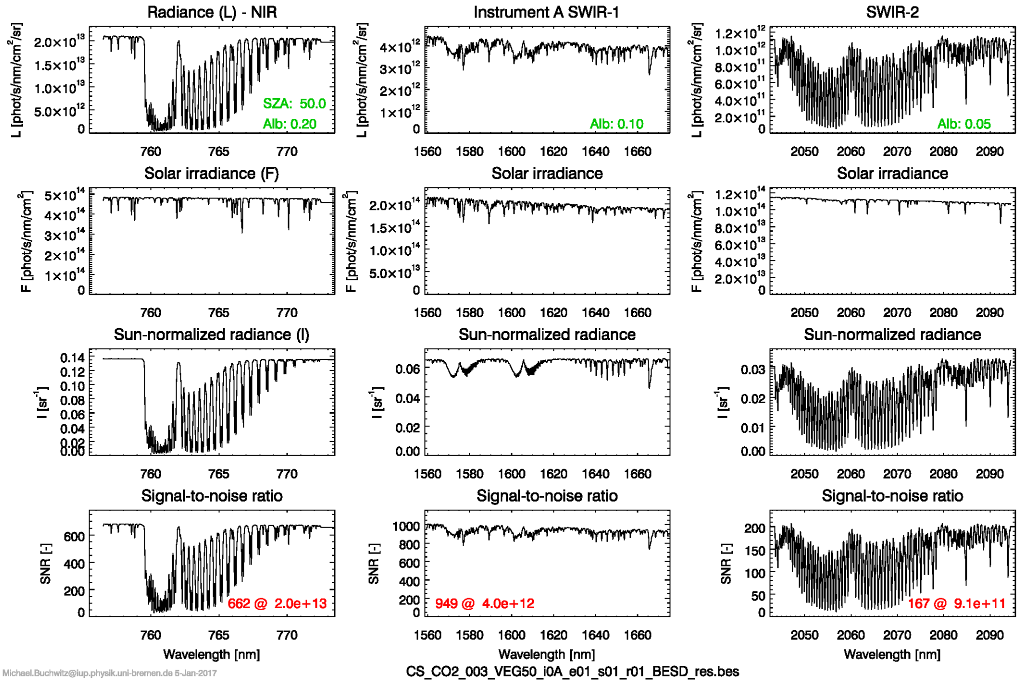

Figure 8: As **Figure 5** but for instrument A.

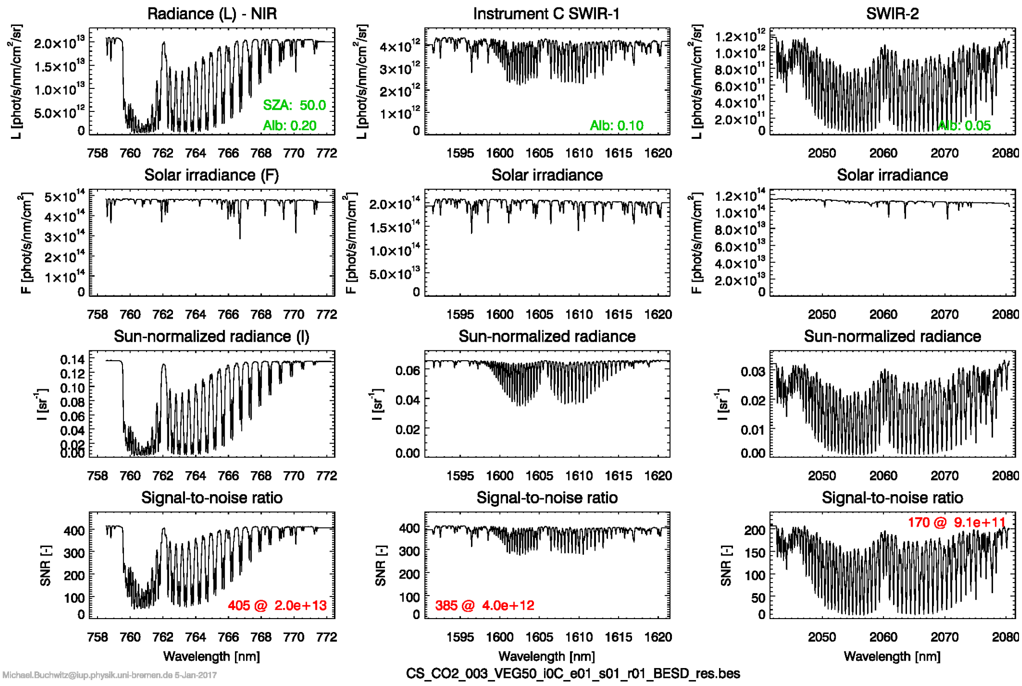

Figure 9: As **Figure 5** but for instrument C.

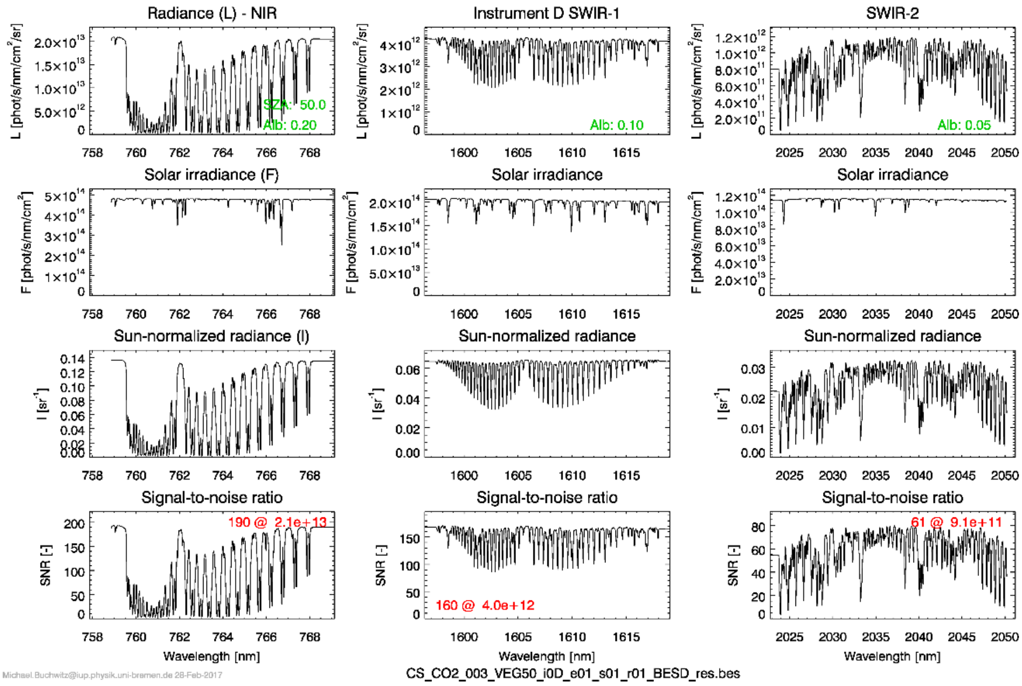

Figure 10: As **Figure 5** but for instrument D.

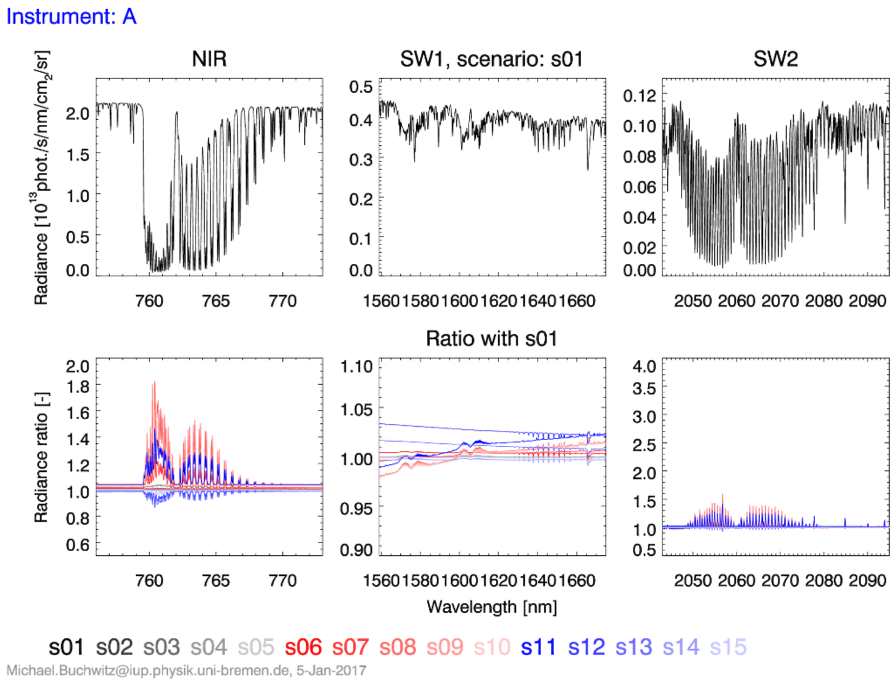

Figure 11: Radiance of scenario s01 for instrument A (top) and radiance ratios of scenarios s02 to s15 w.r.t. s01 (bottom).

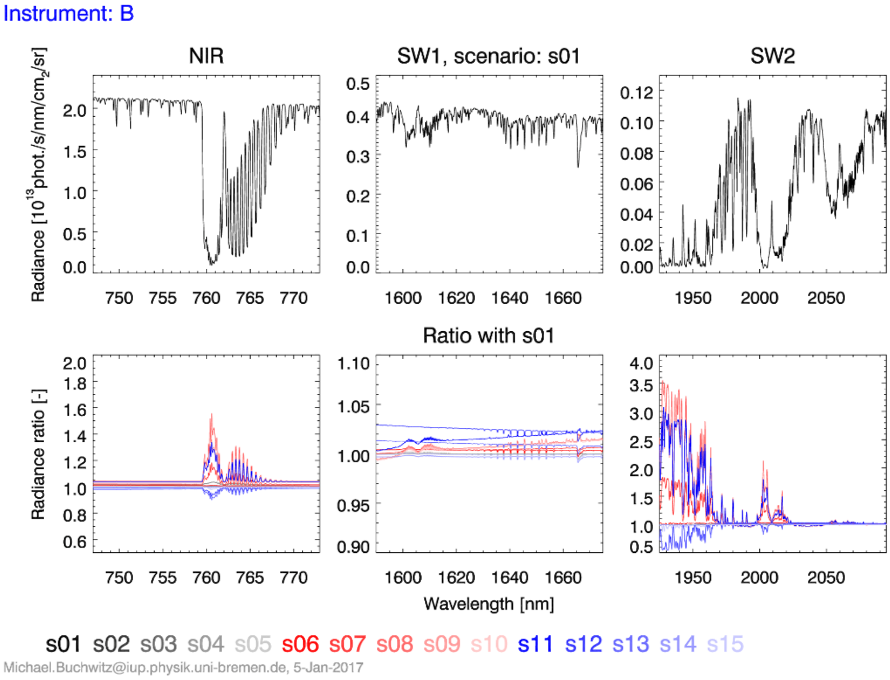

Figure 12: As **Figure 11** but for instrument B.

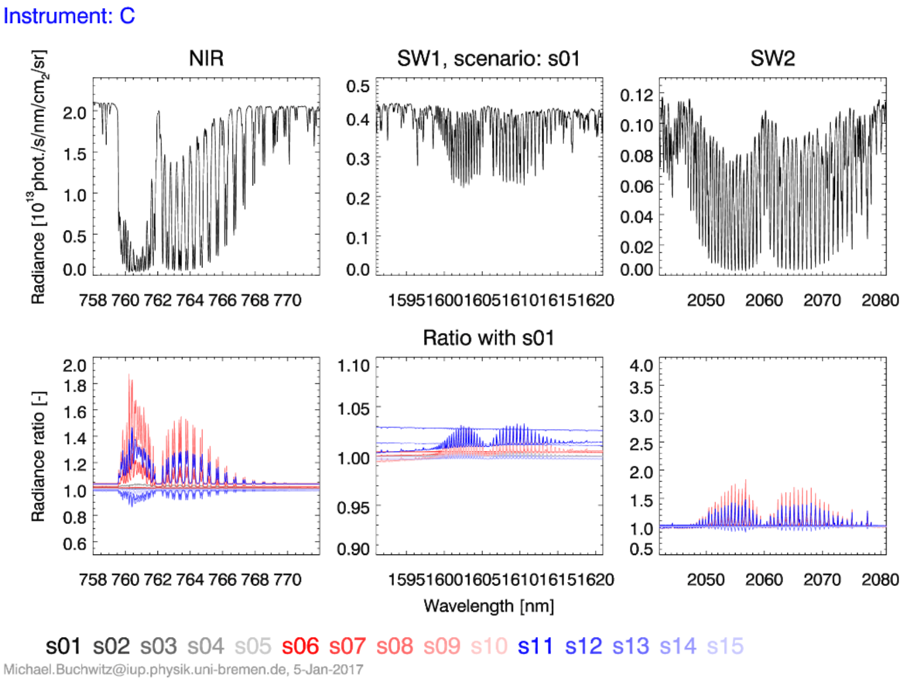

Figure 13: As **Figure 11** but for instrument C.

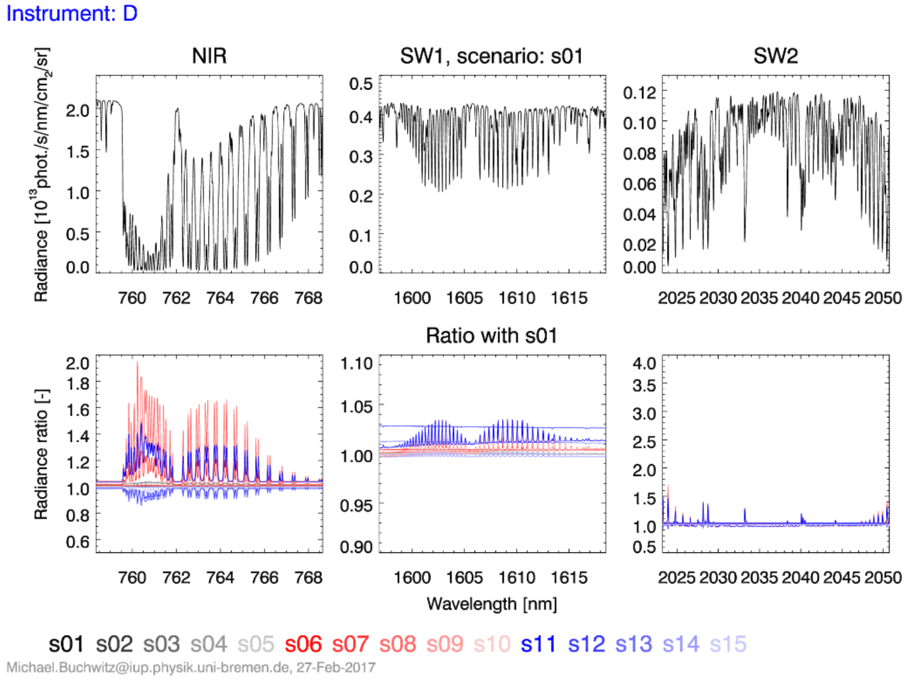

Figure 14: As **Figure 11** but for instrument D.

6. XCO_2 retrieval results ("Iterative abs.")

In this section, the XCO_2 retrieval results are presented for the described 4 instruments (= 4 different spectral sizing points). For each instrument the XCO_2 random and systematic retrieval error has been determined by applying the BESD/C retrieval algorithm to simulated radiances corresponding to the 15 selected scenarios.

The assessment method and results as presented in this section are referred to as **"Iterative abs."** in this document (i.e., absolute XCO_2 biases are presented and discussed originating from application of the iterative BESD/C algorithms to radiance spectra "with errors").

Additional assessment results are presented and explained in Sect. 7, which are referred to as "Iterative diff." and "Linearization" in this document.

6.1. Error source: Instrument noise and geophysical error (GEO)

In this section XCO_2 systematic and random errors are shown for the four instruments (= four spectral sizing points) assuming no systematic instrument related radiance errors.

The single measurement XCO_2 random error - or 1-sigma retrieval precision due to instrument noise - has been computed via the BESD/C retrieval method essentially by mapping the random error of the radiance (i.e., the noise) onto the random error (uncertainty, scatter) of the retrieved XCO_2. This error depends primarily on the radiance noise but to some extent also on the retrieval algorithm.

The retrieved XCO_2 also (typically) has a systematic error or bias. This error is computed as "retrieved – true". Note that the retrieval algorithm is typically not able to provide error free XCO_2 retrievals especially if the scenario used for the generation of the simulated observation does not correspond to the *a priori* assumptions used for the retrieval algorithm (e.g., w.r.t. aerosol type). Note that this is the case for all 15 scenarios (i.e., at least one parameter chosen for the selected scenarios differs from the retrieval assumptions). This source of systematic error – which is present even for error-free radiance spectra - is referred to as "geophysical error" in this document. Note that the bias would typically differ from zero even if the simulated observation would be fully consistent with the *a priori* assumption as some bias typically also originates from the pre-processing algorithms (e.g., surface albedo retrieval).

Before the error analysis results are shown and discussed the BESD/C Jabobian matrix is shown in
Figure 15 for instrument A, in
Figure 16 for instrument B, in
Figure 17 for instrument C and in
Figure 18 for instrument D.

The Jacobians show the change of the radiance due to a change of a retrieval state vector element. The state vector elements are (from bottom to top); CO_2 (3 layers), CH_4 (3 layers), surface pressure (PRE), Vegetation Chlorophyll Fluorescence (VCF or SIF), temperature (TEM), H_20, 2 aerosol parameters, one water cloud parameter (WOD), two cirrus clouds parameters, albedo (3 parameters), low order polynomial coefficients (9 parameter), spectral squeeze (3 parameters), spectral shift (3 parameters) and zero level offset (3 parameters).

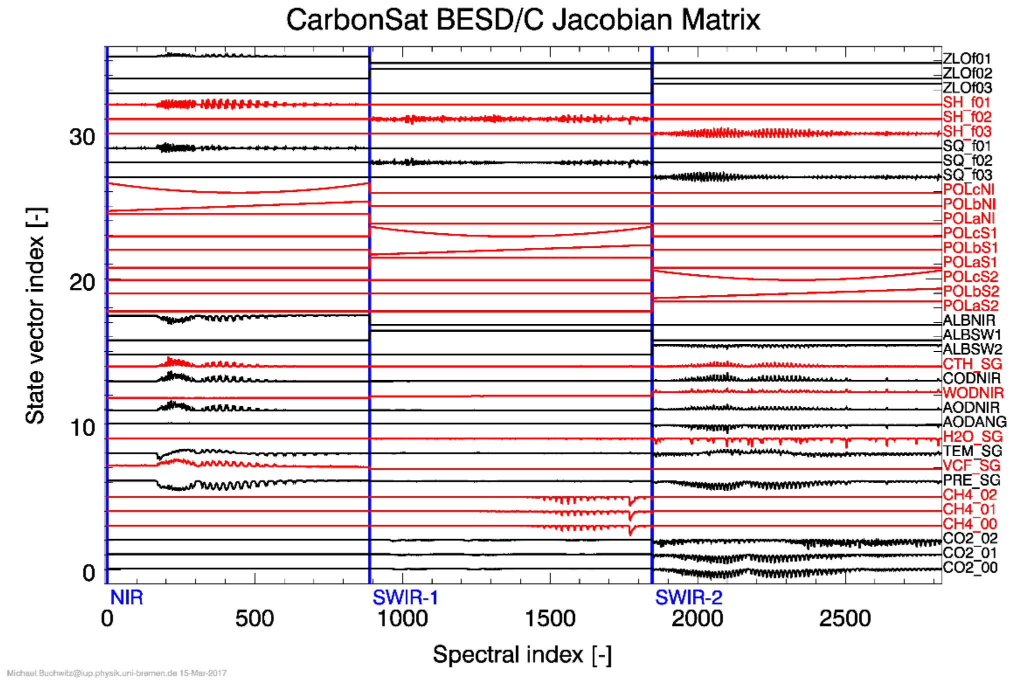

Figure 15: BESD/C Jabobian matrix for instrument A.

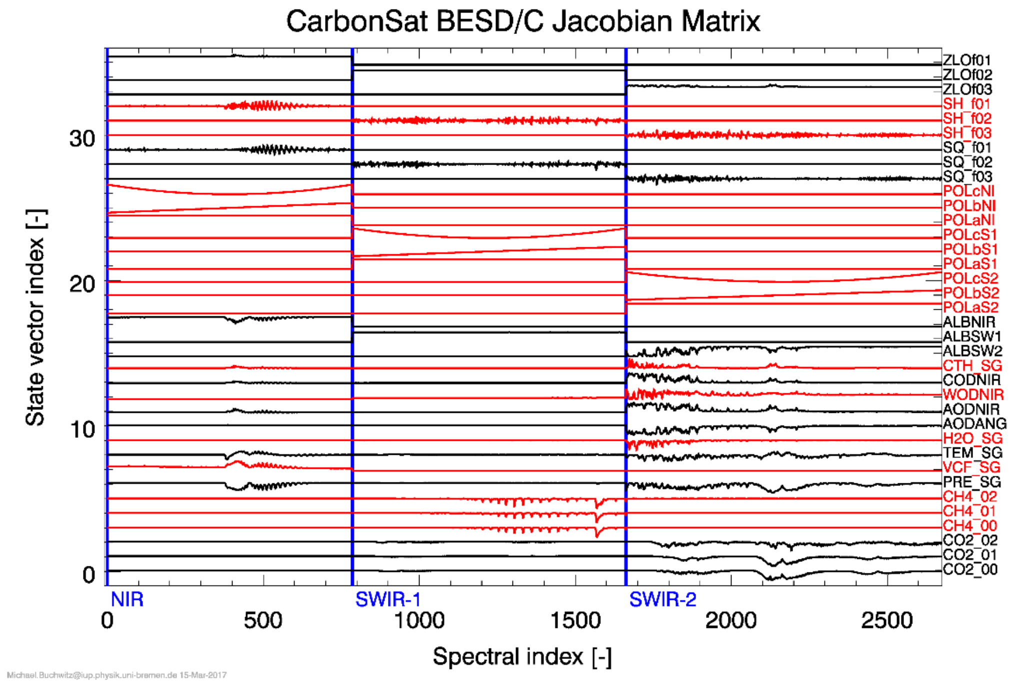

Figure 16: BESD/C Jabobian matrix for instrument B.

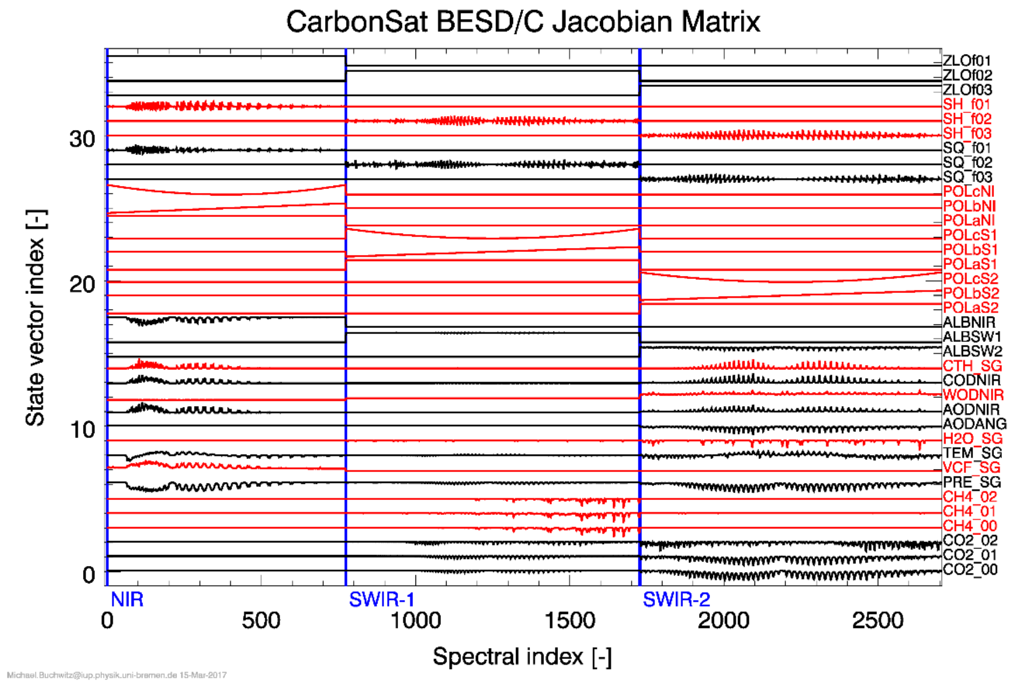

Figure 17: BESD/C Jabobian matrix for instrument C.

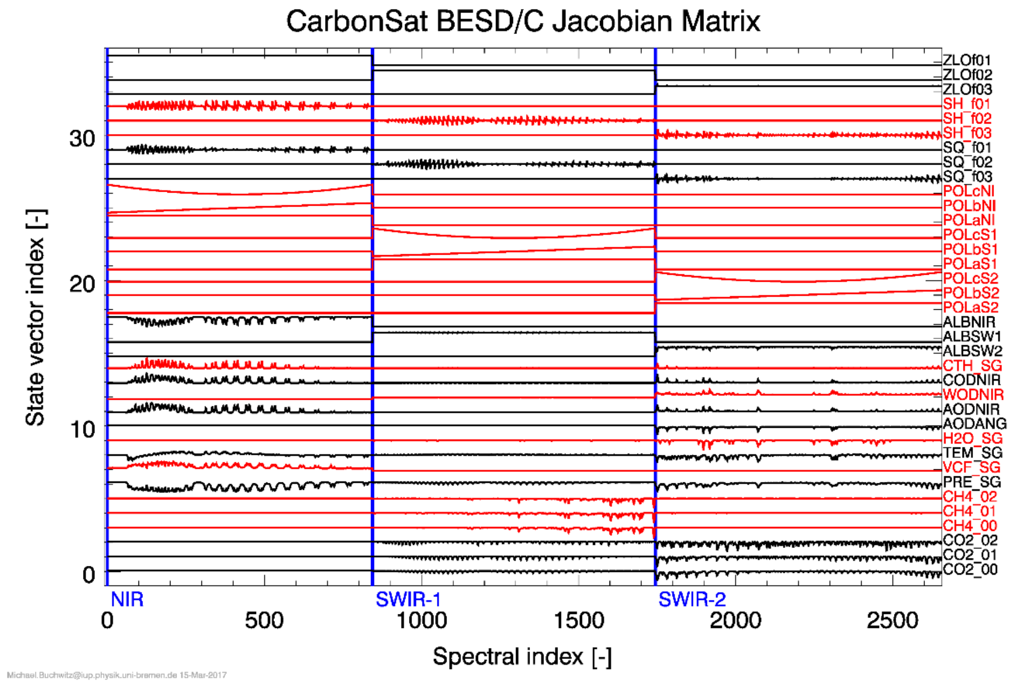

Figure 18: BESD/C Jabobian matrix for instrument D.

Figure 19 shows the error analysis results. As can be seen (top panel), the systematic XCO_2 error depends on the scenario and on the instrument, as expected.

For each instrument three numbers have been computed to characterise systematic errors, namely the mean error (mean bias), the standard deviation of the bias and the root mean square error (RMSE) (or root mean square bias), and the corresponding values are shown on the right hand side.

As can also be seen, instrument B has the smallest XCO_2 bias (in terms of all three metrics) and the smallest XCO_2 random error (i.e., the best precision).

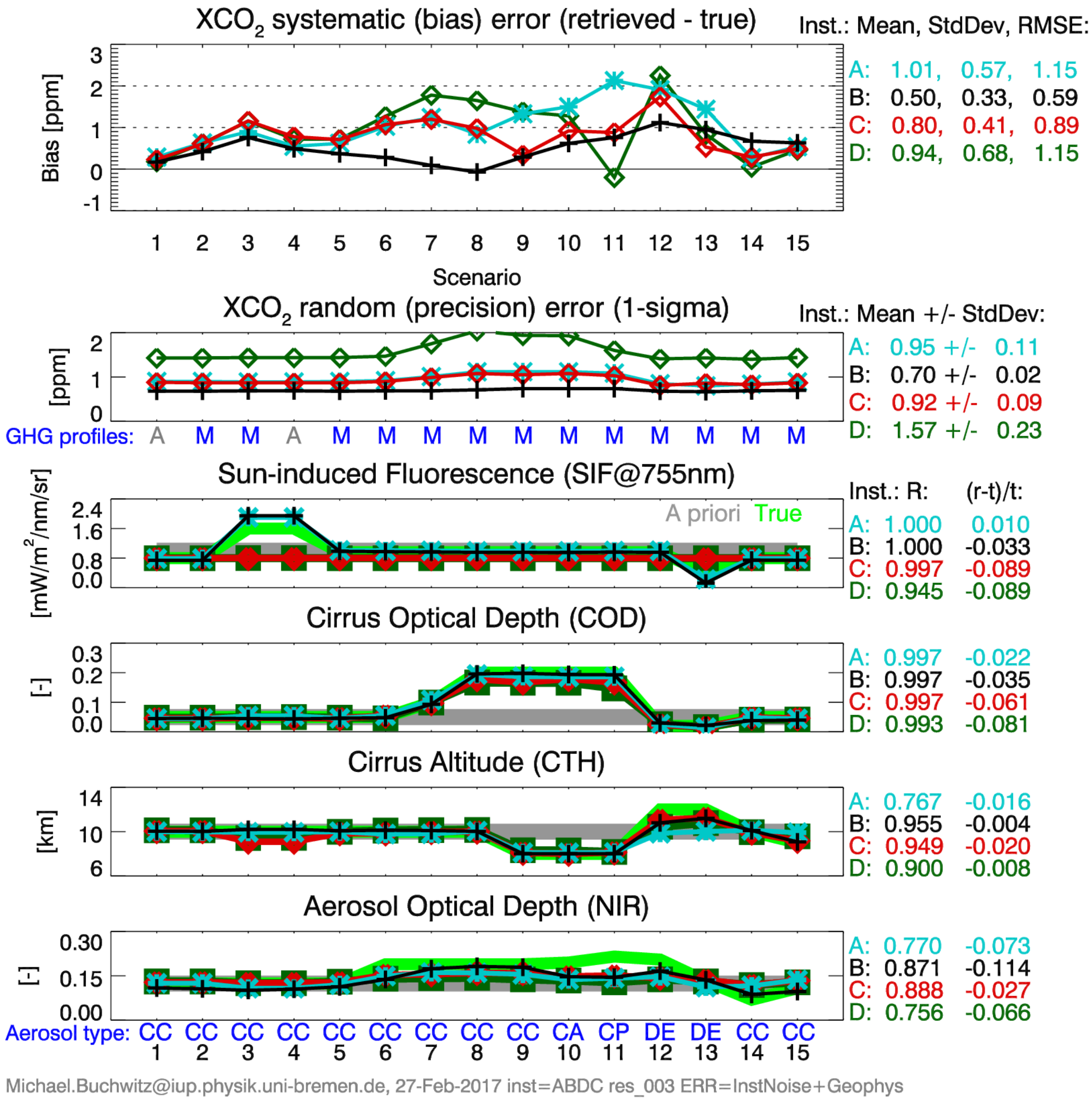

Figure 19: Top panel: XCO_2 systematic error as a function of scenario for the four instruments. In the line below it is listed which GHG profiles have been used (A = *a priori*; M = mid-latitude summer (MLS)). Listed on the right is the mean bias, the standard deviation of the bias and the root-mean-square-error (RMSE). Panel below: As top panel but for XCO_2 random error. Listed on the right is the mean precision and its standard deviation. Following 4 panels: A priori values (grey), true values (green) and retrieved values (for the 4 instruments) for the following 4 parameters: SIF, COD, CTH, AOD(NIR). Listed on the right is the linear correlation coefficient between the retrieved and the true parameters and the mean value of the relative difference ((retrieved-true)/true). At the bottom it is shown which aerosol type has been used for each scenario (note that the *a priori* type is Continental Average (CA)).

6.1. Additional error source: Zero-level-offset (ZLO)

In this section error source "Zero-Level-Offset" (ZLO) has been investigated by adding to each spectral channel the following radiances (see Sect. 1.5 of **/Landgraf et al., 2017b/**):

- NIR: 4.2×10^9 photons/s/nm/cm^2/sr
- SW1: 4.3×10^9 photons/s/nm/cm^2/sr
- SW2: 5.3×10^8 photons/s/nm/cm^2/sr

These radiometric offsets have been added to the radiances as computed for each instrument and each scenario for the e01 simulations and the BESD/C retrieval algorithm has been applied to these radiances.

The retrieval results are shown in **Figure 20**.

As can be seen from **Figure 20** (top panel), instrument B has the smallest XCO_2 bias (in terms of all three metrics) and the smallest XCO_2 random error (best precision).

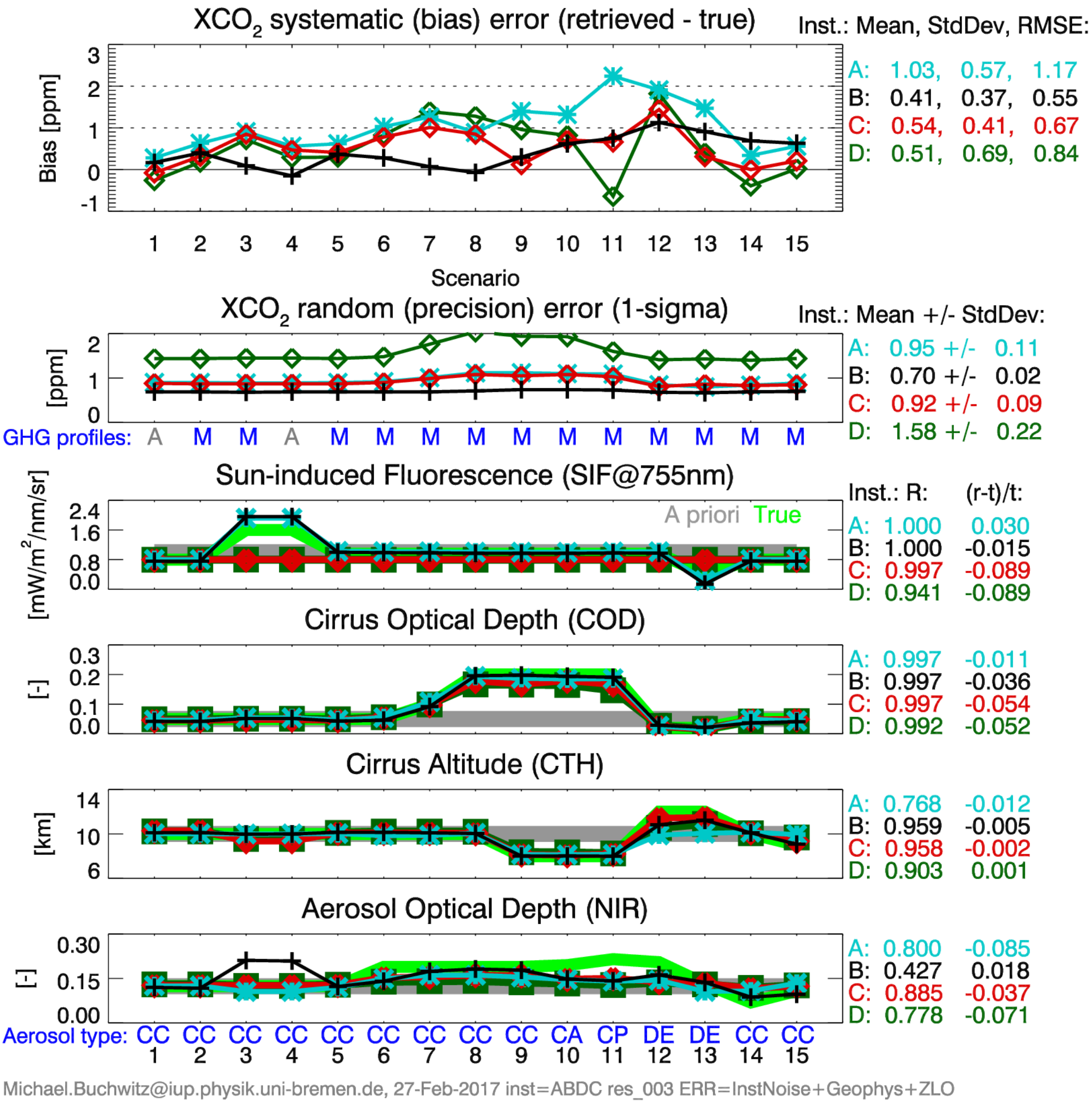

Figure 20: As
Figure 19 but also considering ZLO as an additional error contribution.

6.2. Additional error source: ISRF distortion (ISRF)

In this section error source "Instrument Spectral Response Function distortion" (ISRF distortion) has been investigated by computing simulated radiance observations using ISRF anti-symmetrical distortion No. 3 and symmetrical distortion No. 1 as given in Sect. 1.2 of **/Landgraf et al., 2017b/** (see **Figure 21**).

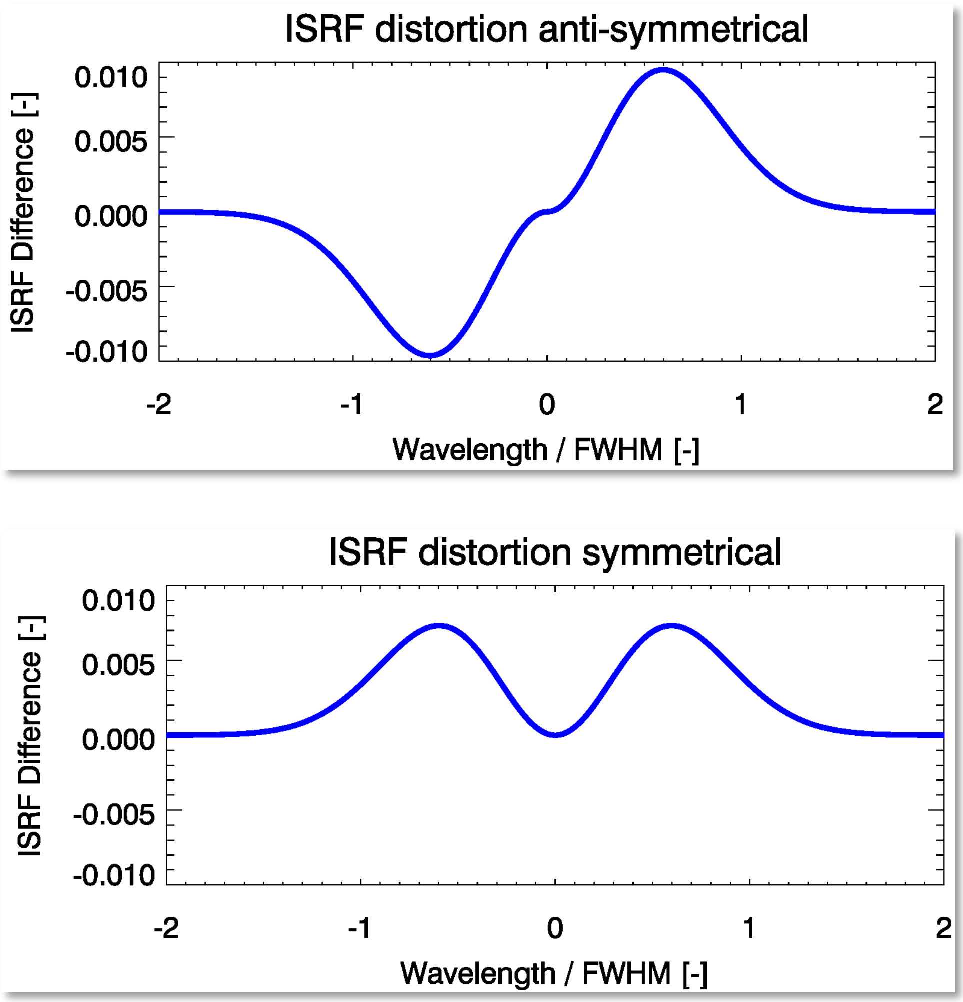

Figure 21: Illustration of ISRF distortion No. 3 (top, anti-symmetrical) and No. 1 (bottom, symmetrical). Source: **/Landgraf et al., 2017b/**.

The retrieval results for the anti-symmetrical ISRF distortion are shown in **Figure 22**. As can be seen from **Figure 22** (top panel), instrument B has the smallest XCO_2 bias (in terms of all three metrics) (but StdDev is identical for instrument A) and the smallest XCO_2 random error (best precision).

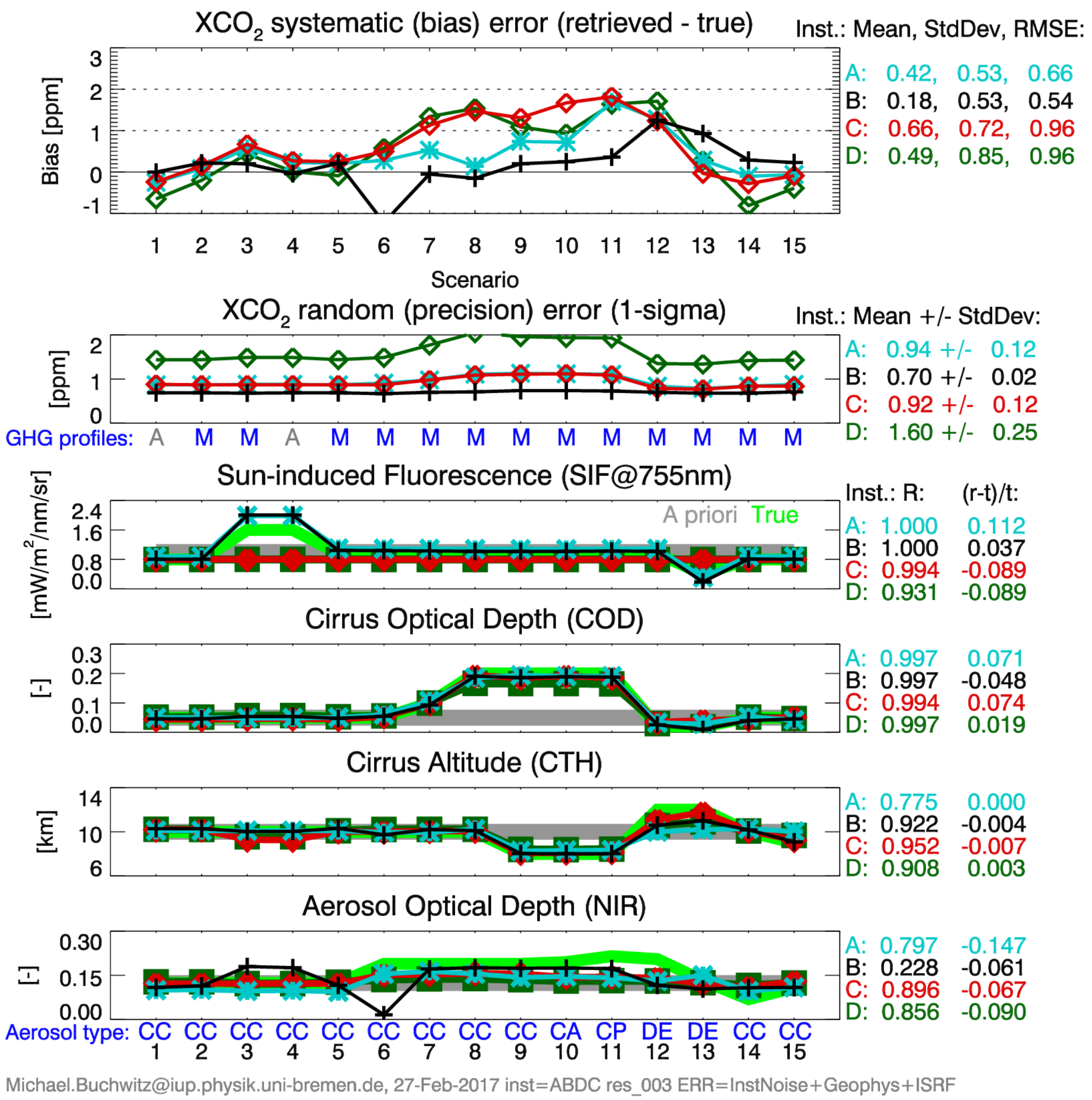

Figure 22: As
Figure 19 but also considering anti-symmetrical ISRF distortions as additional error contributions.

The retrieval results for the symmetrical ISRF distortion are shown in **Figure 23**. As can be seen from **Figure 23** (top panel), instrument B has the smallest XCO_2 mean bias and RMSE and instrument A has the smallest standard deviation of the bias. Instrument B has the smallest XCO_2 random error (best precision).

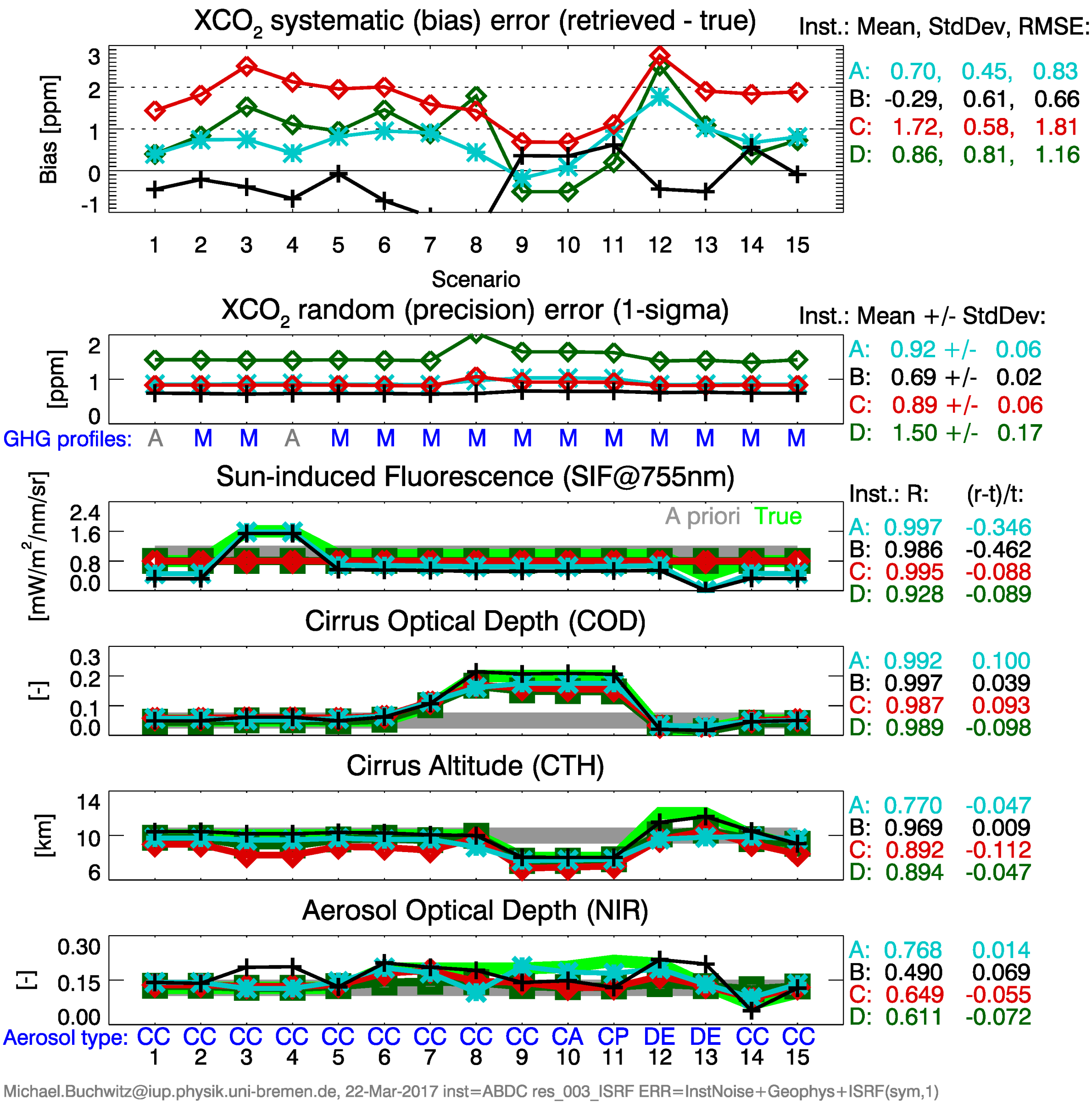

Figure 23: As
Figure 19 but also considering symmetrical ISRF distortions as additional error contributions.

6.3. Additional error source: Detector non-linearity (NL)

In this section error source “Detector non-linearity” (NL) has been considered for the simulated retrievals by using the radiance dependent systematic errors as specified in **/Landgraf et al., 2017b/** (see **Figure 24**).

(a) Detector non-linearity for SWIR-1 and instruments A and B

(b) Detector non-linearity for SWIR-2 and instruments A and B

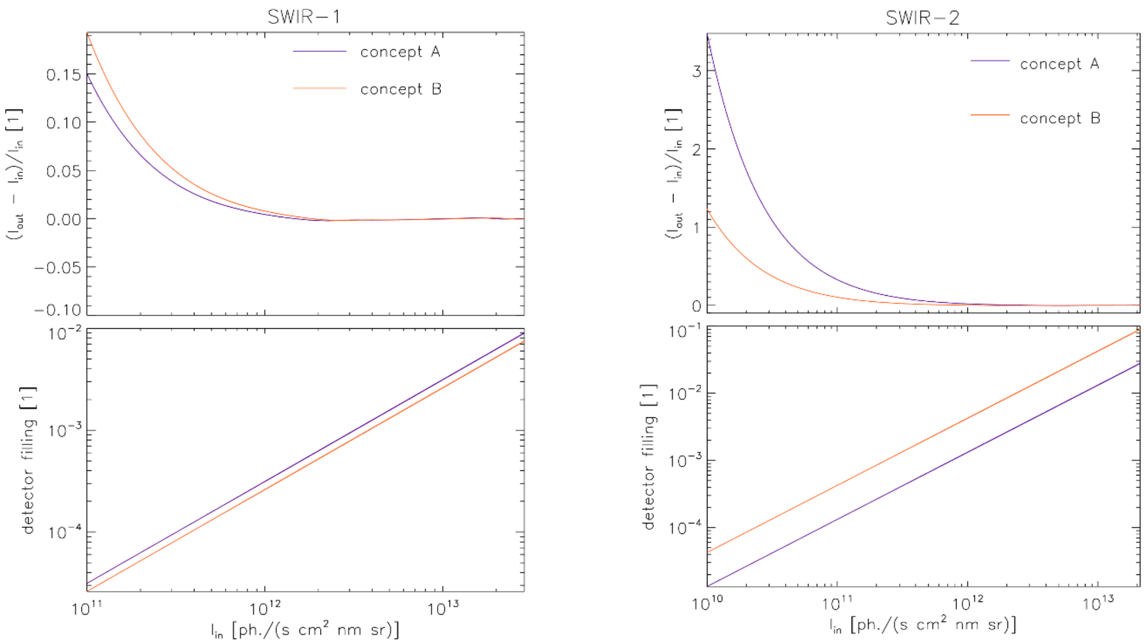

Figure 24: Detector non-linearity for the SWIR-1 (a) and SWIR-2 (b) bands for instruments A and B (source: **/Landgraf et al., 2017b/**).

These errors have been used to modify the radiances as computed for each instrument and each scenario for the e01 simulations and the BESD/C retrieval algorithm has been applied to these radiances.

The spectral dependence of the error is shown in
Figure 25.

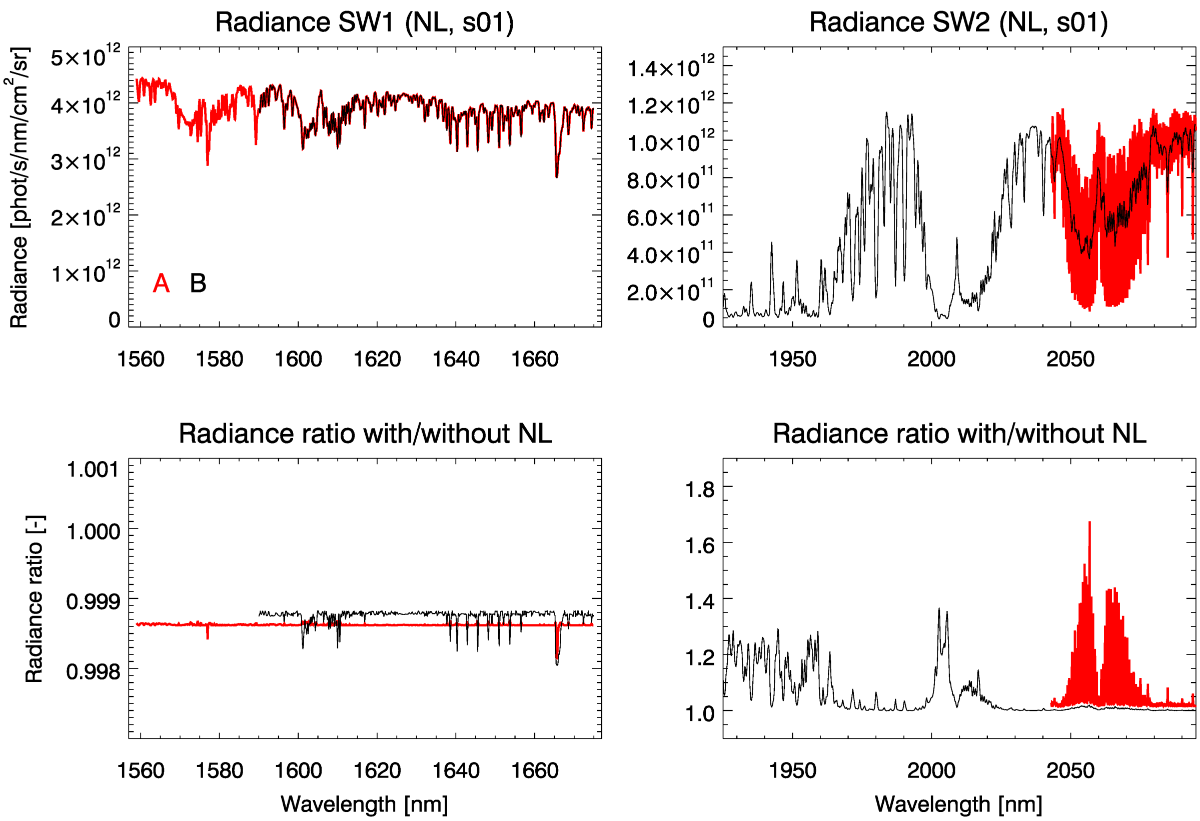

Figure 25: Radiance spectra (top) and radiance ratios (bottom) for the SWIR-1 (left) and SWIR-2 (right) bands for instrument A (red) and B (black), where ratio is the radiance ratio for a radiance with and without non-linearity error.

The retrieval results are shown in
Figure 26.

As can be seen from
Figure 26 (top panel), instrument B has the smallest XCO_2 bias (in terms of all three metrics) and the smallest XCO_2 random error (best precision).

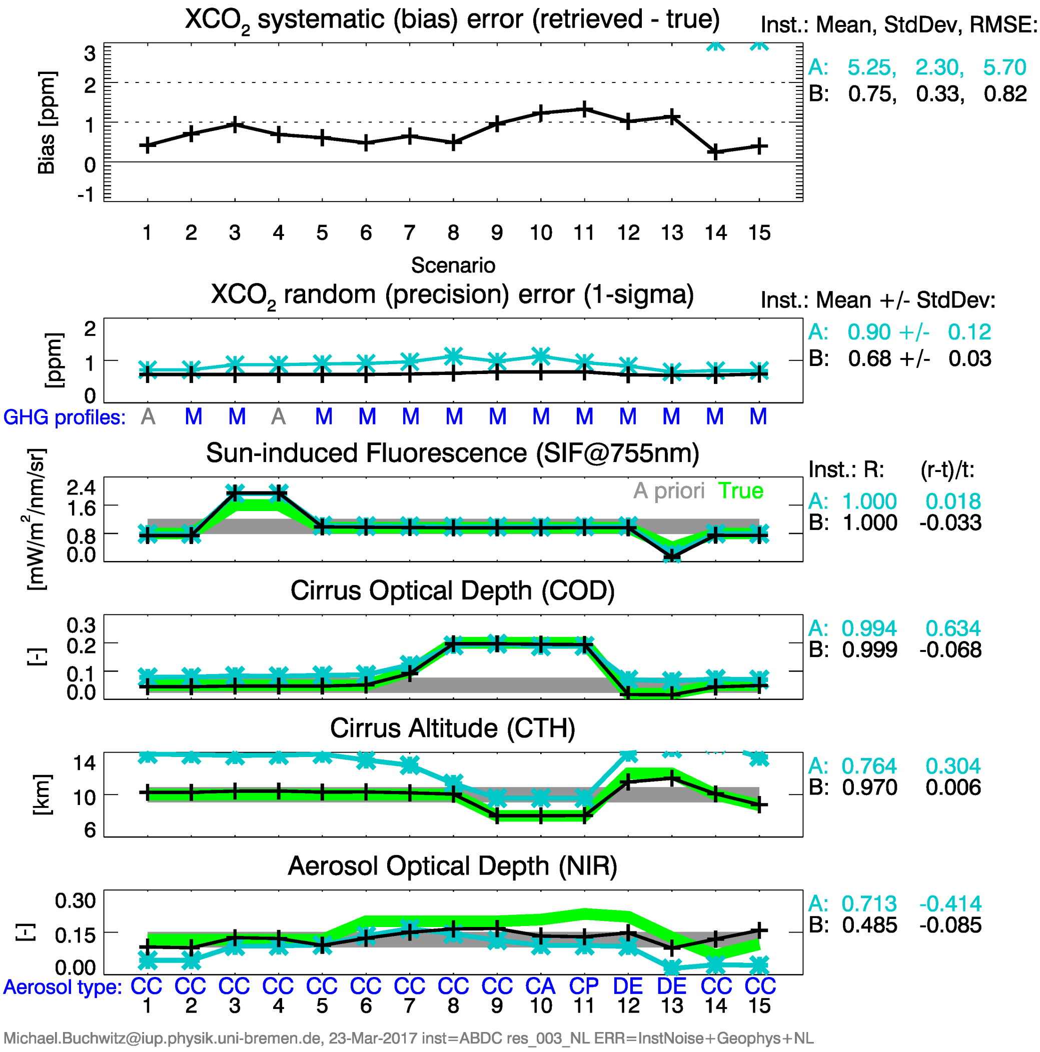

Figure 26: As
Figure 19 but also considering detector non-linearity as an additional error contribution.

6.4. Additional error source: Polarization (POL)

In this section error source "Polarization" (POL) has been considered for the simulated retrievals by using the radiance dependent systematic errors as specified in **/Landgraf et al., 2017b/**. Radiance errors *δI* (see **/Landgraf et al., 2017b/**) are assumed to result from an instrument, which is not perfectly polarization insensitive, i.e., from instrument Mueller matrix elements *M01* and *M02*, which are not zero:

$$\delta I = M01/M00 * Q + M02/M00 * U \qquad \text{Eq. 1}$$

Here *M01, M00* and *M02* are wavelength dependent instrument Mueller Matrix elements (see **Figure 27**) and *Q* and *U* are radiance Stokes vector elements (i.e., differences of radiance spectra). For the results shown in this section radiances *Q*, *U* and *I* have been calculated with the radiative transfer model SCIATRAN (version 3.4) **/Rozanov et al., 2014/** assuming a polarizing vegetation surface. The Mueller matrix elements correspond to parameters ACT field = 8.584° and ALT field = 0.208°.

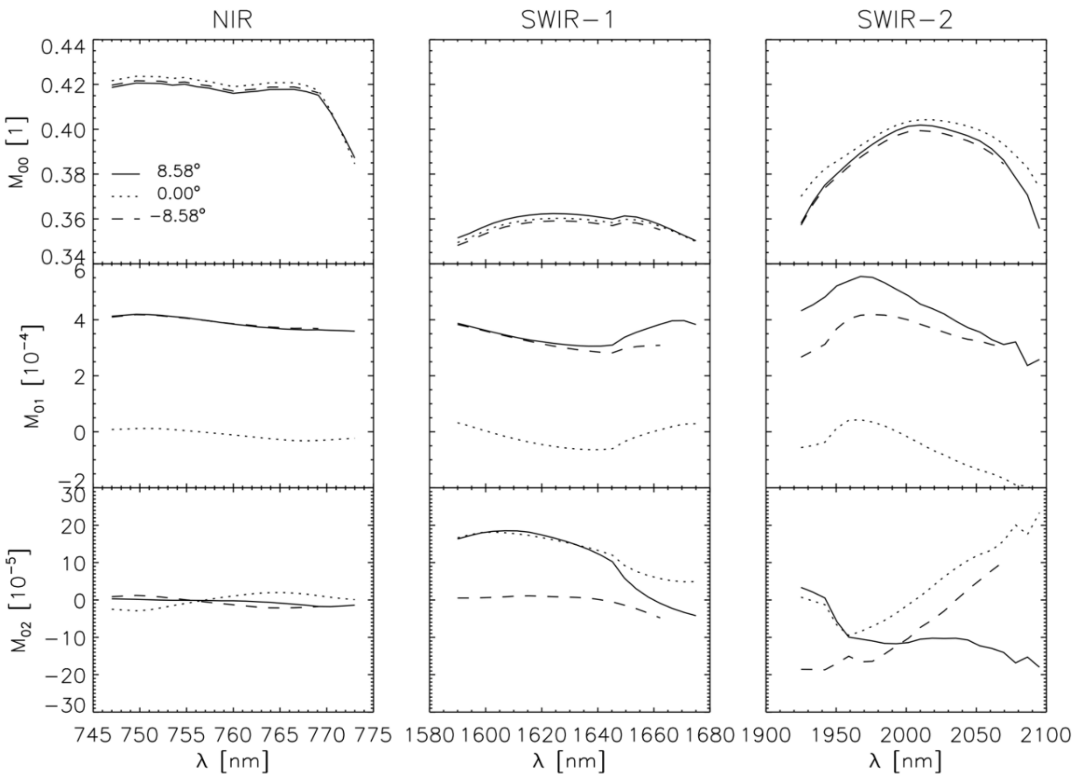

Figure 27: Instrument Mueller matrix elements (source: **/Landgraf et al., 2017b/**).

The polarization related errors have been used to modify the radiances as computed for each instrument and each scenario for the e01 simulations and the BESD/C retrieval algorithm has been applied to these radiances.

The spectral dependence of the radiance error is shown in
Figure 28 **-**
Figure 30 for the three bands. It can be seen that - as expected (see **Figure 27**) - the radiance errors are very small, on the order of 10^{-4} for the NIR band, essentially zero for the SWIR-1 band and on the order of 10^{-3} for the blue part of the SWIR-2 band.

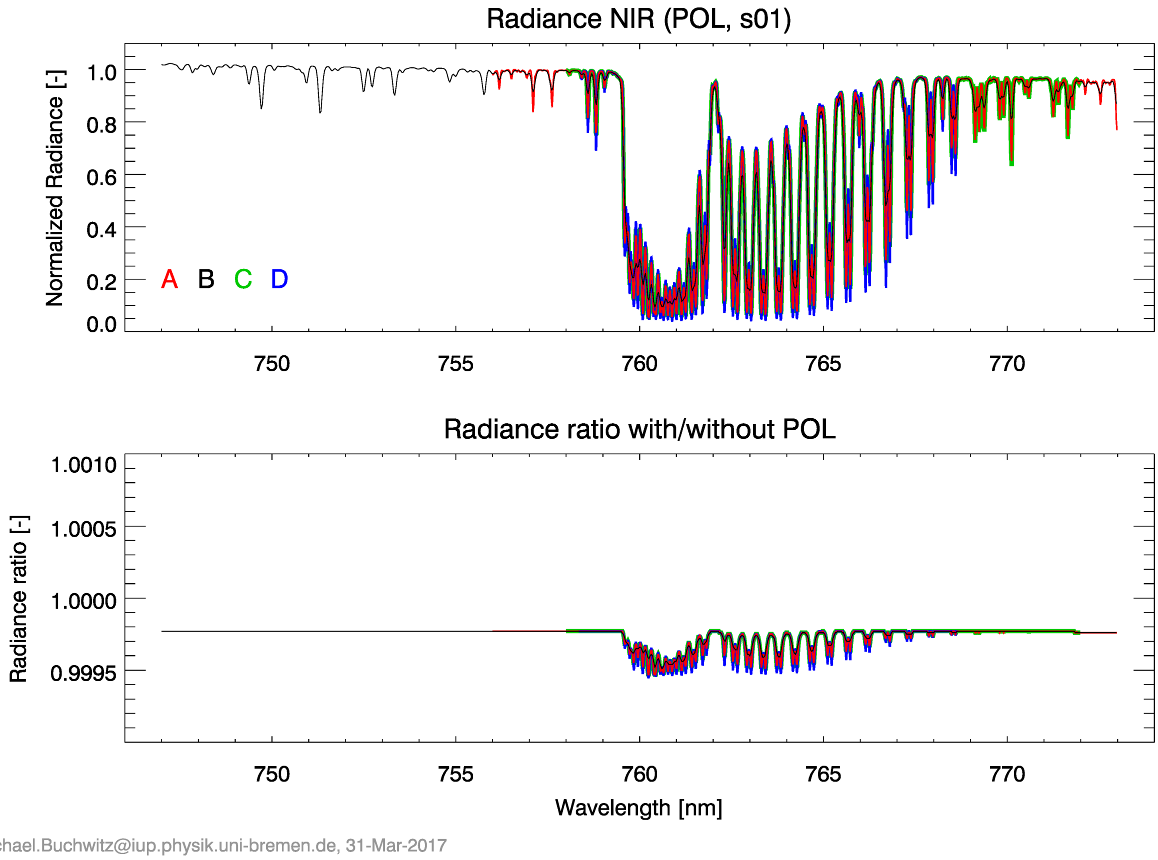

Figure 28: Radiance spectra in the NIR band of all four instruments (top) and ratios of radiance spectra (bottom) for radiances with and without adding radiance polarization error *δI* (see Eq. 1).

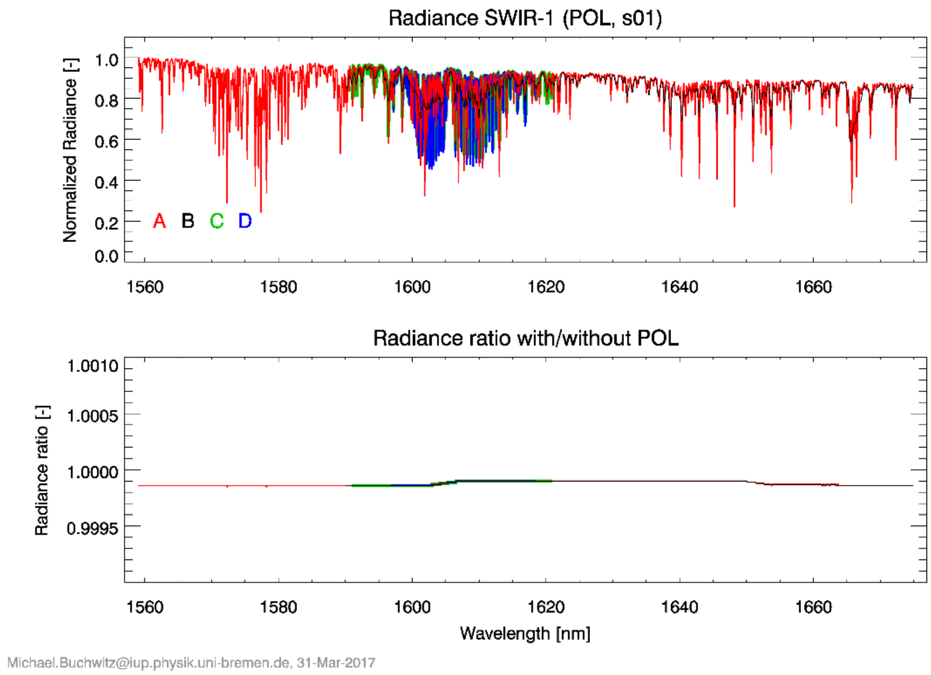

Figure 29: As
Figure 28 but for the SWIR-1 band.

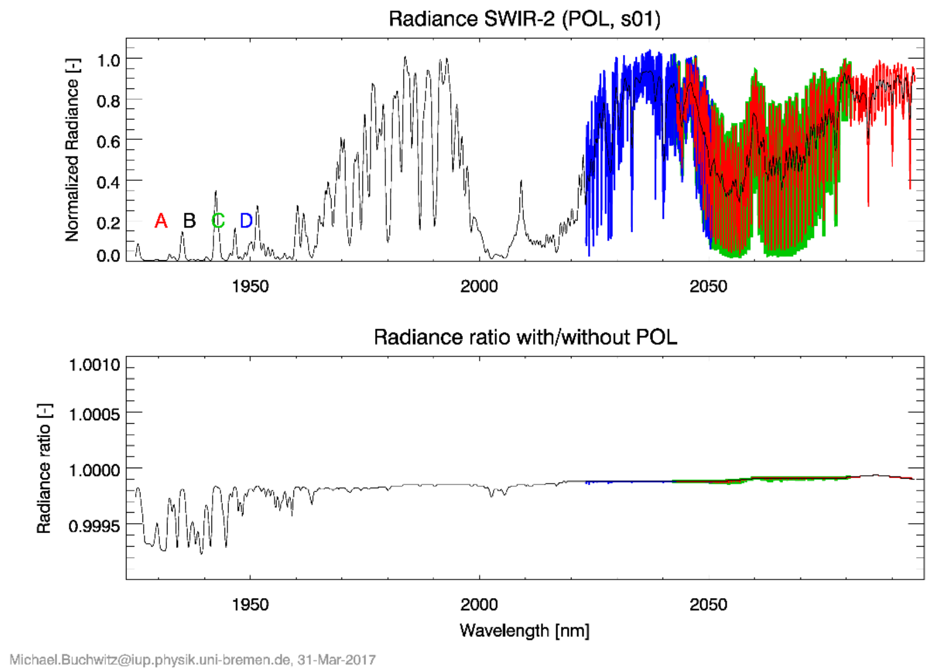

Figure 30: As
Figure 28 but for the SWIR-2 band.

The retrieval results are shown in
Figure 31.

As can be seen from
Figure 31 (top panel), instrument B has the smallest XCO_2 bias (in terms of all three metrics) and the smallest XCO_2 random error (best precision).

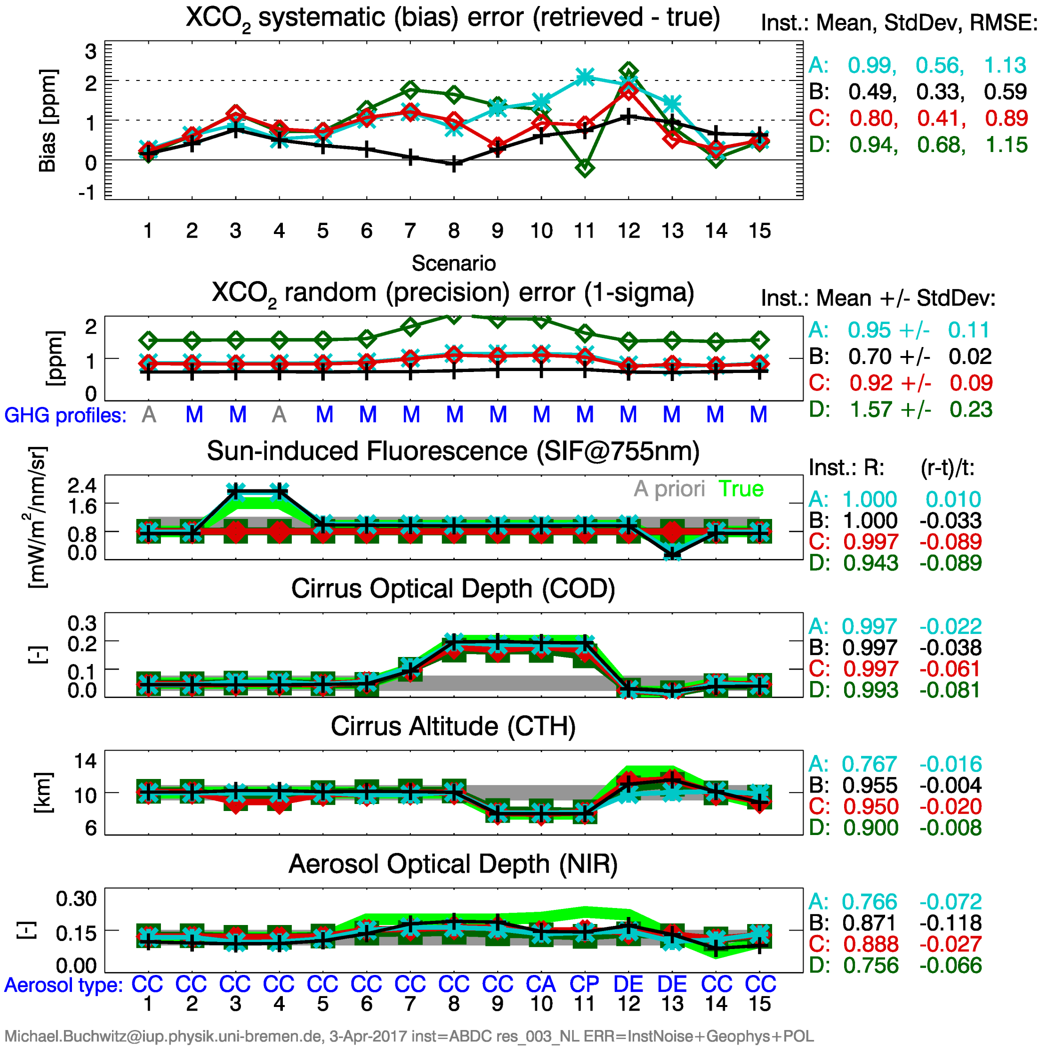

Figure 31: As
Figure 19 but also considering polarization as an additional error contribution.

6.5. Additional error source: Straylight (STRAY)

In this section error source “Straylight” has been considered for the simulated retrievals by using straylight as specified in **/Landgraf et al., 2017b/** using a scaling (straylight correction) factor of *a* = 1/5 (see **/Landgraf et al., 2017b/** for details). The radiance of the observed scene is contaminated from spectral straylight and from spatial straylight according to the straylight kernel (see **/Landgraf et al., 2017b/**). The observed scene is located close (5 SSD away) to a bright scene (on one side) corresponding to a desert scene with much higher albedo, which is 0.6 in all three bands. The bright scene is therefore approximately a factor of 3 (= 0.6/0.2) brighter in the NIR, a factor of 6 (=0.6/0.1) brighter in the SWIR-1 and a factor of 12 (0.6/0.05) brighter in the SWIR-2 band.

The following modifications (i.e., differences w.r.t. to the description given in **/Landgraf et al., 2017b/**) have been applied based on information from ESA (e-mail B. Sierk, 18-June-2017):

- Instrument independent straylight kernels have been used (by setting factors $\Delta\lambda_B/\Delta\lambda$ and $\Delta x_B/\Delta x$ in Formula (13) to 1.0)
- The straylight kernels have been normalized to “Total Intensity Scatter” (TIS) 0.9% for the NIR bands, 0.7% for the SWIR-1 bands and 0.5% for the SWIR-2 bands.

The resulting straylight spectra of the three bands are shown in **Figure 32 - Figure 34** for scene s01.

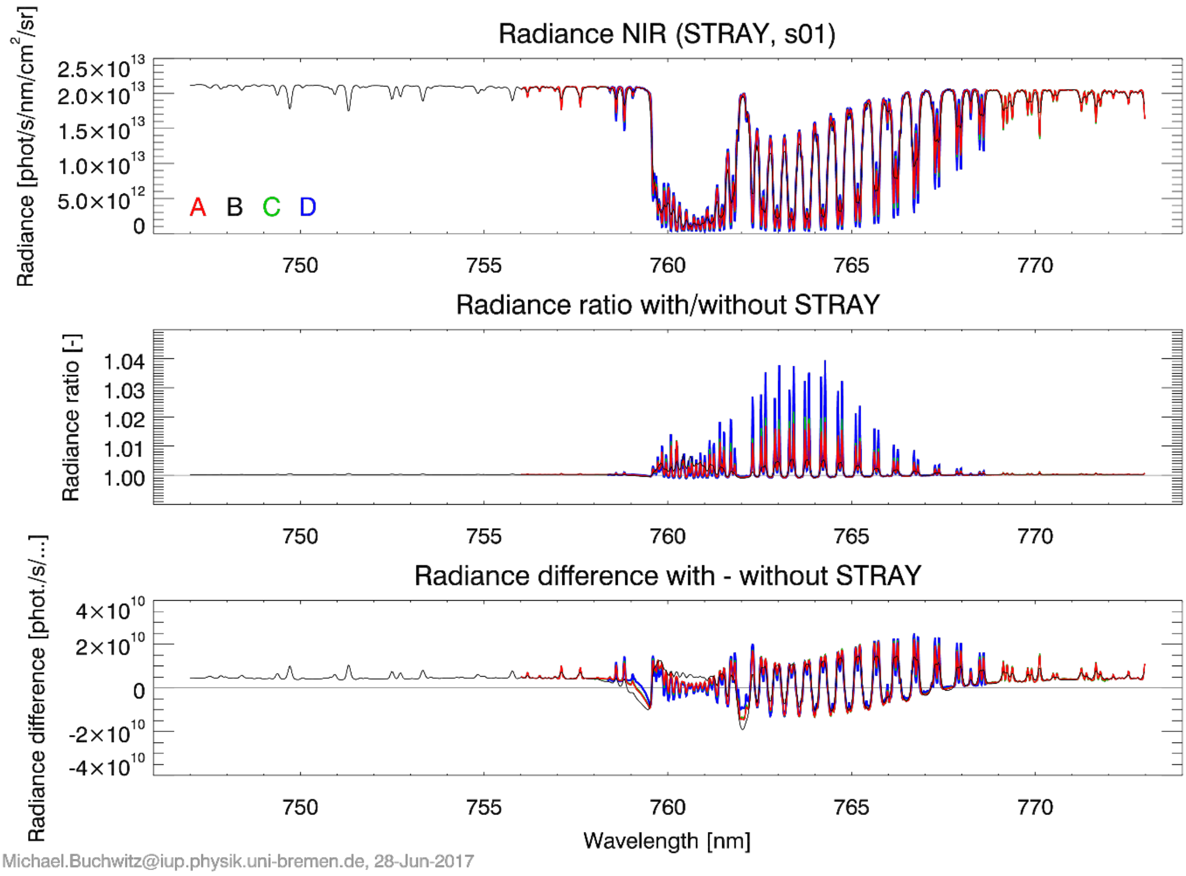

Figure 32: Radiance spectra of all four instruments (top) and corresponding straylight spectra (bottom) for the NIR bands.

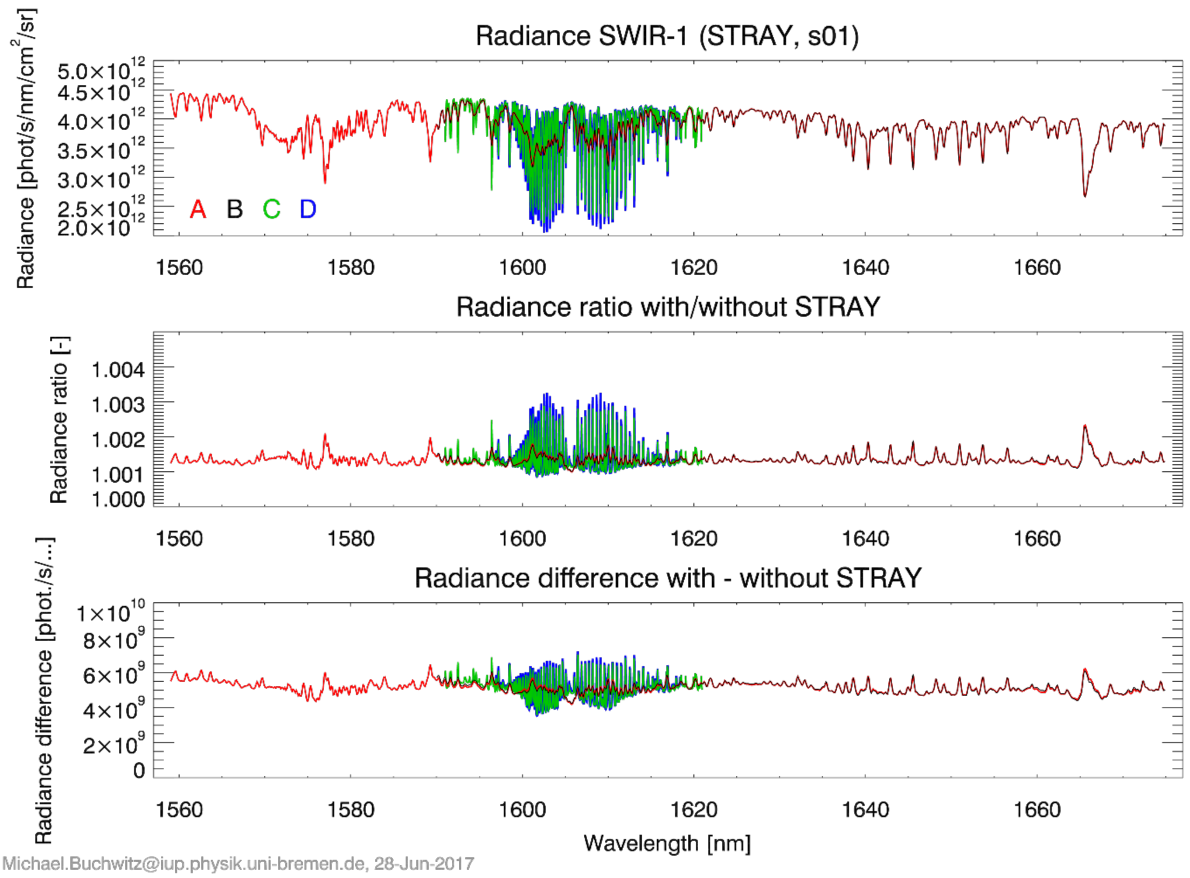

Figure 33: As
Figure 32 but for the SWIR-1 bands.

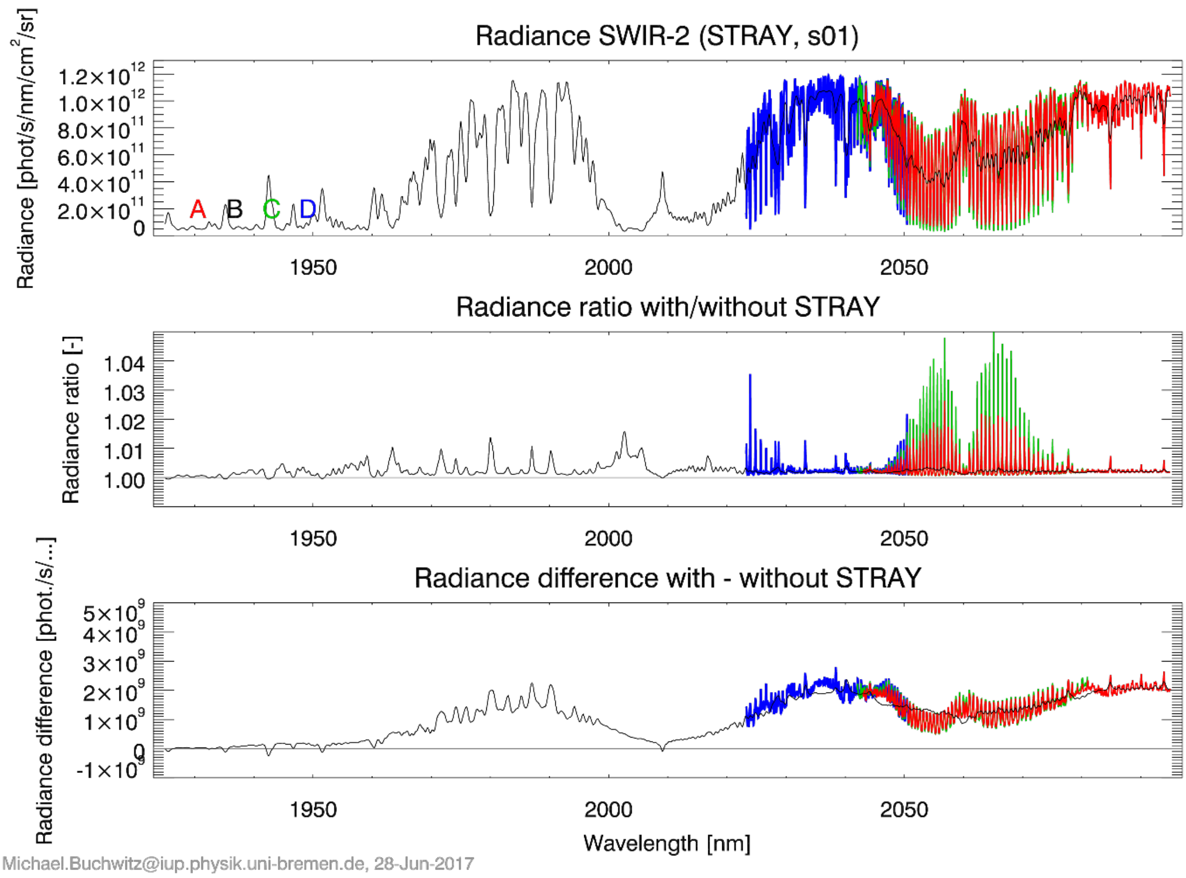

Figure 34: As
Figure 32 but for the SWIR-2 bands.

Simulated retrievals have been performed using the straylight contaminated radiance spectra as observations. The results are shown in
Figure 35.

As can be seen from
Figure 35 (top panel), instrument D has the smallest XCO_2 mean bias, instrument B has the smallest standard deviation of the bias, and instrument D has the smallest root-mean-square-error. As can also be seen, instrument B has the smallest XCO_2 random error (best precision).

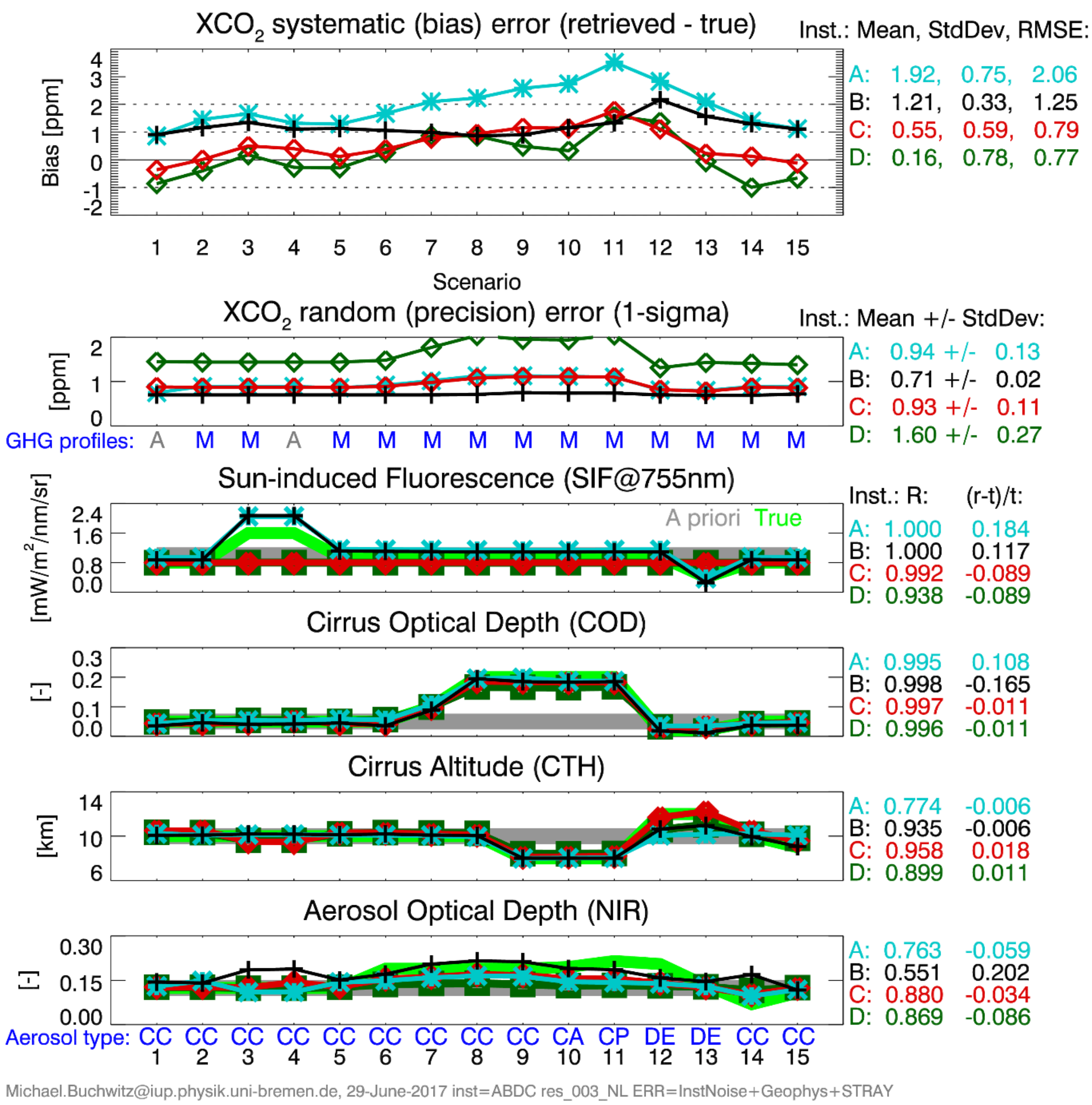

Figure 35: As
Figure 19 but also considering straylight as an additional error contribution.

6.6. Summary of "Iterative abs." results

The results presented in the previous sub-sections, which are summarized in **Figure 36**, show that instrument B has smallest XCO_2 random error ("best precision", green bars in **Figure 36**) for all investigated cases and the smallest XCO_2 systematic error for nearly all investigated cases (red bars in **Figure 36**).

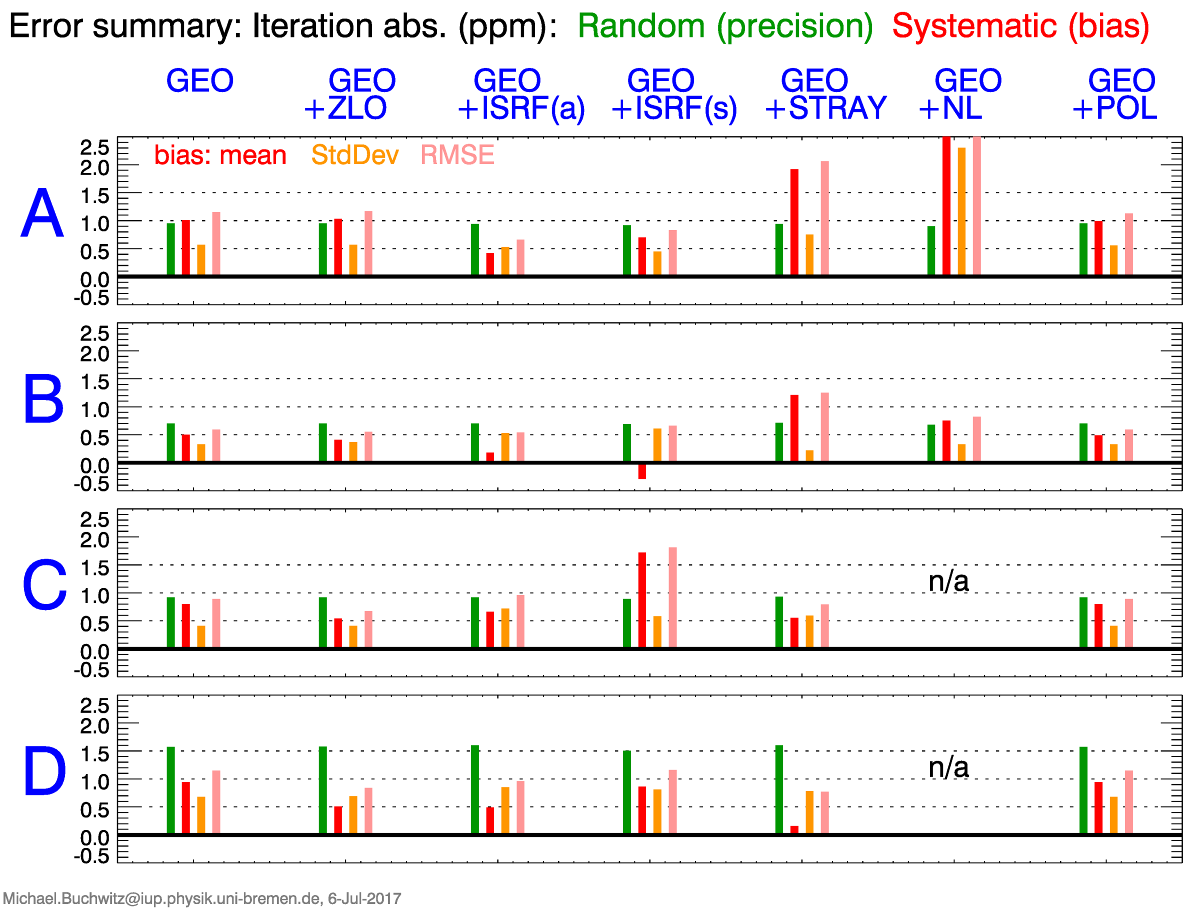

Figure 36: Summary of the "Iterative abs." error analysis results for instruments A, B, C, D (from top to bottom) and all investigated error sources, which are (from left to right): geophysical (Geo), i.e., errors due aerosols, clouds, etc., and the following additional instrument/calibration related error sources: zero level offset (ZLO), Instrument Spectral Response Function (ISRF) anti-symmetrical ("a") and symmetrical ("s") distortions, straylight (stray), detector non-linearity (NL) and polarization (Pol). The XCO_2 random error ("precision") is shown in green, the three metrics for XCO_2 systematic error are shown in red (from left to right: mean bias, standard deviation of bias, root-mean-square-error).

The presented results suggest that instrument B is the preferred instrument concept of the four instrument concepts, which have been investigated in this study.

However, it needs to be noted that concepts C and D seem somewhat less sensitive to straylight than concept B (assuming that the approach to consider straylight related errors is realistic).

Nevertheless, before drawing any final conclusions - it may be worthwhile to carry out some additional investigations and these are described in the following section.

7. Additional error analysis

As shown in the previous section, instrument B has smallest random error ("best precision") compared to the other three instruments. This is a robust finding as (typically) the random error is dominated by the instrument signal-to-noise performance and not so much by the retrieval algorithm (at least if a "good" algorithm is used).

For XCO_2 biases this is less clear as biases critically depend on the used retrieval algorithm. This means that it is less clear (compared to random errors) if the systematic errors shown in the previous section are primarily due to the different instrument concepts or due to the retrieval algorithm. For example it could be that the BESD/C algorithm as used to generate the results shown in the previous section is somehow "better" to better deal with (pre-defined) "GEO scenarios" (see **Sect. 6.1**) for instrument B compared to the other three instruments. If this would be the case than instrument B would be the "winner" for GEO errors. If in addition the additional instrument related errors are relatively small (compared to GEO related errors) than instrument B would also be the winner for all instrument related errors, i.e., instrument B would be the overall winner.

It therefore seems important to aim at disentangling instrument/calibration related errors from GEO errors, i.e., from errors due to aerosols and clouds, etc. This can be achieved by

(i) computing the difference of the ("absolute") XCO_2 biases shown in the previous section w.r.t. the GEO biases (i.e., "GEO + instrument error" minus "GEO error" = "instrument error"). These bias differences are called "Iterative diff." results in this document and these results are obtained by computing differences of the "Iterative abs." results. The disadvantage of this approach is that the disentangling is far from perfect (due to pre-processing related errors and potential influence of the iterative scheme).

(ii) computing instrument related biases directly by applying the "retrieval Gain matrix" to radiance error spectra. These biases are called "Linearization" results in this document. This approach has the advantage that it is independent of the iteration method as implemented for the BESD/C retrieval method and the results do not suffer from pre-processing related errors. Arguably, this is the best method to quantify the instrument related errors.

The corresponding results are presented in the following sub-sections.

7.1. Close loop scenario s00

For retrieval studies based on simulations it is always interesting (or even mandatory) to perform a “close loop” (CL) test. This means that the retrieval algorithm is applied to synthetic radiance observations which have been computed using a model atmosphere (and other parameters/conditions such as surface reflectivity) which is fully consistent (ideally identical) with the retrieval algorithm assumptions (i.e., “true” = *a priori* for all parameters (CO_2, aerosols, clouds, SIF, …)).

Therefore, an additional “close loop scenario” s00 has been defined, which is identical with the assumptions as used in the BESD/C retrieval.

Note that scenario s01 is nearly identical with scenario s00. The only difference of s00 compared to s01 is the aerosol type. For s00 the aerosol type is “continental average with 70% humidity” (CA70) instead of “continental clean with 90% humidity” (CA90) as used for s01.

The corresponding XCO_2 ZLO-related biases for scenario s00 are shown in **Table 8**.

Row “GEO” lists the XCO_2 biases for all four instruments without any instrument related systematic radiance error. In this case one would ideally expect zero biases for all four instruments. However, as can be seen, the biases are small but not zero. This is because of the pre-processing steps, which typically result in small biases (as, for example, the surface albedo retrieval is not “perfect”). Note that the retrievals have been done as before, i.e., using the BESD/C retrieval program, but without iteration (i.e., the option to iterate has been “switched off”).

Row “ZLO” shows the biases if error source ZLO is added and row “ZLO bias via e02-e01” lists the difference of biases as listed in the first two rows, i.e., the “isolated” ZLO error.

Here the “isolated” ZLO related biases are computed from the difference of two biases but these ZLO related biases can also be estimated “directly” using “gains” as shown in the last row.

The last row “ZLO bias via GMM” shows the ZLO bias as computed with the Gain Matrix Method (GMM) (details are given in the following **Sect. 7.2**).

Comparison of the last two rows shows that the two methods “ZLO bias via e02-e01” and “ZLO bias via gains” give similar but not exactly identical results (because of pre-processing related errors present in “ZLO bias via e02-e01”).

The advantage of the gain method is that it permits "direct" computation of XCO_2 biases from instrument/calibration specific radiance errors without introducing "additional errors", e.g., due to pre-processing.

The gain method is explained and applied in the following sub-sections and the resulting "Linearization" method biases are compared with "Iterative diff." biases.

XCO_2 ZLO-related biases for Close Loop scenario					
Error source	**A**	**B**	**C**	**D**	**Comment**
GEO (e01)	0.03	-0.14	0.00	-0.04	Close loop
GEO+ZLO (e02)	0.04	-0.13	-0.23	-0.48	
ZLO bias via e02-e01	0.01	0.01	-0.23	-0.44	
ZLO bias via GMM	0.04	0.07	-0.35	-0.44	

Table 8: XCO_2 ZLO related biases for Close Loop (CL) scenario s00 (see main text for details).

7.2. Linearization via Gain Matrix Method (GMM)

The Gain Matrix Method (GMM) as used here is described and used also in **/Buchwitz et al., 2015/**.

Using a Gain Matrix (GM), G, the relative error of the reflectance spectrum, Δy (a vector), can be mapped onto the error of a geophysical parameter of interest, Δx:

$$\Delta x = G\ \Delta y$$

Here, Δy (which is dimensionless) is the multiplicative reflectance (or radiance) relative error spectrum (i.e., a value of 0.01 corresponds to a +1% error) or the ratio of a spectrum with error divided by the error-free spectrum (in this case a +1% error corresponds to 1.01).

To illustrate how Δy is defined, here some examples, using reflectance (or radiance) ratios:

- If Δy = 1.0 (for certain wavelengths), the reflectance has no (systematic) error (at these wavelength).
- If Δy = +1.001 (for certain wavelengths), the reflectance has a (systematic) error of +0.1% (at these wavelengths).
- If Δy = +0.999 (for certain wavelengths), the reflectance has a (systematic) error of -0.1% (at these wavelengths).

Matrix G is defined by the following three G row or gain vectors G0, G1 and G2:

- G0 is the “Normalized CO_2 vertical column” “G”; G0 is a (1-dimensional) vector with number of elements = number of spectral samples of all three CarbonSat bands (concatenated).
- G1: same as G0 but for methane (CH_4).
- G2: same as G0 but for Surface Pressure (PRE) or, equivalent, the normalized (dry) air (AIR) column.

Recipe how to use the three gain vectors

For each of the three G row vectors (i.e., G0, G1, G2), compute the following three numbers (scalars) by computing the scalar product (<|>) of each G row vector with the reflectance error spectrum (vector) Δy as follows (the sum extends over all elements of the vectors = number of elements of vector Δy):

- $\Delta x0 = \langle G0 \mid \Delta y \rangle := \Sigma_i\ G0_i \times \Delta y_i$
- $\Delta x1 = \langle G1 \mid \Delta y \rangle := \Sigma_i\ G1_i \times \Delta y_i$ (not used here)
- $\Delta x2 = \langle G2 \mid \Delta y \rangle := \Sigma_i\ G2_i \times \Delta y_i$

These three numbers can be interpreted as follows:

- Δx0 is the relative error of the CO_2 vertical column (i.e., if Δx0 = +0.01, the retrieved CO_2 column would have a systematic error of +1%)
- Δx1: as Δx0 but for methane (not used here)
- Δx2: as Δx0 but for the surface pressure / air column (e.g., if Δx2 = -0.01 the retrieved surface pressure / air column would have a systematic error of -1%)

Computation of the XCO_2 bias:

- B^{XCO2} := XCO_2 bias in ppm = ((1+Δx0)/(1+ Δx2) -1)

A GMM overview is shown in **Figure 37**.

For illustration, **Figure 38** to **Figure 41** show BESD/C gain vectors for instruments A to D.

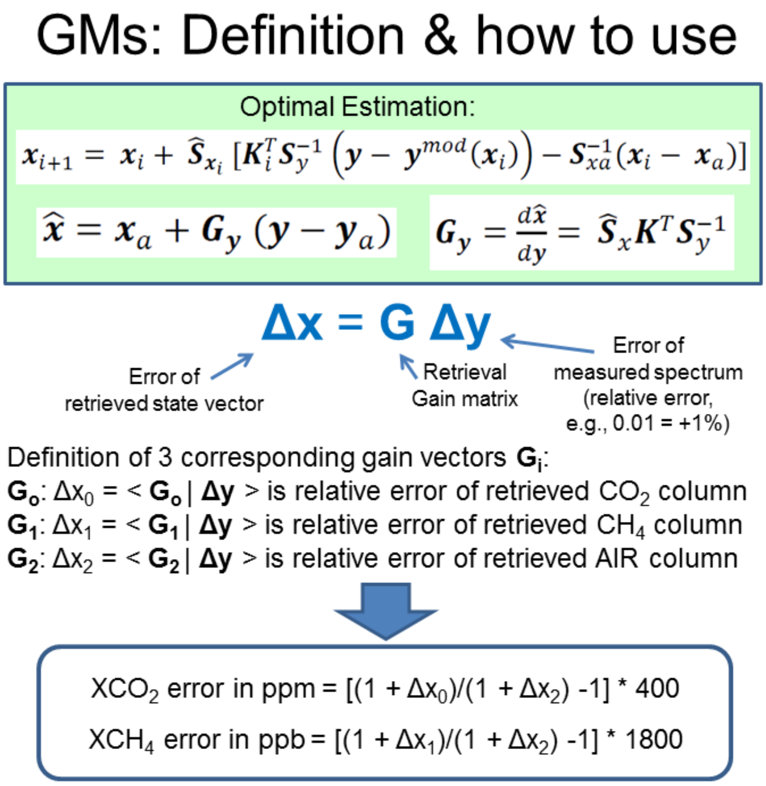

Figure 37: Gain Matrices (GMs): Definition and how to use.

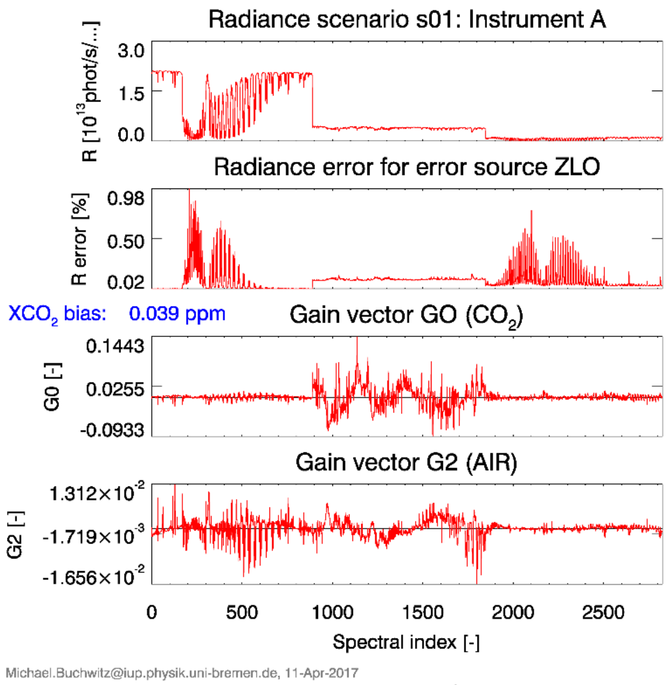

Figure 38: Radiance (top), ZLO radiance error (2nd row), and the gain vectors G0 for the CO_2 column (3rd row) and G2 for surface pressure or dry air column (bottom) for instrument A.

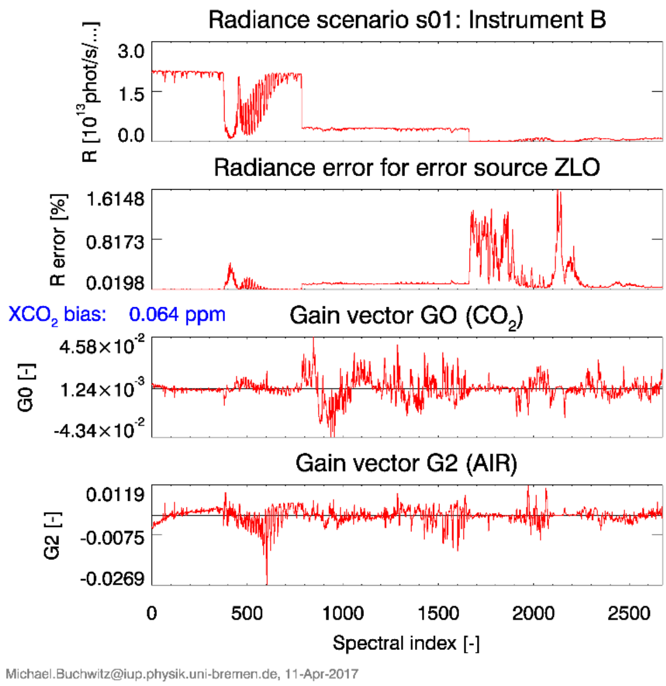

Figure 39: As **Figure 38** but for instrument B.

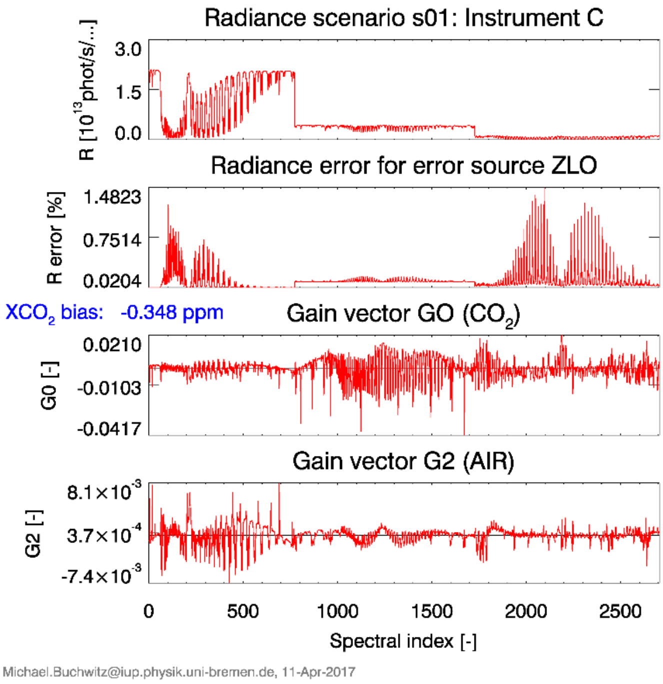

Figure 40: As **Figure 38** but for instrument C.

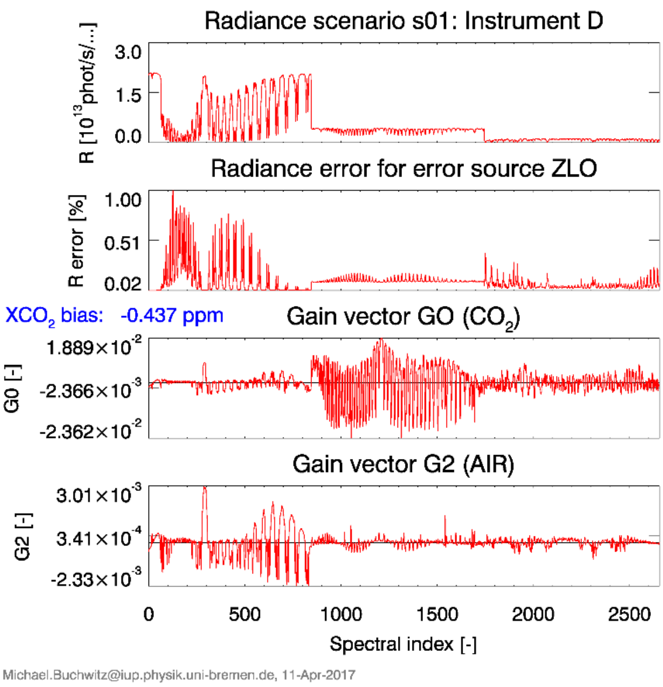

Figure 41: As **Figure 38** but for instrument D.

7.3. Additional error analysis results via Linearization and „Iterative diff.“

Figure 42 shows ZLO-related XCO_2 biases computed via gains (top), i.e., using linearization, and via the “Iterative diff.” method (bottom). The results for the latter method have been computed using the “Iterative abs.” results shown in **Sect. 6**.

Specifically, the results shown in
Figure 42 bottom have been computed as the difference of the biases for “GEO+ZLO” (**Figure 20**) minus the GEO-biases (**Figure 14**). As can be seen, the “Iterative diff.” biases exhibit significantly more scenario dependence compared to the linearized results. This is because the “Iterative diff.” results have been computed using full iterative BESD/C retrievals including pre-processing (as needed to obtain first guess and *a priori* values for surface albedo and other parameters) whereas for the linearized results it is essentially assumed that only one error source (here ZLO) exists. As can also be seen, instrument D shows by far the largest scenario dependence for the “Iterative diff.” results. It is not clear, why this is the case.

As already explained earlier, the “Iterative diff.” approach to isolate the XCO_2 biases originating from specific instrument/calibration related errors is not optimal. For this purpose, the linearization approach is much better. The linearization approach ensures that the bias is zero if the radiance error is zero, which is not the case for the “Iterative diff.” approach.

Similar results as shown in
Figure 42 are shown in
Figure 43 to
Figure 46 for the other instrument related errors ISRF distortion (anti-symmetrical and symmetrical), straylight, and polarization.

The various bias results are summarized and classified in the following section via “scoring”.

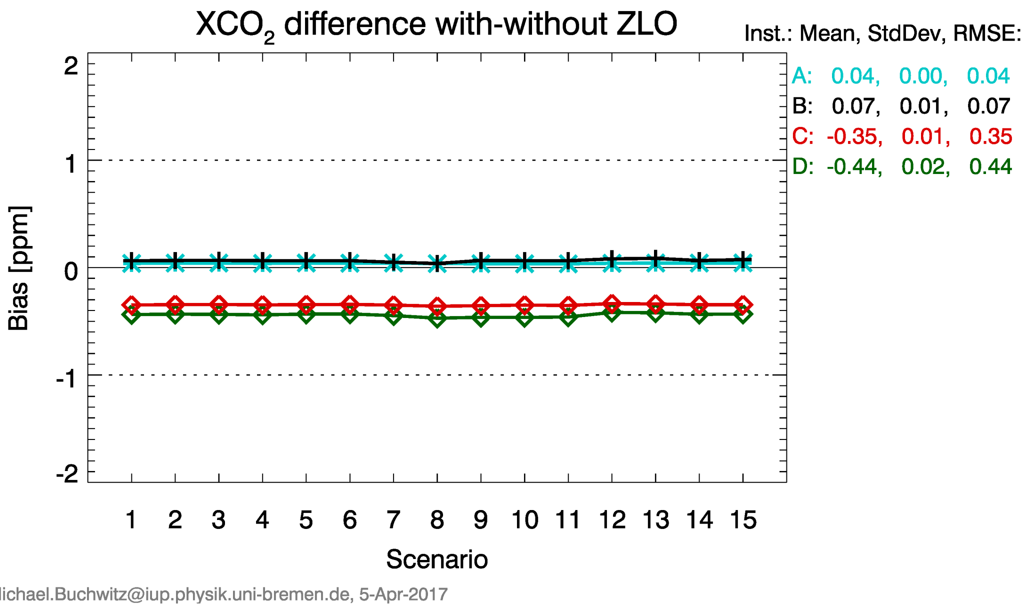

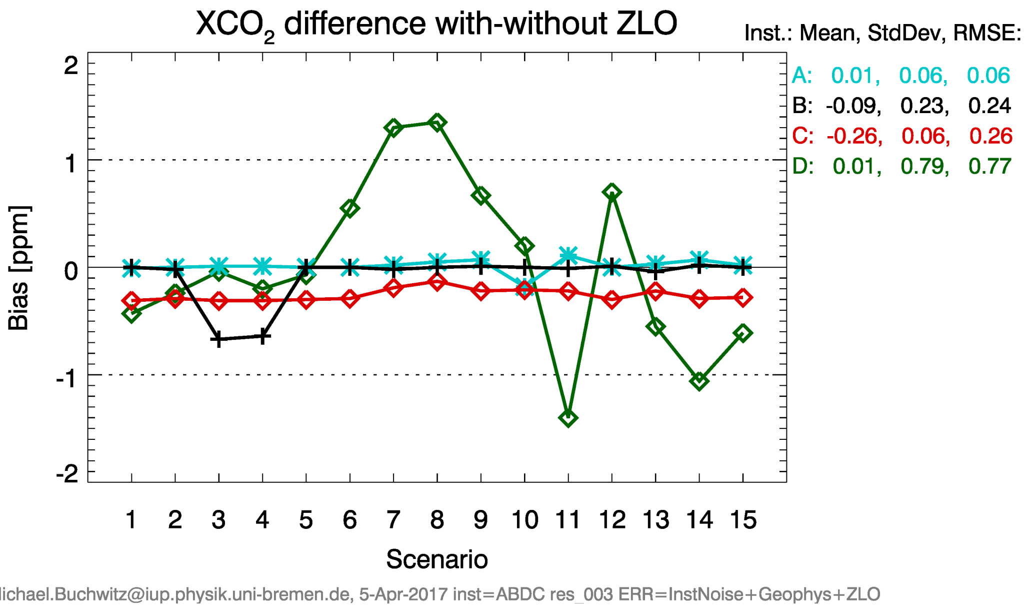

Figure 42: Top: XCO_2 biases for error source ZLO computed with “gains”, i.e., using linearization. Listed are three figures of merit to characterize the biases: (i) mean bias, (ii) standard deviation of bias and (iii) root-mean-square error (RMSE). Bottom: As top panel but using the “Iterative diff.” method.

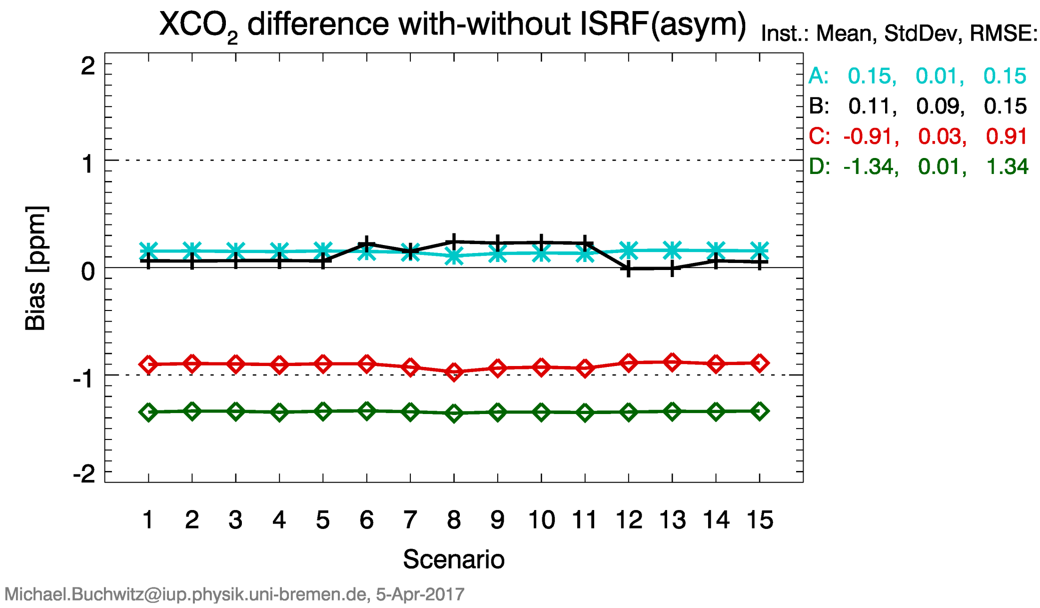

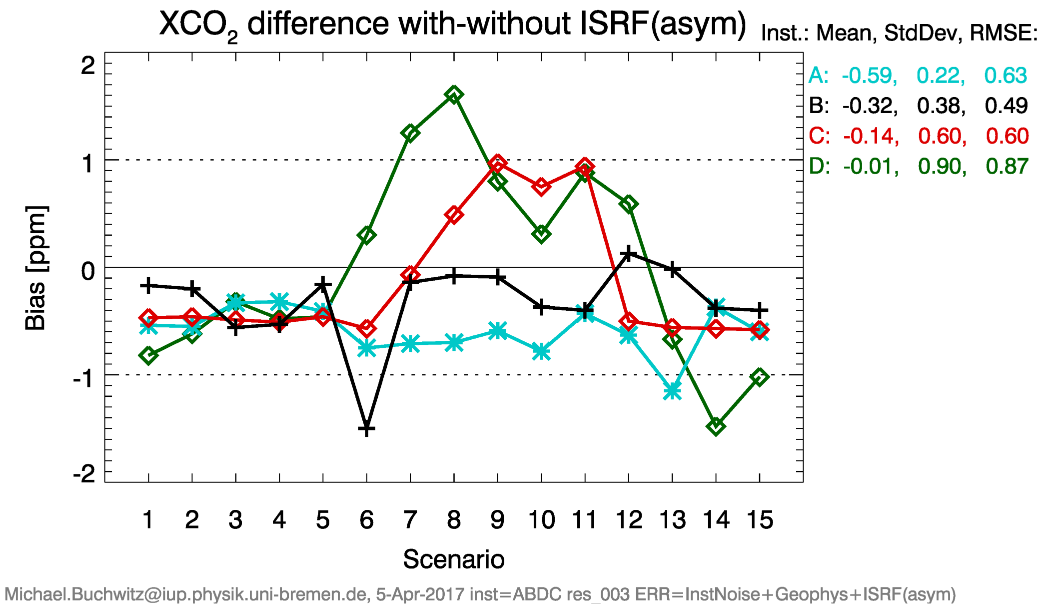

Figure 43: As
Figure 42 but for error source asymmetrical ISRF.

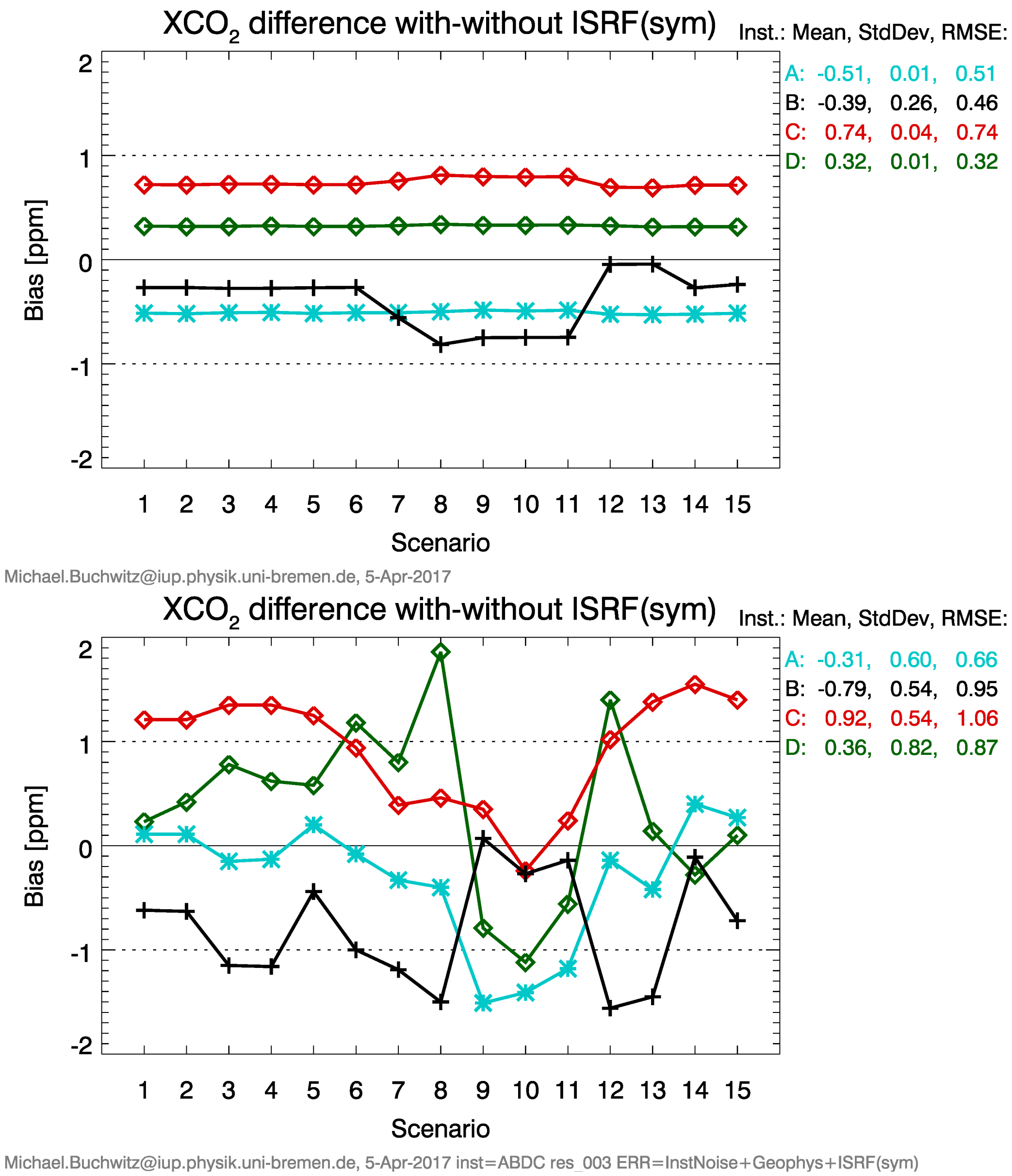

Figure 44: As
Figure 42 but for error source symmetrical ISRF.

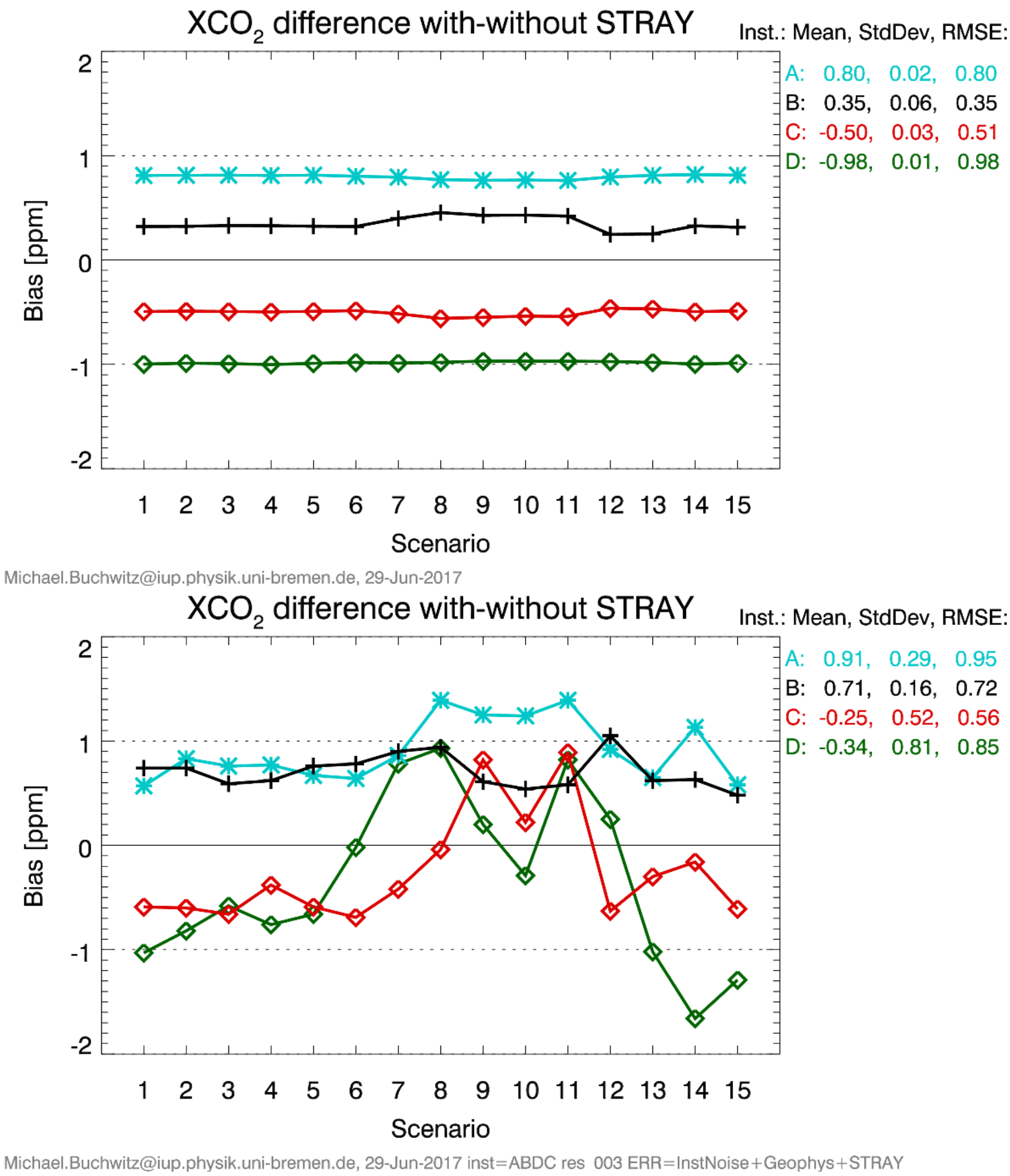

Figure 45: As
Figure 42 but for error source straylight.

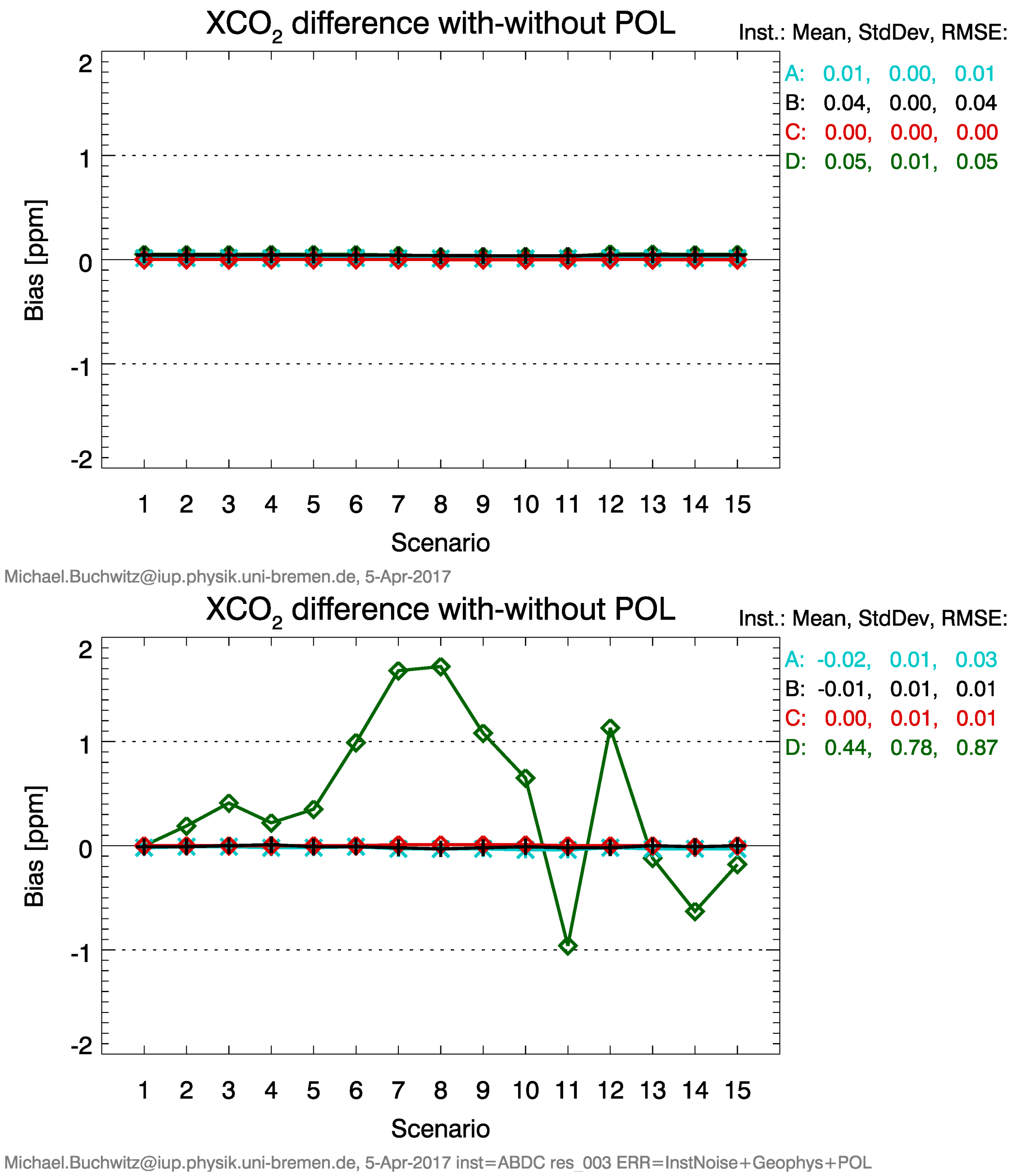

Figure 46: As
Figure 42 but for error source polarization.

Figure 47 summarizes the results of the linear error analysis. As can be seen, these results do not confirm that concept D has smallest sensitivity to straylight in contrast to the "Iterative abs" analysis shown earlier in this document. According to linear error analysis results instrument B has the smallest sensitivity to straylight.

This indicates that overall not strong conclusions can be drawn w.r.t. the best instrument concept in terms of smallest straylight related biases.

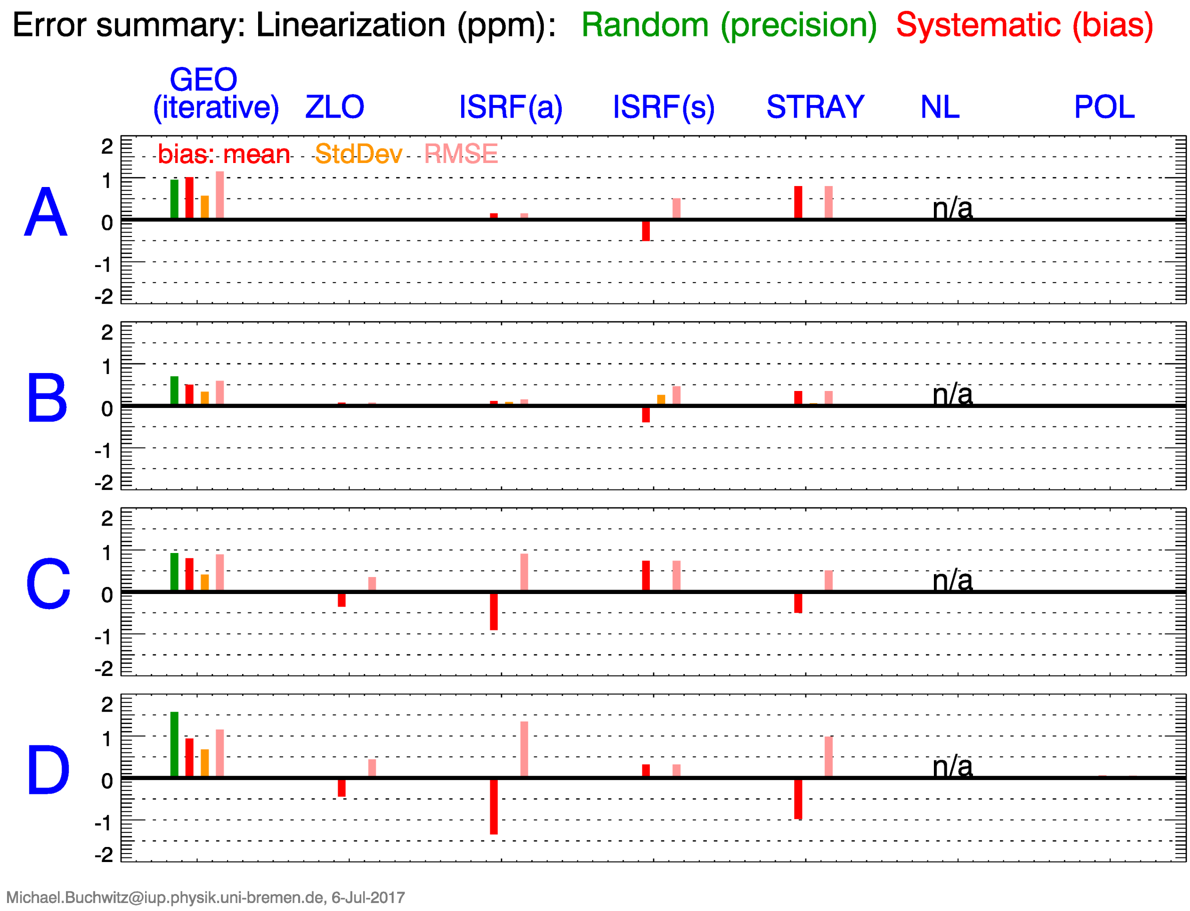

Figure 47: Summary of linear error analysis results. Note that for error "GEO" the "Iterative abs." results are shown including random error and that the "POL" errors have also been added but are too small to be visible.

8. Summary of all instrument A-D results

In **Sect. 6** various XCO_2 bias results are shown for method "Iterative abs." and in **Sect. 7** the corresponding biases as obtained for the "Iterative diff." and "Linearization" methods are presented.

To get an overview about all results in a clear and condensed way a simple scoring scheme has been defined and applied to the various bias results. This scheme and its results are presented in the following sub-section.

8.1. Scoring

8.1.1. Scoring method

The scoring scheme is defined and applied only to the various XCO_2 biases.

For the XCO_2 random error scoring is not needed as it is obvious from the results shown in **Sect. 6** that instrument B has smallest random error („best precision") for all scenarios.

The scoring scheme for biases is as follows:

- Score = 0 for all instruments except if:
  - +1 if the mean bias is smallest (for a given comparison of the four instruments)
  - -1 if the mean bias is largest
  - +1 if the standard deviation of the bias is smallest
  - -1 if the standard deviation of the bias is largest
- If more than one instrument is the winner (looser) for a given error source than all "equivalent" winners (looser) get +1 (-1)

Note:

- The RMSE is not used as this quantity is redundant
- Only the „mean bias" is used for the linearization results as here the scenario dependence is typically very small (the standard deviation of the biases are typically close to zero as can be seen from the figures shown in **Sect. 7.3**)

The scoring results are shown in the following section.

8.1.2. Scoring results

The XCO_2 bias scoring results are shown in **Table 9** to **Table 11** for the three used methods. The overall scoring results are shown in **Figure 48**.

The higher the score, the lower the biases, i.e., the better the instrument.

As can be seen from **Figure 48**, instrument B has by far the highest score for method "Iterative abs." (see detailed results in **Sect. 6**). For "Linearized" instruments A, B and C are essentially equally good (see detailed results in **Sect. 7.3**).

Instrument A has the highest score for method "Iterative diff." followed by B and C (identical scores). However, as already explained, method "Iterative diff." is not appropriate to determine "which instrument is better" in terms of instrument related biases.

Instrument D has lowest score for all three methods.

Following the explanations given earlier, namely that method "Linearized" is the best of the used methods to quantify instrument/calibration related XCO_2 biases, it is concluded from the results shown here that instrument B seems to be as good as instruments A and C. In terms of random errors instrument B is the winner.

In summary, the results of this study show that there is no indication that instrument B is worse than any of the other three instruments.

Error source	Mean bias	StdDev bias
GEO	+1: B -1: A	+1: B -1: D
GEO+ZLO	+1: B -1: A	+1: B -1: D
GEO+ISRF(asym)	+1: B -1: C	+1: AB -1: D
GEO+ISRF(sym)	+1: B -1: C	+1: A -1: D
GEO+STRAY	+1: D -1: A	+1: B -1: D
GEO+POL	+1: B -1: A	+1: B -1: D

Table 9: Scores for method “Iterative abs.”. Result: A: -1; B: 11; C: -2; D: -7.

Error source	Mean bias	StdDev bias
ZLO	+1: AD -1: C	+1: AC -1: D
ISRF(asym)	+1: D -1: A	+1: A -1: D
ISRF(sym)	+1: A -1: C	+1: BC -1: D
STRAY	+1: C -1: A	+1: A -1: D
POL	+1: C -1: D	+1: ABC -1: D

Table 10: Scores for method “Iterative diff.”. Result: A: 6; B: 2; C: 2; D: -5.

Error source	Mean bias
ZLO	+1: A -1: D
ISRF(asym)	+1: B -1: D
ISRF(sym)	+1: D -1: C
STRAY	+1: B -1: D
POL	+1: C -1: D

Table 11: Scores for method "Linearization". Result: A: 1; B: 2; C: 0; D: -3.

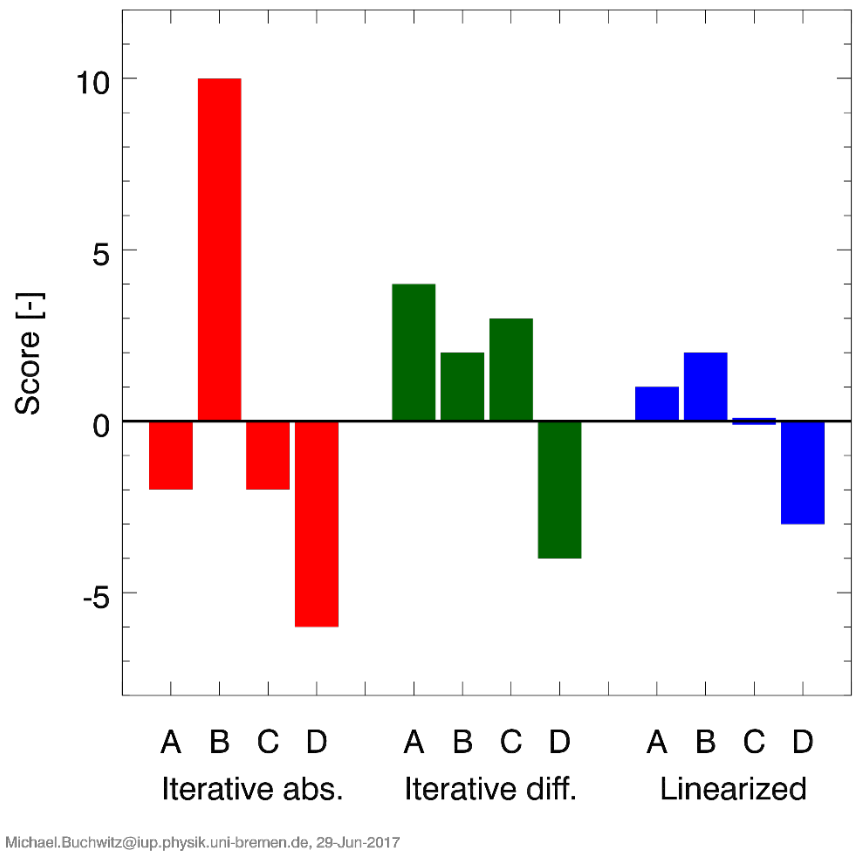

Figure 48: Scoring results for instruments A-D for the three methods "Iterative abs." (red), "Iterative diff." (dark green) and linearization (blue). The higher the score, the better the performance in terms of XCO_2 biases.

8.2. Overall summary and context

As shown in this document, instrument B has the smallest XCO_2 random error (see **Sect. 6**) of all four investigated instrument concepts.

Concerning XCO_2 systematic errors the situation is less clear and the findings can be summarized as follows: Overall, instrument B often has the smallest biases for the investigated scenarios as concluded from applying the full iterative BESD/C retrieval algorithm (with pre-processing) to simulated radiance spectra with various types of geophysical and instrument/calibration related errors present (see **Sect. 6**). As this approach is not optimal to "isolate" instrument/calibration related biases from other ("geophysical") biases also a linearized error analysis has been conducted (see **Sect. 7**). According to the linear error analysis instrument B shows good performance in terms of XCO_2 biases (see also **Sect. 8.1.2**) but here the differences to the other instrument concepts is much less pronounced compared to full iterative retrievals (in fact, instruments A, B and C have very similar performance).

Instrument B has the lowest spectral resolution but the highest signal-to-noise ratio (SNR) and covers the largest spectral range in the NIR (around 760 nm) and SWIR-2 (around 2000 nm) spectral regions.

Spectral resolution cannot be seen in isolation as a higher spectral resolution spectrum does not contain more information if much noisier. Therefore, also other aspects such as signal-to-noise performance and spectral coverage need to be considered. The findings of this study are therefore not necessarily a surprise. This study confirms results obtained in previous studies (see in particular the Final Reports of the two CarbonSat L1L2 studies (**/Bovenmann et al., 2014, 2015/**)). As shown in **/Bovenmann et al., 2014/**, simulated retrievals for several instrument configurations have been performed and it has been found that an instrument with lower spectral resolution can give superior performance in terms of XCO_2 random and systematic errors if the signal-to-noise ratio is high enough and spectral coverage is appropriately selected. These conclusions have been drawn by applying independently two different retrieval algorithms (the one from Univ. Bremen and the one from Univ. Leicester).

In **/Bovenmann et al., 2014/** also results from SRON are shown based on an analysis of real GOSAT data which were later also published in a peer-reviewed publication (**/Galli et al., 2014/**). Here the following has been concluded **/Galli et al., 2014/**: "For GOSAT spectra, the most notable effect on CO_2 retrieval accuracy is the increase of the standard deviation of retrieval errors from 0.7 to 1.0 % when the spectral resolution is reduced by a factor of six. The retrieval biases against atmospheric water abundance and air mass become stronger with decreasing resolution. The error scatter increase for CH_4 columns is less pronounced. … . For both GOSAT and synthetic measurements, retrieval accuracy decreases with lower spectral resolution for a given signal-to-noise ratio, suggesting increasing interference errors. … A countermeasure for instruments with a lower spectral resolution than GOSAT is to aim at a higher SNR. …”. A limitation has been highlighted in **/Bovenmann et al., 2014/**: “The GOSAT data have a SNR of 300 at continuum level for an SZA of 30 degress and an albedo of 0.3. In this report, we did not test whether the increase of error scatter caused by spectral degradation can be mitigated if the SNR for CarbonSat were better than for GOSAT. For this purpose, a representative global ensemble of synthetic spectra, combined with exact CarbonSat instrument settings would be necessary”.

Very strong evidence that high spectral resolution is not mandatory for precise and accurate XCO_2 retrieval is provided by a comparison of the XCO_2 performance as obtained for XCO_2 retrieval from SCIAMACHY compared to GOSAT (using real satellite data). As can be seen from **Table 12**, similar random (around 2 ppm) and systematic (around 0.5 ppm) errors have been obtained for SCIAMACHY and for GOSAT XCO_2 although the spectral resolution of SCIAMACHY is much worse compared to GOSAT - and also significantly worse compared to instrument B investigated in this study by a factor of 4-5 in the NIR and SWIR-1 bands.

GHG-CCI: Estimates of achieved data quality (#): CRDP#4 XCO_2

Sensor	Algorithm	Random error [ppm]	Systematic error [ppm]	Stability [ppm/year]		Details (section)
				Long-term drift	Year-to-year	
SCIAMACHY on ENVISAT	BESD v02.01.02	1.9 1.9 2.0 1.9	0.37 - 0.56 0.38 – 0.40 0.39 – 0.43 0.4 – 0.8	-0.03 +/- 0.06 (*) -0.13 +/- 0.28 (?) -0.02 +/- 0.33 (?) -0.01 +/- 0.08 (*)	0.32 +/- 0.08 0.34 (?) 0.23 (?) 1.68 +/- 2.03 (*)	VAL (Sect. 3) DP (6.1.1) EMMA (6.1.5) QA/QC (7.1)
SCIAMACHY on ENVISAT	WFMD V4.0	2.7 2.6 2.9 3.0 2.7	0.57 – 0.71 0.48 – 0.52 0.60 – 0.75 0.60 – 0.63 0.5 – 1.0	-0.03 +/- 0.10 (*) [0.00, 0.04] (?) 0.14 +/- 0.21 (?) 0.23 +/- 0.42 (?) -0.04 +/- 0.09 (*)	0.31 +/- 0.11 0.21 (?) 0.46 (?) 0.33 (?) 1.86 +/- 2.41 (*)	VAL (3) DP (6.1.2) DP (6.1.1) EMMA (6.1.5) QA/QC (7.1)
TANSO on GOSAT	OCFP v7.0 (UoL-FP)	1.8 1.9 1.8 1.7	0.36 - 0.58 0.47 0.36 – 0.42 0.3 – 0.5	-0.07 +/- 0.07 (*) 0.11 (?) -0.15 +/- 0.11 (?) -0.09 +/- 0.08	0.29 +/- 0.06 0.9 (?) 0.23 (?) 1.48 +/- 2.06 (*)	VAL (3) DP (6.1.3) EMMA (6.1.5) QA/QC (7.1)
TANSO on GOSAT	SRFP v2.3.8 (RemoTeC)	2.0 1.9 2.1 1.9	0.36 - 0.51 0.43 0.28 – 0.48 0.4 – 0.5	0.02 +/- 0.04 (*) -0.05 +/- 0.12 (*) 0.00 +/- 0.16 (?) -0.06 +/- 0.11 (*)	0.27 +/- 0.12 0.34 +/- 0.12 0.24 (?) 1.30 +/- 2.11 (*)	VAL (3) DP (6.1.4) EMMA (6.1.5) QA/QC (7.1)
SCIAMACHY & GOSAT	EMMA v2.2a	2.0 2.4	0.37 - 0.45 0.47 – 0.54	0.08 +/- 0.22 (*) -0.30 +/- 0.64 (?)	0.18 +/- 0.12 0.25 (?)	VAL (3) EMMA (6.1.5)
SCIAMACHY & GOSAT	EMMA v2.2b	1.7 1.8	0.29 - 0.38 0.32 – 0.40	-0.08 +/- 0.20 (*) -0.13 +/- 0.42 (?)	0.16 +/- 0.11 0.20 (?)	VAL (3) EMMA (6.1.5)
TANSO on GOSAT	EMMA v2.2c	1.7 1.8	0.30 - 0.39 0.24 – 0.44	-0.14 +/- 0.20 (*) -0.04 +/- 0.16 (?)	0.16 +/- 0.12 0.26 (?)	VAL (3) EMMA (6.1.5)
Required	G / B / T	< 1 / 3 / 8	< 0.2 / 0.3 / 0.5	< 0.2 / 0.3 / 0.5		/URD GHG-CCI v2.1/
Required	Target	< 0.5 ppm (uncertainty; 1-sigma)		< 0.15 ppm/year		**/GCOS-200/**

(#) As estimated (mostly) by comparison with ground-based TCCON observations neglecting TCCON accuracy (1-sigma) of 0.4 ppm
(*) NOT significant; (?) Significance unclear
Green numbers: at least URDv2.1 threshold requirement met; single values random and systematic errors are 1-sigma

Table 12: Comparison of SCIAMACHY and GOSAT XCO_2 data quality (source: **/Buchwitz et al., 2017/**).

9. Additional sizing points: Instruments B2 and B3

ESA has defined additional sizing points and the corresponding results are provided in this section.

The corresponding instrument concepts are in this document referred to as:

- B2c1: Instrument B2 from "industrial consortium 1"
- B2c2: Instrument B2 from "industrial consortium 2"
- B3c1: Instrument B3 from "industrial consortium 1"
- B3c2: Instrument B3 from "industrial consortium 2"

The differences of the B2 sizing points to instrument B (see previous sections) are:

- SWIR-2 starts at 2043 nm (instead of 1925 nm).
- The spectral sampling ratios (SSR) are 3.0 pixel/FWHM in all three bands (instead of 3.x nm, see **Table 7**).
- New SNR A and B coefficients (as provided by ESA).

All other parameters are identical (for instruments B, B2 and B3) including the spectral resolution, which is 0.1 nm in the NIR, 0.3 nm in the SWIR-1 and 0.55 nm in the SWIR-2.

The only difference between instruments B3 and B2 are:

- B3: SWIR-2 starts at 1990 nm (instead of 2043 nm for B2)

Radiances, solar irradiances and SNR spectra for these instruments (including instrument B) are shown in **Figure 49 - Figure 53**. The scenario is s00 for VEG50. The s00 scenario is identical to s01 (see previous sections, e.g., XCO_2: 390 ppm, H_2O column: $4.8x10^{22}$, AOD@550 nm: 0.2, cirrus at 10 km with COD=0.05) with the following exception:

- The aerosol type is "continental average" (CA, also used as *a priori* aerosol type in BESD/C) and not "continental clean" (CC).

In the captions of **Figure 49 - Figure 53** the corresponding XCO_2 retrieval precisions are listed. The retrieval results have been generated with the same BESD/C algorithm as also used for the instrument B study results shown in previous sections with the following exception:

- No cirrus pre-processing (as the 1939 nm is not available for the B2 instruments)

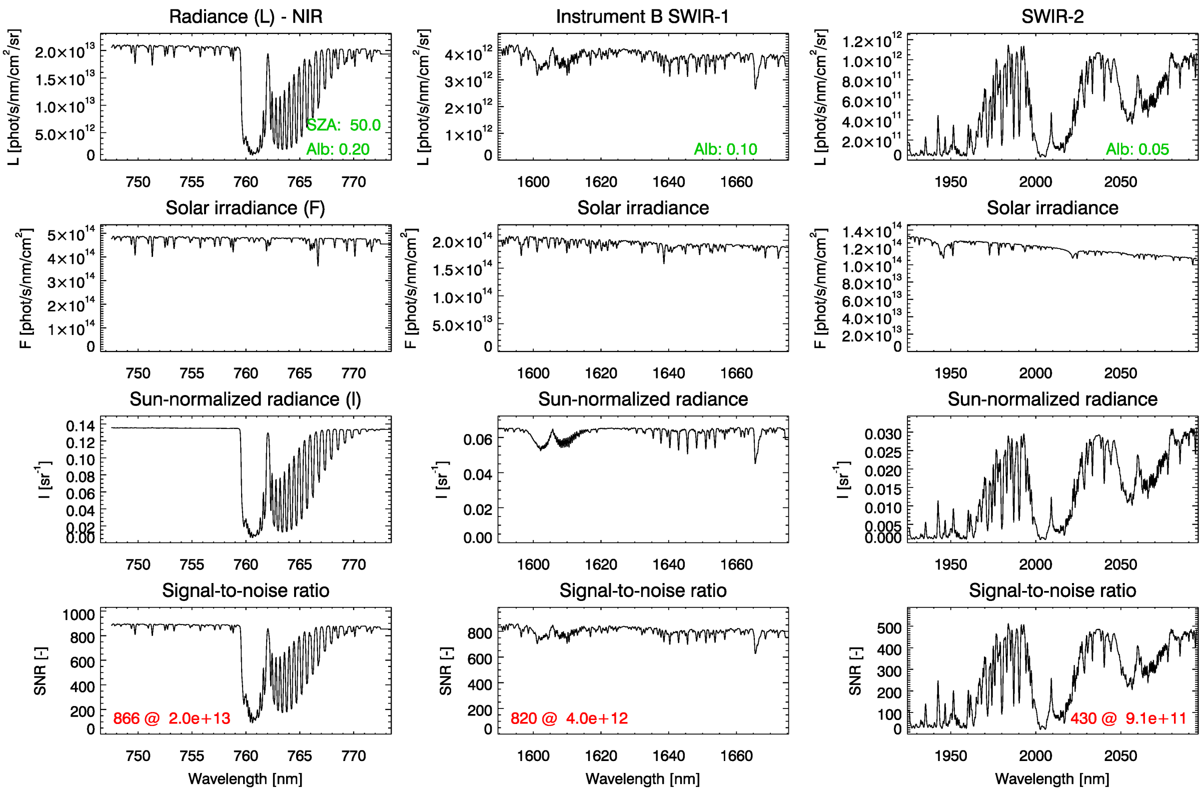

Figure 49: Instrument B spectra (see main text for details). The corresponding BESD/C XCO_2 retrieval precision (total uncertainty, i.e., including smoothing and interference errors): 0.69 ppm.

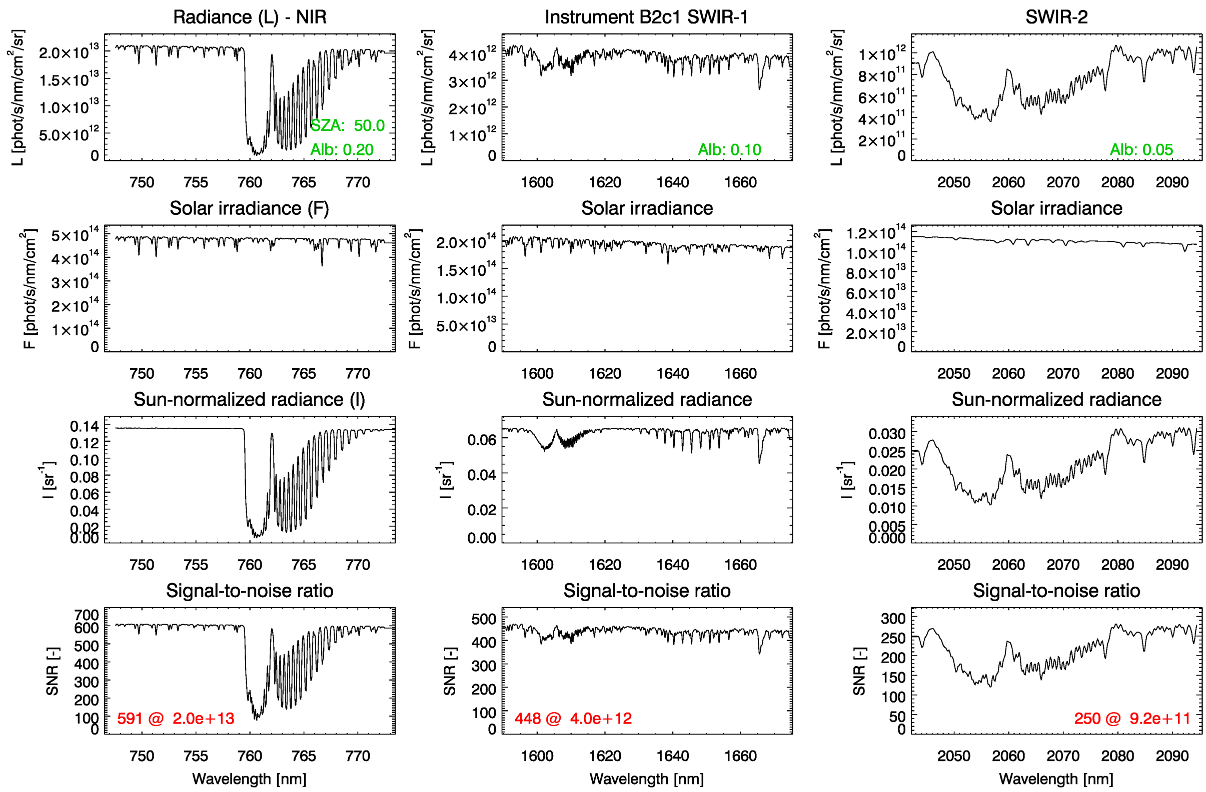

Figure 50: As **Figure 49** but for instrument B2c1. XCO_2 precision: 1.58 ppm.

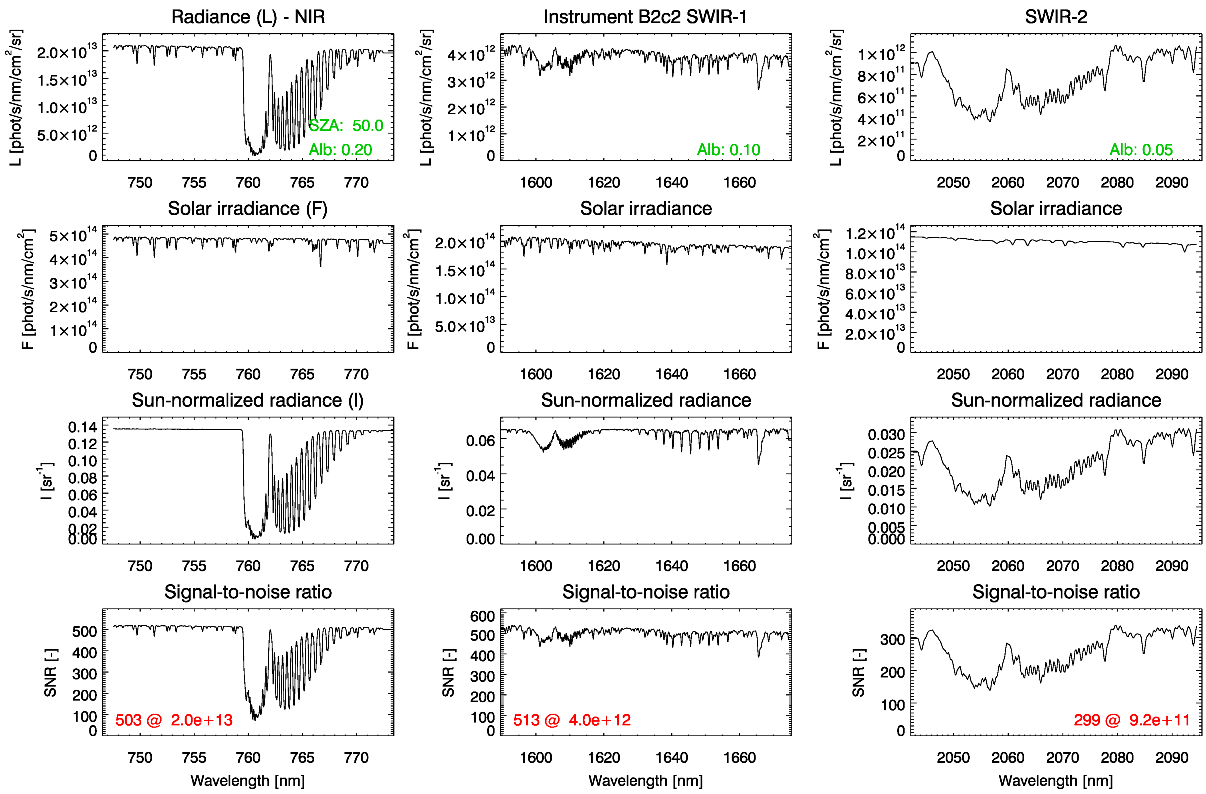

Figure 51: As **Figure 49** but for instrument B2c2. XCO_2 precision: 1.47 ppm.

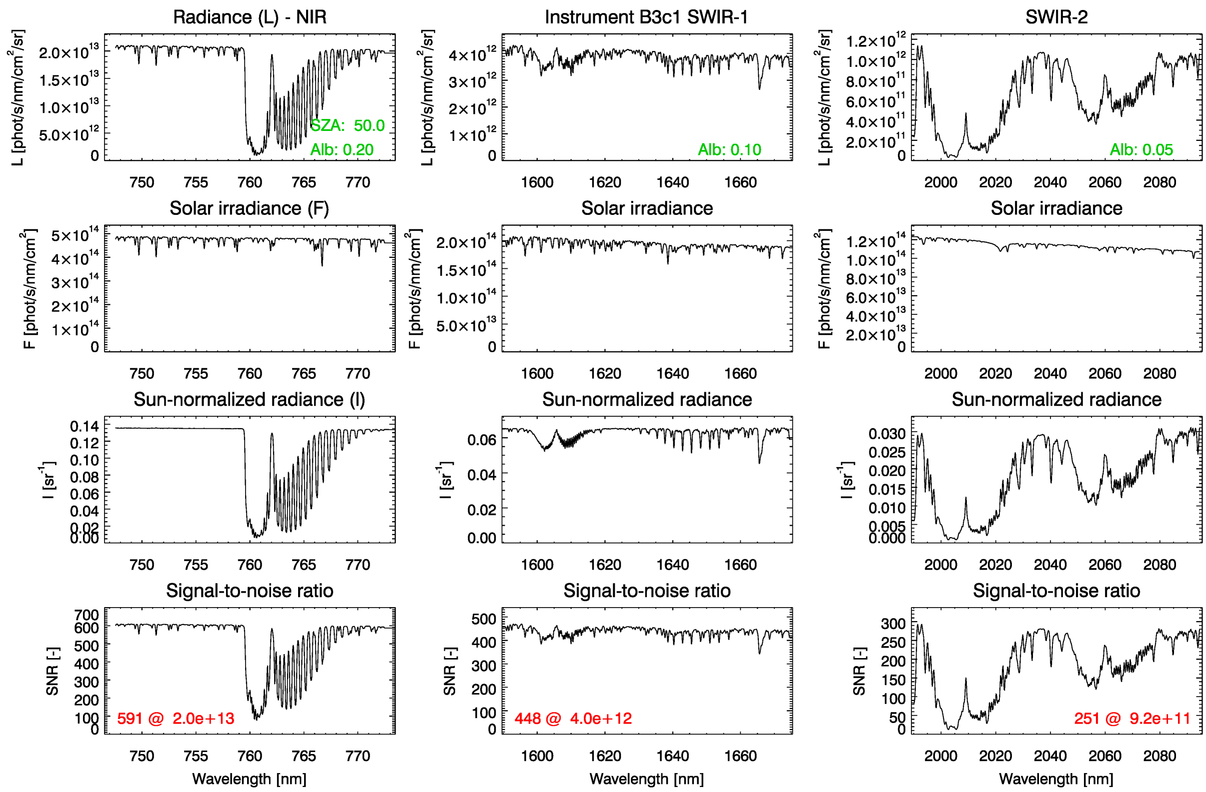

Figure 52: As **Figure 49** but for instrument B3c1. XCO_2 precision: 1.11 ppm.

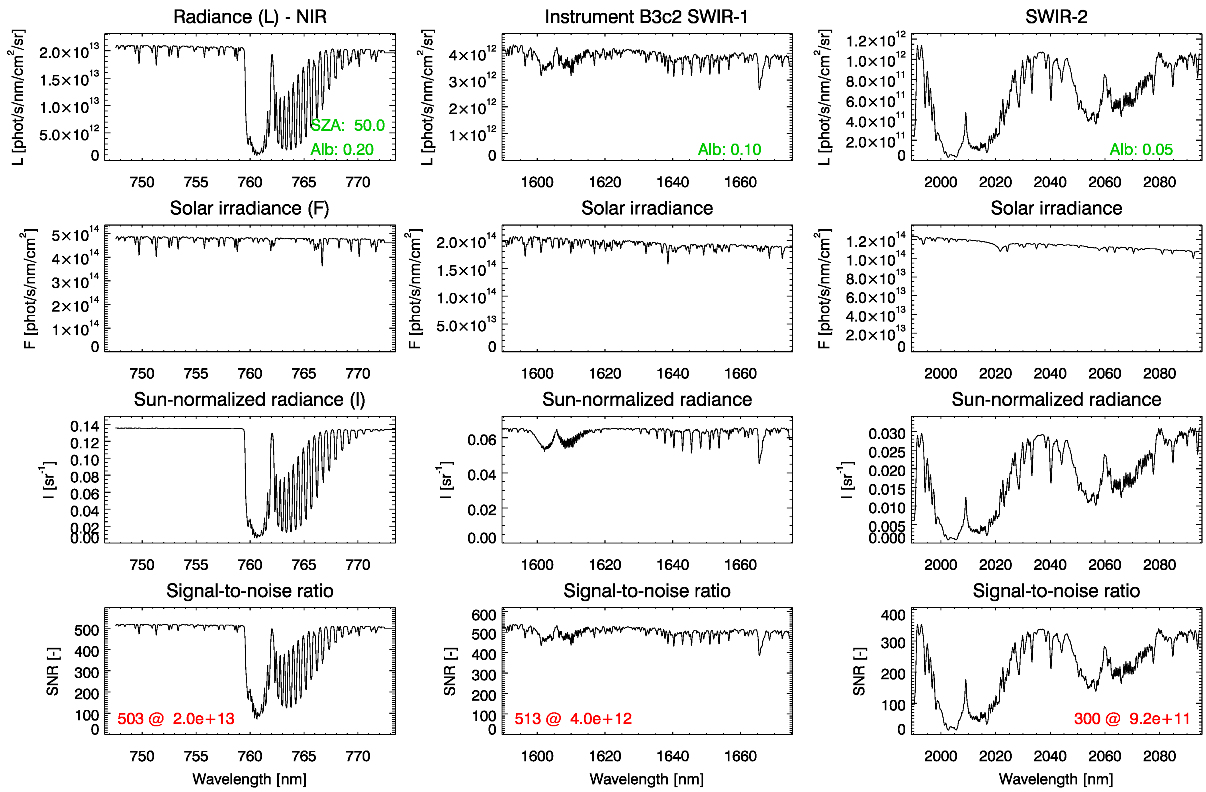

Figure 53: As **Figure 49** but for instrument B3c2. XCO_2 precision: 1.04 ppm.

The “XCO_2 precision” is defined as the overall XCO_2 random error, which has three components (see, e.g., **/Rodgers and Connor, 2003/**):

- Instrument noise (depending on SNR)
- XCO_2 smoothing error (depending on CO_2 and surface pressure state vector elements and their *a priori* uncertainty; note that surface pressure is strongly constrained so that essentially only the uncertainties of the CO_2 state vector elements matter; these are 10% for the lowest layer (lower troposphere) and 0.5% above)
- Interference error (depending on non-CO_2 state vector elements and their *a priori* uncertainty)

How the retrieval precision and the CO_2 column instrument noise errors depends on the BESD/C retrieval settings is shown in **Table 13**. From this the following can be concluded:

- From No. 1-3: Strong dependence on SWIR-2 start wavelength
- From 1, 5-7: Strong dependence on retrieval state vector

No.	BESD/C retrieval settings	XCO_2 precision [ppm]	CO_2 column instrument noise error [%] / [ppm]
1	Instrument B2c1 (SW2 start @ 2040 nm) & BESD/C default settings (= Algorithm Baseline 1 = ABL1)	1.58	0.32% / 1.25
2	As 1 but SW2 start @ 1990 nm	1.11	0.20% / 0.78
3	As 1 but SW2 start @ 1920 nm	0.87	0.15% / 0.59
4	As 1 but BESD/C without ZLO & Sh&Sq	1.20	0.24% / 0.94
5	As 4 but BESD/C without albedo parameters	0.96	0.22% / 0.86
6	As 5 but BESD/C without scattering parameters, TEM, H2O, SIF (remaining: CO_2, CH_4, surface pressure, polynomial)	0.73	0.17% / 0.65
7	As 6 but without polynomial (remaining: CO_2, CH_4, p_s)	0.46	0.10% / 0.32

Table 13: XCO_2 precision and CO_2 column noise error for several BESD/C retrieval settings.

Additional results are shown in **Table 14**. Note that retrieval setting used for No. 1.6 are **"Algorithm Baseline 2" (ABL2)**, which is identical with ABL1 (used in previous sections of this document). For ABL2 the following state vector elements have been removed compared to ABL1: ALB (= albedo; 3 elements, one per band) and ZLO (= zero level offset; 3 elements, one per band).

No.	BESD/C retrieval settings	XCO_2 precision [ppm]	CO_2 column instrument noise error [%] / [ppm]
1.1	For instrument B2c1 with SW2 start wavelength 1990 nm and BESD/C algorithm baseline 1 (ABL1)	1.11	0.20% / 0.80
1.2	As 1.1 but VCF (= SIF) removed from state vector (#)	1.11	0.20% / 0.80
1.3	As 1.2 but albedo (ALB) removed from state vector (#)	0.99	0.21% / 0.82
1.4	As 1.3 but ZLO removed from state vector (*)	0.76	0.16% / 0.64
1.5	As 1.4 but enhanced SNR in NIR / SW1 / SW2: 11% / 0% / 0% 0% / 11% / 0% 0% / 0% / 11% 0% / 11% / 11% 0% / 15% / 15% 0% / 20% / 20%	 0.76 0.73 0.74 0.71 0.70 0.68	 0.16% / 0.64 0.16% / 0.61 0.16% / 0.61 0.15% / 0.58 0.15% / 0.57 0.14% / 0.55
1.6	As 1.4 but VCF (= SIF) added = Algorithm Baseline 2	0.76	0.16% / 0.64
2.1	As 1.4 but with SW2 start wavelength 2043 nm	0.96	0.22% / 0.86
2.2	As 2.1 but enhanced SNR in NIR / SW1 / SW2: 0% / 40% / 40% 0% / 55% / 55% 0% / 60% / 60%	 0.74 0.70 0.67	 0.16% / 0.64 0.15% / 0.59 0.14% / 0.56
2.3	As 2.1 but VCF (= SIF) added	0.96	0.22% / 0.86

Table 14: Additional XCO_2 precision and CO_2 column noise error for several BESD/C retrieval settings. (#) Assumption: Not mandatory as good *a priori* & first guess via pre-processing. (*) Not clear if really needed / if adding ZLO to state vector is the best approach to deal with ZLO related errors.

10. Relevance of SWIR-2a spectral region

The SWIR-2a spectral region (around 1939 nm) covers a strongly absorbing ("saturated") atmospheric water vapour band, which can be used in BESD/C via a pre-processing step in order to obtain an *a priori* / first guess value of the cirrus optical depth (COD) as input for the subsequent BESD/C 3-band retrieval (see **Sect. 3.2**).

Saturated water bands have been and are used in the context of XCO_2 retrieval from real satellite data: For example, the 1.9 µm spectral region is used for cirrus cloud detection and sub-sequent quality filtering (leading to rejection of the corresponding ground pixel depending on a pre-defined threshold) using a simple threshold technique for BESD XCO_2 retrievals from real GOSAT data **/Heymann et al., 2015/** and for the same reason the 1.4 µm spectral region has been used for WFM-DOAS XCO_2 retrievals from SCIAMACHY **/Heymann et al., 2012/**. As shown in **/Heymann et al., 2012/** the method is sensitive to thin (COD > 0.05) and high (CTH > 4 km) clouds if the water column is > 1.14 g/cm^2 (corresponding to 3.8×10^{22} molecules/cm^2). These findings are consistent with the findings of **/Guerlet et al., 2013/**. They concluded - based on simulated and real GOSAT data - that their detection and filtering method efficiently detects high altitude scattering layers (> 5 km) that are most likely cirrus (or occasionally aerosol volcanic plumes) and is efficient even in the case of relatively dry scenes. In summary, the use of strongly saturated water bands is well established and used in the context of satellite XCO_2 retrievals primarily for the detection and flagging of scenes contaminated with high concentrations of elevated (high altitude) atmospheric scatterers such as cirrus clouds.

Nevertheless, not all satellite XCO_2 retrieval algorithms use saturated water bands for detection and flagging of cirrus contaminated scenes. Examples are **/Reuter et al., 2010/** and **/Reuter et al., 2011/** for SCIAMACHY and all OCO-2 algorithms (e.g., **/Eldering et al., 2017/ /Reuter et al., 2017a/ /Reuter et al., 2017b/**).

Saturated water bands are also used for more general purposes, e.g., the 1.38 µm spectral region is used to generate the Visible Infrared Imaging Radiometer Suite (VIIRS) Cloud Mask data product **/VIIRS Cloud Mask ATBD, 2014/**.

The relevance of the SWIR-2a spectral region for XCO_2 retrieval has been further investigated in this study using simulations and the results are shown in the following.

Figure 54 shows radiance spectra and radiance ratios for several cirrus optical depth (COD). As can be seen, the radiance strongly increases almost linearly with COD, in particular for wavelengths below 1950 nm. The BESD/C retrieval algorithm takes advantage of this by retrieving COD from radiances around 1939 nm using a very simple algorithm, which computes COD from the 1939 nm radiance assuming a linear relationship (more details on this algorithm are given below). The resulting COD values are used as *a priori* and first guess values for the full BESD/C 3-band retrieval (where COD is also a state vector element) as this has the potential to further improve the accuracy of the retrieved COD and therefore also of the retrieved XCO_2.

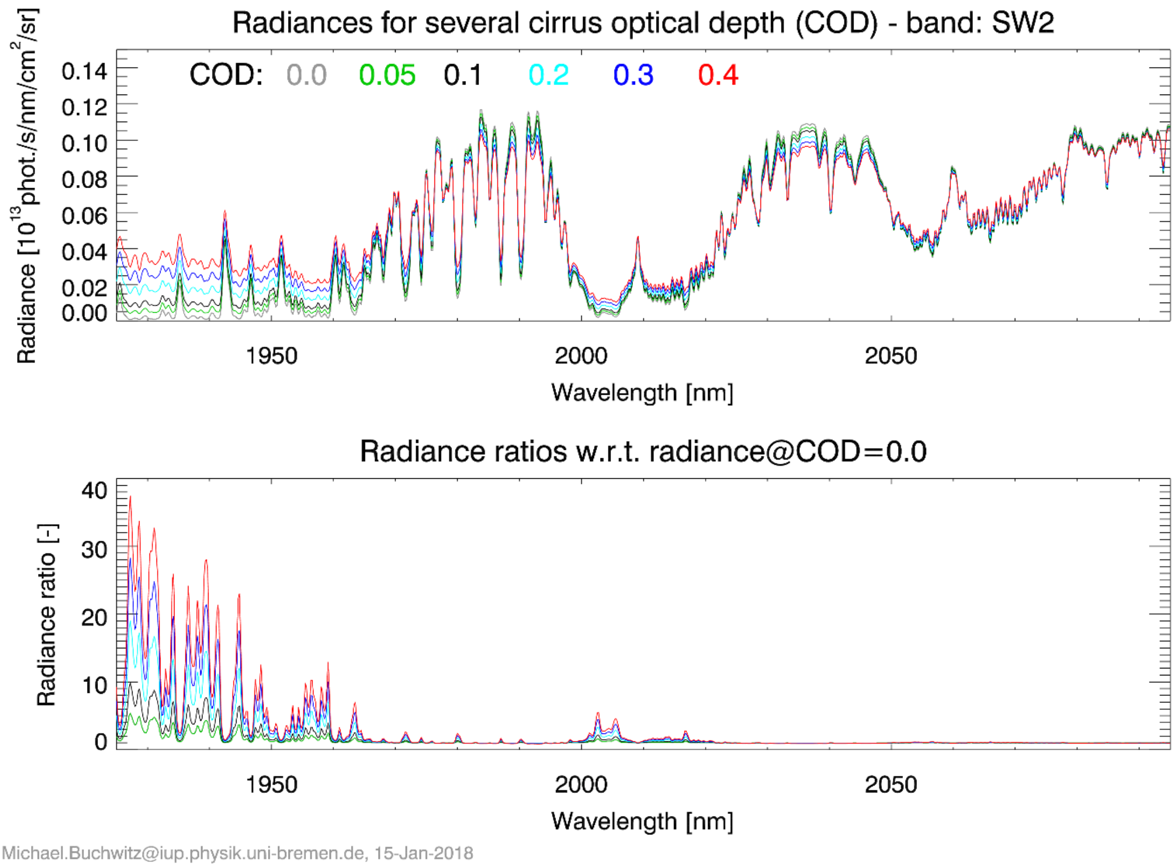

Figure 54: SWIR-2 band radiance spectra and radiance ratios. Top: Radiance spectra (resolution 0.55 nm) for different cirrus optical depths (COD). Other parameters: H_2O column: 4.8x10^{22} molecules/cm^2 (US Standard Atmosphere), SZA 50°, vegetation albedo, cirrus altitude 10 km, default aerosol ("s00": AOD 0.2, type: continental average).

Figure 55 shows a spectral zoom into **Figure 54** including radiance noise error (top) for instrument B2c1 and the corresponding SNR spectra (bottom). As can be seen, the SNR is good enough to distinguish the various radiance levels corresponding to different cirrus optical depths. **Figure 56** shows the corresponding results for the NIR band and **Figure 57** for the SWIR-1 band.

As can be seen, also the NIR band is very sensitive to cirrus but the radiance change is typically less specific compared to the SWIR-2 band as other parameters can lead to similar radiance perturbations. Nevertheless, also the NIR band provides information on cirrus and to what extent this is "good enough" for accurate XCO_2 retrieval if the SWIR-2a spectral region around 1.9 µm is not available has been investigated. The results are presented and discussed in the following.

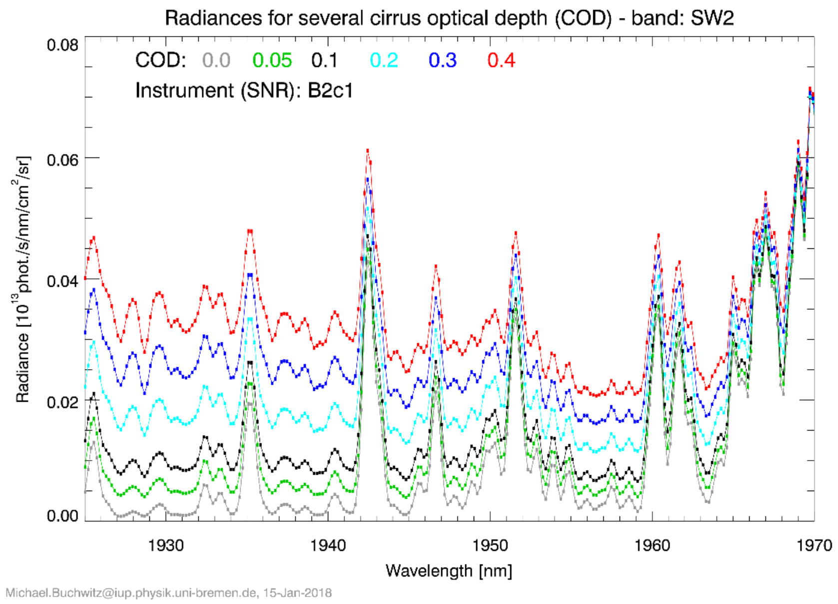

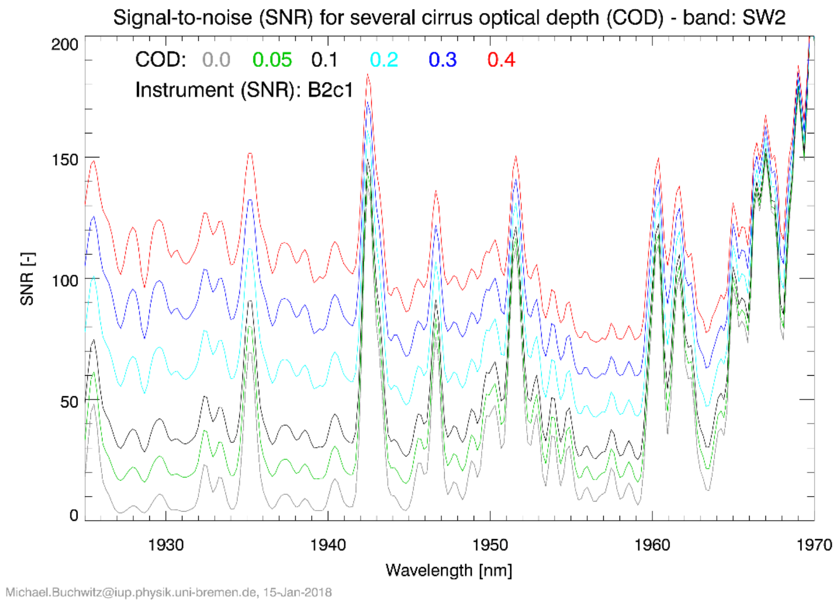

Figure 55: Top: As **Figure 54** but restricted to the first part of the SWIR-2 spectral range and with 1-sigma radiance noise error added. Bottom: Corresponding SNR.

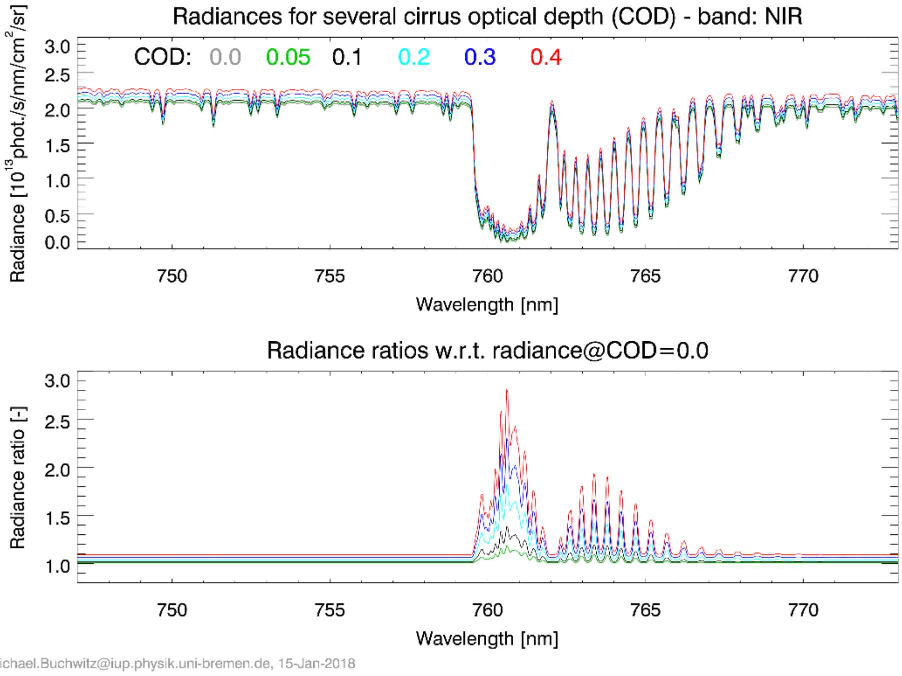

Figure 56: As **Figure 54** but for the NIR band.

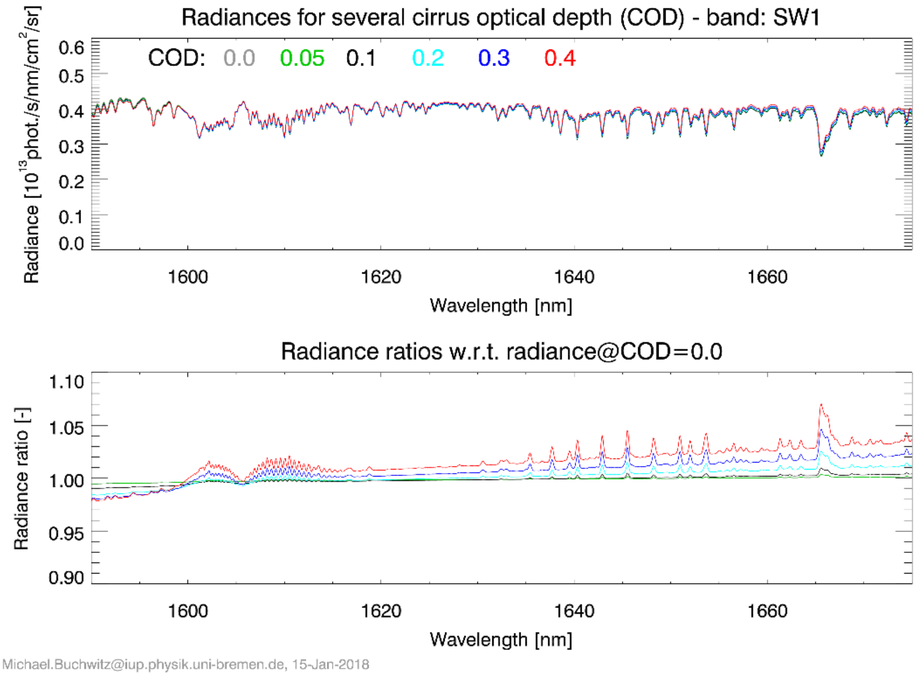

Figure 57: As **Figure 54** but for the SWIR-1 band.

As can be seen from the previous figures, the radiance in the SWIR-2a spectral region increases approximately linearly with COD. BESD/C takes advantage of this by retrieving COD in a pre-processing step from the mean radiance obtained from the 1938 – 1940 nm spectral region according to this equation:

$$COD^a = 0.2 \text{ x } RAD / (1.85\ 10^{11})$$

Here RAD is the (mean) radiance given in photons/s/nm/cm^2/sr and COD^a is the dimensionless cirrus optical depth as obtained from the SWIR-2a spectral region.

COD^a can then be used as *a priori* and first guess value for the BESD/C 3-band retrieval instead of the default value of COD, which is 0.05 +/- 0.05, i.e., assuming 100% *a priori* uncertainty (1-sigma).

To investigate if COD^a from SWIR-2a can be used to improve the accuracy of the XCO_2 retrievals and to find out if this likely also helps to increase the yield, i.e., to see if this has the potential to increase the number of ground-pixels where "good" XCO_2 retrievals are possible, the following has been done:

Retrievals have been performed for two cases:

- Case 1: An ideal case where the simulated radiance observations are fully consistent with the retrieval assumptions (same surface and atmospheric conditions except for COD, no measurement errors, etc.)
- Case 2: A nearly ideal case, which differs from Case 1 in only one aspect: Here the cirrus is located at 6 km whereas the retrieval assumes as *a priori* and initial guess that the cirrus is located at 10 km.

To make sure that the resulting XCO_2 bias is only due to COD errors, all other errors have been eliminated. In particular, errors resulting from the (other) pre-processing steps used to obtain initial values for surface albedo and SIF have been eliminated (i.e., it is assumed here that surface albedo and SIF are perfectly known).

The results shown in the following are for the VEG50 scenario (= surface albedo corresponding to vegetation, SZA 50^o) and for instrument B2c1 with the SWIR-2 fitting window starting at 2043 nm. It can however be assumed that the resulting general conclusions (given at the end of this section) are also valid for similar other instruments (e.g., B2c2) and other (shorter) SWIR-2 fitting window start wavelengths.

Figure 58 shows XCO_2 biases as a function of true COD (top panel) for the ideal case (Case 1). As can be seen, use of SWIR-2a results in lower biases (green curve) compared to retrievals, where SWIR-2a has not been used (red curve). **Figure 59** shows results for the same case but with iteration. As can be seen, the iteration reduces the biases for the case where SWIR-2a has not been used (red curve) but does not change the biases for the case where SWIR-2a has been used (as the iteration does not succeed to further reduce the cost function).

As can also be seen from these figures, the SWIR-2a spectral region provides improved *a priori* and first guess values of COD (compare the blue bars with the black bars in the middle and bottom panels). As can also be seen, good COD values can also be obtained if the SWIR-2a band is not used (compare the red bars with the black bars in the middle panels).

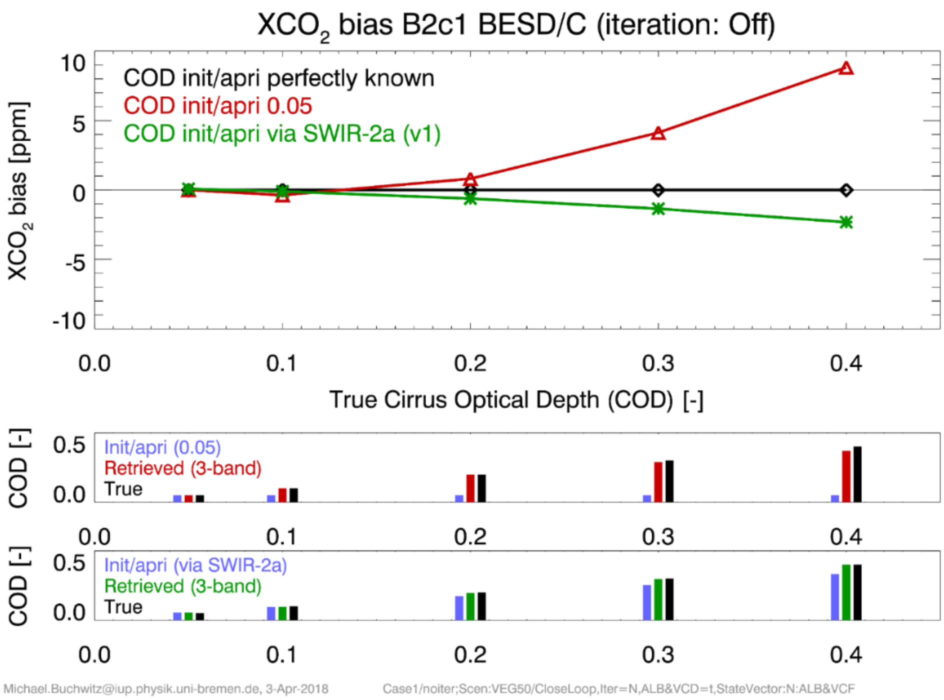

Figure 58: Top: XCO_2 bias versus true COD. The black line corresponds to results obtained with BESD/C 3-band retrievals, where COD is perfectly known. In this case, the resulting XCO_2 biases are all zero, as it should be. The red line shows the XCO_2 biases obtained assuming a default COD *a priori* and initial guess value of 0.05. The green line shows the XCO_2 bias if the SWIR-2a spectral region is used to obtain *a priori* and initial guess values for COD assuming that the COD^a *a priori* uncertainty is 100% (of the retrieved COD^a value). As can be seen, the biases are smaller compared to the case, where the SWIR-2a region has not been used (red curve). Middle panel: COD values for the case where the SWIR-2a region has not been used. Bottom panel: COD values for the case where the SWIR-2a region has been used. The BESD/C retrieval have been performed without iteration.

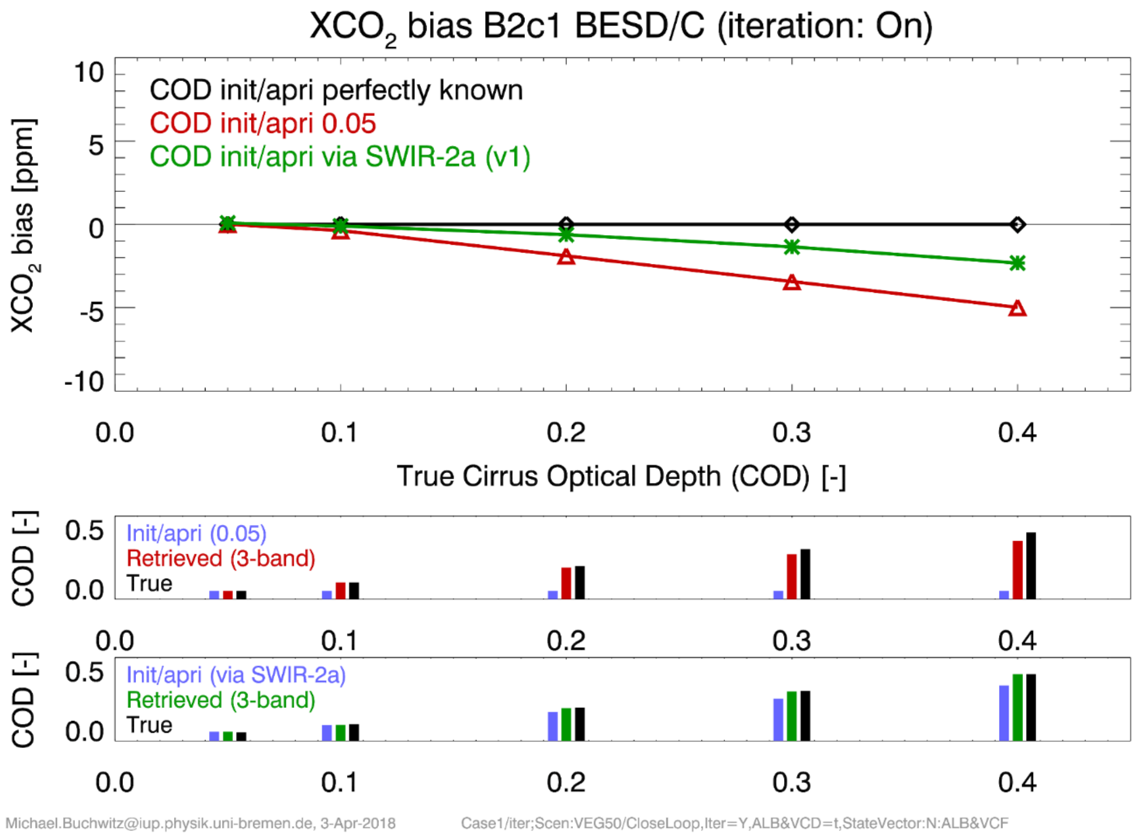

Figure 59: As **Figure 58** but with iteration.

Figure 60 (without iteration) **Figure 61** (with iteration) show the corresponding results for the less ideal case, i.e., for Case 2. As can be seen, even the black curve does not show error zero any more (because the cirrus altitude is not exactly known). As can also be seen, the biases shown by the green curve (use of SWIR-2a) are in this case larger than for the retrievals where SWIR-2a has not been used (red curve). The green curves shown in **Figure 60** and **Figure 61** correspond to retrievals where the assumed *a priori* uncertainty of COD^a is 100%. **Figure 62** and **Figure 63** show the corresponding results for 30% *a priori* uncertainty. As can be seen, the results are essentially the same, i.e., they do not significantly depend on the assumed *a priori* uncertainty.

It was expected that at least for nearly ideal cases it can be shown that the accuracy can be clearly improved. However, as shown by the results in this section, this is apparently not the case for simulated BESD/C retrievals. It is therefore concluded that the SWIR-2a band is useful for detection and flagging of cirrus contaminated scenes but not to improve the accuracy of the XCO_2 retrieval for individual footprints.

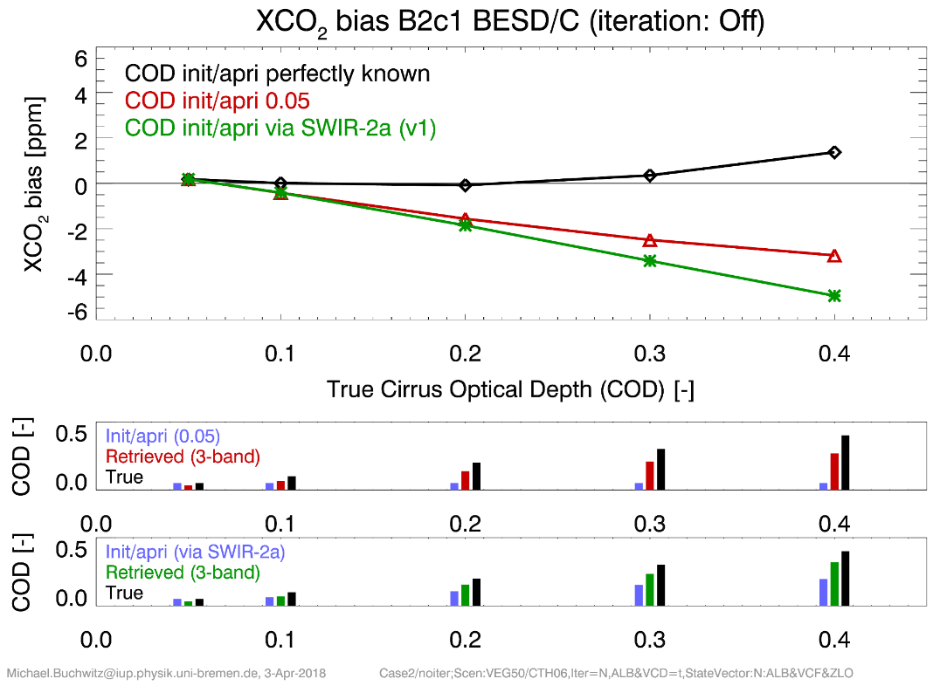

Figure 60: As **Figure 58** but for a slightly less ideal case. Here the cirrus is located at 6 km whereas the retrieval assumes that is it located at 10 km (= BESD/C default value).

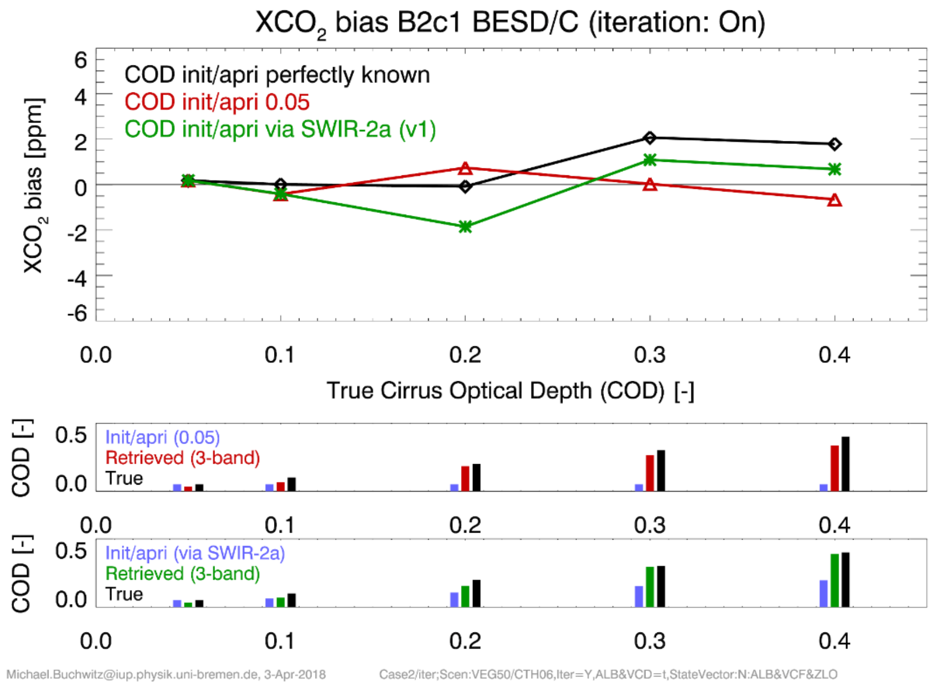

Figure 61: As **Figure 60** but with iteration.

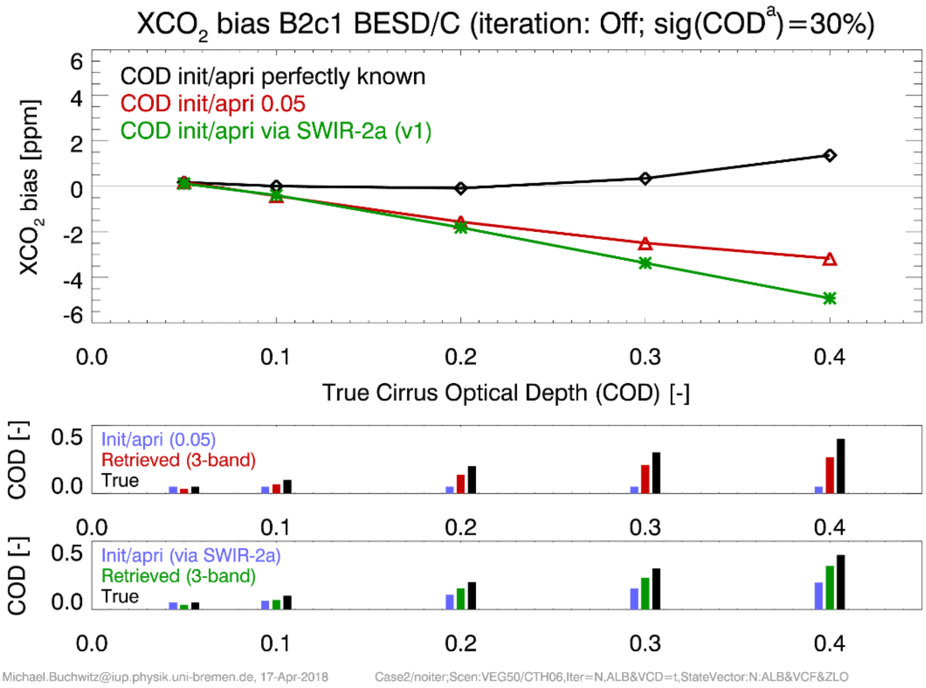

Figure 62: As **Figure 60** but assuming 30% a priori uncertainty for COD[a].

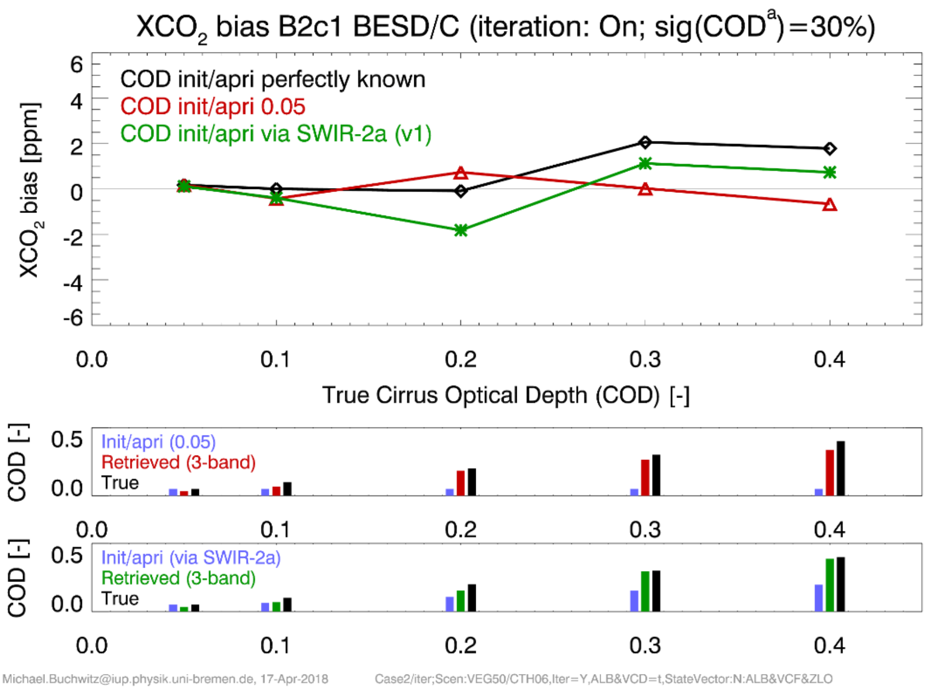

Figure 63: As
Figure 62 but with iteration.

10.1. Summary and conclusions SWIR-2a

It is clear – from published investigations using simulated and real satellite data – that strongly saturated water (SSW) bands (e.g., SWIR-2a) provide information on elevated (> 4-5 km) scattering layers (cirrus, elevated aerosols).

Currently SSW bands are used by some XCO_2 algorithms for identification and flagging (removal) of scenes contaminated by elevated scattering layers.

Note:

- Even „only“ detection and flagging is important as it ensures reliable detection of (potentially) very problematic scenes (footprints). Information on such scenes would be available prior to time consuming 3-band retrievals. This is relevant as processing time will be an issue (as each of the foreseen CO_2 satellites will have approximately 10 times the number of OCO-2 footprints).

The following has been investigated in this study (apart from the literature study results summarized above): Can SWIR-2a also help to improve the XCO_2 single footprint accuracy and/or to increase the yield via improved *a priori* information on cirrus optical depth (COD) from the SWIR-2a spectral region ?

The results shown in this section suggest that the answer is No.

Reason: The simulated retrievals have not shown any robust improvements. In fact, it has been shown that biases can even be worse for nearly ideal cases (where, for example, all is perfectly known except cirrus altitude). This is interpreted as a clear indication that improving the accuracy will hardly be possible.

The underlying reason for this is that COD information from other spectral regions (in particular from the NIR band) is already very good (at least for simulations) and that additional information from SWIR-2a does not to help to improve the accuracy.
Note that this conclusion is consistent with (unpublished) findings from SRON & UoL based on real GOSAT data

Based on these results the following is recommended for the MRD: Coverage of the SWIR-2a spectral region (e.g., the 1938-1940 nm region investigated here) should be included as a goal requirement but not necessarily as a threshold requirement („very good to have but not mandatory“).

11. Acronyms and abbrevations

Acronym	Meaning
ABL	Algorithm Baseline
AOD	Aerosol Optical Depth
ATBD	Algorithm Theoretical Basis Document
BESD	Bremen optimal EStimation DOAS
BESD/C	BESD algorithm used for CarbonSat assessments
BL	Boundary Layer
CA	Continental Average (aerosol scenario)
CarbonSat	Carbon Monitoring Satellite
CC	Continental Clean (aerosol scenario)
CCI	Climate Change Initiative (of ESA)
CL	Close Loop
CNES	Centre national d'études spatiales
COD	Cloud Optical Depth
CP	Continental Polluted (aerosol scenario)
CS	CarbonSat
CTH	Cloud Top Height
DE	Desert (aerosol scenario)
DES	Desert (surface albedo)
DOAS	Differential Optical Absorption Spectroscopy
DOF	Degrees of Freedom
EE8	Earth Explorer No. 8 (satellite)
ENVISAT	Environmental Satellite
ESA	European Space Agency
FR	Final Report
FWHM	Full Width at Half Maximum
GHG	Greenhouse Gas
GHG-CCI	Greenhouse Gas project of ESA's Climate Change Initiative (CCI)
GM	Gain Matrix
GMM	Gain Matrix Method
GOSAT	Greenhouse Gases Observing Satellite
ISRF	Instrument Spectral Response Function
IUP-UB	Institute of Environmental Physics (Institut für Umweltphysik), University of Bremen, Germany
MLS	Mid-latitude summer (profiles)
MODIS	Moderate resolution Imaging Spectrometer
MRD	Mission Requirements Document
NIR	Near Infra Red (band)
OCO	Orbiting Carbon Observatory
OE	Optimal Estimation

OPAC	Optical Properties of Aerosol and Clouds
RfMS	Report for Mission Selection
RMSE	Root Mean Square Error
RTM	Radiative Transfer Model
SCIAMACHY	Scanning Imaging Absorption Spectrometers for Atmospheric Chartography
SCIATRAN	Radiative Transfer Model under development at IUP
SIF	Sun-Induced Fluorescence
SNR	Signal to Noise Ratio
SSI	Spectral Sampling Interval
SSP	Spectral Sizing Point
SSR	Spectral Sampling Ratio
SW1 or SWIR-1	SWIR 1 band
SW2 or SWIR-2	SWIR 2 band
SWIR	Short Wave Infrared
SZA	Solar Zenith Angle
TOA	Top of atmosphere
VCF	Vegetation Chlorophyll Fluorescence
VEG	Vegetation (surface albedo)
VIIRS	Visible Infrared Imaging Radiometer Suite
VMR	Volume Mixing Ratio

12. References

/Bovenmann et al., 2010/ Bovensmann, H., Buchwitz, M., Burrows, J. P., Reuter, M., Krings, T., Gerilowski, K., Schneising, O., Heymann, J., Tretner, A., and Erzinger, J., A remote sensing technique for global monitoring of power plant CO_2 emissions from space and related applications, Atmos. Meas. Tech., 3, 781-811, 2010.

/Bovenmann et al., 2014/ Bovensmann, H., M. Buchwitz, M. Reuter, T. Krings, J. Heymann, H. Boesch, J. Landgraf, CarbonSat Earth Explorer 8 Candidate Mission “Level-2 and Level-1B Requirements Consolidation Study“, Final Report ESA Study CarbonSat Earth Explorer 8 Candidate Mission “Level-2 and Level-1B Requirements Consolidation Study “, ESA Contract No 4000105676/12/NL/AF, Version 2.2, Date: 18. July 2014, Doc.ID: IUP-CS-L1L2-FR-01, 2014.

/Bovenmann et al., 2015/ Bovensmann, H., M. Buchwitz, M. Reuter, T. Krings, J. Heymann, H. Boesch, J. Landgraf, CarbonSat Earth Explorer 8 Candidate Mission “Level-1 Level-2 (L1L2) Performance Assessment Study “, Final Report ESA Study, ESA Contract No 4000109814/13/NL/FF/lf, Version 1.0, Date: 11. December 2015, Doc.ID: IUP-CS-L1L2-II-FR-01, 2015.

/Buchwitz et al., 2013a/ Buchwitz, M., M. Reuter, H. Bovensmann, D. Pillai, J. Heymann, O. Schneising, V. Rozanov, T. Krings, J. P. Burrows, H. Boesch, C. Gerbig, Y. Meijer, and A. Loescher, Carbon Monitoring Satellite (CarbonSat): assessment of atmospheric CO_2 and CH_4 retrieval errors by error parameterization, Atmos. Meas. Tech., 6, 3477-3500, 2013.

/Buchwitz et al., 2013b/ Buchwitz, M., H. Bovensmann, M. Reuter, J. Heymann, O. Schneising, et al., CARBONSAT: ERROR ANALYSIS FOR PRIMARY LEVEL 2 PRODUCTS XCO_2 AND XCH_4 AND SECONDARY PRODUCT VEGETATION CHLOROPHYLL FLUORESCENCE FOR NADIR OBSERVATIONS OVER LAND, ESA Living Planet Symposium, Sept 9-13, 2013, Edinburgh, UK, conference proceedings ESA Special Publication SP-722 (on CD-ROM), link: http://www.iup.uni-bremen.de/sciamachy/NIR_NADIR_WFM_DOAS/2846996buchwitz.pdf, 2013.

/Buchwitz et al., 2015/ Buchwitz, M., Bovensmann, T. Krings, M. Reuter, V. V. Rozanov, P. Liebing, J. Landgraf, F. Alkemade, Mission Requirements Analysis and Level 2 Error Characterization for CarbonSat Nadir Observations over Land - WP 1100, 2000 & 4100 Report, ESA Study CarbonSat Earth Explorer 8 Candidate Mission “Level-1 Level-2 (L1L2) Performance Assessment Study“ ESA Contract No 4000109814/13/NL/FF/lf, Version 1.2, 3 Dec 2015, Doc ID: IUP-CS-L1L2-II-TNnadir, 2015.

/Buchwitz et al., 2017/ ESA Climate Change Initiative (CCI) Product Validation and Intercomparison Report (PVIR) for the Essential Climate Variable (ECV) Greenhouse Gases (GHG) for data set Climate Research Data Package No. 4 (CRDP#4), Version 5.0, 9. Feb. 2017, link: http://www.esa-ghg-cci.org/?q=webfm_send/352, 2017.

/Ciais et al., 2015/ Ciais, P., et al.: Towards a European Operational Observing System to Monitor Fossil CO_2 emissions - Final Report from the expert group, http://www.copernicus.eu/main/towards-european-operational-observing-system-monitor-fossil-co2-emissions, pp. 68, October 2015, 2015.

/CS MRD v1.0, 2011/ ESA, CarbonSat – Candidate Earth Explorer Opportunity Mission – Mission Requirements Document, Issue 1, Revision 0, 8 July 2011, ESA Mission Science Division, Reference EOP-SMA/2232/PI-pi, 2011.

/CS MRD v1.2, 2013/ ESA, CarbonSat – Candidate Earth Explorer Opportunity Mission – Mission Requirements Document, Issue 1, Revision 2, 23 May 2013, ESA Mission Science Division, Reference EOP-SMA/2232/PI-pi, 2011.

/CS RfMS, 2015/ ESA, Report for Mission Selection: CarbonSat, ESA SP-1330/1 (2 volume series), European Space Agency, Noordwijk, The Netherlands. link: http://esamultimedia.esa.int/docs/EarthObservation/SP1330-1_CarbonSat.pdf, 2015.

/Eldering et al., 2017/ Eldering, A., O'Dell, C. W., Wennberg, P. O., Crisp, D., Gunson, M. R., Viatte, C., Avis, C., Braverman, A., Castano, R., Chang, A., Chapsky, L., Cheng, C., Connor, B., Dang, L., Doran, G., Fisher, B., Frankenberg, C., Fu, D., Granat, R., Hobbs, J., Lee, R. A. M., Mandrake, L., McDuffie, J., Miller, C. E., Myers, V., Natraj, V., O'Brien, D., Osterman, G. B., Oyafuso, F., Payne, V. H., Pollock, H. R., Polonsky, I., Roehl, C. M., Rosenberg, R., Schwandner, F., Smyth, M., Tang, V., Taylor, T. E., To, C., Wunch, D., and Yoshimizu, J.: The Orbiting Carbon Observatory-2: first 18 months of science data products, Atmos. Meas. Tech., 10, 549-563, https://doi.org/10.5194/amt-10-549-2017, 2017.

/Galli et al., 2014/ Galli, A., Guerlet, S., Butz, A., Aben, I., Suto, H., Kuze, A., Deutscher, N. M., Notholt, J., Wunch, D., Wennberg, P. O., Griffith, D. W. T., Hasekamp, O., Landgraf, J., The impact of spectral resolution on satellite retrieval accuracy of CO_2 and CH_4, Atmos. Meas. Tech., Volume 7, Issue 4, pp.1105-1119, 2014.

/Guerlet et al., 2013/ Guerlet, S., Butz, A., Schepers, D., et al., Impact of aerosol and thin cirrus on retrieving and validating XCO_2 from GOSAT shortwave infrared measurements, J. Geophys. Res., VOL. 118, 4887–4905, doi:10.1002/jgrd.50332, 2013.

/Hess et al., 1998/ Hess, M., P. Koepke, and I. Schult, Optical Properties of Aerosols and Clouds: The software package OPAC, Bull. Am. Met. Soc., 79, 831-844, 1998.

/Heymann et al., 2012/ Heymann, J., H. Bovensmann, M. Buchwitz, J. P. Burrows, N. M. Deutscher, J. Notholt, M. Rettinger, M. Reuter, O. Schneising, R. Sussmann, and T. Warneke SCIAMACHY WFM-DOAS XCO_2: reduction of scattering related errors, Atmos. Meas. Tech., 5, 2375-2390, 2012.

/Heymann et al., 2015/ Heymann, J., M. Reuter, M. Hilker, M. Buchwitz, O. Schneising, H. Bovensmann, J. P. Burrows, A. Kuze, H. Suto, N. M. Deutscher, M. K. Dubey, D. W. T. Griffith, F. Hase, S. Kawakami, R. Kivi, I. Morino, C. Petri, C. Roehl, M. Schneider, V. Sherlock, R. Sussmann, V. A. Velazco, T. Warneke, and D. Wunch, Consistent satellite XCO_2 retrievals from SCIAMACHY and GOSAT using the BESD algorithm, Atmos. Meas. Tech., 8, 2961-2980, 2015.

/Landgraf et al., 2017/ Landgraf, J., J. aan de Brugh, A. Butz, K. Graf, Specification of Instrument Spectral Sizing Concepts, Spectral Errors and Geo-Physical Scenarios, Technical Note, SRON-CSS-TN-2016-002, 21-Feb-2017, version 3, pp. 20, 2017.

/Landgraf et al., 2017b/ Landgraf, J., J. aan de Brugh, A. Butz, K. Graf, Specification of Instrument Spectral Sizing Concepts, Spectral Errors and Geo-Physical Scenarios, Technical Note, SRON-CSS-TN-2016-002, 20-May-2017, version 4, pp. 21, 2017.

/Rascher et al., 2009/ Rascher, U., Agati, G., Alonso, L., Cecchi, G., Champagne, S., Colombo, R., Damm, A., Daumard, F., de Miguel, E., Fernandez, G., Franch, B., Franke, J., Gerbig, C., Gioli, B., Gomez, J. A., Goulas, Y., Guanter, L., Gutierrez-de-la-Camara, O´ ., Hamdi, K., Hostert, P., Jimenez, M., Kosvancova, M., Lognoli, D., Meroni, M., Miglietta, F., Moersch, A., Moreno, J., Moya, I., Neininger, B., Okujeni, A., Ounis, A., Palombi, L., Raimondi, V., Schickling, A., Sobrino, J. A., Stellmes, M., Toci, G., Toscano, P., Udelhoven, T., van der Linden, S., and Zaldei, A.: CEFLES2: the remote sensing component to quantify photosynthetic efficiency from the leaf to the region by measuring sun-induced fluorescence in the oxygen absorption bands, Biogeosciences, 6, 1181–1198, doi:10.5194/bg-6-1181-2009, 2009.

/Reuter et al., 2010/ Reuter, M., Buchwitz, M., Schneising, O., Heymann, J., Bovensmann, H., and Burrows, J. P., A method for improved SCIAMACHY CO_2 retrieval in the presence of optically thin clouds, Atmos. Meas. Tech., 3, 209-232, 2010.

/Reuter et al., 2011/ Reuter, M., Bovensmann, H., Buchwitz, M., et al. (2011), Retrieval of atmospheric CO_2 with enhanced accuracy and precision from SCIAMACHY: Validation with FTS measurements and comparison with model results, J. Geophys. Res., 116, D04301, doi:10.1029/2010JD015047.

/Reuter et al., 2017a/ Reuter, M., M. Buchwitz, O. Schneising, S. Noel, V. Rozanov, H. Bovensmann, J. P. Burrows, A Fast Atmospheric Trace Gas Retrieval for Hyperspectral Instruments Approximating Multiple Scattering - Part 1: Radiative Transfer and a Potential OCO-2 XCO_2 Retrieval Setup, Remote Sens., 9, 1159, doi:10.3390/rs9111159, 2017.

/Reuter et al., 2017b/ Reuter, M., M. Buchwitz, O. Schneising, S. Noel, H. Bovensmann, J. P. Burrows, A Fast Atmospheric Trace Gas Retrieval for Hyperspectral Instruments Approximating Multiple Scattering - Part 2: Application to XCO_2 Retrievals from OCO-2, Remote Sens., 9, 1102, doi:10.3390/rs9111102, 2017.

/Rodgers 2000/ Rodgers, C. D.: “Inverse Methods for Atmospheric Sounding: Theory and Practice”, World Scientific, Singapore, 2000.

/Rodgers and Connor, 2003/ Rodgers, C. D. and B. J. Connor, Intercomparison of remote sounding instruments, J. Geophys. Res., Vol. 108, No. D3, 4116, pp. 1-13, 2003.

/Rozanov et al. 2014/ Rozanov, V.V., A.V. Rozanov, A.A. Kokhanovsky, J.P. Burrows: Radiative transfer through terrestrial atmosphere and ocean: Software package SCIATRAN. Journal of Quantitative Spectroscopy and Radiative Transfer, http://dx.doi.org/10.1016/j.jqsrt.2013.07.004, Vol. 133, p. 13–71, 2014.

/VIIRS Cloud Mask ATBD, 2014/ GSFC JPSS CMO, Joint Polar Satellite System (JPSS) VIIRS Cloud Mask (VCM) Algorithm Theoretical Basis Document (ATBD), Aug. 5, 2014, Revision E, Goddard Space Flight Center, Greenbelt, Maryland, 2014.

***** End of Document *****

Study on Spectral Sizing for CO_2 Observations (CSS)

D9 - Preliminary Recommendations

Jochen Landgraf and Joost aan de Brugh
SRON Netherlands Institute for Space Research, Utrecht, The Netherlands

Andre Butz and Kaspar Graf
DLR German Aerospace Center, Oberpfaffenhofen, Germany

Michael Buchwitz
Institute of Environmental Physics (IUP) / Institute of Remote Sensing (IFE), University of Bremen, Bremen, Germany

Hartmut Bösch
University of Leicester, Leicester, United Kingdom

Abstract:

This document provides the preliminary conclusions of the error performance analysis for different spectral sizing concepts for CO_2 observations from space. It summarises the analysis of work package 2000, using different XCO_2 retrieval algorithms and different test ensembles. Details about the results can be found in the reports of the sub work packages. Concerning instrument related systematic errors, we found overall no clear indication of a significantly worse performance of instrument concept B. All instrument concepts suffer similarly from systematic instrument and calibration related errors but the exact values of the errors depend on the retrieval algorithm and the investigated scenarios. Instrument B appears to be less sensitive to errors of the Instrument Spectral Response Function but shows a larger sensitivity to straylight (to be confirmed). Moreover, for all spectral sizing concepts, the aerosol and cirrus induced error is significant and requires an appropriate mitigation strategy.

1 Introduction

The retrieval of dry-air column-average mole fractions of carbon dioxide (XCO_2) from solar backscatter soundings in the near and shortwave infrared spectral range from current and future satellites is a major challenge of satellite remote sensing. Small temporal and spatial variations of the global and regional CO_2 distribution have to be resolved to infer information on natural and anthropogenic source and sink processes of CO_2 from satellite observations, which results in demanding requirements on the XCO_2 product as formulated in RD-1 and reported in Table 1. To meet these requirements, dedicated ESA sensitivity studies have already been performed, which led to the proposal of the European XCO_2 CarbonSat mission as one of the two candidates of ESA's 8th Earth Explorer mission. Compared to other CO_2 dedicated missions in space, the CarbonSat instrument concept differs in its extended spectral coverage and its superior signal-to-noise performance but at cost of lower spectral resolution in all three spectral channels of the spectrometer. The CarbonSat concept was evaluated by detailed trade-off studies (RD-2, RD-3, RD-4) and the present study provides the reconsolidation of the concepts in the context of the spectral sizing of the spectrometer.

For this purpose, we investigated how random noise errors, systematic aerosol- and cirrus induced errors and instrument related radiometric biases propagate into XCO_2 errors for four candidate instrument concepts (A,B,C,D) of a future CO_2 monitoring satellite. These instrument concepts differ in particular in their spectral sizing (spectral coverage, spectral resolution, signal-to-noise-ratio). Concept A and B are derived from the early and the later CarbonSat concept (RD-5 and RD-6), respectively. Concept B proposes relative low spectral resolution and thereby gains spectral coverage and signal-to-noise. Concepts C and D are adapted from the OCO-2 (Orbiting Carbon Observatory) and the MicroCarb concepts, both featuring relatively high spectral resolution and narrower spectral coverage. The spectral sizing points are summarized in Table 2.

Table 1: requirements on satellite observations of XCO2 for regional source/sink determination. The table is adapted from RD-1. G, B, and T means goal, break-through, and threshold requirement.

Parameter	Req. type	Random error ("Precision") Single obs.	Random error ("Precision") 1000^2 km^2 monthly	Systematic error	Stability
XCO_2	G	< 1 ppm	< 0.3 ppm	< 0.2 ppm (absolute)	As systematic error but per year
	B	< 3 ppm	< 1.0 ppm	< 0.3 ppm (relative §))	-"-
	T	< 8 ppm	< 1.3 ppm	< 0.5 ppm (relative #))	-"-

Table 2: Spectral sizing points. Concept A and B is simulated for the same readout noise of the detector of 150 electrons. The signal to noise ratio of the radiance measurements L is given by $SNR = \frac{aL}{\sqrt{aL+b}}$ with parameters a and b given in the table.

Instrument sizing point		A	B	C	D
Spectral bands [nm]	NIR	756-773	747-773	758-772	758.35-768.65
	SW-1	1559-1675	1590-1675	1591-1621	1596.85-1618.55
	SW-2	2043-2095	1925-2095	2042-2081	2023.25-2050.75
Resolution [nm]/ sampling ratio	NIR	0.045/2.5	0.1/3.14	0.042/2.5	0.032/2.905
	SW-1	0.30/2.5	0.3/3.14	0.076/2.5	0.067/2.914
	SW-2	0.13/2.5	0.55/3.29	0.097/2.5	0.085/2.924
SNR coefficients a and b (Eq. 1)	NIR	2.81E-15/160540	4.47E-15/160540.	8.36E-016 / 2944.	8.423E-16 / 657350
	SW-1	2.88E-14/ 333979	2.29E-14/ 333297	4.15E-015 / 20277.	3.571E-15 / 654978
	SW-2	1.22E-14/ 324402	3.91E-14/ 323636	6.39E-015 / 56295.	5.670E-15 / 648609
Remark/reference		Adapted from AD-1	Adapted from AD-2	Adapted from RD-2, RD-3, RD-4, RD-5	Adapted MicroCab performance, pers. (B. Sierk, email 20.02.2017)

The study team comprises all European expert groups on CO_2 remote sensing from shortwave infrared measurements using different retrieval algorithms and test data sets to evaluate and ensure a broad consensus on the study conclusions. The study uses the RemoTeC algorithm (RD-7, RD-8, RD-9, RD-10), BESD/C algorithm (RD-11, RD-2) and UoL algorithm (RD-12, RD-13), respectively, where the XCO_2 retrieval performance is analyzed for simulated measurements with global and regional coverage and for dedicated test ensembles also used in previous CarbonSat studies.

2 Study results

For a global ensemble of geophysical test cases designed to try the RemoTeC retrieval performance for realistic aerosol and cirrus loaded scenes for the month January, April, July and October, the XCO_2 noise errors for concepts A, B, and C are typically less than 1 ppm (0.5 ppm) for more than 90% (75%) of the geophysical test cases. Concept D shows significantly larger noise errors with about 75% (50%) of the cases below 1 ppm (0.5 ppm) implying particularly large errors for low sun and dark surfaces i.e. under high-latitude and winter conditions. Figure 1 summarizes our findings on noise errors. Moreover, the analysis of XCO_2 retrieval noise for 15 dedicated CarbonSat test cases supports these finding showing the best XCO_2 noise performance with a mean precision of 0.70 ppm for concept B followed by concept C (0.92 ppm), concept A (0.95), and concept D (1.57).

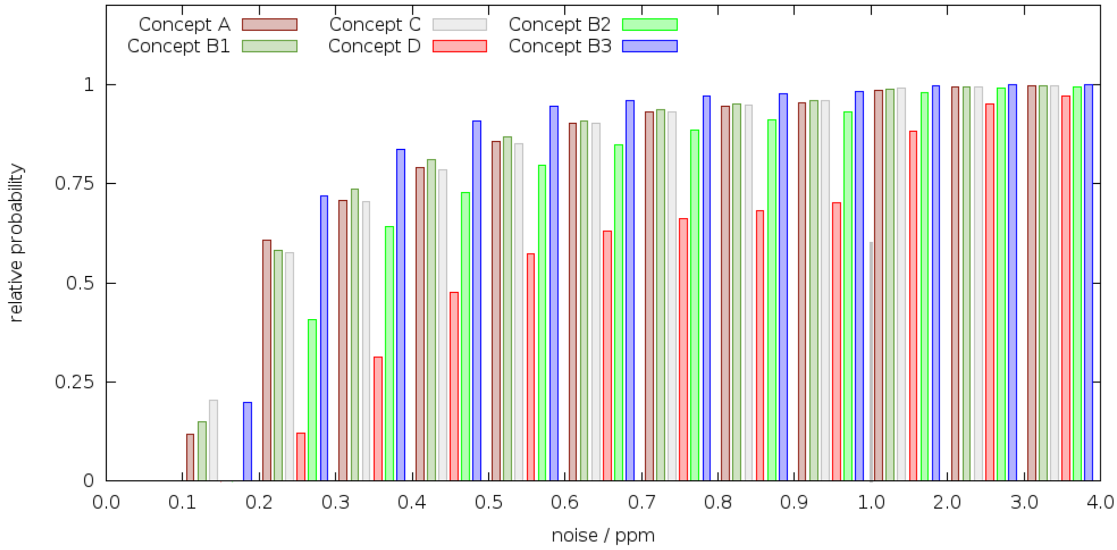

Figure 1: Cumulative histogram of the RemoTeC XCO_2 noise errors for the retrieval concepts A, B1, B2, B3, C, and D. B1, B2, and B3 are retrieval configurations that choose different retrievals sub-windows out of the SW-2 band of concept B (B1=1990-2095nm, B2=2022-2095nm, and B3=1925-2095nm). Please note the change in the x-axis scale at values of 1 ppm.

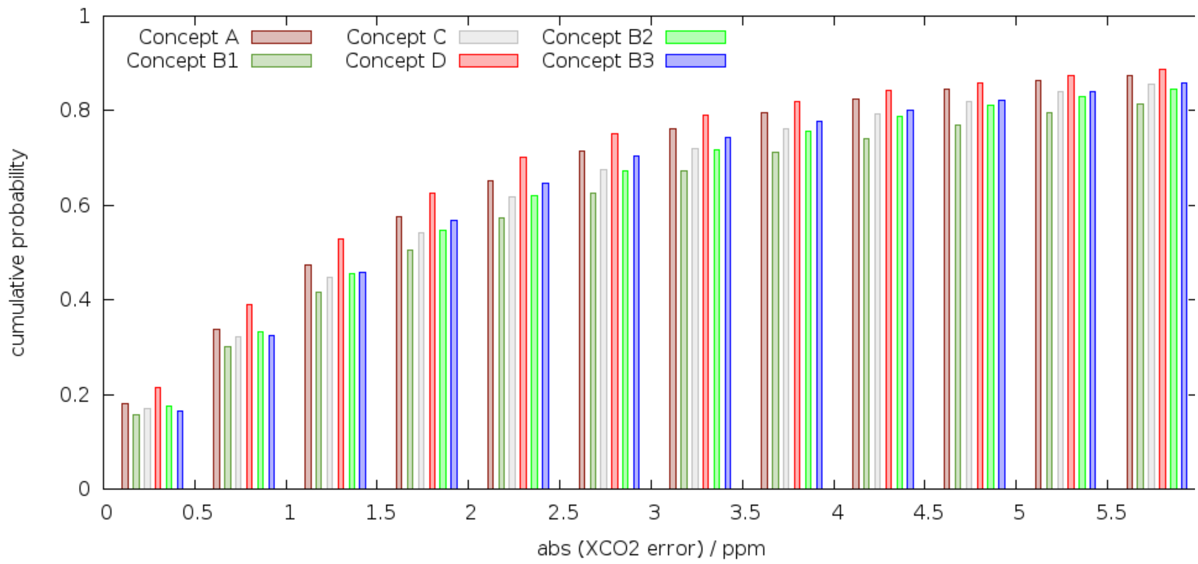

Figure 2: Cumulative histogram of the RemoTeC aerosol and cirrus induced XCO_2 error for the retrieval concepts A, B1, B2, B3, C, and D. B1, B2, and B3 are retrieval configurations that choose different retrievals sub-windows out of the SW-2 band of concept B.

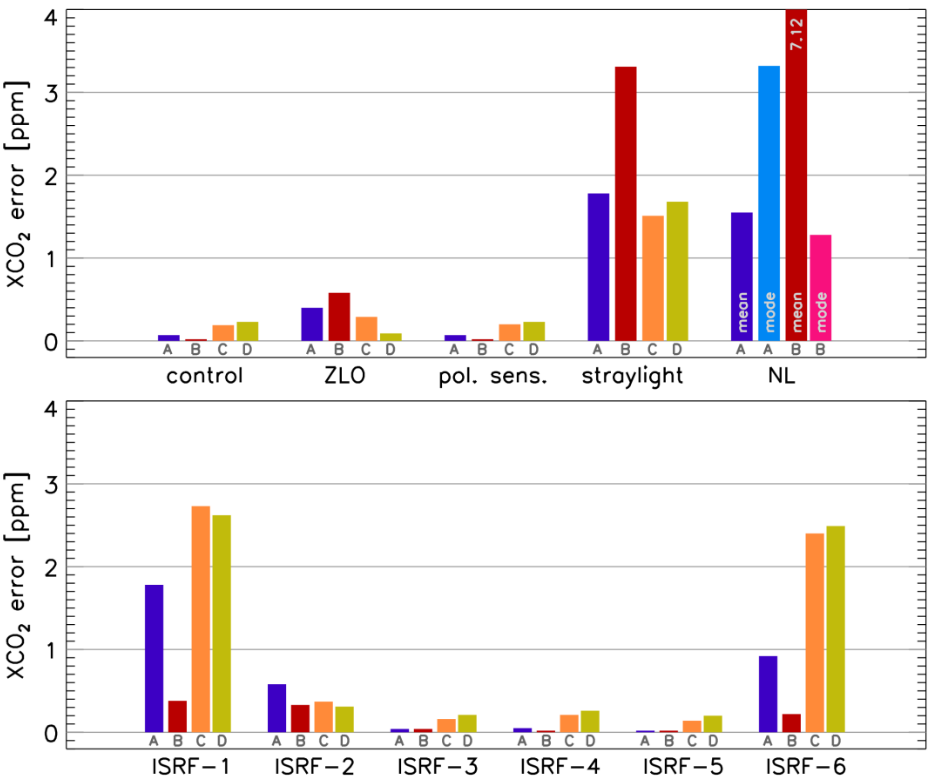

Figure 3: XCO_2 retrieval biases due to instrumental errors for spectral sizing concept A, B, C and D, derived with the RemoTeC retrieval algorithm for global and in case of straylight regional test ensembles. The figure includes the mean bias for the control runs, radiometric offset (ZLO), the polarization sensitivity, spectrometer straylight, detector non-linearity (NL), and six different ISRF distortions. For detector non-linearity, also the mode of the XCO2 bias distribution is depicted.

The systematic aerosol and cirrus induced errors of XCO_2 are depicted in Figure 2 for the four spectral sizing concepts (A, B, C, D) and for the same global test ensemble as used in Figure 1. All concepts show substantial errors < 2 ppm for 50 % (< 4 ppm for 70 %) of the ensemble members, where the performance differences among the concepts are small. Here, concept D (63% < 2 ppm, 82% < 4ppm) is slightly better than A (58% < 2 ppm, 80% < 4ppm), A is slightly better than C (54% < 2 ppm, 76% < 4 ppm), C is almost equal to B (B1: 51% < 2 ppm, 71% < 4 ppm; B2: 55% < 2 ppm, 76% < 4 ppm; B3: 57% < 2 ppm, 78% < 4 ppm).

To disentangle XCO_2 retrieval biases due to instrument related errors from aerosol and cirrus induced biases, we omitted cirrus in the global ensemble and simplified the aerosol simulations such that no systematic errors are induced for an ideal instrument limited by random measurement errors only. The validity of the approach is tested by dedicated RemoTeC control runs with mean errors < 0.1 ppm for concept A and B and < 0.2 ppm and 0.25 ppm for concept C and D, respectively. Subsequently for each spectrum of the ensemble, we considered radiometric errors due to

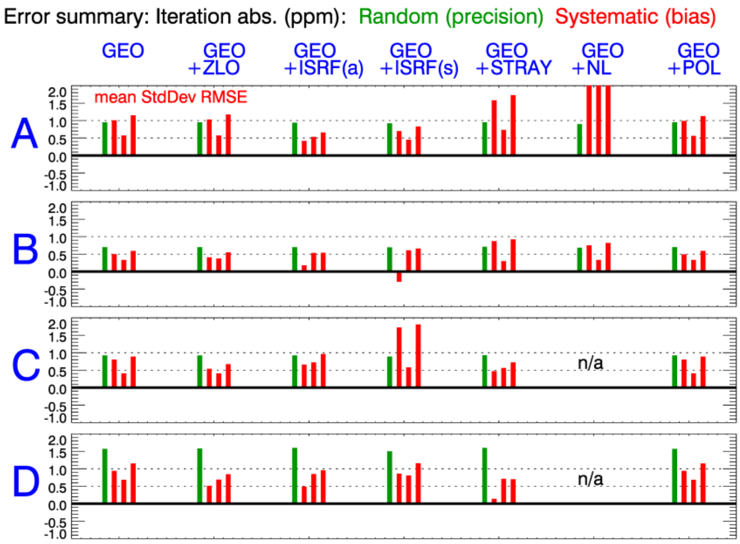

Figure 4: Error analysis for the full-iterative BESD/C retrievals. Rows represent the four instruments A, B, C and D, column corresponds to a certain systematic error or combination of errors: GEO: geophysical error (i.e., XCO_2 error due to aerosols, clouds, etc.), GEO+ZLO: zero-level-offset (radiance) error in addition to GEO error, ISRF: Instrument Spectral Response Function (two type of ISRF errors have been investigated (a = anti-symmetrial shape error, s = symmetrical error)), STRAY: straylight, NL: detector non-linearity (only input data for the instruments A and B were available), and POL: polarization related radiance error. The green bars show the XCO_2 random error ("precision"). The red bars show the three XCO_2 bias charcteristics (from left to right): mean bias, standard deviation of bias and root-mean-square error.

(1) Six different distortions of the instrument spectral response function (ISRF)
(2) A radiometric offset (zero level offset, ZLO) as defined in the mission requirements of CarbonSat (RD-6)
(3) Detector non-linearity derived for concept A and B adapted from a CarbonSat instrument performance analysis
(4) Instrument polarization sensitivity from CarbonSat instrument analysis (concept B)
(5) Straylight within the spectrometer from CarbonSat (concept B).

Figure 3 summarizes the mean of the global bias distribution for the different error sources. Here, the XCO_2 retrieval performance is mostly sensitive to three instrumental errors:

(1) The detector non-linearity. Here the core of the bias distributions indicates better performance of concept B with a mode error of 1.28 ppm compared to concept A with a mode error of 3.32 ppm. However, the XCO_2 biases of concept B include more outliers and so has a mean bias of 7.12 ppm compared to 1.55 ppm for concept A. For the interpretation of these results it is important to note that RemoTeC does not adjust a radiometric offset to the measurements simulation. In case the radiometric offset is fitted, the corresponding XCO_2 error sensitivity diminishes.
(2) The shape of the ISRF. From the investigated six different ISRF distortions, we find largest error sensitivity for ISRF deformations including a symmetrical compression (ISRF distortion 1 and 6 in Figure 3). The induced XCO_2 biases are smallest for the low resolution spectral sizing of concept B with mean biases < 0.35 ppm. Generally, ISRF distortion introduces biases with significant regional dependence as depicted in Figure 5 for the spectral sizing concept C and for the global test ensemble of this study.

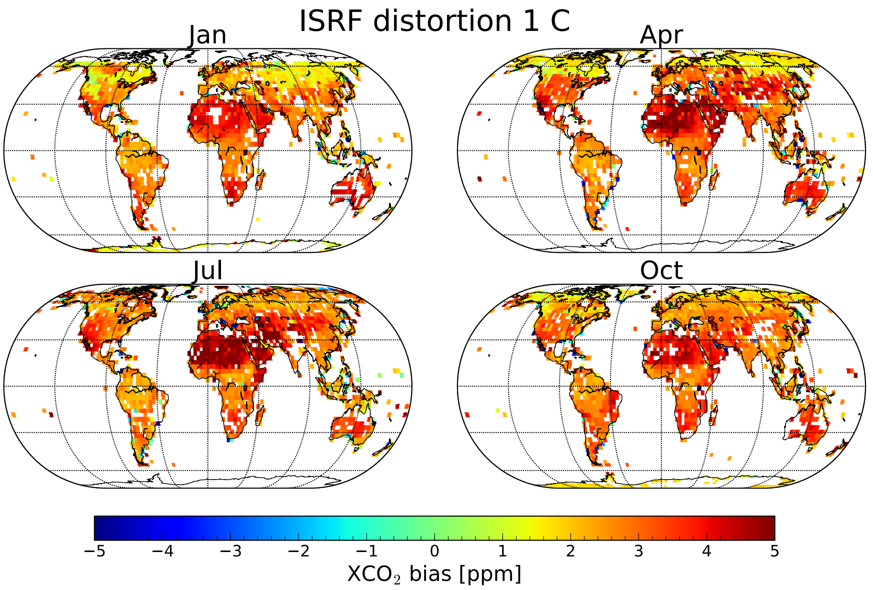

Figure 5: XCO_2 bias for instrument concept C and ISRF distortion 1 derived with the RemoTeC algorithm.

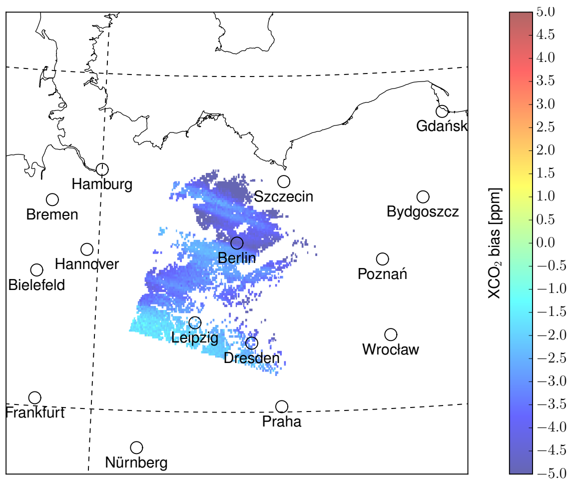

Figure 6: XCO_2 bias due to uncorrected stray light simulated with RemoTeC. Data gaps are due to cloud contaminated scene, which are filtered out.

(3) The spectrometer straylight. Our analysis, performed for a data granule of an orbit simulation, indicates significant XCO_2 biases for all concept. Here, the biases of sizing point A, C, and D with fine spectral resolution are smallest with 1.78, 1.51, and 1.68 ppm respectively and reaches 3.31 ppm for spectral sizing concept B. Due to different cloud coverage within a swath, straylight introduces stripe pattern in the XCO_2 biases as indicated in Figure 6. This XCO_2 retrieval property needs to be confirmed by the other algorithms used in this study.

Most of the error sources described above are also investigated with the BESD/C algorithm for the 15 CarbonSat references scenarios. In spite of the different test ensembles, the BESD/C and RemoTeC mean

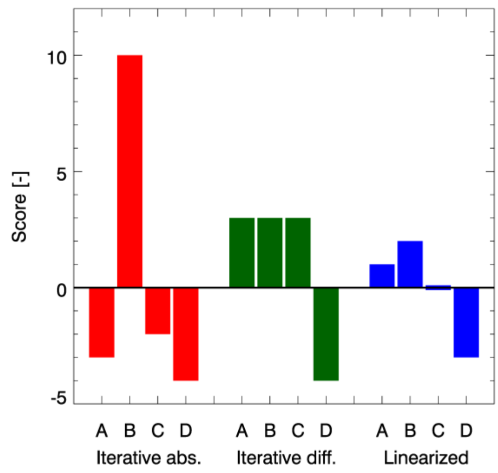

Figure 7: Summary of the BESD/C error analysis results using scores. The red bars show the scores for full iterative retrievals including forward model and aerosol induced errors. The green and blue bars indicate the corresponding scores of the differential biases of full iterative retrievals with respect to retrieval results of an unbiased instrument performance and the linear error analysis, respectively.

biases are similar and the performance analyses agree for most of the error sources. For example, the superior performance of concept B for the ISRF distortion 1 results from both investigations. Also, the relative small biases due to radiometric errors caused by the instrument polarization sensitivity is confirmed by the BESD/C findings. The RemoTeC results concerning detector non-linearity and radiometric offsets cloud not be reproduced, which is likely due to the different fitting approaches. BESD/C infers a radiometric offset from the simulated measurements, whereas RemoTeC does not account for this. Obviously, this difference in the approach affects the XCO2 sensitivity to both instrumental errors.

To summarize the BESD/C XCO_2 bias results, a scoring method is applied, which gives highest scores to the sizing concepts with smallest biases. Figure 7 illustrates the scoring results for different analyses of the BESD/C retrieval biases. For the ‘iterative difference’ method, which is most comparable with the RemoTeC analysis, concept A, B, and C score equally well, whereas concept D has the lowest score.

Finally, Figure 8 summarizes corresponding retrieval simulations employing the UoL algorithm, where the results are derived for a test ensemble of measurement simulations of different atmosphere scenarios and different solar geometry. In the case of known aerosol type, the XCO_2 biases are < 0.2 ppm, which corresponds to the RemoTeC results of the control runs. Also for divergent aerosol types in retrieval and measurement simulations, the induced biases are small for all spectral sizing concepts and so in this case does not confirm the RemoTeC findings. However, here only one particular aerosol type was investigated and so the UoL error analysis does not aim to provide an estimate for a global error performance. Also for the investigated instrumental errors we observe divergent results. For the symmetric ISRF distortion, the UoL algorithm shows best XCO2 performance for the spectral sizing point A and B and worst performance of C. The radiometric offset introduces very similar XCO2 biases for the different spectral concepts, which overall agrees with the BESD/C and RemoTeC performance results.

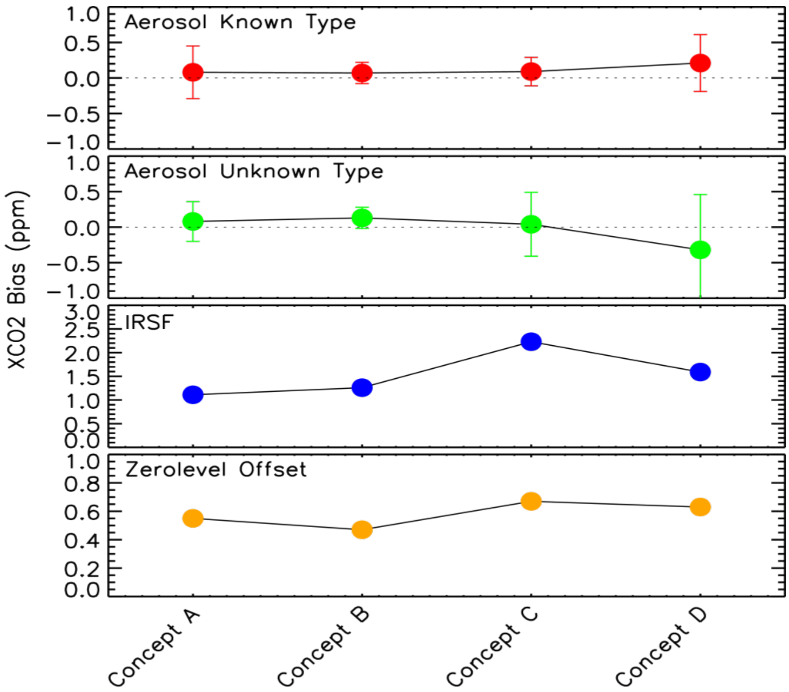

Figure 8: Summary of the UoL error analysis. (Top panel) XCO_2 bias for full-end-to-end retrievals and for measurement simulations assuming an aerosol type consistent with the assumptions of the retrieval, (second panel) same as top panel but for inconsistent aerosol types, (third panel) RMS of XCO_2 biases induced by a symmetric single-band ISRF distortion using linear error propagation, (bottom panel) XCO_2 biases due to the radiometric offset in all three spectral bands using linear error propagation.

3 Summary

The study proposal included consciously different algorithms applied to different test ensembles refraining from any harmonisation of the approaches. This explains the overall agreement of the performance analyses but also is the reason for the different results for certain error sources. Overall, we draw the following preliminary conclusions concerning the error performance for the different spectral sizing concepts A, B, C, and D:

1) For a global ensemble of clear sky measurements, concept A, B, and C show similar performance for the precision of XCO_2. Concept D performs clearly worse than the other. For dedicated CarbonSat test scenarios, we obtained a superior noise performance for concept B.
2) For the different sizing concepts and the global measurement ensemble, the aerosol and cirrus induced error is substantial. We estimated that only for 50 % of all clear sky measurements the bias is < 2 ppm (and for 70 % < 4 ppm).
3) For most of the instrument-induced XCO2 biases, we found no indication that spectral sizing point B is worse than any of the other three sizing point. However, for a regional measurement ensemble, the RemoTeC spectrometer straylight showed a factor 2 larger XCO2 biases for sizing concept B compared to the other sizing point. It needs to be investigated if this can be confirmed by BESD/C using the recently updated formula for the straylight kernel.

4 References

RD-1 GHG-CCI: User Requirements Document for the GHG-CCI project of ESA's Climate Change Initiative, pp. 38, version 2.1, 19 Oct. 2016, 2016.

RD-2 Buchwitz, M., M. Reuter, H. Bovensmann, D. Pillai, J. Heymann, O. Schneising, V. Rozanov, T. Krings, J. P. Burrows, H. Boesch, C. Gerbig, Y. Meijer, and A. Loescher, Carbon Monitoring Satellite (CarbonSat): assessment of atmospheric CO_2 and CH_4 retrieval errors by error parameterization, Atmos. Meas. Tech., 6, 3477-3500, 2013.

RD-3 Buchwitz, M., H. Bovensmann, M. Reuter, J. Heymann, O. Schneising, et al., CARBONSAT: ERROR ANALYSIS FOR PRIMARY LEVEL 2 PRODUCTS XCO_2 AND XCH_4 AND SECONDARY PRODUCT VEGETATION CHLOROPHYLL FLUORESCENCE FOR NADIR OBSERVATIONS OVER LAND, ESA Living Planet Symposium, Sept 9-13, 2013, Edinburgh, UK, conference proceedings ESA Special Publication SP-722 (on CD-ROM), link: http://www.iup.uni-bremen.de/sciamachy/NIR_NADIR_WFM_DOAS/2846996buchwitz.pdf, 2013.

RD-4 Buchwitz, M., Bovensmann, T. Krings, M. Reuter, V. V. Rozanov, P. Liebing, J. Landgraf, F. Alkemade, Mission Requirements Analysis and Level 2 Error Characterization for CarbonSat Nadir Observations over Land - WP 1100, 2000 & 4100 Report, ESA Study CarbonSat Earth Explorer 8 Candidate Mission "Level-1 Level-2 (L1L2) Performance Assessment Study" ESA Contract No 4000109814/13/NL/FF/lf, Version 1.2, 3 Dec 2015, Doc ID: IUP-CS-L1L2-II-TNnadir, 2015.

RD-5 ESA, CarbonSat – Candidate Earth Explorer Opportunity Mission – Mission Requirements Document, Issue 1, Revision 0, 8 July 2011, ESA Mission Science Division, Reference EOP-SMA/2232/PI-pi, 2011.

RD-6 ESA, CarbonSat – Candidate Earth Explorer Opportunity Mission – Mission Requirements Document, Issue 1, Revision 2, 23 May 2013, ESA Mission Science Division, Reference EOP-SMA/2232/PI-pi, 2011.

RD-7 Butz, A., O. P. Hasekamp, C. Frankenberg, I. Aben, Retrievals of atmospheric CO2 from simulated space-borne measurements of backscattered near-infrared sunlight: accounting for aerosol effects, Appl. Opt., 48, 18, 3322 – 3336, 2009

RD-8 Butz, A., S. Guerlet, O. Hasekamp, D. Schepers, A. Galli, I. Aben, C. Frankenberg, J.-M. Hartmann, H. Tran, A. Kuze, G. Keppel-Aleks, G. Toon, D. Wunch, P. Wennberg, N. Deutscher, D. Griffith, R. Macatangay, J. Messerschmidt, J. Notholt, and T. Warneke, Toward accurate CO2 and CH4 observations from GOSAT, Geophys. Res. Lett., L14812, doi:10.1029/2011GL047888, 2011

RD-9 Guerlet, S., A. Butz, D. Schepers, S. Basu, O. P. Hasekamp, A. Kuze, T. Yokota, J.-F. Blavier, N. M. Deutscher, D. W. T. Griffith, F. Hase, E. Kyro, I. Morino, V. Sherlock, R. Sussmann, A. Galli, and I. Aben, Impact of aerosol and thin cirrus on retrieving and validating XCO2 from GOSAT shortwave infrared measurements, J. Geophys. Res., 118, 10, 4887-4905, doi:10.1002/jgrd.50332, 2013

RD-10 Guerlet, S., S. Basu, A. Butz, M. Krol, P. Hahne, S. Houweling, O. P. Hasekamp and I. Aben, Reduced carbon uptake during the 2010 Northern Hemisphere summer from GOSAT, Geophys. Res. Lett., 40, 2378–2383, doi: 10.1002/grl.50402, 2013

RD-11 Bovensmann, H., Buchwitz, M., Burrows, J. P., Reuter, M., Krings, T., Gerilowski, K., Schneising, O., Heymann, J., Tretner, A., and Erzinger, J., A remote sensing technique for global monitoring of power plant CO_2 emissions from space and related applications, Atmos. Meas. Tech., 3, 781-811, 2010.

RD-12 Boesch, H., D. Baker, B. Connor, D. Crisp, and C. Miller, Global characterization of CO_2 column retrievals from shortwave-infrared satellite observations of the Orbiting Carbon Observatory-2 mission, Remote Sensing, 3 (2), 270-304, 2011.

RD-13 Boesch, H., Toon, G. C., Sen, B., Washenfelder, R. A., Wennberg, P. O., Buchwitz, M., de Beek, R., Burrows, J. P., Crisp, D., Christi, M., Connor, B. J., Natraj, V., and Yung, Y. L.: Space-based near-infrared CO_2 measurements: Testing the Orbiting Carbon Observatory retrieval algorithm and validation concept using SCIAMACHY observations over Park Falls, Wisconsin, J. Geophys. Res., 111, D23302, doi:10.1029/2006JD007080, 2006.

XCO_2 retrieval uncertainty under different spectral sizing concepts

Lianghai Wu[1], Joost aan de Brugh[1], Otto Hasekamp[1], Andre Butz[2] and Jochen Landgraf[1]
1 SRON Netherlands Institute for Space Research
2 University Heidelerg, Institut für Umweltphysik, Im Neuenheimer Feld 229, 69120 Heidelberg, Germany

Abstract: In light of the proposed space segment of Europe's future CO_2 monitoring (CO2M) system, we investigate the spectral resolution of the dedicated CO_2 spectrometer, which measures Earthshine radiance in the three relevant spectral bands at 0.76, 1.61 and 2.06 μm. The Orbiting Carbon Observatory-2 (OCO-2) mission covers these bands with fine spectral resolution but limited spatial coverage, which hampers the monitoring of localized anthropogenic CO_2 emission. To improve this aspect, a moderate spectral resolution of 0.1, 0.3 and 0.55 nm in the three spectral bands was proposed by Buchwitz et al. (2013), with adjusted band width and signal-to-noise performance. To assess this choice in the context of the CO2M mission, we use real and synthetic OCO-2 satellite observations, which we spectrally degrade to the envisaged lower spectral resolution. We evaluate the corresponding CO_2 retrieval accuracy by taking the Total Carbon Column Observing Network (TCCON) observations as reference. Here, a lower spectral resolution enhances the scatter error of the retrieved CO_2 column mixing ratio (XCO_2) but has little effect on the station-to-station variation of the biases. We show that the scatter error gradually increases when decreasing spectral resolution. Part of the scatter error increase can be attributed to the retrieval noise error which can be mitigated by a future instrument with improved signal-noise-ratio (SNR). The investigation using measurements from the Greenhouse gases Observing SATellite (GOSAT) and synthetic measurements confirms our finding and indicates that one major source of uncertainties regarding CO_2 retrieval is the insufficient information on aerosol properties that can be inferred from the observations.

Table of Contents

[redacted]Introduction

Carbon dioxide is one of the most important anthropogenic greenhouse gases. Due to fossil fuel combustion and changes in land use, its concentration is increasing in the atmosphere. The consequences of increasing carbon dioxide include global temperature rising, ocean acidification, increased extreme weather and et al. However, our knowledge on its sources and sinks is still limited. Using satellite observations can help us to globally monitor its concentration in the atmosphere and improve our current knowledge on reginal sources and sinks. To achieve this, satellite observations need to provide measurements with high precision and accuracy, good spatial coverage, and high spatial resolution (Ciais et al. (2015); Crisp et al. (2018)).

Carbon dioxide information can be derived from reflected solar radiation in short-wave infrared (SWIR) spectral regions. Currently, the Greenhouse Gases Observing Satellite (GOSAT, Yokota et al. (2009)) and the Orbiting Carbon Observatory-2 (OCO-2, Crisp et al. (2017)) missions are in orbit, dedicated to observing XCO_2 from space. Additionally, the Carbon Monitoring Satellite (CarbonSat, Bovensmann et al. (2010); Buchwitz et al. (2013)) was proposed to the European Space Agency (ESA) with the objective to advance our knowledge on the natural and man-made sources and sinks of CO_2 from regional and country down to local scales, but was not selected for mission implementation. Table 1 includes the spectral and spatial properties of the three satellite instruments, observing the Earth-reflected sunlight in the oxygen (O2) A-band around 0.765 μm, the weak CO_2 absorption band around 1.61 μm and the strong CO_2 absorption band around 2.06 μm. Among those instruments, the CarbonSat concept has the largest swath with good spatial resolution but with significantly reduced spectral resolution compared to GOSAT and OCO-2. The design introduces the risk of XCO_2 errors due to spectral interference with other absorbers and enhanced aerosol induced errors. To evaluate this risk Galli et al. (2014) analyzed a spectral degradation of GOSAT observations and the induced error on XCO_2.

In this study, we investigated the retrieval performance of OCO-2 observations degraded to different spectral resolutions building upon the work by Galli et al. (2014). We evaluate the XCO_2 retrieval accuracy and precision using both OCO-2 measurements and produce spectra with the reduced spectral resolution and the sampling ratio as listed in Table 1, which in the remainder of the study will be referred to as the moderate spectral resolution (MSR) concepts. We start with simulated OCO-2 and MSR type measurements for a global ensemble. For satellite observations, the differences between retrieved XCO_2 and collocated ground-based observations from the Total Carbon Column Observing Network (TCCON) are used to estimate the retrieval uncertainty. A corresponding analysis is done for GOSAT observations to relate our analysis to the previous work done by Galli et al. (2014).

Table 1 Spectral and spatial sizing points of MSR type, GOSAT and OCO-2 instrument [ref1]

Instrument	MSR				GOSAT	OCO-2
	a	b	c	d		
Spectral bands [nm]	747-773				758-775	758-772
	1590-1675				1560-1720	1591-1621
	1925-2095				1920-2080	2042-2081
Resolution [nm]	0.1/3.14	0.1/3.14	0.1/3.14	0.1/3.14	0.015/1.4	0.042/2.5
	0.3/3.14	0.3/3.14	0.3/3.14	0.3/3.14	0.08	0.076/2.5
	0.097/2.5	0.15/3.14	0.30/3.3	0.55/3.29	0.1	0.097/2.5
Swath [km]	Goal: 500 (4 km^2 per pixel)				750 (5-point observation in cross track)	10.6 (8 cross-track footprints)

[redacted]Degradation of spectral resolution and retrieval method

2.1 Spectra with different spectral resolutions

Since different spectral sizing measurements used here are obtained by convolving available satellite measurements with a window function, the transforming procedure should well represent the way in which the satellite instruments record the radiance. For spectrometers, the transformation from the physical radiance $\boldsymbol{I}_{lbl}$ to observation $\boldsymbol{I}_{ob}$ can be described by following convolution,

$$\boldsymbol{I}_{ob}(\lambda_i) = (\boldsymbol{S}_i * \boldsymbol{I}_{lbl})(\lambda_i) = \int d\lambda\, \boldsymbol{S}_i(\lambda_i - \lambda)\boldsymbol{I}_{lbl}(\lambda) \tag{1}$$

$\boldsymbol{S}_i(\lambda_i - \lambda)$ is the spectral response function (ISRF) of spectrometer at wavelength λ_i. The spectral resolution of spectrometer depends on full width half maximum (FWHM) of the ISRF. The ISRF of modeled spectrometer $\boldsymbol{S}_i^d$ can be obtained by convolving the original ISRF with a Gaussian instrumental line shape function f_w with a broader FWHM.

$$\boldsymbol{S}_i^d = \boldsymbol{S}_i * f_w \tag{2}$$

here f_w has following format,

$$f_w = A\delta(m_{\lambda_c})\, e^{-(\lambda-\lambda_c)^2/(2\sigma^2)} \tag{3}$$

λ_c is central wavelength; $\delta(m_{\lambda_c})$ is pixel mask with m_{λ_c}=0 for good pixel; A is a normalization factor and σ is the width of the Gaussian window.

Combing equations (1) and (2), the spectra recorded by the modeled spectrometer can be described by,

$$\boldsymbol{I}_{ob}^d(\lambda_i) = \left(\boldsymbol{S}_i^d * \boldsymbol{I}_{lbl}\right)(\lambda_i) = (\boldsymbol{S}_i * f_w * \boldsymbol{I}_{lbl})(\lambda_i) = f_w * \boldsymbol{I}_{ob}(\lambda_i) \tag{4}$$

For the above procedure, we can see that spectra with coarse spectral resolution can be obtained by convolving fine resolution spectra with a Gaussian window function with a broader FWHM. The resulted spectra are also resampled under the spectral resolution of target instrument concept. The corresponding covariance matrix $\boldsymbol{e}_{ob}^d$ describing the retrieval noise is deduced from the measurement noise of the original OCO-2 measurements by $f_w \boldsymbol{e}_{ob} f_w^T$.

In the forward model, the simulated physical radiance at the top of atmosphere is subjected to the same convolution as Eq. (4) before comparing with degraded spectra. Both the measurement and the forward model as part of the retrieval are adapted accordingly.

Figure 1 shows spectra and ISRF examples of the OCO-2 and corresponding examples of the concept B instrument in all three spectral bands. Here, we convolved original spectra and corresponding forward model simulation with an added Gaussian window with a sigma of 0.039, 0.125, and 0.225 nm, respectively. The effective FWHM of the resulting ILS are shown in the title. For GOSAT measurements, we use the same method.

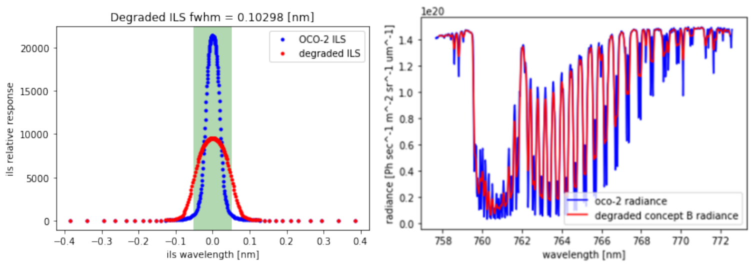

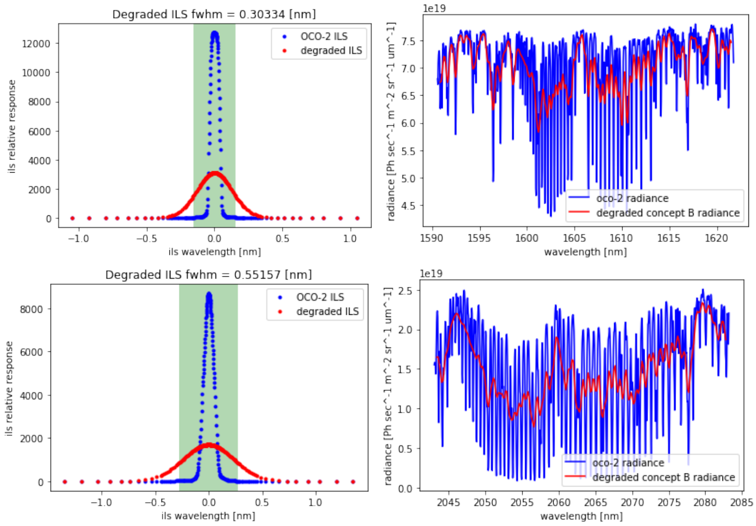

Figure 1. Instrument line shape and spectrum examples from original OCO-2 instrument (in blue) and that of MSR-d (in red).

2.2 Retrieval method and setting up

To retrieve CO_2 columns from space-borne Earth-shine radiance observations in the 0.76, 1.61 and 2.06 µm spectral ranges with different spectral resolutions, we use the RemoTeC full-physics retrieval algorithm (Hasekamp and Butz, 2008), which was first applied for GOSAT measurements and later extensively used for greenhouse gas retrievals of different missions including GOSAT, OCO-2 and Sentinel-5P (Butz et al., 2009; Guerlet et al., 2013; Wu et al., 2018; Hu et al., 2018). The algorithm employs an iterative inverse scheme combined with an efficient forward radiative transfer model developed by Landgraf et al. (2001); Hasekamp and Landgraf (2005); Hasekamp and Butz (2008); Schepers et al. (2014). For a given model atmosphere, the forward model simulates the intensity vector field, including its Stokes parameter Q and U on a line-by-line spectral sampling, and its derivatives with respect to both the amount of all relevant trace gases and the optical properties of spherical aerosols in different layers of the model atmosphere. Moreover, RemoTeC infers state parameters of the atmosphere by minimizing the difference between forward model and satellite observations. Due to the different spectral coverage of the 1.61 µm band and corresponding sensitivities, for GOSAT measurements 12-layer profiles of CO_2 and CH4 partial column are retrieved whereas for OCO-2 measurements we only infer the corresponding CO_2 profile. Apart from that, the algorithm setup is the same for both missions, which infers additionally: H2O total column, surface properties, spectral shifts, intensity offsets and aerosol optical properties. To describe the size distribution of the atmospheric aerosol, RemoTeC uses a power-law size distribution ($n(r) \propto r^{-\alpha}$ with the particle radius r and retrieves the size parameter α, total amount of aerosol particles *N*. For the aerosol height distribution, we assume a Gaussian profile with a full-width-half-maximum of 2 km and retrieve its center height. For this study, we consider only satellite observations over land, where we assume a Lambertian surface reflection model with describing the inter-band spectral dependence of the surface albedo as a second order polynomial.

In terms of spectral calibration, we adjust spectral shifts for both the Earth radiance measurement and solar reference model in each spectral band while an intensity offset is only fitted in the 0.76 µm band for both GOSAT and OCO-2 spectra. These RemoTeC retrieval settings were also used in GOSAT retrievals by Butz et al. (2011); Schepers et al. (2012); Guerlet et al.(2013); Buchwitz et al. (2017). It should be noted that in the recent study by Wu et al. (2018) we found that retrieving an intensity offset in all three OCO-2 bands significantly improves the accuracy of the data product. In this study, however, we use the same retrieval settings for both GOSAT and OCO-2 data for the following reasons:

1. A consistent retrieval setting can help to identify the origin of the product uncertainties. Assuming that the error analysis differs significantly for two satellite missions, it seems likely to be an instrument specific issue rather than due to the algorithm itself;
2. It turns out to be difficult to fit an intensity offset in the 2.06 µm band for spectra with a coarse spectral resolution of 0.55 nm;
3. The primary target of the study is to understand the impact of a reduced spectral resolution and so the relative change of retrieval performances with spectral resolution is the main focus of this study.

To account for line mixing as well as collision-induced absorption of O_2 and CO_2 we employ the spectroscopic model by Tran and Hartmann (2008). The molecular absorption database HITRAN 2008 is used for CH_4 and H_2O considering the Voigt line shape model. The algorithm also requires auxiliary information on vertical profiles of pressure, temperature and humidity, and surface wind speed, which are adapted from the European Centre for Medium Range Weather Forecasts (ECMWF). Surface elevation information is taken from the 90-meter digital elevation data of NASA's Shuttle Radar Topography Mission (Farr et al., 2007). Prior information on CO_2 and CH_4 profiles are interpolated from CarbonTracker and the TM5 model for the years 2013 and 2010 (Peters et al., 2007; Houweling et al., 2014), while prior information of the surface albedo is estimated from the mean radiance of the observation. Aerosol priors are the same for all retrievals.

Cloud-contaminated observations are rejected by strict data filtering using prior non-scattering retrievals (Schepers et al.,2012) and so clouds do not need to be considered in the retrieval algorithm. Here, the cloud clearing relies on the fact that the difference of CO_2 and H_2O columns, retrieved independently from the 1.61 and 2.06 µm bands for a non-scattering model atmosphere, indicates the measurement contamination by clouds. Furthermore, the difference between the O_2 column inferred from the O_2 A-band with a non-scattering atmosphere and the corresponding column derived from the ECMWF surface pressure can be used for cloud filtering. Additionally, we reject spectra with low signal-to-noise ratio, extreme viewing geometry, cirrus contamination and high aerosol load to avoid large retrieval errors. The data screening is described in more detail by Detmers and Hasekamp (2015) and Wu et al. (2018) for the GOSAT and OCO-2 retrievals, respectively, where for OCO-2 the data screening does not rely on the intensity offsets in the 1.61 and 2.06 µm bands because it is not retrieved from the measurement in the context of this study.

[redacted] Data

For our study, we considered OCO-2 observations only over land in the period from September 2014 to October 2017, which are spatio-temporally collocated within 3 × 3 degrees longitude-latitude and within 2 hours with XCO_2 ground-based observations of the TCCON network. Here, we use OCO-2 version 8 L1b data and obtained about 463, 000 collocated soundings. Analogously, we proceeded with GOSAT land observations (L1b version V201) for the years 2009-2016 using only high-gain measurements of the instrument. Given the sparse spatial sampling of GOSAT, we employed a coarse spatial collocation criteria within 5 degrees latitude-longitude which results in 270, 000 individual observations collocated with observations from different TCCON stations. As part of the processing chain, the data were filtered further with respect to latitudinal position, impact from regional CO_2 sources and terrain roughness. For both data sets, we retrieved the column densities of CO_2 and in the case of GOSAT also CH_4 using the RemoTeC algorithm for measurements at their original resolutions. Subsequently, we reduced the spectral resolution to that of the MSR spectral sizing point of Table 1 assuming a fixed sampling ratio, as described in the previous section, and repeated the retrieval. To better understand the impact of the spectral resolution on CO_2 retrieval quality, the different MSR spectral sizing points included first a spectral degradation of the 0.76 um band and 1.6 um band of the original OCO-2 data to a resolution of 0.1 and 0.3 nm, respectively

(MSR-a), and subsequently we gradually degraded the spectral resolution in the 2.06 um band to 0.15, 0.30 and 0.55 nm while retaining the spectral resolutions in the 0.76 um band and 1.6 um band (MSR-b, MSR-c, MSR-d).
In order not to be affected by unknown instrument related issues such as spectrometer stray light, we generated simulated spectra for a global ensemble as described by Butz et al. (2009). The ensemble comprises 11, 036 spectra and is designed to estimate retrieval errors induced by aerosol and cirrus for four typical days representing four seasons (Butz et al., 2012). In the ensemble, the description of aerosol and cirrus is much more complex than in the retrieval and so the assessment of the induced XCO_2 retrieval error can be used to estimate the scattering induced error for different spectral resolutions of the measurement. More details on the ensemble can be found in Butz et al. (2009, 2012); Hu et al. (2016).

[redacted]XCO_2 retrieval uncertainties under different spectral resolutions

4.1 Synthetic study

First, we studied the XCO_2 retrieval error for synthetic spectra calculated for the OCO-2 spectral ranges and resolutions and for the MSR-d type spectra derived from simulated OCO-2 measurements. The reported XCO_2 retrieval error is induced by the limited aerosol information that can be inferred from the measurement and the different sensitivity to the assumed measurement noise, which is on the level of the OCO-2 instrument (Mandrake et al., 2015). Any systematic error due to e.g. erroneous molecular spectroscopy or instrument calibration errors is not addressed here. For performance evaluation, we considered the global ensemble as described in data section without cirrus contamination and performed three different retrieval analyses: test-1 No radiometric offsets in the measurements. test-2 The OCO-2 radiance offsets identified by Wu et al. (2018) of 0.15%, 0.5% and 0.14% of the mean radiance of each band is added to the 0.76, 1.6 and 2.06 μm bands respectively. No radiometric offset is fit. test-3 Same radiometric offset as above but including a radiometric offset fit. Table 2 shows the bias, single sounding accuracy and mean retrieval noise of synthetic OCO-2 and MSR-d measurements for the three test cases. We included all converged cases in our analysis without applying extra quality filtering.

Table 2. Spectral degradation study using calculated synthetic spectrum.

	Bias [ppm]		Standard deviation [ppm]		Percentage of convergence	
	OCO-2	MSR-d	OCO-2	MSR-d	OCO-2	MSR-d
Test 1	0.04	0.05	2.69	3.09	81%	77%
Test 2	-2.70	-2.30	2.83	2.97	82%	77%
Test 3	-0.01	-0.44	2.10	1.97	69%	66%

For test-1, aerosols induced a scatter in the retrieved XCO_2 with a single sounding accuracy of 2.7 and 3.1 ppm for OCO-2 and MSR-d synthetic measurements, respectively. Albeit with different sampling ratios, the mean retrieval noises are quite similar between OCO-2 and MSR-d synthetic measurements. When adding intensity offsets but not accounting for the offset in the retrieval (test-2), the OCO-2 and MSR-d retrievals exhibit similar single sounding accuracy as in test-1 but with an increased negative bias of −2.70 and −2.30 ppm, respectively. The results of test-3 indicate that for simulated measurements the radiometric offset can be fully mitigated by fitting a radiometric offset in each band as additional elements of the state vector for both OCO-2 and MSR-d measurements. However, we cannot prove this for MSR-d type measurements reproduced from real OCO-2 observations. Moreover, test-1 and test-2 have similar noise-propagated errors but decreased single sounding precision in the case of moderate spectral sizing. Partly, this may be mitigated by an improved SNR performance of the instrument for the MSR-d sizing with respect to the OCO-2 measurement simulation.

4.2 Study using OCO-2 measurements

Due to the spatial sampling approach of the OCO-2 instrument with a continuous sampling in flight direction and with eight cross-track samplings, we typically obtain several collocations of OCO-2 measurements with TCCON observations for our collocation criteria. To evaluate the data quality, we consider overpass-averages both for the OCO-2 and TCCON XCO_2 data. This averaging helps to reduce the impact of random and representation errors in our comparison, where we assume that the latter shows a pseudo-random error pattern.

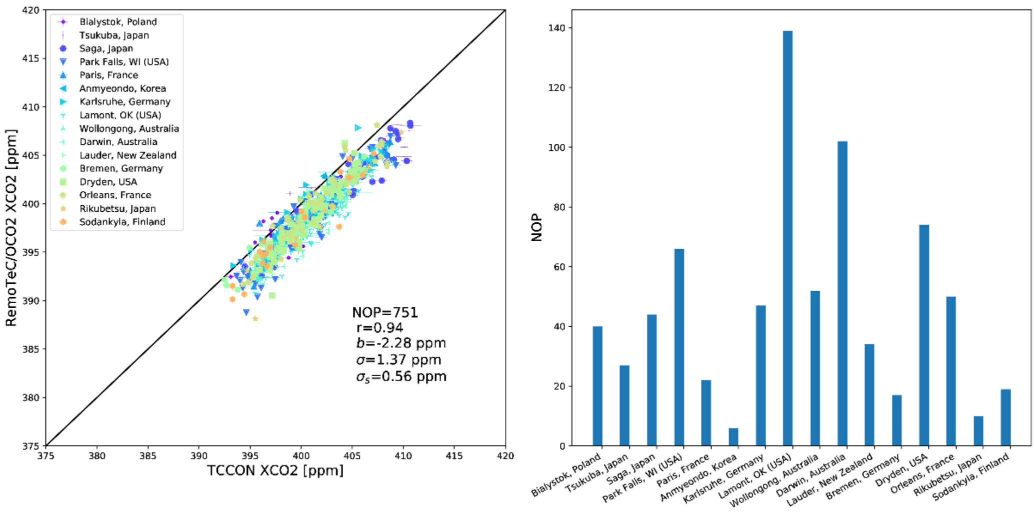

Figure 2. XCO_2 retrievals from OCO-2 measurements under original resolutions. The left panel shows the overall validation and the right panel shows the number of observations per station. In the left panel we included the total number of overpass (NOP), overall bias (b), single sounding accuracy (σ), station-to-station variability (σ_s), Pearson correlation coefficient (r) and the one-to-one line.

For OCO-2 around 386, 600 of the retrievals converged and 313, 500 finally passed the a posteriori quality filtering and are classified as 'good' quality data. Here, the overall data yield is similar to that reported by Wu et al. (2018). The OCO-2 retrievals as shown in Fig. 2 have a global bias of −2.50 ppm, an averaged single sounding precision of σ a = 1.37 ppm, a mean retrieval noise of 0.25 ppm and a station-to-station variability of σ_s = 0.56 ppm. We first degraded the spectral resolution of the 0.76 µm band and 1.61 µm band but used the original measurements of 2.06 µm band (MSR-a). Subsequently, we gradually degraded the spectral resolution in the 2.06 µm band as described for the spectral sizing points MSR-b, MSR-c and MSR-d. We applied the same RemoTeC algorithm settings and similar quality filtering options as above. The filtering is adjusted to guarantee that the percentage of good quality retrievals in all four MSR type retrievals are around 67% as for the original OCO-2 data, although the number of overpasses per station can still differ for the different spectral sizing points.

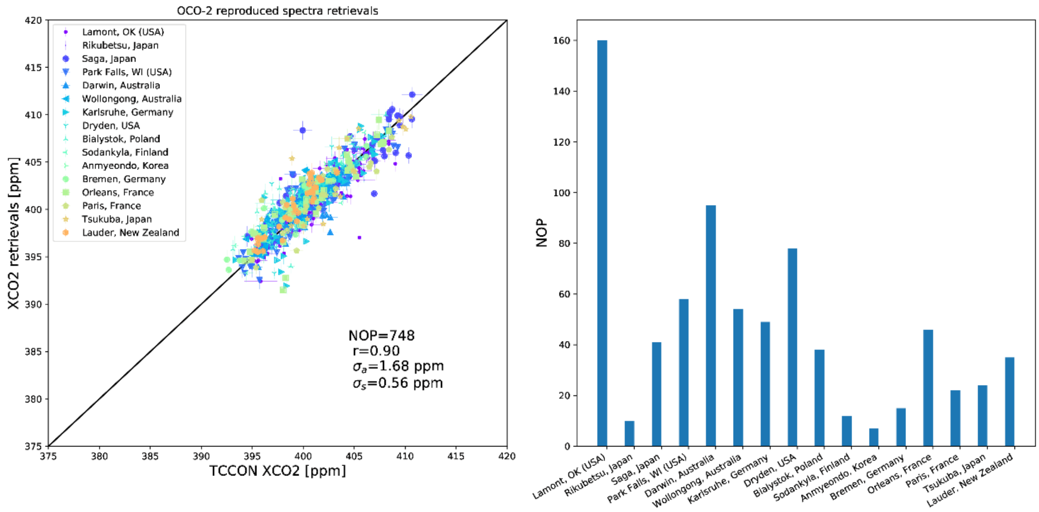

Figure 3. XCO_2 retrievals from MSR-d type spectra reproduced from OCO-2 measurements. Here, a global bias of −6.97 ppm is subtracted in the plot.

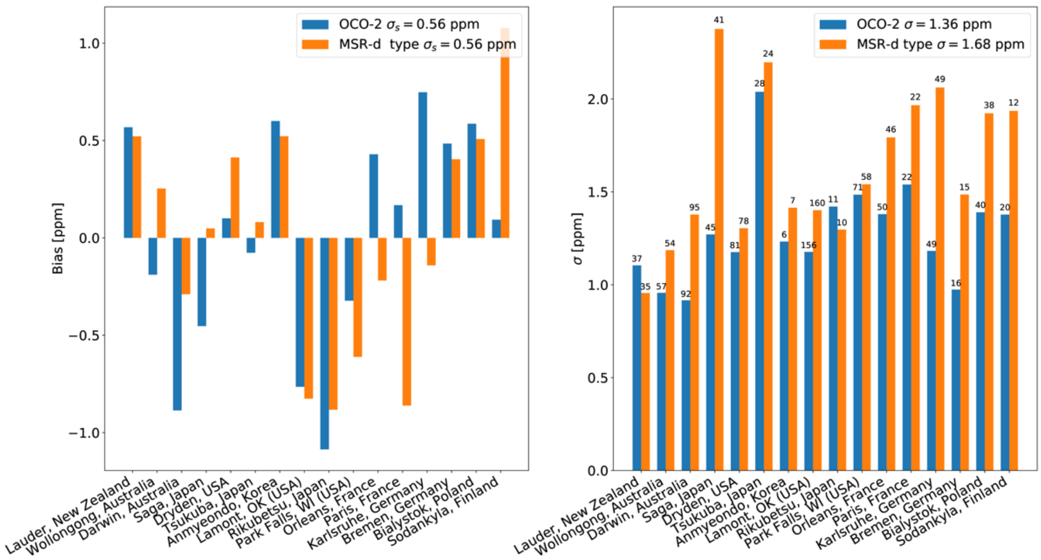

Figure 4. Bias and standard deviation (σ) at different TCCON stations for OCO-2 and MSR-d type retrievals. Overpass frequencies over each site are listed at bar top in the right-hand panel. Here, MSR-d type measurements are reproduced from OCO-2 measurements.

Figure 3 summarizes XCO_2 retrieval performance for the MSR-d sizing point with an average single precision accuracy of σ=1.68 ppm, a retrieval noise error of 0.83 ppm and a station-to-station variability of σ_s=0.56 ppm. Here, the XCO_2 data product has a large negative global bias of −6.97 ppm, which is subtracted in the plot. The variation of biases between 16 different stations is depicted in Fig. 4 while the station-to-station variability σ_s is more-or-less the same as OCO-2 retrievals. To better understand these results and in particular the increase of the global bias, Table 3 summarizes the XCO_2 retrieval performance for OCO-2 and all MSR type measurements, i.e. also the MSR-a, MSR-b and MSR-c spectral sizing points. Here the overall data yield is very similar for the different data sets although differences may occur due to different algorithm convergence. Therefore, we also analyzed the results for the subset of identical data points, shown in Table 4. From MSR-a type retrievals, we see that degrading the 0.76 µm band and 1.61 µm band has limited impact on the XCO_2 retrieval performance. For both selection approaches, lowering the spectral resolution in the 2.06 μm band causes an increase in single sounding precision, mean retrieval noise and mean bias, where the station-to-station variability shows little sensitivity to the different resolutions. Part of the scatter error can be attributed to retrieval noise, which is also gradually increased when lowering the spectral resolution. This part of the uncertainty may be reduced by an instrument with better SNR, which is the advantage of the MSR-type instruments.

Table 3. XCO_2 retrieval performance for OCO-2, MSR-a, MSR-b, MSR-c and MSR-d type measurements under similar throughput. Here,MSR type measurements are generated using OCO-2 measurements.

	Bias [ppm]	σ_a[ppm]	σ_s[ppm]	Mean retrieval noise [ppm]	Overpass	Single sounding accuracy [ppm]
OCO-2	-2.50	1.37	0.56	0.25	783	2.14
MSR-a	-1.46	1.55	0.49	0.42	782	2.16
MSR-b	-3.79	1.60	0.57	0.46	778	2.29
MSR-c	-6.03	1.70	0.55	0.54	745	2.26
MSR-d	-6.97	1.68	0.56	0.80	748	2.31

Table 4. Similar as Table 3, but for the intersection between OCO-2 and MSR type retrievals.

	Bias [ppm]	σ_a[ppm]	σ_s[ppm]	Mean retrieval noise [ppm]	Overpass	Single sounding accuracy [ppm]
OCO-2	-2.00	1.33	0.55	0.25	669	2.05
MSR-a	-1.17	1.39	0.46	0.39	669	2.08
MSR-b	-3.52	1.47	0.54	0.44	669	2.23
MSR-c	-5.73	1.55	0.59	0.59	669	2.34
MSR-d	-6.73	1.58	0.59	0.83	669	2.41

The discrepancy in the mean bias could be for a large part due to intensity offset in the 2.06 μm band of OCO-2. As shown in Tables 3 and 4, the global mean bias increases greatly only when we degrade the 2.06 μm band. As reported by Wu et al. (2018), fitting additive intensity offsets to the two CO_2 absorption bands can improve both the accuracy and the single sounding precision of the XCO_2 retrieval. The fitted intensity offsets are also highly correlated ($r > 0.70$) with the mean signal in each band. This may hint at a stray light related radiometric error. Not fitting such an intensity offset reduces the depth of telluric absorption lines with respect to the continuum and so leads to an underestimation of the CO_2 column. The sensitivity to this radiometric error seems higher for low resolution spectra.

4.3 Study using GOSAT

Finally, to compare our findings with independent GOSAT retrievals, we use, analogously to Galli et al. (2014), 270,000 GOSAT-TCCON collocations, where about 250, 000 successful retrievals pass the a posteriori quality filtering and are classified as ’good’ quality retrievals. Although methane columns are retrieved simultaneously as in previous studies, we will focus here on the XCO_2 retrievals only. As shown in Fig.5, the difference with TCCON measurements shows an overall mean bias of $b=-2.25$ ppm, a single sounding accuracy of $\sigma=2.05$ ppm, a mean retrieval noise of 0.62 ppm and a station-to-station variability of

σ_s=0.42 ppm. Compared with OCO-2 retrievals, GOSAT retrievals have similar mean bias but increased scatter and retrieval noise which is probably due to a higher noise level.
We convert GOSAT measurements to MSR-d measurements and repeat the full-physics retrieval and quality filtering. Figure 6 summarizes the MSR-d XCO_2 retrieval quality and number of observations per station. Almost the same number of observations converge and pass the quality filtering as for the original GOSAT retrievals. Figure 7 shows the variation of the bias and standard deviation among all TCCON stations. Compared to the GOSAT retrievals, the global bias of the MSR retrieval decreases by 0.31 ppm while the station-to-station variability values increase slightly by 0.10 ppm. The mean retrieval noise increased to 1.22 ppm which is not shown in the figure. The reduced spectral resolution affects mainly the single sounding precision of XCO_2, which rises on average by 0.86 ppm and is exhibited at all TCCON stations. This agrees with the finding by Galli et al. (2014) and with the results from simulated measurements. The increase in the scatter of the errors for low resolution spectra was already found for the simulated measurement ensemble and agrees with the OCO-2 findings of Section 4.2. In contrast to the OCO-2 analysis, we see for GOSAT data that the lower resolution has only a minor impact on the global mean bias. In turn, this suggests that the origin of this bias is not due to the interference of molecular spectroscopy but is most likely due to an OCO-2 specific feature, which did not occur in the corresponding GOSAT analysis.

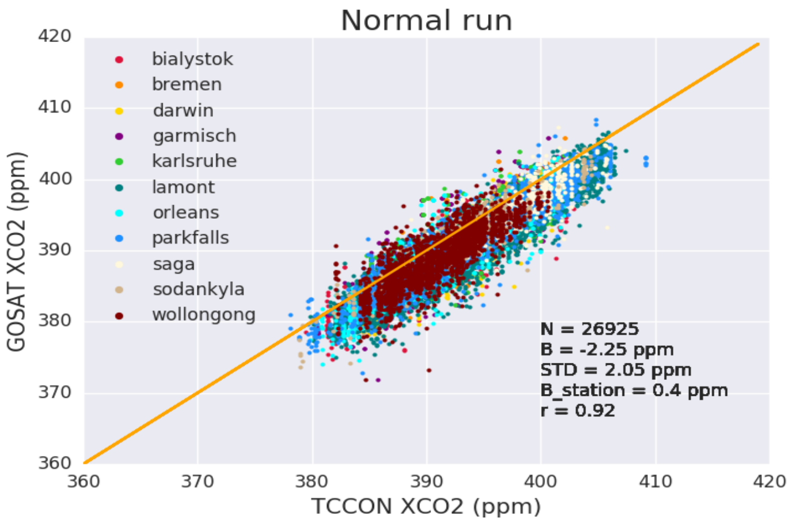

Figure 5. GOSAT reference run. The overall comparision with TCCON has a mean bias of -2.25 ppm, a standard deviation of 2.05 ppm and a station-to-station bias of 0.4 ppm.

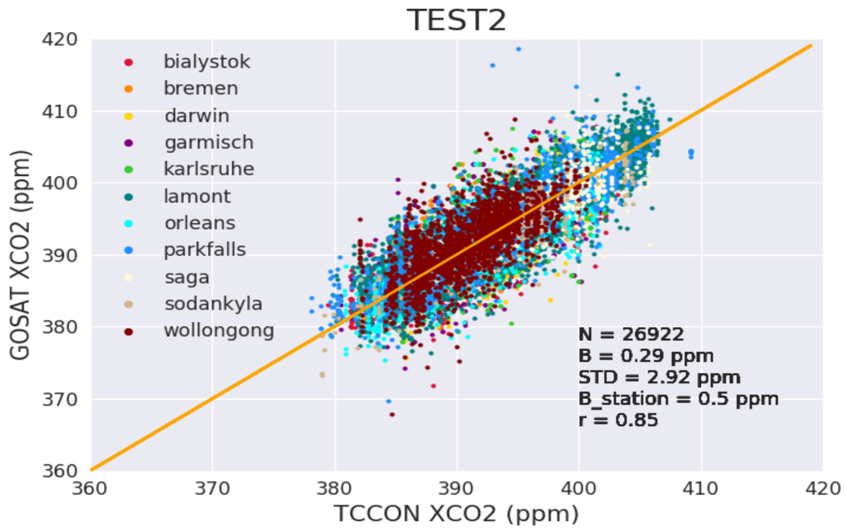

Figure 6. XCO_2 retrieval under spectral resolution of MSR-d type instrument.

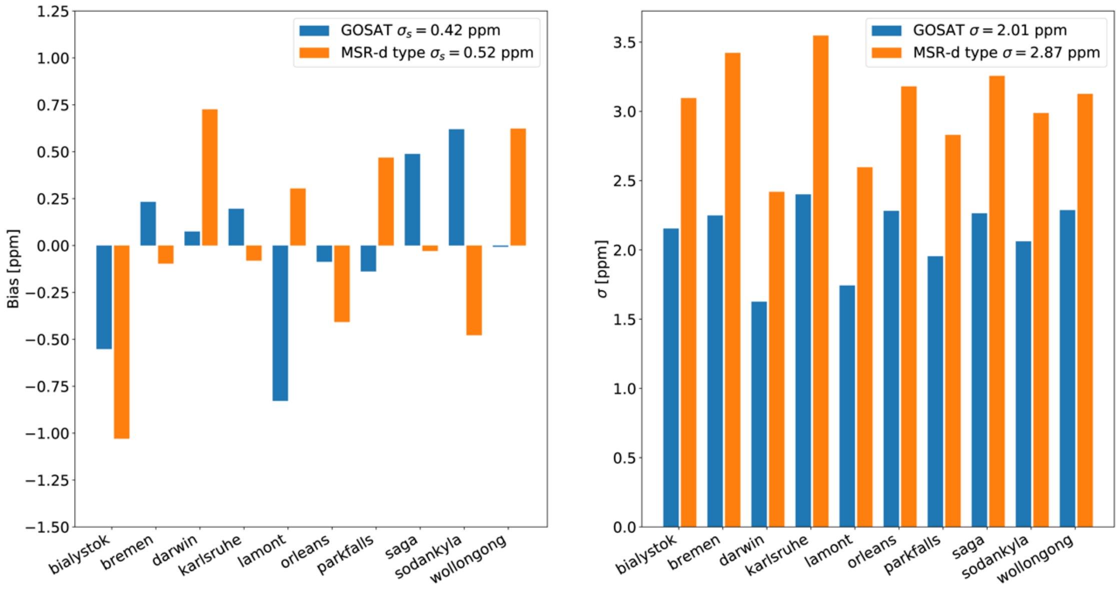

Figure 7. Bias and standard deviation (σ) at different TCCON stations for GOSAT and MSR-d type retrievals. Mean biases of −2.28 and 0.31 ppm are subtracted accordingly for GOSAT and MSR-d type retrievals to show the bias variation on the same reference level.

[redacted] Conclusion

We investigated the impact of spectral resolution on XCO_2 retrieval accuracy with current on-orbit satellite observations and synthetic measurements. From the study with GOSAT, OCO-2 and synthetic measurements, we conclude that the lower resolution of 0.1, 0.3 and 0.3-0.55 nm in the 0.76, 1.61 and 2.06 µm spectral bands mainly induces a larger scatter in the XCO_2 retrieval error, where the scatter gradually increases with lower spectral resolution. Both for GOSAT and OCO-2 measurements, the station-to-station variability is largely insensitive to a coarser spectral resolution. For GOSAT, the global XCO_2 bias differs little for the different spectral resolutions. This is not the case for OCO-2 measurements, which show a significant increase in the mean bias for decreasing spectral resolution. Most likely this increase is due to instrument related errors such as a radiance offset in the different bands. The analysis for synthetic measurements confirms that single sounding precision increases for low resolution and the presence of intensity offsets in the different bands can bring a large bias when not fitted.

[redacted]Reference

[1] CarbonSat Mission Requirements Document, EOP-SMA/2232/PI-pi, version 1.2

[2] Buchwitz, M., et al. "Carbon Monitoring Satellite (CarbonSat): assessment of scattering related atmospheric CO_2 and CH_4 retrieval errors and first results on implications for inferring city CO_2 emissions." Atmospheric Measurement Techniques 6.12 (2013): 3477-3500.

[3] Galli, A., et al. "The impact of spectral resolution on satellite retrieval accuracy of CO_2 and CH_4." (2014): 1105.

[4] Bovensmann, H., et al. "Report for mission selection: CarbonSat-An earth explorer to observe greenhouse gases." (2015).

[5] Orbiting Carbon Observatory–2 (OCO-2) Data Product User's Guide, Operational L1 and L2 Data Versions 8 and 8R. December, 2017.

[6] Boesch, H., Baker, D., Connor, B., Crisp, D., and Miller, C.: Global characterization of CO_2 column retrievals from shortwave-infrared satellite observations of the Orbiting Carbon Observatory-2 mission, Remote Sensing, 3, 270\u2013304, 2011.

[7] Butz, A., et al.: Toward accurate CO_2 and CH_4 observations from GOSAT, Geophysical Research Letters, 38, https://doi.org/10.1029/2011GL047888,l14812, 2011.

[8] Hasekamp, O. P. and Butz, A.: Efficient calculation of intensity and polarization spectra in vertically inhomogeneous scattering and absorbing atmospheres, Journal of Geophysical Research: Atmospheres, 113, n/a–n/a, https://doi.org/10.1029/2008JD010379, d20309, 2008.

[9] Wu, L., et al.: Carbon dioxide retrieval from OCO-2 satellite observations using the RemoTeC algorithm and validation with TCCON measurements, Atmospheric Measurement Techniques, 11, 3111–3130, https://doi.org/10.5194/amt-11-3111-2018, 2018.

[10] Crisp, D., et al. A Constellation Architecture For Monitoring Carbon Dioxide And Methane From Space, technical note, p. 173, http://ceos.org/ourwork/virtual-constellations/acc/, accessed: 2018-10-10, 2018.

[11] Cox, P. M., Betts, R. A., Jones, C. D., Spall, S. A., and Totterdell, I. J.: Acceleration of global warming due to carbon-cycle feedbacks in a coupled climate model, Nature, 408, 184–187, 2000.

Requirement study for the Multi-Angle-Polarimeter

Stephanie Rusli, Hein van Heck, Otto Hasekamp, Jochen Landgraf
SRON Netherlands Institute for Space Research

Table of Contents

1 Introduction

This Technote is a joint delivery of ESA's *CO2M requirement consolidation and error budget study* and the CO_2 spectral sizing study. It addresses the requirements for the multi-angle polarimeter (MAP) for aerosol and cirrus cloud observations in support of the CO_2 monitoring (CO2M) mission. The presence of aerosol and cirrus leads to scattering that modifies the path of the backscattered light. MAP collects the necessary information on aerosol properties to correct the light path. Therefore, MAP observations as a part of the CO2M mission are expected to improve the accuracy of the CO_2 measurements. We derive the requirements for MAP using study cases where we consider multiple geophysical and atmospheric scenarios, presented in section 2. Section 3 and 4 briefly describe the measurement setup of the CO_2 instrument and the state variables used in this study. The XCO_2 accuracy for all the scenarios is assessed using a linear error analysis (section 5). We investigate different aspects of MAP observations, i.e. measurement errors, number of viewing angles, and wavelength range (section 6). The analysis is conducted for two MAP concepts, i.e. modulation (MAP-mod) and bandpass (MAP-band), which are presented individually here. Section 7 presents a summary and conclusions

2 Study cases

We use three aerosol cases that represent different atmospheric scenes in this requirement study. In all cases, we assume a bimodal lognormal size distribution of aerosols consisting of a coarse and a fine mode. All of the fine-mode particles are assumed spherical while the coarse mode is a mixture of spheroids and spheres. The aerosol particles of each mode are distributed vertically following a Gauss distribution parametrized by a mean height and a full width at half maximum (FWHM). The latter is fixed at 2 km. The size distribution, parametrized by the effective radius and effective variance, is assumed constant with height. Case 1 represents boundary layer aerosols in which both modes are located at 1-km height. The coarse mode of Case 2 is representative of an elevated cirrus layer at 8 km. In Case 3, the coarse mode aerosols are located at an intermediate height of 4 km and the size of the fine-mode particles are slightly greater than in Case 1 or 2. For each aerosol case, we study the effect of changing the aerosol column concentration. This is done by varying the fine-mode aerosol optical thickness in Case 1, or by varying the coarse-mode optical thickness in Case 2 and Case 3, to 5 different values. Table 1 specifies the aerosol properties and Figure 1 provides the sketches of the aerosol height distributions in Case 1,2 and 3.

To take the Earth surface reflection into account, we consider a 'vegetation' and a 'soil' type surfaces. They are Lambertian surfaces with albedo (0.1385, 0.2979, 0.2585) for soil and (0.4503, 0.2302, 0.0634) for vegetation at wavelengths (765, 1600, 2000) nm. Solar zenith angle (SZA) is fixed to either 30 or 60 degrees. Given the variety in aerosol cases, optical thickness (τ_{tot}) values, surface types, and SZAs, there is a total of 60 scenarios, based on which the requirements are derived.

Table 1: Aerosol properties adopted in three study cases

Aerosol parameter	Case 1		Case 2	
	fine mode	coarse mode	fine mode	coarse mode
effective radius [micron]	0.12	1.6	0.12/0.2	1.6
effective variance	0.2	0.6	0.2	0.6
spherical fraction	1.0	0.05	1.0	0.05
ref. index @ 765nm	(1.5,10-7)	(1.53,2.54·10-3)	(1.5,10-7)	(1.53,2.54·10-3)
ref. index @ 1600nm	(1.5,10-7)	(1.40,1.56·10-3)	(1.5,10-7)	(1.40,1.56·10-3)

ref. index @ 2000nm	(1.5,10-7)	(1.30,2.00·10-3)	(1.5,10-7)	(1.30,2.00·10-3)
layer width (FWHM) [m]	1000	1000	1000	8000/4000
layer width (FWHM) [m]	2000	2000	2000	2000
optical thickness @ 550nm	0.05, 0.1, 0.15, 0.25, 0.5	0.02	0.2	0.02, 0.04, 0.06, 0.10, 0.15

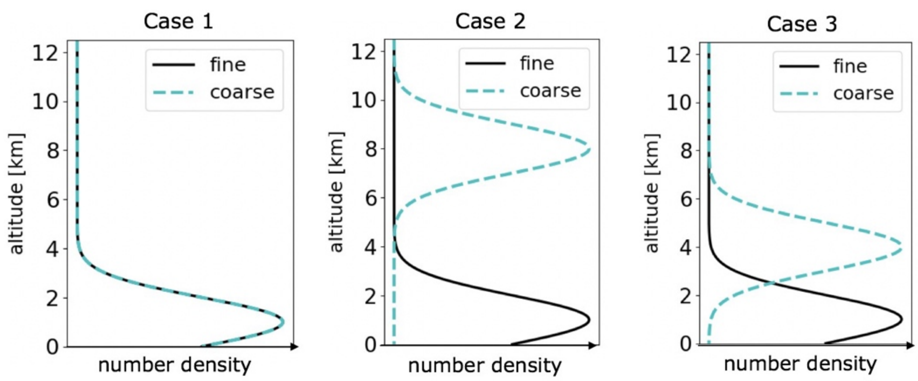

Figure 1: Sketches of the vertical distribution of the coarse- and fine-mode aerosols in Case 1,2 and 3

3 Measurement setups

MAP provides radiance and polarization (degree of linear polarization or DLP) measurements at multiple wavelengths and at multiple observation/viewing zenith angles (VZA). The composition of these measurements is determined by the MAP setup, which is the subject of this requirement study and therefore explored in more detail in section 7.5.

Regarding the setup for the CO_2 instrument, the relevant aspects are given in Table 2. We employ the noise model in which the SNR for TOA radiance follows SNR AI/(AI + B),

where I is the radiance. The values of A and B for each spectral window are provided in Tab. 2.

Table 2: Setup of the CO_2 instrument

Band ID	Spectral range [nm]	Spectral resolution [nm]	Spectral sampling ratio	A [phot./cm2 s nm sr]	B [-]
NIR	747-773	0.10	3.14	$4.47 \cdot 10^{-8}$	160540
SWIR-1	1590-1675	0.30	3.14	$2.29 \cdot 10^{-7}$	333297
SWIR-2	1993-2095	0.55	3.14	$3.91 \cdot 10^{-7}$	323636

4 State vector definition

There are two state vectors, one for the aerosol and the other for the XCO_2 retrievals. The common/ overlapping elements in the two state vectors are the aerosol parameters of interest (see Table 1). Aerosol layer width (FWHM) of both modes as well as the spherical fraction and the layer height of the fine mode are not included in the state vector (assumed known). Apart from the aerosol parameters, the MAP state vector also contains surface BRDF and BPDF parameters. State variables specific to the XCO_2 retrieval include the CO_2 column concentration, surface albedo and its first-order spectral dependence, and the spectral shifts in the three spectral windows.

5 Linear error analysis

We compute the error in XCO_2 by linearly propagating the measurement errors of MAP and of the CO_2 instrument (spectrometer), taking the prior errors into account. This is done in a two-step approach. The first step represents the aerosol retrieval using MAP and the second step corresponds to the XCO_2 retrieval using the prior knowledge of aerosol from MAP. It follows that the derived XCO_2 error reported here is the aerosol-induced error, and it includes the random and systematic error components. In this framework, the error of the retrieved aerosol properties comprises the part that comes from the prior errors and the part that is propagated from the MAP measurement errors. The error component due to the prior uncertainties is formulated as follow

$$\boldsymbol{S}_{aer}^{sm} = (\boldsymbol{G}_{MAP}\boldsymbol{K}_{MAP} - \boldsymbol{I})\boldsymbol{S}_{a,MAP}(\boldsymbol{G}_{MAP}\boldsymbol{K}_{MAP} - \boldsymbol{I})^T \quad (7.1)$$

while the error component due to the measurement errors is written as

$$\boldsymbol{S}_{aer}^{ns} = \boldsymbol{G}_{MAP}\boldsymbol{S}_{y,MAP}\boldsymbol{G}_{MAP}^T \quad (7.2)$$

$\boldsymbol{S}_{a,MAP}$ is the covariance matrix of the MAP prior error. The off-diagonal elements are zero and the diagonal elements consist of the squared prior errors of the state vector elements, which include aerosol parameters. The prior errors of these aerosol parameters are assumed to be approximately 100% of their prior values. $\boldsymbol{S}_{y,MAP}$ is the covariance matrix of the MAP measurement error. The diagonal elements consist of the squared radiometric and the polarimetric (degree of linear polarisation) errors. We assume no correlation among the measurements. $\boldsymbol{K}_{MAP}$ is the Jacobian matrix that describes the sensitivity of the MAP measurements to changes in the MAP state variables. $\boldsymbol{K}_{MAP}$ is calculated for each scenario and for a particular MAP measurement setup. $\boldsymbol{K}_{MAP}$ is the gain matrix that relates the MAP measurement errors with the noise in MAP state parameters and it is formulated as

$$\boldsymbol{G}_{MAP} = (\boldsymbol{K}_{MAP}^T\boldsymbol{S}_{y,MAP}^{-1}\boldsymbol{K}_{MAP} + \boldsymbol{S}_{a,MAP}^{-1})^{-1}\boldsymbol{K}_{MAP}^T\boldsymbol{S}_{Y,MAP}^{-1} \quad (7.3)$$

The total error on the retrieved aerosol parameters is then represented by the sum of $\boldsymbol{S}_{sm}$ and $\boldsymbol{S}_{ns}$, i.e.

$$\boldsymbol{S}_{aer}^{tot} = \boldsymbol{S}_{aer}^{ns} + \boldsymbol{S}_{aer}^{sm} \quad (7.4)$$

The total aerosol uncertainties from Eq. 7.4 are then passed on to the CO_2 retrieval step. At this stage, they are mapped into spectrometer measurement errors using the CO_2 Jacobian matrix for the aerosol parameters $\boldsymbol{K}_{CO2,aer}$, and the measurement errors are in turn mapped into the errors on the CO_2 state variables using the CO_2-instrument gain matrix $\boldsymbol{G}_{CO2}$. Mathematically, this error propagation is expressed as

$$\boldsymbol{S}_{CO2}^{aer} = \boldsymbol{G}_{CO2}\boldsymbol{K}_{CO2,aer}\boldsymbol{S}_{aer}^{tot}\boldsymbol{K}_{CO2,aer}^{T}\boldsymbol{G}_{CO2}^{T} \quad (7.5)$$

The XCO_2 error reported in this document follows from taking the square root of the diagonal element of $\boldsymbol{S}_{CO2}^{aer}$ that is associated with the CO_2 column concentration. This approach of linear error analysis mimics as close as possible the joint retrieval of aerosol and CO_2 using MAP and spectrometer simultaneously.

6 Requirements

We investigate requirements for three aspects of the MAP observations, i.e. the measurement accuracy (radiometric and polarimetric uncertainties), number of viewing angles, and wavelength range. These requirements are derived based on the stringent precision target of the CO2M mission, i.e. 0.7 ppm or better. In this work, we set the target value for the aerosol-induced XCO_2 error (Eq. 7.5) to 0.1% *maximally 0.15%), which includes both the systematic and random errors. For a total CO_2 column of 400 ppm, an XCO_2 error between 0.1% and 0.15% corresponds to an error between 0.4 ppm and 0.6 ppm, and hence within the mission precision target of 0.7 ppm. XCO_2 errors are calculated using the linear error analysis in section 7.4 for the geophysical and aerosol scenarios in section 7.1, from which the requirements follow. The results for the two MAP concepts are presented separately below.

6.1 Modulation concept (MAP-mod)

6.1.1 Baseline setup

As a reference, we define a baseline setup for MAP-mod. This is specified in Table 3.

Table 3: MAP-mod baseline setup

Features	Baseline setup
Number of VZAs	5 (-60 to 60 degrees)
Spectral range	385-765 nm
Radiance spectral resolution	5 nm
DLP spectral resolution	15nm@395nm, 30nm@765nm
Number of radiance measurements	77
Number of DLP measurements	19
Total number of measurements	480

6.1.2 Radiometric and polarimetric uncertainties

This section addresses requirements S7MR-OBS-380M, S7MR-OBS-390M, S7MR-OBS-400M, and S7MR-OBS-410M in the **MRDv1.0**. To derive requirements for MAP measurement uncertainties, we perform the error analysis by varying $\boldsymbol{S}_{y,MAP}$(equation 7.2). The radiance errors are varied to 0.5%,1%,2%, 4% and degree of linear polarization (DLP) errors are set to values ranging from 0.001 to 0.005. For this exercise, the baseline setup (Table 3) is used in which the five VZAs consist of 0,+/-40,+/-57 degrees.

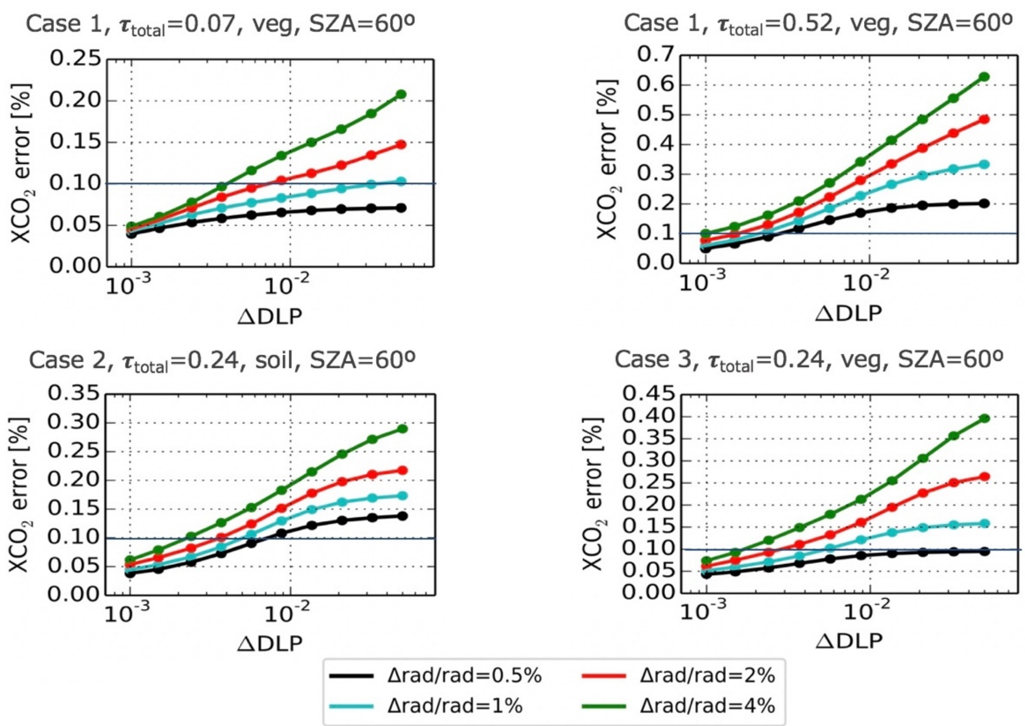

*Figure 2: Performance of the MAP-mode baseline setup for four selected study cases. Each panel represents one study case where XCO_2 errors are shown as a function DLP uncertainties (**Δ**DLP) for different values of radiance errors (±**Δ**rad/rad).*

The results of the error analysis are displayed in Fig. 2, which shows that XCO_2 accuracy decreases with increasing DLP and radiance errors in the three aerosol cases. For large radiance and DLP uncertainties, XCO_2 error can be as high as ~0.6%. When radiance and DLP errors are not greater than 2% and 0.003, respectively, XCO2 errors do not increase beyond 0.15%; in most cases, the target XCO_2 error of 0.1% is in fact met. Relaxing the radiance and DLP errors to 0.003 and 0.0035 still results in XCO_2 errors of ≤0.15% for the majority of the study cases.

The reported radiance and DLP errors are the total errors. Assuming equal contributions from random and systematic components, the 0.0035 DLP errors can be broken down to a noise component of ~0.0025 (or SNR=400) and a systematic error of ~0.0025. Similarly, the radiance error of 3% comprises ~1.7% (SNR~50) noise and ~1.7% systematic component. However, since the required DLP error is smaller, the total SNR requirement is driven by DLP. For a radiometric precision of ~0.0025 (SNR=400), the systematic component is then the dominant part of the total radiance error.

6.1.3 Number of viewing angles

This section addresses requirement S7MR-OBS-340M in the **MRDv1.0**. For this investigation, the spectral range and resolution of the baseline setup (Table 3) are adopted. Changing the number of viewing angles implies adding or removing measurements, which would influence the aerosol and hence the CO2 retrieval. To study this effect, we vary the number of VZAs from 3 to 8 and compute a Jacobian matrix $\boldsymbol{K}_{MAP}$ for each.

The viewing angles are limited to between -60 and 60 degrees. Table 4 specifies the viewing angles and the corresponding number of measurements.

Table 4: Number of viewing angles studied for MAP-mod

Number of VZA	VZAs	Total number of measurements
3	0, ±57	288
4	±19, ±57	384
5	±0, ±20, ±57	480
6	±11, ±34, ±57	576
7	0 ±19, ±38, ±57	672
8	±8, ±24, ±41, ±57	768

Following the discussion above, we assume a radiance error of 2% and a DLP error of 0.3% in the error analysis. Figure 3 shows the resulting XCO_2 errors as a function of number of viewing angles for several selected cases.

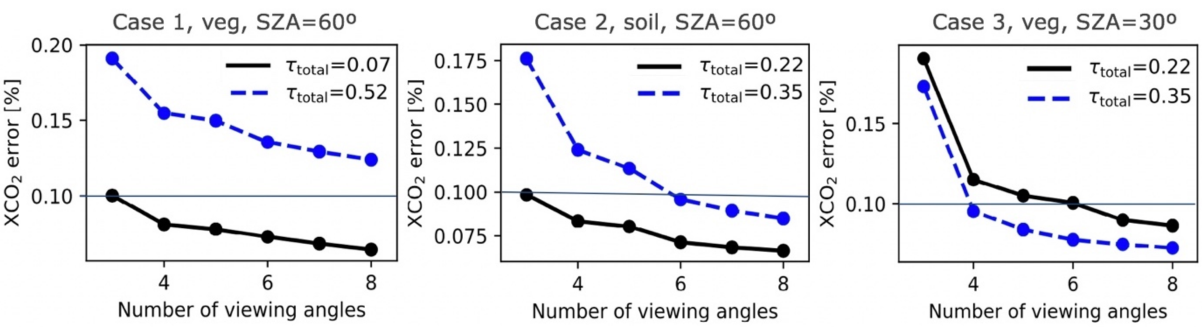

Figure 3: XCO_2 errors as a function of number of viewing angles assuming a radiance error of 2% and a DLP error of 0.003 for the MAP-mod concept. Each panel shows the XCO_2 errors for a particular study case.

The plots in Fig. 3 show that there is a sharp drop of XCO_2 error from 3 to 4 viewing angles. From 4 to 8 viewing angles, XCO_2 errors decrease more mildly. The baseline setup has 5 viewing angles and this choice meets the target XCO_2 error. Having more than 5 viewing angles leads only to a marginal improvement in XCO_2 accuracy. This behavior is seen not just in the selected cases shown here, but also in all the other study cases. An odd number of viewing angles is preferred to an even number to allow for the inclusion of nadir view.
One can then conclude that 5 viewing angles is the minimum necessary to achieve the target XCO_2 error.

6.1.4 Spectral range

This section addresses requirements S7MR-OBS-350M, S7MR-OBS-360M and S7MR-OBS-370M in the **MRDv1.0**. To assess the effect of changing the spectral range on the XCO_2 accuracy, we explore three options, i.e.

- expand the baseline spectral range so it extends further into the UV down to 350nm ('≥350nm'),
- truncate the baseline spectral range at 490nm to exclude UV ('≥490nm'),

- extend the baseline spectral range to include SWIR, i.e. add radiance and DLP measurements at 1640 and 2250nm ('with SWIR').

Table 5: Spectral ranges studied for MAP-mod

Setup	Spectral range [nm]	Number of radiance measurements	Number of DLP measurements	Total number of measurements
≥350nm	350-765	84	22	530
≥490nm	490-765	56	12	340
with SWIR	385-2250	79	21	500
baseline	385-765	77	19	480

Table 5 summarizes the setups that represent the three options, along with the baseline for comparison. For this exercise, all of the setups include 5 viewing angles at 0, +/-40, and +/-60 degrees to conform to requirement S7MR-OBS-350M. The baseline DLP spectral resolution is retained when excluding or including more UV wavelengths. In the error analysis, the radiance and DLP errors are assumed at 3% and 0.003, respectively. Fig. 4 and 5 show the resulting XCO_2 errors as a function of optical depth for all the study cases using the three setups above, compared with the baseline setup.

It can be seen in Fig. 4 that when compared to the baseline setup, including more UV wavelengths down to 350nm leads to little gain in XCO_2 accuracy, while removing UV wavelengths altogether leads to a considerable loss of XCO_2 accuracy. Excluding UV can increase XCO_2 error to around 0.25% for Case 3, vegetation with SZA=60 degrees. Fig. 5 shows that XCO_2 accuracy improves with the additional SWIR channels, but only
marginally, which might not justify the added financial cost of including them. One can then conclude that the optimal choice of setup for MAP-mod is the baseline setup with spectral range from 385 to 765 nm.

6.2 Bandpass concept (MAP-band)

6.2.1 Baseline setup

As a reference, we define a baseline setup for MAP-band. This is specified in Table 6. In this bandpass concept, both radiance and DLP measurements are taken at each bandpass or wavelength.

Table 6: MAP-band baseline setup

Feature	Baseline setup
Number of VZAs	13
Viewing angles [degrees]	0, ±10, ±20, ±30, ±40, ±50, ±60
Bandpass/wavelengths [nm]	410, 440, 490, 550, 669.9, 863.4, 1640, 2250
Number of radiance measurements	8
Number of DLP measurements	8
Total number of measurements	208

6.2.2 Radiometric and polarimetric uncertainties

This section addresses requirements S7MR-OBS-380B, S7MR-OBS-390B, S7MR-OBS-400B, and S7MR-OBS-410B in the **MRDv1.0**. To derive requirements for MAP measurement uncertainties, we perform the error analysis by varying $\boldsymbol{S_{y,MAP}}$ (equation 2). The radiance errors are varied to 0.5%,1%,2%,4% and degree of linear polarization (DLP) errors are set to values ranging from 0.1% to 5%. For this exercise, the baseline setup (Table 6) is used. The results of the error analysis are displayed in Fig. 6, which shows that XCO2 accuracy decreases with increasing DLP and radiance errors in the three aerosol cases. For large radiance and DLP uncertainties, XCO2 error can be as high as ~0.6%. When radiance and DLP errors are not greater than 2% and 0.003, respectively, XCO2 errors do not increase beyond 0.15%; in most cases, the target XCO2 error of 0.1% is in fact met. Relaxing the radiance and DLP errors to 3% and 0.0035 still results in XCO2 errors of ≤0.15% for the majority of the study cases. The reported radiance and DLP errors are the total errors. Assuming equal contributions from random and systematic components, the 0.0035 DLP errors can be broken down to a noise component of ~0.0025 (or SNR=500) and a systematic error of _0.0025. Similarly, the radiance error of 3% comprises ~1.7% (SNR~40) noise and ~1.7% systematic component. However, since the required DLP error is smaller, the total SNR requirement is driven by DLP. For a radiometric precision of ~0.0025 (SNR=500), the systematic component is then the dominant part of the total radiance error

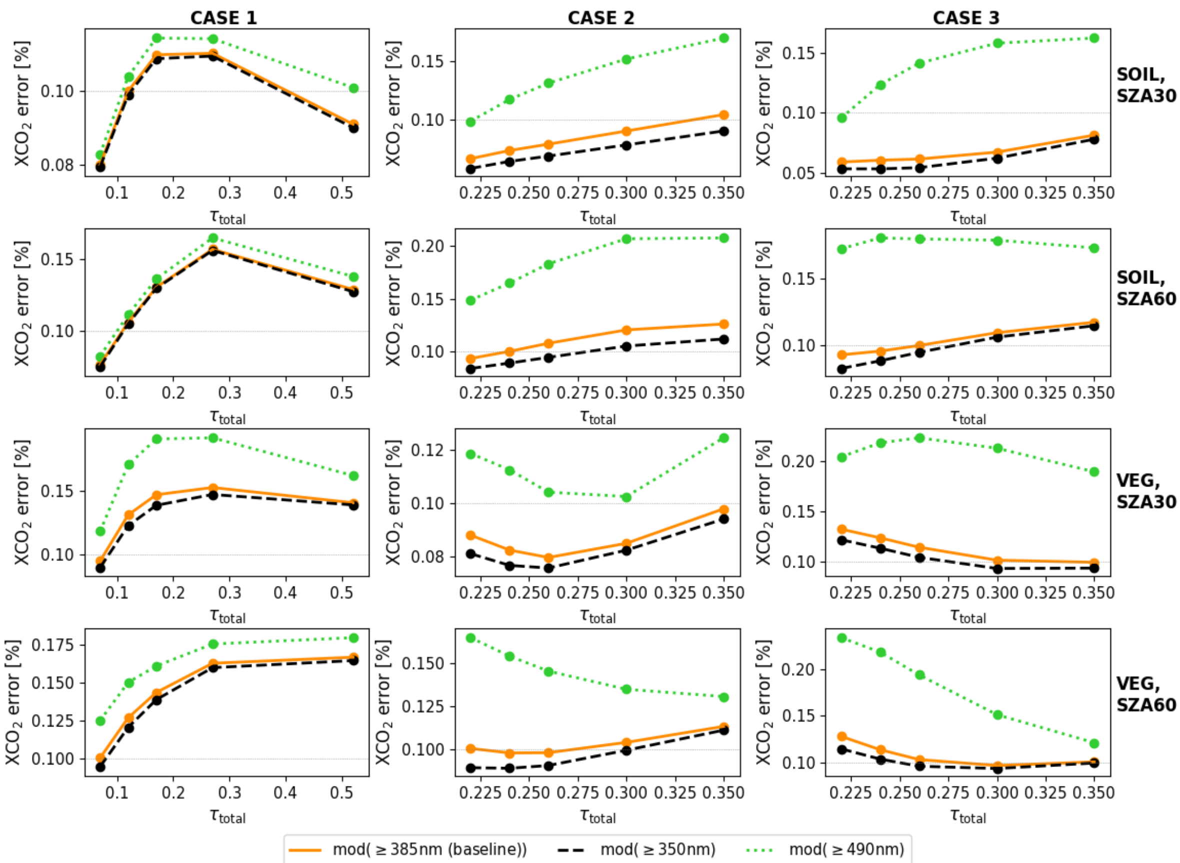

Figure 4*: Performance comparison among the baseline, ≥350nm, ≥490nm setups of MAP-mod, represented by the different lines. XCO_2 errors as a function of aerosol total optical thickness is shown for all the study cases as indicated at the top and on the right side. The magnitude of the radiance and DLP uncertainties are assumed 3% and 0.003, respectively.*

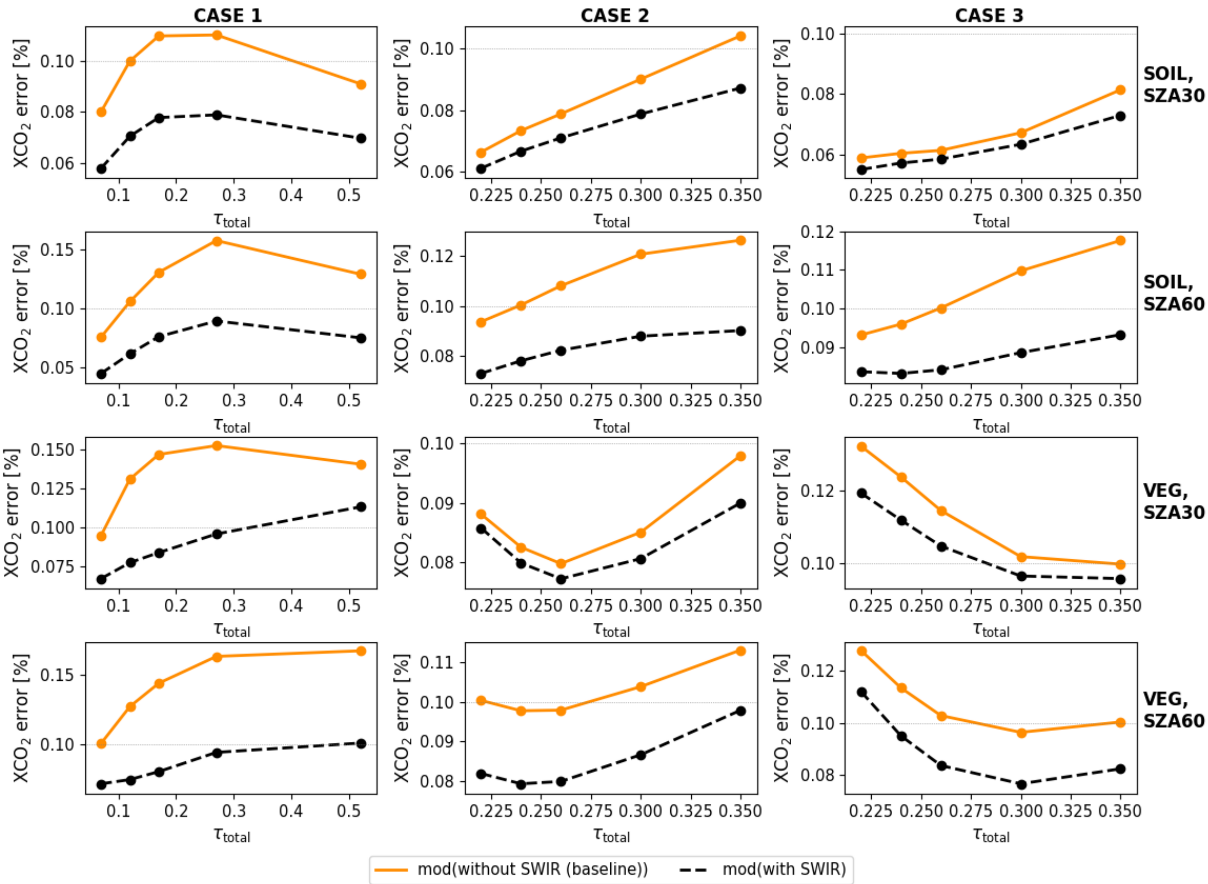

Figure 5: Performance comparison between baseline and with-SWIR setups of MAP-mod concept, represented by the different lines. XCO2 errors as a function of aerosol total optical thickness is shown for all the study cases as indicated at the top and on the right side. The magnitude of the radiance and DLP uncertainties are assumed 3% and 0.003, respectively.

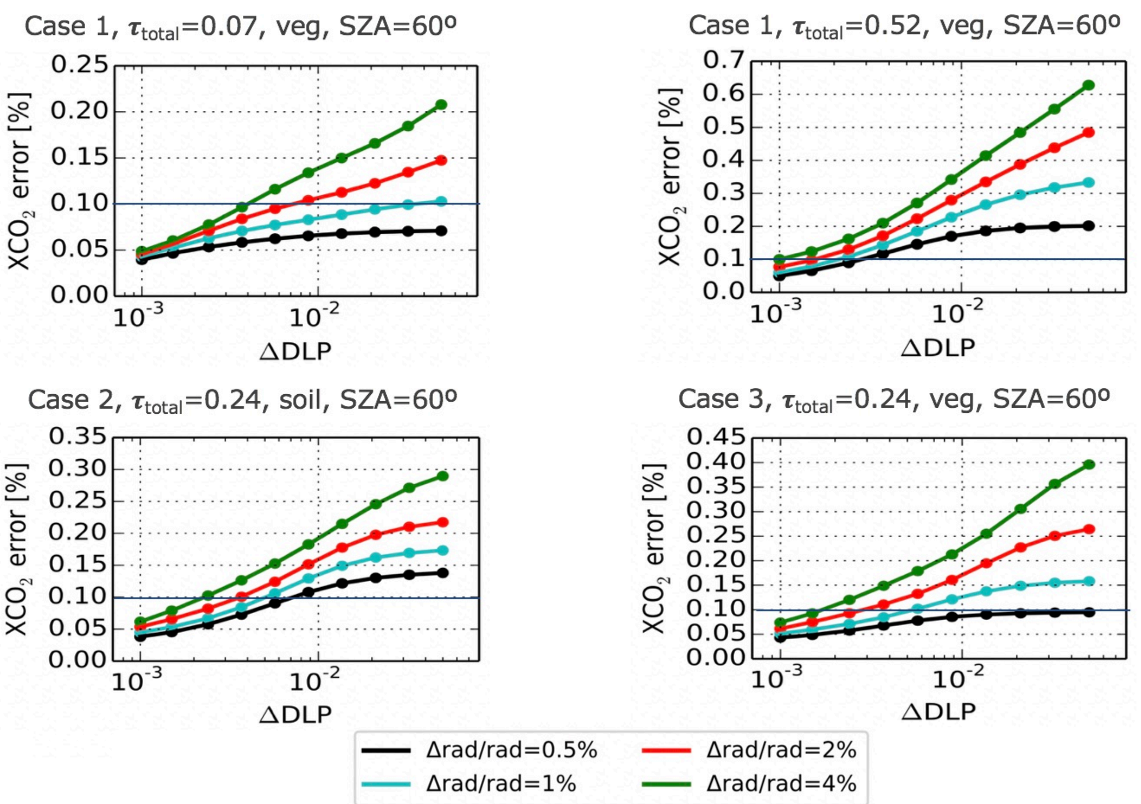

Figure 6: Performance of baseline MAP-band setup for four selected study cases. Each panel represents one study case where XCO_2 errors are shown as a function DLP uncertainties for different values of radiance errors.

6.2.3 Number of viewing angles

Table 7: Number of viewing angles studied for MAP-band

Number of VZAs	VZAs	Number of measurements
10	±7, ±20, ±33, ±47, ±60	160
11	0, ±12, ±24, ±36, ±48, ±60	176
12	±5, ±16, ±27, ±38, ±49, ±60	192
14	±5, ±14, ±23, ±32, ±42, ±51, ±60	224
15	0, ±9, ±17, ±26, ±34, ±43, ±51, ±60	240
16	±4, ±12, ±20, ±28, ±36, ±44, ±52, ±60	256

This section addresses requirements S7MR-OBS-340B and S7MR-OBS-350B in **MRDv1.0**. For this investigation, the bandpass/wavelength selection of the baseline setup (Table 6) is adopted. Changing the number of viewing angles implies adding or removing measurements, which would influence the aerosol and hence the CO2 retrieval. To study this effect, we vary the number of VZAs from 10 to 16 and compute a Jacobian matrix $\boldsymbol{K}_{mat}$ for each. The viewing angles are equally spaced and the outermost angles are fixed to -60 and 60 degrees to conform to requirement S7MR-OBS-350B. Table 7 specifies the individual viewing angles along with the corresponding number of measurements.

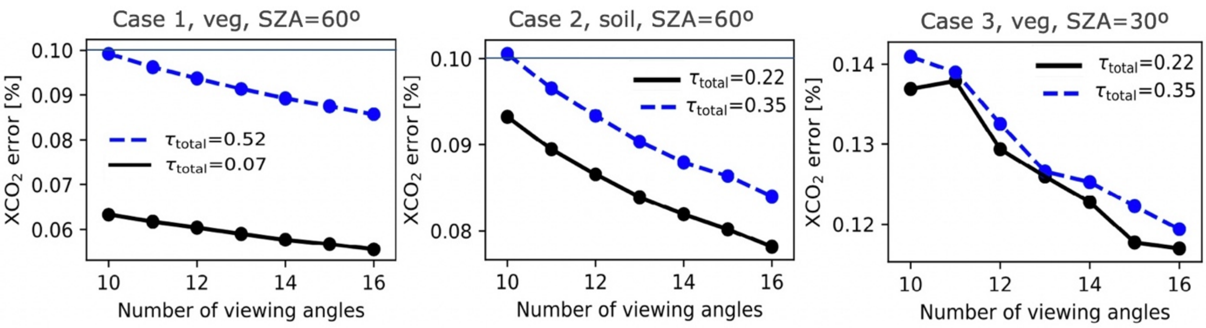

Figure 7: XCO_2 errors as a function of number of viewing angles for a radiance error of 2% and a DLP error of 0.003, for the MAP-band concept. Each panel shows the XCO_2 errors for a particular study case.

Following the discussion above, we assume a radiance error of 2% and a DLP error of 0.003 in the error analysis. Figure 7 shows the resulting XCO_2 errors as a function of number of viewing angles for several selected cases. The plots in Fig. 7 show that XCO_2 accuracy improves with increasing number of viewing angles in an almost linear fashion. From 10 to 16 angles, the improvement in XCO_2 accuracy is quite small. With ten viewing angles, the target XCO_2 error is in fact already met. This behavior is seen not just in the selected cases shown here, but also in all the other study cases.

An odd number of viewing angles is preferred to an even number to allow for the inclusion of nadir view. One can conclude that, given the baseline bandpass selection, having 11 viewing angles is sufficient to deliver the desired XCO_2 accuracy. Note that the requirement on the number of viewing angles is coupled with the requirement on the bandpass/ wavelength range. Here, the number of viewing angles is assessed for a given set of wavelengths and in
the following section, the wavelengths selection is assessed for a given number of viewing angles. In section 7.6, we provide examples of how the interplay between these two aspects affects XCO_2 accuracy.

6.2.4 Wavelength range

This section addresses requirements S7MR-OBS-360B in the **MRDv1.0**. To assess the effect of changing the wavelength range, we explore three options, i.e.

- expand the baseline wavelength range so it extends further into the UV down to 350nm ('≥ 350nm'),
- truncate baseline wavelength range at 490 nm to exclude UV ('≥490nm'),
- narrow down the baseline wavelength range by excluding SWIR wavelengths, i.e. remove radiance and DLP measurements at 1640 and 2250nm.

Table 8 summarizes the setups that represent the three options, along with the baseline for comparison. Radiance and polarization measurements are taken at each of the selected wavelengths. Following the results in section 6.2.3, in this exercise we use 11 viewing angles in all three setups and the baseline setup. The individual angles are given in Table 8.

Table 8: MAP-band bandpass selections for a variety of wavelength ranges

Setup	Bandpass selections	Total number of measurements
≥ 350nm	350, 380, 410, 440, 490, 550, 669.9, 863.4, 1640, 2250	220
≥490nm	490, 550, 669.9, 863.4, 1640, 2250	132
without SWIR	410, 440, 490, 550, 669.9, 863.4	132
baseline	410, 440, 490, 550, 669.9, 863.4, 1640, 2250	176

In the error analysis, the radiance and DLP errors are assumed at 3% and 0.003, respectively. Fig. 8 and 9 show the resulting XCO2 errors as a function of optical depth for all the study cases for the three setups above, compared with the baseline setup. It can be seen in Fig. 8 that when compared to the baseline setup, including more UV wavelengths down to 350nm leads to little gain in XCO_2 accuracy, while removing UV wavelengths altogether leads to a considerable loss of XCO_2 accuracy. Excluding UV can increase XCO_2 error to around 0.25% for Case 3, vegetation with SZA=60 degrees. Fig. 9 shows that XCO_2 accuracy drops considerably when the SWIR channels (1640 and 2250 nm) are removed. For Case 3, vegetation, SZA=60 degrees, the XCO_2 error can even increase to 0.51%. It is therefore important to keep the SWIR measurements in place.

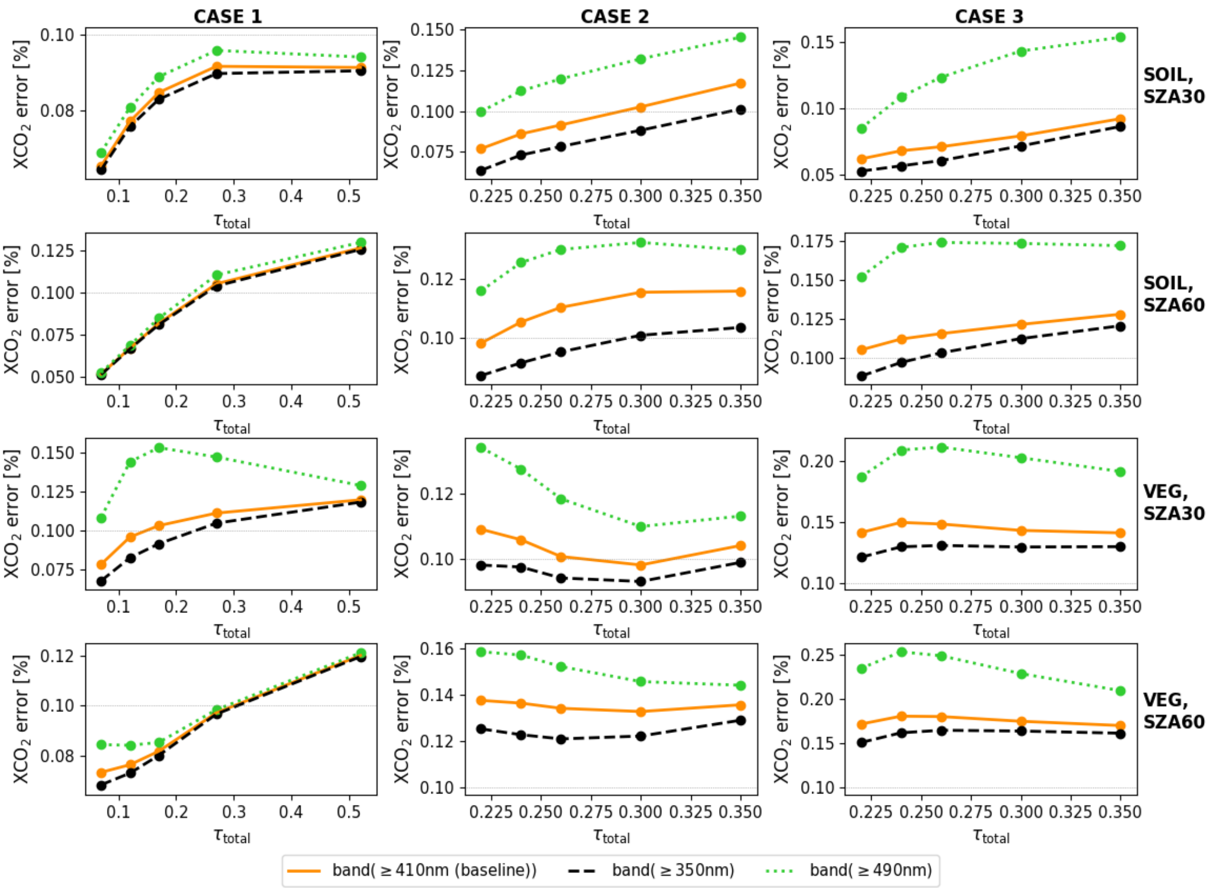

Figure 8: Performance comparison among the baseline, ≥350nm, ≥490nm setups of MAP-band, represented by the different lines. XCO_2 errors as a function of aerosol total optical thickness is shown for all the study cases as indicated at the top and on the right side. The magnitude of the radiance and DLP uncertainties are assumed 3% and 0.003, respectively.

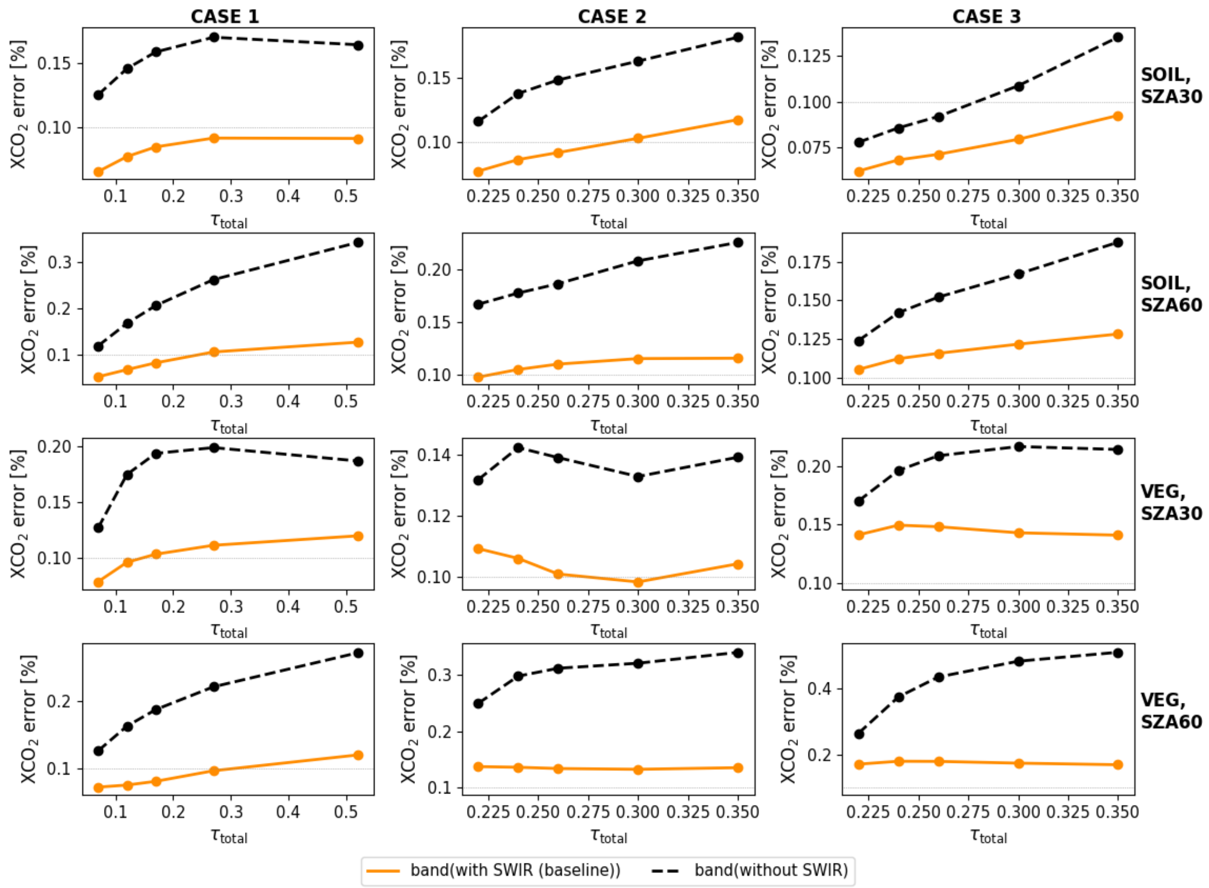

Figure 9: Performance comparison between baseline and without-SWIR setups of MAP-band, represented by the different lines. XCO2 errors as a function of aerosol total optical thickness is shown for all the study cases as indicated at the top and on the right side. The magnitude of the radiance and DLP uncertainties are assumed 3% and 0.003, respectively.

6.2.5 Alternative setups to MAP-band

Given the analysis regarding the spectral/wavelength range in section 6.1.4 and 6.2.4, it appears that the SWIR channels hold a greater importance in the MAP-band than in the MAP-mod concept. We experiment with the possibility of removing the SWIR channels in MAP-band without compromising the retrieved XCO2 accuracy significantly. This is done by increasing the number of viewing angles to a point where the total number of measurements approximately matches that of the baseline setup of MAP-mod. The total number of measurements in the baseline MAP-mod is used as reference here because in this setup SWIR channels are not present. The baseline MAP-mod has a total of 480 measurements. With only 6 wavelengths (after the removal of SWIR bands), 40 viewing angles are needed to arrive at the same number of measurements (this setup is referred to as 'band40' in the rest of this document). The resulting XCO_2 errors as a function of optical depth is shown in Figure 10. The plots show that the XCO_2 errors obtained using the setup 'band40' are comparable with those obtained using the baseline setup of MAP-mod or MAP-band. This means that the substantial loss of performance when SWIR channels in MAP-band are removed can be prevented by adding more viewing angles.

We extend this experiment to investigate what we call the hybrid setup. Here we increase the number of wavelengths and decrease the number of viewing angles while maintaining approximately the same total number of measurements as the baseline MAP-mod or as the band40 setup (i.e. 480). More specifically, this hybrid setup has 11 wavelengths (at 410, 440, 465, 490, 520, 550, 610, 669, 735, 800, 863 nm), at which both radiance and DLP are measured, and 21 viewing angles (equally spaced from -60 and 60 degrees and includes nadir). The total number of measurements is then equal to 462. It is shown in Fig. 10 that the hybrid setup results in XCO2 errors that are very similar to those in the band40 setup.
To summarize, there are 3 possible implementations for the MAP-band concept. The first is the baseline setup with 8 wavelengths that include SWIR. The second is the removal of 2 SWIR wavelengths while having 40 viewing angles (band40), and the third solution is the setup with 11 wavelengths and 21 viewing angles (hybrid). One common feature here is the total number of measurements that is kept approximately the same.

6.2.6 Inclusion of 753-nm wavelength

To allow for a cross-calibration between MAP and the CO_2 instrument, radiance measurement at a common wavelength is needed. This particular wavelength is expected to be at 753 nm. We investigate the accuracy of XCO_2 when this wavelength is used in place of one the 6 wavelengths in the band40 setup. For this exercise we experiment with replacing the last three wavelengths (555, 669.9, 863.4 nm), with 753 nm one by one, keeping the viewing angles and the total number of measurements in the band40 setup intact. It is assumed that both radiance and DLP are measured at 753 nm.
XCO_2 errors are plotted as a function of aerosol optical depth for the different sets of wavelengths in Figures 28 and 29. Fig. 11 shows that having 753nm replace 670 nm degrades the performance noticeably for the vegetation scenes. The surface albedo for vegetation at 753nm is high, resulting in small DLP and this appears to have a negative effect on the XCO_2 accuracy. Fig. 12 compares the other two sets of wavelengths where we
replace either 550 nm or 863 nm with 753 nm. It is evident that in most of our study scenarios, replacing 550 nm leads to smaller XCO_2 errors compared to substituting 863 nm. It can then be concluded that among the three wavelengths (550, 670, 865 nm), replacing 550 nm would deliver the highest XCO_2 accuracy.

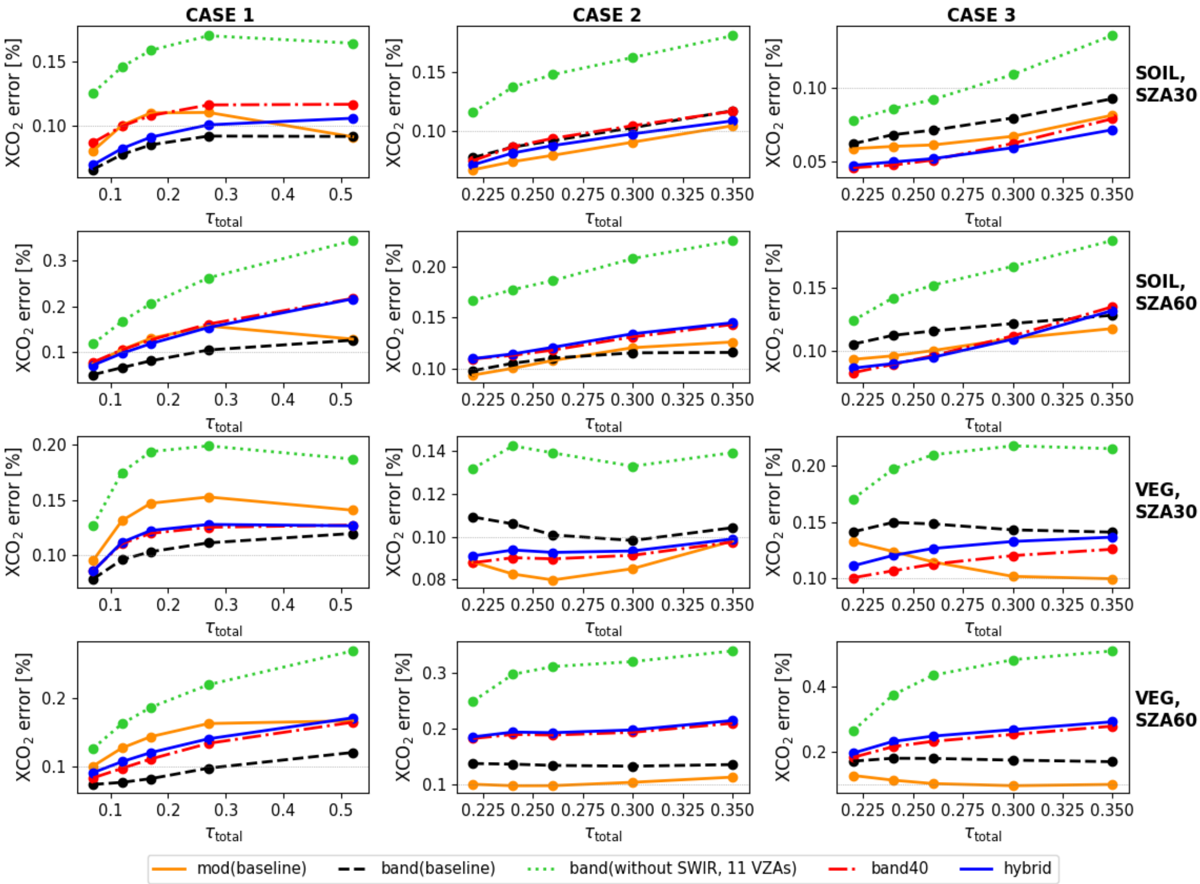

Figure 10: Performance comparison among the baseline setups, without SWIR, and the alternative setups without SWIR, represented by the different lines. XCO_2 errors as a function of aerosol total optical thickness is shown for all the study cases as indicated at the top and on the right side. The magnitude of the radiance and DLP uncertainties are assumed 3% and 0.003, respectively.

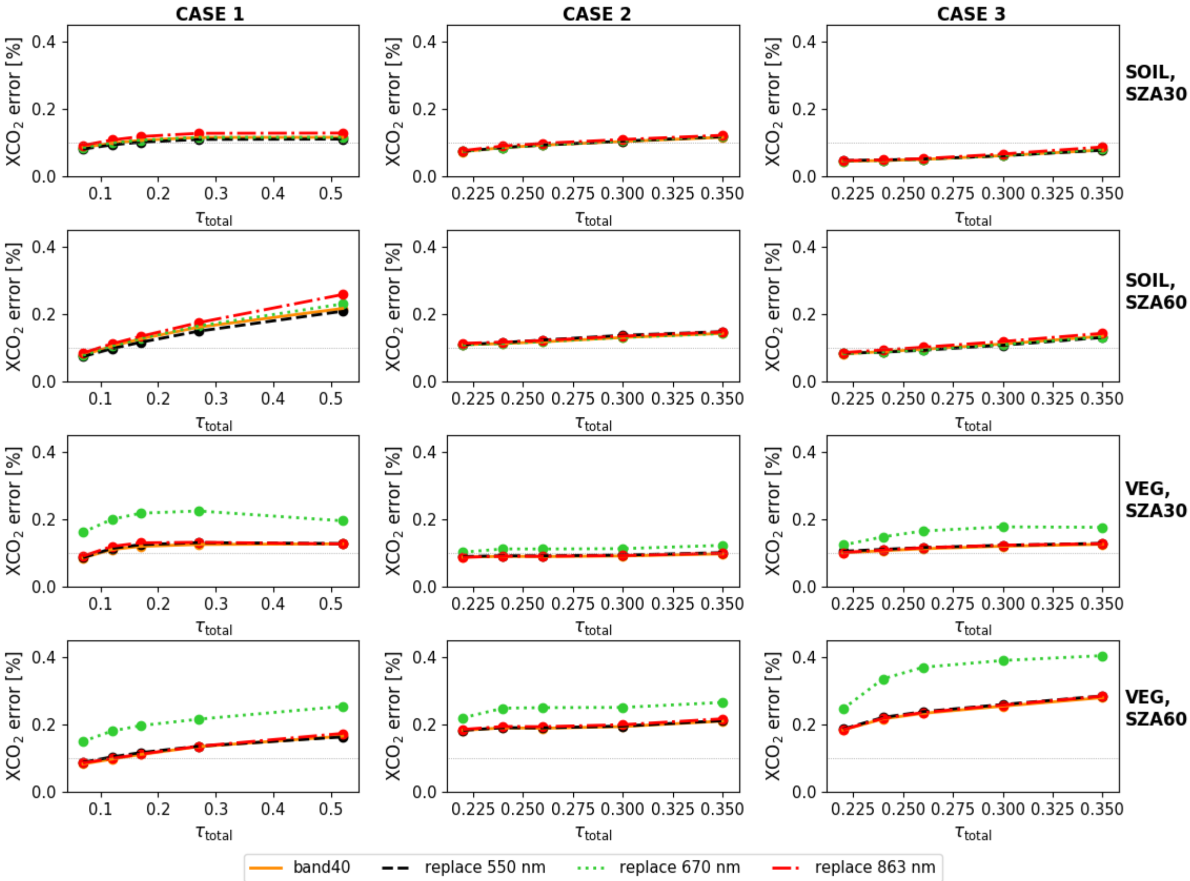

Figure 11: Performance comparison among the different bandpass selections for the band40 setup, represented by the different lines. XCO_2 errors as a function of aerosol total optical thickness is shown for all the study cases as indicated at the top and on the right side. The magnitude of the radiance and DLP uncertainties are assumed 3% and 0.003, respectively.

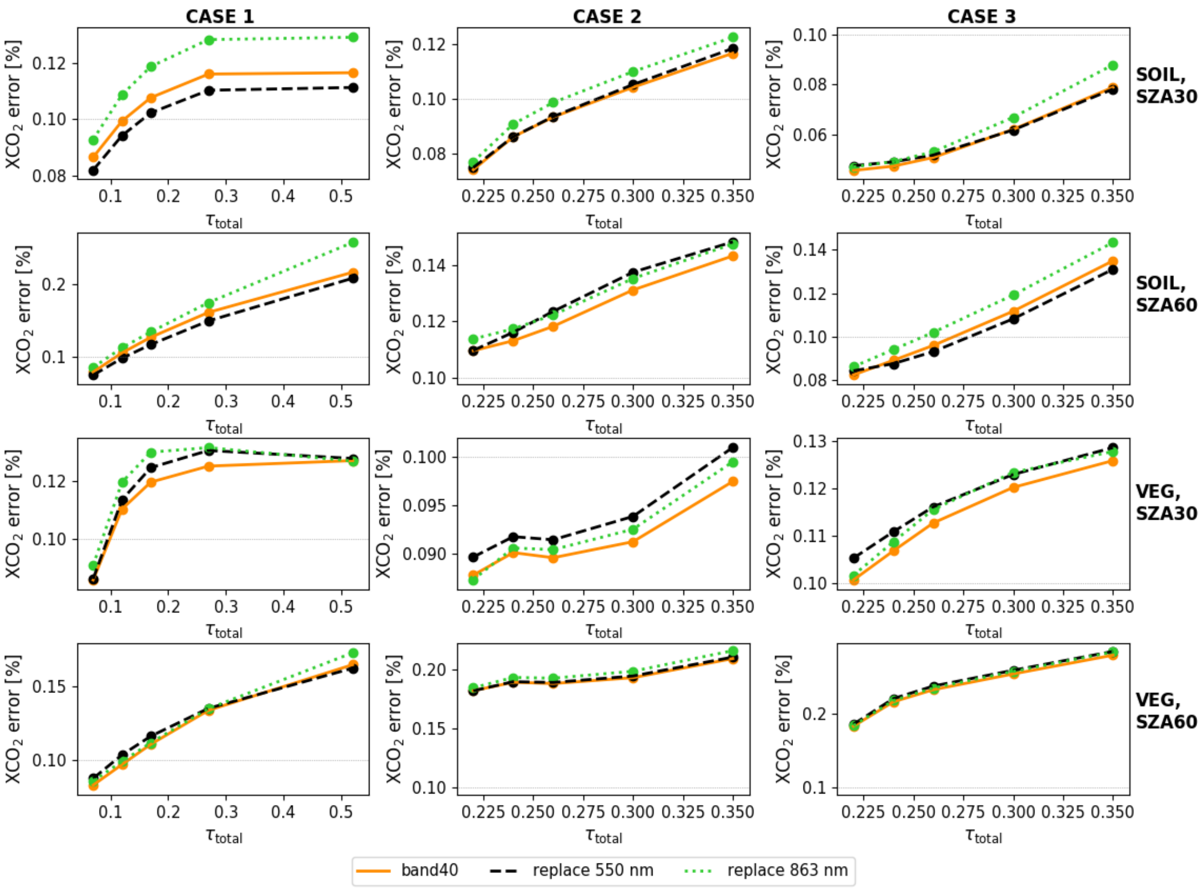

Figure 12: Performance comparison among the different bandpass selections for the band40 setup, represented by the different lines. XCO_2 errors as a function of aerosol total optical thickness is shown for all the study cases as indicated at the top and on the right side. The magnitude of the radiance and DLP uncertainties are assumed 3% and 0.003, respectively.

6.3 Spatial oversampling

To estimate the error induced by spatial resampling of radiance and polarization measurements, we consider two scene examples: first a randomized chess-board scenario and second a Sentinel-2 scene in the Northwest of Shanghai.

6.4 Chess-board scenario

The chess-board scenario assumes a 16×16 km^2 spatial domain with an underlying sampling of 20×20 m^2, which are combined to 300×300 m^2 homogeneous spatial scenes. The fine 20×20 m^2 sampling is required by the convolution of the top-of-atmosphere (TOA) radiometric quantities to the spatial resolution of the MAP instrument. Next, we assume that the scene consists of a randomly assigned radiometric pattern of three reference spectra, calculated for five different viewing angles, VZA = 0, ±40, ±60 degrees. The radiometric allocation is depicted in Fig. 13. As reference scene, we selected a vegetation, soil, and sand BDRF to describe different types of surface reflection. Figure 14 shows examples of the radiance and degree of linear polarization (DLP) spectra for VZA = +60 degree. In the remaining of the study, the radiometric scene is investigated in more detail for four wavelengths $\lambda = 350$, 450, 550, 800 nm.

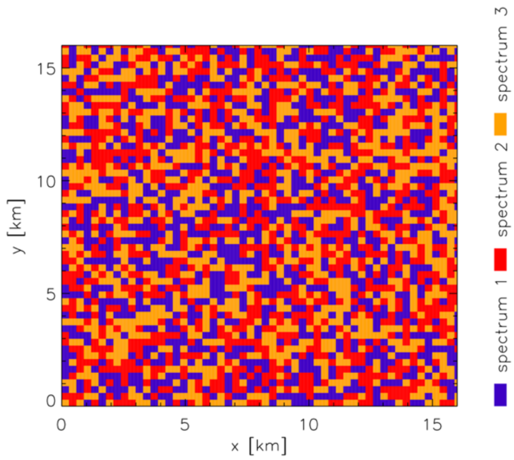

Figure 13: Randomized chess-board scenario where three radiometric scenes are randomly assigned to 300×300 nm homogenous ground scenes. In this study we assume that spectrum 1 represents a vegetation scene and spectrum 2 and 3 a soil and sand scene, respectively.

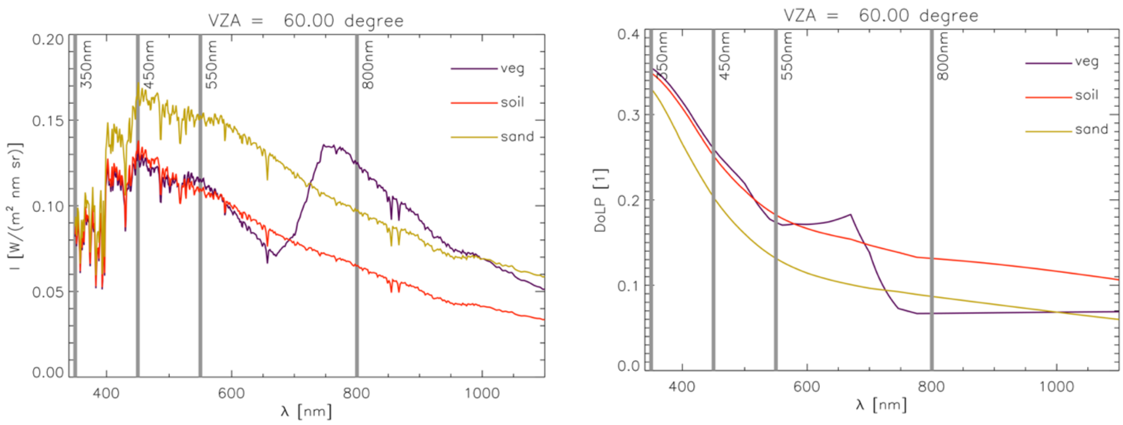

Figure 14: Radiance (left) and DLP (right) reference scene for a vegetation (veg), soil and sand surface BDRF. The depicted simulations are performed for a solar zenith angle of 50 degree and a VZA = 60 degree. Four wavelength λ = 350, 450, 550 and 800 nm are selected for further investigations.

Subsequently, the TOA radiometric scene is convolved with a two-dimensional Gaussian to degrade the scene to the spatial resolution of the MAP. Currently, we assume a full width at half maximum (FWHM) of 2 km in both spatial dimensions. Figure 15 shows the smoothed radiometric scene sampled on a 20×20 m spatial grid.

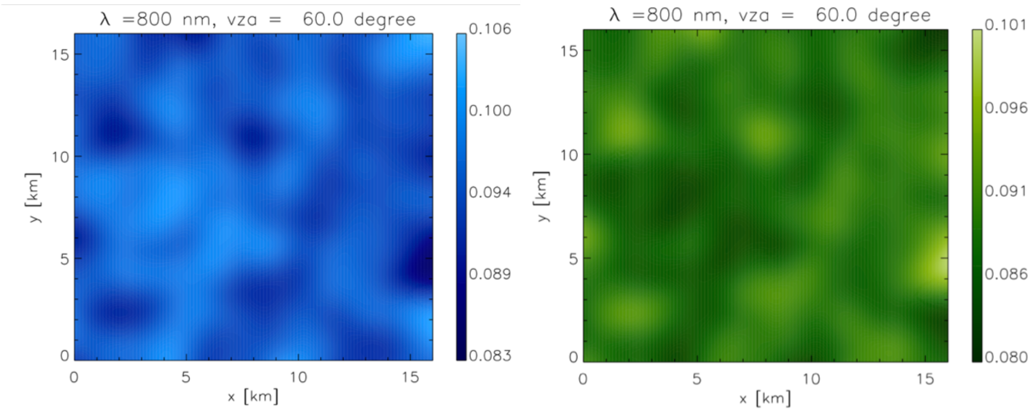

*Figure 15: Convolved radiance (left) and DLP (right) radiometric scenes for **λ** =800 nm and VZA = 60 degree.*

Obviously, the MAP measurements will be sampled on a much coarser grid and based on the generated data set any sampling scheme can be applied. This study considers two regular sampling schemes with a sampling distance of 2 km (1 FWHM) and 1 km (0.5 FWHM), so a spatial oversampling ratio of 1 and 2 in both spatial directions. Subsequently, the sampled data set is used as input for a bilinear interpolation scheme to fill the gaps between the sampling point. Thus, comparing the interpolated radiance scene with those of Fig. 14 can be used to estimate resampling error of this simple scheme. Figure 15 shows an example of the resampling error of the radiance and DLP fields for a VZA of 60 degree at 800 nm for the two sampling distances. Errors are substantial, exceeding ±4 % in the radiance and ±0.004 in the DLP. Enhancing the sampling ratio to 2 reduces the error significantly with a resampling error ≤ 2 % in the radiance field and ≤0.001 in the DLP field.

Finally, Fig. 16 summarizes the resampling error for the chess-board experiment. It shows the maximum and the error standard deviation for the ensemble of resampled radiance and DLP error for all VZAs and for the different wavelengths. Considering the standard deviation as the relevant quantity to formulate MAP requirements, we conclude that for the sampling ratio of 1, errors are too large requiring too large contribution from the radiometric error budget. However, for a spatial oversampling ratio of 2, the induced radiance error standard deviations are < 0.5 % and the corresponding DLP errors are <0.0006, which is acceptable.

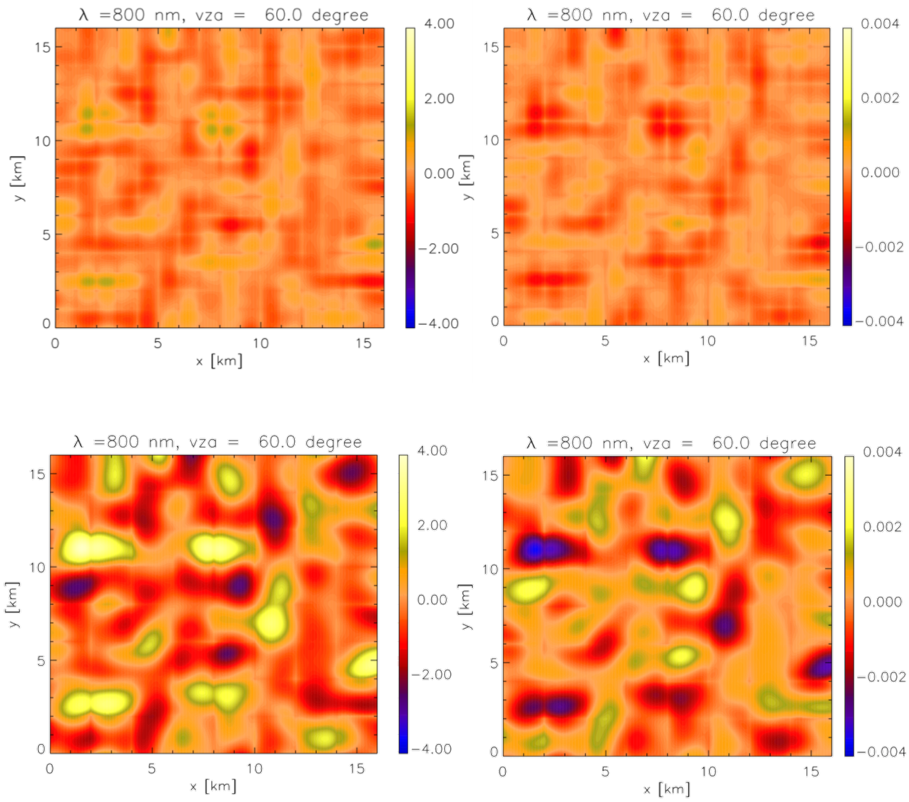

Figure 16: Resampling error for the radiance (left) and DLP (right) for an oversampling ratio of 2 (upper) and 1 (lower).

6.5 Sentinel 2 scenario

The chees-board experiment has a major shortcoming. The radiometric gradients of the ensemble are randomly selected and so introduces a certain arbitrariness in our analysis. To address this problem, a first preliminary analysis was performed for the scenario observed by Sentinel-2 around Shanghai, depicted in Fig. 17. It comprises nine tiles of surface albedo around 780 nm (band 7), which is used to derive a near-infrared (NIR) surface albedo map for the surrounding of Shanghai with a spatial sampling of 20×20 m^2, shown in Fig. 18. The ensemble is much too large for any analysis of the resampling error, and so we selected an area in the Northwest of Shanghai for further investigation. Figure 18 shows the RGB zoom-in region given by the Apple maps service and the corresponding S2 data and indicates that the area includes mainly crop vegetations with a village in the upper left corner.

To assign model spectra to each Sentinel-2 pixel depending on the NIR albedo, we simulated vegetation reference spectra assuming the surface BDRF

$$BDRF(\lambda, \vartheta_{in}, \vartheta_{out}, \Delta\varphi) = A(\lambda) + \sum_{i=1}^{2} f_i \; R_i(\vartheta_{in}, \vartheta_{out}, \Delta\varphi)$$

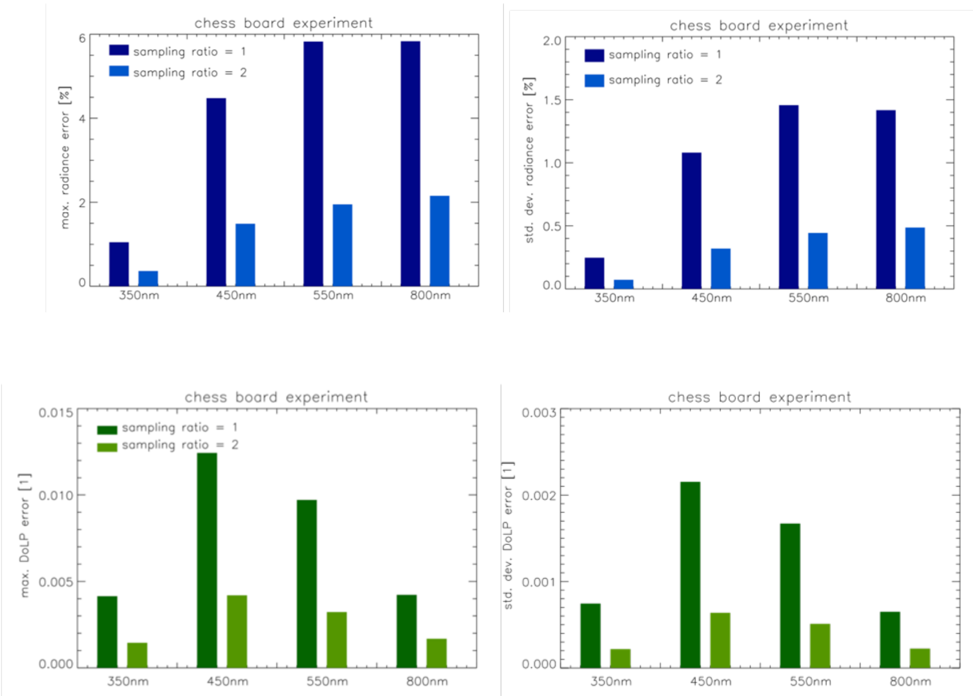

Figure 17: Overview of the resampling errors for the chess-board experiment for all VZAs and the two sampling ratios as indicated in the legend. Maximum error (left), error standard deviation (right), radiance (top) and DLP (bottom).

which comprises the two spectral independent vegetation kernels R_1 and R_2 with corresponding weights f_i. Here, $A(\lambda)$ is the spectral dependent Lambertian albedo. Using this model for surface reflection, we calculated reference spectra scaling the albedo term to cover the range 0.0< $A(\lambda_{NIR}) < 1.0$ in steps of 0.025. Figure 19 illustrates two examples for an NIR surface albedo of 0.10 and 0.25. With the albedo map of Fig. 18, we can assign to each ground pixel a corresponding model spectra and so could generate radiometric scenes, which corresponds to the spatial scales as observed by Sentinel-2.

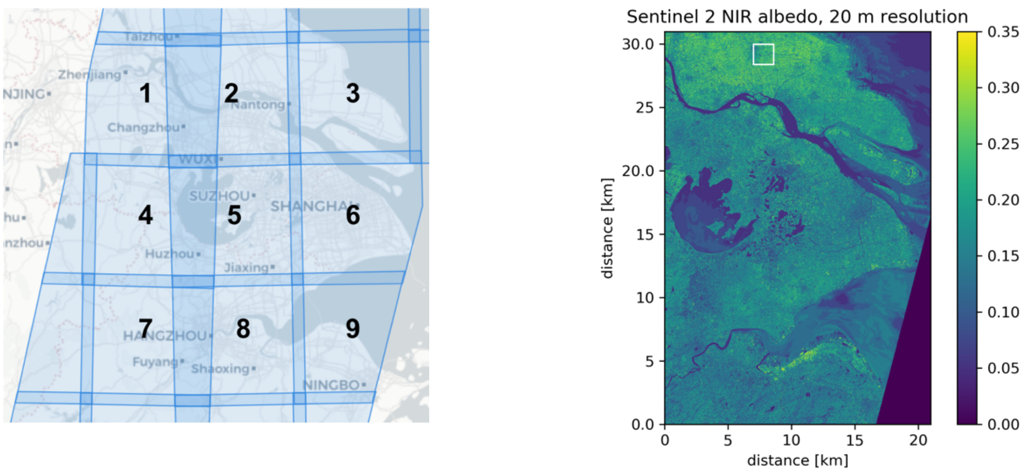

Figure18: (Left) Nine Sentinel-2 tiles over the Shanghai region (right) Sentinel 2 NIR albedo.

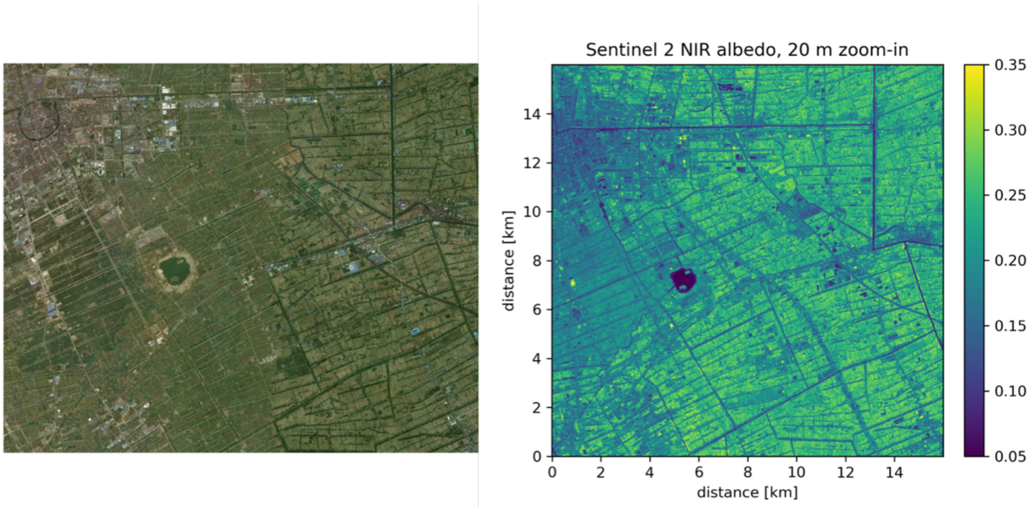

Figure 19 (Left) RGB Apple map service image of the zoom-in, (right) Sentinel 2 NIR albedo for zoom-in.

Finally, we apply the same analysis as already described Sec. 2. Figure 21 shows the 800 nm radiance scene on Sentinel 8 resolution, convolved with the two-dimensional Gaussian response function, and resampled with a spatial sampling ratio of 1 and 2, analogous to Sec. 7.6.1.

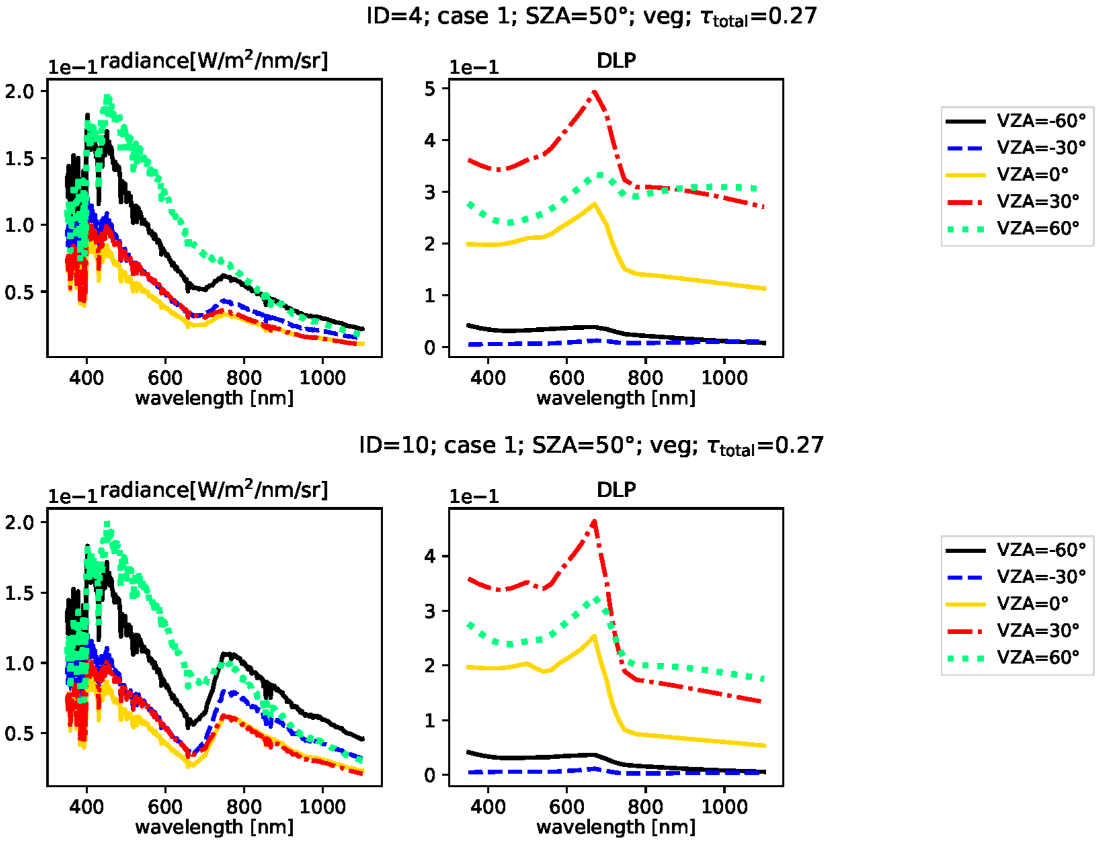

Figure 20: Example of MAP reference spectra for five viewing angles 0, ±30, ±60 degree and two NIR albedo values 0.1 (top) and 0.25 (bottom).

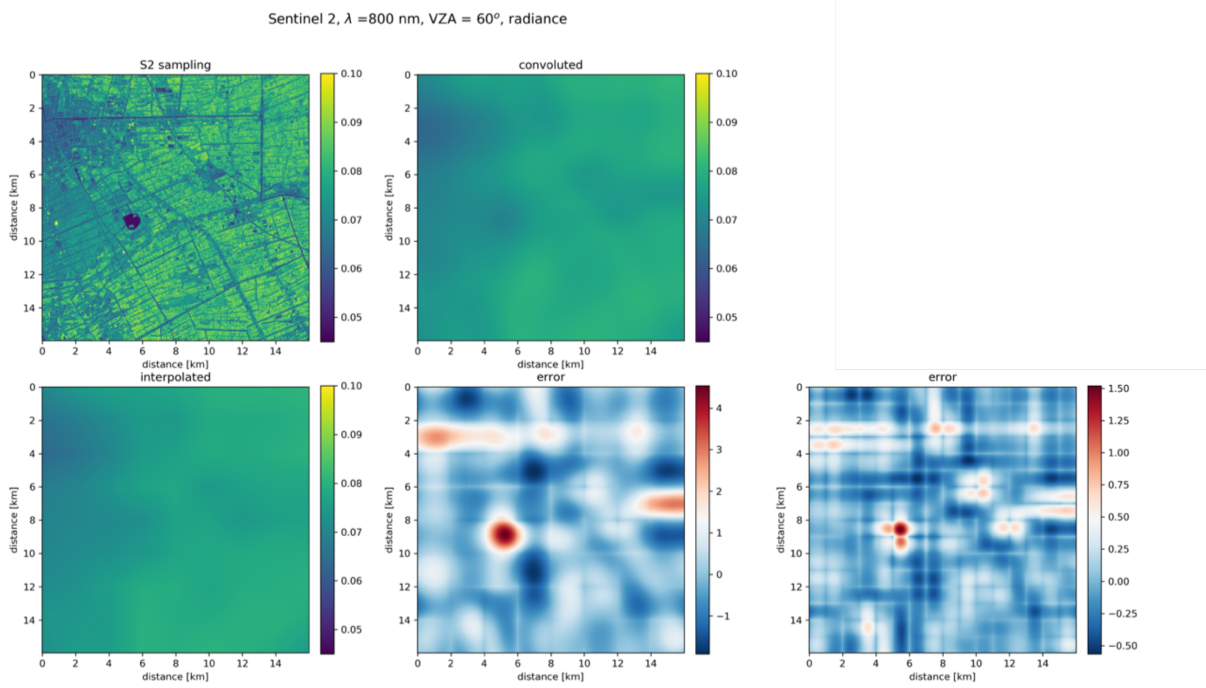

Figure 21: Radiance resampling error for the Sentinel 2 ensemble of Fig. 18. (Top left) Radiance ensemble at 800 nm and for a VZA of 60 degree [W/(m^2 nm sr)], (top middle) convolved radiances assuming a 2D Gaussian spatial response of the MAP instrument with a FWHM of 2 km in both dimensions, (bottom left) resampled radiances assuming an spatial oversampling ratio of 1 in both directions, (bottom middle) radiance resampling error for an oversampling ratio of 1, (bottom right) radiance resampling error for an oversampling ratio of 2.

For a sampling ratio of 1, the mean error is 0.048 % with a standard deviation of 0.79 % whereas for a sampling ratio of 2 the mean error is 0.008 % with a standard deviation of 0.23 %. Thus, the error standard deviation is about a factor 2 smaller than for the chess-board experiment. Figure 21 shows the corresponding results for the sampling error of DLP. Also for the polarization measurements a spatial oversampling ratio of 2 is required to reduce the resampling errors of up to 0.01 to the required accuracy range <0.02.

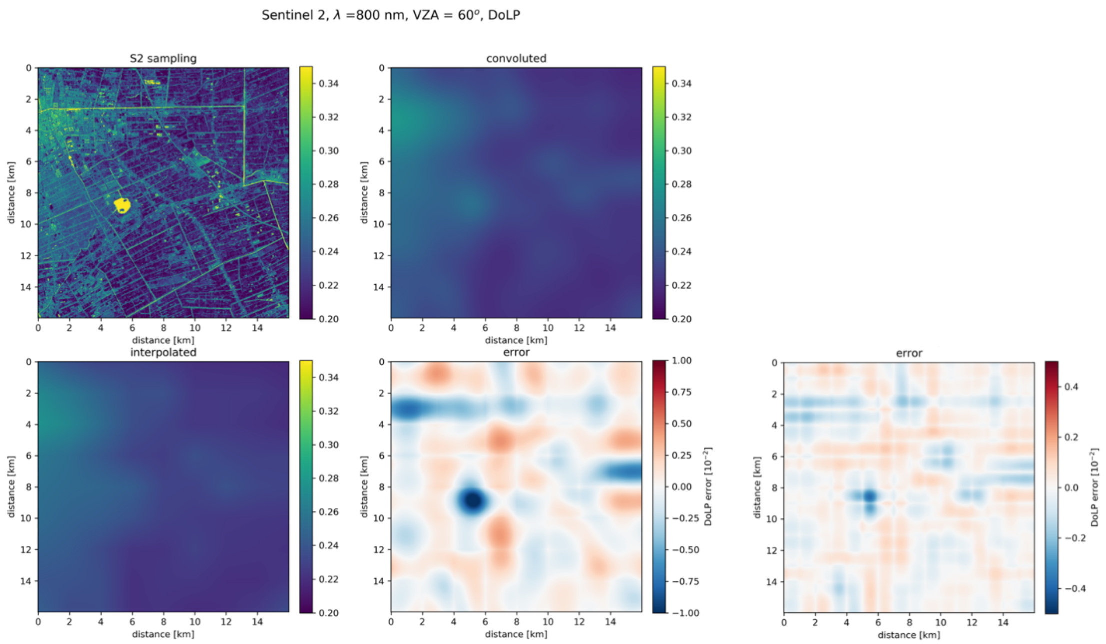

Figure 22: Same as Fig 37 but for DoLP.

6.6 Relative pointing accuracy

To evaluate the relative pointing accuracy, we consider a spatial displacement of the Sentinel 2 ensemble introduced in Sec. 7.6. Figure 22 shows the induced radiance and DLP error due to a spatial shift in the horizontal dimension of the image by $\delta x = 600$, 400 and 200 m. Here, the radiance error standard deviation is 1.07, 0.72, 0.36 %, and the DoLP error is 0.0026, 0.0018, 0.0009. For a corresponding scene displacement in the vertical dimension, we obtained 0.82, 0.55, 0.28 % radiance error standard deviations and 0.0020, 0.0014, 0.007 DoLP error standard deviation. Considering the technical feasibility of a relative pointing accuracy of 200 m, we propose a tightening of the corresponding MRD requirement to 200 m keeping at the same time the contribution to the overall error budget as little as possible.

6.7 ISRF Knowledge Requirement

Overall, the ISRF knowledge is less relevance for the MAP instrument than for the CO_2 spectrometer. To demonstrate this, we consider radiance error induced by ISRF knowledge errors between 1 % and 6 % as depicted in Fig. 23. The induced radiance error increases from 0.02 % to 0.14 % with a maximum error between 0.1% and 0.6 % at the Calcium K and L Fraunhofer lines at 382 nm and 393 nm (see Figure 20). We consider this error as a minor contribution to the total error budget and thus propose an overall knowledge error of the ISRF to be better than 4 % of its maximum value, which causes a standard deviation of the radiance error of 0.1%.

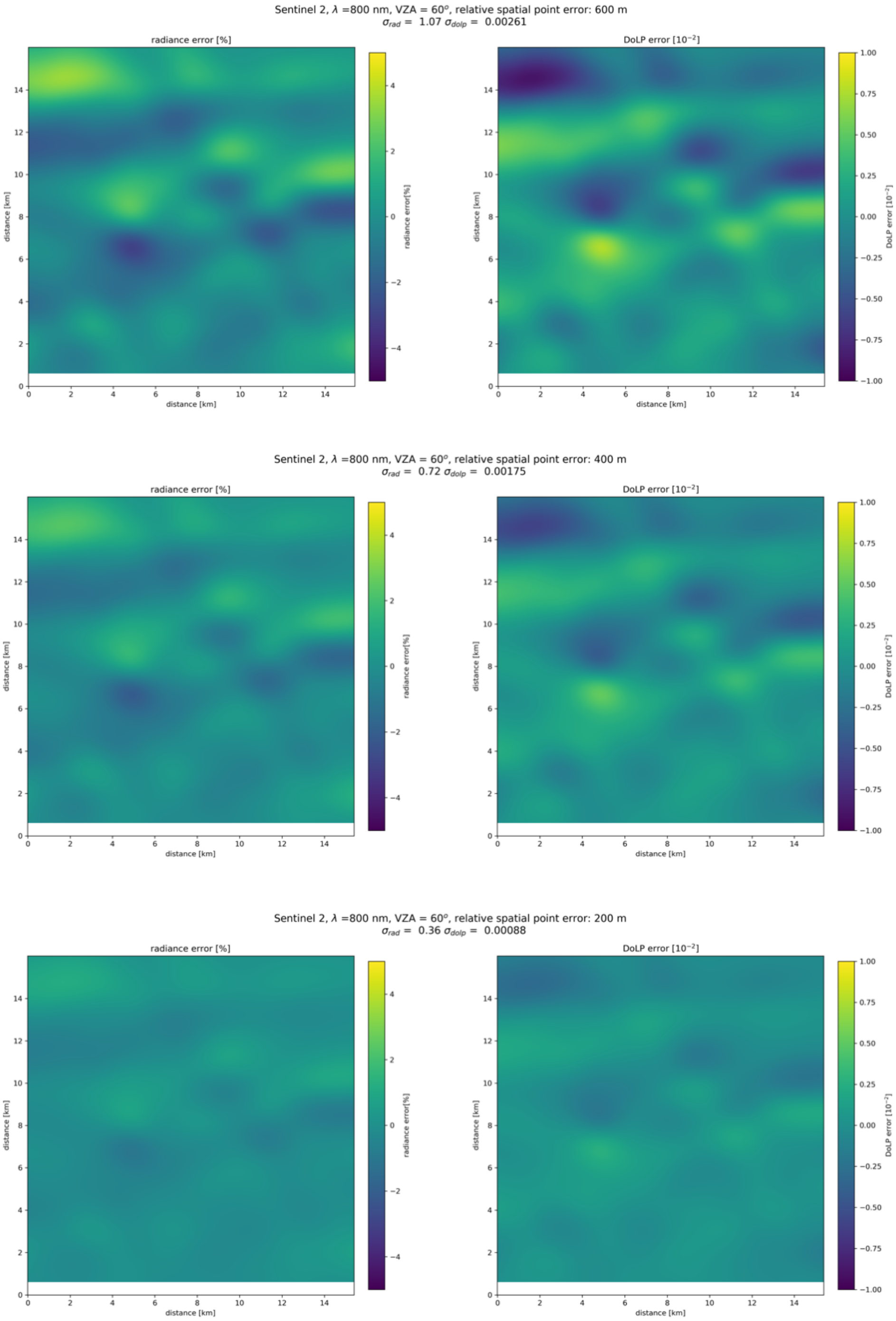

Figure 23: Radiance (left) and DLP (right) error due to a horizontal spatial displacement of the Sentinel-2 scene by 600m (top), 400m (middle), 200m (bottom).

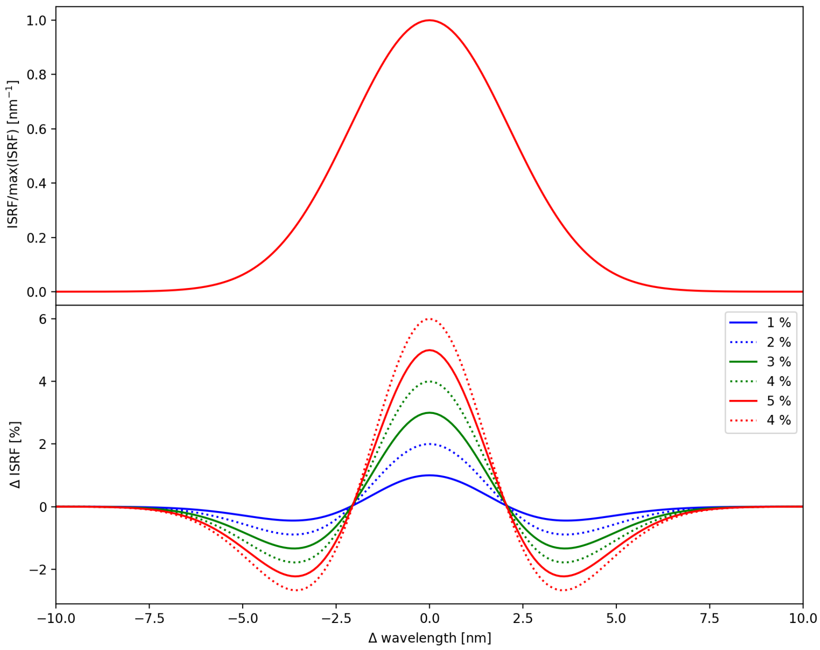

Figure 24: ISRF distortion. (Top) Gaussian ISRF with a FWHM of 5 nm and (bottom) different ISRF distortions with knowledge error between 1-6% (bottom).

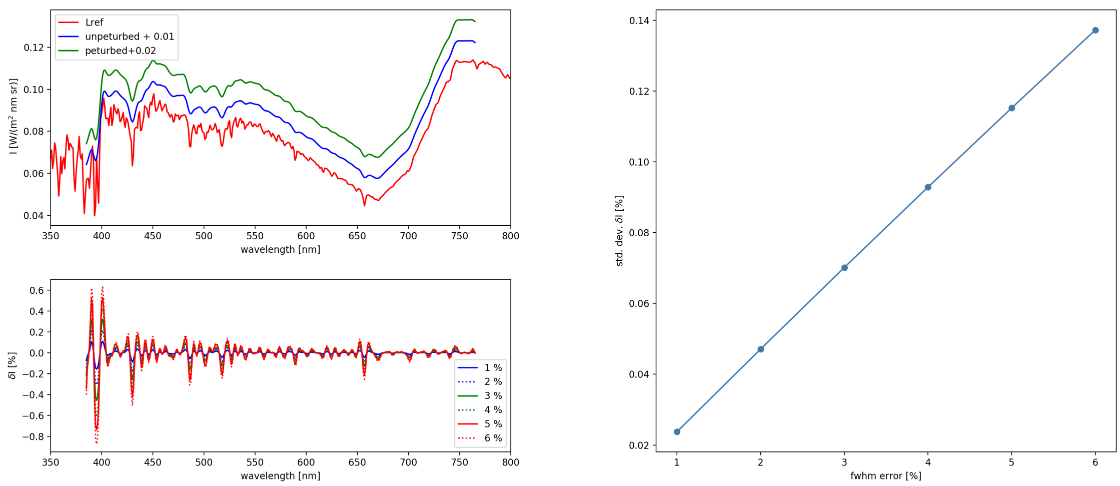

Figure 25: (Left) Radiance error due to ISRF knowledge error shown in Fig. 24. (Right) Standard deviation of the ISRF radiance error as a function of the ISRF knowledge error.

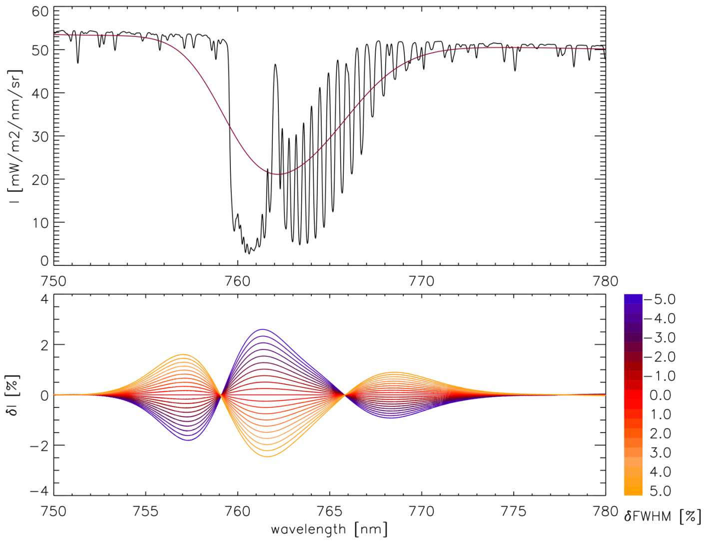

Figure 26: MAP-mod radiance error in the NIR. (Top) Simulation of the MAP-mod radiance measurement from line-by-line radiance simulation assuming a spectral resolution of 5 km. (Bottom) Radiance errors for errors in the FWHM of the ISRF between ±5 % calculated with respect to the maximum radiance in the spectrum.

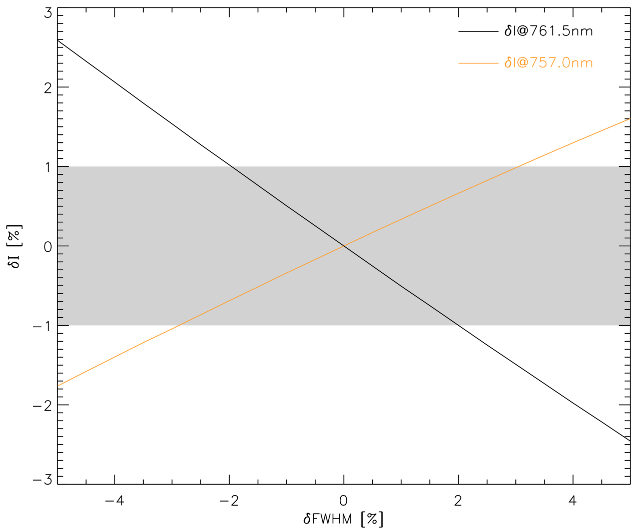

Figure 27: MAP-mod radiance error at 761.5 nm and 757.5 nm as a function of the FWHM error.

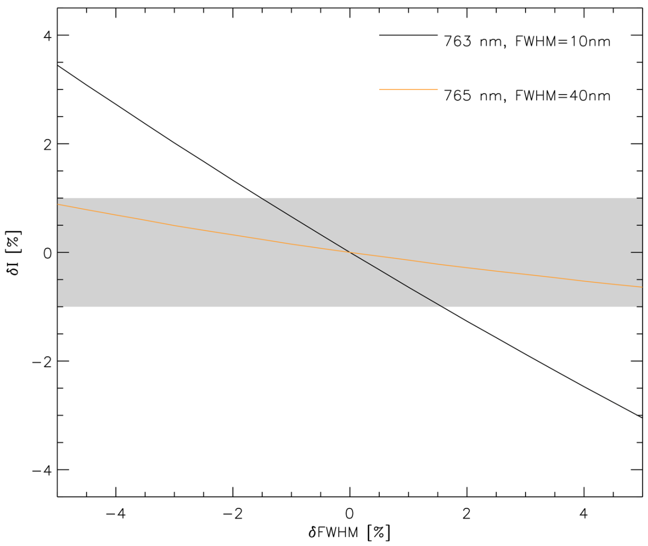

Figure 28: Same as Fig. 27 but for band 6 and 7 of the MAP-band concept as defined in MRDv1.0.

Particular attention must be given to the ISRF knowledge in the NIR. Here measurements around the O_2 A band are intended to be used for cross calibration between the CO_2 and MAP instrument. In the light of the required accuracy of the MAP radiance measurements of 3 %, we assume that radiance errors induced by ISRF knowledge uncertainties must be < 1%, which leads to a dedicated requirement on the ISRF knowledge of the MAP instrument in the spectral range of the O_2 A band. Figure 42 shows the ISRF induced radiance error due to uncertainties between ±5% in the FWHM of the ISRF. Here, the radiance error, given with respect to the continuum value, shows maxima at the center and in the wings of the O_2 A band. Hence, considering the error at 761.5 nm and 757.5 nm in Fig. 28, we conclude that the FWHM of the ISRF must be known with an accuracy of 2 % for instrument cross calibration. The analogous analysis of the MAP-band concept is shown in Fig 28 and results in same requirement for band 6 with the narrow bandwidth of 10 nm. For band 7 with a bandwidth of 40 nm a knowledge requirement of 4 % is sufficient.

7 Summary and conclusions

The CO2M requirements of the MAP instrument have been analyzed with respect to the XCO2 performance. The analysis accounts for two different instrument concepts using the spectral modulation technique and bandpass polarimetry.

For the modulation concept, we conclude that the radiance uncertainty must be < 3 % and the DLP uncertainty < 0.0035. We have broken down this requirement to a radiance precision and bias requirement to be <1.7 %, and a DLP precision and bias requirement to be < 0.0025. The instrument must measure radiance and DLP in at least 5 viewing angles in the spectral range 385-765nm.

For the bandpass concept, the same radiometric requirements hold, i.e. the radiance uncertainty must be < 3 % and the DLP uncertainty < 0.0035 with a breakdown to radiance precision and bias requirement to be <1.7 % and a DLP precision and bias to be < 0.0025. This instrument concept must measure radiance and

DLP in a least 21 viewing angles at 11 wavelengths (410, 440, 465, 490, 520, 550, 610, 669, 735, 800, 863 nm). For instrument cross calibration it is desirable to have one particular measurement at 753 nm. In case an already existing band must be omitted for this implementation, replacing the 550 nm has the smallest impact on the CO2M performance.

Independent on the MAP concept, the radiance and polarization measurements must the spatially resampled, both for a consistent interpretation of the different viewing angles and for a co-alignment with the CO2 measurements. For this purpose, a spatial oversampling of a factor 2 is required.

Aerosol induced XCO_2 errors: A literature review

Jochen Landgraf
SRON Netherlands Institute for Space Research

Abstract: Absorption spectroscopy generally, in particular CO_2 remote sensing from the shortwave infrared spectra range requires knowledge of the light path through the atmosphere to properly interpret the depth of the telluric absorption features of Earthshine radiance spectra. The very demanding CO_2 requirements on accuracy to be better than 0.5 ppm can only be realized after strict cloud filtering of the data and therefore the effect of atmospheric aerosol and optically thin cirrus is only relevant for the retrieval of CO_2. In this review, we summarize study results on the aerosol induced error and on different mitigation approaches.

Table of Contents

1 Introduction

The first dedicated mission observing CO_2 by means of space-borne measurements in the shortwave infrared range of the solar spectrum was the Greenhouse Gases Observing Satellite (GOSAT, Yokota et al., 2004), which is in orbit since 23 January 2009, while the Orbiting Carbon Observatory (OCO, Crisp et al., 2004) suffered from a launch failure on 24 February 2009. The spectral measurements comprise three spectral bands including the O_2 A band at 765 nm (NIR), the moderate strong CO2 absorption bands at 1.61 μm (SWIR-1) and the corresponding strong absorption band at 2,06 μm (SWIR-2) depicted in Fig. 1. Here, the SWIR-1 band provides information on the vertically integrated amount of CO_2, whereas the NIR and SWIR-2 band are used to infer effective aerosol parameters to characterize the atmospheric light path. Moreover, the SWIR-2 band also constrains the CO_2 column amount and its precision. Considering the complexity of atmospheric aerosol given by its diverse chemical composition, size and shape, several microphysical parameters are required to characterize its optical properties. Typically, the three-band concept allows to infer 2-3 effective aerosol parameters, depending on surface albedo, which are by far not sufficient to fully describe all aerosol properties. Although the main aerosol effect on the light path can be captured by this concept, an aerosol induced XCO_2 error remains, which is the subject of this review. Section 2 summarizes estimates of the aerosol induced error using simulated measurements. Results from OCO-2 measurements is the subject of in Section 3 including different bias corrections for error mitigation. Finally, Section 4 describes mitigation strategies using supplementary measurements of a cloud imager and Section 5 summarizes results of an error sensitivity study of a multi-angle radiance concept. Section 6 summarizes our literature review.

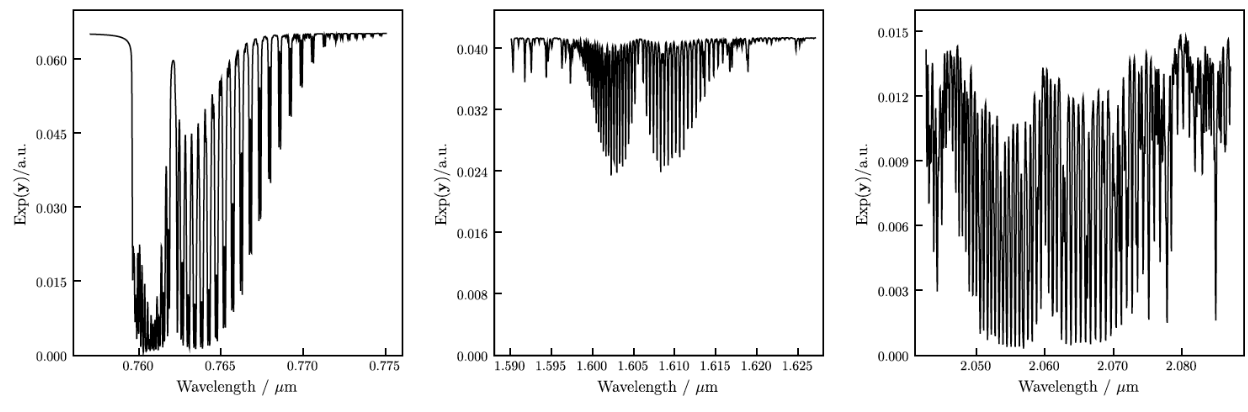

Figure 1: GOSAT and OCO-like exemplary spectra of the O2 A band (left panel), the moderately strong absorbing CO2 band (middle panel), and the strongly absorbing CO2 band (right panel). Spectra are modelled for a grass surface observed at nadir and solar zenith angle 30° (Fig 1 from Butz et al., 2009).

2 Aerosol induced error: An estimate using simulated measurements

The XCO_2 aerosol induced error was discussed in detail by Butz et al., 2009 for the RemoTeC algorithm and O'Dell et al., 2012, for the ACOS algorithm, which is used for operational data processing of OCO-2. Figure 2 shows the RemoTeC XCO_2 error as a function of the aerosol scattering optical depth for a non-scattering retrieval, i.e. a retrieval which does not account for any atmospheric scattering. Already for aerosol optical depth (AOD) < 0.05 the XCO_2 error exceeds the 1 % level, which is indicated by the dashed lines. Retrieving effective aerosol properties by the 3-band RemoTeC approach mitigates XCO_2 errors significantly, such that for AOD < 0.30 the XCO2 error stays within a 1 % error range. However, for the stringent CO2M requirement the XCO2 performance is not compliant for any AOD. These early findings are confirmed by the results of WP-2200 of this study. Obviously, the non-scattering error is a direct consequence of light scattering in the atmosphere and so the enhancement of the light path by aerosols. Thus, non-scattering errors and the remaining aerosol induced error of the full-physics 3-band approach correlate and in a certain sense, the non-scattering XCO_2 error is a proxy for aerosol induced errors in the XCO_2 data product.

Figure 3 shows the corresponding results using the operational OCO-2 algorithm ACOS for a test data set of OCO radiance simulations of 10 orbits with a total of 6522 soundings over land. The upper panel depicts the aerosol induced error for a non-scattering retrieval and shows an increase in the XCO_2 error with increasing AOD, which can be improved by the retrieval of effective aerosol properties as indicated in the lower panel of figure. Although in the meantime both algorithms have been improved in the performance, overall, we can conclude that with the current 3 band retrievals, the CO2M mission requirement on XCO_2 accuracy cannot be met without any further mitigation effort.

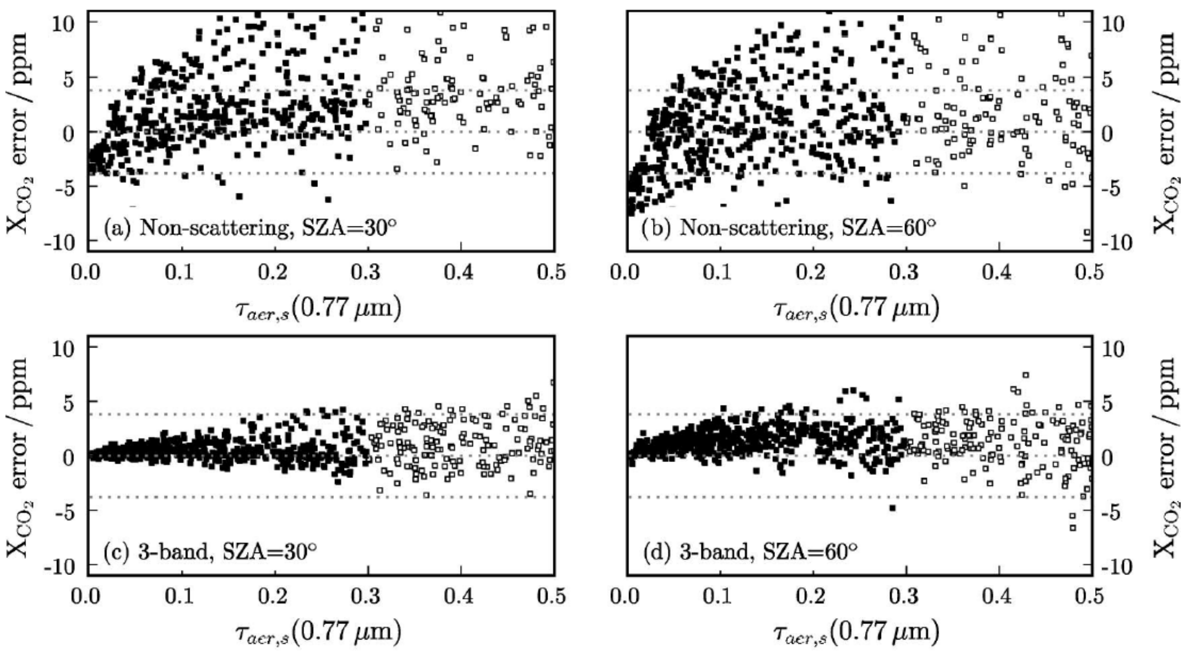

Figure 2: Aerosol induced error for a non-scattering retrieval from GOSAT and OCO-like measurements (top panels) and for the RemoTeC 3-band retrieval (Fig. 8 in Butz et al, 2009)

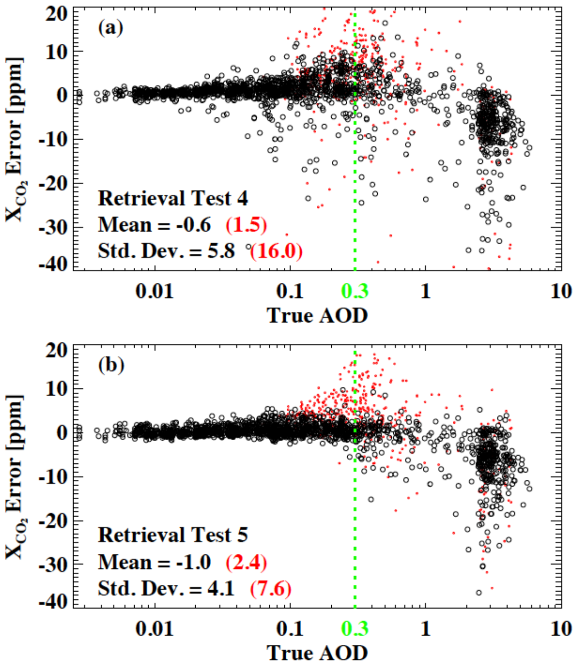

Figure 3: XCO_2 retrieval error as a function of aerosol optical depth at 760 nm. Black and red symbols indicate data points which passed or failed the cloud filter. The upper panel shows XCO_2 error for the clear-sky retrieval (test 4), in which clouds and aerosols are not included (non-scattering retrieval), the bottom panel depicts corresponding results for the standard 3-band full-physics ACOS retrieval (Figure 8 in O'Dell et al., 2012).

From the results in Fig. 2 and 3 one may conclude that the aerosol induced XCO_2 error only become evident in a dependence on AOD. Obviously, AOD is not the only aerosol properties which describes its scattering properties but other microphysical quantities may change the induced XCO_2 error as well. Even more important is fact that the amount of aerosol information, which can be inferred from the observed spectra changes with the brightness of the surface scene. Nanda et al., 2018 showed the sensitivity of a reflectance measurement with respect to scattering height z, optical depth τ and the single scattering albedo of an aerosol scattering layer. Similar results were reported by Corradini et al., 2006 and Sanghavi et al., 2012. Figure 4 indicates clearly an albedo range between 0.2 and 0.3, where the measurement loses its sensitivity to the aerosol optical depth. As a result, prior assumptions on the atmospheric aerosol may introduce XCO_2 biases as function of the surface albedo in agreement with the findings of Aben et al., 2007. As a result, a dependence of the XCO_2 bias on surface albedo is induced in the data product.

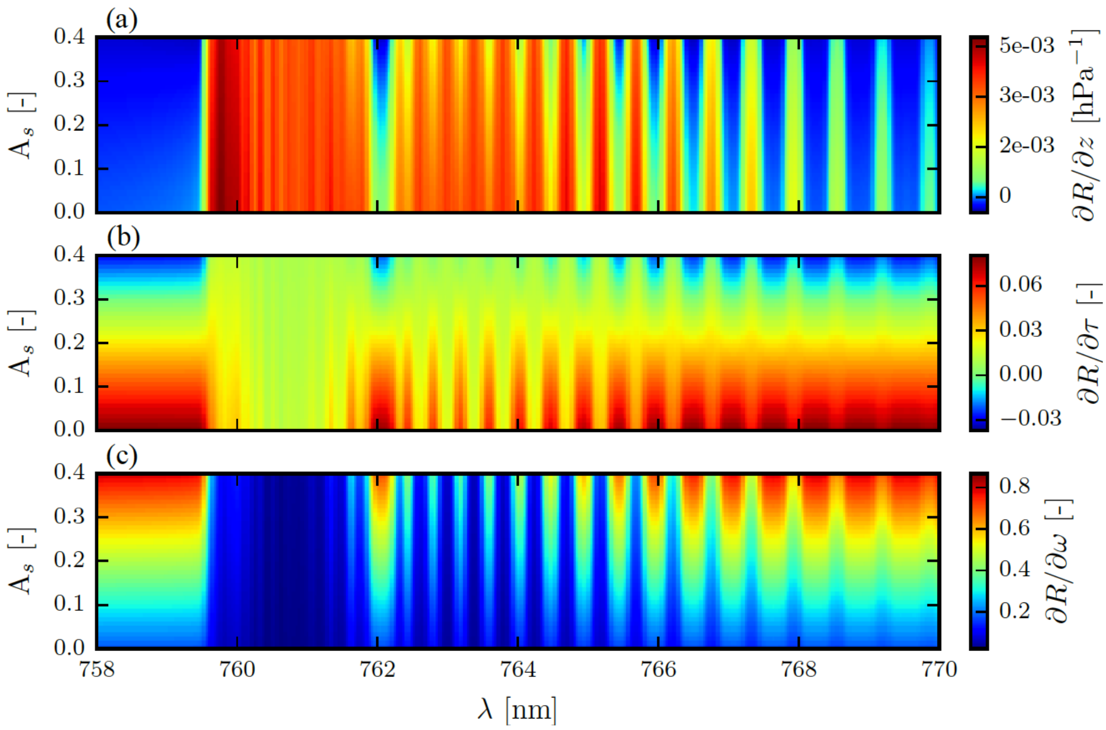

Figure 4: Derivative of reflectance with respect to aerosol properties for different surface albedos A. The z is centred around 600 hPa, with $\boldsymbol{\tau} = 1.0$ $\omega = 0.95$*, and a Henyey–Greenstein phase function with g =0.7. The solar zenith angle is 45º and the viewing zenith angle is 0º. (a) Derivative of reflectance with respect to z. (b) Derivative of reflectance with respect to τ. (c) Derivative of reflectance with respect to ω (Figure 4 in Nanda et al., 2014).*

3 Mitigation approach 1: Posteriori bias correction

To improve the data accuracy, bias corrections are considered as an essential element of the data processing. The approach relies on a data set of XCO_2 retrieval products and collocated reference measurements. Figure 5 shows the XCO_2 biases of the GOSAT RemoTeC data product with respect to TCCON reference measurements as a function of key parameters describing the algorithm performance, like the air mass, the water vapor and molecular oxygen column, the difference of the retrieved surface albedo in the NIR and SWIR-, and effective aerosol parameters (Guerlet et al., 2013). Assuming the ability to generalize the result to the overall data product, a parametrized bias correction can be derived from these results. Similar parametric bias corrections are proposed by Wunch et al., 2011, Cogan et al., 2012, Reuter 2017, Wu et al., 2018. Here a non-trivial fraction of the correction accounts for retrieval algorithm specific problems.

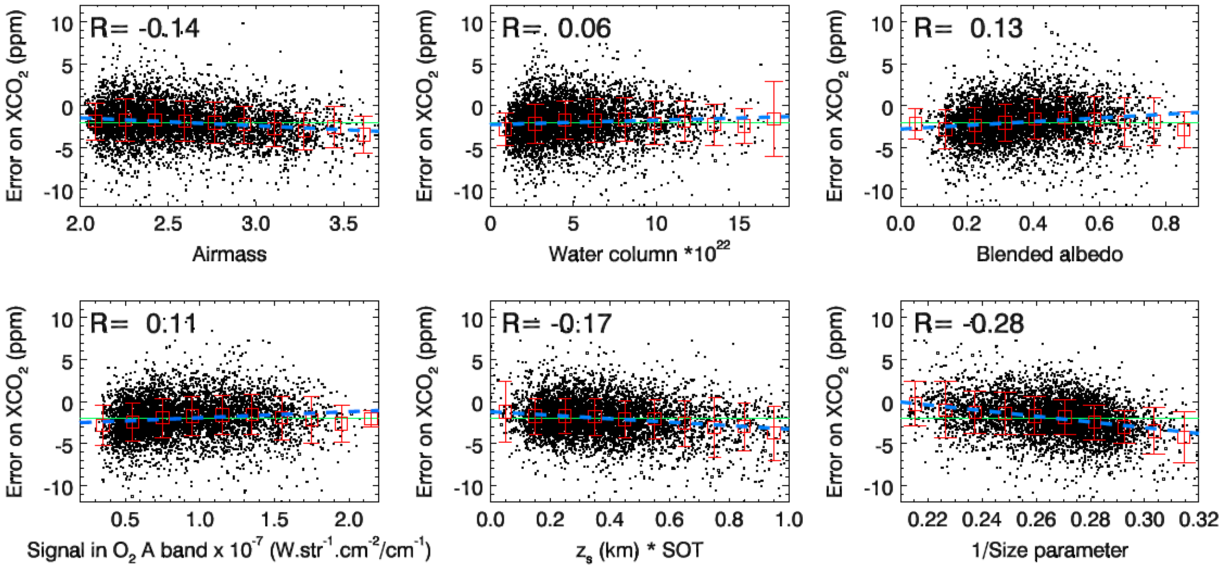

Figure 5: Error on XCO_2, defined as the difference between collocated GOSAT and TCCON retrievals, as a function of six parameters: air mass, water column, blended albedo, signal in O_2 A-band, aerosol scattering optical thickness (SOT) times aerosol layer height z_s, and the reciprocal aerosol size parameter. The green solid line represents the mean error, and the blue dashed line is a linear regression fit to the data. Correlation R with each variable is given in the upper right of each panel. (Figure 11 in Guerlet et al., 2013).

O'Dell et al. 2018, applied a more advanced bias correction to the ACOS OCO-2 B8 data product. Here, the training set comprises collocations with TCCON data, models, models in the Southern Hemisphere only, and a validation method called "small area approximation". This approach assumes that XCO_2 can be considered to be uniform over an area not larger than 100 km assuming to be away from strong known sources. Worden et al. 2017 found that for these circumstances XCO_2 varies by less than 0.1 ppm examine GEOS-5 simulations. The approach is well suited to correct for bias variation on the 100 km scale but is insensitive to biases on larger scales. Overall, the ACOS OCO-2 B8 bias correction per observation mode write as:

$$X_{\mathrm{CO_2,bc}} = \frac{X_{\mathrm{CO_2,raw}} - C_{\mathrm{P}}(\mathrm{mode}) - C_{\mathrm{F}}(j)}{C_0(\mathrm{mode})}$$

where $X_{CO_2,raw}$ are the raw OCO-2 data, $X_{CO_2,bc}$ indicates the bias corrected product, $C_p(mode)$ represents the mode dependent parametric correction as a function of e.g. surface pressure, band dependent albedo quantities, and aerosol parameter, $C_F(mode)$ is the footprint dependent bias correction as a result of the small area approximation, and $C_0(mode)$ is a mode dependent global scaling factor. Figure 5 summarizes the XCO2 bias dependence versus selected filter variables explained in detail by O'Dell, 2018.

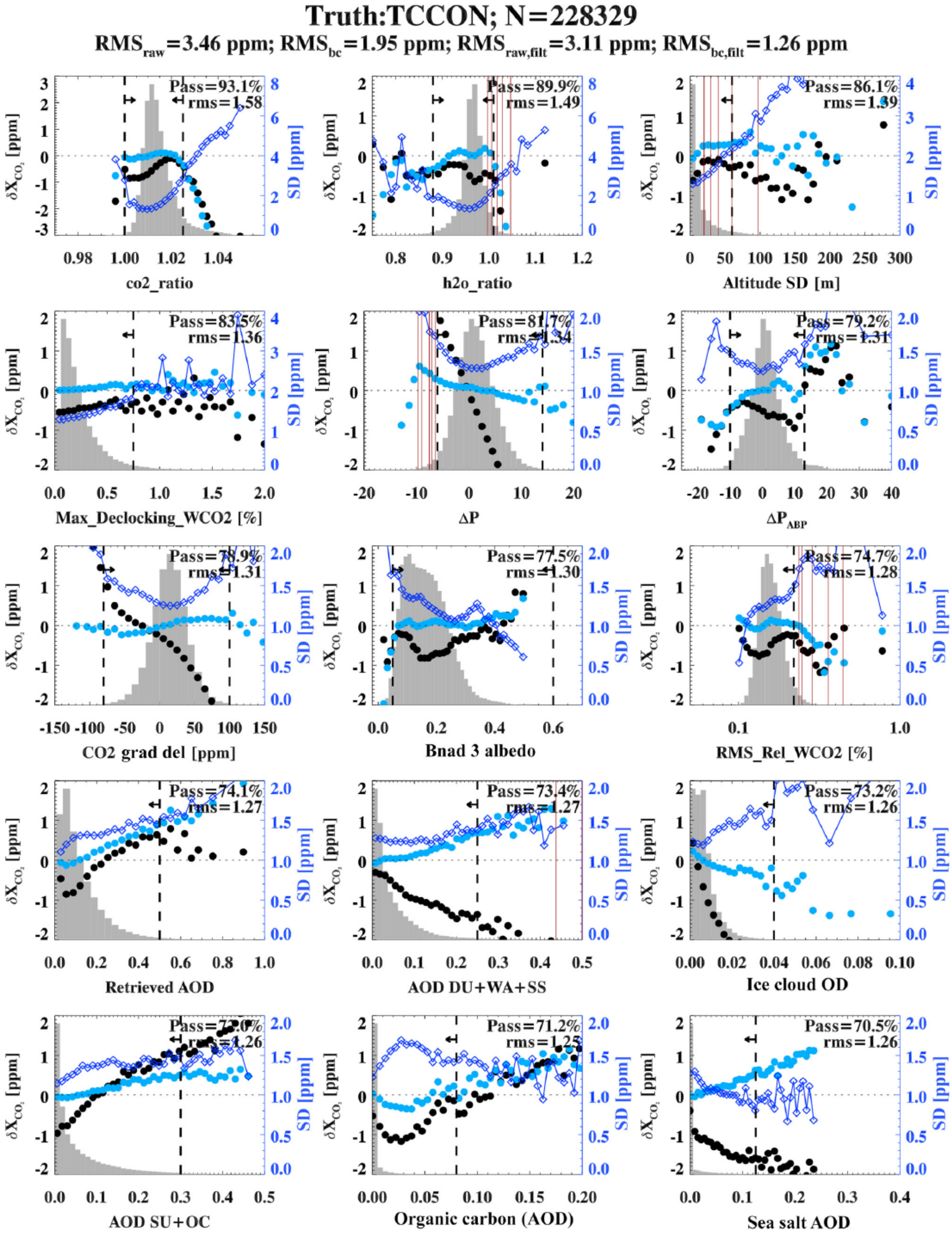

Figure 6: XCO_2 bias versus select filtering variables for land (nadir+glint) data, using TCCON as a truth proxy. Shown are the mean bias in each parameter bin for both raw (black circles) and bias-corrected (light blue circles) XCO_2 as well as the standard deviation of the bias-corrected XCO2 (dark blue diamonds). The histogram of each parameter is shown in gray. The vertical black dashed lines denote filtering thresholds for the XCO_2 quality flag, while the thin red solid lines show filtering thresholds for the warn levels. The quality flag filters are applied cumulatively from left to right and top to bottom. The fraction passing at each step, as well as

the rms error of the bias-corrected XCO2, are shown in the upper right corner of each panel (Figure 10 in O'Dell et al., 2018).

The risk induced by any bias correction is that the set of reference measurements does not have the ability to generalize the biases for the entire XCO2 product. This was illustrated by Guelet et al., 2013 using the difference between a non-scattering and 3-band full-physics retrieval as a proxy for the aerosol induced error. Figure 7 shows this proxy as a function of the SWIR-1 surface albedo for one year of GOSAT data, where different ranges of the aerosol scattering optical depth is color coded with a third order polynomial fitted to each set of data point. The different rectangles highlight the range of errors and albedo for this global data set (solid lines) for the surrounding of sites TCCON using the large colocation box with additional constraints from XCO_2 model fields to identify same air masses (dashed line); or using the 5° colocation area (dotted lines). Obviously, this selection of data sets effects the overall estimate of the bias dependence and thus can introduce significant errors, when extrapolating to cases with the larger albedo and larger aerosol scattering optical depth.

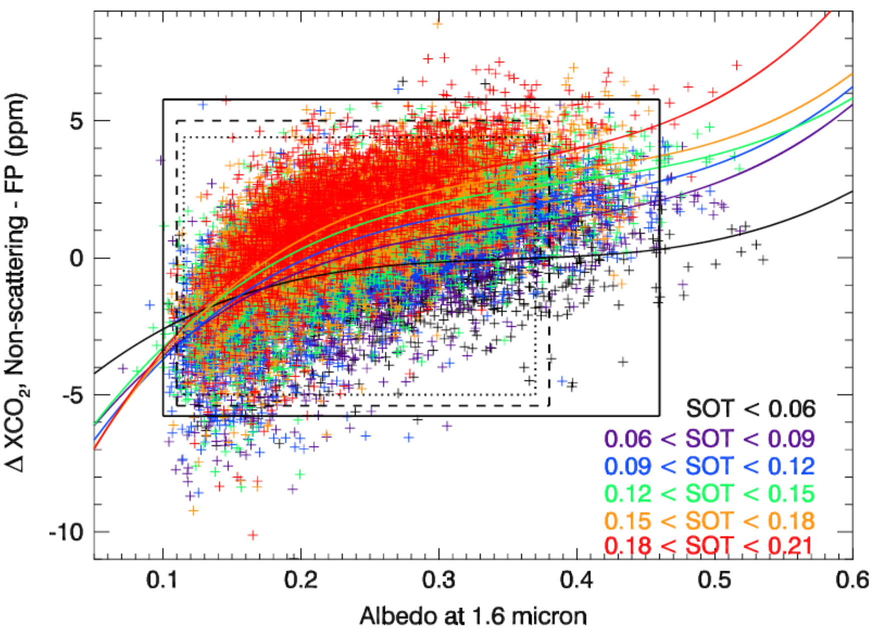

Figure 7: Difference between non-scattering retrievals and RemoTeC XCO_2 as a function of albedo, with SOT colour coded, for 1 year of global retrievals between June 2009 and May 2010 (land data, high gain only). See text for further explanation (Figure 16 in Guerlet et al., 2013).

Obviously, not only the ability to generalize but also the accuracy of the reference data is a critical element of any bias correction. Kiel et al., 2019 investigated the ACOS B8 bias correction with respect to surface pressure in detail, which corrects the data by

$$\mathrm{XCO}_{2,bc} = \mathrm{XCO}_{2,raw} - c_{surf}(p_{surf} - p_{prior})$$

with c_{surf} is a regression coefficient defined by comparison the raw data to a reference data set, p_{surf} is the retrieved surface pressure of the ACOS algorithm and p_{prior} is e.g. the collocated surface pressure from a forecast model. Obviously, any bias in p_{prior} introduces a corresponding bias in the bias corrected product $\mathrm{XCO}_{2,bc}$, where the relative errors in the surface pressure estimates propagate nearly one-to-one into relative errors in bias-corrected XCO_2. Given the precision we need to achieve in XCO2 measurements, seemly insignificant issues cannot necessarily be ignored. Kiel et al, 2019 identified two main reasons by bias correction using surface pressure introduces additional biases. First, they identified errors in the

ACOS B8 bias correction due to erroneous surface pressure estimates due to knowledge error of the pointing of the observatory (up to ~ 130 arcsec). This introduces XCO_2 biases in regions with rough terrain, as illustrated in Fig 8. The surface height around Lauder, New Zealand, changes up to 200 m over small distances. Considering XCO2 data which are not correct for biases we observe a nearly uniformly distribution of XCO2 with a standard deviation of 0.92 ppm, which increases after bias corrections to 1.35 ppm with maximum enhancements of 3 ppm correlated with the underlying the topographic slopes. The errors can be reduced by an improved point accuracy as illustrated by Kiel et al, 2019. Additionally, temporal sampling errors of the surface pressure of meteorological forecast and errors due atmospheric tides, are of crucial importance For example, the mean canopy height of the Amazon rain forest is ~25m and temporal changes due to fires or deforestation cannot be ignored as well as usual tidal range in the open ocean. For example, at sea level, altitude variations of ~ 8m correspond to changes in surface pressure of ~ 1 hPa, which might introduce errors in XCO_2 on the order of 0.4 ppm, which is already close to the accuracy requirement of the CO2M mission.

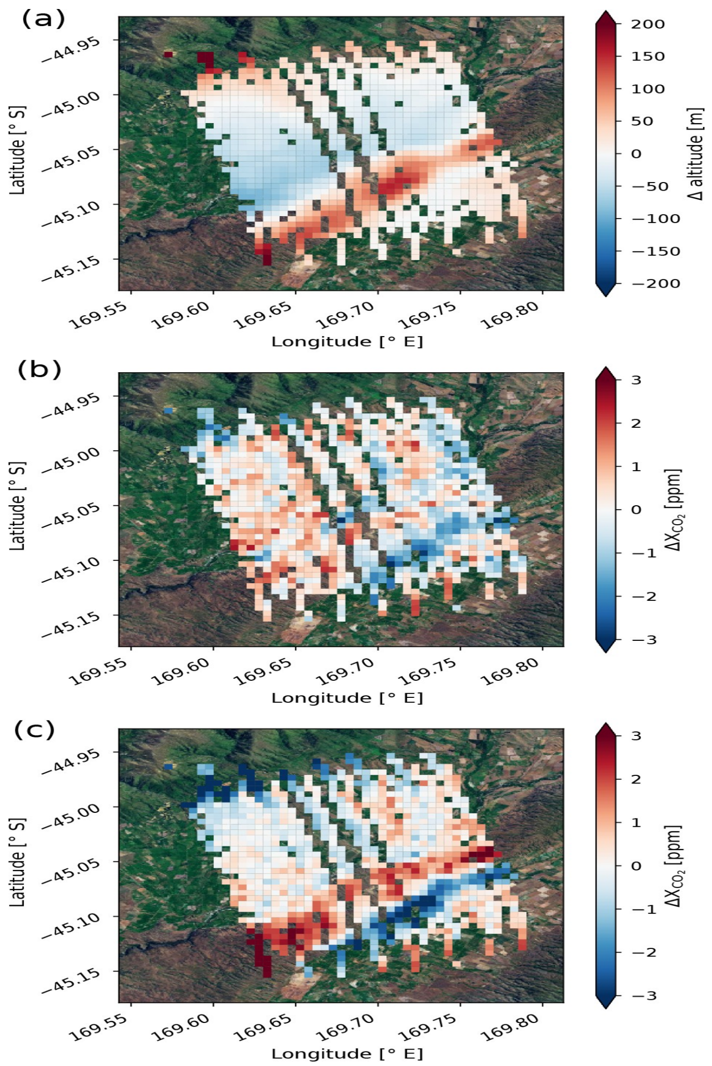

Figure 8 OCO-2 target mode observation over Lauder, New Zealand, on 17 February 2015. Panel (a) shows the altitude deviation (defined as the sounding altitude minus the median altitude of all soundings in the given latitude and longitude limits). Panels (b) and (c) show the variation of raw and bias-corrected OCO-2 v8 XCO_2 (defined in the same way as for the altitude) after applying the

v8 filters. Individual soundings are aggregated into 0.005x 0.005 latitude–longitude square grids (Fig. 4 in Kiel et al., 2019)

4 Mitigation approach 2: Cloud imager data

To mitigate aerosol induced errors, Kim et al, 2016 proposed to use aerosol information from the TANSO-CAI Cloud and Aerosol Imager as prior input to a three-band full-physics retrieval from TANSO-FTS observations, both payload of the GOSAT mission. The study focuses on Asia and North-Africa where aerosol concentrations are persistently high. Therefore, the effect of aerosols on data coverage and data quality is expected to be highest in the region.

The study employs the YCAR (Yonsei Carbon Retrieval) full-physics retrieval algorithm, which is modified to YCAR-CAI to exploit synergies between both instruments. The CAI imager has four spectral bands (0.380, 0.674, 0.870, and 1.600 µm), where the UV band is not used in this study. Thus, employing the bands at 0.674, 0.870, and 1.600 µm, the YCAR-CAI algorithm selects the appropriate aerosol type from four different, prescribed types. After the type selection, the AODs are retrieved from the pre-calculated look-up table. In Figure 9, a comparison of CAI AOD over ocean with MODIS data for the years 2010 and 2011 show a reasonable agreement, with correlation coefficients of 0.80–0.82 and regression slopes of about 1.2. Subsequently, the CAI aerosol information is used as priori information to the full-physics retrieval, which infers the volume mixing ratio CO2 profile, surface albedo, AOD profiles, water vapor scaling factor, surface pressure, temperature offset, wavenumber shift, wavenumber squeeze, and zero-level offset from the GOSAT NIR, SWIR-1 and SWIR-2 data.

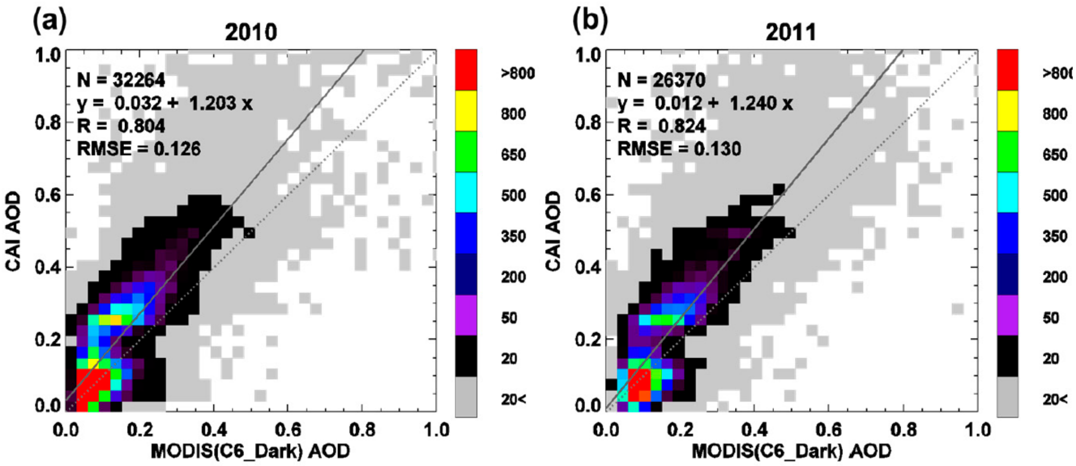

Figure 9: Comparison of AOD from CAI and MODIS over ocean. 2011. Colors represent the frequency of compared results (Fig. 1 in Kim et al, 2016).

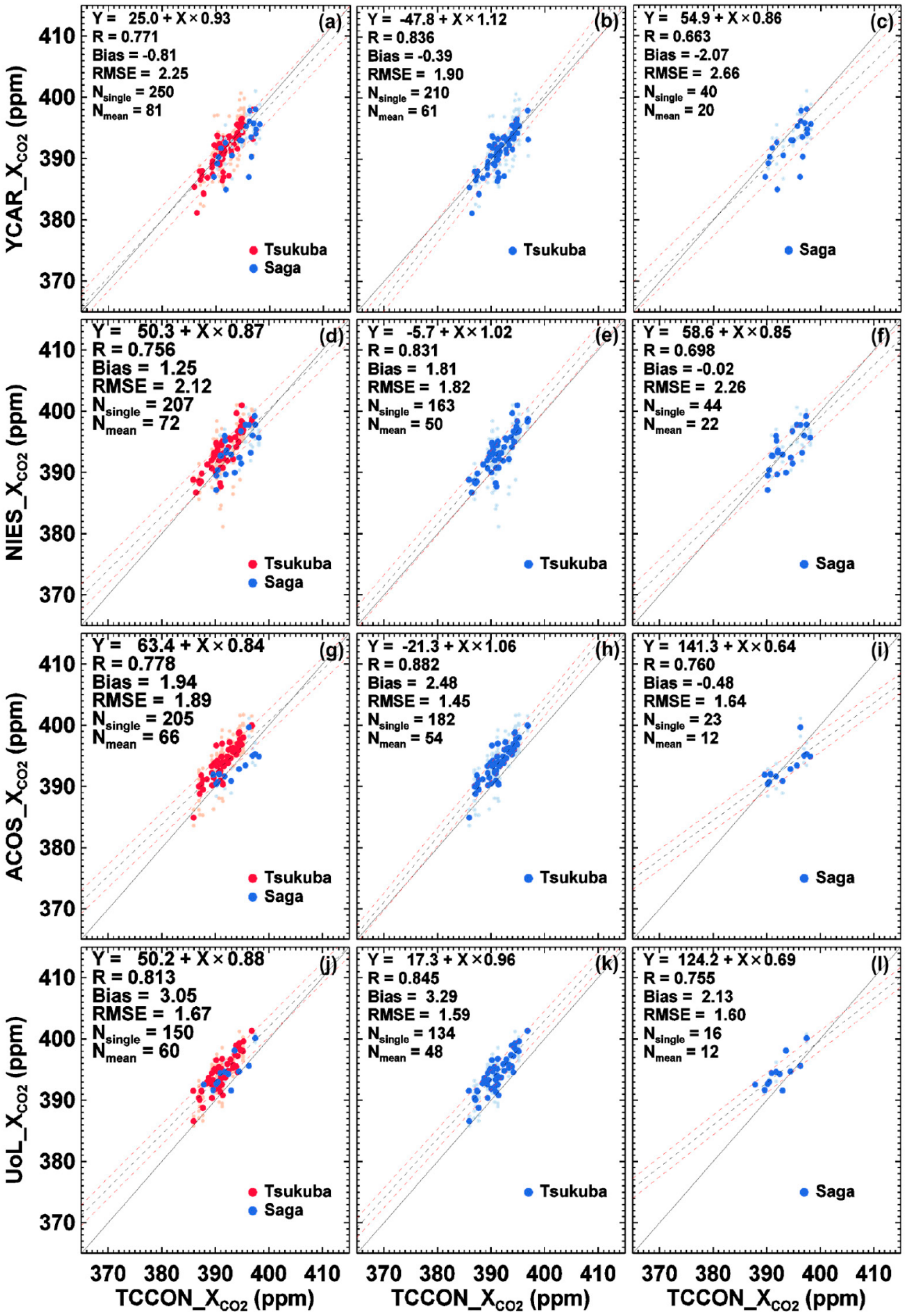

Figure 10: Comparison of retrieved XCO_2 from GOSAT algorithms ((a–c) YCAR-CAI; (d–f) NIES; (g–i) ACOS; and (j–l) UoL) with TCCON XCO_2 for two TCCON sites: Tsukuba (middle), Saga (right), and both (left). All individual sounding GOSAT data are shown as small faded dots, and daily average values are shown as large distinct colored dots. Black dotted line is the best-fit line calculated from robust fitting and red dotted lines are RMSE range of best-fit line. The solid line is linear identity function. (Figure 4 from Kim et al, 2016).

The YCAR-CAI results were validated against TCCON measurements at Tsukuba and Saga with a root mean square error of RMSE=2.25, a bias of b=- 0.81 ppm for in total N = 250 data point with a Pearson correlation r = 0.771, which is similar to the accuracy of other current algorithms (RMSE= 2.12, b = 1.25, N = 212, r = 0.756 for NIES L2 v2.21, RMSE= 1.94, b = 1.94, N = 205, r = 0.778 for ACOS L2 V3.4, and RMSE = 1.67, b = 3.06, N = 150, r = 0.813 for UoL L2 V6.0).

Overall, the present study of Kim et al, 2016 presents a new strategy in the use of aerosol information for XCO2 retrieval, where aerosol information from a different sensor on the same platform is used to improve the prior information of a full-physics 3 band retrieval. For a final assessment of the data quality, the validation must be extended to more TCCON sites with a better global coverage, such that the station-to-station variation of the XCO_2 bias can be evaluated.

5 Mitigation approach 3: Multi-angle radiance observations

Frankenberg et al. 2012 proposed an alternative approach to mitigate the aerosol induced error. They investigated a combined aerosol and greenhouse gas retrieval using multiple satellite viewing angles simultaneously and found that this method, hitherto only applied in multi-angle imagery such as from POLDER or MISR, greatly enhances the ability to retrieve aerosol properties by 2–3 degrees of freedom. The authors conclude that instead of focusing solely on improvements in spectral and spatial resolution, signal-to-noise ratios or sampling frequency, multiple angle observations reduce uncertainty in space-based greenhouse gas retrievals more effectively and provide a new potential for dedicated aerosols retrievals.

For simplicity, Frankenberg et al. only used 3 different viewing geometries; namely strict nadir as well as 30° fore and aft viewing zenith angles at 0° and 180° azimuths (i.e., strictly North-South). The measurement covers the NIR, SWIR-1 and SWIR-2 band of a GOSAT/OCO-type of instrument with a SNR=200 for all bands and viewing angles. For the nadir-only observation mode the SNR is adapted to a corresponding SNR to eliminate any SNR effect in the comparison (i.e., comparable to a $\sqrt{3}\,200 = 350$ SNR). The analysis is performed for the 3-band retrieval, i.e. the combination of the NIR, SWIR-1 and SWIR-2, and a 2-band retrieval, which combines the NIR and SWIR-1 and drops the strong CO2 bands in the SWIR-2.

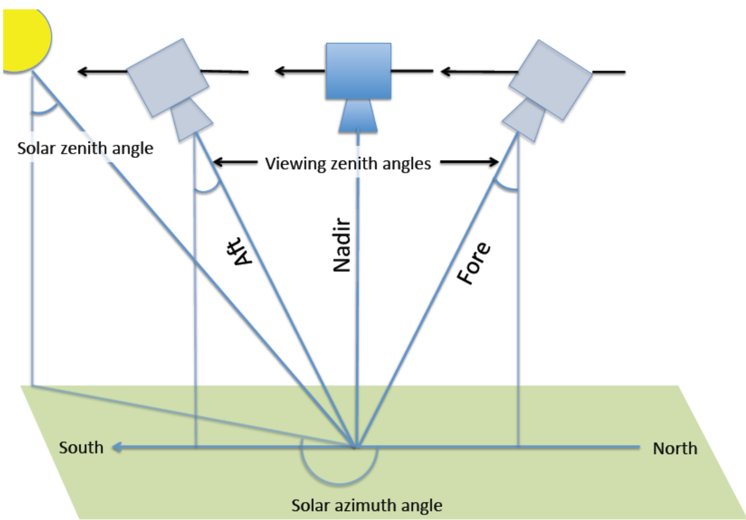

Figure 11: Schematics of the multi-angle viewing observation geometry using the satellite motion in low earth orbit instead to record the same scene at various angles (similar to the OCO-2 target mode). Satellite viewing

azimuth angles in this case are 0º and 180º for aft and fore viewing modes, respectively (Fig. 1 in Frankenberg et al., 2012)

The gain in aerosol information can be well illustrated when analyzing the sensitivity of the retrieved aerosol parameter to its true value, i.e. the corresponding diagonal element of the averaging kernel. Figure 11 shows that for a 2-parameter gamma size distribution, nearly all aerosol parameters can be retrieved independently, which is a major improvement with respect to the 3-band nadir concept, where the averaging kernel element of most parameters is in the range 0.4-0.6. Moreover, the analysis shows that the 2-band concept in combination with one viewing mode only provide little information on the aerosol, underlining the importance of the SWIR-2 band to account for atmospheric scattering. Also, for a 2-band concept, observations in multiple viewing angles add significant aerosol information.

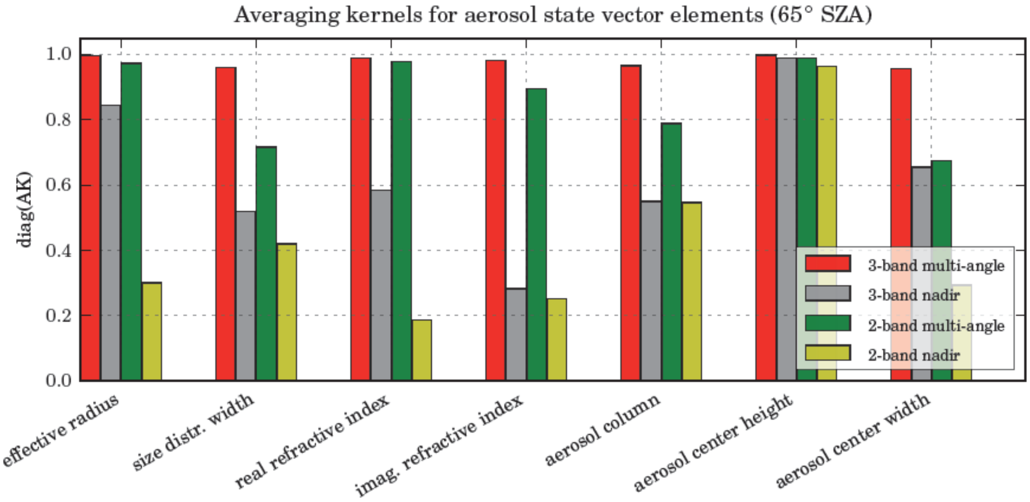

Figure 12: Averaging kernel diagonal elements related to aerosols for low sun (SZA = 65º) with a spectral resolution of 0.04 nm, 0.075 nm and 0.1 nm in the O2 A-band, weak CO2/CH4 band and strong CO2 band, respectively and a 2.5 spectral samples per FWHM. The SNR = 200 for each spectral band (Fig. 6 in Frankenberg et al., 2012).

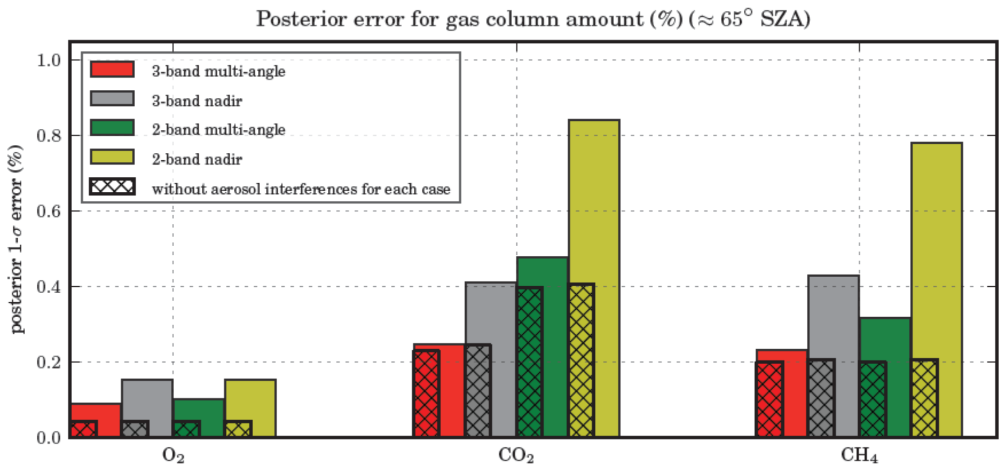

Figure 13: Posterior error estimates (1σ) of trace gas total column amount in % for a winter gas with a SZA = 65º. The simulation assumes OCO-2 spectral resolutions and SNR = 200 for each spectrum (Fig. 10 in Frankenberg et al., 2012).

The gain of aerosol information leads to reduced XCO_2 errors as shown in Figure 13. Here the posteriori error on the CO_2 column is halved for the 3-band multi-angle concept with respect to the 3-band nadir concept and is close to the error induced by the measurement noise only. A similar error reduction is achieved when going from the 2-band nadir to the 2-band multi-angle approach.
Overall the study of Frankenberg et al, 2012 quantified the potential of multi-angle high spectral resolution retrievals to both improve aerosol retrievals and reduce interference errors in trace gas retrievals. The obvious application to OCO-2 target mode observations is hampered by the fact that the observations of the different viewing modes are spatially not collocated. Due to the low spatial sampling with respect to the spatial resolution of the OCO-2 instrument, a spatial resampling induces large errors, which counteracts the potential gain on aerosol information.

6 Conclusions

This review focused on the discussion of the aerosol induced error in the literature discussed in the recent years. We conclude that

- The aerosol induced error is a key XCO_2 error contribution of the 3-band full-physics retrieval approach, which requires mitigation approaches
- A bias correction to a level of accuracy as required for the CO2M mission is a major challenge. The correction approach must have the ability to generalize the identified biases for a training set to all circumstances of the CO2M data product. Here, the level of accuracy of the available reference data, like surface pressure, is a challenge.
- The use of additional measurements from collocated aerosol measurements from a nadir imager is already discussed in the literature. However, a comprehensive assessment of the gain in XCO2 accuracy is not yet provided and only performed for TCCON reference measurements at two site in Asia.
- A multi-angle viewing radiance concept is discussed in the literature with the objective to be applied to OCO-2 target mode measurements. A theoretical study showed that spatiotemporal collocated GOSAT/OCO-2 type of measurements provides a gain in aerosol information which leads to a significant improvements in XCO_2 accuracy. Attempts to demonstrate thus for OCO-2 target measurements failed because of collocation errors between the observations with viewing angle.

The stringent accuracy requirement of <0.5 ppm for the CO2M mission makes it necessary to investigate alternative mitigation strategies, e.g. using collocated aerosol measurements to improve our knowledge on the atmospheric light path. here, a multi-angle polarimeter MAP can provide useful ancillary aerosol information in support to the CO2 3-band spectrometer. Therefore, sensitivity studies are required to evaluate the improved XCO2 performance for certain choices of the MAP instrument.

References

Aben, I., Hasekamp, O., Hartmann W., Uncertainties in the space-based measurements of CO_2 columns due to scattering in the Earth's atmosphere, J. Quant. Spectrosc. Radiat. Transfer 104, 450–459 (2007).

Butz, A., Hasekamp, O. P., Frankenberg, C., Aben, I.: Retrievals of atmospheric CO2 from simulated space-borne measurements of backscattered near-infrared sunlight: Accounting for aerosol effects. Applied Optics, 48, 3322, 2009.

Crisp, D., Atlas, R.M., F.-M. Bréon, F-M., Brown, L.R., Burrows, J.P., Ciais, P., Connor, B.J., Doney, S.C., Fung, I.Y., Jacob, D.J., Miller, C.E., D. O'Brien, S. Pawson, J. T. Randerson, P. Rayner, R. J. Salawitch, S. P. Sander, B. Sen, G. L. Stephens, P. P. Tans, G. C. Toon, P. O. Wennberg, P., Wofsy, S.C., Yung, Y.L., Kuang, Z., Chudasama, B., Sprague, G., Weiss, B., Pollock, R., Kenyon, S., Schroll, S. The Orbiting Carbon Observatory (OCO) mission, Adv. Space Res. 34, 700–709, 2004.

Cogan, A. J., Boesch, H., Parker, R. J., Feng, L., Palmer, P. I., Blavier, J.-F. L., Deutscher, N. M., Macatangay, R., Notholt, J., Roehl, C., Warneke, T., and Wunch, D.: Atmospheric carbon dioxide retrieved from the Greenhouse gases Observing SATellite (GOSAT): Comparison with ground-based TCCON observations and GEOS-Chem model calculations, J. Geophys. Res., 117, D21301, https://doi.org/10.1029/2012JD018087, 2012.

Corradini, S. and Cervino, M.: Aerosol extinction coefficient profile retrieval in the oxygen A-band considering multiple scattering atmosphere. Test case: SCIAMACHY nadir simulated measurements, J. Quant. Spectrosc. Ra., 97, 354–380, https://doi.org/10.1016/j.jqsrt.2005.05.061, 2006.

Frankenberg, C., Hasekamp, O., O'Dell, C., Sanghavi, S., Butz, A., and Worden, J.: Aerosol information content analysis of multi-angle high spectral resolution measurements and its benefit for high accuracy greenhouse gas retrievals, Atmos. Meas. Tech., 5, 1809-1821, https://doi.org/10.5194/amt-5-1809-2012, 2012.

Guerlet, S., Butz, A., Schepers, D., Basu, S., Hasekamp, O. P., Kuze, A., Yokota, T., Blavier, J.-F., Deutscher, N. M., Griffith, D. W., Hase, F., Kyro, E., Morino, I., Sherlock, V., Sussmann, R., Galli, A., and Aben, I.: Impact of aerosol and thin cirrus on retrieving and validating XCO2 from GOSAT shortwave infrared measurements, J. Geophys. Res., 118, 4887–4905, https://doi.org/10.1002/jgrd.50332, 2013.

Kiel, M., O'Dell, C. W., Fisher, B., Eldering, A., Nassar, R., MacDonald, C. G., and Wennberg, P. O.: How bias correction goes wrong: measurement of XCO2 affected by erroneous surface pressure estimates, Atmos. Meas. Tech., 12, 2241-2259, https://doi.org/10.5194/amt-12-2241-2019, 2019.

Kim W , J.Kim , Jung Y, Boesch H, Lee H, Lee S., T.-Y. Goo 4 , Jeong U, Kim M, Cho C.-H. , Ou M.-L. Retrieving XCO2 from GOSAT FTS over East Asia Using Simultaneous Aerosol Information from CAI, Remote Sens., 8, 994; doi:10.3390/rs8120994, 2016

Nanda, S., de Graaf, M., Sneep, M., de Haan, J. F., Stammes, P., Sanders, A. F. J., Tuinder, O., Veefkind, J. P., and Levelt, P. F.: Error sources in the retrieval of aerosol information over bright surfaces from satellite measurements in the oxygen A band, Atmos. Meas. Tech., 11, 161–175, https://doi.org/10.5194/amt-11-161-2018, 2018.

O’Dell, C. W., Connor, B., Bösch, H., O’Brien, D., Frankenberg, C., Castano, R., Christi, M., Eldering, D., Fisher, B., Gunson, M., McDuffie, J., Miller, C. E., Natraj, V., Oyafuso, F., Polonsky, I., Smyth, M., Taylor, T., Toon, G. C.,Wennberg, P. O., andWunch, D.: The ACOS CO2 retrieval algorithm – Part 1: Description and validation against synthetic observations, Atmos. Meas. Tech., 5, 99–121, https://doi.org/10.5194/amt-5-99-2012, 2012.

O'Dell, C. W., Eldering, A., Wennberg, P. O., Crisp, D., Gunson, M. R., Fisher, B., Frankenberg, C., Kiel, M., Lindqvist, H., Mandrake, L., Merrelli, A., Natraj, V., Nelson, R. R., Osterman, G. B., Payne, V. H., Taylor, T. E., Wunch, D., Drouin, B. J., Oyafuso, F., Chang, A., McDuffie, J., Smyth, M., Baker, D. F., Basu, S., Chevallier, F., Crowell, S. M. R., Feng, L., Palmer, P. I., Dubey, M., García, O. E., Griffith, D. W. T., Hase, F., Iraci, L. T., Kivi, R., Morino, I., Notholt, J., Ohyama, H., Petri, C., Roehl, C. M., Sha, M. K., Strong, K., Sussmann, R., Te, Y., Uchino, O., and Velazco, V. A.: Improved retrievals of carbon dioxide from Orbiting Carbon Observatory-2 with the version 8 ACOS algorithm, Atmos. Meas. Tech., 11, 6539-6576, https://doi.org/10.5194/amt-11-6539-2018, 2018.

Reuter, M., Buchwitz, M., Schneising, O., Noël, S., Bovensmann, H., and Burrows, J.: A Fast Atmospheric Trace Gas Retrieval for Hyperspectral Instruments Approximating Multiple Scattering – Part 2: Application to XCO2 Retrievals from OCO-2, Remote Sens., 9, 1102, https://doi.org/10.3390/rs9111102, 2017.

Sanghavi, S., Martonchik, J. V., Landgraf, J., and Platt, U.: Retrieval of the optical depth and vertical distribution of particulate scatterers in the atmosphere using O2 A- and B-band SCIAMACHY observations over Kanpur: a case study, Atmos. Meas. Tech., 5, 1099–1119, https://doi.org/10.5194/amt-5-1099-2012, 2012.

Wunch, D., Wennberg, P. O., Toon, G. C., Connor, B. J., Fisher, B., Osterman, G. B., Frankenberg, C., Mandrake, L., O’Dell, C., Ahonen, P., Biraud, S. C., Castano, R., Cressie, N., Crisp, D., Deutscher, N. M., Eldering, A., Fisher, M. L., Griffith, D. W. T., Gunson, M., Heikkinen, P., Keppel-Aleks, G., Kyrö, E., Lindenmaier, R., Macatangay, R., Mendonca, J., Messerschmidt, J., Miller, C. E., Morino, I., Notholt, J., Oyafuso, F. A., Rettinger, M., Robinson, J., Roehl, C. M., Salawitch, R. J., Sherlock, V., Strong, K., Sussmann, R., Tanaka, T., Thompson, D. R., Uchino, O., Warneke, T., and Wofsy, S. C.: A method for evaluating bias in global measurements of CO2 total columns from space, Atmos. Chem. Phys., 11, 12317–12337, https://doi.org/10.5194/acp-11-12317-2011, 2011.

Wu, L., Hasekamp, O., Hu, H., Landgraf, J., Butz, A., aan de Brugh, J., Aben, I., Pollard, D. F., Griffith, D. W. T., Feist, D. G., Koshelev, D., Hase, F., Toon, G. C., Ohyama, H., Morino, I., Notholt, J., Shiomi, K., Iraci, L., Schneider, M., de Mazière, M., Sussmann, R., Kivi, R., Warneke, T., Goo, T.-Y., and Té, Y.: Carbon dioxide retrieval from OCO-2 satellite observations using the RemoTeC algorithm and validation with TCCON measurements, Atmos. Meas. Tech., 11, 3111–3130, https://doi.org/10.5194/amt-11-3111-2018, 2018

Yokota,T., Oguma, H., Morino, I., Higurashi, A., Aoki, T., Inoue, G., Test measurements by a BBM of the nadir-looking SWIR FTS aboard GOSAT to monitor CO_2 column density from space, Society of Photo-Optical Instrumentation Engineers (SPIE) Conference Series, S. C. Tsay, T. Yokota, and M.-H. Ahn, eds., Vol. 5652, pp, 182–188, 2004

WP A600

Adopting External Aerosol Data in the UoL Retrieval Algorithm and Intercomparison to RemoTeC

Technical note

Leif Vogel (Kaioa Analytics), Hartmut Bösch (University of Leicester)

Document version 1.02

October 29th, 2020

Leif Vogel
Kaioa Analytics
Goiko Kalea 58, 3°
48360 Mundaka
Bizkaia, España
Tel. +34-633261825
Email: contact@kaioa-analytics.org
VIES: ESY4179160M

University of Leicester
Earth Observation Science Group
Department of Physics & Astronomy,
University of Leicester,
University Road,
Leicester, LE1 7RH,
United Kingdom.
Tel.: +44 (0)116 252 3506
Fax: +44 (0)116 252 2770
Email: hartmut.boesch@le.ac.uk

Document version 1.02

October 29th, 2020

Change Log

Version	Date	Changes	Reason for changes
1.01	May 5th 2019	Removal of duplicated figures.	A number of figures appeared duplicated in PDF version of document.
1.02	October 29th 2020	Change in table 1, removal of duplicated figures	Comments incorporated by Yaska Mejer

Table of Contents

A Introduction

A.1) Applicable Documents

The following documents, listed in order of precedence, contain requirements applicable to the activity:

AD-1 CarbonSat Mission Requirements Document, EOP-SMA/2232/PI-pi, version 1.0

AD-2 CarbonSat Mission Requirements Document, EOP-SMA/2232/PI-pi, version 1.2

AD-3 CarbonSat Earth Explorer Opportunity MissionPhase A/B1 System Study System Requirements Document, EOP-SFP/2011-04-1574/AL/al, version 1.2

A.2) Reference Documents

The following documents were consulted by the Contractor as they contain relevant information:

RD-1 Towards a European Operational Observing System to Monitor Fossil CO2 emissions, Final Report from the expert group, October 2015 available at http://www.copernicus.eu/sites/default/files/library/CO2_Report_22Oct2015.pdf

RD-2 Final report of CarbonSat Earth Explorer 8 Candidate Mission "Level-2 and Level-1B Requirements Consolidation Study ", IUP, version 2.2, 18 July 2014

RD-3 Technical Note of CSL1L2 study "CarbonSat: Balancing requirements (SNR, spatial and spectral, other)", version: 2.0, Doc ID: IUP-CS-L12-TN-3d, 27 April 2012

RD-4 CarbonSat Reference Spectra IUP-CS-RS-TN-001, version 1.0

A.3) Acronyms and Abbreviations

AD	Applicable Document
ESR	Executive Summary Report
FR	Final Report
HITRAN	HIgh-resolution TRANsmission molecular absorption (database)
KA	Kaioa Analytics
MAP	Multiangle spectro-polarimetry (auxiliary aerosol instrument)

NIR	Near InfraRed
PM	Progress Meeting
RD	Reference Document
RemoteTec	SRON retrieval algorithm
SNR	Signal-to-Noise Ratio
SoW	Statement of Work
SWIR	Short-Wave InfraRed
TCCON	Total Carbon Column Observing Network
TOA	Top-of-Atmosphere (radiance)
UoL	University of Leicester
UoL-FP	University of Leicester Full-Physics retrieval
XCO_2	dry-air column averaged mixing ratios of CO2

A.4) Executive Summary

The work package A600 general task is to assess the performance of the UoL retrieval algorithm using external aerosol information which would be provided by a MAP (Multi-Angle Photopolarimetric) aerosol sounder. To this end, the work package consists of the following points:

- Adjustment of the UoL retrieval method to use external aerosol information as provided by the MAP instrument
- Conduct a series of geophysical simulations covering different aerosol scenarios, surface types and geometries. The details of the geophysical scenarios will be agreed with SRON.
- Retrieve XCO_2 from the simulated spectra assuming uncertainties for aerosol parameters according to the MAP retrieval uncertainties
- Evaluate the obtained retrieval results against RemoTeC results

In order to assess the performance of the CO_2 retrieval, spectra for a range of geophysical scenarios have been simulated using the forward model of the Full-Physics retrieval algorithm from the University of Leicester [UoL-FP][2–5] . The specifications of the instrument are laid out in section B and respective reference documents RD.

The geophysical scenarios follow simulations by SRON to allow easy intercomparison of results. Respective parameters are described in section C.

This study assesses the performance of the retrieval using additional a priori information on aerosols from the simulated MAP instrument for a range of geophysical scenarios. One of

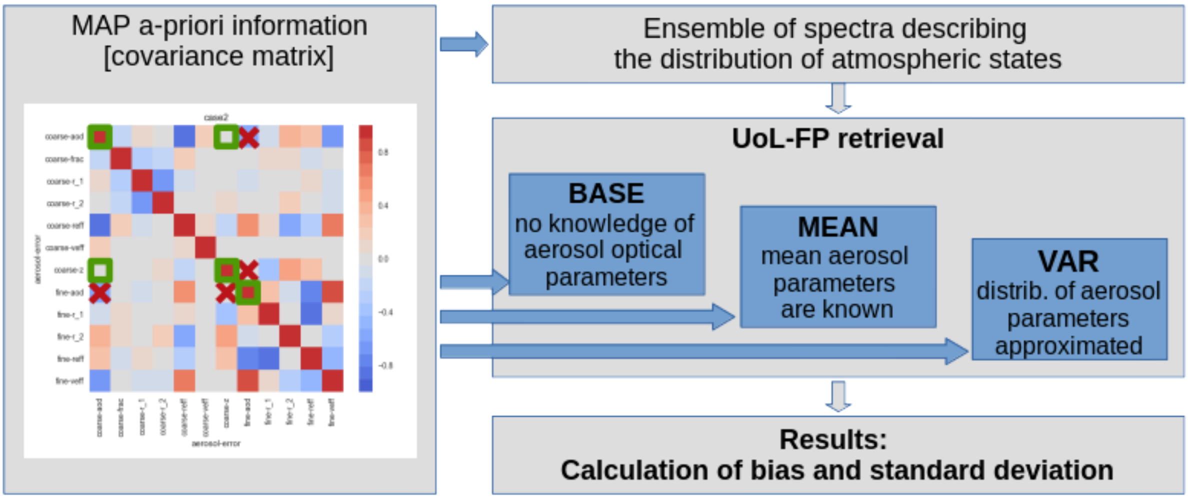

Figure 1: Schematic overview of the work flow of the study. For each geophysical scenario, the given a-priori information is described as an ensemble of spectra. These ensembles are processed using different retrieval setups, and the results compared.

the main challenges result from the inherent differences in the treatment of aerosol information in the UoL retrieval and the a priori information provided by the MAP instrument (section D). The standard UoL retrieval setup is described inD.1, additional information provided by the MAP instrument is laid out in D.2. These challenges are overcome by the workflow outlined in Figure 1. First, the distribution of atmospheric states (due to different aerosol states) as predicted by the MAP a-priori information is described as an ensemble of spectra, which encompass these distributions. A detailed description of this approach is given in Section D.3.

Retrievals are run for the full ensembles of spectra for the respective geophysical scenarios. Three different degrees of a-priori knowledge are assumed (see Section E). A) no knowledge of aerosol optical parameters [BASE], B) the mean aerosol parameters are assumed to be known [MEAN], and C) [VAR]: all uncertainties of the aerosol properties are translated to a-priori information / retrieval setup.

Figure 2 depicts the results for BASE and VAR retrieval setups at SZA 30° and 60°, respectively, which corresponds to retrievals employing no a-priori aerosol information and retrievals with approximately full a-priori information. The figures show the combined biases for the individual retrievals in the ensembles for all geophysical scenarios and aerosol AOD variations. In order to filter out outliers, the shaded areas show the respective 25%-75% percentile range, whereas the solid line depicts the mean of all biases. It is obvious that the BASE retrieval does not lead to acceptable results for the gross of scenarios and aerosol loads. If the uncertainty of aerosol parameters is taken into account with the VAR retrievals, however, biases are obtained which meet the 0.1% XCO_2 threshold values and show significant lesser spread. All results are described and compared in Section F.

Comparison of the error ranges obtained with the RemoteTec algorithm confirm the gain by additional a-priori information. In general, standard deviation of results by the VAR retrieval are within a factor of 2 below error ranges of the RemoteTec algorithm, meeting goal requirements.

These results of the different retrieval setups, from no aerosol optical properties information, mean properties known and approximation of full use of additional a-priori information, clearly highlight the improvements in performance of the UoL retrieval when employing external aerosol information.

Figure 2: Combined biases for all geophysical scenario ensembles and retrieval setups BASE and VAR. The upper panel depicts results for SZA 30°, the lower panel for SZA 60°. The solid line denotes the respective median and the shaded area the 25%-75% percentiles of all retrievals.

B Instrumental setup

An instrument similar to Sentinel 7 is assumed. The applied instrumental properties are summarized in Table 1. The random noise *N* of each pixel of the instrument has been simulated according to equations

$$
\begin{aligned}
N &= \sqrt{a * R + b}/a \\
SNR &= a \cdot R/\sqrt{a * R + b}
\end{aligned}
$$

where *R* is the radiance of a pixel and the constants *a* and *b* are given in Table 1.

Examples of calculated spectra, where the forward model (see section D.1) employs these values are given in Figure 3 and Figure 4 for two different geophysical scenarios (section C).

	NIR	**SWIR1**	**SWIR2**
Window lower wavelength [µm]	0.747	1.59	1.99
Window upper wavelength [µm]	0.773	1.625	2.09
Pixel step width [µm]	0.0318E-3	0.0955E-3	0.167E-3
ILS FWHM [µm]	0.10E-3	0.30E-3	0.55E-3
Noise slope (a)	4.47E-15	2.29E-14	3.91E-14
Noise base (b)	1.6054E5	3.33297E5	3.23636E5

Table 1: Spectral windows of simulated instrument. ILS width denotes the width of a Gaussian instrumental slit function.

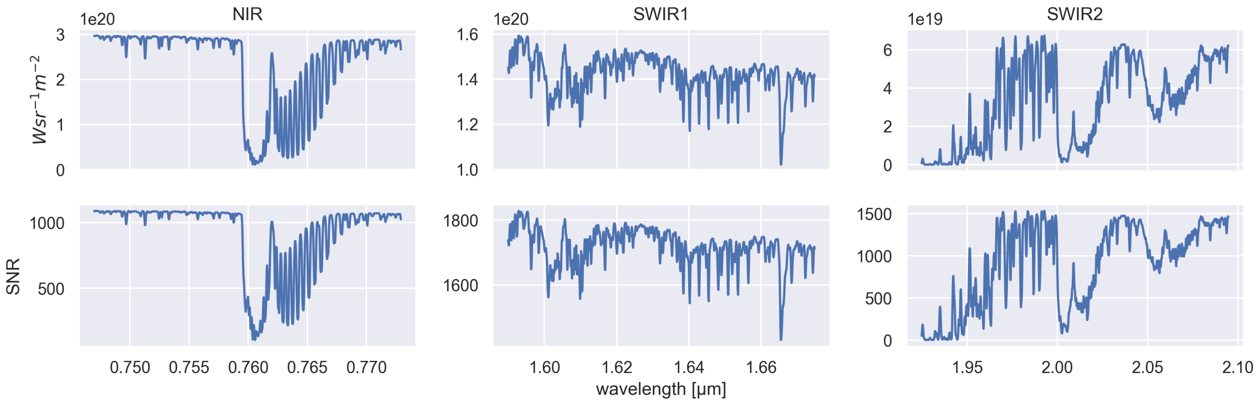

Figure 3: Modelled spectra for geophysical scenario case 1, employing a BRDF for soil, total AOD 0.07 and a SZA 30°. The lower panels show the respective signal-to-noise ratios.

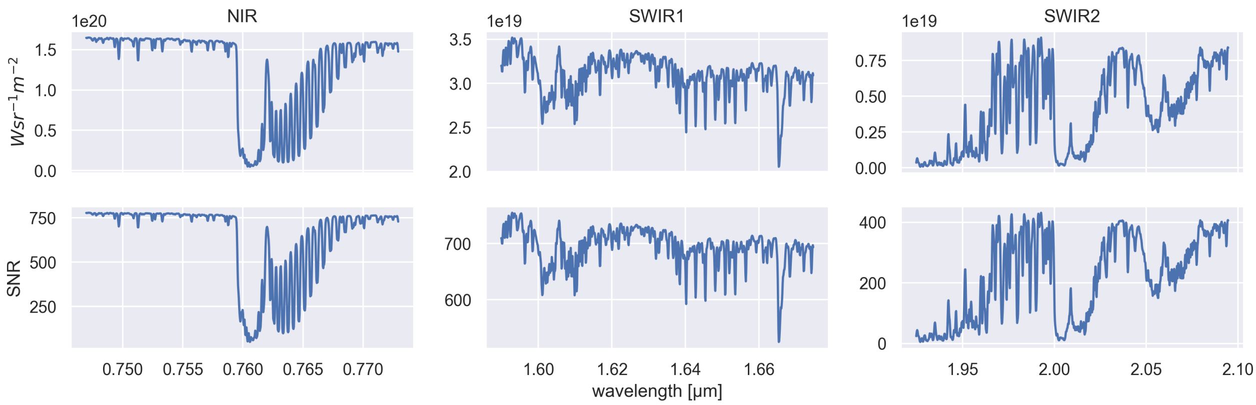

Figure 4: Modelled spectra for geophysical scenario case 3, assuming a Lambertian albedo for vegetation, total AOD 0.3 and SZA 60°. The lower panels show the respective signal-to-noise ratios.

C Geophysical scenarios

Following the study conducted by SRON, the same geophysical scenarios are used with the UoL-FP algorithm to allow a direct comparison for the individual scenarios. Three different cases of aerosol distributions (see Table 2) are studied for different surface Lambertian albedos (henceforth denoted as albedo), soil and vegetation, and two different solar zenith angles (SZA) at 30° and 60°. Since each aerosol case includes 5 different aerosol loadings, the study consists of a total of 60 different scenarios. The same, standard atmospheric profiles where used for all scenarios (see Figure 5).

The aerosol optical parameters for aerosols are derived from a database look-up table [1] which has been calculated originally for AERONET and is also used in the RemoteTeC retrieval. Assumed is a bimodal, log-normal aerosol size distribution. The default values are given in Table 3, and resulting optical properties at respective wavelengths are depicted in Figure 6 and 7.

Here, we use the same database of aerosol optical properties as SRON for the RemoteTeC retrieval. Thus, the microphysical properties are translated to the same optical properties (extinction, scattering, scattering matrices, and wavelength dependencies etc) as used in the RemoteTeC retrieval.

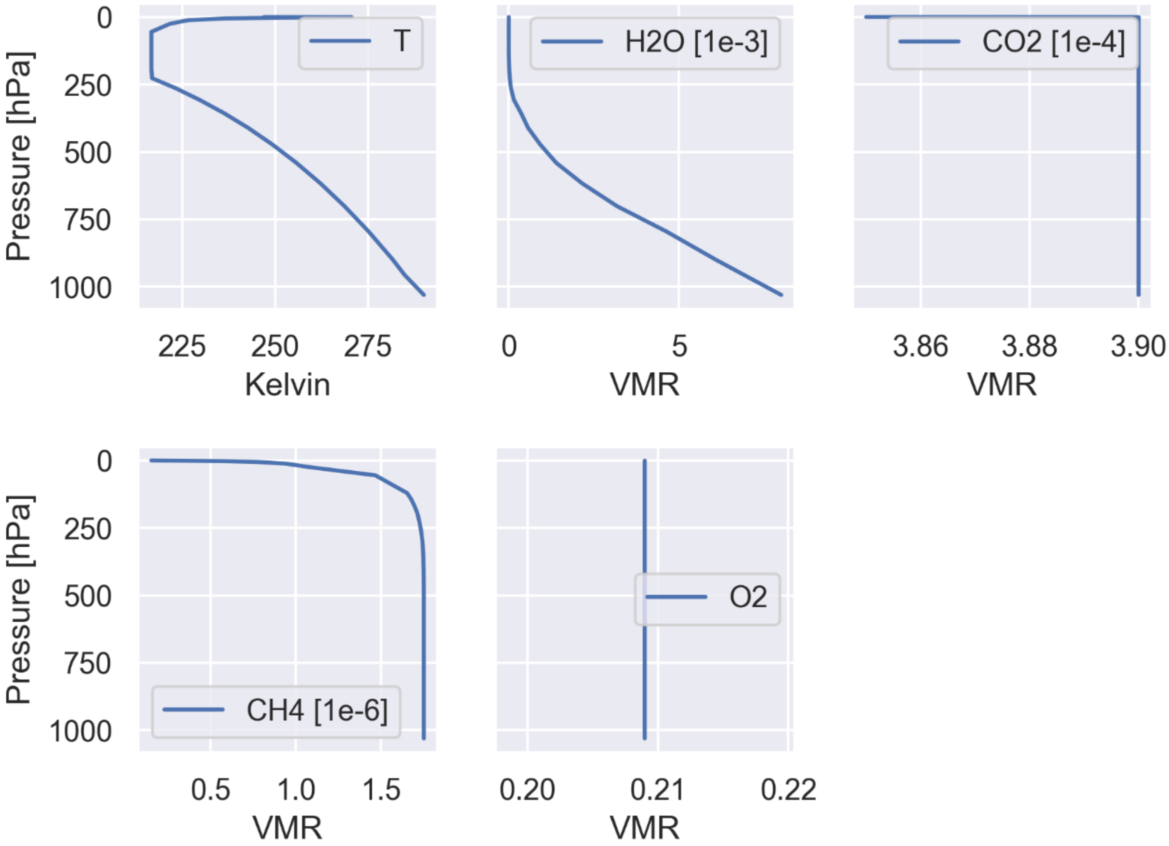

Figure 5: Standard atmosphere used in all geophysical retrieval setups.

Aerosol Profile	Fine / Boundary Layer			Coarse / Free troposphere		
	AOD	Height [km]	Width [km]	AOD	Height [km]	Width [km]
Case 1 Boundary Layer	0.05, 0.1, 0.15, 0.25, 0.5	1	2	0.02	1	2
Case 2 Upper Troposphere	0.2	1	2	0.02, 0.04, 0.06, 0.1, 0.15	8	2
Case 3 Middle Troposphere	0.2	1	2	0.02, 0.04, 0.06, 0.1, 0.15	4	2

Table 2: Aerosol profile setup for the different geophysical scenarios. A Gaussian profile is assumed for each aerosol at a certain AOD, height and width. For the fine aerosol, the effective mean radius of the aerosol size distribution (R_{eff}) also differs for case3.

Aerosol properties		**Fine**	**Coarse**
r_{eff}		Case 1: 0.12 Case 2,3: 0.2	1.6
v_{eff}		0.2	0.6
Refractive index (real, imaginary)	0.774µm	1.5, 1E-7	1.53, 2.7E-3
Refractive index (real, imaginary)	1.675µm	1.5, 1E-7	1.38, 1.7E-3
Refractive index (real, imaginary)	2.096µm	1.5, 1E-7	1.25, 2.3E-3
Fraction of spheres		100%	5%

Table 3: Properties of default aerosols types used in the geophysical scenarios

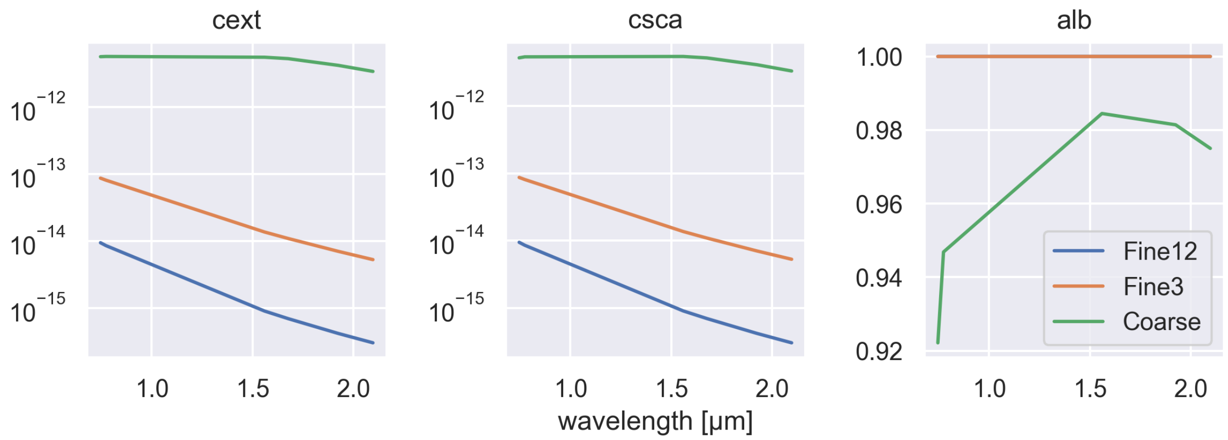

Figure 6: Extinction, scattering and singe scattering albedo coefficients for default aerosol types in the geophysical scenarios. Fine12 denotes the fine aerosol type used in cases 1 & 2, whereas Fine3 denotes the fine aerosol type employed in case 3.

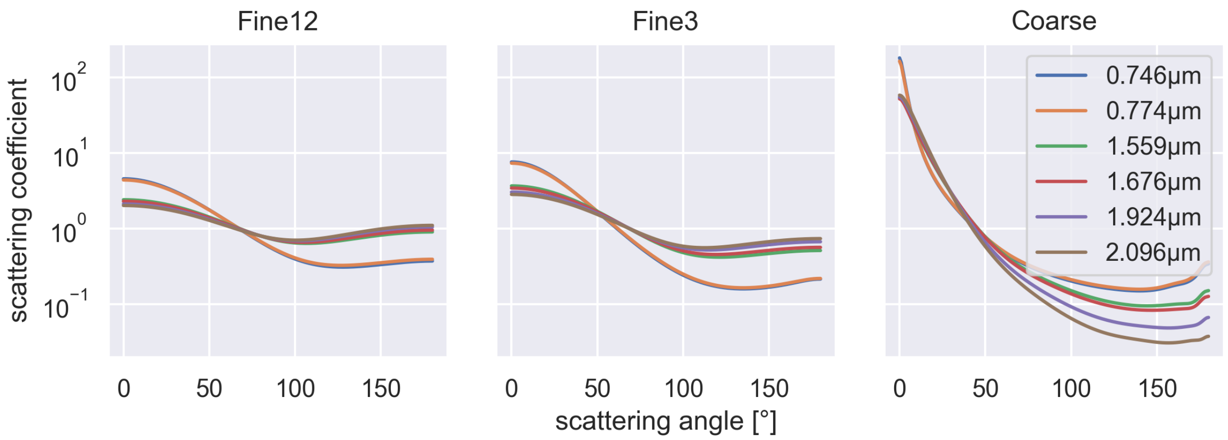

Figure 7: Scattering matrices for default aerosol types in the geophysical scenarios. Fine12 denotes the fine aerosol type used in cases 1 & 2, whereas Fine3 denotes the fine aerosol type employed in case 3.

D General retrieval scheme

The UoL-FP retrieval employs a different aerosol retrieval scheme than the RemoTeC retrieval and cannot readily process the a priori information provided by the MAP instrument. In this section, first the standard UoL retrieval setup is described in D.1 and information given of the characteristics of the MAP a-priori information (D.2)).

Section D.3 provides a detailed description of how these challenges are overcome, namely the construction of an ensemble of spectra which reflects the distribution of atmospheric states as given by the MAP a-priori information.

D.1) UoL-FP retrieval scheme

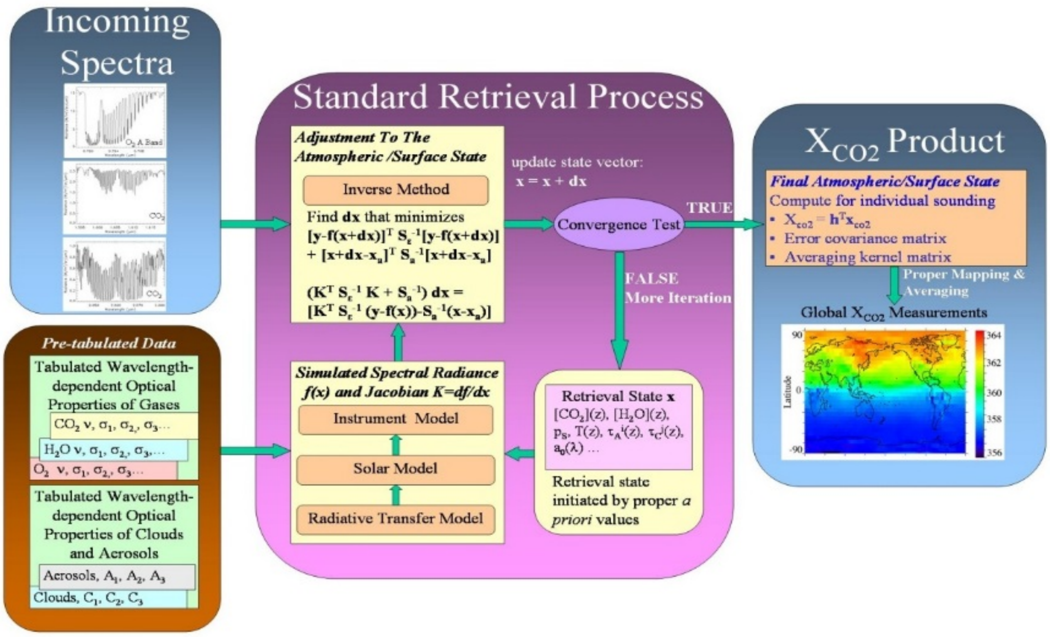

Figure 8: Schematic of the UoL-Retrieval scheme.

The UoL-FP retrieval scheme has been detailed in [3–5]. In a nutshell, it employs an iterative approach consisting of forward modelling a spectrum, comparing to measured values and adapting the parameters of the model's state vector until a best fit is obtained. It retrieves XCO_2 from a simultaneous fit of the near-infrared O_2-A Band spectrum at 0.76 µm and the CO_2 bands at 1.61 and 2.06 µm. It is based on an iterative retrieval scheme using Bayesian optimal estimation to determine a state vector x combined of a set of atmospheric/surface/instrument parameters. The main components of the algorithm are a forward model and inverse method. The forward model describes the physics of the measurement process and describes radiances for a state vector x. It consists of a radiative transfer (RT) model coupled to a model of the solar spectrum to calculate the monochromatic spectrum of light that originates from the sun, passes through the atmosphere, reflects from the Earth' surface or scatters back from the atmosphere, exits at the top of the atmosphere and enters an instrument. The top of atmosphere (TOA) radiances are then passed through the instrument model to simulate the measured radiances at the spectral resolution (see Figure 8).

The UoL full physics retrieval employs two aerosol particles types and atmospheric profiles to estimate aerosol scattering, which can be roughly categorized as a small/fine and large/coarse particle (with large and small Ångström coefficients). The combination of these two types allows to mitigate the effect of radiative scattering in greenhouse gas retrievals [4]. Previously, the two aerosols employed in the UoL FP had fixed optical properties. They consisted of a small, carbonaceous, sooty continental mixture and a large, carbonaceous, dusty continental mixture as described in [6] called mixture 5b and 2b respectively. Both particles were assigned an a priori Gaussian-shaped profile of a certain aerosol optical depth (AOD), height, width. Here, we used these fixed aerosol properties as a baseline retrieval assuming that no further information of the optical aerosol properties is available. In current UoL-FP retrievals of XCO_2, observation dependent aerosol types and profiles are employed to achieve a more realistic a-priori properties and profiles. Aerosol fields as modelled by MACC/CAMS provide the basis for the small and large aerosol types used in the retrieval of satellite observations.

It is important to note that the UoL-FP retrieval is set up to retrieve only certain aerosol profile parameters, here Gaussian shapes, of a number of different aerosol types with fixed aerosol micro-physical and corresponding optical properties. That is to say, the true optical path in the atmosphere is estimated by adjusting the different aerosol profile shapes and not the type optical properties. This is one of the major differences to the RemoTeC algorithm used in other parts of the CO_2 sizing study.

D.2) MAP a priori information

The aim of this work package is to assess the improvements in retrieval performance by employing the MAP instrument a priori information. Assuming that the MAP instrument correctly predicts the mean aerosol parameters, errors in the CO_2 retrieval are determined by mapping the MAP a priori covariances to retrieved CO_2 values.

The MAP instrument provides a priori information and error covariance matrices for a number of profile parameters and aerosol micro-physical properties. In the following, the MAP instrument or MAP a priori information always refers to aerosol information as measured by the MAP instrument (MAP-mod) with a radiometric error=3% and DLP error=0.3%. Employed are MAP-mod covariance matrices as provided by SRON for the individual geophysical scenarios.

The information yielded by the MAP instrument consists of two aerosol profiles with respective optical properties of associated aerosol types. This includes a fine/small aerosol type fixed to the boundary layer [BL], and a coarse/large aerosol type which can also be present in the free troposphere [FT], see also geophysical scenarios in section C. The fine aerosol type mostly consists of spherical particles with inorganic characteristics and may include black carbon, whereas the coarse type includes mostly non-spherical, dusty particles and consists only on the order of 5% of spherical particles.

Micro-physical information provided for the individual aerosols are

- Refractive index, described as the sum of two refractive indices with a certain weighting coefficient, called r_1 and r_2 respectively (see Table 4).
- Effective radius of size distribution [r_{eff}]
- Effective variance of size distribution [v_{eff}]
- Fraction of spheres [frac] - only coarse aerosol: percentage of spherical particles (~5% with the rest being non-spherical dust)

Information on gaussian aerosol profiles are given as

- total aerosol optical depth [AOD]
- height [z], only coarse aerosol

Note that width of the gaussian profile is always fixed to 2km, and height for boundary layer aerosol (fine) is also fixed to 1km.

Figure 9 depicts the correlation matrix calculated from mean MAP covariance matrices for the geophysical scenario case 2. It is obvious that strong correlations and anti-correlations exist between some of the parameters. The number of parameters for coarse aerosol are

Refractive indices (real, imaginary)			
Type	**inorganic**	**black carbon**	**dust**
Fine Aerosol	r1	r2	
Coarse Aerosol	r2		r1
wavelength			
0.774µm	1.5, 1E-7	1.75, 0.7	1.53, 2.5E-3
1.675µm	1.5, 1E-7	1.8, 0.7	1.38, 1.7E-3
2.096µm	1.5, 1E-7	1.81, 0.7	1.25, 2.3E-3

Table 4: Refractive indices for used aerosol types. Fine aerosol r1 and r2 correspond to inorganic and black carbon, whereas coarse aerosol r1 and r2 correspond to dust and inorganic, respectively. See also **Figure 9**.

higher than for fine aerosols, because of the it includes gaussian profile height (z) and fraction of spheres (frac) not retrieved for fine aerosols.

Here, we use the same database of aerosol optical properties as SRON for the RemoTeC retrieval, which has been calculated originally for AERONET[1]. Thus, the microphysical properties are translated to the same optical properties (extinction, scattering, scattering matrices, and wavelength dependencies etc) as used in the RemoTeC retrieval.

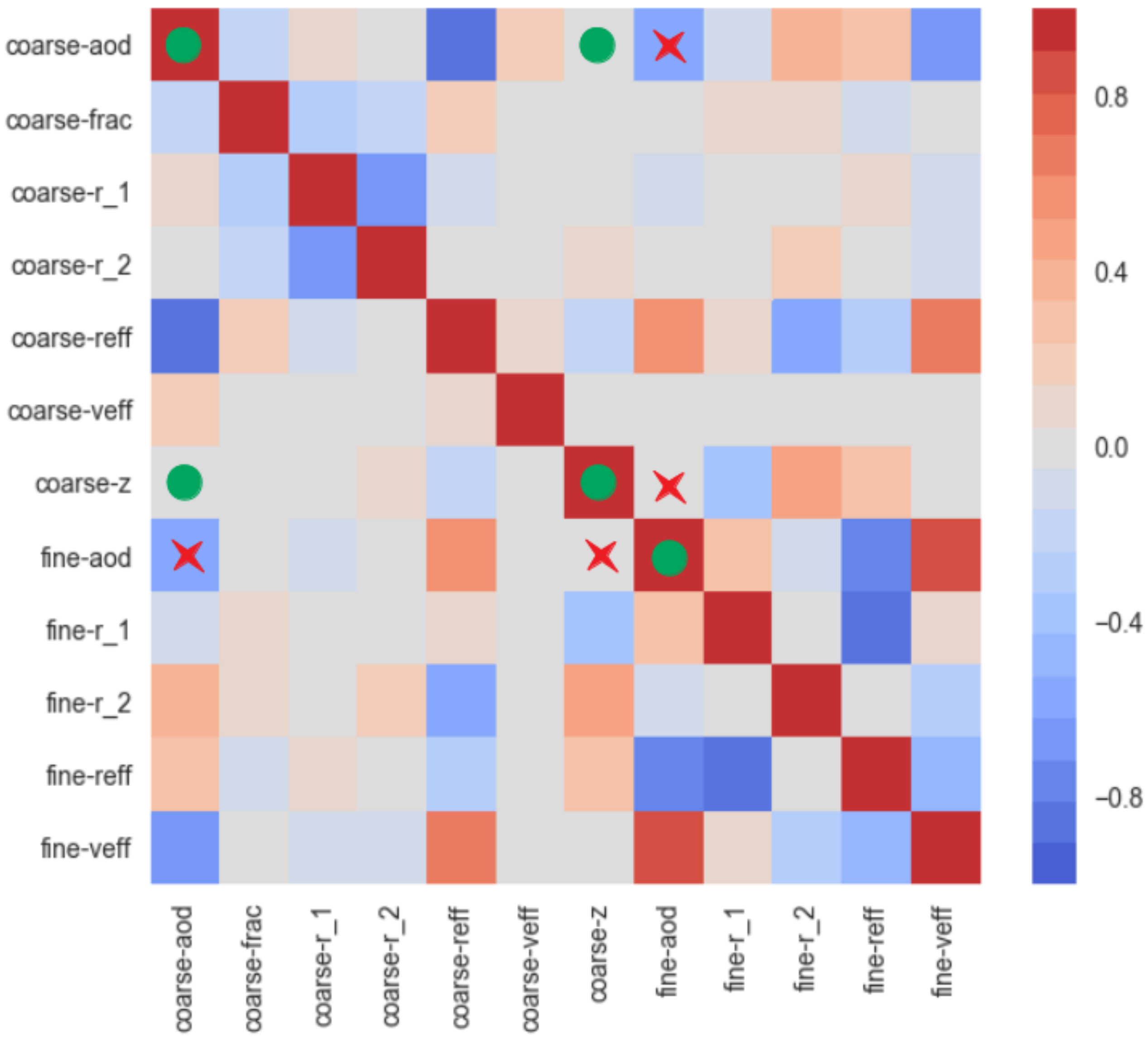

Figure 9: Correlation matrix calculated for the mean MAP covariance matrices for the geophysical scenarios case 2. Correlation instead of covariance has been chosen to better highlight the interaction between parameters of different physical scales. Green dots mark a-priori information which can readily be processed by the UoL-FP retrieval, whereas information under red crosses can only be used after modification of the retrieval algorithm itself (see section D.3).

D.3) Describing the atmospheric state via ensemble of spectra

The main complication when directly applying the MAP instrument covariances to the UoL-FP retrieval arise from the different treatment of aerosol optical properties. Whereas most aerosol profile information, i.e. the AOD, height and width of the Gaussian profile agrees between the MAP-mod and the UoL FP, aerosol optical parameters of the individual types as provided by MAP are not part of the state vector in the UoL-FP retrieval. Furthermore, the UoL-FP retrieval assumes that a priori information of the aerosol profiles is not correlated between profiles of different aerosol types.

Figure 9 depicts all a-priori information with green dots marking errors and covariances which can be readily processed. Information under the red cross could only by used after modifications to the UoL-FP retrieval algorithm, which is not feasible in the scope of this study. In the following, the chosen approach is described which enables the use of the additional aerosol information content (unmarked in Figure 9) of the MAP instrument without significant changes to the UoL-FP retrieval algorithm.

In order to take the MAP information into consideration, an ensemble of spectra is created which describes the variability of the atmospheric state for each individual scenario. Eigenvalue decomposition is used (Section D.3.1) to represent existing correlations between parameters in the MAP covariance matrix. The so generated set of independent observable states of the atmosphere is then fed to the UoL-FP forward model to generate an ensemble of spectra (Section D.3.2).

It must be noted that the following approaches and studies focus on the estimation of the impact of a-priori information on aerosol optical properties, because the impact of a-priori information on aerosol profile can be readily be estimated with the UoL-FP.

$$S = \begin{bmatrix} 1.0 & 0.5 \\ 0.5 & 1.0 \end{bmatrix}$$
$$L = \begin{bmatrix} 0.71 & 0.71 \\ -0.71 & 0.71 \end{bmatrix}$$
$$\Lambda = [0.5 \quad 1.5]$$

Covariance Matrix **S**
Eigenvector matrix **L** (columns)
eigenvalues **Λ**

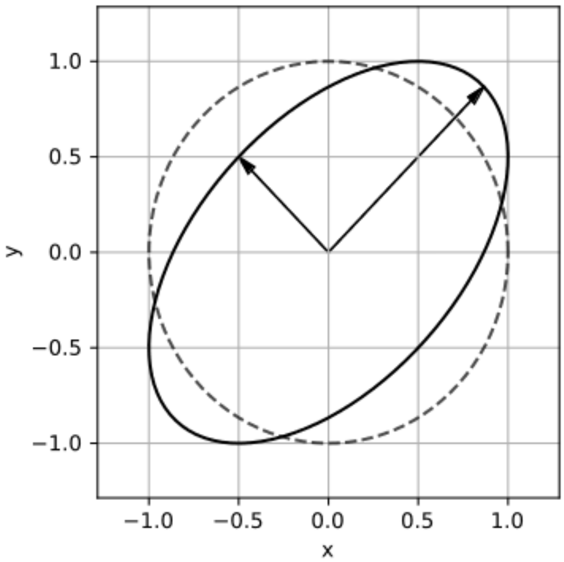

Figure 10: Illustration of correlated errors and eigenvalue decomposition. Left: A covariance matrix S of errors x,y can be expressed as eigenvalues and -vectors. Right: Graphical interpretation, with correlated errors corresponding to S as solid line, uncorrelated errors (non-diagonal entries = 0) as a dashed line. The arrows correspond to the eigenvectors with respective length of eigenvalues.

D.3.1) Eigenvalue decomposition of covariance matrix

An eigenvalue decomposition of the covariance matrix yields independent sets of aerosol error parameters (see [7], chapter 3). In this way, the observed correlations in the covariances matrix can be addressed as independent sets of errors. In a nutshell, a covariance matrix S can be diagonalized, i.e. finding eigenvalues λ and -vectors ***l*** so that $Sl_i = \lambda_i l_i$

$$S = \sum_i \lambda_i \, l_i l_i^T = \sum_i e_i e_i^T \; ; \; e_i = \lambda_i^{\frac{1}{2}} l_i ; \; \epsilon_x = \sum_i e_i$$

where $\boldsymbol{e_i}$ corresponds to orthogonal vectors aka error patters, which can be added to obtain the total error. The approach is illustrated in Figure 10 for the simple case of two correlated errors x, y.

The so generated error patterns include aerosol profile and optical parameter information. Whereas parts of the error patterns containing profile information (coarse AOD, coarse height [z], fine AOD) can be supplied directly to the retrieval, variations in optical parameters need to be assessed in a different manner.

D.3.2) Generation of spectra ensemble for individual scenes

The main challenges in the assessment of the impact of MAP a-priori information employing the UoL-FP algorithm results from the differing treatment of aerosol optical properties and their correlations as provided by the MAP instrument, as has been outlined in the previous sections.

Using the MAP a-priori information for each individual geophysical scenario, an ensemble of spectra is calculated which corresponds to the uncertainty in the atmospheric states as described with the aerosol properties:

Eigenvalue decomposition of the MAP a-priori covariance matrix is used to derive a new set of independent aerosol parameter values. Together with the default setup parameters (see Table 5) for the modelled spectrum R_0 of the respective covariance matrix, a set of observations/spectra $R_{p,i}$ can be modelled which describe the scene including in all relevant aerosol optical property uncertainties e_i.

$$R_{p,\pm i} = R_0 \pm e_i$$

The baseline properties R_0 for each scenario are given in Table 5.

This entails that the number of spectra to be evaluated increases by a factor of 18 (= 9 error patterns from the 9 aerosol optical parameters *2 to allow for positive and negative perturbation of the default value), leading to a total number of 1080 of spectra to be evaluated for 60 scenarios (20 scenarios in each geophysical case).

Because each individual perturbed spectrum belonging to a certain scenario is independent, the sum of their retrieval results yields the bias for the retrieval of the scenario within the boundaries spanned by the respective space of aerosol optical properties.

An example of the different aerosol optical extinction profiles is presented in Figure 11, which depicts the changes in extinction with wavelength for Case 3, albedo vegetation, SZA 60° and total AOD of 0.35. Differences induced by the different EPs are in general more pronounced for coarse aerosol than for fine aerosol.

Figure 12 depicts an example of the so generated ensembles for the scenario of Case 1, albedo: Vegetation, SZA 60° and a fine aerosol AOD 0.5.

Aerosol	Parameter	Geophysical Scenarios		
		Case 1	**Case 2**	**Case 3**
coarse	aod	0.02	variable	
	frac	0.05	0.05	0.05
	r_1	1	1	1
	r_2	0	0	0
	Reff [µm]	1.6	1.6	1.6
	Veff [µm]	0.6	0.6	0.6
	w [km]	2	2	2
	z [km]	1	8	4
fine	aod	variable	0.2	0.2
	frac	1	1	1
	r_1	1	1	1
	r_2	0	0	0
	Reff [µm]	0.12	0.12	0.2
	Veff [µm]	0.2	0.2	0.2
	w [km]	2	2	2
	z [km]	1	1	1

Table 5: Baseline properties R_0 for generation of spectral ensembles. For a description of individual parameters please refer to Section D.2.

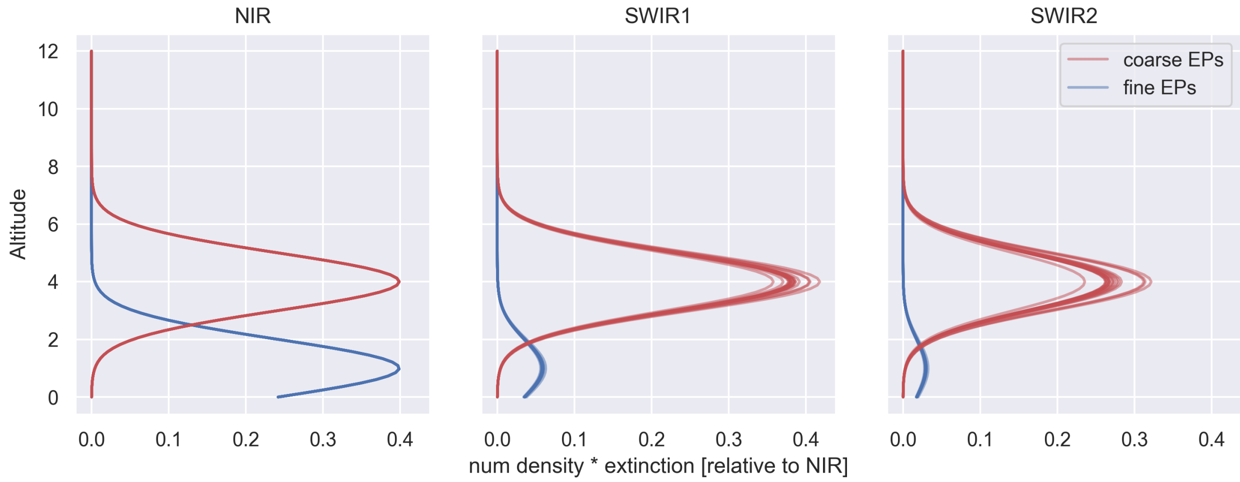

Figure 11: Different aerosol optical extinctions generated with respective error patterns (EPs) at the example of Case3, albedo vegetation, SZA 60°, fine aerosol AOD 0.2, coarse aerosol AOD 0.15. Please note that the total extinction has been normalized to the NIR window for all aerosol types to highlight the different wavelength dependencies of the aerosols.

D.3.3) Calculation of bias from spectra ensemble

The bias is the mean of the differences between retrieved XCO_2 for the different simulations for the distribution of aerosol states as described by the MAP covariance matrix and the true value (390ppm). The spectra in the ensemble are generated from an independent set of parameters, i.e. correlations from the covariance matrix are taken into account employing eigenvalue decomposition. Therefore, the bias can be calculated from retrieved values of each individual spectrum by simply taking the mean.

$$\langle xCO_2 \rangle = {}^{1}/_{n} \sum^{n} xCO_{2_n} - 390ppm$$

with n denoting the individual spectra and respective retrievals. The standard deviation of the retrieved parameters is used as an indication of the uncertainty of the bias. In case that the retrieval does not converge for individual spectra of the ensembles, these values are omitted in calculation of mean bias and standard deviation.

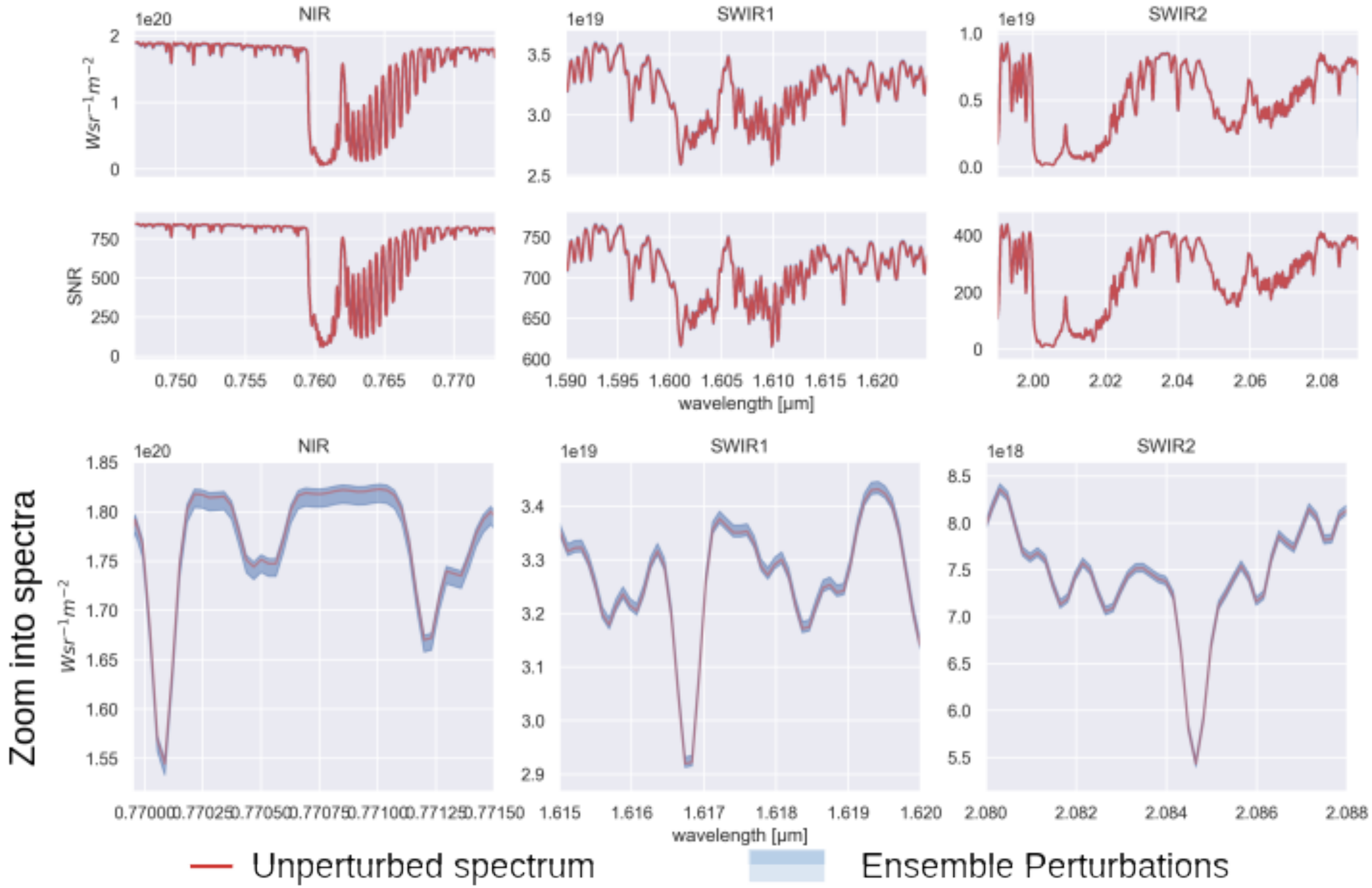

Figure 12: Visualization of an ensemble of spectra at the example of Case 1, BRDF: Vegetation, SZA 60° and a fine aerosol AOD 0.5. The range of spectra encountered by the perturbations is highlighted as blue envelope.

E Retrieval setups with different degrees of a-priori information

As outlined in section D.1, the standard UoL-FP retrieval employs two aerosol retrieval types and atmospheric profiles to estimate aerosol scattering. Both are assumed to consist of a small/fine and large/coarse particle (with large and small Ångström coefficients) and a Gaussian profile at height, width and AOD as modelled in the Geophysical Scenarios (section C). The true aerosol profile and optical properties are therefore estimated as the linear combination of both profile and properties as an "effective aerosol load".

It is obvious that the aerosol approach using two fixed aerosol retrieval types only acts as an estimation for aerosol-related biases for the scenarios studied. Here, differing aerosol optical properties and profiles are assessed, and the use of only two aerosol types with fixed optical properties can only act as an approximation. Retrieval setups BASE (E.1) and MEAN (E.2) employ this two-aerosol approach. To better capture the true variations in aerosol as described in the MAP a-priori covariance matrix, a four-aerosol retrieval has been setup (VAR, E.3) that better approximates the full variability of the atmospheric states.

E.1) Baseline retrieval without using any information of aerosol properties [BASE]

In this baseline approach [BASE] it is assumed that no information on aerosol optical properties are available. The Geophysical scenarios are therefore all evaluated with two, fixed aerosol types. They consisted of a small, carbonaceous, sooty continental mixture and a large, carbonaceous, dusty continental mixture as described in [6] called mixture 5b and 2b respectively. These aerosol types were chosen because they have been successfully used in previous operational GOSAT products and constitute aerosol mixtures with the largest and smallest Ångström coefficients in [6]. In order to map all dimensions of the aerosol optical properties information given in by the MAP instrument, retrievals are run on all perturbed spectra for each scenario (see section D.3.2). Both retrieval types were assigned the true a priori Gaussian-shaped profile (aerosol optical depth (AOD), height, width) for fine and coarse aerosol, respectively.

E.2) Mean aerosol type is known [MEAN]

The BASE retrieval provides only a worst-case picture of retrieved results for the geophysical scenarios. It is more realistic to assume that at least some aerosol a-priori information would be available, e.g. by modelling of aerosol fields, ground based

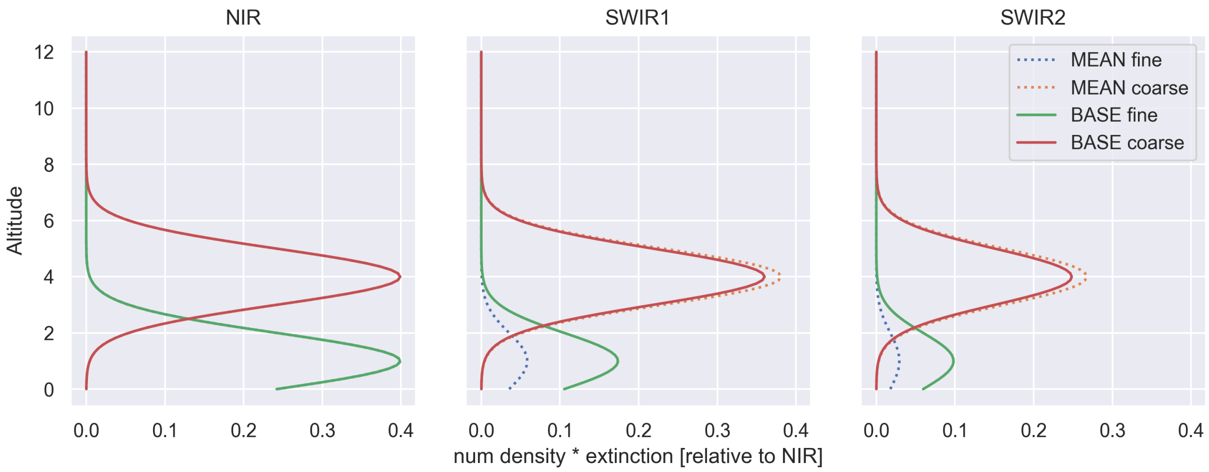

Figure 13: BASE and MEAN aerosol retrieval setup at the example of the extinction profiles for Case 3. Please note that the total extinction has been normalized to the NIR window for both aerosol types. In this way, the different wavelength dependencies of the aerosols becomes apparent.

observations or other space born instruments. Here, the assumption is made that the mean aerosol optical properties and profile are known from MAP – which correspond to the parameters used to calculate the unperturbed spectra for each scenario. Each scenario is evaluated by using these mean aerosol parameters in the retrieval of all perturbed spectra for the respective scenario.

Figure 13 depicts an extinction profiles for BASE and MEAN retrievals for the example of Case3. The profile has been normalized to values in the NIR window in order to highlight the wavelength dependencies of the different aerosol types. Clearly, the BASE fine aerosol type is not well adjusted to the mean fine aerosol properties for all scenarios. The coarse aerosol however shows quite a good agreement in terms of the wavelength dependencies of the extinction coefficient.

E.3) Retrieval with variable aerosol types [VAR]

As described in the previous section, the standard UoL-FP retrieval employs two aerosols types. To better exploit the MAP aerosol information with the UoL-FP retrieval we use four aerosol types instead of two in the retrieval. This allows to better match the encountered variability in the aerosol optical properties in the MAP aerosol information. Basically, the respective fine and coarse aerosol type are described by two aerosol types in the boundary

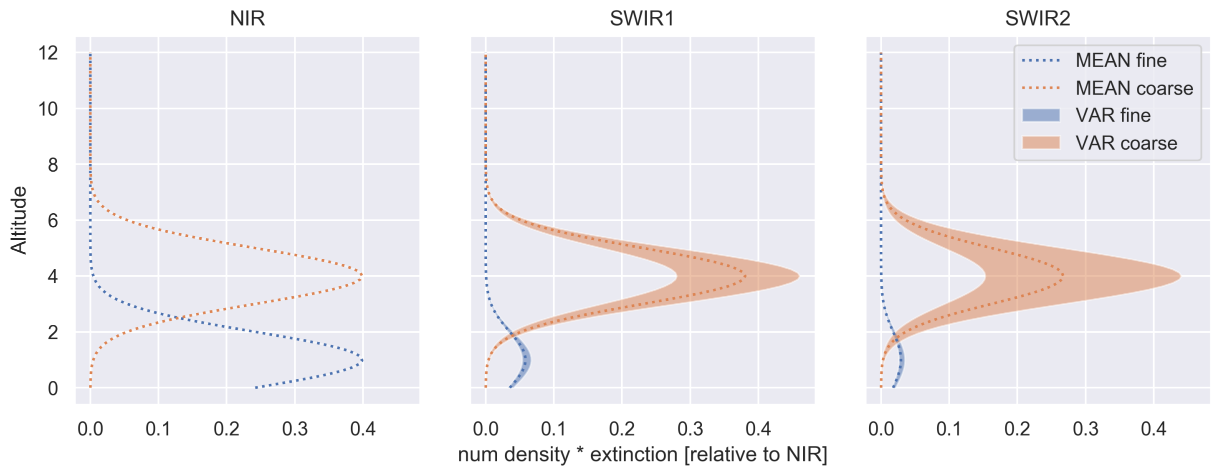

Figure 14: Aerosol retrieval setup VAR at the example of Case3, BRDF vegetation, SZA 60°, fine aerosol AOD 0.2, coarse aerosol AOD 0.15. Please note that the total extinction has been normalized to the NIR window for all aerosol types to highlight the different wavelength dependencies of the aerosols. The shaded area shows the range of extinctions spanned by the respective aerosol types with min.-max. Ångström coefficient.

layer and the free troposphere which encompass the encountered variability in the aerosol parameters.

This extended retrieval therefore has two aerosol types in the boundary layer (fine aerosol) and two in the free troposphere (coarse aerosol) depending on the respective geophysical scenario. The aerosol optical parameters need to allow for a sufficient degree of freedom to encompass the aerosol variations in individual scenarios, but still match the information from MAP instrument. To this end, the maximum uncertainty of the microphysical parameters (given by the diagonal elements of the covariance matrix) are used to create the respective fine and coarse aerosol properties and find a set of fine and coarse aerosols with the maximum and minimum Ångström coefficient.

These parameter sets are specific for each individual scenario. The advantage is that a) the whole ensemble of spectra for an individual scenario is still evaluated with a constant set of aerosol retrieval types, which is consistent with the other retrieval setups; and b) that it resembles an approach which could directly be reproduced for measured spectra and their respective MAP information without changing the retrieval algorithm.

Figure 14 shows an example of how the respective minimum and maximum aerosol type encompass the mean aerosol type. The NIR window seems to only depict the mean curves because of the normalization to that window. Note that the respective distributions of aerosol properties used to construct the ensemble of spectra is depicted in Figure 11. Although the range in Figure 14 is much wider for the coarse aerosol, the objective of constructing an envelope for all true aerosol properties is fulfilled.

F Results and discussion

The resulting biases for all retrieval setups are shown in Figure 15, which depicts the range of encountered results in [-5, 10] ppm XCO_2 as well as a closer look in [-2, 2] ppm XCO_2. The latter highlights actual results of interest and the difference between MEAN and VAR retrieval setups. The respective distribution of individual results from the ensembles are given in Figure 16, which also provides a zoom to the interval [0, 2] ppm XCO_2. All plotted values are also given in Table 6.

Results from the individual retrievals of spectra for all ensembles are shown in Appendix A.

F.1) Results BASE retrieval setup

The results from the BASE setup highlight the need for using appropriate aerosol optical properties. Unacceptable high biases are encountered at higher AODs and in some cases (e.g., Case2 with an albedo for vegetation) for all retrievals.

This is not surprising, since the aerosol optical properties are quite different for both, fine and coarse aerosol types, e.g., comparing Figure 13 showing the extinction properties of aerosols used in the retrieval with the ones employed in constructing the ensemble of spectra (Figure 11), it is obvious that greater differences are present. Especially the fine, boundary layer aerosol used in the retrieval exhibits a much smaller Ångström coefficient (equivalent to lesser reduction of extinction with increasing wavelength) than the ones used in generating the spectra ensemble. This feature is not as prominent for the coarse, free tropospheric aerosol.

For operational retrievals, some a-posteriori filtering would be used to remove these biased retrievals. However, that means also that only a small subset of spectra in the ensemble would pass that filter and the number of observed scenes would be greatly reduced. This is especially true for scenes of interest for the space mission and studying the carbon cycle, like vegetated areas in the northern hemisphere (e.g. albedo vegetation, higher SZA 60°).

F.2) Results MEAN retrieval setup

Observed biases for retrievals applying the MEAN aerosol show a good agreement in most cases (<1ppm XCO_2 bias) and even yield results meeting the threshold criteria (<0.1% or 0.39ppm XCO_2) for geophysical scenarios case 1. However, results for geophysical scenarios case 2 and 3 show biases above 0.1% XCO_2 for higher AODs (>0.25). Although these biases are still small, one can observe greater standard deviations for the results in each ensemble (Figure 16). For cases 2 and 3, these standard deviations can range up to

6ppm XCO_2 and indicate that this retrieval setup is not suitable to capture the whole range of predicted aerosols distributions, even if the mean state of the distribution is known.

Therefore, even mean aerosol optical properties are known via other sources, e.g. models, the retrieval with MEAN setup cannot capture the full distribution.

F.3) Results VAR retrieval setup

The retrieval setup VAR yields very good results. The bias calculated for almost all ensembles remains below the threshold of 0.1% (0.39ppm) XCO_2. Case 1 shows a very small bias for all AODs (~0.15 ppm XCO_2), which shows no significant dependence on true total aerosol AOD. Bias for Case 2 shows greater variation and can breach the threshold in case of vegetation albedo, but remains always below an absolute bias of 1ppm XCO_2. Results for Case 3 meet the threshold requirements. In all cases, the observed standard deviation of individual results in the ensemble are small (< 0.1% XCO_2) and compare very well against the other retrieval setups.

In the scenarios for Case2, albedo vegetation, the VAR retrieval setup shows some deficiencies compared to its performance in the other scenarios. In general, a trend can be observed where for Case 2 and Case 3 where the results show a positive bias for low total aerosol AODs, which decreases as the total aerosol load in the scenarios increases. Because the fine aerosol load is kept fixed when generating the spectra ensemble, this may indicate that the approach does not fully capture the true aerosol optical properties of the fine, boundary layer aerosol leading to a certain bias best observed at low coarse, free tropospheric aerosol load. Observed anti-correlation of bias with increasing total aerosol AOD for case 2 and 3 indicate anti-correlation of bias with coarse aerosol AOD. This feature becomes more prominent the higher the aerosol layer in altitude (case 2 vs case 3) and less light is reflected from the ground (albedo soil vs vegetation).

One has to keep in mind that the chosen approach was born out of the necessity to merge the MAP a-priori information with the UoL-FP retrieval rather than adapting the retrieval code itself to make use of the a-priori information. Therefore, these results must be understood as an upper limit because the retrieval algorithm itself has not been adjusted to make full use of the a-priori information. Nevertheless, the results are very promising and highlight the potential of employing improved a-priori information.

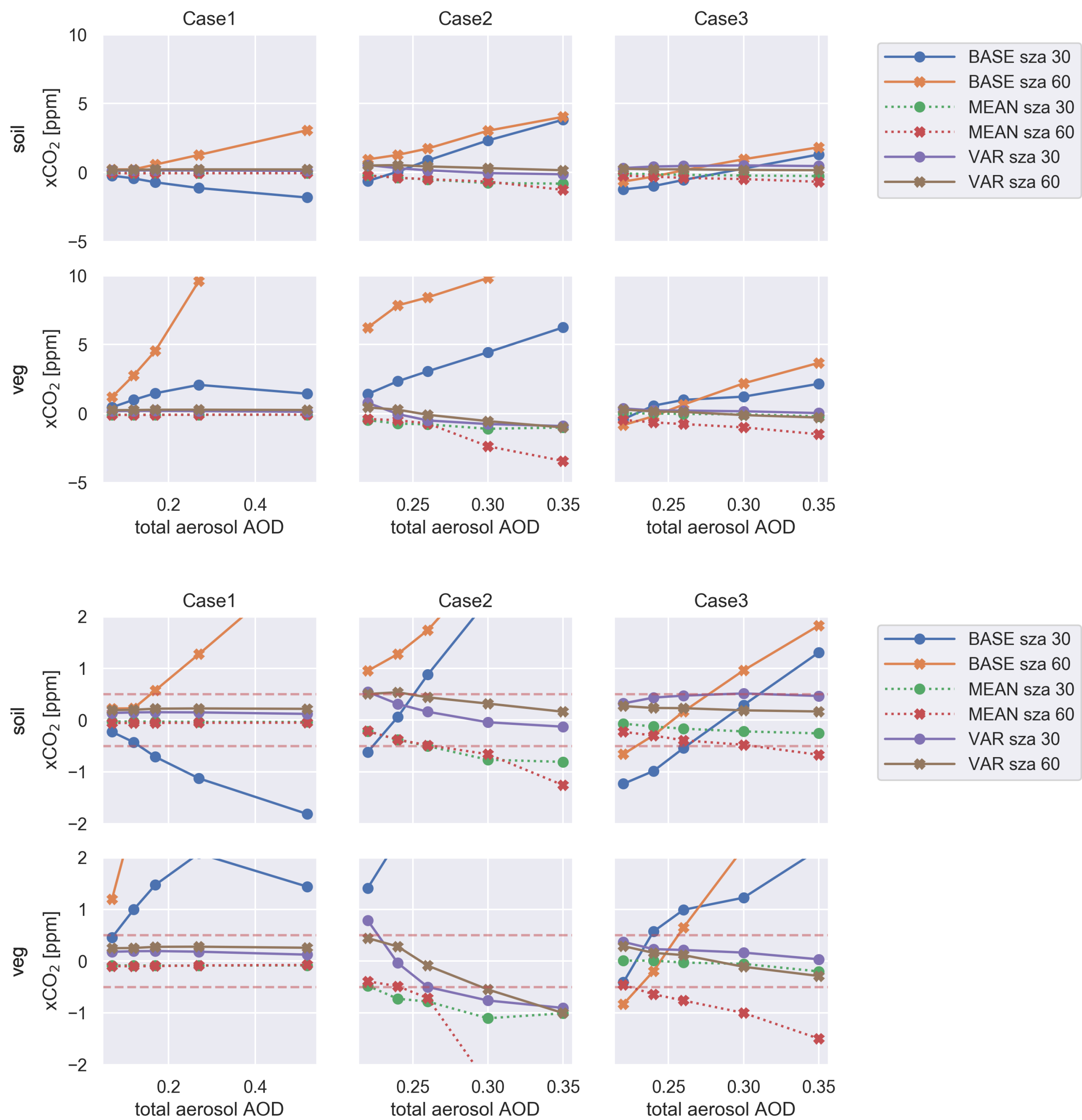

Figure 15: Resulting biases for all geophysical scenarios and retrieval setups, with bias as retrieved - true XCO_2 (390ppm). The top panel depicts the calculated bias in the range of [-5, 10] ppm XCO_2 in order to show encountered values. The bottom panel highlights the range of [-2, 2] ppm XCO_2, which allows to study actual ranges of interest and the differences between MEAN and VAR. The dotted horizontal line marks ±0.1% (0.39 ppm) XCO_2.

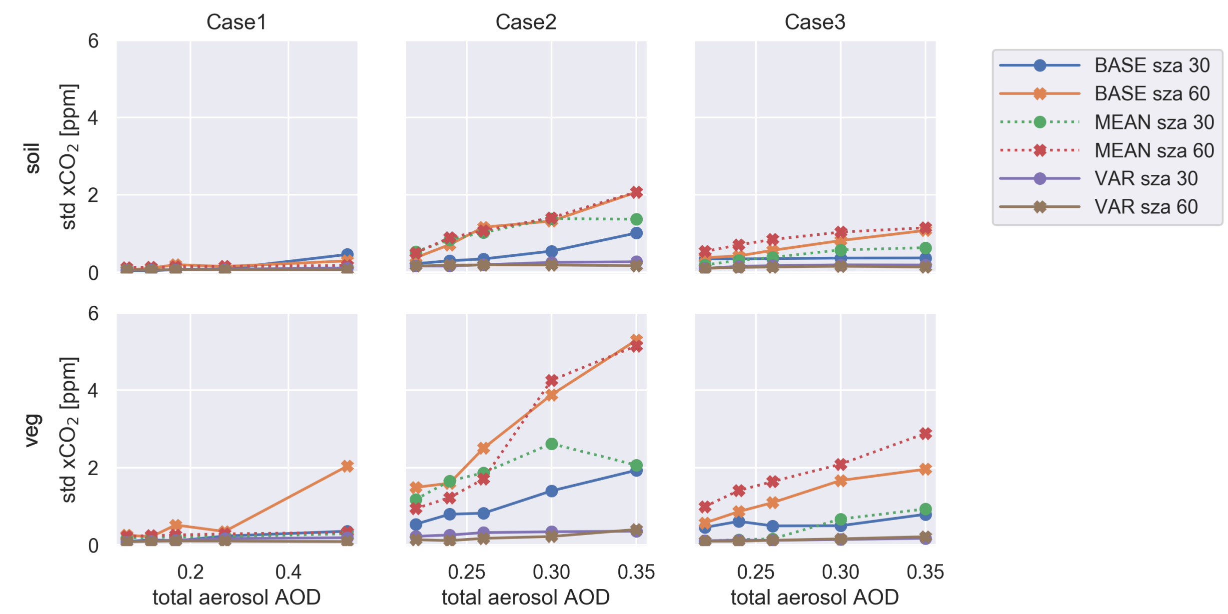

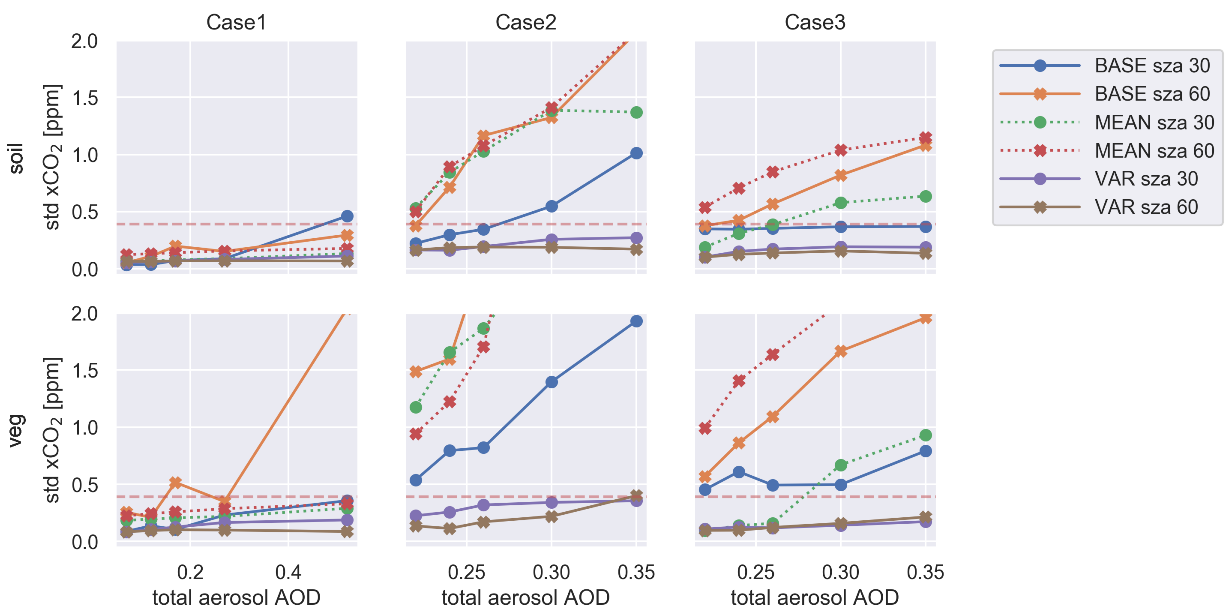

Figure 16: Standard deviation of retrieved XCO_2 values for the respective ensemble. The top figures show the full encountered range, the bottom panel depicts the interval of [0, 2] ppm XCO_2. The dotted line represents 0.1% = 0.39 ppm XCO_2 of the true value .

Table 6: Tabulated results for the different geophysical scenarios and retrieval setups. Bias refers to the mean retrieved XCO_2 for respective ensemble minus 390ppm XCO_2, standard deviation to the encountered standard deviation of results.

				BASE		MEAN		VAR	
Case	**BRDF**	**SZA**	**total AOD**	**Bias [ppm]**	**std [ppm]**	**Bias [ppm]**	**std [ppm]**	**Bias [ppm]**	**std [ppm]**
Case1	**soil**	**30**	**0.07**	-1.715E-01	2.288E-02	-2.790E-02	6.380E-02	1.375E-01	5.483E-02
			0.12	-3.630E-01	2.533E-02	-2.802E-02	7.155E-02	1.481E-01	6.212E-02
			0.17	-9.245E-01	4.671E-02	-3.022E-02	7.832E-02	1.522E-01	6.854E-02
			0.27	-1.466E+00	4.439E-02	-3.438E-02	8.873E-02	1.485E-01	8.187E-02
			0.52	-3.150E+00	6.221E-01	-3.603E-02	1.332E-01	1.194E-01	1.116E-01
		60	**0.07**	2.489E-01	4.066E-02	-5.616E-02	1.237E-01	1.921E-01	6.466E-02
			0.12	3.046E-01	5.573E-02	-5.589E-02	1.318E-01	1.989E-01	6.456E-02
			0.17	3.293E-01	5.578E-02	-5.430E-02	1.404E-01	2.205E-01	6.868E-02
			0.27	7.156E-01	5.627E-02	-5.238E-02	1.563E-01	2.251E-01	6.975E-02
			0.52	3.763E+00	1.314E-01	-4.980E-02	1.776E-01	2.171E-01	6.819E-02
	veg	**30**	**0.07**	4.560E-01	9.850E-02	-8.186E-02	1.844E-01	1.807E-01	8.326E-02
			0.12	1.198E+00	1.566E-01	-8.407E-02	1.963E-01	1.917E-01	1.053E-01
			0.17	1.330E+00	1.171E-01	-8.557E-02	2.066E-01	1.951E-01	1.261E-01
			0.27	1.339E+00	1.094E-01	-8.552E-02	2.194E-01	1.827E-01	1.661E-01
			0.52	2.283E+00	1.865E-01	-8.184E-02	2.905E-01	1.256E-01	1.882E-01
		60	**0.07**	1.366E+00	1.737E-01	-9.635E-02	2.250E-01	2.498E-01	8.499E-02
			0.12	2.509E+00	2.953E-01	-9.938E-02	2.439E-01	2.544E-01	9.567E-02
			0.17	2.987E+00	2.350E-01	-9.496E-02	2.587E-01	2.767E-01	1.030E-01
			0.27	9.168E+00	3.102E-01	-8.305E-02	2.869E-01	2.793E-01	1.000E-01
			0.52	2.028E+01	4.989E-01	-7.317E-02	3.301E-01	2.590E-01	8.745E-02
Case2	**soil**	**30**	**0.22**	-1.554E-01	2.920E-01	-2.148E-01	5.315E-01	5.442E-01	1.647E-01
			0.24	4.927E-01	3.701E-01	-3.803E-01	8.432E-01	3.112E-01	1.621E-01
			0.26	1.285E+00	4.206E-01	-5.023E-01	1.029E+00	1.603E-01	1.946E-01
			0.30	2.629E+00	5.271E-01	-7.661E-01	1.387E+00	-4.242E-02	2.577E-01
			0.35	4.034E+00	8.443E-01	-8.072E-01	1.371E+00	-1.275E-01	2.720E-01
		60	**0.22**	7.497E-01	3.933E-01	-2.138E-01	5.002E-01	5.041E-01	1.630E-01
			0.24	1.523E+00	5.700E-01	-3.783E-01	8.929E-01	5.373E-01	1.860E-01
			0.26	2.211E+00	8.754E-01	-4.857E-01	1.076E+00	4.391E-01	1.901E-01
			0.30	3.095E+00	1.293E+00	-6.591E-01	1.411E+00	3.187E-01	1.880E-01
			0.35	3.759E+00	1.470E+00	-1.258E+00	2.073E+00	1.609E-01	1.714E-01
	veg	**30**	**0.22**	2.202E+00	5.499E-01	-4.762E-01	1.174E+00	7.865E-01	2.251E-01
			0.24	3.165E+00	9.312E-01	-7.259E-01	1.655E+00	-3.602E-02	2.580E-01
			0.26	3.829E+00	9.739E-01	-7.803E-01	1.864E+00	-4.989E-01	3.197E-01
			0.30	5.157E+00	1.471E+00	-1.103E+00	2.618E+00	-7.601E-01	3.420E-01
			0.35	6.520E+00	1.905E+00	-1.007E+00	2.061E+00	-9.035E-01	3.563E-01
		60	**0.22**	4.001E+00	1.006E+00	-3.893E-01	9.413E-01	4.454E-01	1.363E-01
			0.24	4.719E+00	1.367E+00	-4.839E-01	1.223E+00	2.827E-01	1.137E-01
			0.26	6.516E+00	3.652E+00	-7.143E-01	1.703E+00	-8.793E-02	1.721E-01
			0.30	1.187E+01	5.017E+00	-2.370E+00	4.254E+00	-5.477E-01	2.200E-01
			0.35	1.481E+01	5.647E+00	-3.433E+00	5.143E+00	-1.003E+00	4.015E-01

Table 6, continued: Tabulated results for the different geophysical scenarios and retrieval setups. Bias refers to the mean retrieved XCO_2 for respective ensemble minus 390ppm XCO_2, standard deviation to the encountered standard deviation of results.

				BASE		MEAN		VAR	
Case	BRDF	SZA	total AOD	Bias [ppm]	std [ppm]	Bias [ppm]	std [ppm]	Bias [ppm]	std [ppm]
Case3	soil	30	0.22	2.423E-02	2.147E-01	-6.879E-02	1.887E-01	3.224E-01	1.016E-01
			0.24	2.685E-01	2.136E-01	-1.246E-01	3.097E-01	4.340E-01	1.524E-01
			0.26	6.565E-01	2.202E-01	-1.664E-01	3.859E-01	4.725E-01	1.721E-01
			0.30	1.326E+00	4.031E-01	-2.190E-01	5.785E-01	5.145E-01	1.927E-01
			0.35	2.128E+00	4.665E-01	-2.564E-01	6.357E-01	4.661E-01	1.891E-01
		60	0.22	-2.703E-01	1.821E-01	-2.275E-01	5.388E-01	2.709E-01	1.020E-01
			0.24	2.651E-01	3.760E-01	-2.987E-01	7.069E-01	2.341E-01	1.265E-01
			0.26	5.816E-01	4.280E-01	-3.916E-01	8.488E-01	2.301E-01	1.380E-01
			0.30	1.227E+00	5.512E-01	-4.774E-01	1.038E+00	1.879E-01	1.560E-01
			0.35	1.988E+00	7.344E-01	-6.700E-01	1.150E+00	1.664E-01	1.357E-01
	veg	30	0.22	3.845E-01	8.202E-01	1.045E-02	9.594E-02	3.719E-01	1.087E-01
			0.24	5.683E-01	2.847E-01	1.030E-02	1.397E-01	2.319E-01	1.270E-01
			0.26	9.483E-01	3.751E-01	-2.720E-02	1.595E-01	2.159E-01	1.191E-01
			0.30	1.689E+00	5.794E-01	-5.266E-02	6.709E-01	1.652E-01	1.421E-01
			0.35	2.664E+00	8.786E-01	-1.979E-01	9.303E-01	3.583E-02	1.737E-01
		60	0.22	-3.492E-01	6.188E-01	-4.600E-01	9.902E-01	2.900E-01	9.720E-02
			0.24	3.665E-02	7.414E-01	-6.392E-01	1.406E+00	1.601E-01	9.841E-02
			0.26	1.097E+00	1.093E+00	-7.608E-01	1.638E+00	1.169E-01	1.229E-01
			0.30	2.545E+00	1.271E+00	-1.000E+00	2.087E+00	-1.089E-01	1.587E-01
			0.35	3.973E+00	1.674E+00	-1.497E+00	2.882E+00	-2.870E-01	2.144E-01

F.4) Comparison with results obtained with the RemoteTeC algorithm

Results for the geophysical scenarios using the RemoTeC algorithm have been described elsewhere (e.g., see presentation by Stephanie Ruesli during progress meeting on May 30th 2018). Table 7 compares the range of errors obtained with a linear error approximation with the RemoTeC algorithm with the standard deviation of respective UoL retrieval scenario. It can be observed that error ranges of the UoL retrievals are comparable to RemoTeC for many cases, but certain systematic deviations occur. Whereas the error by RemoTeC varies around 0.1% XCO_2 without much dependencies on the scenarios, one can observe several trends for the UoL retrievals. For Case 1, all UoL retrieval setup show a similar or lower range of errors than RemoTeC. The BASE and MEAN setups show highly increased ranges for Case 2 and Case 3, especially at conditions with increased sensitivity to aerosols like albedo vegetation and SZA of 60°. The standard deviation of VAR retrieval does not exceed 0.1% XCO_2 and remains commonly about a factor 2 - 3 below ranges observed with RemoTeC.

It is difficult explain the observed differences between RemoTeC and the VAR setup without further tests. This is especially true given the differences in retrieval methods. One could speculate that the covariances in the VAR setup overly constrained the aerosol profile. Although this setup provides a good adaptation of the a-priori information to the UoL retrieval, some deficiencies remain due to its experimental nature.

However, the relative ranges of the different retrieval setups (BASE > MEAN > VAR) together with the same order of magnitude with the RemoTeC errors highlight the use of the additional a-priori information of the MAP instrument.

Albedo	SZA	Retrieval	Case 1	Case 2	Case 3
Soil	30	RT	0.08 – 0.11	0.07 – 0.10	0.06 – 0.08
		UoL BASE	0.01 - 0.16	0.07 - 0.22	0.05 - 0.12
		UoL MEAN	0.02 - 0.03	0.14 - 0.36	0.05 - 0.16
		UoL VAR	0.01 - 0.03	0.04 - 0.07	0.03 - 0.05
	60	RT	0.08 – 0.16	0.09 – 0.13	0.09 – 0.12
		UoL BASE	0.01 - 0.03	0.10 - 0.38	0.05 - 0.19
		UoL MEAN	0.03 - 0.05	0.13 - 0.53	0.14 - 0.29
		UoL VAR	0.02 - 0.02	0.04 - 0.05	0.03 - 0.04
Vegetation	30	RT	0.09 – 0.15	0.08 – 0.10	0.10 – 0.13
		UoL BASE	0.03 - 0.05	0.14 - 0.49	0.07 - 0.23
		UoL MEAN	0.05 - 0.07	0.30 - 0.67	0.02 - 0.24
		UoL VAR	0.02 - 0.05	0.06 - 0.09	0.03 - 0.04
	60	RT	0.10 – 0.17	0.10 – 0.11	0.10 – 0.13
		UoL BASE	0.04 - 0.13	0.26 - 1.45	0.16 - 0.43
		UoL MEAN	0.06 - 0.08	0.24 - 1.32	0.25 - 0.74
		UoL VAR	0.02 - 0.03	0.03 - 0.10	0.02 - 0.05

Table 7: Range of errors in % of true XCO_2. Shown are both, results from the RemoteTec (RT) algorithm for the mod-MAP instrument as well as standard deviation of results obtained with the UoL retrieval.

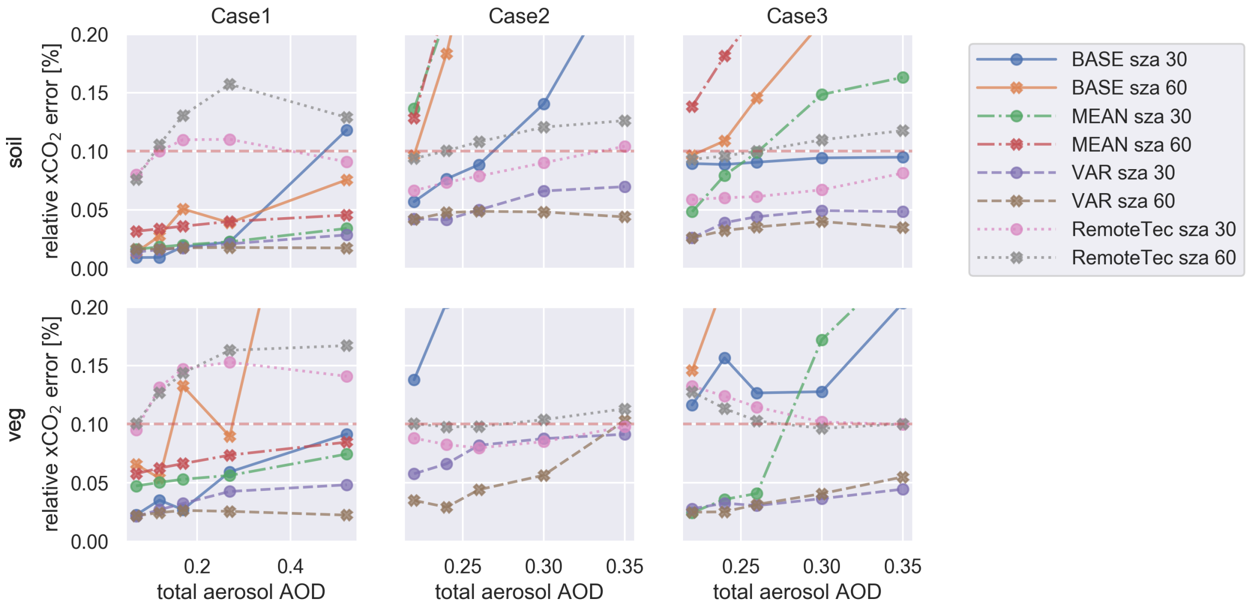

Figure 17: Comparison of UoL standard deviation of each ensemble versus error obtained with the RemoteTeC retrieval.

G Conclusion

This tech note describes the work performed to allow an assessment of the gain in performance by improved aerosol a-priori knowledge. To this end, the information provided by a fictional MAP instrument for a range of geophysical scenarios was translated into ensembles of spectra, which were evaluated with the UoL-FP algorithm under different setups. Setup BASE does not employ any additional a-priori aerosol information and indicates performance for a generic retrieval. Setup MEAN uses the mean aerosol parameters for the geophysical scenarios, which are also used in the generation of the MAP a-priori information. This setup indicates performance in case of reduced a-priori information, because it reflects the values retrieved with a MAP instrument, but not their covariance matrix. The VAR setup employs a range of aerosol optical properties and reflects the variances observed with the MAP instrument. It is designed to allow a consistent retrieval for all spectra of an ensemble, encompassing the encountered range of aerosol properties. The VAR retrieval setup constitutes a best approximation of the use of additional a-priori information without modifying the UoL-FP algorithm itself.

Figure 18 and Figure 19 depict results for BASE and VAR retrieval setups at SZA 30° and 60°, respectively. The figures show the combined biases for the individual retrievals in the ensembles for all geophysical scenarios and aerosol AOD variations. In order to filter out outliers, the shaded areas show the respective 25%-75% percentile range, whereas the solid line depicts the mean of all biases. It is obvious that the BASE retrieval does not lead to acceptable results for the gross of scenarios and aerosol loads. If the uncertainty of aerosol parameters is taken into account with the VAR retrievals, however, biases are obtained which meet the 0.1% XCO_2 threshold values and show significant lesser spread. It must be noted that certain discontinuities are visible with increasing total aerosol AOD. The reason is that the geophysical scenarios have been assessed at different total aerosol loads. Case 1 simulates AOD ranges between 0.07 and 0.52, whereas case 2 & 3 are restricted to 0.22 – 0.35. Therefore, values for total AODs lesser than 0.22 and greater than 0.35 only show results for case 1.

Comparing the bias results from the different retrieval setups in more detail (Figure 15 and Figure 16), confirm that the BASE setup, i.e., the one without further aerosol information, would only yield acceptable results for low aerosol AODs and under certain scenarios. Especially for observations of greater interest like measuring XCO_2 over vegetation more a-priori information is needed. If the average of aerosol properties is known (retrieval setup MEAN), the observed bias is greatly reduced and remains below 0.1% XCO_2 for most scenarios. Increased bias is still observed under conditions especially sensitive to aerosols like albedo vegetation, SZA 60° and/or aerosol profiles with higher AODs and altitude (Case

2, 3). Furthermore, individual results from the ensemble show a higher variability as indicated by higher standard deviation. If the VAR setup is used, which adapts the UoL retrieval setup to employ the given a-priori information, the observed bias meets the 0.1% XCO_2 criteria in all but the most extreme cases together with low standard deviation of the individual ensemble results.

Comparison of the error ranges obtained with the RemoteTec algorithm confirm the gain by additional a-priori information. In general, standard deviation of results by the VAR retrieval are within a factor of 2 below error ranges of the RemoteTec algorithm, meeting goal requirements.

These results of the different retrieval setups, from no aerosol optical properties information, mean properties known and approximation of full use of additional a-priori information, clearly highlight the improvements in performance of the UoL retrieval when employing external aerosol information.

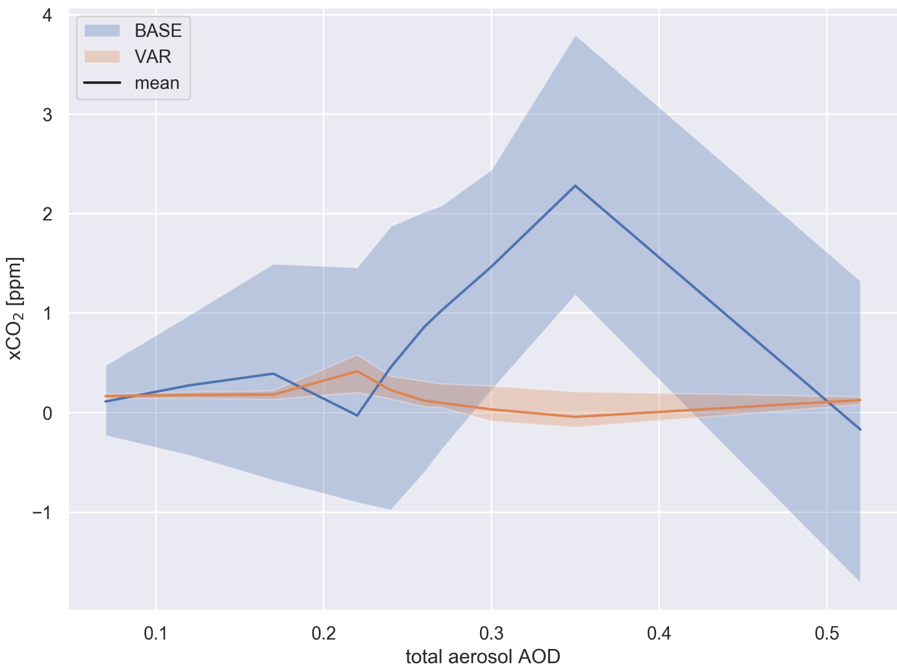

Figure 18: Combined biases for SZA 30° for all geophysical scenario ensembles and retrieval setups BASE and VAR. The solid line denotes the respective median and the shaded area the 25%-75% percentiles of all retrievals.

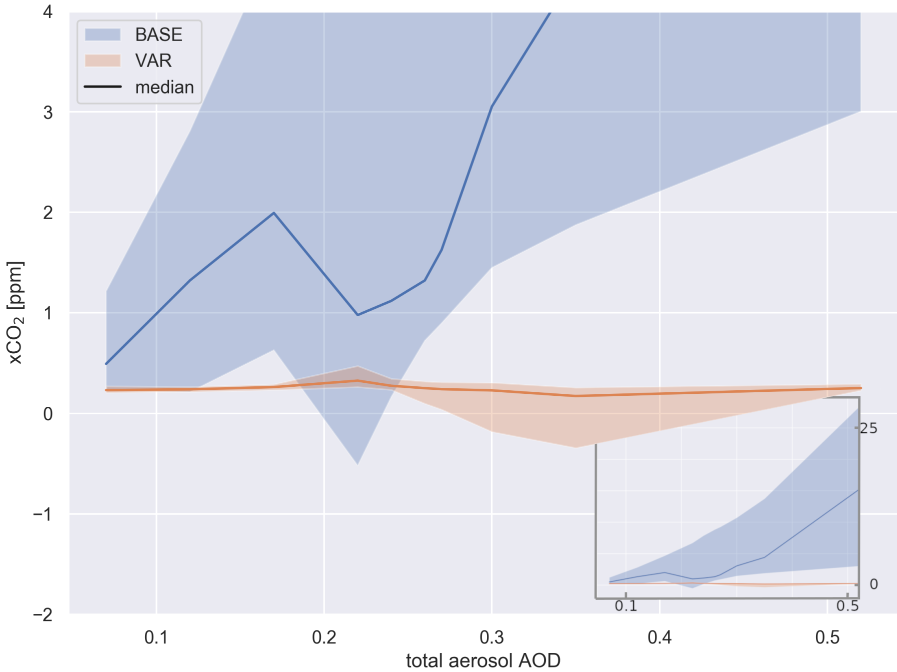

Figure 19: Combined biases for SZA 60° for all geophysical scenario ensembles and retrieval setups BASE and VAR. The solid line denotes the respective median and the shaded area the 25%-75% percentiles of all retrievals. The inlay in the lower right corner depicts the full range of the results at a range up to 25ppm XCO_2.

H References

1. Dubovik, O. *et al.* Application of spheroid models to account for aerosol particle nonsphericity in remote sensing of desert dust. *Journal of Geophysical Research: Atmospheres* **111**, (2006).
2. Connor, B. J. *et al.* Orbiting carbon observatory: Inverse method and prospective error analysis. *J. Geophys. Res.-Atmos.* **113**, D05305 (2008).
3. Boesch, H., Baker, D., Connor, B., Crisp, D. & Miller, C. Global Characterization of CO2 Column Retrievals from Shortwave-Infrared Satellite Observations of the Orbiting Carbon Observatory-2 Mission. *Remote Sens.* **3**, 270–304 (2011).
4. Cogan, A. J. *et al.* Atmospheric carbon dioxide retrieved from the Greenhouse gases Observing SATellite (GOSAT): Comparison with ground-based TCCON observations and GEOS-Chem model calculations: GOSAT OBSERVATIONS. *Journal of Geophysical Research: Atmospheres* **117**, n/a-n/a (2012).
5. Hartmut Boesch *et al. OCO-2 Level 2 Full Physics Retrieval Algorithm Theoretical Basis, Version 2.0 Rev 2*. (Jet Propulsion Laboratory California Institute of Technology Pasadena, California, 2015).
6. Kahn, R., Banerjee, P. & McDonald, D. Sensitivity of multiangle imaging to natural mixtures of aerosols over ocean. *Journal of Geophysical Research: Atmospheres* **106**, 18219–18238 (2001).
7. Rodgers, C. D. *Inverse Methods for Atmospheric Sounding: Theory and Practice*. (WORLD SCIENTIFIC, 2000). doi:10.1142/3171

Appendix A Error pattern ensembles; retrieval results for individual spectra

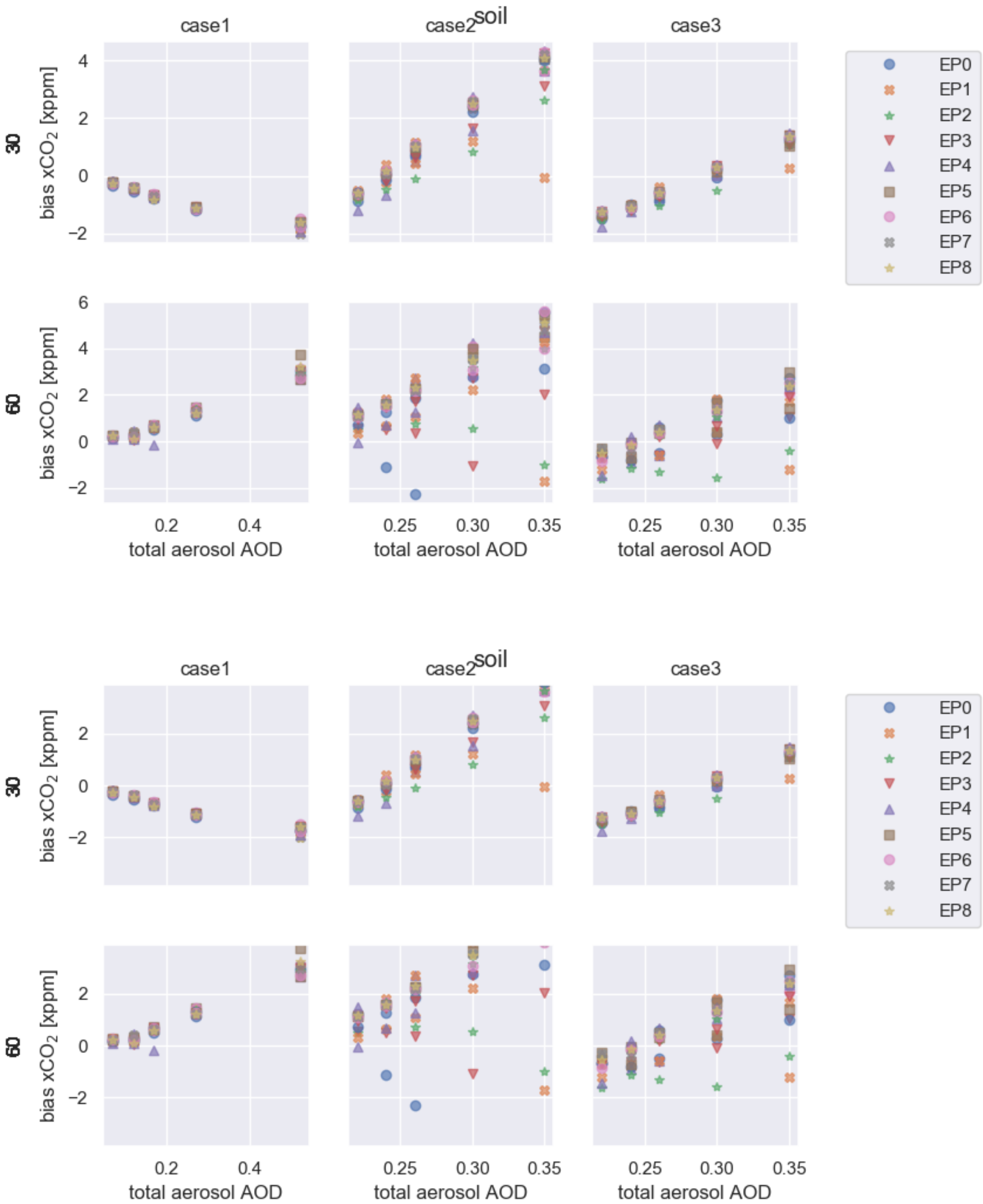

Figure 20: BASE retrieval of the EP ensemble with BRDF soil. The top panel shows the full range of retrieved values, whereas the bottom graph focuses only on a bias of ±3.9 ppm XCO_2 (±1%).

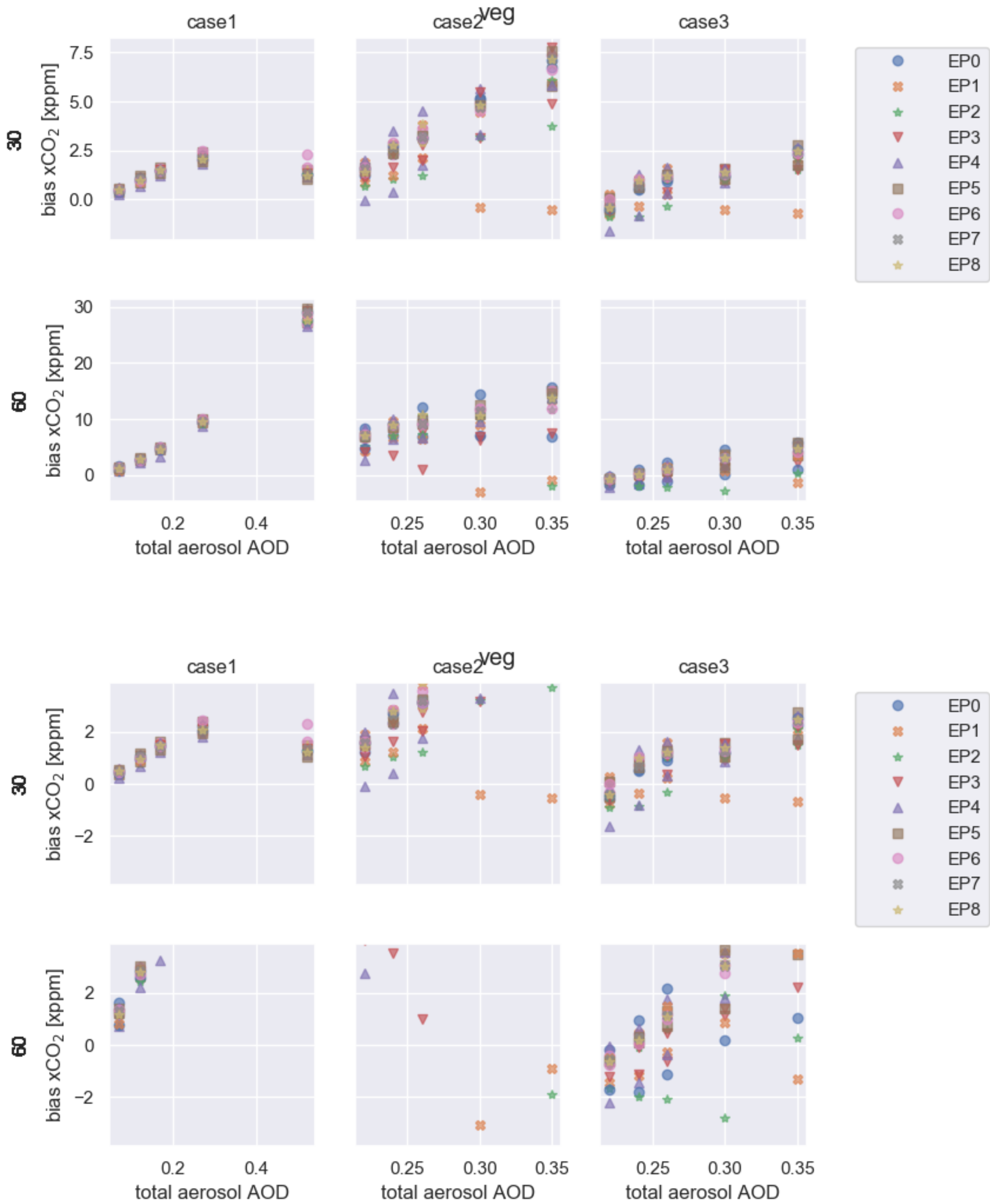

Figure 21: BASE retrieval of the EP ensemble with BRDF vegetation. The top panel shows the full range of retrieved values, whereas the bottom graph focuses only on a bias of ±3.9 ppm XCO_2 (±1%).

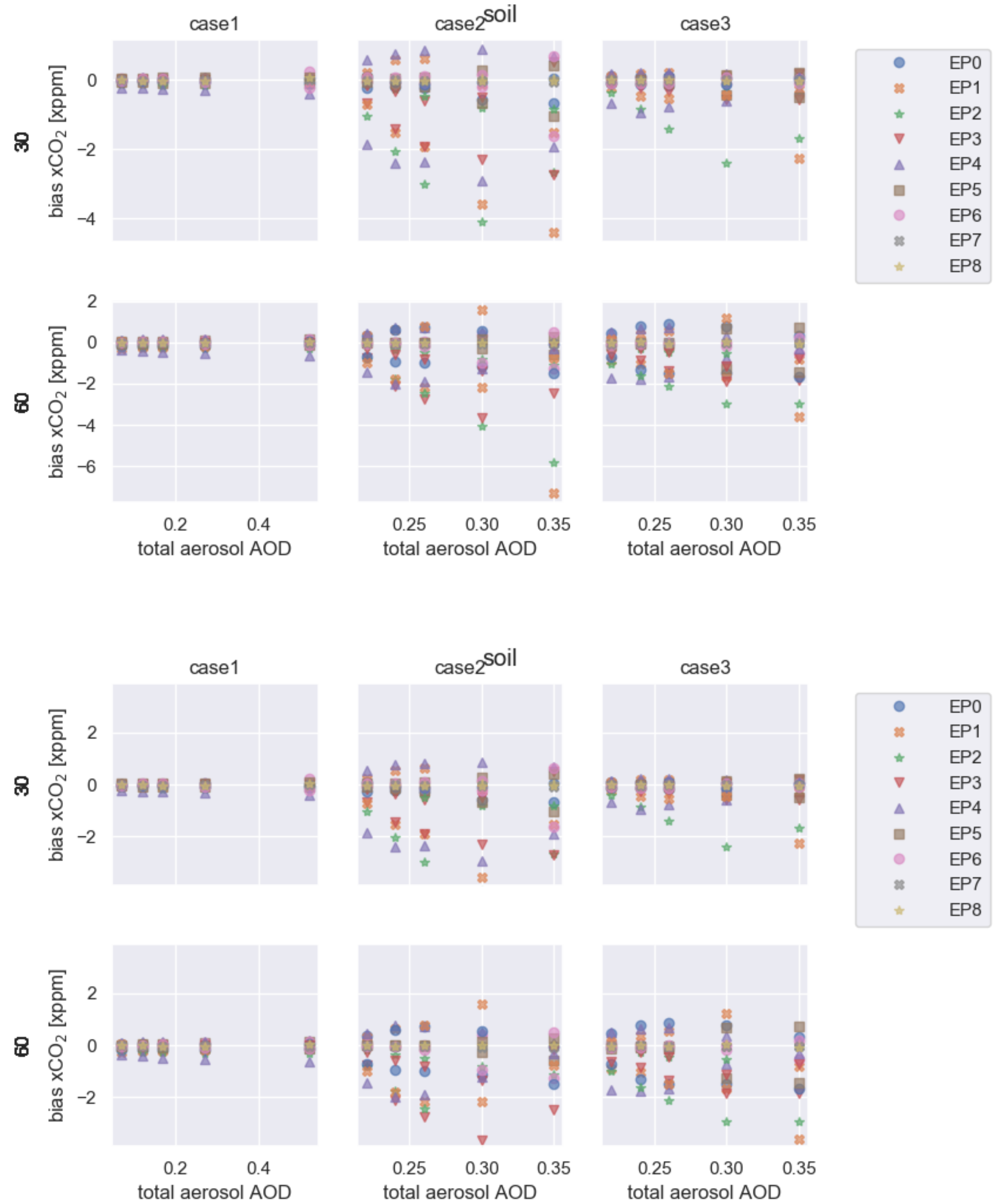

Figure 22: MEAN retrieval of the EP ensemble with BRDF soil. The top panel shows the full range of retrieved values, whereas the bottom graph focuses only on a bias of ±3.9 ppm XCO_2 (±1%).

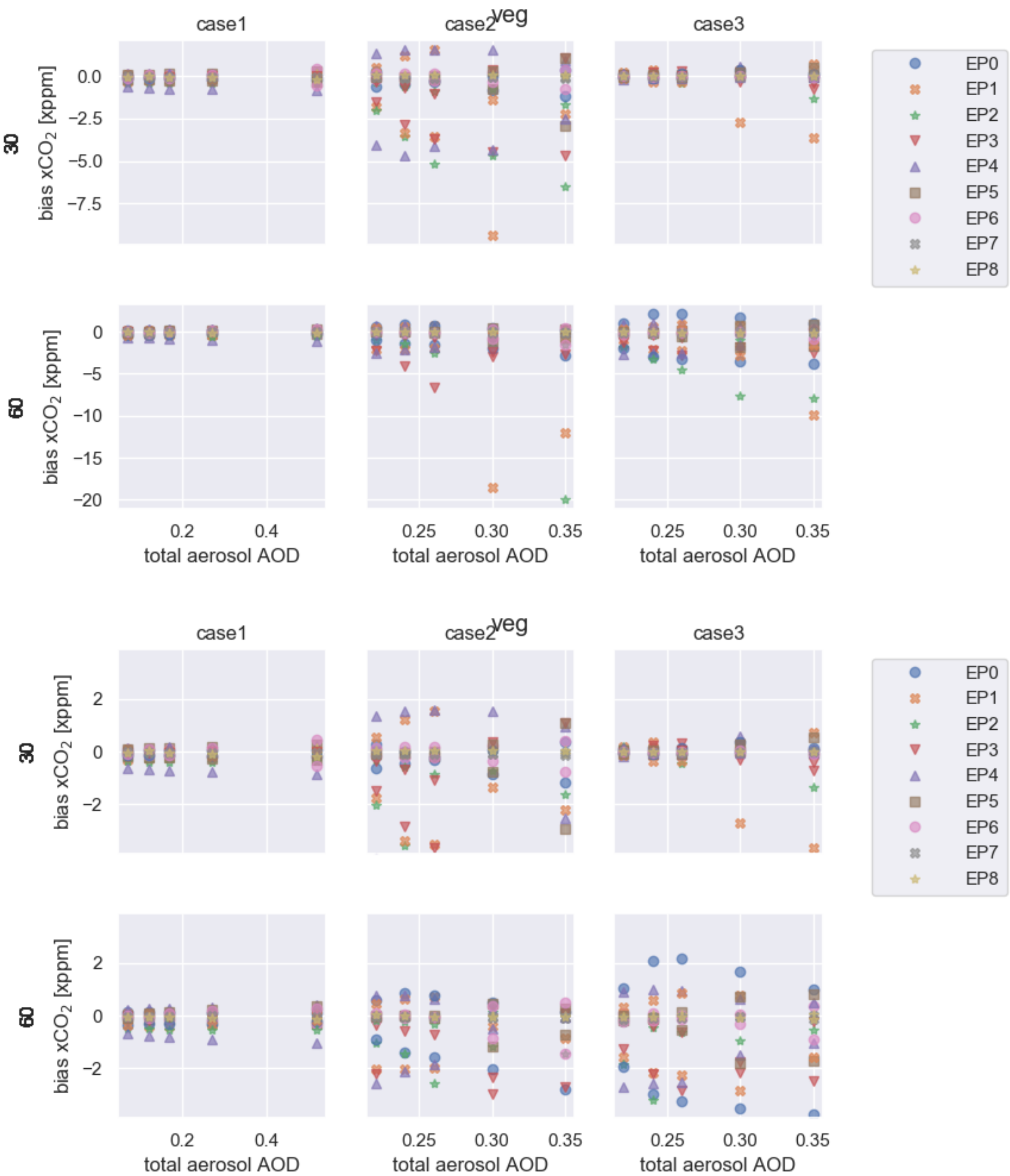

Figure 23: MEAN retrieval of the EP ensemble with BRDF vegetation. The top panel shows the full range of retrieved values, whereas the bottom graph focuses only on a bias of ±3.9 ppm XCO_2 (±1%).

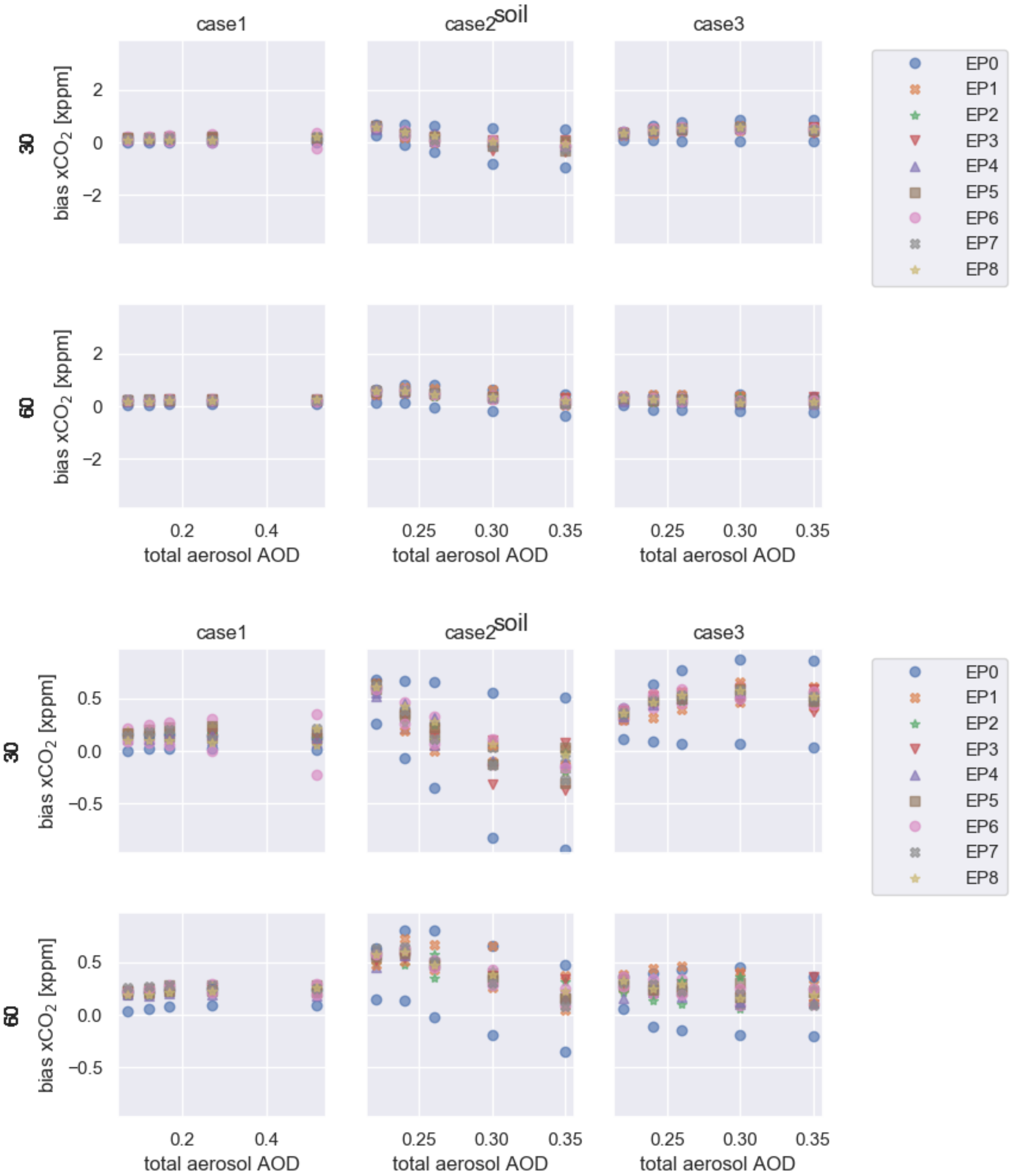

Figure 24: VAR retrieval of the EP ensemble with BRDF soil. The top panel shows the bias on a range of ±3.9 ppm XCO_2 (±1%) for comparison with the previous graphs. The bottom graph depicts a range of ±0.975 ppm XCO_2 (±0.25%).

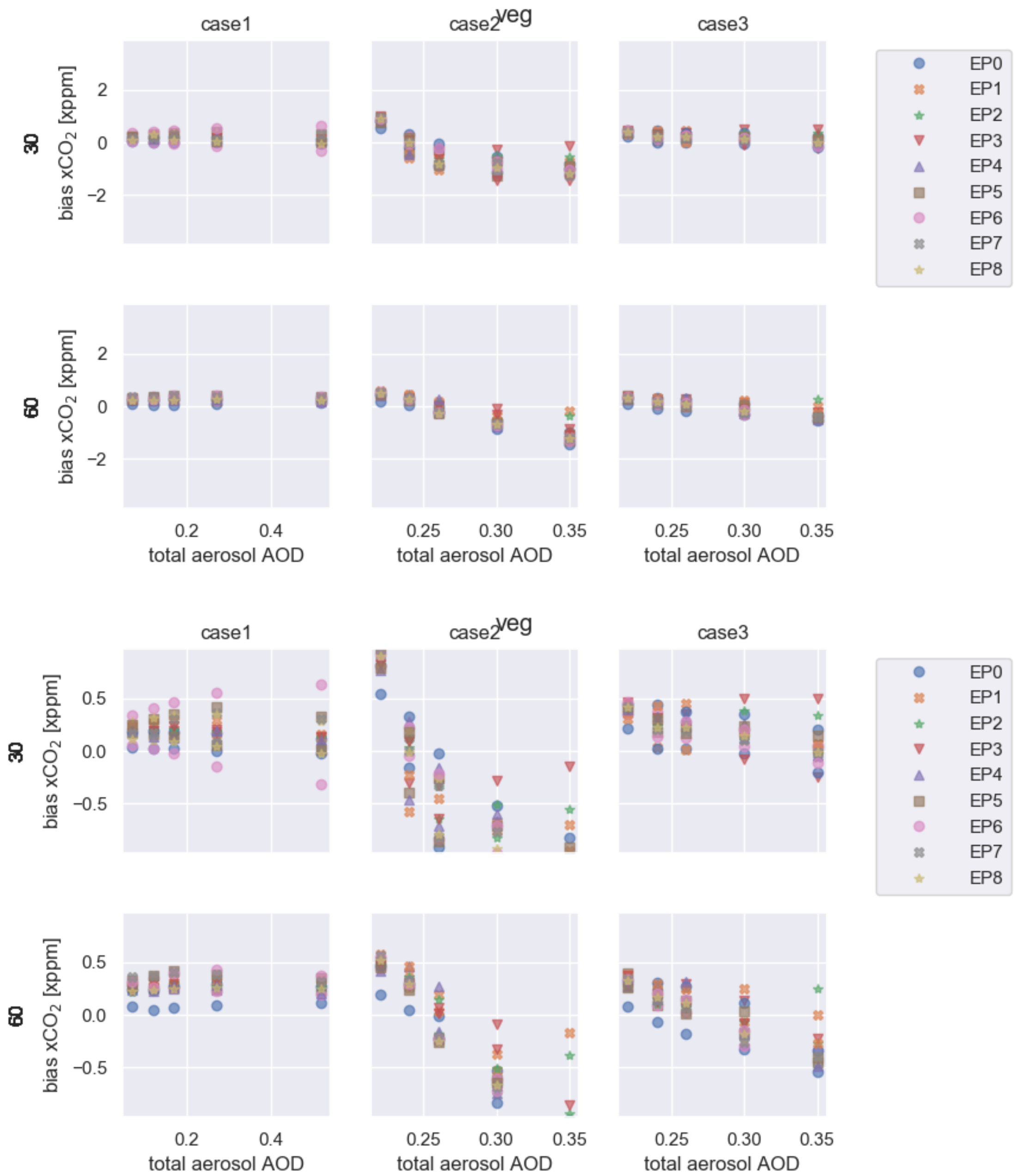

Figure 25: VAR retrieval of the EP ensemble with BRDF vegetation. The top panel shows the bias on a range of ±3.9 ppm XCO_2 (±1%) for comparison with the previous graphs. The bottom graph depicts a range of ±0.975 ppm XCO_2 (±0.25%).

Appendix B Linear error analysis

Linear error analysis relies on the approximation of linearity forward model with respect to the various parameters involved. Given that this assumption holds, the propagation of a-priori covariances can be assessed by $S_{CO_2} = G_{CO_2} \cdot K_{CO_2} \cdot S_{MAP} \cdot K^T_{CO_2} \cdot G^T_{CO_2}$, where G and K represent the Gain and Jacobian (Kernel) matrix, respectively. The entries in the matrices correspond to the state vector parameters of the forward model. However, since the UoL-FP retrieval does not include many parameters of the supplied MAP a-priori, a simplified version of the linear error analysis can be derived making use of the eigenvalue decomposition of the aerosol parameters as described earlier.

The UoL-FP algorithm's forward model can be used to calculate spectra which have are based on unperturbed aerosol parameters (R_0) and ones generated with perturbed aerosol parameters (R_p). I. e., by aerosol parameters which have been perturbed by the error patterns of the eigenvector decomposition. Given the gain matrix G_R translating spectral changes to changes in XCO_2, the impact of a-priori error on retrieved CO_2 can be assessed.

$$\begin{aligned} S_{CO_2,P} &= G_R \cdot (R_0 - R_P) \\ S_{CO_2} &= \sum S_{CO_2,P} \\ &= \sum G_R \cdot (R_0 - R_P) \end{aligned}$$

This approach comes at the cost of calculating individual spectra for all perturbations in question. Furthermore, additional errors are introduced because the gain matrix G_R assumes only aerosol parameters as defined for the unperturbed case and, because of the restrictions of the retrieval - does not allow for variations of the micro-physical aerosol parameters. This means that results by this direct approach can only serve as an upper error limit and will most likely heavily overestimate errors. Results from linear error analysis are not shown here because they produced very high errors, suffering from the described insufficiencies in the approach. Linear error analysis proved to be not suitable in this study with the given retrieval restrictions.

Other approaches must be taken because A) the translation of micro-physical aerosol information to XCO_2 is strongly non-linear or B) the Gain matrix G_R cannot account sufficiently for the introduced perturbations, because it is based on state vectors which do not include these perturbations.

Aerosol Variability Analysis
(CO_2 Spectral Sizing Study)

Cheng Chen, David Fuertes, Yana Karol and Oleg Dubovik GRASP SAS

Aerosol_Variability_CO_2_Spectral_Sizing_Study

Version 1 12.12.2019

Version 2 17.07.2020

Contact
T: +33 667027316
M: office@grasp-sas.com
W: www.grasp-sas.com

Company office
GRASP SAS
20, Impasse de l'Eglise
59830, Bachy, France

Legal Information
RCS: 809 550 270
VAT number: FR33 809550270
No Siret: 809955027000015

Contents

1 Introduction

1.1 Objectives of the study

The objective of the study was the analysis of the aerosol spatial variability in preparation of Copernicus CO2 mission. This mission is aimed at enhancement of global CO2 monitoring. One of the key ideas of this mission is an employment of the simultaneous observations of CO2 spectrometer and multi-angular polarimeter (MAP). The measurements of MAP are expected to be used for advanced correction of the aerosol effects in spectrometric observations of CO2. Indeed, the hyperspectral features of CO2 absorption can be strongly affected by the smooth spectral-continuum-like contributions of atmospheric aerosol features. Those "continuum" features depend in rather complex way on the detailed properties of aerosol and, therefore, cannot be accounted accurately from spectral measurements only. As a result, the current CO2 operational algorithms do not provide the CO2 retrieval in presence of even minor amount of aerosol (AOD(560) $\geq$ 0.2). In these regards, the MAP observations are expected to provide enough information for deriving detailed aerosol information, including information about spectral extinction aerosol optical depth (AOD) and absorption aerosol optical depth (AAOD). Therefore, the MAP observations are planned to be used for accounting for aerosol effects and improving the CO2 retrieval in the conditions of moderate and even large presence of aerosol. Indeed, MAP observations are widely considered as the most suitable for detailed aerosol characterization [e.g. see Dubovik et al., 2019].

The question that needed to be addressed in current study is quite specific: would spatial resolution of 4 km be sufficient for the characterization of aerosol using MAP in frame Copernicus CO2 mission? Alternatively, the observations of MAP could be implemented at 2 km resolution in similar manner as it is planned to be done for CO2 spectrometer. At the same time, obtaining and processing MAP observations at 2 km resolution requires significantly increased resources for data collection, transmission and processing. The former is not attractive perspective especially, taking into account that the reference aerosol databases, such as MODIS [Remer et al., 2005], provide aerosol product at ~10 km spatial resolution and the existent MAPs such as POLDER/PARASOL [Tanre et al. 2011] provided observations at ~6 km. Moreover, even the most advanced MAP future missions [see review by Dubovik et al., 2019] are not intended to provide observation at the spatial resolution significantly higher than 4 km. This also relates to the fact that obtaining multi-angular observations at high spatial resolution is nearly impossible considering the nature of satellite observations (see discussion below in Section 7).

Thus, the explicit objective of this study is to evaluate the aerosol spatial variability at 2 and 4 km scale and to identify and evaluate possible important differences in aerosol characterization.

1.2 Concept of the study

Aerosol particles vary with time and from one to another location due to their short lifetime, dynamic processes, e.g. transport, advection, deposition, convection etc. The dynamic of atmospheric aerosol is highly related with local meteorology and emission sources. The high variability of aerosol in space and time poses significant difficulties for aerosol satellite remote sensing and aerosol transport modeling [Eck et al., 2008]. Therefore, the analyzing the actual time and space variability of ambient aerosol is very challenging task, while the understanding of aerosol temporal and spatial variability is crucial for design of CO2 Copernicus MAP instrument and many next generation observation systems.

The use of ground-based measurements by AERosol RObotic NETwork (AERONET) [Holben et al., 1998] is well recognized as data set providing “ground truth” observations of columnar properties of aerosol. This is why, all main efforts on validations of aerosol remote sensing observation and modeling results relying on AERONET. However, analyzing spatial variability of aerosol using AERONET observations is not obvious task because AERONET generally provides very localized observations. For example, the evaluation of satellite remote sensing aerosol products in ~5 km or ~10 km grid boxes remain one of not fully solved issues of aerosol validation efforts. The in depth discussion of this aspect can be found in the articles by Kinne, al. [2013] and Schutgens et al. [2017]. Those studies attempted to quantify the representativeness of AERONET sites in distance by defining the range score of each AERONET station based on personal experience. However, even those studies were focused on validation of chemical transport model at rather coarse the spatial resolution of ~50 - 100 km.

In this study we estimate the spatial variability aerosol using information about temporal aerosol variability observed at AERONET in point location combined together with available information about local wind speed data from MERRA-2 reanalysis dataset. Similar concept was used in previous study by Smirnov et al. [2003] that relied on the values of surface wind speed to analyze the aerosol temporal and spatial variability over one oceanic AERONET site.

2 General information about aerosol properties and its variability

2.1 Atmospheric aerosol properties

The effect of aerosol on the atmospheric radiances depends, first of all, on the amount of aerosol that characterizes by mass or volume concentration of the aerosol particles. It also depends on the aerosol type that can vary due to differences in aerosol particles sizes, shapes and compositions (related to particle complex refractive index that defines scattering and absorption of particle material). Both the information about amount of aerosol and its type is needed for correction of aerosol effects in CO2 retrieval. The microphysical characteristics such as aerosol concentrations, size distribution, etc. can be obtained from very detailed in situ measurements [e.g. Livingston et al., 2003; Reid, et al., 2003] or from remote sensing observations using sophisticated inversion procedures [e.g. Dubovik and King, 2000]. Therefore, the availability of reliable microphysical data is very limited and most of aerosol studies use relevant optical properties. Namely, in most of aerosol analyzes the aerosol optical depth (AOD) is used as measure of aerosol loading. Similarly, the AOD spectral dependence characterized by the value of Angstrom exponent (AE) is considered as reliable indication of dominant aerosol particle sizes: the smaller the value the larger the particles and vice versa [e.g., see Eck., 1999]. The abilities of aerosol to absorb radiation is characterized by single scattering albedo (SSA), changing from SSA=1 for non-absorbing aerosol to SSA = ~0.65 for highly absorbing aerosol [e.g., see Dubovik et al., 2002]. The variability of AE and SSA is usually employed as a reliable indication of aerosol type variability [Russels et al., 2010]. Therefore, our analysis is focused on investigating variability of the above main parameters AOD, AE and SSA, that are provided by AERONET network.

2.2 AERONET Aerosol Dataset

The Aerosol Robotic Network (AERONET) is a global distributed network of well-calibrated sun photometers [Holben et al., 1998]. By measuring direct Sun radiance, AERONET provides high temporal (every 15 minutes in daytime) multi-wavelength AOD products with reliable accuracy (±0.01 for AOD and ~± 0.1-0.3 for AE) [Eck et al., 1999]. In addition, the almucantar measurements of sky radiances supply the inversion algorithm [Dubovik and King, 2000] for characterizing aerosol microphysical properties, e.g. single scattering albedo, complex refractive index and aerosol size distribution. Generally, the accuracy of AERONET inversion products is related to aerosol loading. The SSA accuracy is estimated at ±0.03 when AOD (440 nm) is higher than 0.2, and ±0.05-0.07 when AOD is lower than 0.2 [Dubovik et al. 2000]. These results were used to established criteria for selecting Level 2 AERONET high quality data [Holben et al., 2006].

2.3 Accuracy limits in knowledge of aerosol property variability

AERONET is widely considered as the source of the most accurate aerosol data for all considered parameters: AOD, AE and SSA. Therefore, AERONET measurement accuracy can be considered as accuracy limits for the analyzed parameters. For example, Figure 1 shows very detailed AOD measurements implemented every 3 min by sun-photometer of GAW network [Kazadzis et al., 2008].

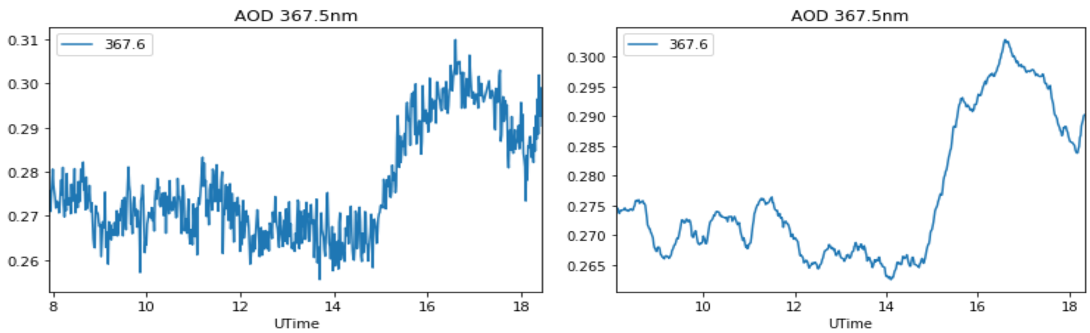

Figure 1. AOD measurement by GAW network. Left panel: instantaneous 3 min AOD measurements; Right panel: the same AOD but smoothed for user convenience.

As one can see on the left panel of Fig. 1 even such accurate and direct measurements of AOD exhibit some instabilities at the order of 0.01 that occur due to both natural variability and measurement uncertainty. Similar situation is for AE. For aerosol SSA, AERONET is nearly a unique data base providing this aerosol properties.

Thus, in present study we assume that variability of AOD, AE and SSA insignificant it is below accuracy limits of AERONET measurements: ± 0.01 for AOD, ± 0.1-0.3 for AE and ± 0.03 for SSA.

3 Data Description

3.1 AERONET Aerosol Dataset

In this report we selected 30 typical AERONET sites to analyze aerosol temporal and spatial variability. In total there are more than 3.5×10^6 measurements collected during more than 10 years of operating time. The information about the selected sites is provided in the Table 1, and their geolocations are shown in Figure 2. We use AERONET Version 3 Level 1.5 (Last access: 2019-07-05) data to conduct our analysis.

3.2 MERRA-2 Reanalysis Wind Speed

The newly released Modern-Era Retrospective Analysis for Research Application, version 2 (MERRA-2) (Gelaro et al., 2017) is a global earth system model based reanalysis dataset with data assimilation. MERRA-2 provides long-term (1980 on ward) reanalysis dataset of climate system. In this report, we will use MERRA-2 10-m wind speed data (Last access: 2019-04-23) to access the aerosol temporal and spatial variability. Figure 2 shows the global mean 10-m wind speed and direction from MERRA-2 dataset.

Figure 3 shows the scatter plots of mean AOD (440 nm) versus mean AE (440/870 nm) and the mean 10-m wind speed for all 30 AERONET sites. Surprisingly, the high wind speed is mainly associated with high AOD and small particles (high AE). Hence, there is an interest to investigate the wind speed related aerosol temporal and spatial variability.

Table 1. List of AERONET sites used in this study

# ID	SiteName	Location	Type	$\bar{\tau}_{440}$ (1σ)	$\bar{\alpha}_{440/870}$ (1σ)	Start Date	N Obs.
1	GSFC	North America	Urban	0.21 (0.21)	1.61 (0.32)	1993.05	187, 382
2	Mexico_City	North America	Urban	0.38 (0.27)	1.58 (0.31)	1999.02	74, 161
3	Guadeloup	Centre America	Dust	0.15 (0.14)	0.35 (0.39)	1997.02	45, 294
4	Alta_Floresta	South America	Biomass burning	0.42 (0.65)	1.39 (0.44)	1993.06	84, 020
5	Africa	South America	Urban	0.25 (0.12)	1.07 (0.23)	1998.05	105, 100
6	CUIABA-MIRANDA	South America	Biomass burning	0.32 (0.48)	1.34 (0.39)	2001.03	66, 681
7	Banizoumbou	Africa	Dust	0.46 (0.33)	0.35 (0.25)	1995.10	181, 836
8	Capo_Verde	Africa	Dust	0.34 (0.26)	0.28 (0.23)	1994.10	97, 458
9	Dakar	Africa	Dust/BB	0.44 (0.28)	0.35 (0.24)	1996.12	169, 199
10	Ilorin	Africa	Dust/BB	0.80 (0.48)	0.66 (0.32)	1998.04	100, 815
11	Mongu	Africa	Biomass burning	0.34 (0.30)	1.70 (0.34)	1995.06	110, 302
12	Santa_Cruz_Tenerife	Africa	Coastal	0.18 (0.18)	0.58 (0.36)	2004.07	158, 225
13	REUNION_ST_DENIS	Africa	Coastal	0.08 (0.05)	0.72 (0.40)	1997.06	85, 645
14	FORTH_CRETE	Europe	Coastal/Urban	0.21 (0.11)	1.15 (0.50)	2003.01	82, 167
15	Granada	Europe	Urban	0.16 (0.10)	1.11 (0.45)	2004.12	151, 660
16	Lille	Europe	Urban	0.22 (0.17)	1.29 (0.41)	1994.11	88, 864
17	Moscow_MSU_MO	Europe	Urban	0.24 (0.25)	1.43 (0.31)	2001.08	69, 277
18	Rome_Tor_Vergata	Europe	Urban	0.21 (0.13)	1.32 (0.41)	2001.02	127, 681
19	Thessaloniki	Europe	Urban	0.27 (0.16)	1.56 (0.36)	2003.06	104, 444
20	Beijing	East Asia	Urban/Dust	0.67 (0.71)	1.12 (0.31)	2001.03	107, 885
21	Shirahama	East Asia	Coastal	0.29 (0.20)	1.24 (0.36)	2000.10	111, 010
22	XiangHe	East Asia	Urban/Dust	0.70 (0.72)	1.16 (0.31)	2001.03	139, 280
23	Kanpur	Central Asia	Urban/Dust	0.72 (0.36)	0.99 (0.40)	2001.01	159, 907
24	Silpakorn_Univ	Central Asia	Biomass burning	0.57 (0.37)	1.39 (0.34)	2006.08	118, 425
25	Singapore	Central Asia	Urban/BB	0.51 (0.61)	1.39 (0.32)	2006.11	50, 348
26	IMS-METU-ERDEMLI	West Asia	Coastal/Urban	0.29 (0.17)	1.28 (0.36)	1999.11	112, 828
27	SEDE_BOKER	West Asia	Dust	0.20 (0.13)	0.93 (0.45)	1995.03	259, 871
28	Solar_Village	West Asia	Dust	0.35 (0.21)	0.54 (0.34)	1999.02	182, 322
29	Lake_Argyle	Oceania	Biomass burning	0.14 (0.14)	1.11 (0.45)	2001.10	151, 023
30	Lanai	Oceania	Coastal	0.08 (0.06)	0.52 (0.43)	1996.08	46, 172

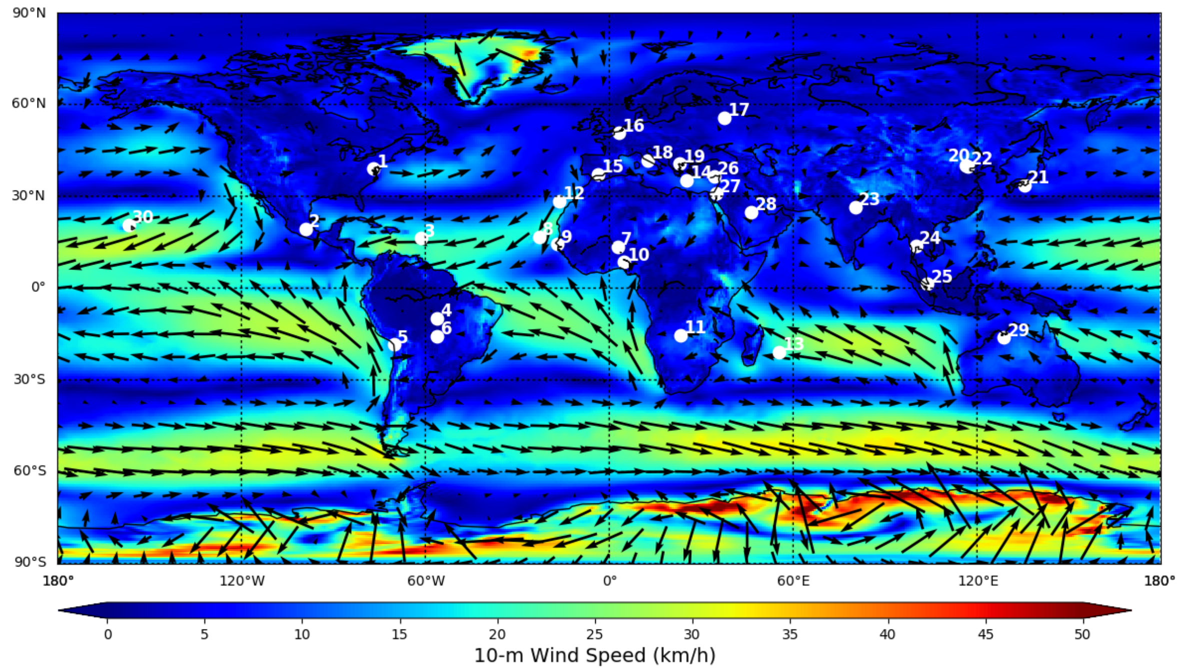

Figure 2. Global mean 10-m wind speed and direction from MERRA-2 reanalysis. The geo-location of 30 AERONET sites are also shown as white circle, and the site numbers are corresponding to #ID in Table 1.

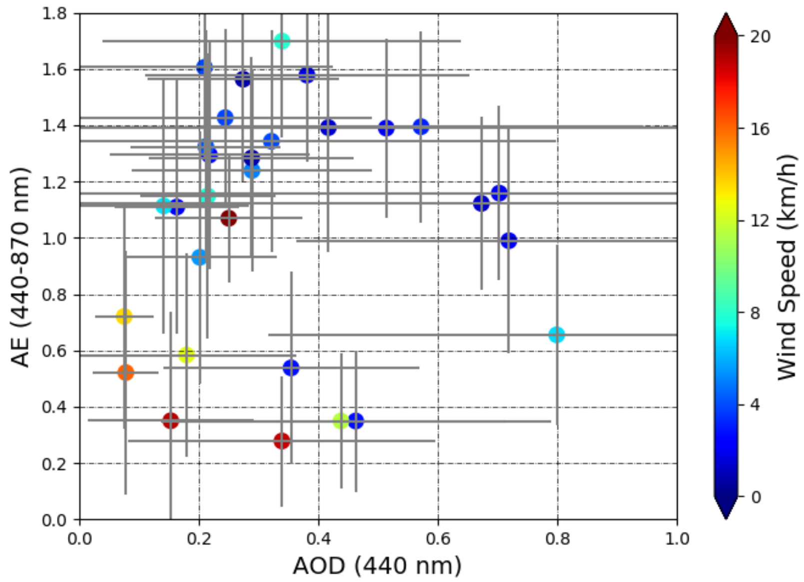

Figure 3. Scatter plots of mean AOD (440 nm) vs. mean AE (440/870 nm) for all 30 sites. The error bar represents standard deviation (1σ), and the color represents mean 10-m wind speed of this site for the data-collecting period.

4 Methodology

In order to study aerosol variability, we have used the most frequent AOD AERONET observations. Namely, using the AERONET AOD measurements obtained at every 15 minutes, we estimated variability of aerosol AOD and AE parameters in series of time windows of 0.5, 1.0, 1.5, 2.0, 3.0, 3.5 and 4.0 hour. The AOD observations obtained each 15 min were used to evaluate aerosol variability within each time window relying on linear interpolation. The obtained slopes of aerosol variability in time were interpreted as characteristics aerosol temporal variability. The information about aerosol SSA is provided by AERONET using sky-scanning diffuse radiances observations [e.g. see Dubovik and King, 2000] that obtained less frequently than direct Sun measurements with the interval of ~ 1h [see details in Holben et al., 1998, 2006]. Correspondingly, these ~1h observations were used for analysis of aerosol SSA variability. Using the above approach, several characteristics were obtained:

(i) Maximum aerosol ***Temporal Variability*** (TV) for AOD (**AOD_TV**), AE (**AE_TV**) and SSA (**SSA_TV**).

Then using the information about wind speed the values of AOD_TV, AE_TV, and SSA_TV were used to estimate maximum aerosol spatial variability:

(ii) Maximum aerosol ***Spatial Variability*** (SV) for AOD (**AOD_SV**), AE (**AE_SV**) and SSA (**SSA_SV**).

Finally, using the values of AOD, AE and SSA measured at 15 minutes interval and information about wind speed the characteristic of aerosol mean variability were estimated:

(iii) Differences between mean AOD, AE and SSA observed in 2 km and 4 km grid boxes, that is called below ***Mean Spatial Variability***: **AOD_MSV**, **AE_MSV** and **SSA_MSV.**

The values of AOD_SV, AE_SV, SSA_SV are intended to show the maximum observed variability at different spatial scales (specifically 2 and 4 km). Correspondigly these values show extreme spatial variability of aerosol. The values AOD_MSV, AE_MSV, SSA_MSV are show the differences between mean values AOD, AE and SSA obtained for 2 km and 4 km grid boxes, that seem to be more appropriate for reflecting the potential differences of observing aerosol at 2 km and 4 km spatial scales.

4.1 Estimation of maximum aerosol Temporal Variability (TV)

AOD temporal variability AOD_TV (unit: ΔAOD/hour), AE temporal variability AE_TV (unit: ΔAE/hour) and SSA temporal variability SSA_TV (unit: ΔSSA/hour) are estimated based on the equations as below:

$$\mathrm{AOD\_TV}(\lambda) = \frac{|\tau_\lambda(t+\Delta t)-\tau_\lambda(t)|_{\max}}{\Delta t}, \quad (1)$$

$$\mathrm{AE\_TV} = \frac{|\alpha(t+\Delta t)-\alpha(t)|_{\max}}{\Delta t}, \quad (2)$$

$$\mathrm{SSA\_TV}(\lambda) = \frac{|\omega_\lambda(t+\Delta t)-\omega_\lambda(t)|_{\max}}{\Delta t}, \quad (3)$$

here $\{\Delta t = 0.5, 1.0, 1.5, 2.0, 2.5, 3.0, 3.5, 4.0 \text{ hour}\}$, and λ represents wavelength. Note that we calculated maximum variability here. The obtained slopes of aerosol variability AOD_TV(t), AE_TV(t) and SSA_TV(t) in time are interpreted as aerosol temporal variability.

4.2 Estimation of aerosol Spatial Variability

The aerosol spatial variability estimation over each AERONET site is based on aerosol temporal variability and the mean wind speed $\bar{v}$. AOD spatial variability AOD_SV (unit: ΔAOD/km), AE spatial variability AE_SV (unit: ΔAE/km) and SSA spatial variability SSA_SV (unit: ΔSSA/km) are estimated based on the equations as below:

$$\mathrm{AOD\_SV}(\lambda) = \mathrm{AOD\_TV}(\lambda)/\bar{v}, \quad (4)$$

$$\mathrm{AE\_SV} = \mathrm{AE\_TV}/\bar{v}, \quad (5)$$

$$\mathrm{SSA\_SV}(\lambda) = \mathrm{SSA\_TV}(\lambda)/\bar{v} \quad (6)$$

where $\bar{v}$ is the mean wind speed (unit: km/h).

4.3 Estimation of aerosol Mean Spatial Variability in 2 km and 4 km grid boxes

The estimation of aerosol mean variability in distance is based on the conversion of the distances to the time window:

$$\Delta t_i = \frac{d_i}{\bar{v}}, \quad \{d_i = 2 \; or \; 4 \text{ km}\} \;, \quad (7)$$

where d_i is the distance in kilometer (e.g. 2 km and 4 km) and $\bar{v}$ is the mean wind speed (unit: km/h). Δt_i is the time window with respect to the corresponding distance:

$$\Delta\tau_\lambda = < \overline{\tau_\lambda(t+\Delta t_{4\mathrm{km}})} - \overline{\tau_\lambda(t+\Delta t_{2\mathrm{km}})} >, \quad (8)$$

$$\Delta\alpha = < \overline{\alpha(t+\Delta t_{4\mathrm{km}})} - \overline{\alpha(t+\Delta t_{2\mathrm{km}})} >, \quad (9)$$

$$\Delta\omega_\lambda = < \overline{\omega_\lambda(t+\Delta t_{4\mathrm{km}})} - \overline{\omega_\lambda(t+\Delta t_{2\mathrm{km}})} >, \quad (10)$$

where $\overline{\tau_\lambda(t+\Delta t_{4\mathrm{km}})}$ and $\overline{\tau_\lambda(t+\Delta t_{2\mathrm{km}})}$ are the mean AOD in 4 km and 2 km; $\overline{\alpha(t+\Delta t_{4\mathrm{km}})}$ and $\overline{\alpha(t+\Delta t_{2\mathrm{km}})}$ are mean AE in 4 km and 2 km; and $\overline{\omega_\lambda(t+\Delta t_{4\mathrm{km}})}$ and $\overline{\omega_\lambda(t+\Delta t_{2\mathrm{km}})}$ represent mean SSA in 4 km and 2 km.

5 Results

Using the approach described in Section 4, we have estimated the maximum aerosol *Temporal Variability*, maximum aerosol *Spatial Variability* and mean aerosol Spatial Variability based on the full archive of the AERONET observation at selected 30 sites listed in Table 1.

5.1 Aerosol maximum Temporal Variability: AOD_TV, AE_TV, and SSA_TV

The calculations were done for 30 sites for AOD_TV and SSA_TV at four standard AERONET wavelengths: 440, 675, 870 and 1020 nm. The values of AE_TV were estimated using AOD at two wavelengths 440 and 870 nm. Figure 4 illustrates the results for AERONET sites Alta Floresta and Beijing. The aerosol time variability AOD/h is among the highest at those two sites. One can see that AOD_TV has significantly higher values at 440 nm. This is why later illustrations will be focused on AOD_TV (440). The values of SSA_TV are actually are higher at 1020 nm. At the same time SSA_TV at different wavelengths differ only by the value of 0.001-0.002 per hour that is very small. Therefore, for consistency with AOD_TV, the illustrations of AOD_SSA are also provided later at 440 nm.

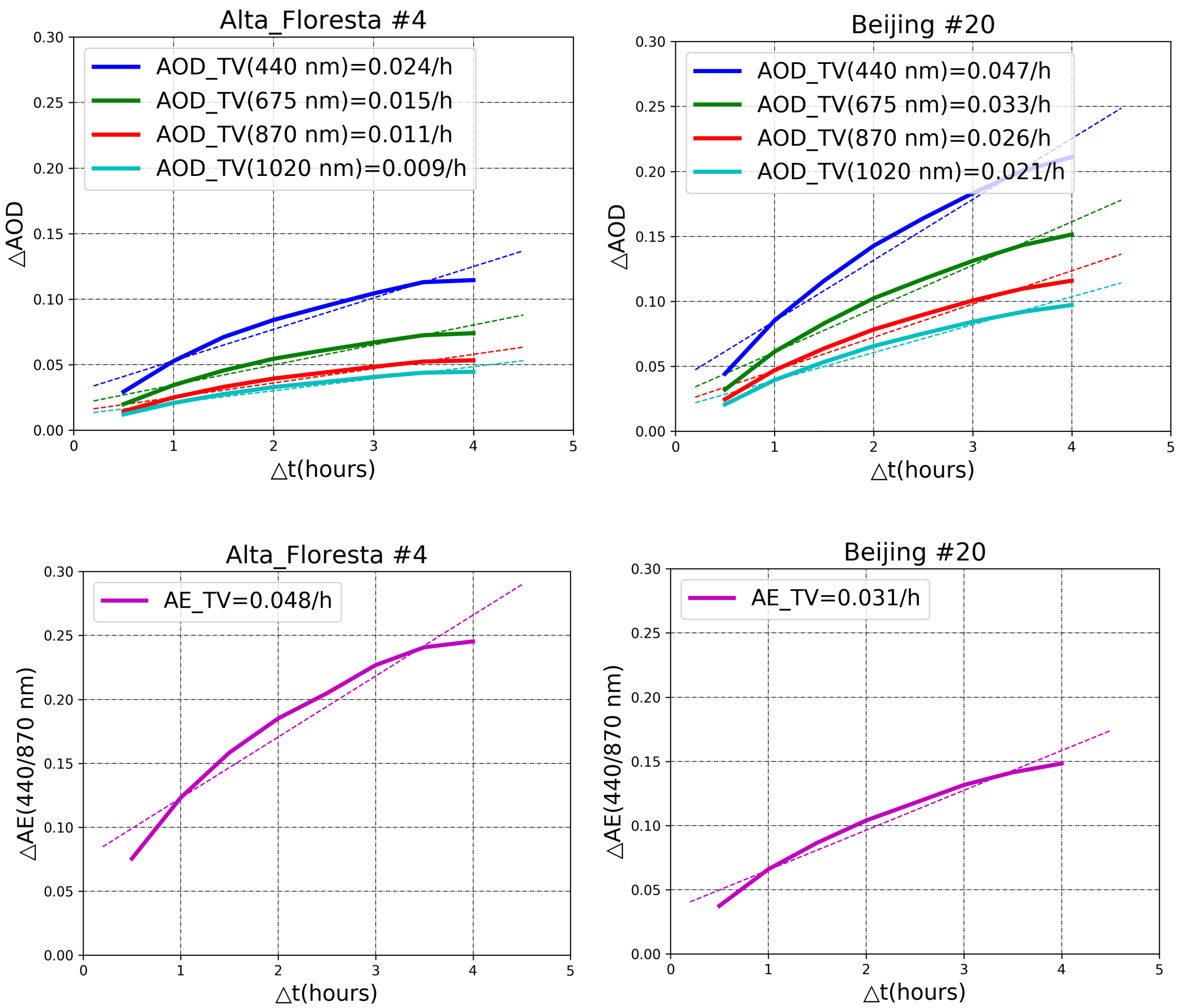

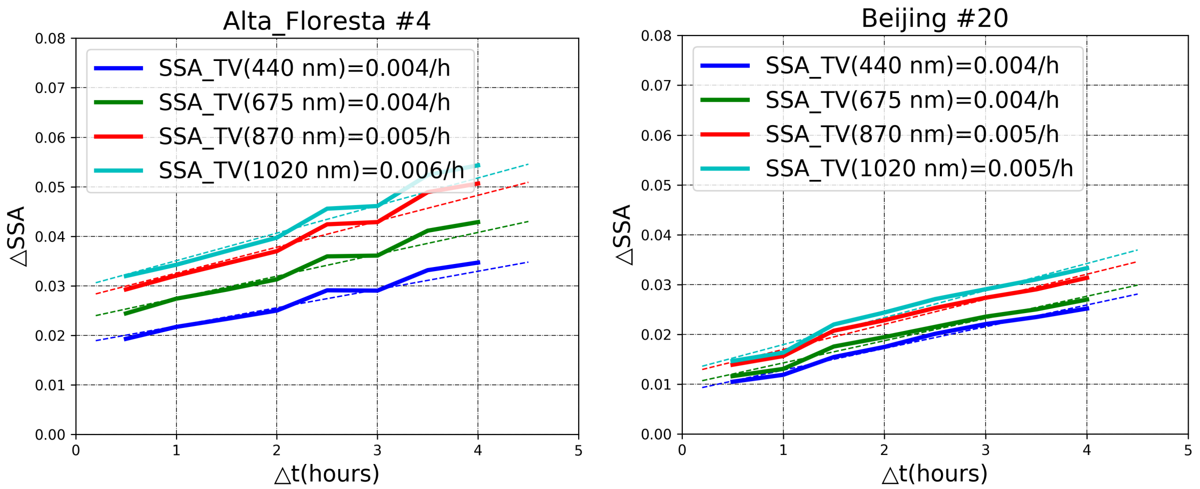

Figure 4. Example of AOD_TV (λ), AE_TV and SSA_TV (λ) estimations over Alta Floresta (# 4) and Beijing (# 20).

Below AOD_TV, AE_TV and SSA_TV are provided for 30 AERONET sites. The means and standard deviations were calculated over all used data for each value.

5.1.1 AOD_TV

The 30 sites mean AOD_TV (440 nm) is ~**0.025 per hour** (**1σ=0.015**). Probability density distribution of AOD_TV values are shown in the left panel of Fig. (5).

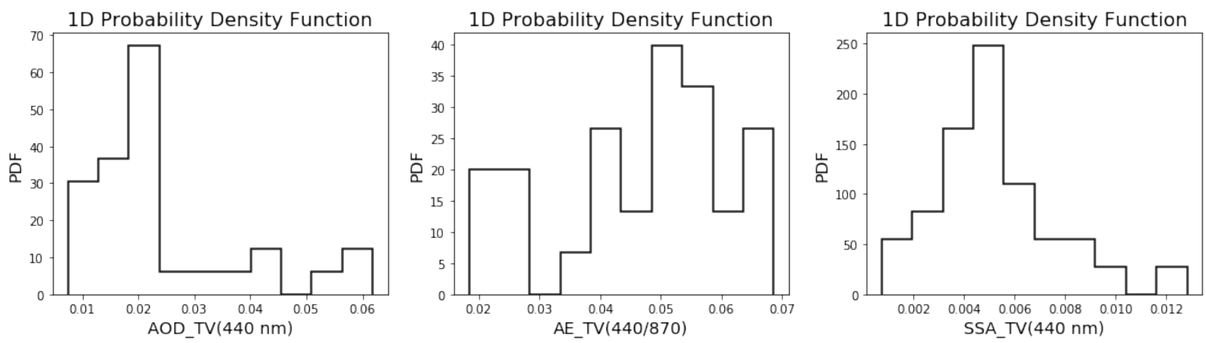

Figure 5. Probability density function of AOD_TV (440 nm), AE_TV (440/870) and SSA_TV (440 nm); the aerosol temporal variability AOD_TV (440 nm), AE_TV (440/870) and SSA_TV (440 nm) are calculated over 30 AERONET sites using all available data.

Figure 6 shows the AOD temporal variability at 440 nm over all considered AERONET sites. The site numbers are corresponding to #ID in the Table 1. The AOD_TV temporal variability (ΔAOD/hour) is relatively high over urban sites (e.g. #2-Mexico_City; #20-Beijing; #22-Xianghe), while AOD_TV is low over oceanic sites (e.g. #13-REUNION_ST_DENIS; #30-Lanai), with highest value ~0.062/h over Beijing and lowest value ~0.008/h over Reunion St Denis. Those tendencies are rather logical since Beijing site has one of the highest mean AOD while Reunion St Denis is the cleanest site with the lowest mean AOD, see Table.1

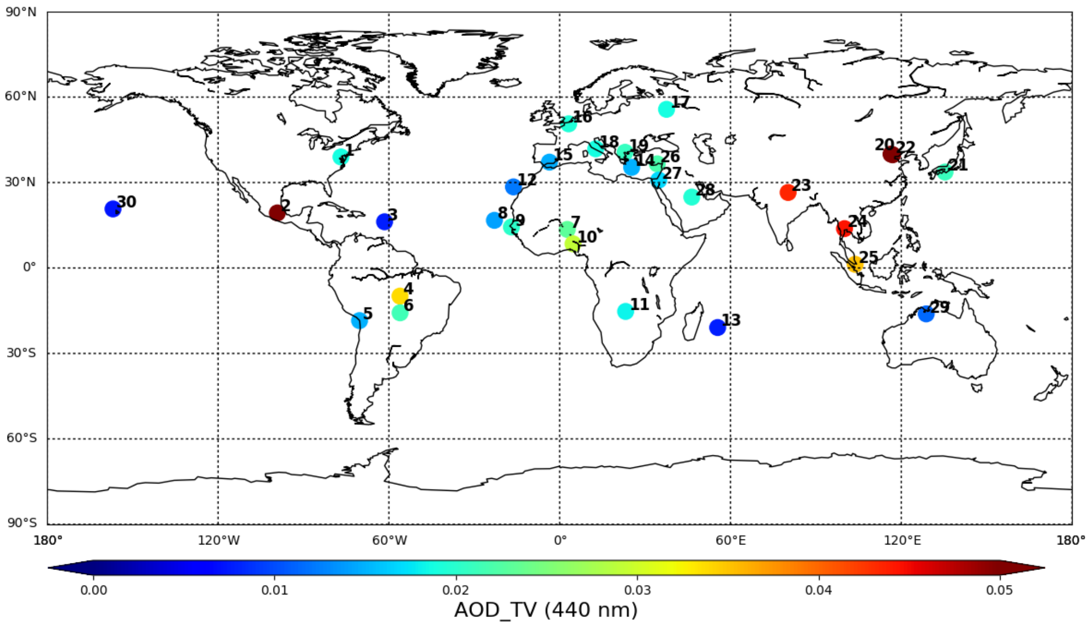

Figure 6. AOD temporal variability at 440 nm (AOD_TV (440 nm), unit: ΔAOD/hour) over 30 AERONET sites; the site numbers are corresponding to #ID in Table 1.

5.1.2 AE_TV

AE (440/870) temporal variability over 30 AERONET sites is present in Figure 7. Over 30 AERONET sites, the mean AE_TV is **0.047 per hour** (**1σ=0.014**). The probability density distribution of AE_TV values are shown in the central panel of Fig. (5). The relatively low values are observed over sites #8 Capo Verde (~0.018/h) and #9 Dakar (~0.022/h). The highest AE_TV (~0.069/h) is observed at site #30 Lanai, which is owing to high wind speed that can be an influx of large particles from the surface [Smirnov et al., 2003].

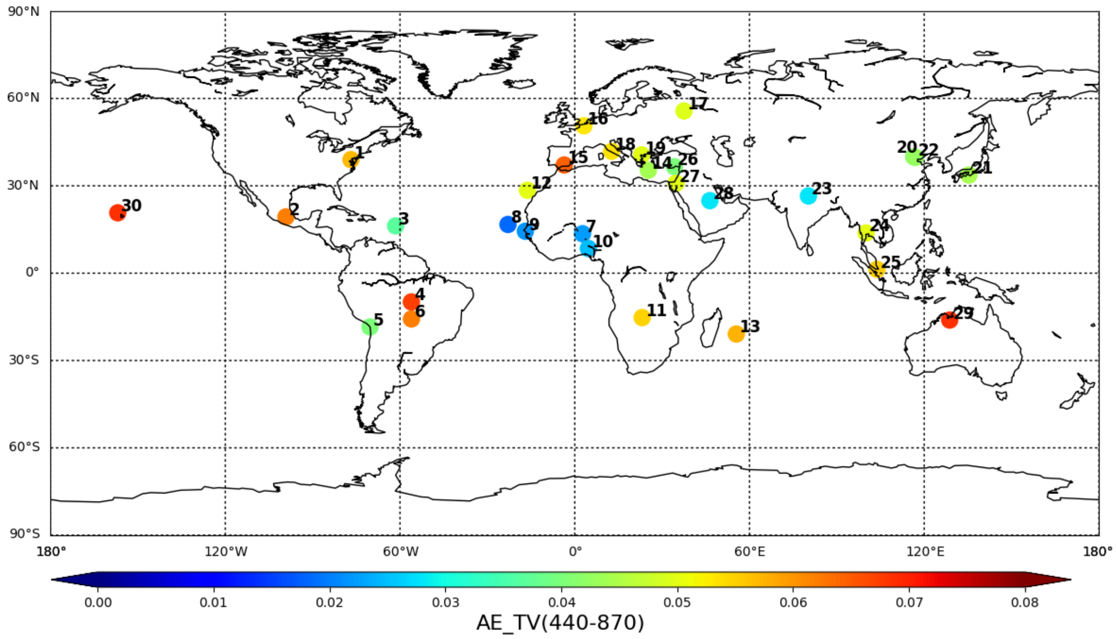

Figure 7. Same as Figure 6, but for AE temporal variability (AE_TV (440/870), unit: ΔAE/hour)

5.1.3 SSA_TV

Figure 8 presents SSA_TV (440 nm) for 30 AERONET sites. All the sites show low SSA variability, that all the values are within the AERONET Level 2 stated accuracy ~0.03. The mean SSA_TV (440 nm) is **0.005 per hour** (**1σ=0.002**). The probability density distribution of SSA_TV values are shown in the right panel of Fig. (5). The maximum value ~0.013/h is observed over biomass burning site #29 Lake Argyle.

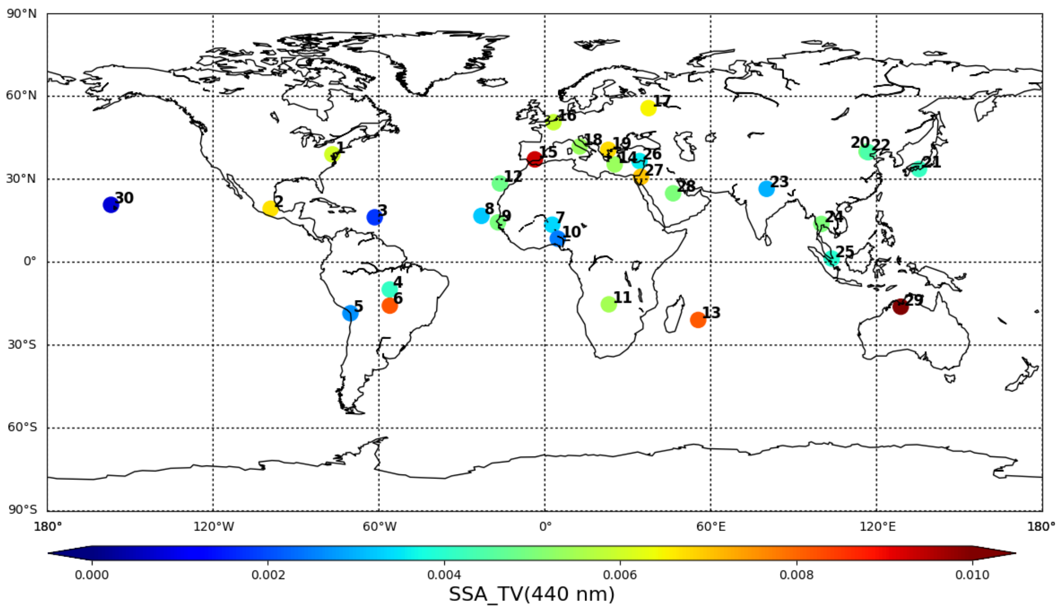

Figure 8. Same as Figure 6, but for SSA temporal variability (SSA_TV (440 nm), unit: ΔSSA/hour).

5.2 Aerosol spatial variability

As shown in Section 4, in this study we evaluate the aerosol spatial variability from the aerosol temporal variability using mean wind speed. This section shows the results of values AOD_SV (ΔAOD/km), AE_SV (ΔAE/km) and SSA_SV (ΔSSA/km) that can provide important information of spatial aerosol variability sought for optimizing design of Copernicus CO2 mission.

Figure 9 provides an interesting qualitative insight obtained using straightforward clustering analysis of AOD_TV, AE_TV, SSA_TV and wind speed. One can see that highest values of AOD_TV are observed for urban polluted and biomass burning aerosol generally characterized by high aerosol loading and variability [Dubovik et al., 2002]. The highest values of AE_TV are observed for urban polluted aerosols that are known to be mixtures of fine and coarse mode aerosols with high AE dynamics. The values of AE_TV are also high for aerosols at low AOD, that are evidently related with the base uncertainty in AOD observations (0.01). Correspondingly at very low AOD, AE can strongly change simply due to the presence of uncertainties and the AOD errors at the absolute level of 0.01 may be a reason for strong changes in AE. The highest values of SSA_TV are observed for urban polluted aerosols and biomass burning that generally exhibit stronger SSA changes due to enhanced absorption by these aerosols [e.g. Dubovik et al., 2002]. Finally, it is interesting to note that most of the highest values of AOD_TV, AE_TV and SSA_TV correspond to the cases with the lowest wind speed. Evidently, in absence of strong winds the activity of local aerosol sources results in high temporal aerosol variability.

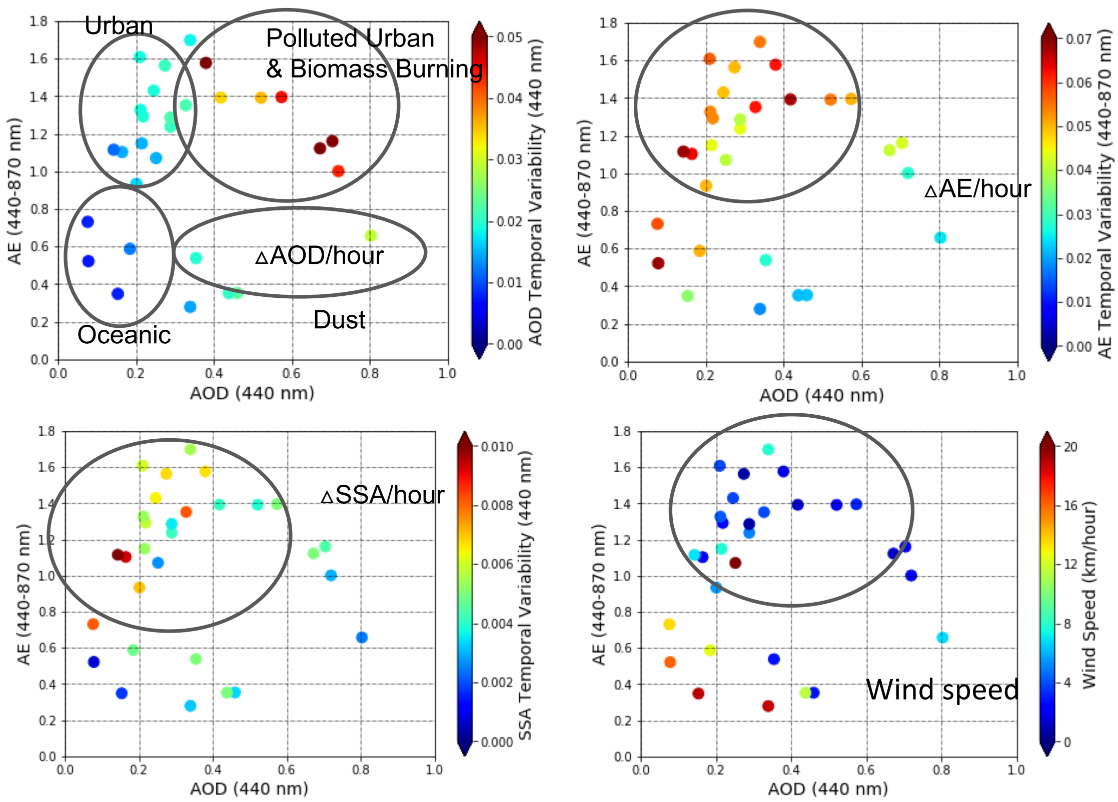

Figure 9. Clustering analysis aerosol time variability and wind speed.

As shown in Section 4.2, using the values of wind speed, the AOD_TV, AE_TV, SSA_TV can provide the information about aerosol spatial variability. Below the values of AOD_SV (ΔAOD/km), AE_SV (ΔAE/km) and SSA_SV (ΔSSA/km) are shown for all 30 AERONET sites. The means and standard deviations were calculated over all used data for each value.

5.2.1 AOD_SV

The mean AOD_SV (440 nm) is estimated at **0.010 per km** (**1σ=0.012**). The probability density distribution of AOD_SV values are shown in the left panel of Fig. (10).

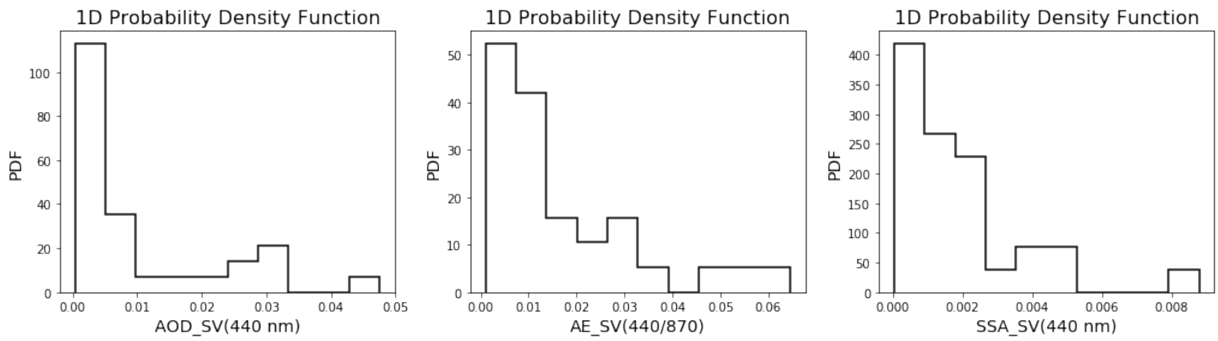

Figure 10. Probability density function of AOD_SV (440 nm), AE_SV (440/870) and SSA_SV (440 nm); the aerosol spatial variability AOD_SV (440 nm), AE_SV (440/870) and SSA_SV (440 nm) are calculated over 30 AERONET sites using all available data.

The AOD maximum spatial variability over 30 AERONET sites is shown in Figure 11. The high AOD spatial variability is observed mainly over urban sites (e.g. #20 Beijing ~0.048; #22 Xianghe ~0.032/km; #2 Mexico City ~0.030/km; #26 IMS-METU-ERDEMLI ~0.030/km; #19 Thessaloniki ~0.027/km); while the low spatial variability is found over costal oceanic sites (e.g. #3 Guadeloup ~0.0004/km; #30 Lanai ~0.0005/km), which suggests that aerosol is more homogeneous than other regions.

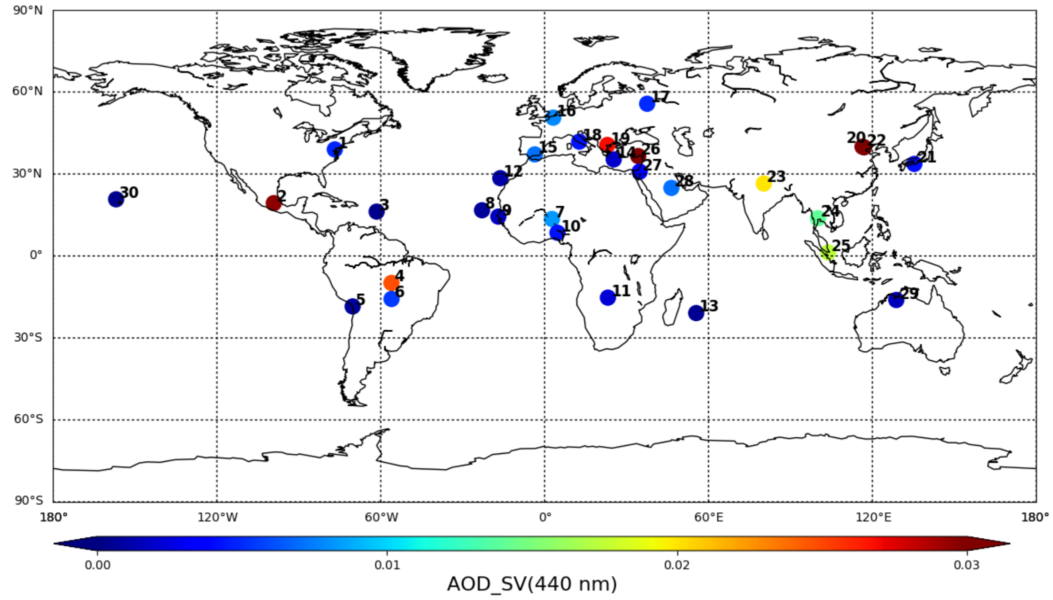

Figure 11. AOD spatial variability at 440 nm (AOD_SV (440 nm), unit: ΔAOD/km) over 30 AERONET sites; the site numbers are corresponding to #ID in Table 1.

5.2.2 AE_SV

Ångström Exponent is a qualitative indicator of aerosol particle size; the smaller the AE, the larger the particle size [Eck et al., 1999; Schuster et al., 2006]. The spatial variability of AE is high over sites where both the fine and coarse mode particles have strong effects. The mean AE_SV (440/870) is **0.017 per km** (**1σ=0.016**). The probability density distribution of AE_SV values are demonstrated in the central panel of Fig. (10).

The distribution of AE_SV over 30 AERONET sites is shown in Fig. (12). The highest value is observed over #19 Thessaloniki ~0.064/km, where coarse mode oceanic aerosol and fine mode urban aerosol are alternate dominant. For AE_TV, we found high AE temporal variability over Lanai #30 ~0.069 per hour, here the spatial variability is low ~0.004 per km, which means that the aerosol particle size varies quickly in time due to high wind speed; however, high wind speed also distribute aerosol evenly spatially.

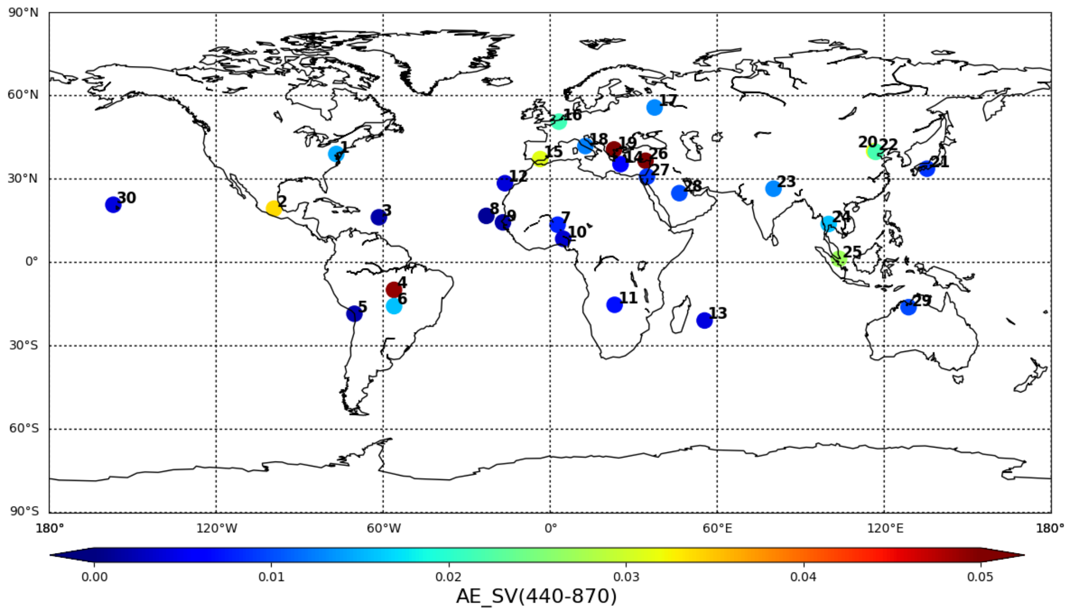

Figure 12. AE spatial variability at 440 nm (AE_SV (440/870), unit: ΔAE/km) over 30 AERONET sites; the site numbers are corresponding to #ID in Table 1.

5.2.3 SSA_SV

The mean SSA_SV(440 nm) is **0.002 per km** (**1σ=0. 002**). The probability density distribution of SSA_SV values are shown in the right panel of Fig. (10). Figure 13 shows the SSA spatial variability over 30 AERONET sites. The highest SSA_SV (440 nm) observed at #19 Thessaloniki ~0.009/km and lowest value at #3 Guadeloup ~0.0001/km; #30 Lanai ~0.0001/km. Overall, the SSA variability is small in 1 km distance.

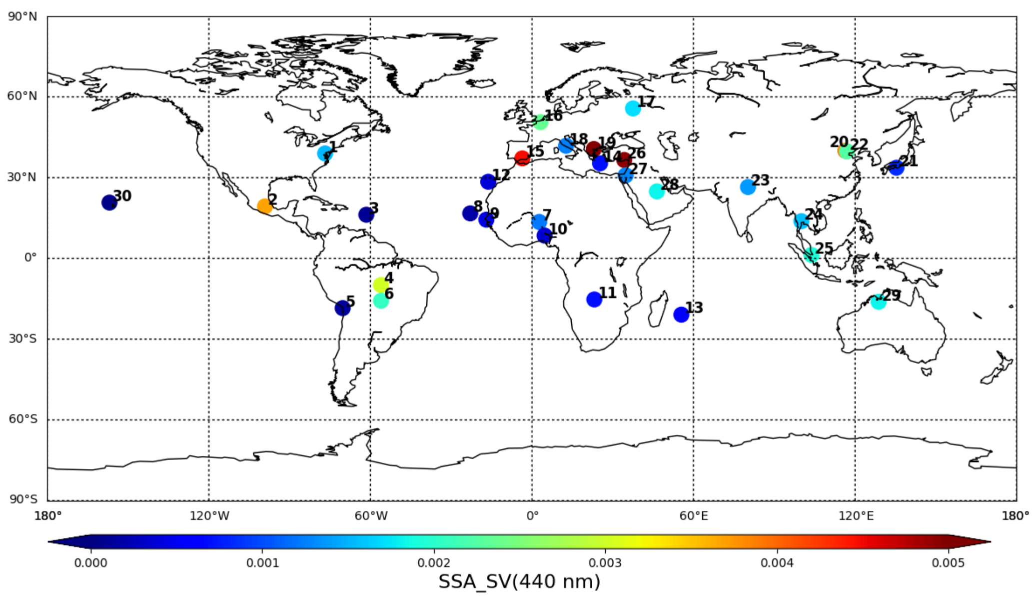

Figure 13. SSA spatial variability at 440 nm (SSA_SV (440 nm), unit: ΔSSA/km) over 30 AERONET sites; the site numbers are corresponding to #ID in Table 1.

5.3 Differences in aerosol mean variability at 2 km to 4 km scales

This section discusses the results of analysis of the aerosol variability between mean AODs calculated for 2 km and 4 km grid boxes. Specifically, the AOD_MSV, AE_MSV and SSA_MSV were estimated for the square greed box of 2 km and larger greed box extended up to for 4 km, as illustrated in Figure 14. It is our understanding that the AOD_MSV, AE_MSV and SSA_MSV are the most adequate values for characterizing the potential uncertainty introduced into aerosol mean values if observation resolution changed from 2 to 4 km scale.

The values of AOD_MSV, AE_MSV and SSA_MSV were calculated for 30 selected AERONET and the details of the results provided below.

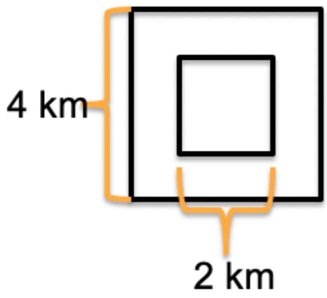

Figure 14. Illustrations of 2 and 4 km greed box concept used for estimating uncertainty introduced into aerosol mean variability if observation resolution changed from 2 to 4 km scale.

5.4 AOD_MSV

AOD_MSV (440 nm) mean is at **0.004** (**1σ=0.005**), which accounts for ~1.2% of AOD. Figure 11 shows the SSA spatial variability over 30 AERONET sites. The probability density distribution of AOD_MSV values are shown in the left panel of Fig. (15).

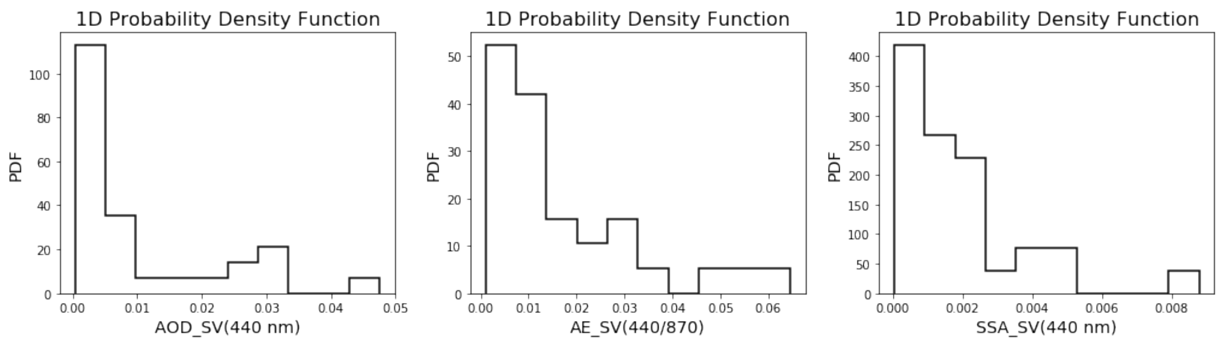

Figure 15. Probability density function of AOD_MSV (440 nm), AE_MSV (440/870) and SSA_MSV (440 nm); The AOD_MSV (440 nm), AE_MSV (440/870) and SSA_MSV (440 nm) are mean differences of aerosol variability between 4x4 vs. 2x2 km^2 and calculated over 30 AERONET sites using all available data.

The values of AOD_MSV for 30 AERONET sites at shown in Fig. (16). The highest AOD_MSV (440 nm) is observed over #20 Beijing ~0.019, accounting for ~2.8% of mean AOD over Beijing and over other urban sites such as #1 GSFC, #2 Mexico_City, #22 Xianghe and #23 Kanpur where AOD_MSV ΔAOD (440 nm) was somewhat greater than 0.01. At the same time, even the highest value of ~0.019 over Beijing is practically within the uncertainty of AOD measurement by AERONET (± 0.01 , see Section 2.3). Thus, the uncertainties of this level in AOD variability can be considered nearly negligible.

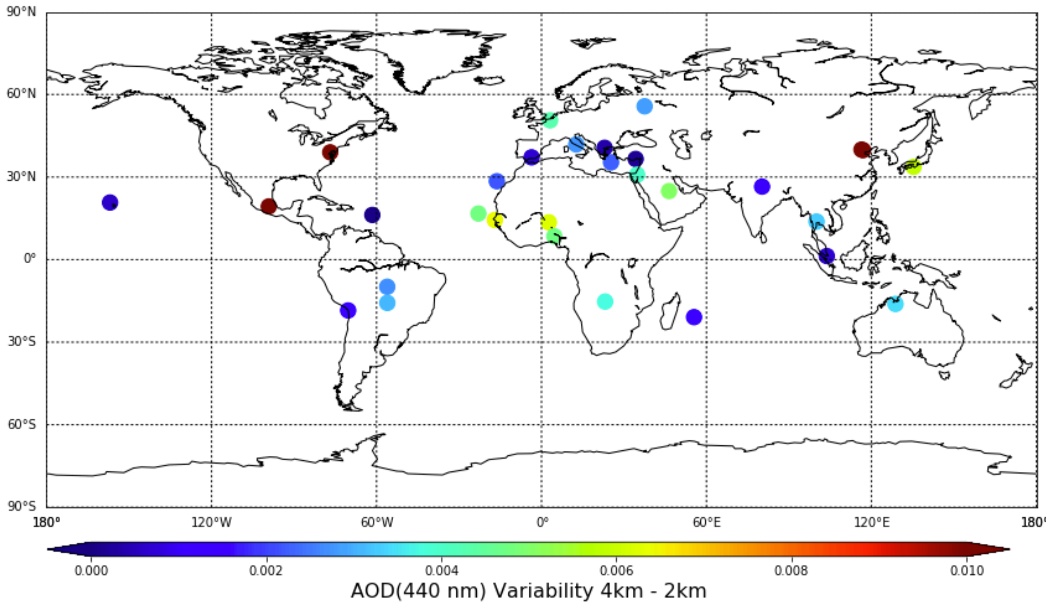

Figure 16. AOD_MSV – variability between 2 and 4 km AOD spatial means obtained for 30 AERONET sites.

5.4.1 AE_MSV

AE_MSV (440/870) mean is at **0.004** (**1σ=0.003**), which is ~0.4% of mean AE. The probability density distribution of AE_MSV values are shown in the central panel of Fig. (15). The values of AE_MSV for 30 AERONET sites at shown in Fig. (17). The highest AE variability is over biomass burning sites, e.g. #11 Mongu AE_MSV = ~0.011 (0.6%) and #24 Silpakorn Univ ~0.014 (1.0%), that can be explained by the fact that biomass burning dominated by fine particles with high values of AE. At the same time, even these apparently maximal values are within AE uncertainty limits (± 0.1 – 0.3, see Section 2.3).

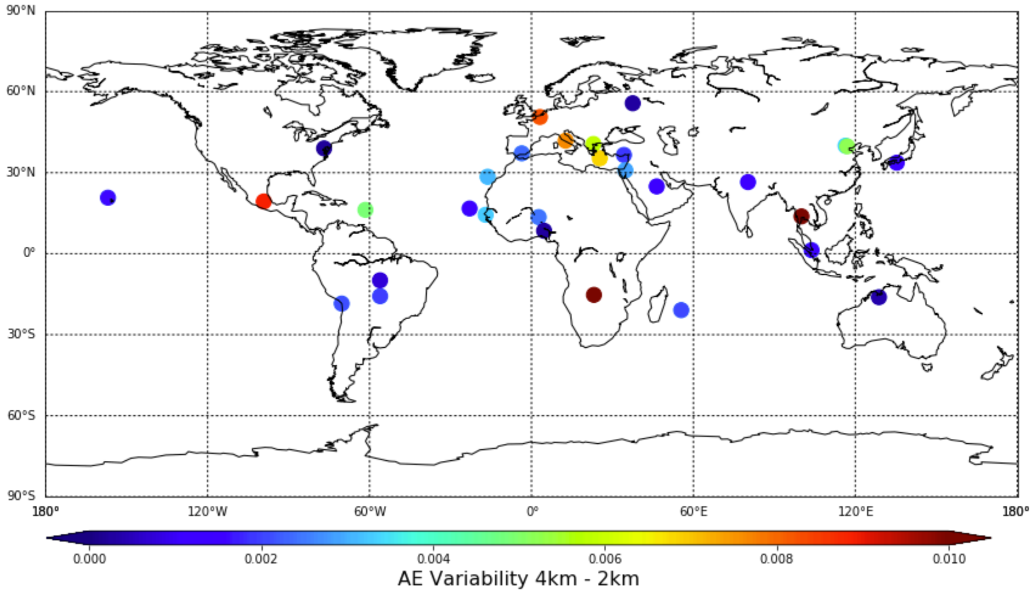

Figure 17. AE_MSV – variability between 2 and 4 km AE spatial means obtained for 30 AERONET sites.

5.4.2 SSA_MSV

SSA_MSV (440 nm) mean is 0.004 (1σ=0.003), which is ~0.4% of mean AE. The probability density distribution of SSA_MSV values are shown in the right panel of Fig. (15). The values of SSA_MSV for 30 AERONET sites at shown in Fig. (18). Similar to AOD_MSV (440 nm), the highest values of SSA_MSV (440 nm) are mainly observed over urban sites such as #20 Beijing ~0.019, #22 Xianghe ~0.017, #1 GSFC ~0.012 and #2 Mexico City ~0.012. At the same time, similarly to situation with AOD_MSV and AE_MSV, the values of SSA_MSV are clearly within the SSA uncertainty limits (± 0.03, see Section 2.3)

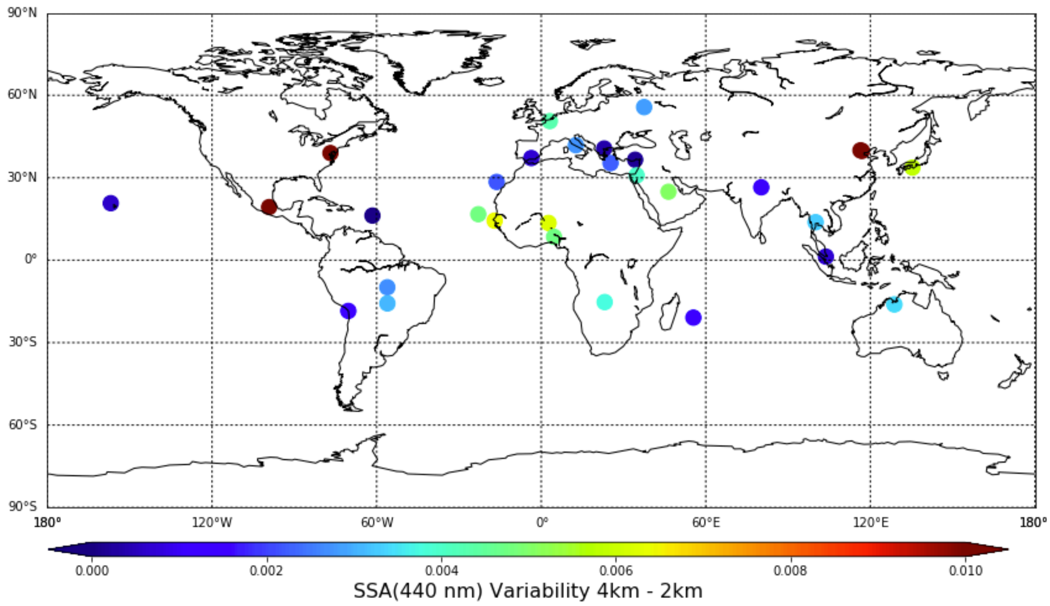

Figure 18. SSA_MSV – variability between 2 and 4 km SSA spatial means obtained for 30 AERONET sites.

6 Discussion

This report presented the study of the aerosol maximum temporal variability estimated using full data archives over 30 representative AERONET sites. Then using the available information about local wind speed, the maximum and mean aerosol variability was estimated at scales of 2 and 4 km and compared. The results of this report can be summarized by the following conclusions:

- ✓ The changes of aerosol type, that were linked in this study to changes of AE and SSA, can be considered negligible or tolerable at scales of 4 km. For example, the maximum AE_SV (440/870) variability in 4 km over 30 sites is 0.068 (1σ=0.064); and the maximum variability for SSA_SV(440 nm) in 4 km is 0.008 (1σ=0. 008). These values are comparable with limits of AE and SSA measurement accuracy (± 0.1-0.3 for AE, ± 0.03 for SSA , see Section 2.3).

- ✓ The mean (over 30 sites) maximum AOD(440 nm) spatial variability within 1 hour at 4 km scale is 0.040 (1σ=0.048), with highest maximum variability of AOD observed over polluted urban sites such as Beijing, Xianghe, Mexico_City and Kanpur with the maximum value reaching ~0.2 that is quite significant. The corresponding values for maximum aerosol variability for the scale of 2km are two time smaller. At the same time, the highest AOD variability observed at the sites with very high dynamic of aerosol and associated only with ~6% in relative changes of AOD.

- ✓ In order to understand more adequately the impact of changes of satellite pixel resolution from 2 km to 4 km, we have analyzed the differences in the means values of aerosol properties (AOD, AE and SSA) obtained for 2 km to 4 km grid boxes. Indeed, mainly the average properties of aerosol located within these grid boxes would affect observations. The results can be summarized:
  - Mean difference of AOD (440 nm) variability between 2 and 4 km grid boxes is only 0.004 (1σ=0.005), which is corresponding to 1.2% of mean AOD value in the grid box. The highest differences between 2 and 4 km means of AOD(440 nm) are mainly found over urban sites such as Beijing 0.019 (2.8%), where typical values of AOD are very high.
  - Mean difference of AE (440/870) variability between 2 and 4 km grid boxes is 0.004 (1σ=0.003), which is equivalent to 0.4% relative AE (440/870). The high AE (440/870) variability from 2 km to 4 km is observed over biomass burning sites, e.g. Mongu ~0.011 (0.6%) and Silpakorn ~0.014 (1.0%).
  - Mean difference of SSA (440 nm) between 2 and 4 km grid boxes is 0.004 (1σ=0.005), and the high SSA variability is also found over urban sites.

All these observed mean aerosol variability differences between 2 and 4 km grid boxes for AOD, AE and SSA are comparable with limits of AOD, AE and SSA measurement accuracy (± 0.01-0.03 for AOD, ± 0.1-0.3 for AE, ± 0.03 for SSA, see discussion in the Section 2.3).

In addition, for considering the impact of changes of satellite spatial resolution from 2 km to 4 km, it is necessary to consider the fundamental limitations of in the multi-angular satellite observations. Indeed, the passive satellite observations collected over one pixel are generally expected to be representative of entire atmospheric column over the pixel. At the same time, as illustrated by Fig.(19), the satellite observations corresponding to different angles of observation corresponds to different light passes. Therefore, since layer of tropospheric aerosol is always elevated (typically it's concentrated in the first 1-5 km), the observations obtained by different angles are affected by aerosol not only over observed pixel and also over neighboring pixels. This phenomenon leads to potential inconsistency of measurement obtained at different geometry (scattering angles) over the same pixel. This is one of challenges of multi-angular polarimetry [e.g., see Dubovik et al., 2019]. Although, in order to understand the importance of so-called coregistration error, an in-depth dedicated analysis is needed for each specific technical and geometrical of multi-angular instrument, it is evident that the coregistration inconsistencies in different angular observation significantly decreases for the sensors with lower spatial resolution. In these regards, using 4 km instead of 2 km MAP sensor resolution seems preferable. For example, *Lang et al.*, [2019] discussed the issues of coregsitration for the Multi-viewing, Multi-channel and Multi-polarisation Imager (3MI) on board the Metop-SG satellites. They have considered diverse uncertainties caused by existing differences in time and geometry of observations at different angles and concluded while the coregistration errors limit the accuracy of 3MI observations, the errors remain acceptable for the 4km spatial resolution.

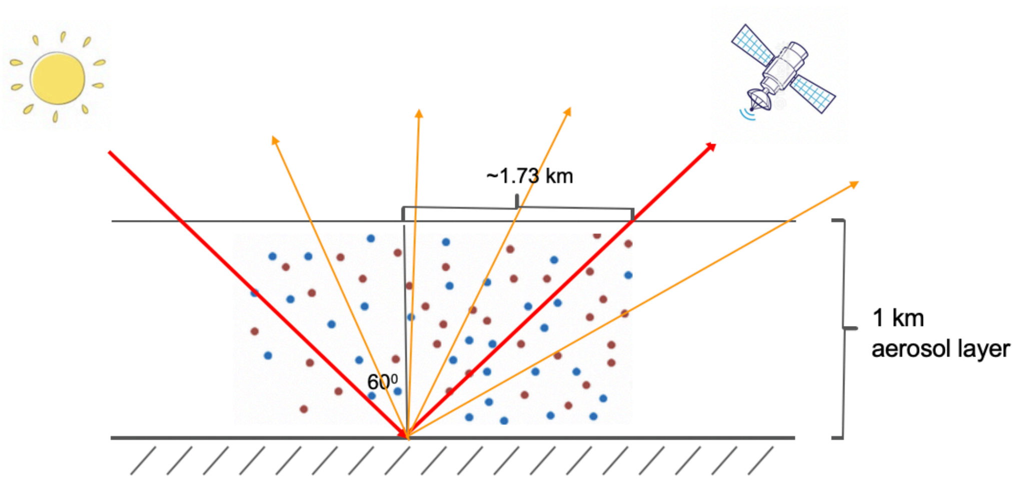

Figure 19. The scheme of the multi-angular satellite observations.

7 Conclusions

Based on the results and analysis conducted in the present study, the spatial variability of the tropospheric aerosol is overall negligible. Specifically, the mean aerosol parameters obtained for 2 and 4 km spatial scale showed very small differences: only 0.004 for AOD (440 nm) , 0.004 for Angstrom Exponent, and 0.004 for aerosol single scattering albedo. Such small differences cannot be reliably detected even using the fundamentally most reliable AERONET observations. Moreover, even the conducted analysis of observed maximum spikes in aerosol variability showed no significant deviations in parameters characterizing aerosol type, that is highly important for characterizing overall aerosol effect and specifically in CO2 correction efforts. In a contrast, the analysis of maximum spatial variation of aerosol concentrations, some nonnegligible spikes up to 0.2 for AOD(440) were observed at spatial scale of 4km. However, those high fluctuation are corresponding to very high aerosol loading event, and remain at ~ 5 to 6% relative level in respect of total AOD. In such situations, decreasing observational resolution to 2 km is unlikely to resolve the issue, especially considering the fact of increasing coregistration errors in multi-angular information for satellite observations with high spatial resolution. Indeed, the light scattered at different angles is affected by aerosol over neighboring pixels and the resulting inconsistency is notably higher at smaller spatial scales and quickly decreases with increase of spatial resolution.

Thus, the performed study suggests that using 4 km spatial resolution for MAP sensor planned to be deployed as part of CO2 Copernicus mission instead of 2 km is sufficient to capture the features in aerosol variability. Moreover, the observations at 4 km scale are expected to provide significantly more consistent multi-angular information than at 2 km spatial scale.

8 References

Dubovik, O. and King, M. D.: A flexible inversion algorithm for retrieval of aerosol optical properties from Sun and sky radiance measurements, J. Geophys. Res. Atmos., 105(D16), 20673–20696, doi:10.1029/2000JD900282, 2000.

Dubovik, O., Smirnov, A., Holben, B. N., King, M. D., Kaufman, Y. J., Eck, T. F. and Slutsker, I.: Accuracy assessments of aerosol optical properties retrieved from Aerosol Robotic Network (AERONET) Sun and sky radiance measurements, J. Geophys. Res. Atmos., 105(D8), 9791–9806, doi:10.1029/2000JD900040, 2000.

Dubovik, O., B. N. Holben, T. F. Eck, A. Smirnov, Y. J. Kaufman, M. D. King, D. Tanré, and I. Slutsker, “Variability of absorption and optical properties of key aerosol types observed in worldwide locations”, J. Atmos. Sci., 59, 590-608, 2002.

Dubovik, O., Z. Li, M. I. Mishchenko, D. Tanre, Y.Karol, B. Bojkov, B. Cairns, D. J. Diner, R. Espinosa, P. Goloub, X. Gu, O. Hasekamp, J. Hong, W. Hou, K. D. Knobelspiesse, J. Landgraf, L. Li, P. Litvinov, Y. Liu, A. Lopatin, T. Marbach, H. Maring, V. Martins, Y. Meijer, G. Milinev-sky, S. Mukai, F. Parol, Y. Qiao, L. Remer, J. Rietjens, I. Sano, P. Stammes, S. Stamnes, X. Sun, P. Tabary, L. D. Travis, F. Waquet, F. Xu, C.Yan and D. Yin, “Polarimetric remote sensing of atmospheric aerosols:instruments, methodologies, results, and perspectives", J. Quant. Spectrosc. Radiait. Transfer, doi.org/10.1016/j.jqsrt.2018.11.024, 474–511, 2019.

Eck, T. F., Holben, B. N., Reid, J. S., Dubovik, O., Smirnov, A., O'Neill, N. T., Slutsker, I. and Kinne, S.: Wavelength dependence of the optical depth of biomass burning, urban, and desert dust aerosols, J. Geophys. Res. Atmos., 104(D24), 31333–31349, doi:10.1029/1999JD900923, 1999.

Eck, T. F., Holben, B. N., Reid, J. S., Sinyuk, A., Dubovik, O., Smirnov, A., Giles, D., O'Neill, N. T., Tsay, S.-C., Ji, Q., Al Mandoos, A., Ramzan Khan, M., Reid, E. A., Schafer, J. S., Sorokine, M., Newcomb, W. and Slutsker, I.: Spatial and temporal variability of column-integrated aerosol optical properties in the southern Arabian Gulf and United Arab Emirates in summer, J. Geophys. Res., 113(D1), D01204, doi:10.1029/2007JD008944, 2008.

Gelaro, R., McCarty, W., Suárez, M. J., Todling, R., Molod, A., Takacs, L., Randles, C. A., Darmenov, A., Bosilovich, M. G., Reichle, R., Wargan, K., Coy, L., Cullather, R., Draper, C., Akella, S., Buchard, V., Conaty, A., da Silva, A. M., Gu, W., Kim, G.-K., Koster, R., Lucchesi, R., Merkova, D., Nielsen, J. E., Partyka, G., Pawson, S., Putman, W., Rienecker, M., Schubert, S. D., Sienkiewicz, M. and Zhao, B.: The Modern-Era Retrospective Analysis for Research and Applications, Version 2 (MERRA-2), J. Clim., 30(14), 5419–5454, doi:10.1175/JCLI-D-16-0758.1, 2017.

Holben, B. N., Eck, T. F., Slutsker, I., Tanré, D., Buis, J. P., Setzer, A., Vermote, E., Reagan, J. A., Kaufman, Y. J., Nakajima, T., Lavenu, F., Jankowiak, I. and Smirnov, A.: AERONET—A Federated Instrument Network and Data Archive for Aerosol Characterization, Remote Sens. Environ., 66(1), 1–16, doi:10.1016/S0034-4257(98)00031-5, 1998.

Holben, B. N., T. F. Eck, I. Slutsker, A. Smirnov, A. Sinyuk, J. Schafer, D. Giles, and O. Dubovik "Aeronet's Version 2.0 quality assurance criteria", Proc. SPIE 6408, Remote Sensing of the Atmosphere and Clouds, 64080Q, https://doi.org/10.1117/12.706524, 2006.

Livingston, J. M., P. B. Russell, J. S. Reid, J. M., Redemann, B. Schmid, D. Allen, O. Torres, R. C. Levy, L. A. Remer, B. N. Holben, A. Smirnov, O. Dubovik, E. J. Welton, J. R. Campbell, J. Wang, S. A. Christopher, Airborne Sun photometer measurements of aerosol optical depth and columnar water vapor during the Puerto Rico Dust Experiment, and comparison with land, air-craft, and satellite measurements, J. Geophys. Res., 108, 8588,10.1029/2002JD002520, 2003.

Kazadzis, S., Kouremeti, N., Diémoz, H., Gröbner, J., Forgan, B. W., Campanelli, M., Estellés, V., Lantz, K., Michalsky, J., Carlund, T., Cuevas, E., Toledano, C., Becker, R., Nyeki, S., Kosmopoulos, P. G., Tatsiankou, V., Vuilleumier, L., Denn, F. M., Ohkawara, N., Ijima, O., Goloub, P., Raptis, P. I., Milner, M., Behrens, K., Barreto, A., Martucci, G., Hall, E., Wendell, J., Fabbri, B. E., and Wehrli, C.: Results from the Fourth WMO Filter Radiometer Comparison for aerosol optical depth measurements, Atmos. Chem. Phys., 18, 3185–3201, https://doi.org/10.5194/acp-18-3185-2018, 2018

Kinne, S., O'Donnel, D., Stier, P., Kloster, S., Zhang, K., Schmidt, H., Rast, S., Giorgetta, M., Eck, T. F. and Stevens, B.: MAC-v1: A new global aerosol climatology for climate studies, J. Adv. Model. Earth Syst., 5(4), 704–740, doi:10.1002/jame.20035, 2013.

Lang, R, G. Poli, B. Fougnie, A. Lacan, T. Marbach, J. Riedi, P. Schlüssel , A. Couto, and R. Munro, The 3MI Level-1C geoprojected product –definition and processing description, J. Quant. Spectrosc. Radiait. Transfer, https://doi.org/10.1016/j.jqsrt.2018.12.022, *225*, 91–109, 2019.

Reid, J. S., H. Halflidi, H. B. Maring, A. Smirnov, D. L. Savoie, S. S. Cliff, E. A. Reid, J. M. Liv-ingston, M. M. Meier, O. Dubovik, and S.-C. Tsay, Comparison of Size and Morphological Measurements of Coarse Mode Dust Particles from Africa, J. Geophys. Res, 108, 8593, 10.1029/2002JD002485, 2003.

Russell, P.B., R. W. Bergstrom, Y. Shinozuka, A. D. Clarke, P. F. DeCarlo, J. L. Jimenez, J. M. Livingston, J. Redemann, O. Dubovik, and A. Strawa, "Absorption Angstrom Exponent in AERONET and related data as an indicator of aerosol composition", Atmos. Chem. Phys., 10, pp 1155-1169, 2010.

Schuster, G. L., Dubovik, O. and Holben, B. N.: Angstrom exponent and bimodal aerosol size distributions, J. Geophys. Res., 111(D7), D07207, doi:10.1029/2005JD006328, 2006.

Schutgens, N., Tsyro, S., Gryspeerdt, E., Goto, D., Weigum, N., Schulz, M. and Stier, P.: On the spatio-temporal representativeness of observations, Atmos. Chem. Phys, 17, 9761–9780, doi:10.5194/acp-17-9761-2017, 2017.

Smirnov, A., Holben, B. N., Eck, T. F., Dubovik, O. and Slutsker, I.: Effect of wind speed on columnar aerosol optical properties at Midway Island, J. Geophys. Res. D Atmos., 108(24), doi:10.1029/2003jd003879, 2003.

Tanré, D., F. M. Bréon, J. L. Deuzé, O. Dubovik, F. Ducos, P. François, P. Goloub, M. Herman, A. Lifermann, and F. Waquet, “Remote sensing of aerosols by using polarized, directional and spectral measurements within the A-Train: the PARASOL mission”, Atmos. Meas. Tech., 4, 1383-1395, 2011.